OAK RIDGE NATIONAL LABORATORY LIBRARY
3 4456 0021550 4

CENTRAL RESEARCH LIBRARY
DOCUMENT COLLECTION
4

ORNL-4316
UC-41 – Health and Safety

HEALTH PHYSICS DIVISION
ANNUAL PROGRESS REPORT
FOR PERIOD ENDING JULY 31, 1968

OAK RIDGE NATIONAL LABORATORY
CENTRAL RESEARCH LIBRARY
DOCUMENT COLLECTION
LIBRARY LOAN COPY
DO NOT TRANSFER TO ANOTHER PERSON
If you wish someone else to see this document, send in name with document and the library will arrange a loan.
UCN-7969
(3 3-67)

OAK RIDGE NATIONAL LABORATORY
operated by
UNION CARBIDE CORPORATION
for the
U.S. ATOMIC ENERGY COMMISSION

Printed in the United States of America. Available from Clearinghouse for Federal Scientific and Technical Information, National Bureau of Standards, U.S. Department of Commerce, Springfield, Virginia 22151
Price: Printed Copy $3.00; Microfiche $0.65

LEGAL NOTICE

This report was prepared as an account of Government sponsored work. Neither the United States, nor the Commission, nor any person acting on behalf of the Commission:

A. Makes any warranty or representation, expressed or implied, with respect to the accuracy, completeness, or usefulness of the information contained in this report, or that the use of any information, apparatus, method, or process disclosed in this report may not infringe privately owned rights; or

B. Assumes any liabilities with respect to the use of, or for damages resulting from the use of any information, apparatus, method, or process disclosed in this report.

As used in the above, "person acting on behalf of the Commission" includes any employee or contractor of the Commission, or employee of such contractor, to the extent that such employee or contractor of the Commission, or employee of such contractor prepares, disseminates, or provides access to, any information pursuant to his employment or contract with the Commission, or his employment with such contractor.

ORNL-4316
UC-41 – Health and Safety

Contract No. W-7405-eng-26

HEALTH PHYSICS DIVISION ANNUAL PROGRESS REPORT

For Period Ending July 31, 1968

K. Z. Morgan, Director
W. S. Snyder, Assistant Director
E. G. Struxness, Assistant Director

OCTOBER 1968

OAK RIDGE NATIONAL LABORATORY
Oak Ridge, Tennessee
operated by
UNION CARBIDE CORPORATION
for the
U. S. ATOMIC ENERGY COMMISSION

OAK RIDGE NATIONAL LABORATORY LIBRARY
3 4456 0021550 4

Contents

SUMMARY ix

PART I. RADIOACTIVE WASTE DISPOSAL

1. FATE OF TRACE ELEMENTS AND RADIONUCLIDES IN TERRESTRIAL ENVIRONMENT 1
   - Phosphate Studies 1
   - Phosphorus in Soils and Sediments 2
2. DISPOSAL BY HYDRAULIC FRACTURING 5
   - Site Evaluation by Water Injection Tests – Theoretical Analyses 5
   - Site Evaluation by Water Injection Testing – Drop in Pressure After Pumping Has Stopped 8
   - Pressure Changes in the Rock Cover Monitoring Wells During an Injection 14
3. DISPOSAL IN NATURAL SALT FORMATIONS 21
   - Project Salt Vault 21
   - Disposal-in-Salt Prototype-Facility Study 27
   - Economics of Disposal in Salt 27
   - Brine Cavity Migration Studies 32
   - Pillar-Model Studies 35
   - Computation of Stresses and Displacements Resulting from the Disposal of Radioactive Solids in a Salt Mine 40
   - Other Rock Types 40
   - Major Conclusions from Studies on Disposal in Natural Salt Formations 42
4. ENGINEERING, ECONOMIC, AND SAFETY EVALUATIONS 47
   - Krypton-85 and Tritium in an Expanding World Nuclear Power Economy 47
   - Release of Tritium in an Expanding Nuclear Power Economy and Its Long Range Behavior in the Environment 50
   - Dissolution of Calcium-Strontium Carbonate and Its Subsequent Movement Through the Ground 51
   - Development of Criteria for the Long-Term Storage of High-Level Radioactive Solid Wastes 54
   - Long-Range Waste Management Study 56
   - Deep-Well Injection of Brine Effluents from Inland Desalting Plants 58

5. EARTHQUAKES AND REACTOR SAFETY 59
Laboratory Studies of Strain Accumulation in Rocks 59

6. DOSE ESTIMATION STUDIES RELATED TO PEACEFUL USES OF NUCLEAR EXPLOSIVES 60
Essential Information for Dose Estimation 60
The EXREM Code for Estimating External Dose 61
The INREM Code for Estimating Internal Dose 62
Search for Critical Radionuclides 63
Estimating Dose Equivalents Received by a Population Exposed to Tritium 65

7. RELATED COOPERATIVE PROJECTS 69
Cooperation of Other Agencies in ORNL Studies 69
Visiting Investigators from Abroad 69
Nuclear Safety Review 69
Participation in Educational Programs 69
Laboratory Projects 69

PART II. RADIATION ECOLOGY

8. RESPONSES OF ANIMAL POPULATIONS TO IONIZING RADIATION 71
Prediction of LD_{50} in Mammals 71
Incorporation of ^{134}Cs by Cotton Rats 72
Effects of Acute Gamma Radiation on Cricket Respiration 74
Honeybee Irradiation Studies 76
Effects of Beta and Gamma Radiation on *Sinella curviseta* (Collembola) 76
Radiation Effects on Carp Reproduction 78
Population Genetics and Radiation Effects Studies 78

9. RESPONSES OF PLANTS TO IONIZING RADIATION 82
Effects of External Beta Radiation on Higher Plants 82
Mineral Uptake by Irradiated Plants 85
Genetic Modification of Growth and Radiosensitivity of *Populus deltoides* 85
Effects of Biotic Complexity and Fast-Neutron Radiation on Cycling of Radionuclides in Microcosms 87

10. RADIONUCLIDE CYCLING IN TERRESTRIAL ECOSYSTEMS 91
Seasonal Shoot Growth in a Tagged Liriodendron Forest 91
Rainfall Transfers from Liriodendron Forest Canopy 92
Dispersal of ^{137}Cs Around the Tagged Liriodendron Forest 94
Energy Content of Dogwood Trees 94
Microbiology of Forest Soil 97
Accumulation of ^{137}Cs by a Soil Fungus Relative to ^{137}Cs in Organic Debris and in Soil Solution 97

Transient Behavior of Radioisotopes in Insect Food Chains 97
Calcium, Potassium, and Sodium Content of Forest Floor Arthropods 98
Prey Preferences of a Forest Centipede 99
Effects of Pesticides on Soil Invertebrate Populations 101
Ingestion Rate of Pine-Mor Detritus by an Oribatid Mite (*Cultroribula juncta*) 102
Behavior of Curium in Plants 104
Distribution of Radiocesium Assimilated by Fescue Foliage 105
Preliminary Estimation of Erosion and Radiocesium Redistribution in a Fescue Meadow 108
Seasonal Change in Roots, Tops, and Dead Biomass of *Andropogon* and *Festuca* Fields 112
A New Instrument for the Aerodynamic Measurement of Water Vapor Flux from and Carbon Dioxide Flux to Undisturbed Vegetation Under Field Conditions 113
Transfer of ^{137}Cs, ^{54}Mn, and ^{32}P in Terrestrial Microcosms 114
Assimilation and Biological Turnover of ^{134}Cs, ^{131}I, and ^{51}Cr by *Acheta domesticus* 115

11. RADIONUCLIDE CYCLING IN AQUATIC ECOSYSTEMS 117
White Oak Lake Studies 117
Uptake and Excretion of ^{60}Co by Black Bullheads (*Ictalurus melas*) 118
Radiotungsten Uptake and Elimination in Black Bullheads (*Ictalurus melas*) 122
Feeding Rates of Snails Determined with ^{60}Co 122
Aquarium Experiments 124
White Oak Lake Periphyton 125

12. WATERSHED AQUATIC HABITAT INTERACTIONS 127
Walker Branch Watershed Project 127

13. SYSTEMS ECOLOGY 138
Indirect Estimation of Energy Fluxes in Animal Food Webs 138
Applications of Compartment Modeling to Population Dynamics 140
Ford Foundation Report on Systems Ecology 142
Compartmental Analysis of Production and Decay of *Juncus roemerianus* 143
Computer Simulation of Phosphorus Cycling in a Douglas Fir Forest Ecosystem in Western Washington 145
Nitrogen Equations of Grassland and Dune Soils 146
Dry Weight Rank Method for Grassland Studies 150
Model of Peat, Standing Dead, and Live Organic Contributions to Subarctic Blanket Bog 153
FORSTAN: A Computer Program for Estimating Forest Stand Dry Weight and Mineral Content 156
Estimated Biomass of Leaf, Branch, Bole, and Roots of Tropical Lower Montane Rainforest, El Verde, Puerto Rico 158

14. FOREST MANAGEMENT 160
Forest Management 160

PART III. RADIATION PHYSICS

15. THEORETICAL RADIATION PHYSICS 161
New Evaluation of Mean Excitation Energies for Use in Radiation Dosimetry 161
Effect of Delta-Ray Buildup in High-Energy Dose Calculations 162
High-Energy Dosimetry 162
Ground-State Energy Eigenvalues and Eigenfunctions for an Electron in the Field of a Stationary Electric Dipole 163
Quantum Theory of the Plasma Resonance Emission Process 165
Radiative Decay of Coulomb-Stimulated Plasmons in Spheres 170
Quantum Treatment of Multiple Real Transitions 170
Electron Mean Free Paths in a Free-Electron Gas 170
Surface Plasmon Resonance Effect in Grating Diffraction 170
Electron Penetration in Metals 172
Secondary Electron Emission Due to the Decay of Coulomb-Stimulated Surface Plasmons 172
Potential Energy Curves for Diatomic Molecules 173
Exchange and Nonadiabatic Polarization Effects in Low-Energy Electron Scattering 173

16. INTERACTION OF RADIATION WITH LIQUIDS AND SOLIDS 177
Optical Properties of Aluminum Oxide 177
Optical Properties of Vacuum-Evaporated Films of Polycrystalline Tellurium 179
Optical and Photoemission Measurements for Copper, Nickel, and Palladium 179
Ultrahigh Vacuum Ellipsometry 184
Evaluation of a Reflection-Type Polarizer for Use in the Ultraviolet 185
Time Studies of the Polarization due to Gratings 187
Grating Anomalies 189

17. ATOMIC AND MOLECULAR RADIATION PHYSICS 190
Scattering of Thermal Electrons by Polar Molecules 190
Dipole and Nondipole Contributions to the Cross Section for Scattering of Slow Electrons from Polar Molecules 190
Electron Attachment to Halogenated Aliphatic Hydrocarbons 193
Electron Attachment to Aromatic Hydrocarbons 194
Dissociative Electron Attachment to Molecules 196
Excited Electronic States of Benzene and Naphthalene 198
Emission from Liquid Benzene and Liquid Benzene and Naphthalene Derivatives Excited by Electron Impact 198

Lifetimes of Liquid Benzene and Liquid Benzene and Naphthalene Derivatives Excited by Electron Impact 201
Ionization Efficiencies of Molecules 203
Transition Yields in Irradiated Gases 203

18. ELECTRON AND ION COLLISION PHYSICS 206
Determination of Diffusion Coefficients of Thermal Electron Swarms in Gases 206
Equilibration of Electron Swarms in Argon to a Thermal Energy Distribution 207
Excitation of Atoms and Molecules by Electron Impact 209
Transient Negative Ion Resonances in Molecules 211
Temporary Negative Ion Lifetimes 213
Studies of Dissociative Electron Attachment 214
Low-Energy Negative Ion Molecule Reactions 215

19. GRADUATE EDUCATION AND VOCATIONAL TRAINING 219
Graduate Education and Vocational Training 219

20. PHYSICS OF TISSUE DAMAGE 223
Electronic Properties of Liquid Water in the Vacuum Ultraviolet 223
Slowing-Down Spectra 225
Low-Energy Electron Transmission in Solids 227

PART IV. RADIATION DOSIMETRY RESEARCH

21. DOSIMETRY FOR HUMAN EXPOSURES AND RADIOBIOLOGY 231
Japanese Dosimetry Program 231
Operation HENRE 234
Nuclear Accident Dosimetry Intercomparisons 238
X Radiation Hazards Associated with the Use of Vacuum Electrical Components 239

22. APPLIED RESEARCH 246
Dosimetry by Thermally Stimulated Exoelectron Emission (TSEE) 246
Lithium Borate Glasses as Radiophotoluminescence (RPL) Dosimeters 249
LET Effects in Radiophotoluminescence Glasses 250
Long-Term Stability of Radiophotoluminescence in Phosphate Glasses 252
Dosimetry at the UT-AEC Agricultural Research Laboratory Variable Dose-Rate Facility 253
Radon and Radon Daughter Personnel Dosimetry with Solid-State Alpha-Particle Detectors 253
Calculation of Probability of Overlapping Tracks in Solids 257
Chemical Processes Involved in Latent Track Formation in Plastics 257
Oxygen and Humidity Effects on the Sensitivity of Organic Nuclear Track Detectors 260
Fast-Neutron Dosimetry by Direct Interaction with Organic Polymers 260

23. SPECTROMETRY DEVELOPMENT AND RESEARCH 264
Van de Graaff Operations 264
Investigation of Organic Scintillators 264
Calculation of Spectra of Recoil Heavy Particles 265
24. HPRR AND DLEA OPERATIONS 267
Health Physics Research Reactor 267
DOSAR Low-Energy Accelerator Analyzing Magnet 268

PART V. INTERNAL DOSIMETRY

25. INTERNAL DOSE ESTIMATION 271
An Estimate of the Systemic Body Burden of ^{239}Pu Resulting from a Contaminated Wound 271
The Effect of Size, Shape, Composition, and Density of Body Organs on the Absorption of Gamma Rays from a Uniform Source in an Organ 274
The Relative Importance of ^{137}Cs Contamination in Various Foodstuffs in Terms of Total Dose for Various Age Groups of a Population 276
Calculation of Microcurie-Days Residence in an Organ Resulting from a Single Intake 281
A Model for Estimation of Mean Activity Present in Segements of the Gastrointestinal Tract at Any Time Postingestion 283
Nuclear Safety Environmental Studies: Biohazards of Aerospace Nuclear Systems 287
Interaction of Airborne Particulates with Gases 288
26. STABLE ELEMENT METABOLISM 290
Patterns of Elemental Excretion in Long-Term Balance Studies 290
Method for Removal of Phosphate from Bone Ash 294

THESES, PAPERS, PUBLICATIONS, AND LECTURES

THESES 295
PAPERS 296
PUBLICATIONS 301
LECTURES 314

Summary

PART I. RADIOACTIVE WASTE DISPOSAL

1. Fate of Trace Elements and Radionuclides in Terrestrial Environment

Fertilized and unfertilized soils, eroded material from unfertilized soils, river sediment, and sediment from a man-made pond were analyzed for their content and forms of phosphorus. Of the sought-for forms – free aluminum, free iron, calcium, organic, and occluded – the fertilized soils were characterized by the presence of all five forms. Sediment from the pond which had received commercial fertilizer differed from the fertilized soils by the very low content of both free aluminum and iron phosphates. The river sediments were characterized by low content of free aluminum phosphate. Unfertilized soil and material eroded from the unfertilized soil were characterized by the low content of calcium phosphate. Results suggest that calcium phosphate is associated with soils and sediments receiving commercial fertilizers and further suggest that eroding material can transport significant quantities of phosphate from soils which have not received commercial fertilizer.

An abundant growth of algae and wild celery, a rooted aquatic plant, occurred in a man-made pond after a generous application of commercial fertilizer. Subsequent reduction of the concentration of phosphate resulted in a decrease in the growth of both wild celery and algae. Results suggest that the form and concentration of phosphate in sediments play a key role in influencing the growth of rooted aquatic plants.

2. Disposal by Hydraulic Fracturing

A considerable amount of information on the underground behavior of hydraulically induced fractures is contained in the pressure histories of the injection and shut-in phases of the operation, particularly if a fluid like water is injected rather than a slurry. The analyses presented in this section represent an effort to develop a basis for interpreting such information in terms of the fracture orientation.

The first part is a theoretical and empirical evaluation of the pressure variations measured in the injection well during pumping. This analysis includes components due to turbulence at the entrance to the fracture, the viscous losses during laminar flow for circular and noncircular fractures, and the effects of vertical gradients, both in the confining rock stresses due to tectonism and in the fracture resulting from changes in elevation. These components were synthesized in various combinations to provide a predicted pressure history for almost any possible (idealized) fracture configuration.

The second part is an empirical graphic analysis of the pressure decay after the water injection was finished and the well shut in. This drop in pressure was very rapid at first but then went more and more slowly, so that after some 70 days the pressure was still over 200 psi. The drop in pressure is presumably principally due to two factors: (1) the continued lateral extension of the fracture due to recoil of the deformed rock cover near the injection well and (2) the water leaking out of the fracture. The first of these mechanisms will stop when the walls of the fracture make contact, which, if the fracture is horizontal, will happen when the pressure reaches that due to the weight of the overlying rock. A discontinuity in the time-pressure curve coming at this pressure would, therefore, be an indication that the fracture was horizontal. A log-log plot of the rate of change of pressure as a function of time did indeed show a change in slope at this critical pressure, suggesting that such an analysis of the pressure decay

data may be of value in determining the orientation of a water-filled fracture.

The so-called rock cover monitoring wells were constructed by cementing in a steel casing to a depth of 550 ft and then drilling an open hole to 650 ft. It was noted that, during a waste injection, the water level in these wells (which had been left full of water) in some cases rose, while, at the same time, it fell in others. An obvious explanation is that, where the grout-filled fracture passed underneath one of the wells, the shale adjacent to the open-hole section of the well was compressed and water was squeezed into the well. In the case of wells located in a direction other than that taken by the grout sheet, a shearing force would be developed in the shale adjacent to the open-hole section of the well, and the vertical load would be reduced, sucking a small amount of water into the shale. By equipping the rock cover monitoring wells with pressure gages and taking readings at intervals during an injection, it was possible to get indications of the direction taken by the fracture; however, these indications have not yet been correlated with the data from the gamma-ray logging of the observation wells.

3. Disposal in Natural Salt Formations

As reported previously (ORNL-4168), the radioactive phase of the demonstration disposal of high-level radioactive wastes was completed by the end of June 1967. By the end of December 1967, the remainder of the mine experiments had been terminated, and preparations were made to place the Carey Salt Company's Lyons, Kansas, mine on a standby basis, beginning February 1968. Arrangements have been made for periodic service of the equipment left on standby and for periodic collection of selected items of data.

During the 19-month operation of the radioactive demonstration, the average dose to the salt over the length of the main array holes was about 8×10^8 rads, and the peak dose was about 10^9 rads. The dose in the array in the old mine floor was about 10^8 rads.

Additional tests were run to determine the effects of water on container corrosion. The simulated-waste container cans have been removed for evaluation of the corroded conditions observed.

The laboratory pillar-model tests have been completed, and the effects of various variables have been analyzed. A completion report (ORNL-TM-2102) has been published.

The study of the economics of disposal in salt has been completed and was published as ORNL-3358. Using present worth considerations and a 4% interest rate, the money to be set aside annually at the time of waste generation ranged from about \$2.4 million to \$2.6 million for one-year-old waste to about \$0.3 million to \$0.4 million for waste 30 years old at the time of disposal. In terms of cost per kilowatt-hour of electricity generated, this corresponds to about 18 to 20×10^{-3} and 2 to 3×10^{-3} mill respectively.

To summarize, it may be said that most of the major technical problems regarding disposal in salt have been resolved. The results have been most encouraging. The feasibility and safety of handling highly radioactive materials in an underground environment have been demonstrated. The stability of the salt under the effects of heat and radiation was shown, as well as the capability of solving minor structural problems by standard mining techniques. The data obtained on the creep and plastic flow characteristics of the salt should make it possible to arrive at a suitable mine design for a disposal facility. A study of the economics of disposal in salt mines indicates that this method will be compatible with competitive nuclear power. All these items combined lead one to the conclusion that burial in salt mines is one of the better methods, if not the best, for the ultimate disposal of high-level solidified wastes.

Based on this conclusion, an examination is now being made of the desirability of establishing an actual prototype disposal facility in the immediate future.

4. Engineering, Economic, and Safety Evaluations

A hypothetical 6-ton/day nuclear fuel reprocessing plant was sited at ORNL, and estimates were made of dose equivalents to a "standard man" working at the Oak Ridge Gaseous Diffusion Plant and residing in Oak Ridge for assumed release conditions of ^{85}Kr and ^{3}H. Modes of exposure considered were ingestion, inhalation, submersion in contaminated air and water, and irradiation from a contaminated surface.

Tritium released to the environment will be expected to be predominantly in the hydrosphere and

will behave much the same as ordinary water. Although the oceans and seas represent the largest reservoirs for dilution of tritium, their long turnover times, even for the surface 75 m which mixes rather rapidly, will prevent attainment of uniform concentration throughout the circulating portion of the hydrosphere.

Laboratory studies have been made on the dissolution and movement of strontium that has been coprecipitated with calcium carbonate in mineral exchange systems. Mineral exchangers have substantial capacities for hydrogen ion buffering. In order to dislodge strontium from such a system, it was found necessary to add sufficient acid to overcome this buffering capacity. Hence, a sudden change in groundwater pH with a coincident release of ^{90}Sr in the waste seepage pit area is highly unlikely.

As a part of the long-range waste management study, projections were made of the nuclear power requirements and the reactor mix that may accommodate these requirements. Estimates were made of the volumes of waste and fission products accumulated to year 2000.

Factors that need to be considered for the long-term, on-site storage of solid high-level wastes are enumerated and discussed in a qualitative manner. On the basis of present information, salt offers the optimum combination of properties for a disposal formation. However, it seems possible that other formations may also be suitable.

A study has been completed of the potential disposal of brine effluents from inland desalting plants by deep-well injection. Present practice, costs, and requirements for a disposal operation were reviewed.

5. Earthquakes and Reactor Safety

A new technique, utilizing microscopic measurements of rock specimens, is being developed for utilization in reactor site evaluations. This technique is based on the premise that certain elastic properties of rocks that are indicative of present stress conditions can be determined and measured in the laboratory.

6. Dose-Estimation Studies Related to Peaceful Uses of Nuclear Explosives

The information requirements for estimating a population's radiation dose resulting from environmental releases of radioactive material have been categorized. Models have been developed and programmed to estimate expected radiation doses to populations in various hypothetical exposure situations related to peaceful uses of nuclear explosives. Radiation doses received from external and internal sources of exposure are estimated with computer codes entitled EXREM and INREM respectively. The modes of exposure considered for external sources are: submersion in contaminated air, submersion in contaminated water, and exposure to a contaminated surface. Ingestion and inhalation are the modes of exposure considered for internal sources. Steps are outlined for utilizing dose estimates obtained with these codes to identify the critical radionuclides in a given exposure situation. A study to determine the radiological-safety feasibility of using nuclear explosives to excavate a sea-level canal across the isthmus of Central America is under way, and those elements whose radioactive isotopes are of greatest radiological importance to that study have been tentatively identified on the basis of results obtained by completing the second step of the four-step critical radionuclide identification procedure. Use of the INREM code is demonstrated in detail with an example estimating the dose received by a population exposed to an atmosphere containing tritiated water vapor. The example illustrates evaluation of the age-dependent parameters and the influence of the age of those exposed upon the resulting dose estimate. The maximum variation among age groups, in this case, is a factor of 1.5.

7. Related Cooperative Projects

Representatives of other agencies continued to participate in the Radioactive Waste Disposal Section's studies. Two alien guests were in residence during the year. One member served as assistant news editor for the United States for *Health Physics* and as an assistant editor of *Nuclear Safety*. One member of the section participated in cooperative programs with the University of Tennessee and Vanderbilt University. Two members of the section participated part time at the Nuclear Safety Information Center.

PART II. RADIATION ECOLOGY

8. Responses of Animal Populations to Ionizing Radiation

Data from hematological and radiation effects studies on mammals were utilized for comparisons of radiation mortality in the hemopoietic death range as typified by $LD_{50(30\text{-}60\ days)}$ observations. An index was obtained by multiplying average interphase chromosome volume (ICV) of the lymphocyte by the elimination constant of ^{59}Fe (λ_b) for each species. This index gives close predictions of LD_{50} (rads) for the species for which data are available. Presently the relationship ICV (Fe λ_b) is linear, but it is anticipated that it will be sigmoid when data are obtained for the extremely radiosensitive and radioresistant species. An interesting observation during hematological studies of cotton rats was the rapid recovery of WBC counts after irradiation of individuals infected with a blood parasite, *Hepatozoon* sp.

It has been hypothesized that the increased life expectancy of animals exposed to low radiation doses was due to a reduction in the respiration rate. This hypothesis was tested by measuring the continuous oxygen consumption of crickets (*Acheta domesticus*) exposed to doses of gamma radiation from 0 to 32 kilorads. A variety of statistical tests failed to demonstrate differences in oxygen consumption among the irradiated crickets. Thus the increased life expectancy of crickets exposed to low dose levels cannot be explained by a reduction in respiration rate.

Responses of honeybees to irradiation could be an important aspect of postattack recovery of agricultural landscapes. Irradiation experiments of samples of about 150 bees showed a reduction of 22% in life-span of bees exposed to 5000 rads of ^{60}Co gamma irradiation. On this basis five entire colonies of bees were exposed to 5000 rads of ^{60}Co irradiation in a large animal irradiator to determine effects of irradiation on pollen collection. Surprisingly, the irradiated colonies ceased to function as social units within two weeks. Pollen collections in the irradiated colonies were 61% of the controls the week before irradiation, but in the week following exposure this dropped to 28%; two weeks post irradiation, pollen collections were 7% of controls, and in the third week no pollen was collected. At the end of three weeks about 200 of the 87,000 irradiated adult bees survived.

The interaction of radiation and competition between two closely related species, *Drosophila melanogaster* and *D. simulans*, was tested in controlled laboratory populations. Although adults of *Drosophila* can survive several kilorads of gamma radiation and populations are easily maintained while receiving an acute or chronic dose of 2000 r every generation, a dose of 1000 rads given every three weeks to adult male *D. melanogaster* was sufficient to eliminate this species when it was in competition with *D. simulans*. In the control population *D. melanogaster* quickly became the most abundant species. These results illustrate the effects of competition interacting with an additional radiation stress.

The *Gambusia* population in White Oak Lake is exposed to a chronic radiation dose of about 11 rads/day. To determine whether White Oak Lake fish had acquired radioresistance, the $LD_{50/30}$ for these fish was compared with *Gambusia* from a nonirradiated population. The $LD_{50/30}$ of both populations was slightly greater than 3000 rads and not significantly different from each other. *Gambusia* as a species appears to be relatively radioresistant.

9. Responses of Plants to Ionizing Radiation

Studies of the effects of external beta radiation on higher plants were initiated to determine radiosensitivities of native plant species and to provide estimates of the ecological effects of postattack fallout on plants. Fallout simulant, consisting of sand (44 to 88 μ in diameter) containing approximately 5 nc of ^{90}Sr per particle, was applied to various organs of white pine, cottonwood, cocklebur, and bean plants. In all cases plant parts which received contact exposures were killed, while other plant organs survived with varying degrees of biological damage depending upon distance from the contaminated area of the plant. Contaminated white pine terminal buds receiving contact doses of 54 to 310 rads/hr started turning brown within five days and by ten days were dehydrated and brittle. Shoot growth from buds below contaminated buds received doses varying between 70 and 200 millirads/hr and showed an average growth reduction of 47% at 30 days. Browning of the

foliage occurred much earlier from the beta radiation than expected on the basis of previous experience with plant exposures to gamma radiation. Furthermore, translocation of ^{90}Sr to other parts of the plant occurred, and in the case of beans the fruit contained 0.4 to 5.0 nc of ^{90}Sr per gram.

Aquatic microcosms containing various combinations of physical components (soil, water, and container surface) and biological components (*Physa heterostropha, Najas flexilis,* and *Elodea canadensis*) were used to determine the effect of increased biotic complexity on ^{60}Co and ^{137}Cs cycling parameters and to test the stability of the cycling parameters under exposure to sublethal and lethal doses of fast-neutron irradiation. Generally, cycling parameters of ^{137}Cs and ^{60}Co were dissimilar in less complex microcosms and converged toward similarity as complexity increased. System stability was related more to the sensitivity of biological interactions than to the sensitivity of individual organisms. On the basis of mineral cycling parameters the simpler microcosms were less stable than the complex ones to a moderate stress (100 rads) but more stable than complex systems when subjected to an extreme stress (1000 rads).

10. Radionuclide Cycling in Terrestrial Ecosystems

Sampling of the tulip poplar forest tagged with ^{137}Cs continued to further define rate constants for the redistribution of ^{137}Cs through the ecosystem. The leaching of ^{137}Cs from leaves by rainfall has been decreasing gradually since 1962, but during July 1967 abnormally heavy rainfall caused more leaching than in 1966. There was no detectable increase in dispersal of radiocesium beyond 20 m outside the experimental plot. Radioactivity in 10 to 20 m from the plot is intermittent and appears to be related to the dispersal of tagged leaves, but within 10 m of the plot a severalfold increase in ^{137}Cs may be related to other botanical or zoological processes.

The weight loss from dogwood leaves during their first four weeks in litter is caused primarily by the leaching of water-soluble material. Weight loss was 37.5 ± 1.7% and energy loss was 27.7 ± 2.0% after 26 weeks, showing that the material removed from the leaves had a relatively low caloric value. Fungi are important in the mobilization of mineral elements in the litter. However, fungi can obtain mineral elements either from the solid substrate or the soil solution. With ^{137}Cs as a tracer, experiments showed that ^{137}Cs uptake by fungi isolated from solid substrates was proportional to the ^{137}Cs concentration in the soil solution. For fungi in direct contact with solid substrate the concentration appears to be proportional to ^{137}Cs availability in the substrate. Availability is a function of decomposability and leachability of ^{137}Cs in the substrate.

Studies of forest floor arthropods included chemical analyses of 37 species for Ca, K, and Na. The calcium content was most variable since some species have well-developed exoskeletons rich in calcium. Because of the variability of ash content, results were expressed as element content per gram of ash-free weight. Excluding Diplopoda, all other arthropods averaged 1.89 mg of calcium per gram. The distribution of sodium among species was symmetrical, with an average of 4.6 mg per gram of ash-free dry weight. The potassium frequency curve was positively skewed, due to the occurrence of high values in a few diplopod species. Generally potassium and sodium concentrations were consistent within and among major taxonomic categories. Whole-body concentrations of potassium and cesium decrease with an increase in trophic level, while sodium increases at the higher trophic level. In addition to trophic level differences, some species exhibited seasonal differences in their chemical composition. These differences were attributed to changing seasonal composition of the food base for the organisms. Food chain transfers of nutrients between trophic levels involve characteristic delays or time lag phenomena. Equations were developed to allow prediction of ^{137}Cs concentrations in successive trophic levels in the cesium forest. A 30-day biological half-life was obtained for the saprovore trophic level, which approximated the biological half-life determined previously for several of the species. This predictive equation may be applicable to the study of environmental pollutants in food chains.

Preliminary estimates of erosion and radiocesium redistribution on a fescue meadow were made to evaluate potential ^{137}Cs losses from this field to be tagged with ^{137}Cs-contaminated sand grains. The four experimental plots will contain 8 curies of contaminant, and estimated losses through

eroded soil and runoff water were 1.7 mc/year. Agreement between these results and those predicted by the Wischmeir and Smith soil-loss equation were relatively good, considering that the predictive model was derived for cultivated systems and that the topographic features of the experimental plots approach the lower limits for which the model is applicable.

11. Radionuclide Cycling in Aquatic Ecosystems

Fish from White Oak Lake are being assayed to determine the body burden of ^{137}Cs, ^{106}Ru, and ^{60}Co. Most emphasis is being placed on ^{137}Cs in bluegills and the comparative metabolism of cesium and potassium. The biological half-life of ^{137}Cs in White Oak Lake bluegills weighing 60 to 70 g (12°C) was 115 days and of 10-g fish 80 days. The excretion curves obtained are essentially linear and do not show the rapid initial elimination of ^{137}Cs ordinarily found in acutely tagged fish. These results suggest that most of the ^{137}Cs in bluegills is associated with the long component in biological half-life curves. Similar excretion experiments with snails and newts chronically contaminated with ^{85}Sr, ^{137}Cs, ^{54}Mn, ^{65}Zn, and ^{60}Co showed similar results in that 80% or more of the radionuclide burden was associated with the long component in the excretion curve. The turnover of potassium by bluegills studied with ^{42}K-tagged fish indicated a biological half-life of about 16 days. This half-life is somewhat shorter than that indicated from potassium balance studies. The feeding habits of White Oak Lake bluegills are being studied to measure feeding rates of fish. About 71% of the diet consisted of chironomid larvae and pupae, 13% other insects and fish, and 16% detritus and algae.

Rates of uptake, sites of deposition, and the biological half-life of ^{60}Co in the black bullhead were determined. Uptake of ^{60}Co was rapid, and near-maximum levels of activity were obtained within one day, but uptake experiments continued for seven days. The most rapid uptake from water was by gills, gut, and stomach. The flesh had a lower concentration, but since it comprises 60% of the body weight, it was a major source of whole-body activity. Excretion of ^{60}Co by fish tagged in water and by those fed tagged food was compared. Fish tagged in water lost 28% of their initial dose in the first day of excretion, while those fed tagged food lost 95.5% of their initial activity. Otherwise the excretion curves were similar, with the first component having a biological half-life of 1.5 to 4 days, a second component of 35 to 48 days, and a third component having a long but undetermined biological half-life. Dissections of White Oak Lake bullheads showed that skin and bone contained proportions of ^{60}Co similar to those in the experimentally tagged fish, while blood, liver, and kidney were higher than in laboratory fish. The kidney of these fish contained a major pool of ^{60}Co; this was confirmed by stable cobalt analyses, which showed that the kidney had more cobalt per gram than any other tissue. Similar experiments are under way to define radiotungsten metabolism by the bullhead.

Feeding rates of snails were determined with a new and simple radioisotopic method. Rocks with their attached aufwuchs were tagged by placing them in a ^{60}Co solution containing 2 to 7×10^4 dis/min of ^{60}Co per milliliter. The rocks were rinsed and placed in clean water, and snails were allowed to feed on the rocks for 1 hr. After feeding, the snails were counted for ^{60}Co activity, samples of the aufwuchs were scraped from the rock and ^{60}Co activity per milligram was determined. Dividing the ^{60}Co activity in the snails by ^{60}Co per milligram of rock yielded the milligrams of aufwuchs consumed per hour. Movement of food through the gut of snails was slight within the 1-hr period and reached a maximum at 2 hr after the start of feeding. Feeding rates of snails determined by this method varied from 0.01 to 0.08 mg of aufwuchs per hour.

12. Watershed Aquatic Habitat Interactions

The paired Walker Branch watersheds were essentially completed as a research facility during the year, and experimental programs were planned and initiated. Two 120° V-notch weirs were constructed, and stage-height recorders and proportional water samplers were installed. Wong precipitation collectors were modified to serve as differential collectors of dry fallout and rain-scavenged materials and were installed at each of the five gage sites. The computer program for data reduction and processing is about 50% complete. An innovation in identification of storm events is through the use of rainfall intensity-duration records rather than the stream hydrograph.

Preliminary chemical analyses show the ionic content of the water is essentially normal for a stream in a limestone formation. The west fork of Walker Branch generally follows expected patterns of calcium and magnesium content as different springs flow into the stream. The east fork has some anomalies in dissolved calcium and magnesium content which may be the consequence of soil formations in area adjacent to the stream. A soft water spring is located in an area of Tarklin soil. This soil has a fragipan, and it was hypothesized that incoming precipitation percolates to the fragipan and then flows laterally to emerge at the spring without contacting the limestone bedrock. A more typical spring nearby is located in an area of highly permeable Bodine soils, and hard water occurs through contact with limestone.

Aquatic fauna of both forks was sampled to determine the biotic resources available for study. Approximately 60 different species were collected and preliminary identifications made. The snail *Goniobasis clavaeformis* is one of the most obvious components of the community. However, a large number of caddis flies, mayflies, and stoneflies are also present.

13. Systems Ecology

The developing systems approach to ecology received added support from a Ford Foundation Grant which permitted a number of visiting investigators to utilize facilities at the Laboratory. In addition to the ongoing programs these investigators were able to summarize data available from a number of ecosystems and in some cases develop models from the empirical data. These models are instructive in several ways, but perhaps most important is the potential for interaction of the model results with experimental programs.

14. Forest Management

The forest management program achieved its mean annual cutting rate of 1,500,000 bd ft of sawtimber for the first time. Thinning of the 20-year-old loblolly and shortleaf pine plantations yielded 3300 cords of pulpwood and fence posts. Forest management is conducted in cooperation with ecological research on the AEC reservation.

PART III. RADIATION PHYSICS

15. Theoretical Radiation Physics

A new evaluation has been made of mean excitation energies for some 36 compounds and mixtures of importance in radiation dosimetry. Dose buildup due to delta rays in a soft-tissue slab bombarded by normally incident high-energy protons has been studied. A simplified model for nuclear interactions has been used to obtain estimates of dose for neutrons and protons in the range from 0.4 to 2 Gev incident upon a soft-tissue slab. Numerical calculations have been made of ground-state energies and eigenvalues for an electron in the field of a stationary electric dipole. The quantum theory of a process in which a photon excites a normal surface plasmon which then undergoes radiative decay by collision with density fluctuations in the plasma has been formulated. The Coulomb excitation and radiative decay of spherical plasmons has been investigated theoretically. A fundamental quantum-theoretic study of the probability of multiple real transitions in an interacting fermion-boson system has been carried out. The mean free path of low-energy electrons in a free-electron gas has been calculated using a Bethe-Goldstone formulation. An explanation of Wood grating anomalies in terms of intermediate resonant surface plasmon states has been given. A Monte Carlo code for calculating the penetration of low- and intermediate-energy electrons in metal-insulator-metal diodes is described. The effect of surface plasmon decay in the spectrum of electrons ejected from a metal by energetic charged particles has been investigated theoretically. Progress in the calculation of internuclear potential energy as a function of nuclear separation in a diatomic molecule using Klein's semiclassical method is described. A theory of exchange and nonadiabatic polarization effects in low-energy electron scattering on an atomic system has been developed and is being applied to scattering on alkali atoms and noble-gas atoms.

16. Interaction of Radiation with Liquids and Solids

Reflectance and/or transmittance measurements have been analyzed to yield optical constants in

the vacuum ultraviolet for anodized and single-crystal Al_2O_3 and for evaporated films of Te, Pd, Ni, and Au. In addition, an ellipsometer has been constructed and used to determine the optical constants of Pd at long wavelengths. Photoemission measurements have been made on Cu, Pd, and Ni over the same energy range as the optical measurements.

The optical constants for Al_2O_3 show characteristics similar to the insulators studied previously. Interpretation is in terms of (1) single-electron exciton and interband transitions and (2) collective plasma oscillations. The optical properties of polycrystalline tellurium are very similar to those of selenium reported previously. In both materials two different volume plasma oscillations can occur involving either two or six valence electrons per atom. Correlation of optical and photoemission data has resulted in the identification of discrete losses suffered by photoexcited electrons prior to emission. These discrete losses are due to the excitation of interband transitions or volume plasma oscillations. In fact, it appears that the inelastic scattering of photoelectrons generated by relatively low-energy photons can be interpreted in terms of the same theory derived for the inelastic scattering of electrons of much higher energies.

The optical data for gold were used to evaluate gold triple-reflection polarizers of different geometries. It is suggested, because of differences observed between different gold films, that measurements should be made of the optical constants of the gold each time that such a reflection-type polarizer is constructed. It was found that in certain wavelength regions it is possible to obtain 99% polarization with approximately 20% transmission of the polarized beam. A triple-reflection polarizer was used to study the polarization, introduced by the grating, of the radiation emerging from a Seya-Namioka monochromator. It was found that the polarization properties of concave diffraction gratings vary with time and are different for different gratings. Generally, there are several sharp peaks in the ratio of the polarized components, some of which may be attributed to the creation and deexcitation of volume or surface plasmons. Studies on gratings are very important, as they constitute the principal optical component in all ultraviolet spectrometers.

17. Atomic and Molecular Radiation Physics

Electron transport in gases yielded the first experimental evidence for the minimum dipole moment necessary to bind an electron to a polar molecule. Studies on the scattering of thermal electrons from 41 pure polar molecules indicated for the first time the possible effect of a potential resonance on the scattering of low-energy electrons from polar molecules. Electron attachment cross sections have been obtained for 21 toxic hydrocarbons, the toxic action of which has been related to their ability to attach electrons to form radical and negative-ion fragments. An increase in cross section has been observed with increasing toxicity. A comprehensive analysis of all the available data on dissociative electron attachment to molecules has been made which demonstrated the effect of level crossing and autoionization on the magnitude of the cross section. Absolute cross sections for parent negative-ion formation to a number of aromatic molecules (including anthracene and 1,2-benzanthracene) have been obtained, and the relation of the attachment cross section to the energy of the first excited π-singlet state as well as to the electron affinity of the molecules studied has been investigated. A comprehensive study of the excited electronic states of benzene and naphthalene excited by photons and electrons has been made, and new electronic transitions have been identified. New techniques have been proposed for the study of ^1X_g states of aromatic molecules. The emission and decay from organic liquids under intense electron bombardment have been found to be characteristic of singlet-state excimers. Emission from triplet-state excimers has been clearly observed for the first time. Lifetimes of excited states of organic molecules excited by electron impact have been measured. Calculations have been made also for transition yields in irradiated gases. Finally, the role of the resonance states of noble gases in the so-called Jesse effect has been demonstrated.

18. Electron and Ion Collision Physics

A number of new techniques have been developed and applied to the study of the interaction of low-energy electrons and negative ions with molecules.

These techniques have provided new information about many important fundamental collision processes and about the structure of the common gases (e.g., water, ammonia, hydrogen chloride, etc.), complex molecules (e.g., benzene, naphthalene, azulene, etc.), and molecules of biological interest (e.g., pyridine).

Employing SF_6 as a scavenger of low-energy electrons, the threshold excitation spectra of benzene, naphthalene, chloronaphthalene, nitrobenzene, azulene, pyridine, and xenon hexafluoride have been studied for the first time. The results exhibited considerable new information about the excited states of these molecules (especially the position of triplet states) and the existence of temporary negative ion states. The degenerate temporary negative ion resonance in benzene was found to be split into two resonances for pyridine – one at the energy of the benzene resonance and another approximately $\frac{1}{2}$ v lower in energy. The temporary negative ion resonance in naphthalene was observed to shift to lower energy with the addition of chlorine or bromine onto one of the ring structures. Transient negative ion states were also studied in ethylene, carbon dioxide, and five fluorobenzene derivatives. The fluorobenzene data provided evidence for a linear increase in the electron affinity with increasing number of fluorines added to the benzene ring.

Nondissociative electron attachment to polyatomic molecules has been the focus of much fruitful study. An electron swarm procedure has been developed to measure electron diffusion and electron attachment rates under zero field conditions where the electron swarm energy distribution is most certainly thermal. Negative ion lifetimes have been determined very accurately for azulene and some eight aromatic and alicyclic fluorocarbon molecules. The latter results exhibited a very striking increase in lifetime with increasing number of atoms in the molecule. Furthermore, the experimental results qualitatively agreed with previous theoretical predictions.

Dissociative electron attachment processes have been studied in ammonia, deuterated ammonia, carbon dioxide, carbon monoxide, nitrogen dioxide, nitrous oxide, naphthalene, chloronaphthalene, bromonaphthalene, a series of fluorocarbons, and xenon hexafluoride. A rather complete study of ammonia and deuterated ammonia yielded the magnitude and energy dependence of the cross sections, the ions formed, kinetic energies of the negative hydrogen ions, and the electron impact excitation spectrum. Measurements of the appearance potentials of O_2^- and NO^- from nitrogen dioxide have provided interesting lower limits to the electron affinities of these molecules.

A new technique has been developed to study negative-ion–molecule reactions in the energy region from 0 to 2 ev. Reactions of H^- (and D^-) ions with H_2O (and D_2O) are shown to lead to OH^- (and OD^-) with a quite large cross section which increases with decreasing energy. A significant isotope effect favoring the $D^- + D_2O \rightarrow OD^- + D_2$ reaction was observed. Simple charge-exchange reactions of O^- with NO_2 leading to NO_2^- have also been studied as a function of the O^- ion energy.

19. Graduate Education and Vocational Training

In the Graduate Education and Vocational Training Program, five AEC Health Physics Fellows came to ORNL for summer training in applied health physics and research. Two came from the University of Rochester and one each from the Universities of California, Illinois, and Vanderbilt. The book *Principles of Radiation Protection: A Textbook in Health Physics* was published in December 1967. This book should be widely used in health physics education. Thirty-five colleges and universities were visited, and health physics research and career opportunities were discussed. Nineteen graduate students conducted thesis research in the Health Physics Division for the M.S. or Ph.D. degree during the year. A total of 38 university personnel ranging from undergraduates to professors spent last summer in the Health Physics Division. Several of our staff assisted the University of Tennessee Physics Department in writing research proposals to government agencies. The Division cooperated with Oak Ridge Associated Universities in screening of applicants for USAEC Fellowships; participation in an eight-week course in Health Physics for college teachers; and assistance in presenting a ten-week course and a three-week course for

state personnel. Lectures were given at several courses for M.D.'s entitled "Medical Radioisotopes." One member of the Division spent six weeks in Bombay, India, giving a series of lectures on radiation physics at the Bhabha Research Center.

20. Physics of Tissue Damage

In the Physics of Tissue Damage program the optical properties of liquid water in the vacuum ultraviolet spectral region were measured for the first time. Two methods were employed. In one the reflectance of water in equilibrium with its vapor was measured over the spectral region from 1050 to 3000 A for three angles of incidence. In the second method quartz or CaF_2 semicylinders were used with the liquid in contact with the flat portion of the semicylinder in a sealed cell. Light was incident and exited from the semicylinder on the curved surface at various angles. These two methods together yielded values of n and k, the real and imaginary parts of the index of refraction; ϵ_1 and ϵ_2, the real and imaginary parts of the dielectric constant; and $-\mathrm{Im}\,(1/\epsilon)$, the imaginary part of the reciprocal complexing dielectric constant. One possible interpretation of the optical data is that there is an exciton transition at 8.3 ev, an interband transition at 9.6 ev, and a band gap of 9 ev. Thus liquid water has optical and electronic properties very much like those of insulators, such as Al_2O_3. Other activities in this program included a recalibration of the electron spectrometer used to measure electron slowing-down spectra with the thought that the anomalously large electron fluxes found in low energy might be attributed to a spurious response of the instrument. However, the instrument was found to respond as expected, and the discrepancy between the Spencer-Fano theory and our results remains. Further measurements were taken on the transmission of very low-energy electrons (2 ev–3000 ev) through thin layers of aluminum and sodium. Approximately 28% transmission was found out to 20 ev, whereupon the transmission decreased to essentially zero at about 50 ev, became unity again between 400 and 1100 ev depending on film thickness, and went negative beyond this energy (more electrons were ejected from the films than were absorbed by the films).

PART IV. RADIATION DOSIMETRY RESEARCH

21. Dosimetry for Human Exposures and Radiobiology

The most significant accomplishment in the dosimetry study for survivors of the nuclear bombings of Hiroshima and Nagasaki was the determination of the energy yield of the Hiroshima bomb; the yield was 12.5 ± 1.25 kilotons. Progress in the evaluation of the shielding afforded by heavy concrete structures was made, and the development of techniques for calculation of doses for the in utero cases was commenced. Analysis of data from Operation HENRE was largely completed; an especially significant finding was a prominent but unexpected gamma-ray peak which was attributed to the reactions $^{16}O(n,\alpha)^{13}C^* \rightarrow n + {}^{12}C^* \rightarrow {}^{12}C$ + 4.43-Mev gamma ray.

22. Applied Research

A highly noteworthy development in these studies was the development of "thermally stimulated exoelectron emission" (TSEE) as a dosimetry system. The system incorporates great sensitivity (can be much less than 1 mr of gamma radiation), low Z (e.g., BeO), wide dose range (over ten orders of magnitude), and, by using different detectors, the capability to distinguish between radiations of different LET.

Another development has been the extension of the etch-pit method of identifying charged-particle tracks in insulating solids to permit alpha dosimetry (i.e., airborne activity such as in uranium mines).

Special "low-Z" glasses of silver-activated lithium borate were developed for gamma-ray dosimetry by the radiophotoluminescence technique; the glasses were found to have promise in neutron dosimetry as well.

23. Spectrometry Research and Development

Except for the reduction and analysis of data from Operation HENRE (see above), the emphasis of the study was on accurate and absolute calibration of both neutron and gamma-ray spectrometers. The 3-Mv Van de Graaff accelerator in the High Voltage Laboratory was used extensively in these studies.

Another important area of investigation was that of developing a good organic scintillator by use of zone-refined quaterphenyl. Thus far, the refining has produced crystals having light output for ^{137}Cs gamma rays as great as that of anthracene to within ±5%.

Calculations of recoil particle spectra in neutron-irradiated tissue have been completed for the cases of 3- and 14-Mev neutrons incident on 30-cm-diam cylinders.

24. HPRR and DLEA Operations

The HPRR was used extensively in dosimetry, radiobiology, and radiobotanical studies. There were no major modifications and no significant changes in operating procedures.

The DLEA was modified extensively to provide for precise energy selection of charged particles to be used in stopping-power studies.

PART V. INTERNAL DOSIMETRY

25. Internal Dose Estimation

The fluctuations of daily excretion levels of plutonium in hospital patients receiving a single intravenous injection of plutonium were studied and reported in 1967 (ORNL-4168, p. 273). Following a single intake to blood, subsequent significant increments of intake would be expected either to change the general trend of the excretion curve or to produce an excess of high values. During the past year a plutonium worker (not an ORNL employee) suffered a minor cut which was contaminated with ^{239}Pu. The excretion data were made available with a request for assessment of the body burden. The interpretation required some changes in the computer code because of the early excision of tissue and treatment with DTPA. Study of the trend of the data and of the distribution of the amounts excreted per day supports the conclusions that the treatment did enhance excretion and that translocation of plutonium from the wound to bone after the first day was minimal.

A Monte-Carlo-type computer program for estimating the absorbed fraction of gamma energy in a "target" organ from a uniform source in a "source" organ was reported in 1967 (ORNL-4168, p. 245). The program is based on a "phantom" and 23 "organs" which are defined by simple mathematical inequalities suitable for fast calculation by the computer. The entire phantom and each of the "organs" have a volume and shape approximating that of the whole body or of the corresponding organ. During the past year the computer program has been modified to allow each "organ" to have approximately the composition and density of the corresponding human organ. This permits one to estimate with more confidence the absorbed fraction for the skeleton and lungs. The results differ from those obtained using the homogeneous model principally in the low-energy region, say when the photon energy is below 0.2 Mev. Results are now available for the source in ten different organs and for 15 photon energies from 0.01 to 4 Mev.

The total dose received by an individual from ^{137}Cs present in a particular food (e.g., meat) will be proportional to the product of four factors: $C \times I \times T_b \times D$, where C is the concentration of ^{137}Cs in the particular food, I is the daily intake of that food, T_b is the biological elimination half-time of ^{137}Cs for the individual, and D is the dose received per disintegration of ^{137}Cs, which is assumed to be uniformly distributed in the body. The variation with age of each of the four factors is summarized, and the variation of total dose or dose commitment per day of exposure is considered for two cases: (1) where a single foodstuff is contaminated (e.g., milk, meat, fresh fruits, fresh vegetables) and (2) for fallout ^{137}Cs present in the Chicago diet as of January 1967 and January 1968.

When a radionuclide is present in an organ and produces daughter nuclides, some fraction of these daughter elements remains in the organ and will be eliminated at rates which may differ from the elimination rates of the parent. A mathematical model has been designed to provide estimates of the activity levels of the parent radionuclide and of the daughter nuclides present in the organ at an arbitrary time post intake of the parent. The model has been programmed for a digital computer for the case in which there is no significant translocation of daughter nuclides from other tissues and when the retention of each nuclide in the organ can be described as a sum of exponentials. Estimates of the total microcurie-days of residence for each radionuclide are provided also.

A model for estimation of the mean activity present in various segments of the gastrointes-

tinal tract following a single oral intake has been developed. The model assumes uniform mixing of the contents in the various segments of the tract or, equivalently, an exponential distribution of residence times for the contents in each segment, as has been suggested by some experimenters. The model is mathematically equivalent to a catenary compartment system, and thus the solution is a sum of exponentials. The model also provides estimates for the mean activity of daughters if they are present.

Studies related to eventual estimation of the hazard posed by ^{238}Pu dioxide particles with diameters in the range of 50 to 250 μ have been conducted to estimate the probability of inhalation of such particles. The theoretical formula takes the settling velocity of the particle into account as well as the breathing rate. Studies of the dose distribution in tissue near such a particle have been carried out.

Sorption of SO_2 gas on aerosol particles of lead oxides, aluminum oxides, platinum, and iron oxide has been studied. Sorption ranges from essentially 100% to 10% or less, depending on the type of aerosol and the conditions of the experiment. Evidence of subsequent release of sorbed SO_2 has also been found in the case of platinum.

26. Stable Element Metabolism

Dietary and excretion data on 25 elements have been obtained for two individuals eating ad libitum during a period of 250 days. The data have been analyzed to study the dietary trends and fluctuations and the resulting patterns of excretion. Regression coefficients relating the intake on a given day to excretion during the next 24 days have been obtained, with multiple correlation coefficients greater than 0.32 ($p < 0.05$) for 10 of the 25 elements.

A practical procedure has been developed for removal of phosphate from solutions of bone ash. This makes it possible to chemically concentrate the trace elements at pH 6.5 rather than at pH 5.2, substantially increases the number of trace elements that can be collected, and eliminates the undesirable coprecipitation of calcium phosphate.

Part I. Radioactive Waste Disposal

K. E. Cowser

1. Fate of Trace Elements and Radionuclides in Terrestrial Environment[1]

Tsuneo Tamura
W. P. Bonner
F. S. Brinkley
E. R. Eastwood

PHOSPHATE STUDIES

Of all the elements present in living organisms, phosphorus is likely to be the most important ecologically.[2] Because of its importance in lakes and rivers in causing pollution and eutrophication and because of our interest in the movement of soil particles from land forms by erosion and runoff, studies were initiated to characterize its amount, form, and distribution in the soil surface, in sediments of a river (Clinch), and in sediments of a man-made pond (ORIC pond).

The procedures normally used in water quality studies distinguish ortho, or free, inorganic and organic phosphates in the water, including suspended solids. Though these analyses characterize a body of water for immediately available (ortho) and total phosphorus content, they do little to distinguish between the several forms of inorganic phosphates nor the behavior of the various forms. In this initial exploratory period, suggested methods, which are designed primarily for soil samples, have been applied to distinguish free iron and aluminum phosphates, occluded iron and aluminum phosphates, calcium phosphate, organic phosphate, and total phosphate. The organic phosphate was determined by difference between total phosphate and inorganic phosphate.

The procedure generally followed was the soil phosphorus fractionation system described by Jackson.[3] Several samples were also examined using modifications suggested by Williams *et al.*[4] and Bauwin and Tyner.[5] The fractionations are based on the solubility differences of the various forms of phosphorus in different extracting media. Three samples of field-moist soil and/or sediment, each weighing the equivalent of 1 g of oven-dried material, are required. The general procedure follows.

[1]Other studies are reported in Sect. 12, as part of cooperative program in land-water interactions.

[2]G. E. Hutchinson, *A Treatise on Limnology*, Wiley, New York, 1959.

[3]M. L. Jackson, *Soil Chemical Analysis*, Prentice-Hall, Englewood Cliffs, N.J., 1958.

[4]J. D. H. Williams, J. K. Syers, and T. W. Walker, "Fractionation of Soil Inorganic Phosphates by a Modification of Chang and Jackson's Procedure," *Soil Sci. Soc. Am. Proc.* **31**, 736–39 (1967).

[5]G. R. Bauwin and E. H. Tyner, "The Nature of Reductant Soluble Phosphorus in Soils and Soil Concretions," *Soil Sci. Soc. Am. Proc.* **21**, 250–57 (1957).

First Sample

After removal of easily soluble phosphorus with 0.5 *N* NH_4Cl, free aluminum phosphate is extracted with neutral 0.5 *N* NH_4F. The aluminum is complexed by the fluoride at neutral pH, releasing phosphate to the solution by the following reaction:

$$6NH_4F + AlPO_4 \longrightarrow AlF_6^{3-} + 6NH_4^{+} + PO_4^{3-} .$$

In neutral to alkaline solutions, the iron fluoride complex is unstable, and phosphate in the iron phosphate form is not released.

Free iron phosphate is next released by extracting with 0.1 *N* NaOH. Since the NH_4F treatment dissolved the aluminum phosphate, only free iron phosphate is released to the NaOH extract. Under certain circumstances, however, the phosphate released in the NH_4F may react with iron and give a higher analysis of iron phosphate.[4] Several of the samples were given a second NaOH treatment using 1.0 *N* solution, as suggested by Williams *et al.*,[4] since they found that all the iron phosphate is not extracted by a single treatment.

Calcium phosphates are soluble in acid solutions but insoluble in neutral-to-alkaline solutions and have thus remained undisturbed during the aluminum- and iron-removal treatments. The solubility of CaF_2 is higher than the calcium phosphate, and thus the NH_4F does not dissolve calcium phosphate. To extract calcium phosphate, the sample is treated with 0.5 *N* H_2SO_4 for 1 hr.

Occluded or interlattice iron and aluminum phosphates are much more difficult to remove than the "free" forms and require a treatment which reduces the iron and dissolves the phosphate; such a treatment is given using $Na_2S_2O_4$ as the reducing agent. After washing with NaCl, the sample is treated with neutral NH_4F to dissolve any occluded aluminum phosphate. Samples which were treated with sodium citrate–dithionite did not give reproducible results for reductant-soluble or occluded phosphate; by substituting sodium tartrate for the citrate as used by Bauwin and Tyner,[5] reproducible results were obtained. Thus, results reported for occluded iron and aluminum phosphates were obtained using the tartrate-dithionite medium.

Second Sample

Organic phosphorus is determined by the difference in the mineral plus organic phosphorus and the mineral phosphorus in the sample. To remove both forms from the sample, extraction is made with concentrated HCl, followed by two extractions with 0.5 *N* NaOH, one of which is an overnight extraction at 90°C. Phosphorus is then determined in the combined extract before (mineral) and after oxidation with $HClO_4$ (mineral plus organic).

Third Sample

Phosphorus in silicates and other forms which are hard to get to is determined by fusing the sample with sodium carbonate. The phosphorus, which includes the organic form, represents the total phosphorus in the sample.

PHOSPHORUS IN SOILS AND SEDIMENTS

Since analytical development and sample analysis were being done simultaneously, results are not directly comparable unless indicated (Table 1.1). These analyses were made to obtain information on the distribution of the different phosphate forms in different environmental media, including soils, eroding material, and bottom sediments. The soil samples marked 1 to 4 represent the 0-to-1-in. layer; samples 1 to 3 are fertilized soils whose runoff drains into ORIC pond, sample 4 represents an unfertilized soil whose runoff is being collected for another study, and the eroded material represents material collected from this runoff. The bottom sediments were obtained from ORIC pond as well as from the Clinch River.

The results in Table 1.1 list the forms of phosphate found in the samples. In the soil samples, the fertilized soils show higher phosphate concentration than the unfertilized soil. In addition, only the fertilized soils show significant quantities of easily removable phosphate which is due to the addition of fertilizers. The high concentration of calcium phosphate in the soil samples also reflects the phosphate due to fertilization. Soil sample 1 was taken on the crest of a hill, and sample 2 was taken near the base of the hill; the difference in phosphate concentration may, therefore, be due to erosion of material from the upper part which accumulated at the lower zone.

The source of the eroded material of Table 1.1 is soil 4; the high concentration of phosphate in

Table 1.1. Amounts and Forms of Phosphate in Selected Samples

Soil or Sediment	Easily Removable	Free Aluminum Phosphate	Free Iron Phosphate		Calcium Phosphate	Occluded Phosphate	Organic Phosphate	Sum of Phosphate	Total Phosphate
			First	Second					
Soil 1	0.054	0.285	0.258	N.d.	0.355		0.494	1.446	2.191
Soil 2	0.0301	0.545	0.586	N.d.	0.918		1.011	3.090	3.930
Soil 3	0.0389	0.391	0.490	N.d.	0.960		0.518	2.397	2.911
Soil 4	0.002	0.265	0.279	0.086	0.100	0.732	0.311	1.775	1.610
Eroded material	0.002	0.564	0.909	0.367	0.063	1.088	0.724	3.677	3.833
Bottom sediment (ORIC)	0.000	0.019	0.029	N.d.	0.298		0.372	0.718	1.358
CRM 48.8	0.000	0.087	0.435	N.d.	0.150		0.347	1.019	1.840
CRM 15.5	0.000	0.086	0.462	N.d.	0.126		0.384	1.058	1.528
CRM 7.5	0.003	0.192	0.263	0.037	0.085	0.676	0.130	1.386	1.303

this sample is likely due to selective removal of finer particles of the soil which contains the phosphate.

The bottom sediment in ORIC pond derives its material from soils 1 to 3. The interesting feature in the phosphate distribution is the higher concentration of calcium phosphate in ORIC pond than in the Clinch River. Since ORIC pond was fertilized with 10-10-10 fertilizer during the summer months of 1962 through 1964, this may account for its presence. The absence of detectable amounts of easily removable phosphate in the ORIC pond sediment is probably due to the higher calcium carbonate content. Calcium carbonate can adsorb phosphate and prevent its leaching with NH_4Cl. The sediment from Clinch River Mile (CRM) 7.5 was obtained during the coring operations of 1962, in contrast to the dredged samples of CRM 48.8 and 15.5 obtained in 1968. The differences in amounts and forms of phosphate may thus be due to the influence of time as well as location.

The results thus far obtained, though suggesting more work be done, are encouraging in providing clues to the distribution of phosphate, which differs in forms. Results suggest that calcium phosphate is associated with systems receiving commercial fertilizers and may be an indicator of potential pollution. The ORIC pond, discussed more fully in the next section, has produced abundant aquatic weeds and calcium phosphate in the predominant inorganic form in the sediment. Results further suggest that eroding material can transport significant quantities of phosphate from soils which have not received commercial fertilizers. The availability of the phosphates associated with sediments needs to be evaluated, especially since aluminum and iron phosphates are relatively insoluble in acidic systems of soils but increase in solubility with increase in pH, which is noted in ORIC pond and the Clinch River.

ORIC Pond Studies

ORIC pond, created in the fall of 1961 to beautify the area between the east entrance to ORNL and Building 6000, has at times become a turbid and thus a rather unattractive pond. Evidences of abundant production have been exhibited by masses of aquatic plants floating on the pond.

The pond has a surface area of approximately 2.5 acres, a maximum depth of 8 ft, and a total capacity of about 2,500,000 gal. The primary source of water is a spring located at the northeast end of the pond under Eighth Street. The flow is discharged into

the pond through a 12-in. culvert at a depth of about 4 ft. A wet-weather spring located across Bethel Valley Road contributes flow intermittently during the winter months. The remaining sources are derived from precipitation on the pond and runoff from approximately 9 acres of grassed watershed.

During 1962 to 1964, 300 lb of 10-10-10 fertilizer was added to the pond each month during the months of May through September. In addition, each fall the grass on the watershed was fertilized at the rate of 500 lb/acre with the same fertilizer. Each 300 lb of fertilizer added to the pond could, assuming complete solution of the fertilizer, increase the concentration of PO_4 and NO_3 in the pond by approximately 4.3 and 6.4 mg/liter. This concentration of PO_4 is generally recognized as being from 1 to 2 orders of magnitude above that necessary to produce an abundant growth of algae.

In the spring of 1966, 2000 wild celery tubers were introduced into the pond to provide food for the ducks and swans. In 1967, sago pond plant tubers, giant burweed roots, marsh smartweed root, duck potato tubers, and water iris tubers were also introduced into the pond. Of these plants only the wild celery survived, and by the fall of 1966 it had grown so rapidly that some of it had to be raked from the pond and hauled off to prevent the floating masses from becoming a nuisance. A weed killer, Karmex [active ingredient 3-(3,4-dichlorophenyl),1-dimethyl urea], which was applied to the pond in June 1967 helped to control the growth of aquatic plants at a tolerable level during 1967

During the summer of 1966 and 1967, studies were initiated to establish the trophic level of the pond, especially since an abundant growth of wild celery had been observed. These data have been analyzed and some of the results tabulated in Table 1.2. The data show that the NO_3 concentration remained relatively constant, presumably due to the high input of NO_3 from the spring, while the PO_4 showed a significant decrease in 1967. The concentration of other elements showed only minor changes.

Table 1.2. Some Chemical Characteristics of Water from ORIC Pond[a]

	1966	1967
Orthophosphate	0.096	0.017
CO_2	7.7	5.1
D.O.	8.6	6.4
pH range	7.75–8.35	7.5–8.3
NO_3	0.14	0.14
NO_2	<0.01	0.014
Free NH_3	0.07	0.13
Organic NH_3	0.02	0.04

[a]All units are milligrams per liter except for pH.

Agriculturalists have shown that nitrogen and phosphorus play a key role in producing growth in agricultural crops. The rooted aquatic plants which were introduced into the pond in 1966 and 1967 would therefore be expected to show a similar response to fertilization in this system. The high concentration of PO_4 in 1966 suggests that the abundant growth of wild celery was likely due to overfertilization. Data which have been obtained since 1967 and which are not included in Table 1.2 substantiate the decrease in concentration of PO_4 which was observed in 1967 and further suggest that the concentration of PO_4 may decrease sufficiently to prevent the recurrence of an overabundant growth of aquatic weeds and algae.

Proportional samples and flow measurements are being obtained on both the influent and effluent streams of the pond. The data from these will be used to make a material balance of nutrients. The data are being fitted to a mathematical model in order to permit the prediction of the status of the pond with time and to evaluate the contribution of the several nutrient inputs. From this information, a fertilization program to prevent excessive production in the pond will be developed.

2. Disposal by Hydraulic Fracturing

Wallace de Laguna W. C. McClain

SITE EVALUATION BY WATER INJECTION TESTS – THEORETICAL ANALYSES

W. C. McClain

Although hydraulic fracturing is now being successfully used as a waste-disposal technique at Oak Ridge National Laboratory, it is not possible to guarantee its applicability at any other location without first carrying out a site testing and evaluation program. This is because the technique is predicated upon the formation of essentially horizontal fractures deep in the ground when the waste slurries are pumped through a slot in the cased injection well. The development of vertical fractures would represent a breach of the containment and isolation barrier provided by the overlying rocks, thereby negating the principal advantage of hydraulic fracturing.

The orientation of hydraulically induced fractures is controlled primarily by the state of stress in the earth's crust;[1] and, since there is no way to predict that stress state, it will be necessary to prove that the induced fractures are horizontal at any proposed waste-disposal site as a part of the site examination procedure.

At the Oak Ridge facility, the horizontality of the fractures was confirmed by the core drilling that was conducted as part of the experimental program. In this case, several grout injections, each identified by a chemical dye and an isotopic tag, were intersected at approximately the same depth in a number of core holes drilled from the surface. At any other proposed hydraulic fracturing site, it may be necessary to perform a similar core-drilling program in order to conclusively prove that the fractures are horizontal. This core-drilling program is both time consuming and very expensive. The purpose of this investigation was therefore an attempt to develop a method whereby a fairly reliable indication of the fracture orientation could be obtained by some other method. In this way, it should be possible to significantly reduce the number of core holes and hence the expense of proving the applicability of hydraulic fracturing at a proposed site.

For a number of reasons, it appeared that an analysis of the pressure history data obtained from a water-injection test would offer the best approach to the problem. Preliminary examination indicated that the mechanics of even the horizontal fracturing taking place at ORNL is not amenable to a complete theoretical analysis. Consequently, an experimental water-injection test was conducted in December 1967 to supply the empirical data required to complete the analysis.

Dynamic Mechanics of Horizontal Fractures

The simplest configuration of the fracture for waste-disposal operations is a single horizontal fracture extending outward equally in all directions from the injection well, that is, a circular fracture, which is parallel to the surface and axially symmetrical about the injection well. The evidence[2] available suggests that, whereas this configuration is not actually obtained at the Oak Ridge facility, it is a reasonable first approximation of

[1] W. C. McClain, Internal Memorandum, 1967.

[2] Wallace de Laguna *et al.*, *Engineering Development of Hydraulic Fracturing as a Method for Permanent Disposal of Radioactive Wastes*, ORNL-4259 (1968).

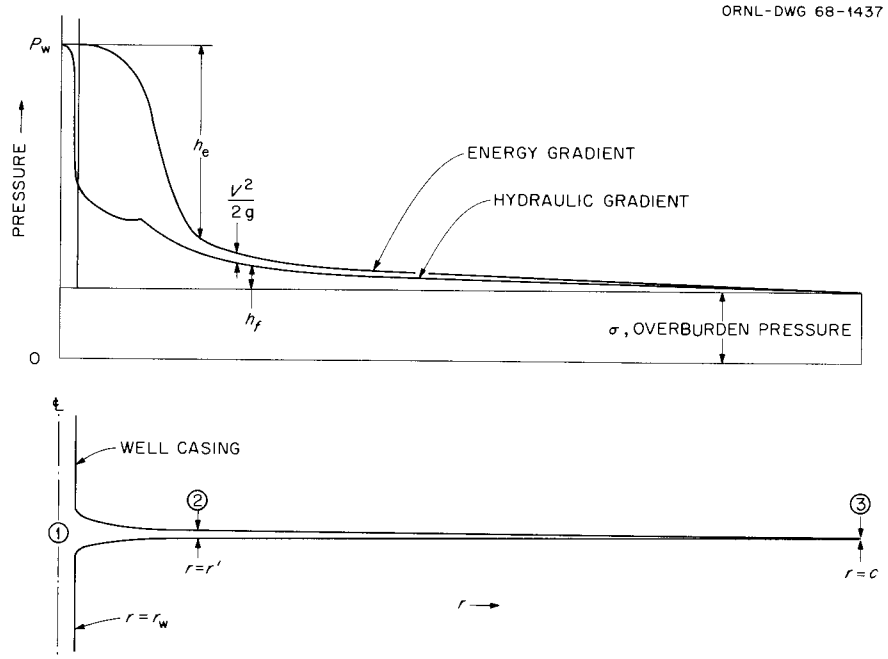

Fig. 2.1. Pressure Relationships for a Circular Horizontal Fracture.

the grout sheet for analysis purposes. The pressure relationships in this type of fracture are illustrated in Fig. 2.1, where P_w is the fluid pressure at the center of the injection well at the level of the slot, h_e is the pressure loss in the turbulent region resulting from both entrance and friction losses, and h_f is the friction loss in the remainder of the fracture where the flow is laminar.

Since the pressure at the tip of the fracture ($r = c$) must be almost exactly equal to the overburden pressure (σ), the fluid pressures at the various locations indicated in Fig. 2.1 can be expressed:

$$P_3 = \sigma ,$$

$$P_2 + \frac{\gamma V_2^2}{2g} = P_3 + \gamma h_f + \gamma \delta Z , \qquad (1)$$

$$P_w = P_2 + \frac{\gamma V_2^2}{2g} + \gamma h_e + \gamma \delta Z ,$$

where γ is the density factor for water (0.433 psi/ft).

These expressions reduce to

$$P_w = \sigma + h_e + h_f \qquad (2)$$

because there is no difference between the velocity head nor the elevation as measured at the center of the well ($r = 0$) and the tip of the fracture ($r = c$). Since the overburden pressure (σ) can be estimated from the depth, it remains only to evaluate the two components of the losses h_e and h_f.

An expression for the laminar losses (h_f) has been derived,[3] based on the method of Perkins and Kern,[4] as a function of the total volume injected:

$$h_f = \frac{\sqrt{3}}{8} \ln \frac{c}{r'} \left[\frac{E}{(1 - \nu^2)c} \right]^{3/4} [\pi^2 \mu Q]^{1/4} , \qquad (3)$$

[3]W. C. McClain, *The Interpretation of Water Injection Tests in Site Evaluation for Waste Disposal by Hydraulic Fracturing*, ORNL-CF (in press).

[4]T. K. Perkins and L. R. Kern, "Widths of Hydraulic Fractures," *J. Petrol. Technol.* 13, 937–49 (1961).

where

$$c = \left[\frac{9E\Delta^4}{\pi^2(1-\nu^2)\mu Q}\right]^{1/9} \tag{4}$$

= radius of circular fracture,

μ = absolute viscosity of water (2.0886×10^{-5} lb-sec/ft^2),

Q = flow rate of injection (ft^3/sec),

Δ = total volume injected (ft^3),

E, ν = modulus of elasticity and Poisson's ratio of the rock,

ρ = bulk density of water (1.95 lb-sec^2/ft^4),

$$r' = \frac{Q\rho}{2000\pi\mu}. \tag{5}$$

If the horizontal fracture is noncircular, being constrained in one horizontal direction but with the injection well located at the center, Eqs. (3) and (4) reduce to[3]

$$h_f = \frac{1}{\Psi}\left[\frac{4(2.546)^2\, E^3\, \mu Q(c - r')}{3\pi(1-\nu^2)^3}\right]^{1/4}, \tag{6}$$

$$c = 3\left[\frac{4E\Delta^4}{\pi^3\Psi^4\mu Q(1-\nu^2)(2.546)^2}\right]^{1/5}, \tag{7}$$

where Ψ = narrow, restricted dimension of the noncircular fracture (ft). If the injection well is located at one end of the elongated fracture, the laminar losses h_f will be double those given by Eq. (6).

Only an empirical evaluation of the turbulent losses h_e in the region $r \leqq r'$ is possible, because the shape of the fracture in this zone and even the configuration of the slot in the casing is unknown. The empirical data from the experimental water injection test were fitted to[3]

$$h_e = \frac{\gamma}{2g} B Q^{2m} \Delta^{2n}, \tag{8}$$

where

γ = density factor for water (0.433 psi/ft),

g = acceleration of gravity,

B, m, n = arbitrary constants; their values determined as

$$B = 1.1175 \times 10^6, \quad m = 0.07, \quad n = -0.09. \tag{9}$$

When the appropriate expressions for the laminar losses h_f [Eq. (3) or (6)] and the turbulent losses h_e [(Eq. (9)] are substituted into Eq. (2), the pressure in the well during injection of water into a horizontal fracture is obtained as a function of (1) total injected volume, (2) flow rate, and (3) rock properties.

Mechanics of Nonhorizontal Fractures

The relationship between the injection pressure and the other injection parameters discussed in the previous section can be broadened to include the behavior of nonhorizontal fractures if the original state of stress in the ground and its variation with depth are known. If $\sigma_{\theta w}$ is assumed to be the earth stress acting perpendicular to the fracture plane at the injection point (regardless of the orientation of the fracture) and if K' is similarly assumed to be the linear vertical gradient of that stress, then the expression for the injection pressure becomes

$$P_w = \sigma_{\theta w} + h_e + h_f + \delta Z(\gamma - K'), \tag{10}$$

where Z is the change in elevation of the fracture tip.

Figure 2.2 shows the plot of Eq. (10) for vertical fractures for what are probably the limiting values of K'. When $K' = 0$, there is no change in the horizontal earth stress with depth, and the pumping pressure decreases rapidly with increasing injected volume. Under these conditions the fracture will propagate itself downward away from the injection well without additional pumping. When the vertical gradient of the horizontal earth stress is equal to the density of the rocks, $K' = \gamma_R$ (i.e., a hydrostatic earth stress), a vertical fracture will be propagated upward toward the ground surface, but the pumping pressure (measured at the depth of the slot) will increase rapidly during the injection because of the increasing static head. When the vertical gradient of the horizontal earth stress is exactly equal to the density factor of water $K' = \gamma$,

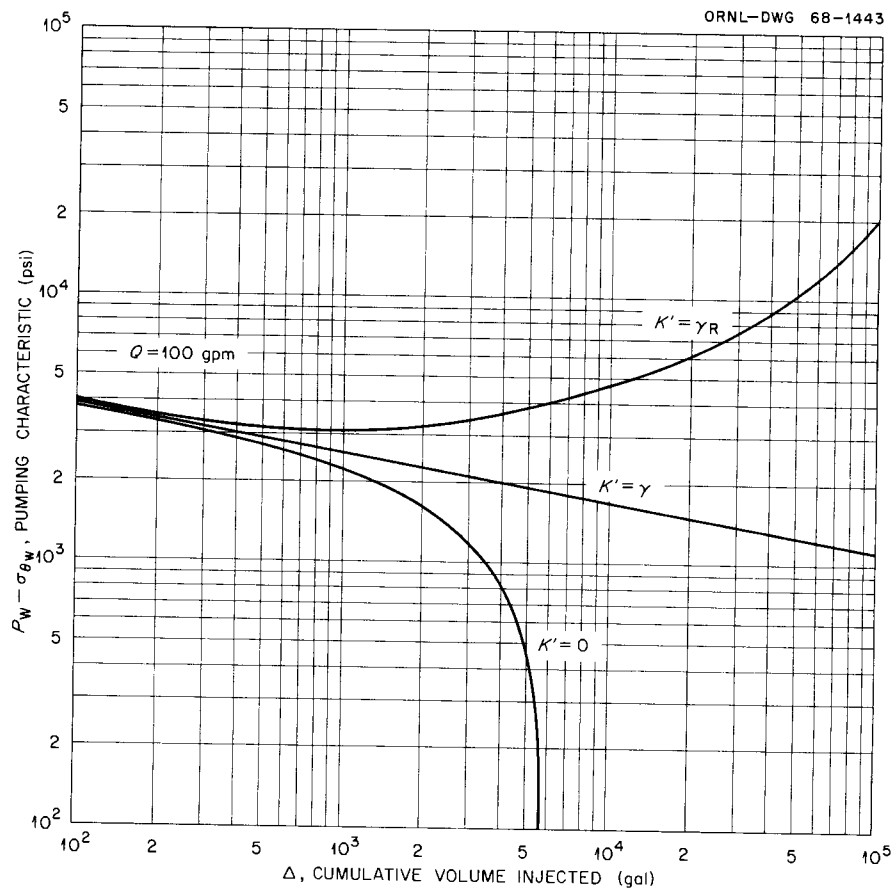

Fig. 2.2. Pumping Characteristics for Vertical Fractures.

a vertical fracture will be propagated both up and down from the injection point, and the injection pressure will appear exactly the same as for a horizontal fracture.

Conclusions

Based on this analysis,[3] it should be possible to distinguish between a horizontal fracture and a steeply dipping one if the value of the parameter K' at the location being tested is sufficiently different from the density factor of the injection fluid.

At the present time the analysis summarized here represents a hypothesis which has not yet been tested. It is anticipated that this testing of the hypothesis will take place coincidentally with the testing of any proposed sites for waste disposal by hydraulic fracturing. Field testing will doubtless result in some refinements and modifications of the theory. However, it is felt that the analysis provides the basis for what may become an efficient and inexpensive method for screening the suitability of hydraulic fracturing sites.

SITE EVALUATION BY WATER INJECTION TESTING – DROP IN PRESSURE AFTER PUMPING HAS STOPPED

Wallace de Laguna

After injection of the fracturing fluid has stopped and the well is shut in, the pressure at the wellhead drops, rapidly at first and then more and more slowly. At least two factors are believed to be responsible for this pressure drop. While liquid is

being pumped into the well, there must be a pressure gradient in the fracture between the point of entry at the injection well and the tip of the fracture; indeed, a significant gradient may be required to drive the fluid a distance of up to several hundred feet through a fracture believed to be only a few tenths of an inch wide near the well. At the tip of the fracture, if the fracture is essentially horizontal, the fluid pressure must be equal to or slightly greater than the pressure due to the weight of the overburden if the pressure is to split and lift the rock. Near the well, therefore, the pressure must be somewhat greater than the pressure required to propagate the fracture. This excess pressure compresses and deforms the rock more than would the fracture extension pressure alone, and energy is required for this additional deformation. When pumping stops, this stored energy is released, driving the liquid from the vicinity of the well out to the tip of the fracture, and the fracture continues to extend. In other words, after pumping stops, the shape of the fracture will change, but the volume of the fracture will remain constant, unless other factors are considered. As the fracture extends and as the walls come closer and closer, the pressure in the fracture will drop. When the walls of the fracture make contact, the pressure should equal the weight of the overburden, and this process should cease.

The shale rock is nearly, but not completely, impermeable, so that during the pumping and also during the subsequent self-extension of the fracture, liquid must be slowly leaking out into the wall rock. The rate of leakage will be a function of the pressure gradient of the fluid in the rock immediately adjacent to the fracture and to the surface area of rock exposed, both of which will be constantly changing. Also, the permeability of the shale is greater parallel to the bedding than normal to the bedding, so that the direction of fluid flow and the direction of the related pressure gradient in the fluid will not be isotropic. As fluid leaks out of the fracture, relatively rapidly at first and then more and more slowly, the pressure in the fracture will drop. Unlike the pressure drop due to the change in shape of the fracture, the leaking of the fluid will continue to lower the pressure after the pressure has reached the weight of the overburden, and, indeed, the pressure should eventually reach the "formation pressure," although what is meant by formation pressure in a rock of such low porosity and permeability may be difficult to define.

When pumping stops and the well is shut in, the subsequent drop in pressure is some very complex function of the change in shape and in volume of the fracture. With so many poorly known parameters to consider, it is futile at this time to attempt a detailed mathematical analysis of the processes involved. However, we do know that the change in shape of the fracture will cease to be an important factor after the pressure has dropped to the pressure equal to the weight of the overburden, and that the subsequent drop in pressure will very largely be governed by the decrease in volume of the fracture due to loss of fluid. The rate of pressure drop in a horizontal fracture may, therefore, show some discontinuity as the pressure drops below the weight of the overburden, and if such a discontinuity can be identified, it should be evidence that the fracture is horizontal.

Following the water injection test of December 1967, the well was shut in and the pressure recorded, at first at 1-min intervals and then at longer and longer intervals as the rate of drop in pressure declined. These measurements were continued for about 70 days, at which time the rate of drop in pressure was only about 1 psi/day. The initial rate of pressure drop was about 60 psi in 1 min, so that the rate of drop in pressure varied over about five orders of magnitude during this shut-in second part of the injection test. Figure 2.3 is a plot of the fluid pressure vs the time since pumping stopped, time being represented on a logarithmic scale. The first part of the curve is convex upward; the second part is concave. The point of inflection was first estimated as coming after about 5×10^3 min, when the pressure was approximately 700 psi. The pressure at the wellhead corresponding to the weight of the overburden at a depth of 852 ft is about 610 psi. However, the change in slope of the curve is gradual, and the point of inflection may well come at 8×10^3 min, at which time the pressure was very close to 610 psi. At first my impression was that this point of inflection, falling as it does close to the pressure at which some change was anticipated, was indeed the sign or index for which I was searching, but I have been informed by our Mathematics Division that such a point of inflection on a semilogarithmic plot has no physical significance.

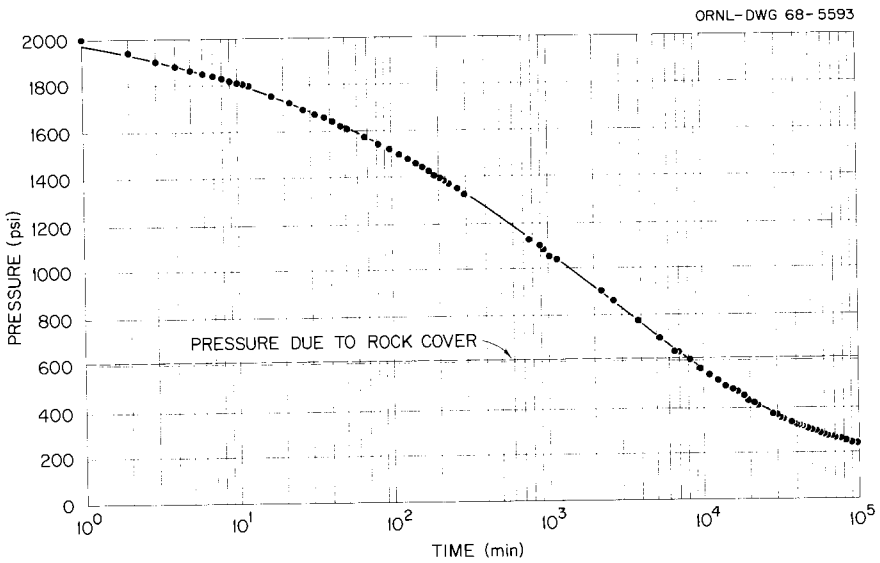

Fig. 2.3. Pressure Decay; Water Injection Test, December 1967.

Figure 2.4 is a plot of the pressure, on a linear scale, vs the rate of change in pressure on a logarithmic scale. This curve is very similar in shape to the preceding curve except that the point of inflection comes at a pressure of about 1000 psi. And, in any case, this point also has no physical significance but is an arbitrary product of the method of plotting.

Figure 2.5 is a plot of the rate of change of pressure as a function of time, both plotted on a logarithmic scale. The first part of the plot, out to about 8×10^3 min, is a straight line with a slope of very nearly 45°. This suggests that up to this time the rate of change of pressure is approximately inversely proportional to time, although this apparently simple relation may well be fortuitous. After 8×10^3 min the plot continues, not as a straight line but as a curve convex upward, showing that the rate of change of pressure decreases with time and is no longer a simple inverse proportion of the time. This change may well have a physical significance, although there is nothing in the graph to indicate just what mechanisms or factors are involved. However, the change comes at a pressure of just over 600 psi (see Fig. 2.3 for the pressure after 8×10^3 min) and is the kind of change that one might anticipate if one of two mechanisms responsible for the drop in pressure had ceased. The relation may well be fortuitous, but it does suggest a possible empirical method for using the rate of pressure decline after pumping has stopped to determine if the fracture is more likely to be horizontal than vertical. Like all empirical methods, it will have to be tested a number of times under a variety of known circumstances before any reliance can be placed in it.

In April of 1968 some 130,000 gal of waste-cement slurry, followed by about 1200 gal of water, was pumped into the same fracture at 852 ft into which the water injection test had been made some four months earlier. After pumping had stopped and the well was shut in, pressure measurements were made much as in the case of the water injection test, although they were only continued for 28 days, as the pressure fell somewhat more rapidly.

The problem of the rate of pressure drop in a fracture filled with a self-hardening cement slurry is even more complex than in the case of a water-filled fracture. Since the consistency of the slurry is somewhat thicker, one might expect that the injection pressures, at the same pumping rate, would be higher for the slurry than for water, but this does not seem to be the case. Direct comparison is, however, difficult because of the deliberate variations in pumping rate during the water injection test.

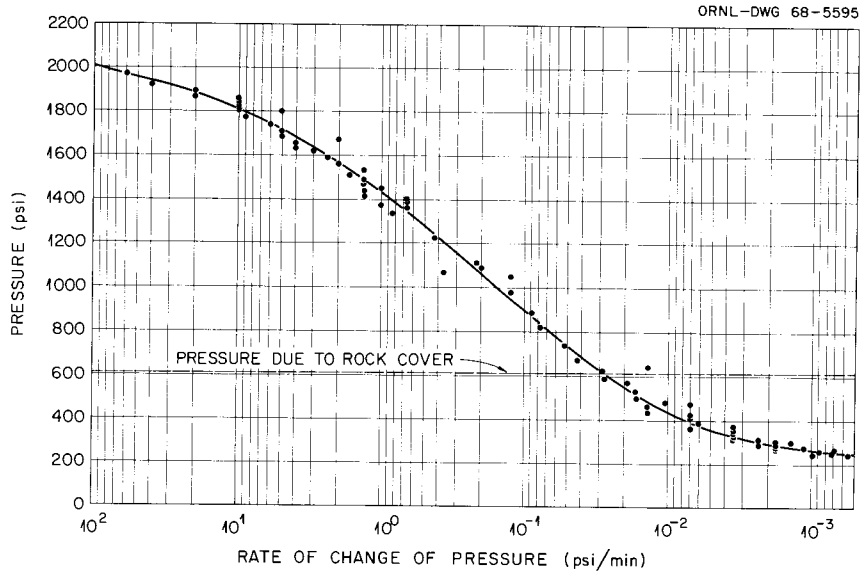

Fig. 2.4. Rate of Pressure Drop as a Function of Pressure; Water Injection Test, December 1967.

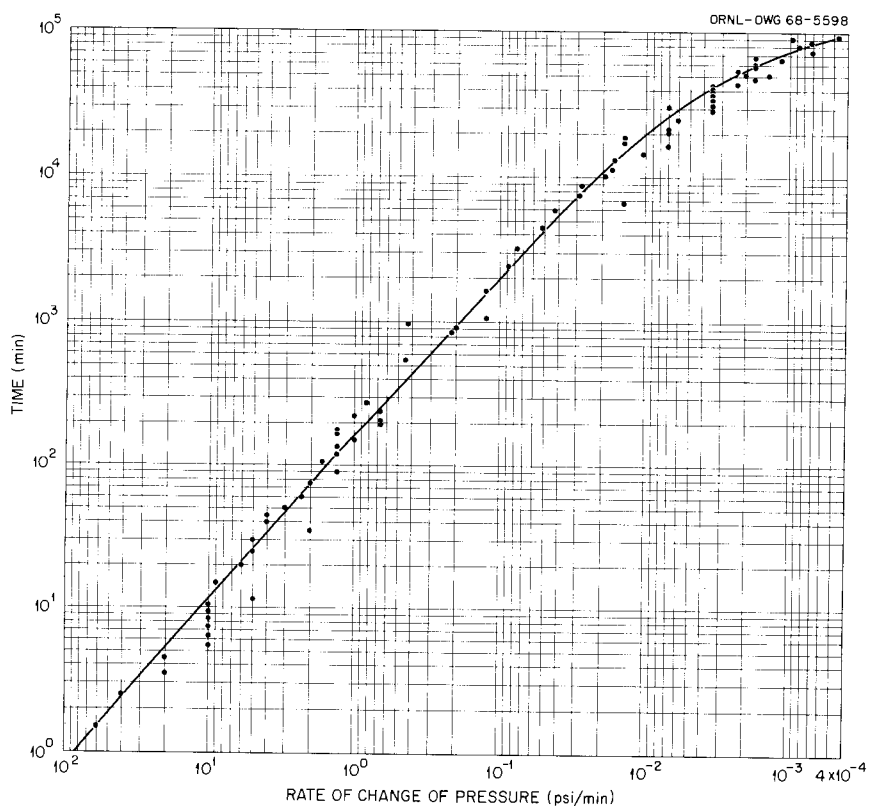

Fig. 2.5. Rate of Change of Pressure as a Function of Time; Water Injection Test, December 1967.

As far as we know, the injection of 50,000 gal of water forms a single fracture. Evidence from core drilling, however, shows that large injections of slurry form multiple fractures, in general parallel but separated by thin layers of shale up to 1 or 2 ft thick. Apparently, the slurry at the leading edge of the fracture is thickened, as water is squeezed out into the shale, until it can no longer flow easily, when the advance of this fracture is blocked and a new fracture forms, probably back near the injection well.

When the pumping is stopped, the fracture, which is then actively taking the slurry, presumably continues to extend as in the case of a water-filled fracture; but, as the shape of the fracture changes and the fracture becomes narrower, the slurry in the fracture may, because of the solids contained, start to carry directly some of the vertical load some time before the rock walls of the fracture actually make contact. This is equivalent to saying that the pressure distribution in the fracture is no longer hydrostatic and that the pressure as measured at the wellhead is not a true indication of the pressure at the tip of the fracture available for fracture extension. Of course, once the cement starts to set, the slurry will lose its fluidity, but the loss of even a small proportion of the liquid phase to the wall rock may appreciably reduce the mobility of the slurry prior to the time when the cement first starts to gel. For all these reasons, the mechanism which produces a change in shape of the fracture and a consequent drop in pressure may be expected to halt before the pressure has dropped to the weight of the overburden.

Figure 2.6 is a plot of the pressure in the fracture as a function of time, with time plotted on a logarithmic scale. The curve is very similar to that shown in Fig. 2.3 for the water-injection test, except that the pressure falls more rapidly, particularly in the time interval from 10 to 1000 min after pumping stops, and the point of inflection comes after only about 150 min, when the pressure is about 1100 psi. The more rapid drop in pressure, so early in the shut-in phase, was unexpected and cannot be easily explained. It can hardly be due to a more rapid change in the shape of the fracture or to a more rapid loss of the fluid phase to the wall rock. The more rapid pressure drop may be related to the fact that the slurry is a non-Newtonian fluid or to the more complex fracture pattern formed with a slurry, but it can hardly be related to the setting of the cement, for even the start of the formation of the initial cement gel is not believed to begin until after an hour or two; the true hardening of the cement would not begin until after several hours.

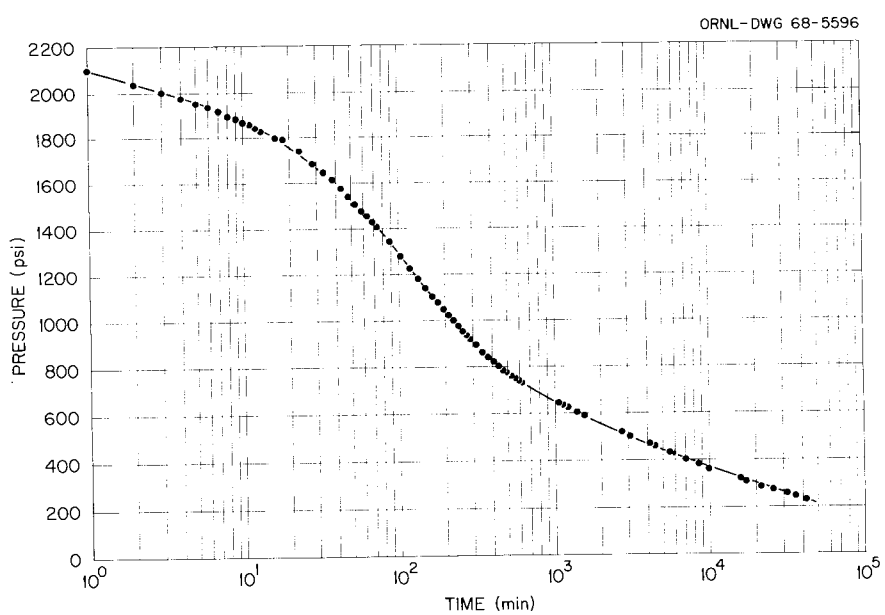

Fig. 2.6. Pressure as a Function of Time; Injection ILW-4B, April 1968.

Figure 2.7, showing the rate of change of pressure plotted on a logarithmic scale as a function of the pressure, is similar to Fig. 2.4, the equivalent curve for the water-injection test. The difference reflects the more rapid drop in pressure in the case of the slurry injection.

Figure 2.8 is a plot of the rate of change of pressure as a function of time, both plotted on a logarithmic scale. This graph appears to consist of two straight line segments with a change in slope coming about 100 min after pumping stopped. The first segment has a slope of about 60°, again an indication of the more rapid pressure drop following the slurry injection. The graph from 100 min out to 4×10^4 min, or 28 days, is also a straight line segment, in this case with a slope of about 40°. The break in slope at 100 min is unmistakable, despite the scatter of the plotted points. This decrease in the rate of change in pressure almost certainly has some physical significance. It may represent the formation of a gel, which is the first stage in the complex process of the setting of the cement. This gel at first is very weak, but it is capable of giving the slurry some of the properties of a solid. Even a weak gel would greatly reduce the rate of change in the shape of the fracture and also the rate at which the fluid phase can seep out into the wall rock. There is no simple way of telling which of these factors was responsible for the change in slope of the plot, and both may be involved. At the time of change in slope, that is, 100 min after pumping stopped, the pressure at the wellhead was about 1300 psi, well above the fracture extension pressure.

A time of 100 min is a little short for the start of gelling by the cement, although this time is very sensitive to even minor changes in the chemical composition of the slurry. The change in slope may be a consequence of the loss of fluid into the wall rock, for the loss of even a small proportion of the liquid phase can change markedly the thixotropic properties of the slurry so that, in a confined space, the slurry would have some shear strength and could exert an upward supporting pressure greater than the pressure as measured by the pressure gage.

These attempted explanations of the variations in rate of drop in pressure in a fracture after pumping has stopped are not significant in themselves; too many variables and too many uncertainties are involved. They do suggest, however, a rational method of examining such data; and, when the results from a number of injections are available, it may be possible to eliminate some of the uncertainties.

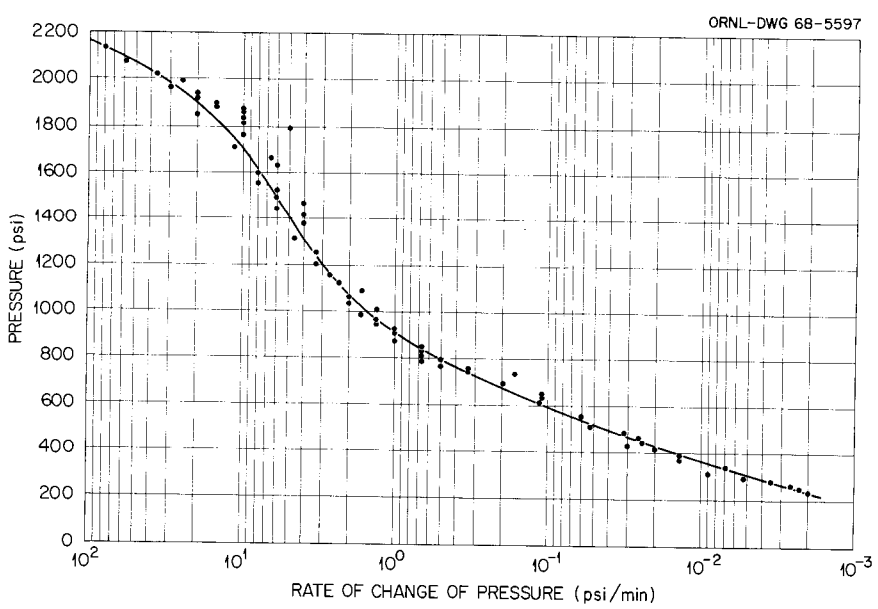

Fig. 2.7. Rate of Change of Pressure as a Function of Pressure; Injection ILW-4B, April 1968.

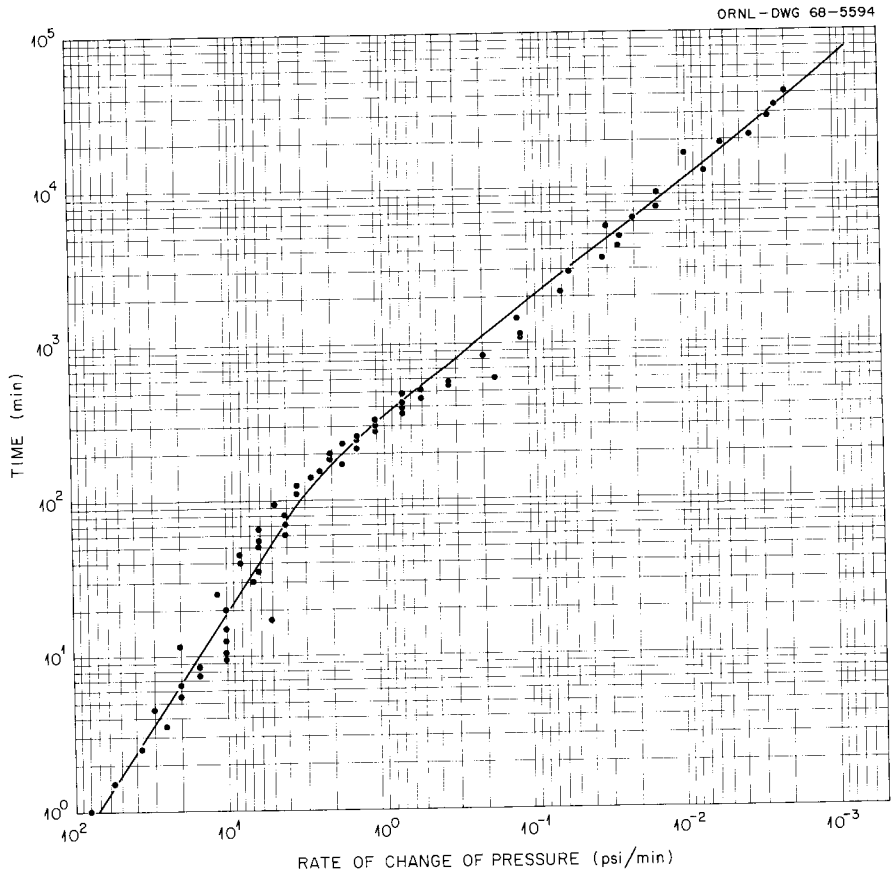

Fig. 2.8. Rate of Change of Pressure as a Function of Time; Injection ILW-4B, April 1968.

In particular, it is worth noting that the most useful and informative plot is one showing the rate of change of pressure as a function of time, both plotted on logarithmic scales.

PRESSURE CHANGES IN THE ROCK COVER MONITORING WELLS DURING AN INJECTION

Wallace de Laguna

The so-called rock cover monitoring wells were constructed by cementing a 4-in. casing into a 6½-in. hole down to a depth of about 550 ft and then drilling 100 ft of uncased hole down to a depth of 650 ft. The rock cover, which provides an impermeable seal overlying the red shale into which the disposal injections will be made, is the gray shale which lies between the surface and the limestone marker beds at a depth of 700 ft (see Fig. 2.9). Attempts were made to pump water into each of these wells at an arbitrary standard pressure of 75 psi, and the volume accepted by the well was carefully measured. In the first hour the wells accepted from 2 to 3 gal, and over a 3- to 4-hr period they accepted a total of 5 to 10 gal, after which the rate of acceptance was negligible. Qualitatively this means that the shale was effectively impermeable, even in a direction parallel to the bedding. These attempted injections will be repeated periodically, and any faulting or fracturing of the cover rock adjacent to one of the monitoring wells will result in an increase in the rate of fluid accepted by that well.

Four of these monitoring wells have been constructed: one 200 ft north and a little east of the the injection well (N 200 E), one 175 ft to the northwest (NW 175), one 200 ft to the south (S 200),

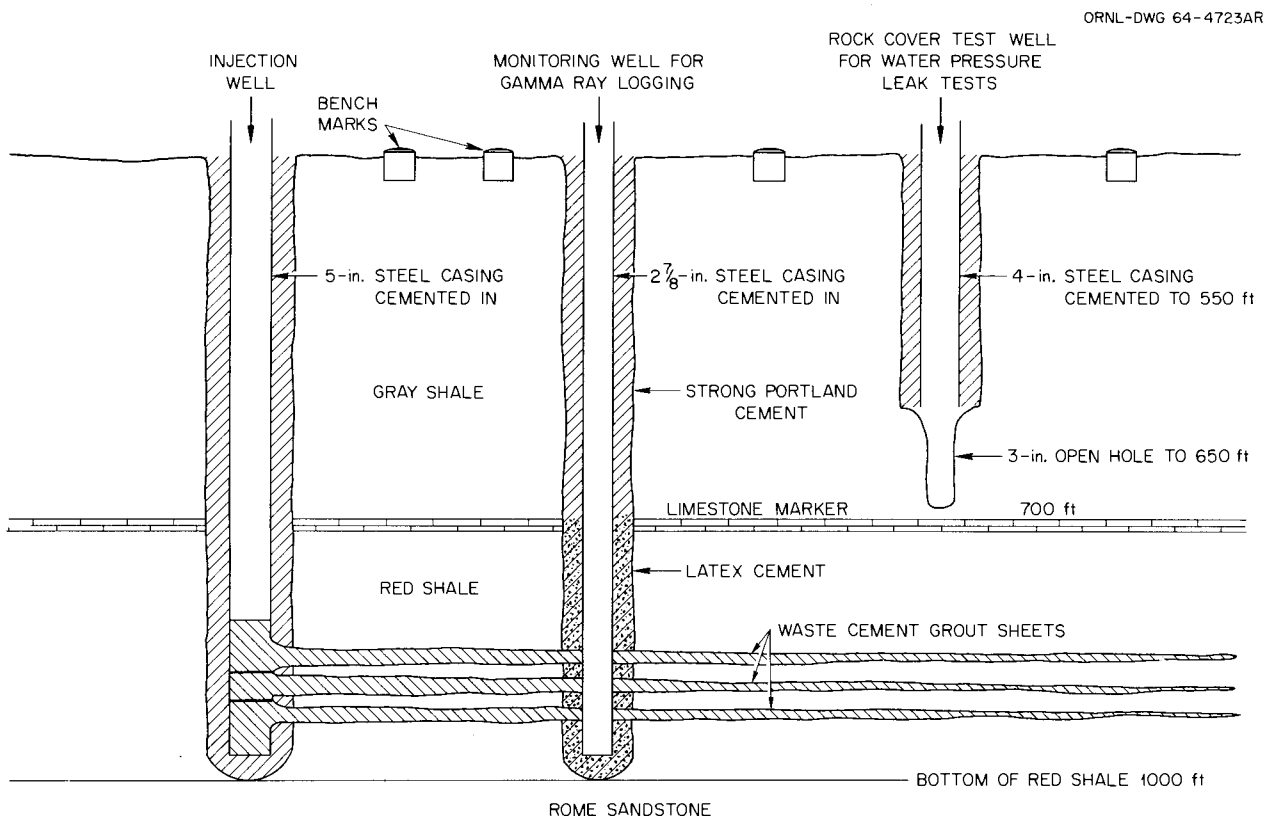

Fig. 2.9. Relation of Rock Cover Monitoring Wells to Injections.

and one 125 ft to the northeast (NE 125). During some of the early test injections the water levels in these wells were observed to change; sometimes the water level rose and the well overflowed; sometimes the water level fell. In April of 1967 three of the four wells were carefully filled to the top with water and equipped with pressure gages. Figure 2.10 shows the changes in pressure observed in these three wells during injection ILW-2A. The pressure in well N 200 E started to increase rapidly shortly after the injection started and continued to rise for about 270 min, after which the pressure declined slowly. The pressure in well NW 175 started to rise very slowly after about 160 min; the pressure in well S 200 decreased very slowly. There is no comparable record for well NE 125, as it was left open, but the water level was observed to rise during the injection, and the well overflowed. The next day the well was still flowing very slowly. A pressure gage was installed, and the pressure rose to 13.5 psi, where it remained steady.

Injection ILW-2A was made into a fracture at a depth of 862 ft and comprised a total volume of about 122,000 gal. This fracture is about 200 ft below the level of the bottom of the rock cover monitoring wells. When the fracture passes below the bottom of one of the monitoring wells, the overlying shale is compressed, a little water is squeezed out of the shale into the uncased bottom portion of the well, and either the water level rises or, if the well is closed in, the pressure rises. However, if the fracture moves out from the injection well in a direction away from one of the monitoring wells, the cover rock is uplifted and slightly deformed in such a way as to reduce the vertical strain on the uncased portion of the well, a small volume of water is taken into the shale, probably along the bedding planes, and the pressure drops. The theoretical changes in the verti-

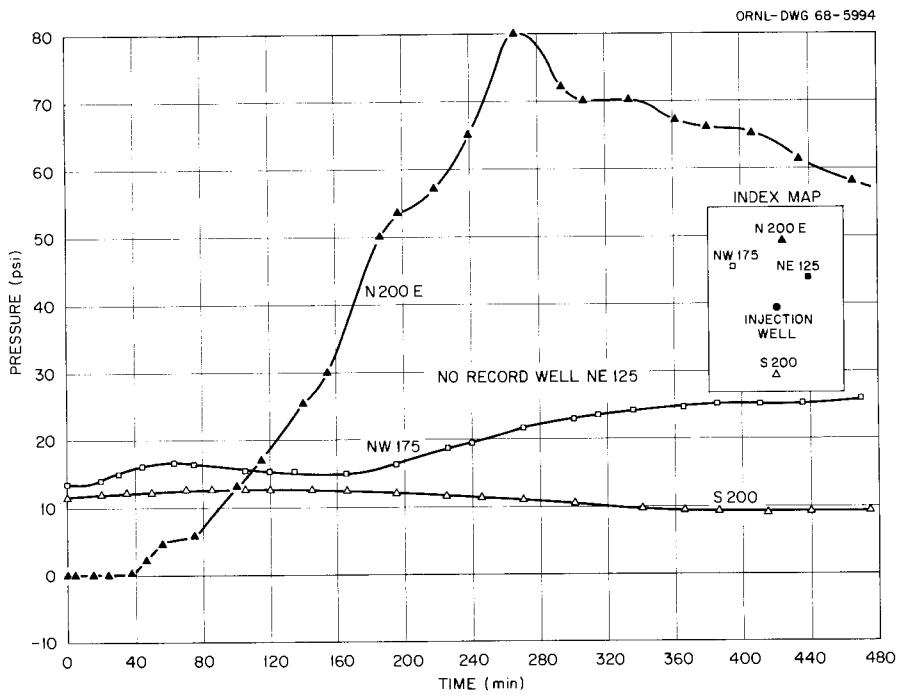

Fig. 2.10. Pressure Changes in Rock Cover Monitoring Wells; Injection ILW-2A, Apr. 20, 1967.

cal strain in the shale in the general vicinity of a fracture resulting from the formation of the fracture are shown in the right-hand side of Fig. 2.11, taken from McClain.[1] The record of pressure changes in the three rock cover monitoring wells shown in Fig. 2.10 and the observed rise in water level in well NE 125 strongly suggest that this fracture, at least at first, moved out from the injection well to the north and northeast. The drop in pressure in well N 200 E after about 270 min of pumping suggests that at this time a new fracture formed which probably moved to the east and northeast but not to the north. We know from earlier work that a single fracture does not move out in all directions from the injection but that it has the shape of a fan, with an angle at the well in some cases perhaps as narrow as 30° and in other cases perhaps as wide as 100°.

Figure 2.12 shows the pressure changes in the rock cover monitoring wells during injection 2B, which was made into the same slot at 862 ft and which comprised a little over 100,000 gal of slurry. After about 280 min the pressure in well NW 175 started to rise. There was a slight drop in pressure in well N 200 E; the pressure in the other two wells changed very slightly. This fracture apparently moved out to the northwest.

Figure 2.13 shows the pressure changes in the rock cover monitoring wells associated with injection ILW-3A, when about 40,000 gal of slurry was injected also into the fracture at 862 ft. This injection appears to have gone out to the northwest. Injection 3B, made the next day into the same slot, comprised a little over 100,000 gal of slurry; the data shown in Fig. 2.14 suggest that this injection went out to the east, because there is a pressure rise in wells NE 125 and S 200, although the rise is not as large as some of those observed previously in other rock cover monitoring wells. The condition of the shale adjacent to the uncased section of each of the rock cover monitoring wells undoubtedly affects the observed magnitude of the pressure change.

The injection of about 50,000 gal of water into a new fracture at 852 ft, to judge from the data shown in Fig. 2.15, produced a fracture which

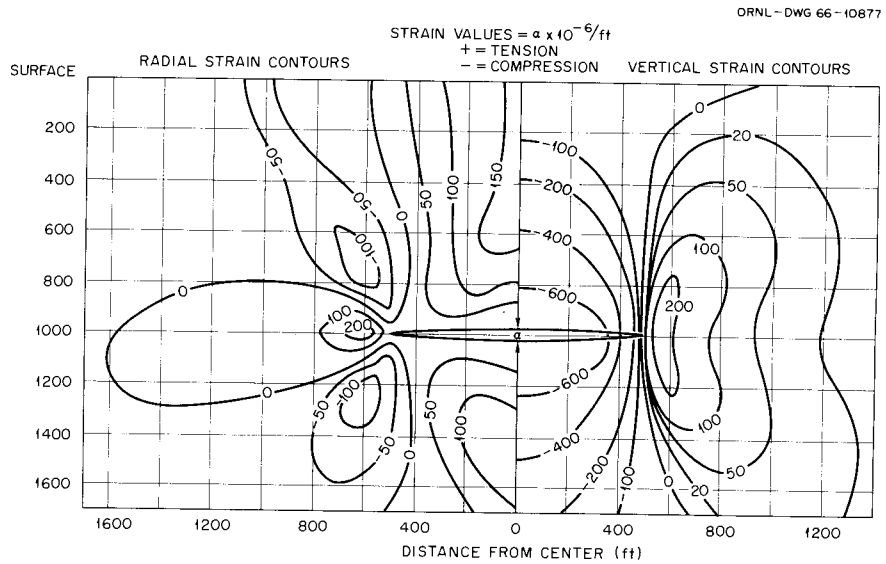

Fig. 2.11. Theoretical Strain Distribution in the Vicinity of a Horizontal Fracture.

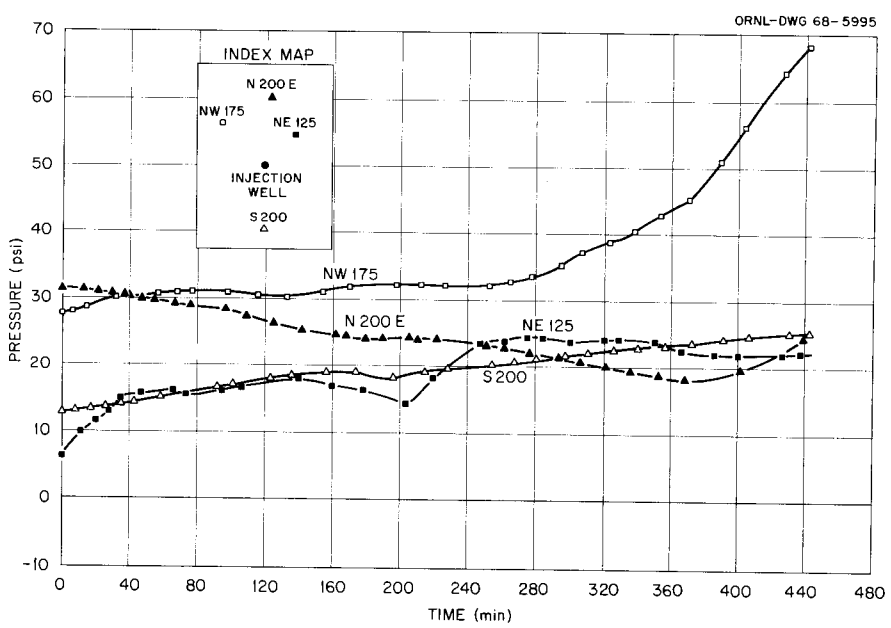

Fig. 2.12. Pressure Variations in Rock Cover Monitoring Wells; Injection ILW-2B, Apr. 24, 1967.

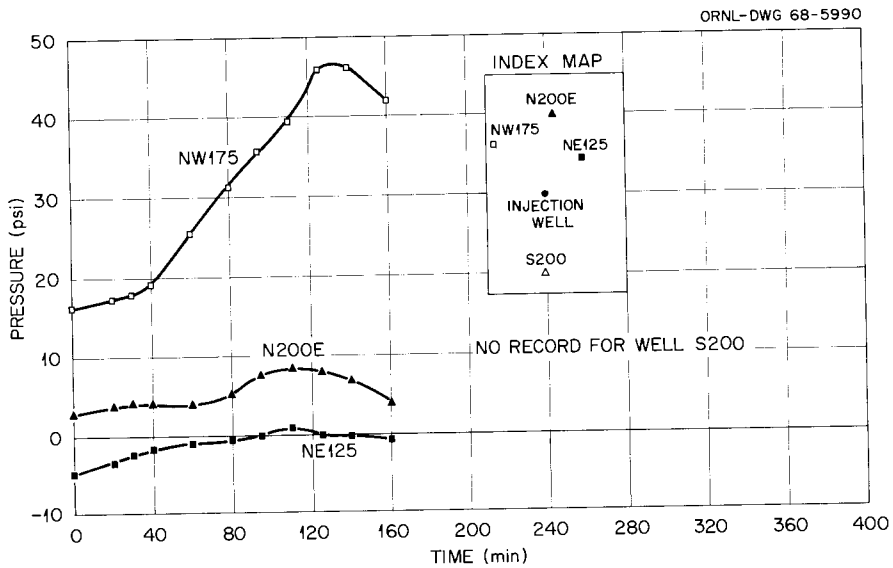

Fig. 2.13. Pressure Changes in Rock Cover Monitoring Wells; Injection ILW-3A, Nov. 28, 1967.

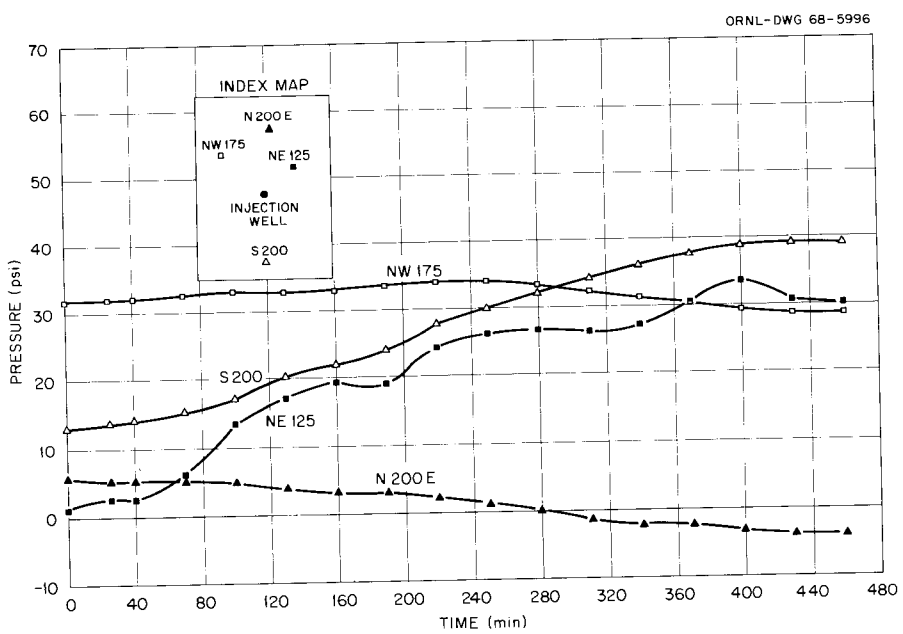

Fig. 2.14. Pressure Variations in Rock Cover Monitoring Wells; Injection ILW-3B, Nov. 29, 1967.

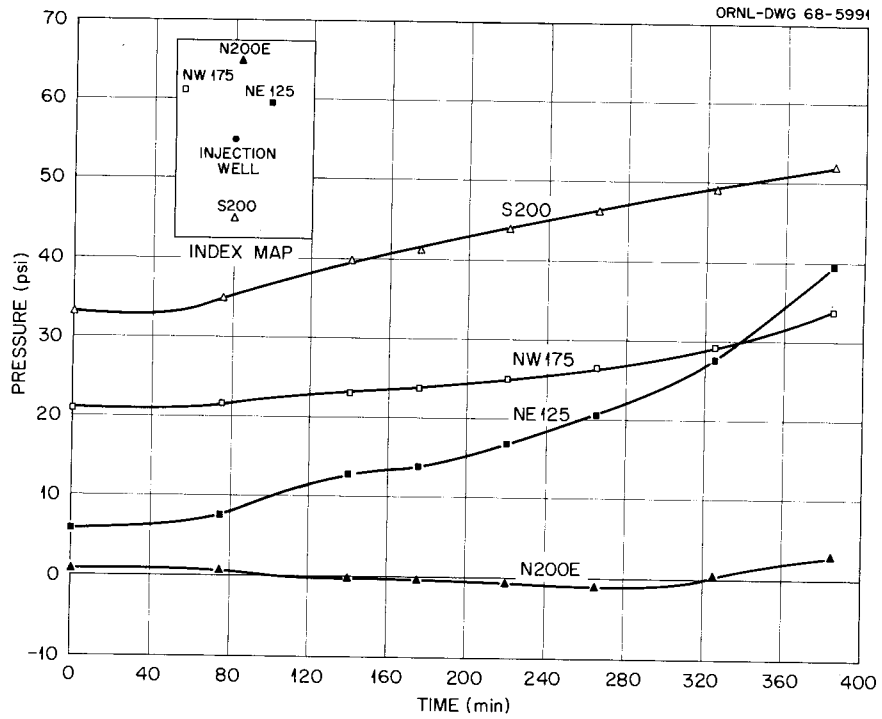

Fig. 2.15. Pressure Variations in Rock Cover Monitoring Wells; Water Injection Test, Dec. 13, 1967.

moved out to the east. The pattern of pressure changes in the four rock cover monitoring wells was similar to that produced by the previous injection, ILW-3B (Fig. 2.14). The next injection, ILW-4A, was made at 852 ft and comprised only 30,000 gal. It produced increases in pressure in wells S 200 and NE 125 and presumably spread out to the northeast, east,and south (Fig. 2.16). Injection ILW-4B, at 852 ft, made the following day, had a volume of about 67,000 gal (Fig. 2.17). In this case the most marked rise in pressure was seen in well NE 125 during the first 200 min of pumping. Following this, the pressure in well NE 125 remained constant as did the pressure in well NW 175, which earlier had risen slightly. The pressure in well N 200 E rose slowly and then fell. The pressure in well S 200 remained nearly constant for the first 120 min of pumping and then started to rise slowly. Apparently for the first 120 to 200 min the fracture moved out to the northeast, and then a new fracture formed which moved out to the south.

The preceding discussion is certainly much oversimplified. We know that during the injection of a slurry a series of fractures is formed, perhaps as many as five or six when over 100,000 gal of slurry is injected. A new fracture may move out in the same general direction as its predecessor, separated from it by a thin layer of shale, or it may move out in a new direction. The shale is certainly neither homogeneous nor isotropic, so that the changes of stress in the rock cover are probably more complex than is suggested by Fig. 2.9. The pressure changes of the water in one of the monitoring wells are probably more of a qualitative than a quantitative indication of the change in stress in the shale adjacent to the uncased section of the well. There is every indication, however, that these pressure changes can provide a potentially valuable insight into what happens when waste is injected into a deep subsurface fracture.

To date, there has been no attempt to correlate the apparent direction taken by any of the fractures, as estimated above, with the location of the fractures as determined by gamma-ray logging. At best the correlation will be difficult, since there are not enough of either type of well for

detailed plotting, the fracture pattern resulting from any one injection is complex, and the gamma-ray logging probe, until recently, would not plot properly the very high radiation fields produced in the observation wells by the waste-filled fractures. The correlation will, however, be undertaken in the near future.

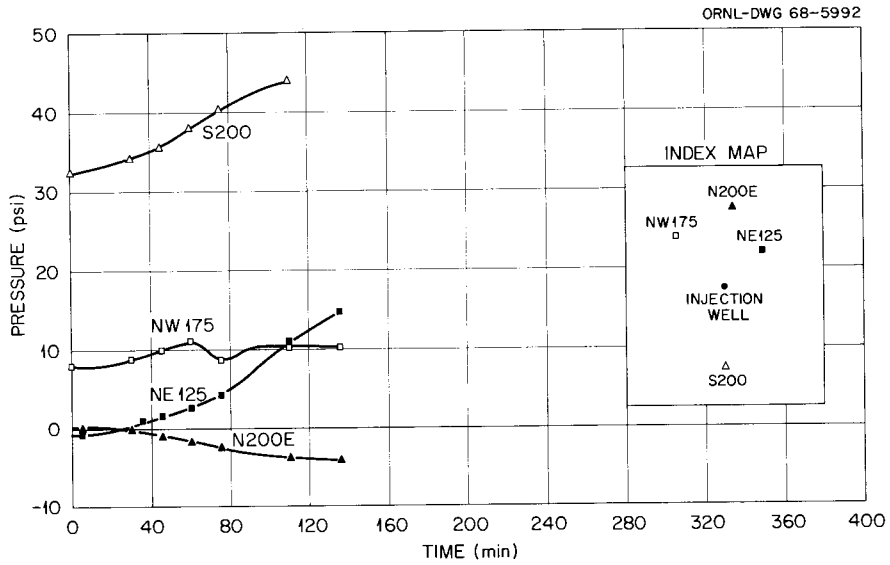

Fig. 2.16. Pressure Variations in Rock Cover Monitoring Wells; Injection ILW-4A, Apr. 3, 1968.

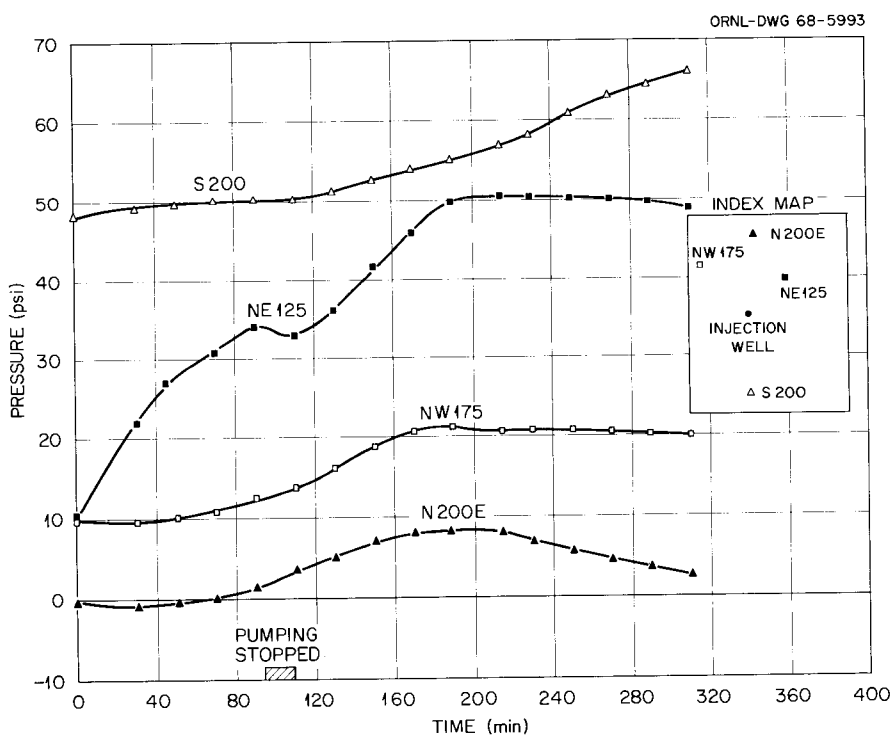

Fig. 2.17. Pressure Variations in Rock Cover Monitoring Wells; Injection ILW-4B, Apr. 4, 1968.

3. Disposal in Natural Salt Formations

R. L. Bradshaw
J. O. Blomeke[1]
W. J. Boegly, Jr.
F. M. Empson
T. W. Hodge, Jr.
B. L. Houser
T. M. Kegley[2]
T. F. Lomenick
W. C. McClain
J. J. Perona[1]
Florentino Sanchez[3]
A. M. Starfield[4]
H. J. Wyrick

PROJECT SALT VAULT

F. M. Empson
B. L. Houser
T. W. Hodge, Jr.
R. L. Bradshaw
W. C. McClain
T. M. Kegley

As reported previously,[5] the radioactive phase of the demonstration disposal of high-level radioactive wastes was completed by the end of June 1967. By the end of December 1967, the remainder of the mine experiments had been terminated, and preparations were made to place the Carey Salt Company's Lyons, Kansas, mine on a standby basis, beginning February 1968. Arrangements have been made for periodic service of the equipment left on standby and for periodic collection of selected items of data.

Radiation Dose to Salt

The radiation doses accumulated in the salt are shown in Fig. 3.1. The curve determined by the solid circles shows the originally calculated theoretical two-year dose based on Engineering Test Reactor (ETR) fuel having nominal irradiation. It

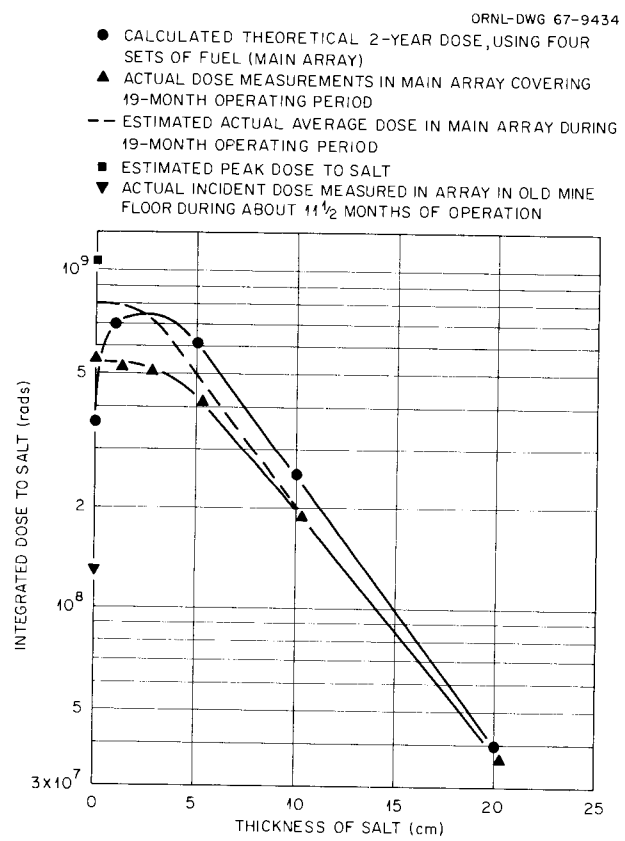

Fig. 3.1. Comparison of Measured and Calculated Doses to Salt.

[1]Chemical Technology Division.

[2]Metals and Ceramics Division.

[3]Oak Ridge Associated Universities Summer Student Trainee.

[4]Consultant, University of Minnesota, Minneapolis, Minn.

[5]K. Z. Morgan *et al.*, *Health Phys. Div. Ann. Progr. Rept. July 31, 1967*, ORNL-4168, pp. 18–31.

was expected that the peak dose to the salt would be about 7 or 8×10^8 rads at a depth of $2\frac{1}{2}$ cm into the salt, due to the buildup factor. The curve with upright triangles, based on actual measurements, indicates that the peak dose after about 19 months of operation in the mine was approximately $5\frac{1}{2} \times 10^8$ rads, occurring at the wall of the hole. The estimated actual average dose to the salt over the length of the hole is shown by the dashed line and is about 8×10^8 rads, for reasons explained in the next paragraph. The peak salt dose is shown by the square and is about 10^9 rads. The measured dose at the wall of the hole in the array in the old mine floor which received the ETR fuel after it had remained about six months in the main array in the experimental area was a little over 10^8 rads, as shown by an inverted triangle. The average dose over the length of the hole would be higher.

Since the incident dose is measured at a point even with the junction between the fuel assemblies, the value read is below the average along the canister.[5] The peaks occur at the midpoint of the fuel assemblies, due to nonuniform flux in the reactor. The average dose over the can length is about 1.4 times the dose at the junction, and the peak dose is about 1.9 times the junction dose.

Disassembly of Demonstration Equipment

The three arrays were completely disassembled, and a detailed examination was made of the equipment. No serious deterioration of the equipment was found. The following observations were made:

1. The lower liners from the arrays in rooms 1 and 5 showed no sign of significant corrosion. The surfaces were generally bright, and mill stencils could still be clearly seen on the surfaces. No electric heaters had failed, and the equipment was good for continued operation.
2. The carbon steel lower liners in the room 4 array had the general appearance of a piece of hot steel left in a salt mine for a period of months. They were covered with a heavy coat of rust. There was no sign of pitting or other accelerated corrosion.

The thermocouple cables were removed and stored on reels, and the temperature recorders were placed on a standby basis. Other equipment was either returned to ORNL or surplused.

Heated Pillar Test

The heated pillar test was terminated on October 9, 1968, after 11 months of operation. The movement of salt in the 20-ft-thick heated pillar and of the floor and roof of the two adjacent rooms is shown in Fig. 3.2. Since the 33-kw heating rate, divided equally along the two sides of the pillar, represents approximately three times the heat flux into the pillar if the rooms were filled with actual solidified waste, the movement shown by Fig. 3.2 is greater than would be expected to occur in an actual disposal operation over the same time period.

The 22 heaters operated throughout the experiment without difficulty. The carbon steel units are rusty but show no sign of penetration. All of the heaters were removed from the holes, and selected ones were returned to ORNL for further examination.

Effect of Water Release

Two modified pillar heaters (heaters installed in sealed cans and backfilled with salt as in an actual disposal operation) were operated as a part of the pillar-heating test with the added objective of evaluating the effect of water in relatively pure salt on 304L stainless steel and on carbon steel. The heater made of carbon steel operated approximately 16 months, maintaining pressure throughout the period. When removed from the hole, the surfaces of the heater and of the pipe and the conduit to the surface were superficially corroded, but they showed no sign of serious attack.

The second modified heater, fabricated of stainless steel, lost pressure about three months after being placed in operation. The heating elements did not fail, however, and the heater remained in service for the duration of the test. The leak was found to be due to severe corrosion of the $\frac{1}{2}$-in. sched 40 pipe which constituted the connection to a pressure gage at the floor level. In addition to the severe corrosion of the pipe and of the conduit, a crack was found in the wall of the end section (unpressurized) of the heater can.

An additional group of heaters (designated as the Simulated Waste Container Test or SWCT) were operated in the original mine floor and in the pure salt floor of the experimental area. Six heaters

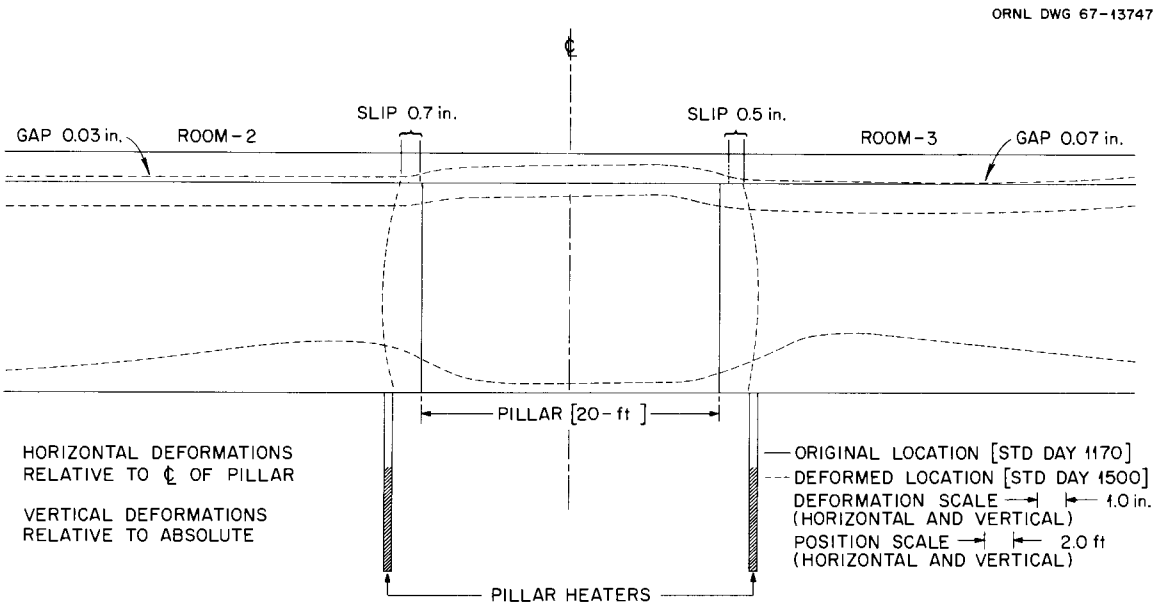

Fig. 3.2. Deformation of Pillar and Adjacent Rooms in Heated-Pillar Test.

were utilized, three of 304L stainless steel and three of carbon steel. Two of each were located in the original mine floor in a square array of 10-in.-diam by 12-ft-deep holes about 50 ft from the room 5 (floor) array. One of each was located in the experiment entry near the electrical (room 4) array. These heaters were fabricated of 6-in. sched 40 pipe, with electrical heaters installed in a sealed section about 6 ft long. An open extension of the heater can, equipped with a gasketed cover plate, served as a terminal box for heater leads, which were conducted to the floor through a plastic tube. A pressure connection was made to the floor level through a $\frac{1}{4}$-in. steel tube.

The two heaters in the experimental entry were located in similar holes with the bottom 12 ft below the floor. Those in the original mine floor were located approximately 1 ft higher in order to place the center of the heated section at the same elevation as a major shale seam. The holes were backfilled with crushed salt after placing the heaters.

Design of the SWCT called for a power input of 4.3 kw per can, with a possible increase of the power in the two experimental area cans to 8 kw per can. It was expected that 4.3 kw should give a wall-of-the-hole temperature of about 200°C after several months. However, it was not possible to follow this design because of difficulty with the heaters. The main difficulty was loss of heaters due to shorting or failure of heater terminals resulting from leakage of moisture into the enclosed, but not sealed, section containing the terminals. In addition, leaks in the pressure connections occurred, similar to that encountered with the stainless steel modified pillar heater.

In the experimental entry, can and salt wall temperatures for heater 1 were approximately 200°C before failure of one heater element. Heater 2 reached a maximum can temperature of about 300°C and a salt wall temperature of 240°C before leveling out at about 220°C can wall temperature and 190°C salt temperature. The four heaters in the original mine floor operated more erratically, due to failure of individual heater elements. Maximum can temperatures were in the range of 360 to 400°C; salt wall temperatures were 250 to 280°C.

The SWCT cans were removed for evaluation of the corroded conditions observed.

Metallurgical Examination of Pillar and SWCT Heaters

Examination of the modified pillar heaters and SWCT heaters revealed that gross cracking had occurred in both the 304L stainless steel pillar heater (operated in the pure salt of the experimental area) and in one of the 304L SWCT heaters. Also, the 304L $\frac{3}{4}$- and $\frac{1}{4}$-in. pipes used on the modified pillar heater as electrical conduit and for a pressure connection to the floor were severely corroded. The cracking and severe corrosion were in those parts of the heaters which were cooler and at which water may have condensed. Figure 3.3 shows the crack in the cold section of the modified pillar heater. A similar crack was observed in one of the SWCT heaters. The lower section of heater, to the left of the weld in the picture, and the similar section of the SWCT were pressurized with air during the investigation and showed no loss of pressure in more than 72 hr. Metallographic examination of the 304L stainless steel modified pillar heater revealed the presence of stress corrosion cracking. Transgranular cracks were found in a metallographic sample removed from the center of the sealed heated portion, as well as in the cool portion, of the heater assembly. Although the sealed heated portion had held air pressure, more than half of the wall thickness was penetrated by the cracks. Also, pits as great as 0.14 mm (Fig. 3.4) deep were observed at the center of the heated portion. Figure 3.5 shows a stress corrosion crack penetrating about half the wall thickness.

Metallographic examination of the carbon steel modified pillar heater showed a corroded outer surface but no evidence of penetration. There was apparently little, if any, loss of wall thickness to corrosion. Measurement of a section taken 40 in. below the top of the sealed heated portion indicated a thickness of 0.239 in. as compared with a nominal wall thickness of 0.237 in. for 4-in. sched 40 pipe.

Metallographic examination of the 304L stainless steel SWCT heater from the original mine floor also revealed transgranular stress corrosion cracks. The sample of the heated portion taken 2 ft below the top of the heated section contained

Fig. 3.3. Crack in the Cold Section of the Modified Pillar Heater.

Fig. 3.4. Pits, 0.14 mm Deep, at the Center of the Heated Portion of 304L Stainless Steel Modified Pillar Heater.

cracks penetrating half of the wall thickness and pits as great as 0.4 mm deep. Cracks almost completely penetrating the wall were found in the pressurized section near the cool end of the heater.

Figure 3.6 shows stress corrosion cracks occurring in the heated section of the stainless steel SWCT in the original floor. Two cracks may be seen partially penetrating the 0.280-in. wall thickness of the heater.

Five conditions must be satisfied for stress corrosion to occur in austenitic stainless steel:[6]

1. The steel must be in a state of tensile stress.
2. Liquid-phase water must be present.
3. An elevated temperature is necessary. The minimum temperature is frequently stated to be 50°C.
4. The water must contain chlorides.
5. Oxygen must be present. Concentrations in the order of parts per million are sufficient.

All the above conditions were met in the experimental operation of the modified pillar heaters and the SWCT heaters. The first condition is always present in practice, since stainless steel parts are stressed in some way during fabrication. The second condition will probably occur during either the heating or cooling part of the operation. The third, fourth, and fifth conditions are inherent in the waste-disposal operation and are unavoidable. The second condition, presence of a liquid water phase, may have been the principal factor in the occurrence of stress corrosion in the modified pillar heater and the SWCT heaters.

[6]T. Marshall, *Corrosion* 14, 61 (March 1958).

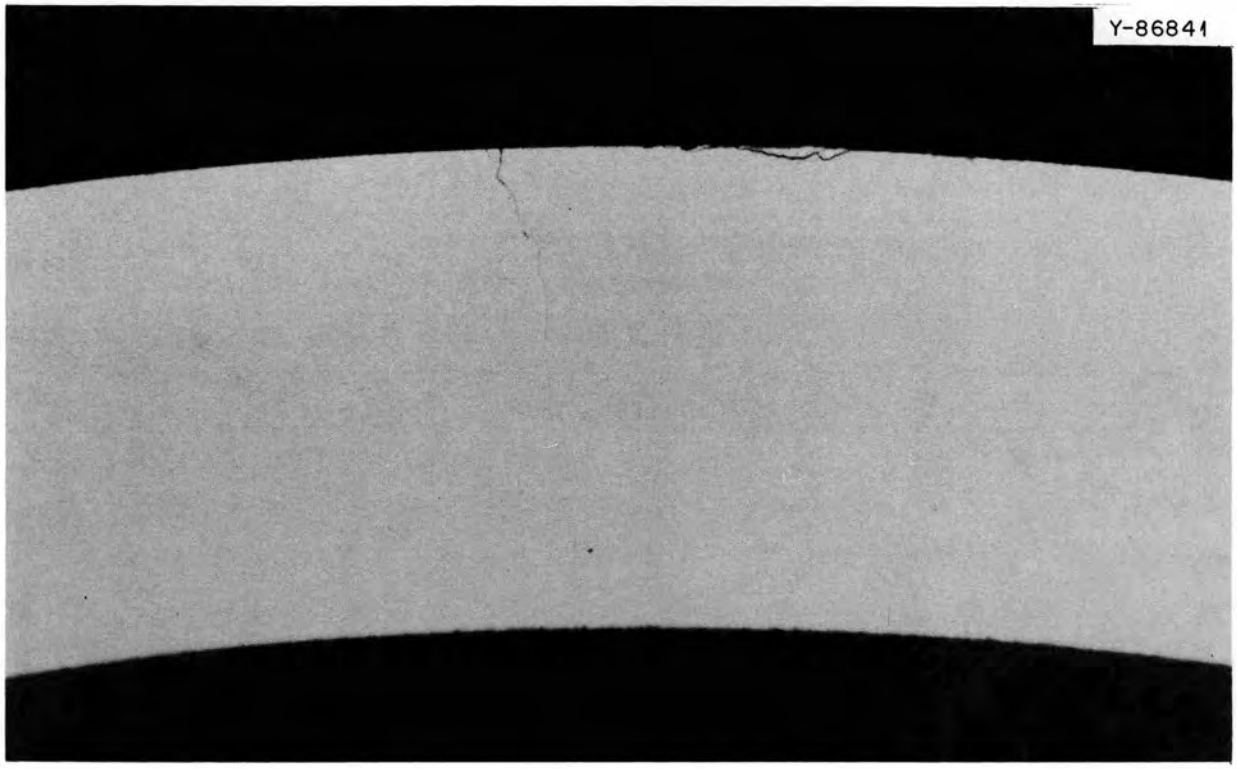

Fig. 3.5. Stress Corrosion Crack Penetrating About Half the Wall Thickness.

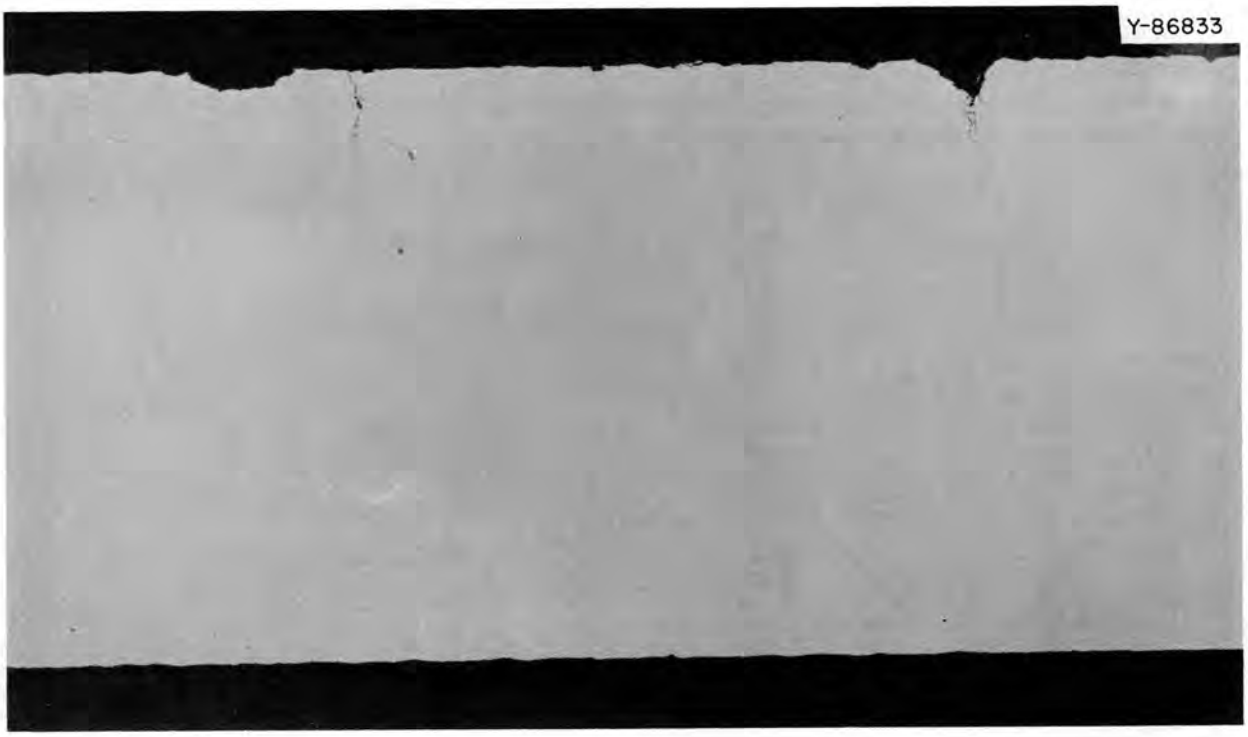

Fig. 3.6. Stress Corrosion Cracks Occurring in the Heated Section of the Stainless Steel SWCT in the Original Floor.

Core Preparation – Environmental Testing

It is planned to carry out environmental tests of containers of actual solidified waste produced in the Waste Solidification Engineering Prototype at Pacific Northwest Laboratories. One of the environments of interest is that which would exist in a disposal facility in a salt mine. Salt cylinders were prepared by drilling 10-in.-diam holes in $15\frac{3}{16}$-in.-diam cores. Five cylinders, 12 ft long, were prepared and shipped to Pacific Northwest Laboratories.

DISPOSAL-IN-SALT PROTOTYPE-FACILITY STUDY

R. L. Bradshaw W. C. McClain
J. O. Blomeke[1]

At the request of the AEC, efforts have been initiated to explore the next step in the development of radioactive waste disposal in natural salt formations. Although the Project Salt Vault experiment successfully demonstrated the technical feasibility of the method, several questions remain to be resolved before salt disposal could be conducted as a routine operation by a commercial concern. The current study is an examination of several alternative sites for an actual disposal facility and includes information on items such as (1) when will a disposal facility be needed, (2) how big should it be, (3) what minimum capital investment is required to begin disposal operations, and (4) what are the relative operating costs of the several alternative sites, considering especially the shipping distance from the point of waste generation.

ECONOMICS OF DISPOSAL IN SALT

R. L. Bradshaw W. J. Boegly, Jr.
J. O. Blomeke[1] J. J. Perona[1]

This is a joint Health Physics and Chemical Technology study of the cost of disposing of high-

level solidified power-reactor wastes produced by the pot calcination process and contained in cylinders ("pots") 6, 12, and 24 in. in diameter and 10 ft long. One disposal facility handles the entire output from a 15,000-Mw (electrical) [56,000 Mw (thermal)] nuclear power economy. The waste products result from the processing of 1500 metric tons/year of 10,000 Mwd/metric ton burnup uranium converter fuel and 270 metric tons/year of 20,000 Mwd/metric ton burnup thorium converter fuel. Disposal of the resulting Purex and Thorex wastes in both acid and neutralized forms and of Thorex wastes made into an alumina-silica-borax-type glass is considered. The study has been completed and published.[7]

A conceptual design of a salt mine especially for disposal of high-level wastes was developed, and the cost of the entire mining and disposal operation was calculated. The mine is 1 sq mile in area and is 1000 ft below the surface. The operating life of the mine for disposal of the wastes from the assumed economy was calculated, using rather conservative mine stability criteria for various waste types, pot sizes, and waste combinations.

[7]R. L. Bradshaw *et al.*, *Evaluation of Ultimate Disposal Methods for Liquid and Solid Radioactive Wastes, VI: Disposal of Solid Wastes in Salt Formations*, ORNL-3358.

The life of the mine was found to range from about $12\frac{1}{2}$ years for waste aged 1 year at the time of burial to about 70 years for wastes aged 30 years at burial (Fig. 3.7). The initial capital outlay required to start waste-disposal operations ranges from about $8.4 million to $10.7 million. Total annual costs for operating the facility (both capital and operating) were found to vary from a range of about $2.5 million to $2.7 million for a 1-year-old waste to a range of about $1.0 million to $1.3 million for 30-year-old wastes, again depending on waste combinations and pot sizes (Table 3.1). The figures in Table 3.1, or for any other waste age and combination, may be obtained by (1) determining the life of the mine from Fig. 3.7 for the waste combination desired, (2) determining the cost as a function of the life of the mine from Fig. 3.8, (3) determining the number of pots per year from Table 3.2, and (4) determining the cost as a function of the number of pots per year from Fig. 3.9.

Using present worth considerations and a 4% interest rate, the money to be set aside annually at the time of waste generation ranged from about $2.4 million to $2.6 million for a 1-year-old waste to about $0.3 million to $0.4 million for a waste 30 years old at the time of disposal (Table 3.1). In terms of cost per kilowatt-hour of electricity generated, this corresponds to about 18 to 20 $\times 10^{-3}$

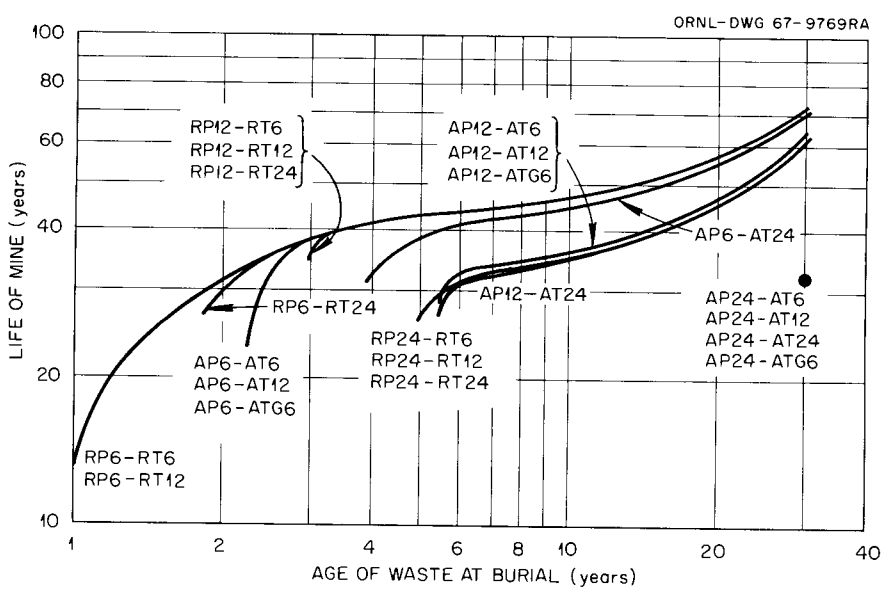

Fig. 3.7. Life of Mine as Function of Age at Burial for Various Combinations of Waste Type and Vessel Diameter.

Table 3.1. Total Costs of Operating the Disposal Facility as a Function of Waste Age at Burial for Waste Combinations Which Give Maximum and Minimum Costs

Age at Burial (years)	Waste Combination[a]	Annual Costs (millions of dollars per year)			Present Value	
		Costs Based on Life of Mine	Costs Based on Pots per Year	Total	Millions of Dollars per Year	Mills per Kilowatt-Hour of Electricity
						$\times 10^{-3}$
1.0	RP6-RT6	2.13	0.55	2.68	2.58	19.5
	RP6-RT12	2.13	0.35	2.48	2.38	18.1
1.8	RP6-RT6	1.19	0.55	1.74	1.62	12.3
	RP6-RT12	1.19	0.35	1.54	1.44	10.9
2.43	RP6-RT6	1.08	0.55	1.63	1.48	11.2
	RP6-RT24	1.10	0.31	1.41	1.28	9.7
3.0	RP6-RT6	1.03	0.55	1.58	1.40	10.6
	AP6-AT12	1.03	0.20	1.23	1.09	8.28
4.0	RP6-RT6	0.98	0.55	1.53	1.31	9.90
	RP12-RT24	0.98	0.19	1.17	1.00	7.58
5.0	RP6-RT6	0.97	0.55	1.52	1.25	9.46
	RP12-RT24	0.97	0.19	1.16	0.95	7.23
5.5	RP6-RT6	0.96	0.55	1.51	1.22	9.24
	RP12-RT24	0.96	0.19	1.15	0.93	7.05
6.0	RP6-RT6	0.96	0.55	1.51	1.19	9.03
	RP12-RT24	0.96	0.19	1.15	0.91	6.88
10.33	RP6-RT6	0.92	0.55	1.47	0.98	7.42
	RP12-RT24	0.92	0.19	1.11	0.75	5.66
20.0	RP6-RT6	0.86	0.55	1.41	0.64	4.83
	RP12-RT24	0.86	0.19	1.05	0.48	3.60
30.33	RP6-RT6	0.78	0.55	1.33	0.40	3.04
	RP12-RT24	0.78	0.19	0.97	0.29	2.21
	AP24-ATG6	1.15	0.22	1.37	0.42	3.16

[a]For explanation of nomenclature, see footnote for Table 3.2.

and 2 to 3×10^{-3} mill respectively (Table 3.1 and Fig. 3.10).

These costs are a relatively small portion of the cost of competitive nuclear power. In fact, previous studies[8] have shown that the estimated cost of the entire waste-management scheme, from conversion to a solid through disposal in salt, represents only about 1% of 2-mill/kwhr power.

The disposal-in-salt costs in this study do not include the effects of charges or credit for the salt which must be disposed of (about 50% of that mined). Since the quality of the salt will likely be poor (containing considerable quantities of shale), it may not be salable. However, if it is necessary to dissolve it and dispose of the brine in a deep porous formation, the additional cost will not be prohibitive.

[8]J. O. Blomeke *et al.*, "Estimated Costs of High-Level Waste Management," *Proceedings of International Symposium on Solidification and Long-Term Storage of Highly Radioactive Wastes, Richland, Washington, February 14–18, 1966*, CONF-660208, pp. 830–43 (November 1966).

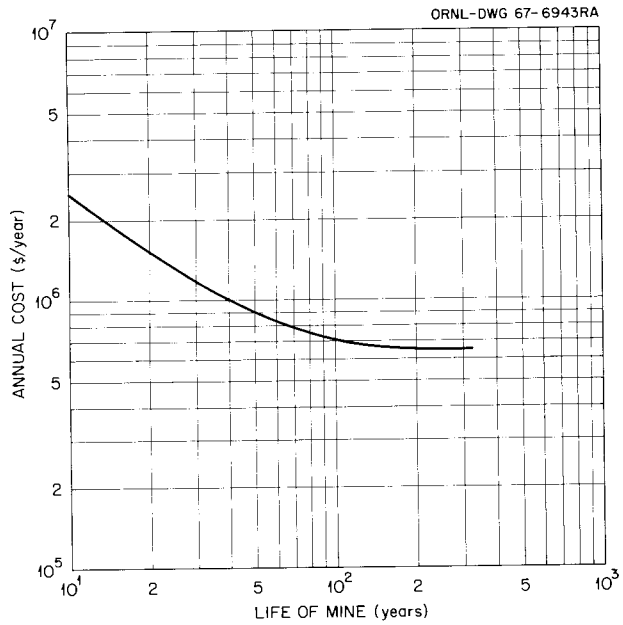

Fig. 3.8. Total Annual Costs for Items Which Are a Function of the Life of the Mine.

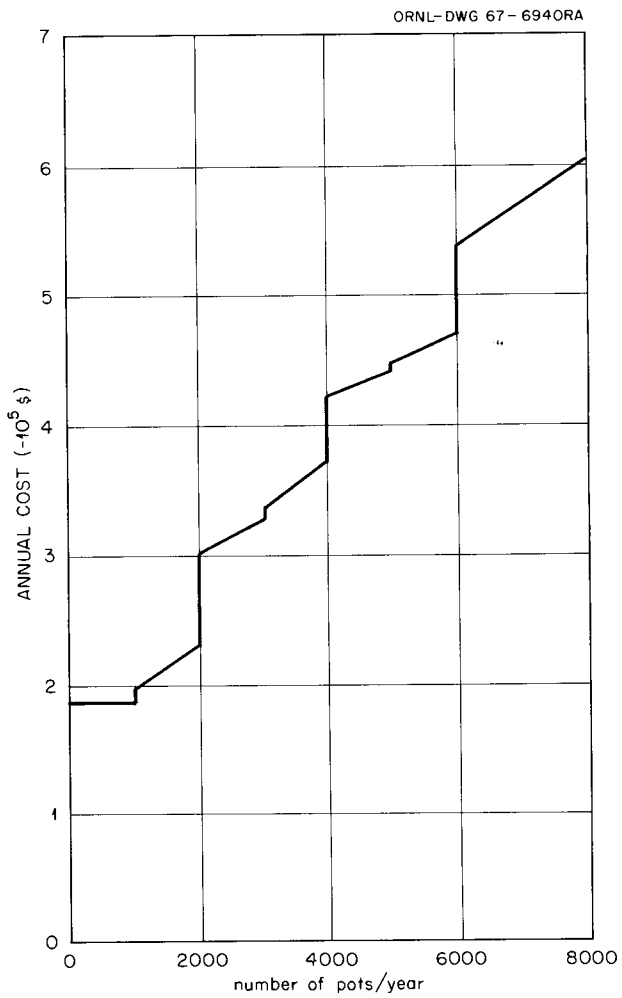

Fig. 3.9. Total Annual Costs for Items Which Are a Function of the Number of Pots per Year.

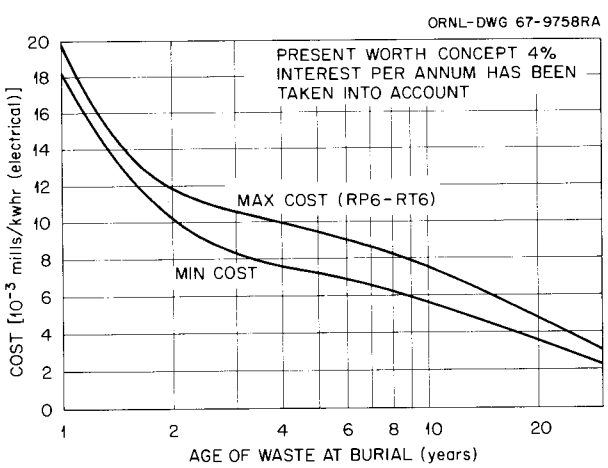

Fig. 3.10. Total Costs Which Must Be Charged to Power Generation for Disposal of Wastes in Salt Mine.

Table 3.2. Life of Mine and Number of Pots per Year for Various Waste Combinations

Age at Burial (years)	Possible Combinations[a]	Life of Mine (years)	Number of Pots per Year
1.0	RP6-RT6	12.5	6430
	RP6-RT12	12.5	3348
1.8	RP6-RT6	29.5	6430
	RP6-RT12	29.5	3348
	RP6-RT24	26.3	2577
2.43	RP6-RT6	34.7	6430
	RP6-RT12	34.7	3348
	RP6-RT24	34.0	2577
	AP6-AT6	30.0	2315
	AP6-ATG6	30.0	2725
	AP6-AT12	30.0	1273
3.0	All previous combinations	37.8	Same as previous combinations
	RP12-RT6	34.8	4690
	RP12-RT12	34.8	1608
	RP12-RT24	34.8	837
4.0	All previous combinations	41.3	Same as previous combinations
	AP6-AT24	31.0	1012
5.0	All combinations possible at three-year age	42.9	Same as previous combinations
	AP6-AT24	38.5	Same as previous combinations
	RP24-RT6	25.5	4255
	RP24-RT12	25.5	1173
	RP24-RT24	25.5	402
5.5	All combinations possible at three-year age	43.3	Same as previous combinations
	AP6-AT24	39.9	Same as previous combinations
	RP24-RT6, 12, or 24	30.0	Same as previous combinations
	AP12-AT6	28.0	1621
	AP12-ATG6	28.0	2031
	AP12-AT12	28.0	579
	AP12-AT24	26.7	318
6.0	All combinations possible at three-year age	43.6	Same as previous combinations
	AP6-AT24	40.8	Same as previous combinations
	RP24-RT6, 12, or 24	31.7	Same as previous combinations
	AP12-AT6, G6, or 12	32.5	Same as previous combinations
	AP12-AT24	31.0	Same as previous combinations
10.33	All combinations possible at three-year age	47.0	Same as previous combinations
	AP6-AT24	44.6	Same as previous combinations
	RP24-RT6, 12, or 24	35.6	Same as previous combinations
	AP12-AT6, G6, or 12	36.1	Same as previous combinations
	AP12-AT24	35.0	Same as previous combinations

Table 3.2 (continued)

Age at Burial (years)	Possible Combinations[a]	Life of Mine (years)	Number of Pots per Year
20.0	All combinations possible at three-year age	56.7	Same as previous combinations
	AP6-AT24	55.0	Same as previous combinations
	RP24-RT6, 12, or 24	45.5	Same as previous combinations
	AP12-AT6, G6, or 12	46.3	Same as previous combinations
	AP12-AT24	45.5	Same as previous combinations
30.33	All combinations possible at three-year age	72.7	Same as previous combinations
	AP6-AT24	71.0	Same as previous combinations
	RP24-RT6, 12, or 24	62.7	Same as previous combinations
	AP12-AT6, G6, or 12	64.3	Same as previous combinations
	AP12-AT24	62.7	Same as previous combinations
	AP24-AT6	31.8	1448
	AP24-ATG6	31.8	1858
	AP24-AT12	31.8	406
	AP24-AT24	31.6	145

[a]AP = acid Purex; AT = acid Thorex; RP = reacidified Purex; RT = reacidified Thorex; ATG = acid Thorex glass. The numbers 6, 12, and 24 refer to the nominal pot diameters, in inches.

BRINE CAVITY MIGRATION STUDIES

R. L. Bradshaw Florentino Sanchez[3]

As mentioned in previous reports, it was found that small quantities of water trapped in so-called "negative crystals" or brine-filled cavities tend to migrate toward a heat source and into the disposal hole. This water posed no problem in the demonstration, since it was removed by the off-gas system, but, in order to determine approximate water inflow rates which might be expected in an actual disposal operation, a theoretical study was made, along with a few experimental measurements.

Theoretical Aspects

Previous theory on the migration of liquid inclusions in ice crystals by Hoekstra, Osterkamp, and Weeks[9] and later modified by Seidensticker[10] has been found applicable, with modifications, to the migration of negative crystals in rock salt. In this case the cavity contains saturated NaCl solution (along with other salts normally associated with evaporite deposits, which we have assumed can be neglected as a first approximation). The driving force for the migration of brine cavities through rock salt under the influence of a temperature gradient is considered to be the difference in solubility between the warm and colder sides of the brine cavity. The flux of solute J may be described by[9]

$$J = cv ,$$

where

c = concentration (g/cc),

v = rate of diffusion (cm/sec),

J = (g/cc × cm/sec) or (cm^2/sec × g/cc-cm).

[9]P. Hoekstra, T. F. Osterkamp, and W. F. Weeks, *J. Geophys. Res.* **70**(20), 5035–41 (1965).

[10]R. G. Seidensticker, *J. Geophys. Res.* **71**(8), 2180–81 (1965).

From Fick's law,

$$J = -D\frac{dc}{dx},$$

where D is diffusion coefficient (cm^2/sec) and dc/dx is concentration gradient (g/cc-cm). Hoekstra's final expression is

$$v(T) = -\frac{D(T)}{c(T)}\frac{dc}{dT}\frac{dT}{dx},$$

where T is temperature and dT/dx is the temperature gradient. The expression is negative, because migration is up gradient.

However, Seidensticker[10] showed that the rate of diffusion of solute is not exactly equal to the rate of migration of the cavity. His argument is based on the fact that the solid and liquid (saturated NaCl solution in our case) have different densities and different thermal gradients. The correction factors are[10]

$$\frac{G_l}{G_s} = \frac{3K_s}{2K_s + K_l}$$

and

$$\frac{\rho_l}{\rho_s},$$

where

G_l = thermal gradient of the saturated solution,

K_l = thermal conductivity of the saturated solution,

ρ_l = density of the saturated solution,

G_s = thermal gradient of the solid,

K_s = thermal conductivity of the solid,

ρ_s = density of the solid.

Our final expression for the rate of migration of negative crystals in rock salt is as shown below:

$$v(T) = -\frac{D(T)}{c(T)}\frac{dc}{dT}\frac{dT}{dx}\frac{3K_s}{2K_s + K_l}\frac{\rho_l}{\rho_s},$$

where

$D(T)$ = diffusion coefficient of NaCl in H_2O,

$c(T)$ = NaCl concentration per unit volume of solution,

dc/dT = rate of change of NaCl concentration as function of temperature,

dT/dx = thermal gradient in salt,

$\frac{3K_s}{2K_s + K_l}$ = factor to correct thermal gradient in salt to gradient in solution,

ρ_l/ρ_s = factor to correct solute (NaCl) diffusion rate to cavity migration rate,

K_s = thermal conductivity of solid NaCl,

K_l = thermal conductivity of saturated NaCl solution,

ρ_l = density of saturated NaCl solution,

ρ_s = density of solid NaCl.

Data on solubility[11] from 0 to 350°C were obtained, and the slope dc/dT of the solubility curve was approximated. Thermal conductivity data on saturated NaCl solutions from 10 to 150°C were found,[12] and above 150°C the thermal conductivity of water[13] was used since both curves follow each other closely. Thermal conductivity data on solid NaCl from 0 to 400°C have been published by Birch.[14] The correction factor for the difference in thermal conductivities is a linear function of temperature. Also, the densities for both solid NaCl from 0 to 50°C and saturated NaCl solutions[11] from 0 to 107°C are approximately linear functions of temperature and have been extrapolated linearly to higher temperatures.

Diffusion coefficients were calculated using the Stokes-Einstein model:[15]

$$D(T) = \frac{kT}{6\pi\eta r},$$

[11] D. W. Kaufmann, *Sodium Chloride*, pp. 592, 597, 612, 617, Reinhold, New York, 1960.

[12] Walter Unterberg, *Brit. Chem. Eng.* 11, 494–95 (June 1966).

[13] W. R. Gambill, *Chem. Eng.* **64**(2), 238 (February 1957) and **66**(7), 139–40 (Apr. 6, 1959).

[14] Francis Birch, *Thermal Consideration in Deep Disposal of Radioactive Waste*, National Academy of Sciences–National Research Council Publication 588, July 1958, p. 13.

[15] R. A. Robinson and R. H. Stokes, *Electrolyte Solutions*, 2d ed., p. 12, Eq. 1.7, Academic, New York, 1959.

where

D = diffusion coefficient,

k = Boltzmann's constant,

T = temperature, °K,

η = viscosity of water, g cm^{-1} sec^{-1},

r = molecular radius.

[In our case, we used the mean ionic radius[11] = $\frac{1}{2}$(0.95 A + 1.81 A) = 1.38 A, where the ionic radius of Na^+ = 0.95 A, Cl^- = 1.81 A.] According to the Stokes-Einstein model, the diffusion coefficient D is nearly exponential with temperature because of the dependence of viscosity[13,16] on temperature from 0 to 300°C.

Theoretical calculations were made with the aid of a computer program in which the solubility of saturated NaCl solution and the viscosity of water were interpolated by Lagrange's method using quadratics. Lagrange's method was also used to find the slope of the solubility curve. The thermal conductivity correction factor, the density of saturated NaCl solution, and the density of solid NaCl were curve fitted by a linear function. The most important characteristic of the model is that the migration rate is a function of temperature and directly proportional to temperature gradient, both of which can be measured directly from the NaCl crystal.

Experimental Aspects

Relatively pure salt crystals from the Hutchinson mine, Kansas, about $2\frac{1}{2}$ cm on a side and containing brine cavities at least 2 mm but not more than 1 cm across were placed on a hot plate. For salt temperatures around 200°C, where the experimental setup was run at room temperature, the four vertical sides were insulated with asbestos tape to slow down heat escape, and the top side was exposed to ambient temperature, because earlier work showed that under room-temperature conditions the surface heat escape of the crystal was not the same even between two opposite surfaces; consequently, unequal temperature gradients were obtained. However, insulation was not necessary below 100°C nor on experiments where the hot plate was enclosed in a temperature chamber, perhaps because the differences between the hot plate temperatures and the ambient temperatures were less; consequently, the differences in heat escape between two opposite surfaces were less. Six type K thermocouples, three on each of two opposite sides, were placed in $\frac{1}{8}$-in.-deep, $\frac{1}{32}$-in.-diam holes, drilled 1 cm apart, along the sides in a vertical direction. Temperature and temperature gradients were recorded on a Brown electronic temperature recorder. Although the temperature of the hot plate was controlled by a Variac, there was little control on the temperature gradient. Smaller gradients at higher temperatures, around 200°C, were obtained by placing the experimental setup in the temperature chamber, where ambient temperatures could be controlled; however, temperature gradients were still not reproducible. For salt temperatures around 100°C or less, a knife-blade heater was used to migrate brine cavities in a horizontal direction; it was interesting to note that cavity migration in a horizontal direction behaves the same as migration in a vertical direction.

Measurements on migration were made to within 0.1 mm with a comparator. The initial position of the negative crystal face nearest to the heat source was marked with a scalpel on the surface of the salt crystal. Measurements were made between the scalpel mark and the final position of the negative crystal face nearest to the heat source. Migrations were usually in the order of millimeters over a period of a day or two; however, at temperatures below 100°C cavities were migrated for about two weeks. Temperatures were read from the thermocouple nearest to the cavity or were taken as the average of the two nearest thermocouples, both on the same side, if the cavity happened to be about halfway between the two. (We are assuming identical temperatures on opposite sides.) Since the thermocouples were 1 cm apart, temperature gradients were taken to be the difference between the two nearest thermocouples, both on the same side. Since salt crystals can be shattered by thermal shock, temperatures on cold salt crystals were raised slowly over a period of about 30 min. Cooling was accomplished over a period of 30 min by turning the power off, but for experiments in the temperature chamber, the fan was left on, and the chamber door was pulled open about a centimeter.

[16] Lange's *Handbook of Chemistry*, 8th ed., p. 1708.

Results

The main objective of the experiment was to compare the results with the diffusion model and the hope was to obtain agreement at least within the right order of magnitude. Although our experimental work was not done with any high precision and even though the experimental setup was rather simple, the results were adequate. The experimental data (see Fig. 3.11) agree with theoretical calculations within the right order of magnitude.

The salt crystals were well maintained at steady-state temperatures within 5°C; and, although the temperature gradients were not reproducible, almost identical gradients, at least along two opposite sides, were obtained; but they were by no means constant with respect to the position along the sides. Therefore, at a given position along a side, the temperature gradient in the salt could only be estimated from the thermocouple readings. Another factor to be considered in comparing results is that measurements were made only on those crystals whose cavities did not rupture but whose cavities generally changed from a cubical shape to an oval shape and sometimes increased in volume due to creep expansions, while the diffusion model does not include the effects of change in shape or volume.

Using the migration rates indicated by the theoretical curve of Fig. 3.11, some calculations were made to determine what might be expected in an actual disposal facility. They were based on the temperature vs time and distance relationships for a typical high-level future solidified waste which were computed as a part of the "Disposal-in-Salt Economic Study Report." Assuming about ½ vol % water in the salt, one might expect a total inflow per disposal hole of perhaps 2 to 10 liters, taking place over a period of 20 to 30 years after burial. The peak inflow rate would occur at around one year after burial and be somewhere in the range of 200 ml to 1 liter per year per hole. This corresponds to about ½ to 3 ml per day per hole, a range similar to that estimated in the demonstration arrays. This water inflow rate would be expected to taper off and approach zero after 20 to 30 years. It is not likely that such volumes and inflow rates will cause any problems in a disposal facility.

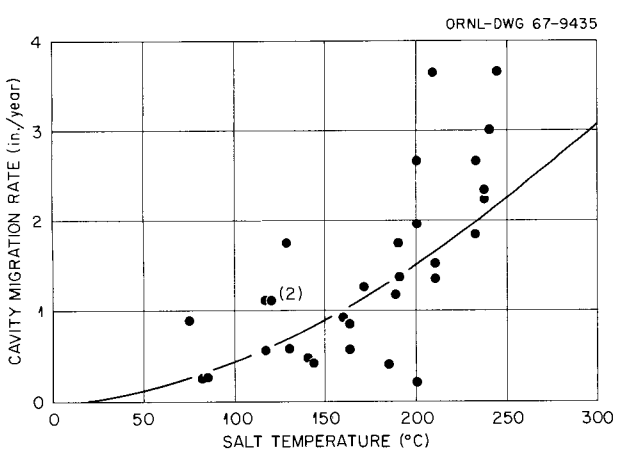

Fig. 3.11. Comparison of Theoretical and Experimental Migration Rates of Brine-Filled Cavities in Rock Salt. Data normalized to salt temperature gradient of 1°C/cm.

PILLAR-MODEL STUDIES[17]

T. F. Lomenick H. J. Wyrick

Effect of Pillar Shapes

In addition to tests on models having various pillar width-to-height ratios,[18] a few models having rectangular-shaped pillars were deformed. (All previously deformed model pillars were cylindrical in shape.) Tests were conducted on models having overall dimensions of 6.45 by 3.94 in. and with pillar dimensions of 5.01 and 2.51 in. The lengths of the pillars were, therefore, approximately twice their widths, and the salt extraction was about 50% or roughly the same as that for the cylindrical samples. Under these conditions, as shown in Fig. 3.12, significant differences in pillar deformation are apparent when the rectangular-shaped specimens are compared with the cylindrical-shaped specimens with the same horizontal cross-section areas. In Fig. 3.12, which shows the deformational curves for a rectangular-shaped specimen and a cylindrical-shaped specimen tested at 4000 psi and 22.5°C, it is apparent that

[17] T. F. Lomenick, *Accelerated Deformation of Rock Salt at Elevated Temperature and Pressure and Its Implications for High-Level Radioactive Waste Disposal* (thesis), ORNL-TM-2102 (March 1968).

[18] F. L. Parker *et al.*, *Health Phys. Div. Ann. Progr. Rept. July 31, 1966*, ORNL-4007, pp. 23–26.

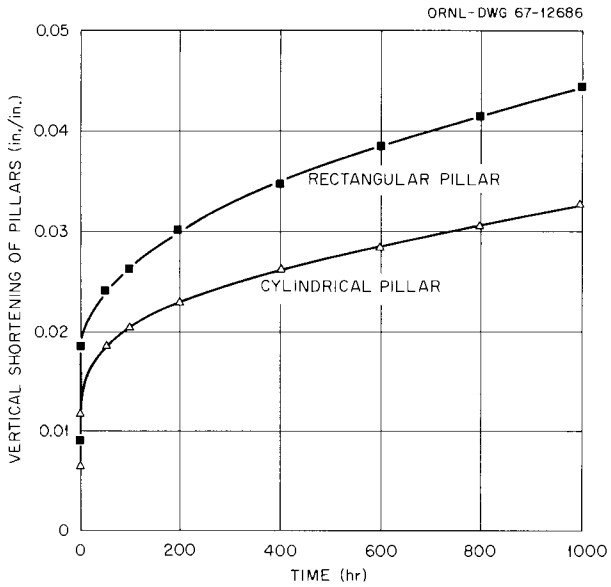

Fig. 3.12. Deformation of Cylindricol and Rectangular Pillor Models at 4000 psi and 22.5°C.

the rectangular-shaped pillar is weaker than its cylindrical counterpart. After 1000 hr of testing, the former had deformed approximately 40% more than the latter. Both samples were fabricated from salt taken in the mine at Lyons, Kansas. The same pattern of deformation was observed in dome salt (Grand Saline, Texas) at an axial load of 6000 psi and a temperature of 22.5°C. The deformation in that case was also about 40% more for the rectangular specimen than for the cylindrical one after about 1000 hr.

The greater strength of cylindrical pillars compared with their rectangular counterparts may be explained, in part, by the apparently high concentrations of stress at the corners of the rectangles, which lead to spalling of the salt at these locations and thus to reductions in the cross-sectional area over which the loads are distributed. Also, it would appear that, as the lengths of rectangular-shaped pillars increase in relation to their widths, the pillars will be correspondingly weaker. This is due, presumably, to reductions in the transmission of confining stresses from the roof and floor portions of the specimens to the pillars, as would be also the case for pillars having width-to-height ratios less than 4. It was shown earlier, in the case of specimens having shale partings at the tops and bottoms of the pillars, that when confining stresses are not transmitted into the pillars from the roofs and floors, the pillars are considerably weaker than when confining stresses are effectively transferred into the pillars.

Comparison of Salt from Various Localities

In order to make a general comparison of the deformational behavior of rock salt from various localities in the United States as well as from European deposits, tests were conducted at 4000 psi and at temperatures of 22.5 and 100°C on model pillars fabricated from salt samples taken in mines at Lyons and Hutchinson, Kansas; Retsof, New York; Detroit, Michigan; Grand Saline, Texas; Cote Blanche, Louisiana; and Asse, Northeast Germany. The Kansas salt is from a bedded deposit of Permian age, while the New York and Michigan salts are bedded and of Silurian age. The Grand Saline and Cote Blanche mines are situated in dome-type deposits. The Asse salt is mined from an anticlinal structure.

For the tests at 22.5°C, shown in Fig. 3.13, it is observed that the deformation curves for the Lyons, Hutchinson, Michigan, Cote Blanche, and Asse II mine deposits are strikingly similar; however, the Grand Saline mine salt deforms at a slightly greater rate, and the salt from the Retsof mine deforms, at least initially, at an even more accelerated rate.

As seen in Fig. 3.14 for the 100°C tests, there is a rather wide spread in the deformation associated with the various types of salt. The Lyons, Hutchinson, Cote Blanche, and Grand Saline curves are similar and show the largest amounts of pillar shortening after about 800 hr. The Retsof sample is observed to deform at a markedly slower rate. The curve for the Detroit salt is distinctly different from the others in that the deformation rate is initially slower, but it does not decrease as rapidly with time. Thus it appears from these tests that the total deformation for the Detroit salt

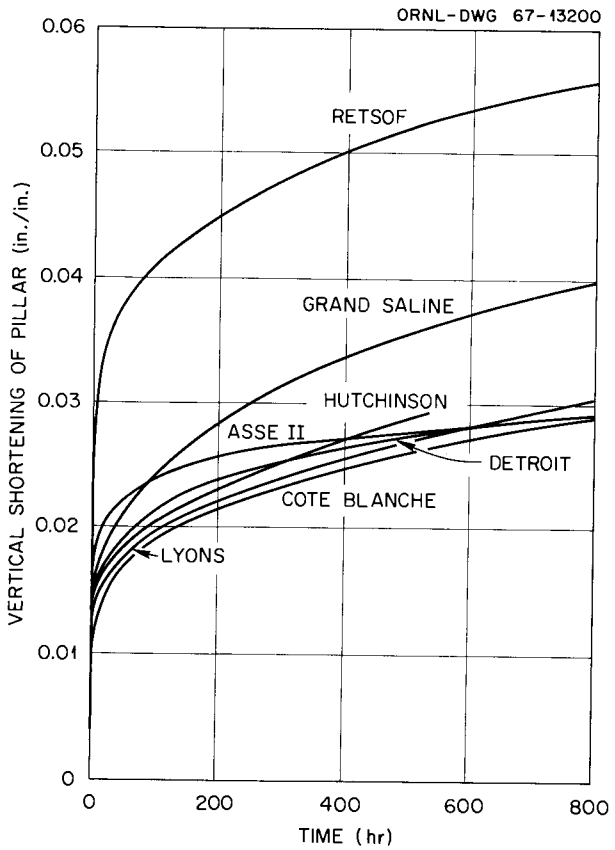

Fig. 3.13. Deformation of Pillar Models from Various Localities at 4000 psi and 22.5°C.

will eventually exceed that of the other deposits. The Asse II salt, under these conditions, appears to be stronger than the others.

The reasons for the differences in the behavior of the salts from the various localities as shown in these tests are not fully understood. The depths of the mines do not vary greatly, most being about 1000 ft deep; thus the overburden loads that the salts have been subjected to in Recent geologic time and the resulting prestrained conditions (before laboratory testing) of the samples would appear to be roughly the same. All of the salts are relatively low in insolubles; therefore the differences in deformation behavior would not appear to be explained by the presence of large quantities of impurities in some deposits. However, it is noted that the Retsof and Asse II salts, which appear to deform after the initial deformation at a slower rate than the other salts, contain about twice the quantity of water insolubles than do the samples from the other localities, with the exception of the Hutchinson salt. Using x-ray diffraction techniques, it was found that anhydrite was the principal water-soluble impurity for all samples except the Asse II salt, which contained polyhalite as its major impurity.

There do not appear to be any consistent differences in behavior related solely to the three structural types of deposits; namely, domal, anti-

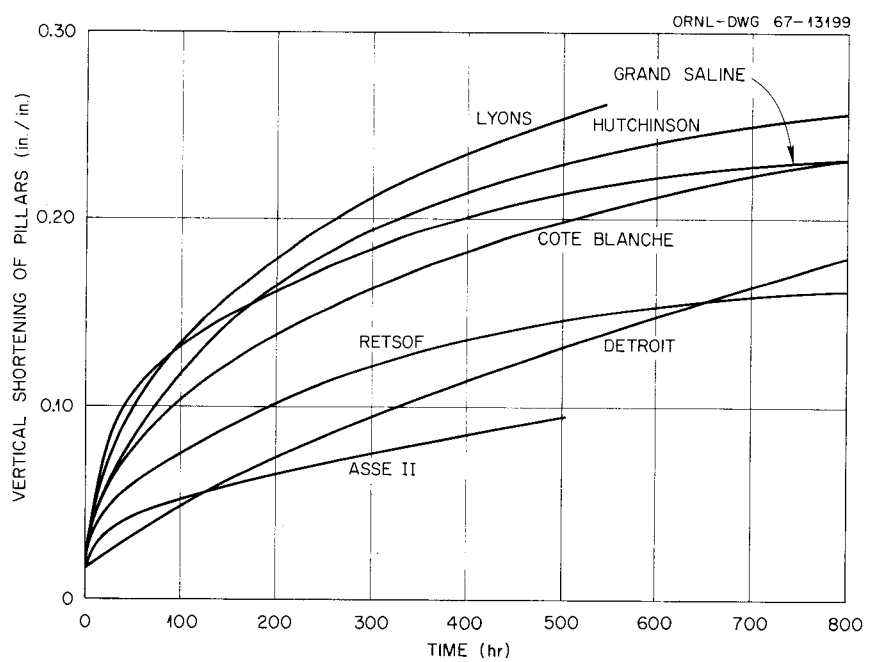

Fig. 3.14. Deformation of Pillar Models from Various Localities at 4000 psi and 100°C.

clinal, or bedded. Differences in grain size may account for some of the variations in deformation; however, all samples are extremely coarse grained, with the exception of the Retsof and Asse II salts. The Retsof salt is unique in that there is a pronounced lack of grain intergrowth, and the grains are apparently not firmly cemented together; thus the texture of the salt is somewhat friable. This may account for the high initial deformation rate of the Retsof salt, since some compaction and reorientation of grains would be expected to occur when the salt is loaded initially. Perhaps the thermal expansion of the salt was instrumental in reducing the intergranular voids for the 100°C test, which did not experience the extremely rapid initial deformation as did the sample tested at 22.5°C.

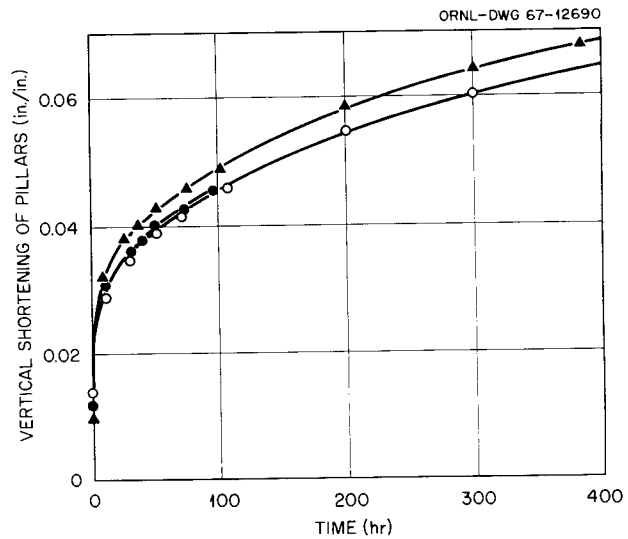

Fig. 3.15. Deformation of Pillar Models at 6000 psi and 22.5°C.

Reproducibility of Results

In order to evaluate, quantitatively, the effects of temperature, axial load, and time on the deformation of salt, it is important that the samples tested be, as near as possible, the same type of salt, including similar grain size, impurities, bedding, etc. All specimens of salt from the Lyons, Kansas, mine, with the exception of a few special samples, were fabricated from a series of 5-ft-long cores, taken in the roof immediately above the thick shale bed in entry 5 of the old mine workings near the experimental site. This part of the salt section in the mine, which also comprises the lower part of the pillars and walls in the experimental area, consists for the most part of coarse-grained crystals of clear halite that range from $\frac{1}{4}$ to $\frac{3}{4}$ in. in size. Finely divided blebs of clay are concentrated in the salt at intervals of about 1 to 6 in. along bedding, giving the salt a characteristic banded appearance. A few stringers of anhydrite and an occasional "pod" of clay also are found in the salt. More rarely, polyhalite blebs can be identified. Specimens from the other localities were prepared from single blocks that appeared to be about the same type of salt throughout.

To obtain an approximate measure of the variation in deformational behavior of model specimens of the same type of salt in the Lyons mine tested under the same conditions, duplicate and even triplicate samples were run at several combinations of pressure and temperature. In Fig. 3.15 the deformation curves for three samples, each tested at 6000 psi and 22.5°C, are shown. The curves for these samples are essentially the same. Good agreement was also shown for the duplicate samples tested at 4000 psi and 22.5°C. Two samples heated to 200°C and loaded to 2000 psi showed that reproducible results can also be obtained for samples tested at elevated temperatures.

Ultimate Strength

The ultimate strength of support systems is of fundamental importance in all underground openings. To determine the ultimate, or breaking, strength of mine pillars in salt, two models, one having a width-to-height ratio of 3 and the other a width-to-height ratio of 4, were loaded at rates of 33 psi/min until failure or extensive deformation occurred. In both cases sudden or brittle pillar failure did not occur, even for loads as high as 15,000 psi; however, considerably more deformation did occur for the smaller-diameter pillar than for the larger one. This verifies the conclusion drawn from other tests, described above, that pillars having a width-to-height ratio of 4 are stronger than those having a width-to-height ratio of 3. Although 100% pillar shortening was not attained for either sample, both were deformed to

the extent that accumulation of spall or small pieces of broken salt from the pillars had filled a part of the cavity opening. Thus the effective pillar diameter for the smaller-diameter pillar had increased to the point that it extended almost the entire width of the excavated cavity. The combined effects of pillar shortening and pillar spall in cavity closure are discussed in more detail later; however, it is concluded that the smaller the width-to-height ratio of the pillars (assuming a greater excavation ratio), the greater the amount of pillar shortening prior to complete cavity closure. The results of these tests also suggest that sudden or brittle pillar failure will not occur in salt pillars having width-to-height ratios of 3 and 4 at loads up to 15,000 psi and perhaps even at any higher loads, although it is recognized that deformation of the pillars through creep of the salt would occur at a very high rate. The ultimate strength or breaking strength of these type pillars thus cannot be determined, since the salt under these conditions will flow very rapidly but will not fail in a brittle manner regardless of the load.

Long-Term Creep

In order to ascertain whether or not creep rates continue to decrease with time for periods in excess of a few thousand hours, creep rates were recorded over a period of $3\frac{1}{3}$ years on a model loaded to 6000 psi at 22.5°C and over a period of 1 year for a model loaded to 4000 psi at 22.5°C. Plots of the cumulative deformation with time for these samples are shown in Fig. 3.16. In both cases it is observed that the rate of deformation continues to decrease with time out to the extent of the test periods. This decrease in creep rates

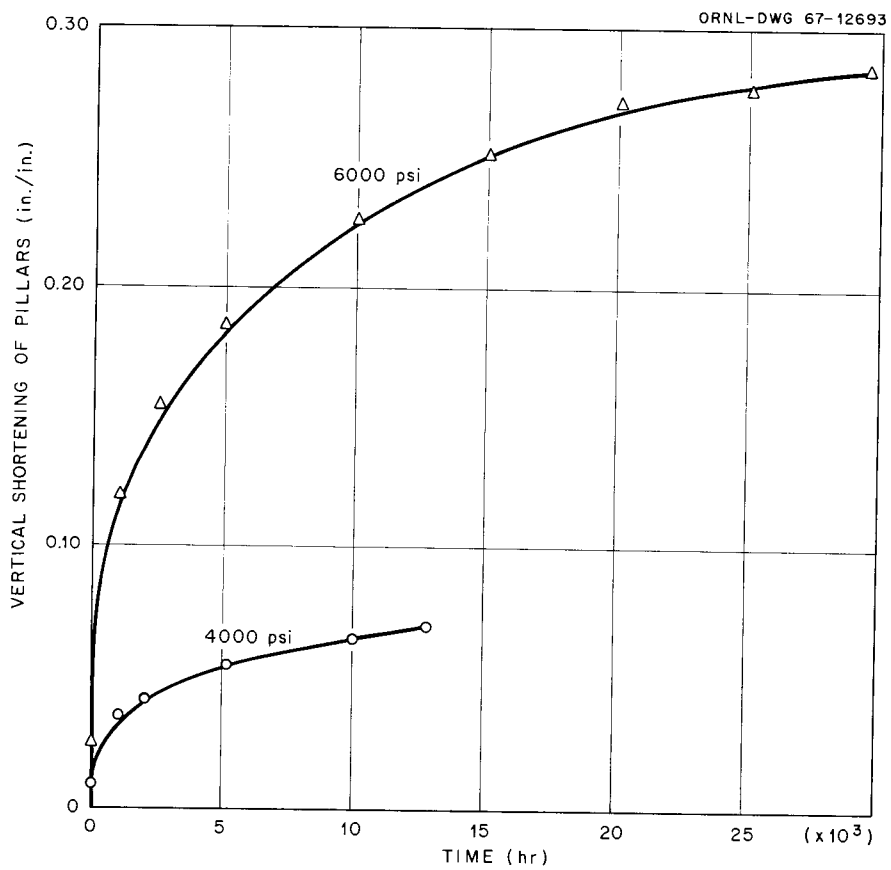

Fig. 3.16. Deformation of Pillar Models at 6000 and 4000 psi and 22.5°C.

with time has also been observed by Bradshaw, Boegly, and Empson in actual mine workings.[19] Their work in the Hutchinson, Kansas, mine shows that in mine openings up to 12 years old there is a continual decrease in the rate of floor-to-ceiling convergence or creep rate.

COMPUTATION OF STRESSES AND DISPLACEMENTS RESULTING FROM THE DISPOSAL OF RADIOACTIVE SOLIDS IN A SALT MINE

A. M. Starfield[20] W. C. McClain
R. L. Bradshaw

This study is concerned with the development of techniques for predicting the pillar loads and convergence rates in room-and-pillar systems which are to be used for the disposal of radioactive waste. These techniques are based on the experimental studies, both in the laboratory and in situ, which have already been made by the Health Physics Division. The approach adopted is one in which the laboratory measurements of creep in model salt pillars are interpreted as providing a phenomenological or qualitative, though not necessarily quantitative, understanding of creep in actual mine pillars. The qualitative relationships obtained from the laboratory measurements are developed into a model of the deformations occurring in and near a mined excavation, and quantitative values for the various parameters of the model should then be obtainable from comparisons with in situ measurements. At the same time, the consistency of agreement between the model and in situ measurements will indicate whether or not the model gives a true reflection of the physical processes contributing to the deformation of the rock salt. (This test of agreement has not yet been done.) If it is valid, the model should then be applicable to the design of disposal layouts under a variety of conditions.

The model should ultimately be capable of predicting the influence on the convergence rate at any time of:

1. the width of the rooms and pillars,
2. the proximity of remnants and abutments (the load carried by the abutments might influence the geometrical layout of the mine),
3. the depth of burial of the waste,
4. the amount of waste which is deposited in a room and the sequence of waste-disposal operations.

Finally, it should be mentioned that if the load-displacement characteristics of the backfill salt can be determined, then the influence of the backfill on the convergence rate after the backfill begins to compress could be included in the analysis.

OTHER ROCK TYPES

T. F. Lomenick H. J. Wyrick

Storage in Rock Types Other Than Bedded Salt

The widespread occurrence of rock salt over the United States has been commonly accepted as one of the principal advantages for the use of these rocks as storage sites for radioactive waste materials. Indeed, salt deposits do underlie a portion of 24 of the 50 states; however, from recent laboratory and field studies on the flowage of rock salt at elevated temperatures and high overburden loads, it is apparent that many of these deposits are unsuitable for disposal sites. At present there are perhaps three principal areas in the United States where disposal in salt would appear to be highly desirable. These areas are (1) the Silurian salt deposits of the Northeast, which underlie parts of New York, Pennsylvania, West Virginia, Ohio, and Michigan; (2) the Permian basin salts which underlie parts of Kansas, Oklahoma, Texas, and New Mexico; and (3) the Gulf Coast Embayment salts which underlie parts of Louisiana, Texas, Arkansas, and Mississippi. The first two named areas are bedded deposits, while the latter contains only salt domes.

Most of the other deposits throughout the United States are less suited because of their great depths below the surface, their numerous inclusions of other rock types, or a general lack of knowledge concerning their extents, depths, etc. In general, mine workings at great depths in salt are initially expensive to open, and accelerated deformation of the salt occurs because of the greater overburden

[19] R. L. Bradshaw, W. J. Boegly, Jr., and F. M. Empson, "Correlation of Convergence Measurements in Salt Mines with Laboratory Creep-Test Data," *Proceedings of the Sixth Symposium on Rock Mechanics*, University of Missouri, Rolla, Missouri, 1964, pp. 501–14.

[20] Consultant, University of Minnesota, Minneapolis, Minn.

loads. The presence of other rock types with the salt beds may further accelerate the deformation of the salt. For instance, in the Williston basin, which covers a part of North Dakota, the minimum depth to salt is 3600 ft; also, the bed is only about 20 ft thick. Thicker deposits occur, but they lie between 4300 and 20,000 ft below the surface. Salt beds are also present in Florida, but they are only about 30 ft thick and occur at depths of 10,000 to 12,000 ft. Even in the Permian basin much of the salt is at great depths below the surface and contains numerous inclusions of other rocks. Perhaps the principal concern in the disposal of waste in bedded deposits is the stability of the structure at elevated temperatures and stresses. This has been found to be especially significant when shale beds occur interbedded with the salt. These shale beds are usually absent in dome deposits, and thus in this respect domes may be favored over bedded deposits for waste-disposal sites. From recent laboratory and field tests, it appears that an efficient and safe operative work in bedded rock salt can be designed; however, there are several problems unique to salt dome deposits that require investigation before a similar operation can be designed for these structures.

More than 300 salt domes are now known to be present in the Gulf Coast Embayment. In addition to the lack of shale beds or the high salt content of these deposits as compared with bedded formations, these domes often occur relatively near to the land surface. Many lie between 500 and 1000 ft below the surface, and, of course, in all, the salt extends to depths of many thousands of feet. A large part of the available mined-out space in salt deposits also exists in salt domes. Approximately 40% of the total space vacated by rock salt mining each year results from workings in the domes of the Gulf Coast region.

The principal technical concern in the disposal of waste to salt domes is in ensuring that migrating waters do not reach stored waste. The recent flooding of the Winnfield, Louisiana, dome mine may serve to illustrate the concern. Also, in Germany, where domal-type salt structures have been mined for many years, at least 20 mines have been reported to have been flooded by groundwater. At present, apparently little is known about the movement of groundwater in the vicinity of salt domes; thus investigations would have to be initiated to ascertain the geohydrological factors or other parameters which were or appeared to be instrumental in the flooding at Winnfield and other salt domes before utilizing them for radioactive disposal media. It is obvious that the distance between mine workings and aquifers is important, but it is not possible to state at this time, for example, what would be the minimum distance under specified conditions of mine depth, structural and stratigraphic conditions of the intruded country rocks, etc. Once the important parameters that bear most directly on mine flooding are identified, laboratory and/or field investigations, if necessary, would have to be initiated to demonstrate that safe and efficient disposals can be made in salt domes.

On a regional basis, it appears that the most promising areas of rock deposits other than salt that would be suitable for radioactive waste storage would include relatively tectonically undisturbed areas such as the midcontinent region of the United States. Other areas, such as the Colorado Plateau, would also appear to be highly desirable. In parts of the arid west, where there is no groundwater recharge from rainfall and where site locations in rock exist above the water table, suitable excavations may also be practicable. In many localities within these areas, it is likely that horizontal shaft-type or tunneling operations may be feasible. This method of excavation is preferable in many respects to vertical shaft mining, since it is generally agreed that mining costs are lower and the openings are more accessible. Tunneling into the faces of hills, escarpments, or other topographic features of high relief is a common means for mining limestone in many areas where horizontal bedding prevails (Fig. 3.17). Many mines of this type in Middle Tennessee have been found to be structurally stable (Fig. 3.18), and, except for some leakage at the mine entrances, they are entirely free of circulating groundwater. On a larger scale, underground excavations in limestone near Kansas City, Kansas, are currently being used as refrigerated cold storage bins. Here, facilities have been provided to accommodate storage of entire rail cars and their refrigerated products in tunneled-out dry cavities.

To determine the effects of gamma radiation on the physical properties of limestone, a series of cylindrical-shaped specimens taken from an operating mine are being tested in the laboratory. The sample specimens, which are 3 in. in diameter

Fig. 3.17. Entrance to Underground Limestone Mine Near Sherwood, Tennessee.

by 3 in. in length, have been fabricated from a representative block of limestone, comprising the mine pillars at the Southern States Lime Corporation mine, Crab Orchard, Tennessee. In this locality, the mined unit, which is a part of the Ste. Genevieve-Gasper formation of Mississippian age, lies essentially horizontal and is very thickly bedded. It is also gray in color and has a dense to crystalline texture.

In general, one testing procedure consists in measuring stress-strain relationships for a series of unirradiated specimens and then comparing them with irradiated specimens of various exposure doses. The sample specimens are irradiated in the ^{60}Co storage facility at the Oak Ridge National Laboratory. The gamma radiation field in the irradiation chamber at the facility is about 6×10^5 r/hr. Thus, by allowing the specimens to remain in the storage garden for periods of up to six months, peak radiation doses of 2.6×10^9 can be attained. Preliminary tests show that the compressive strength of unirradiated specimens is approximately 20,000 psi.

Previous investigations have shown that for temperatures as high as 200°C, there is no significant effect on the strength of model specimens of carbonate rock pillars.[21]

MAJOR CONCLUSIONS FROM STUDIES ON DISPOSAL IN NATURAL SALT FORMATIONS

R. L. Bradshaw

The operation of Project Salt Vault (a demonstration disposal of high-level radioactive waste solids in a Lyons, Kansas, bedded salt mine, using Engineering Test Reactor fuel assemblies in lieu of actual solidified wastes) has successfully demonstrated waste-handling equipment and techniques similar to those required in an actual disposal operation.[22] A total of about 4,000,000 curies of fission product activity in 21 containers, each having an average of about 200,000 curies,

[21] F. L. Parker *et al.*, *Health Phys. Div. Ann. Progr. Rept. July 31, 1966*, ORNL-4007, p. 26.

[22] Some of these conclusions must be regarded as tentative, since the evaluation of the results of Project Salt Vault is still in progress at this time (May 1968).

Fig. 3.18. Interior of Underground Limestone Mine Near Sherwood, Tennessee.

was transferred to the disposal facility in the mine and back to the National Reactor Testing Station at the end of the test. No hot cells were used at the mine; and, even under these conditions, the maximum personnel exposure was about 200 mr to the hands and head. In an actual disposal facility, hot cells *would* be required since the waste containers will offer only single containment. (The fuel cladding plus the sealed canister was considered double containment.)

During the 19-month operation of the radioactive phase of the demonstration, the average dose to the salt over the length of the fuel assembly container holes was about 8×10^8 rads, and the peak dose was about 10^9 rads. Doses dropped off very rapidly with distance out into the salt, with doses at 6 in. into the salt being only about 10^8 rads. As anticipated from the laboratory studies, no significant effects due to the radiation were detected.

Theoretical studies indicate that some free chlorine should be radiolytically produced within the salt structure, but, again confirming predictions based on laboratory studies, no detectable quantities of chlorine were released. Small quantities of what is believed to be a radiolytically produced organic peroxide were detected when the salt temperature exceeded 175°C, but this is expected to be of no consequence in an actual disposal operation. Ultimate doses to the salt with wastes of the future may exceed 10^{10} rads, but the mass of salt involved will still be small, and no detrimental effects are anticipated.

Both theoretical and experimental results indicate that rock salt is approximately equivalent to

concrete as an absorber of gamma radiation.[23] This being the case, approximately 5 ft of solid salt or 7½ ft of crushed salt (assuming ⅓ voids) will give adequate biological shielding to allow unlimited access to a room in a salt mine filled with the most radioactive waste of the future. (It is assumed that the containers are located in backfilled holes in the floor with the tops of the containers at the proper depth and that container spacing is based on fission product decay heat dissipation calculations.)

Field tests have indicated that the in situ heat transfer properties of salt are sufficiently close to the values determined in the laboratory that confidence can be placed on theoretical heat transfer calculations.[23] Calculations to date have generally been approximate and on the conservative side, but the knowledge exists to permit more precise calculations to be made by means of more complex computer programs.

At the beginning of the study of the use of salt for waste disposal, very little was known about the effects of heat on the behavior of salt in mines. It soon became apparent that, due to the unusual quasi-plastic properties of rock salt, there was little hope of developing theoretical solutions for the effects of stress, temperature, and other variables on the behavior of salt in mines. Consequently, the use of laboratory tests on model salt pillars was investigated and found to be applicable. Behavior of model pillars at ambient temperatures was found to correlate with observed phenomena under actual mine conditions.[24] It was thus concluded that the behavior at elevated temperatures could be extrapolated to mine conditions. This conclusion has been borne out by the field tests.

The most significant finding in the field tests regarding the effects of heat on salt behavior is that the insertion of heat sources in the floor of a mine room produces a thermal stress whose effects are instantaneously transmitted around the opening (to the pillars and roof).[24] These stresses produce increased plastic flow rates in the salt and could possibly cause trouble if the roof of the room is too close to a shale layer (a plane of weakness). In the demonstration area such a shale layer existed, but it was found that conventional roof bolting techniques were adequate to handle the problem. In an actual disposal operation it is anticipated that rooms would be filled with waste and then backfilled with crushed salt rapidly enough that roof bolts would probably not be required.

The combined field and laboratory tests have provided sufficient information on the salt flow characteristics to allow the development of both general and specific empirical criteria for design of a disposal facility in almost any bedded salt deposit. (For dome deposits, it is felt that there are some additional unanswered questions.)

In the demonstration it was discovered that small brine-filled cavities (generally roughly cubic in shape, with sizes ranging from a few millimeters down to microscopic) migrate toward a heat source.[25] A typical bedded salt deposit might contain about ½ vol % water. Theoretical studies and laboratory tests of the migration rates as a function of temperature were in reasonable agreement. Based on the theoretical calculations, one might expect a total inflow per waste-disposal container hole of from 2 to 10 liters, taking place over a period of 20 to 30 years after burial. The peak inflow rate would occur at around 1 year after burial and be somewhere in the range of 200 ml to 1 liter per year per hole. Similar migration rates were observed in the demonstration. This water inflow rate would be expected to taper off and approach zero after 20 to 30 years.

The field tests have indicated that once the migrating brine reaches the crushed salt backfilling the hole, it moves upward and condenses in the colder regions above the waste containers. Under some conditions, since the upper regions of the waste containers may not be full of waste, the upper ends of the containers may be located in the condensation zone. If this is the case, then stress corrosion cracking of these portions of stainless steel containers may be anticipated. If the containers are of mild steel, then only

[23] R. L. Bradshaw, F. M. Empson, W. J. Boegly, Jr., H. Kubota, F. L. Parker, and E. G. Struxness, "Properties of Salt Important in Radioactive Waste Disposal," *International Conference on Saline Deposits, 1962*, GSA Special Paper 88 (1968).

[24] R. L. Bradshaw *et al.*, "Model and Underground Studies of the Influence of Stress, Temperature, and Radiation on Flow and Stability in Rock Salt Mines," pp. 429–33 in *Proceedings of the First Congress of the International Society of Rock Mechanics, Lisbon, 25 September to 1 October 1966*, vol. II, 1966.

[25] *Health Phys. Div. Ann. Progr. Rept. July 31, 1967*, ORNL-4168, pp. 18–31.

generalized rusting may be expected, and container integrity should be maintained for an indefinite period of years. Even if containers do perforate, this should not produce any problem in a disposal facility since there should be no gas pressure in the containers, and, even if there is, the 7 to 8 ft of crushed salt above the containers would be expected to act as a filter and adsorber for the released material. Should some hazardous material manage to escape the hole anyway, the anticipated facility operating procedure is that ventilating air never comes in contact with personnel after it passes a filled storage room, and container failure would not be anticipated during the relatively short period of operation in an individual room (typically, about one month).

A study of the economics of a very conservatively designed salt mine facility handling the entire high-level waste output from the United States nuclear power reactor economy in year 1972 [continuous operation of 56,000 Mw (thermal)] has been completed.[26] The mine was assumed to be developed solely for waste disposal and to cover a gross area of 1 sq mile. At this level of waste input, the mine was found to last from about 12 to 70 years for wastes buried at 1 year and 30 years out of the reactor respectively. The initial capital outlay required to start operations was of the order of $10 million. Total annual costs (both capital amortization and operation) were found to range from about $2.5 million for a 1-year-old waste to about $1 million for 30-year-old wastes. In terms of cost per kilowatt-hour of electricity generated, this corresponds to about 0.02 to 0.002 mill/kwhr respectively (using present worth concepts and 4% interest rate). These costs are a relatively small portion of the cost of competitive nuclear power; and, from the standpoint of economics, it should be practical to dispose of wastes in salt at 3 to 4 years out of the reactor. Disregarding safety aspects, the overall economics of waste management indicate that longer interim storage periods are somewhat cheaper, and, in fact, perpetual storage as a liquid in tanks is slightly cheaper than conversion to solid with ultimate disposal in salt. However, since it is generally accepted that solids disposal is the preferred method, the same reasoning would appear to lead to the general conclusion that ultimate disposal as soon as practical is also highly desirable.

Some areas where further work needs to be done include:

1. Complete the analysis of the results of the field and laboratory studies.
2. Develop a more flexible and accurate heat transfer computer program for use in obtaining the desired spacing between waste containers as a function of such parameters as waste history, container size, rate of production, etc. If possible it would be desirable to develop universal design graphs based on the various parameters.
3. Develop both general and specific criteria for room and pillar dimensioning, etc., of a disposal facility in bedded salt deposits. Again, if possible, universal design graphs should be the objective.
4. Operate a prototype disposal facility in order to verify some of the previous conclusions as well as to develop answers to questions of public and governmental acceptability, the evaluation of safety under actual operating conditions, and the development of health and safety regulations in order to provide a basis and incentive for industrial takeover. Waste disposal will not be an economically large operation for some time to come. Assume, for example, that a 5-year interim storage period is chosen. Then, in the year 2000, the wastes being disposed of represent those generated in 1995 (from continuous operation of about $8\frac{1}{2} \times 10^5$ Mw (thermal) of nuclear power). This level of waste could be handled in about 15 mines of the size assumed in the economic study mentioned previously. The total annual cost of operation of each mine facility would range from about $1 to $1.5 million per year, giving a total gross cost for waste disposal in salt in the year 2000 of only about $20 million. (If the interim storage period is longer, the costs are still further reduced.) It is thus obvious that the net profit will not be large enough for several decades to induce industry to step in unless the AEC works out the answers to the basic questions ahead of time.
5. Another possible area of concern is the effect of the large fission product heat source (about

[26] R. L. Bradshaw *et al.*, *Evaluation of Ultimate Disposal Methods for Liquid and Solid Radioactive Wastes, Part VI. Disposal of Solid Wastes in Salt Formations*, ORNL-3358 (May 1968).

two orders of magnitude above the normal geothermal flux) on the geological structure. For example, with a peak salt temperature of 200°C next to containers of waste buried after 10 or more years interim storage, a temperature of 100°C would extend about 100 ft above and below the storage level for a period ranging from about 40 to more than 100 years.

To summarize, it may be said that most of the major technical problems regarding disposal in salt have been resolved. The results have been most encouraging. The feasibility and safety of handling highly radioactive materials in an underground environment have been demonstrated. The stability of the salt under the effects of heat and radiation was shown, as well as the capability of solving minor structural problems by standard mining techniques. The data obtained on the creep and plastic flow characteristics of the salt should make it possible to arrive at a suitable mine design for a disposal facility. A study of the economics of disposal in salt mines indicates that this method will be compatible with competitive nuclear power. All these items combined lead one to the conclusion that burial in salt mines is one of the better methods, if not the best, for the ultimate disposal of high-level solidified wastes.

Based on this conclusion, an examination is now being made into the desirability of establishing an actual disposal facility in the immediate future. The first high-level disposal facility could begin by accepting waste pots from the Pacific Northwest Laboratories' Waste Solidification Engineering Prototype Facility, which may become available about 1970. This phase would also provide an opportunity for working out legal, regulatory, political, and public relations problems which might develop. The facility would have a built-in capability of expansion to meet the demands of the fuel-reprocessing industry and reasonably useful lifetime at or near full capacity. Since an interim storage period of several years will probably be required, this expansion would probably begin toward the end of the 1970's.

4. Engineering, Economic, and Safety Evaluations

K. E. Cowser
W. J. Boegly, Jr.
Jacob Tadmor[1]
Judy Varga[2]
D. G. Jacobs
T. F. Lomenick
J. O. Blomeke[3]
O. M. Sealand

KRYPTON-85 AND TRITIUM IN AN EXPANDING WORLD NUCLEAR POWER ECONOMY

K. E. Cowser Jacob Tadmor

Dose equivalents to man have been evaluated based on the complete release and worldwide distribution of ^{85}Kr and ^{3}H from reprocessing of irradiated fuel (to year 2000).[4] A procedure was developed for estimating average annual downwind air concentrations from a stack release of radionuclides that included the effect of washout and fallout.[5] In the following discussion, the pathways of external and internal exposure are examined for a hypothetical fuel reprocessing plant sited at ORNL.

Dose Estimation Models

Methods described and parameters given in ICRP Publication 2[6] are used to convert concentrations (X in $\mu c/cm^3$) to estimates of dose equivalents to standard man from submersion in a contaminated cloud, from ingestion, and from inhalation. In particular, Eqs. (12), (13), and (20) are used, and equilibrium conditions are assumed where appropriate. These dose equations are summarized in Table 4.1.

Submersion dose rates in contaminated water were calculated by assuming that the body is in the center of a sphere and receives equal quantities of radiation from all directions.[7] Other assumptions included: (1) The radius of the contaminated water is large in comparison with the range of beta particles and with the half-thickness of the water for gamma rays, (2) an effective absorbed energy that is equal to the average energy of the beta particle, and (3) a short penetration distance for the beta particle in the body, thus limiting beta radiation to near-body-surface exposure. The following expressions were derived to calculate dose equivalents at the surface of a body submerged in contaminated water: For ^{85}Kr,

$$R = 0.26 X_w \text{ rems/hr} .$$

For tritium,

$$R = 1.1 \times 10^{-2} X_w \text{ rems/hr} ,$$

where X_w is the concentration in water in microcuries per cubic centimeter.

Hine and Brownell describe the derivation of equations that relate to calculation of dose rates

[1]Visiting scientist on leave from Israel AEC.

[2]Summer employee – ORINS-ORNL Student Trainee.

[3]Chemical Technology Division.

[4]K. E. Cowser, W. J. Boegly, Jr., and D. G. Jacobs, *Health Phys. Div. Ann. Progr. Rept. July 31, 1966*, ORNL-4007, pp. 35–57.

[5]K. E. Cowser *et al.*, *Health Phys. Div. Ann. Progr. Rept. July 31, 1967*, ORNL-4168, pp. 39–43.

[6]*Report of Committee II on Permissible Dose for Internal Radiation*, International Commission on Radiological Protection, Publication 2, Pergamon, London, 1959; *Health Phys.* **3** (June 1960).

[7]K. E. Cowser *et al.*, "Evaluation of Radiation Dose to Man from Radionuclides Released to the Clinch River," pp. 639–71 in *Proceedings of Symposium on Disposal of Radioactive Wastes Into Seas, Oceans, and Surface Waters, May 16–20, 1966, Vienna, Austria*, IAEA, Vienna (1966).

Table 4.1. Equations to Calculate Dose Equivalents (Rems per Week) to Standard Man[a]

Exposure Mode[b]	Critical Organ[b]	40-hr-week Exposure		168-hr-week Exposure	
		^3H	^{85}Kr	^3H	^{85}Kr
Inhalation and skin absorption	Total body	$1.2 \times 10^4 X_a$		$3.6 \times 10^4 X_a$	
Inhalation and skin absorption	Body tissue	$2.0 \times 10^4 X_a$		$5.8 \times 10^4 X_a$	
Ingestion	Total body	$0.67 X_w$		$1.9 X_w$	
Ingestion	Body tissue	$1.1 X_w$		$3.2 X_w$	
Submersion in air	Total body		$9.2 \times 10^3 X_a$		$4.0 \times 10^4 X_a$
Submersion in air	Skin	$3.9 \times 10^2 X_a$		$1.7 \times 10^3 X_a$	
External exposure, 2.5 ft above contaminated ground surface	Total body		$2.4 \times 10^1 X_a$		$1.0 \times 10^2 X_a$

[a]Dose rate in rems per week when the concentration in air X_a or the concentration in water X_w is expressed in units of $\mu c/cm^3$.

[b]Exposure mode and critical organ for inhalation and skin absorption, ingestion, and submersion in air are based on information contained in ref. 6.

in air from beta emitters associated with an infinite plane of negligible thickness.[8] Equations 10, 11, 20, and 21 are selected for calculation, where the energy-dependent parameters are those adapted for dose estimates in soft tissue. Equation 9-30 from Morgan and Turner is used to calculate the dose due to gamma emitters when the source is of infinite planar extent and infinite thickness.[9] External dose equations listed in Table 4.1 for soil contaminated with ^{85}Kr are then derived from the expected soil load (4.8×10^{-11} curie/cm^3) at the maximum air concentration (1.6×10^{-6} $\mu c/cm^3$). The range in aluminum of the average-energy beta particle from ^{85}Kr is used to estimate the thickness of contaminated soil contributing to the beta dose and thus the amount present per unit area. The beta dose rate is calculated by assuming that this amount of ^{85}Kr is spread uniformly at the surface without taking credit for self-absorption within the soil layer.

[8]G. J. Hine and G. L. Brownell, "Discrete Radioisotope Sources," chap. 16, p. 694 in *Radiation Dosimetry*, Academic, New York, 1956.

[9]K. Z. Morgan and J. E. Turner, "Dose from External Sources of Radiation," chap. 9, p. 268 in *Principles of Radiation Protection*, Wiley, New York, 1967.

Estimated Dose Equivalents from Hypothetical Reprocessing Plant

Blanco *et al.* reported on the requirements for nuclear power and fuel reprocessing in the United States in year 2000.[10] A release of 1 curie/sec of ^{85}Kr and 0.03 curie/sec of ^3H is chosen for purposes of this analysis. These release rates correspond to a reprocessing plant size that may be required for the Southeast and Midwest by year 1990, that is, about 6 metric tons/day. All of the ^{85}Kr is assumed to be released to the atmosphere. Blomeke indicates that about 25% of the ^3H has appeared in dissolver off-gas and is released through the stack; 75% appears in low-level aqueous waste.[11] Therefore, it is assumed that 0.0075 curie/sec of ^3H is released to the atmosphere as HTO vapor and that 0.0225 curie/sec of ^3H is discharged to the Clinch River at mile 20.5 (below the Oak Ridge municipal water intake and above the ORGDP water intake) as liquid waste

[10]R. E. Blanco *et al.*, *Survey of a Site for a Nuclear Fuel Reprocessing Plant and Waste Disposal Area at Oak Ridge*, ORNL-TM-1748 (January 1967).

[11]J. O. Blomeke, internal memorandum, 1964.

Table 4.2. Estimated Annual Dose Equivalents (Millirems) Received by Standard Man Due to a Hypothetical 6-metric ton/day Reprocessing Plant Sited at ORNL

Mode of Exposure[a]	Reference Organ[a]	Dose Rate (millirems/year)	
		Employee of ORGDP	Oak Ridge Resident
	^{85}Kr		
Submersion in air	Total body	23	160
Submersion in water	Total body	<0.01	<0.01
Contaminated ground (2.5 ft above surface)	Total body	0.06	0.4
	Tritium		
Inhalation and skin absorption	Body tissue	0.38	1.7
Ingestion of water	Body tissue	8.9	<0.07
Submersion in air	Skin	0.008	0.05
Submersion in water	Skin	0.2	<0.001

[a]Exposure mode and reference organ for submersion in air, inhalation and skin absorption, and ingestion of water are based on information contained in ref. 6.

and is diluted with 4919 cfs of river water. Other schemes of ^{3}H release and corresponding release rates are possible, such as distillation of ^{3}H-bearing liquids and release to the stack as water vapor, and would require an appropriate adjustment in the dose estimates that follow.

Table 4.2 contains the estimated annual dose equivalents to standard man working at ORGDP or residing in Oak Ridge due to the release of 1 curie/sec of ^{85}Kr and 0.03 curie/sec of ^{3}H to the environment. Periods of occupancy are 40 hr/week and 50 weeks/year for the employee at ORGDP and 168 hr/week and 50 weeks/year for the Oak Ridge resident. A "less than" sign preceding certain values reflects a conservative estimate. The critical modes of exposure are submersion in air for ^{85}Kr and inhalation and skin absorption for ^{3}H. The estimated total-body exposure of standard man residing in Oak Ridge due to releases from a hypothetical 6-metric ton/day plant operating at ORNL in 1990 is about 160 millirems/year. For a 1-metric ton/day plant operating in 1970, total-body exposure due to ^{85}Kr would be approximately 10 millirems/year.

Current guidance for total-body exposure to ^{85}Kr limits the maximum permissible dose of individuals in the general population to 500 millirems/year (and of average population groups to 170 millirems/year).[6,12] However, it is unlikely that a dose potential of 160 millirems/year from a single source would be considered acceptable; present practice is to minimize exposure. An additional uncertainty in support of this conservative practice is the apportionment of dose to single and eventually to multiple sources of ionizing radiation as industry growth continues.

Potential dose from the release of ^{3}H in liquid waste is small, because credit can be taken for dilution in the Clinch River, in which flow is substantial (4919 cfs), and the river is not used as a source of municipal water. Dose estimates by the ingestion of water (5.4 millirems/year) at ORGDP would increase in direct proportion to reduction in flow and increase by a factor of 3 if the water is used as a municipal water supply. Disposal of ^{3}H in water vapor released to the stack may be one way to reduce the potential exposure from ingestion of water.

Even though verification will be necessary of some assumptions made to estimate dose, it seems

[12]*Background Material for the Development of Radiation Protection Standards*, Report No. 1, Staff Report of the Federal Radiation Council (May 18, 1960).

clear that complete stack release of ^{85}Kr from a 6-ton/day reprocessing plant sited at ORNL may create unnecessarily high population exposures in Oak Ridge. Economic benefits would be expected to accrue from large reprocessing plants, and remote siting (with adequate surface water flow) may not be a practical method to avoid population exposures in the future. There is justification, therefore, to continue research and development studies now in progress to reduce the amounts of ^{85}Kr and ^{3}H released and to understand more completely the fate of these radionuclides after discharge to the environment.

RELEASE OF TRITIUM IN AN EXPANDING NUCLEAR POWER ECONOMY AND ITS LONG RANGE BEHAVIOR IN THE ENVIRONMENT

D. G. Jacobs

Tritium is produced in light-water reactors primarily by ternary fission. Some of the tritium may penetrate fuel element claddings and escape into the coolant, but most of it is apparently retained until the fuel is reprocessed, when it follows ordinary water and is released to the environment in low-level aqueous waste streams.[13-14] Some of the tritium may be released through stacks. Although most of the stack release is expected to be in the form of tritiated water vapor, part of the release may be as HT.[15,16] Tritium released as HT gas would be expected to oxidize at a rate ranging from 0.2 to 3% per day.[17,18] Once the tritium is oxidized, it will become dispersed in much the same manner as ordinary water.

Tritium released to the upper limits of the troposphere from the stratosphere has a mean residence time estimated to range from 21 to 40 days.[19-24] As a consequence, the fallout of tritium released to the troposphere is limited to the general latitude of release. Practically all continental deposition of natural and fallout tritium occurs due to precipitation.[19] This may not be the case in local situations where tritium is released through a stack, because downward diffusion may cause the plume to impinge on the ground surface before washout by rain occurs.[25] Tritium may also be transferred between the air and the earth's surface by vapor exchange. Eriksson[26] estimates that vapor exchange may account for two-thirds of the tritium removed into the oceans. Vapor exchange over continental areas is not so likely, since the upper layers of the groundwater are not mixed as rapidly or throughout as large a reservoir as is the case of the oceans and other large bodies of water.

Because of the pattern of exchange of tritium from the stratosphere into the troposphere, about half of the tritium released from detonations of thermonuclear devices has been deposited between 30 and 50° north latitude.[19] This 10% of the earth's surface includes most of the United States and much of Europe and will likely receive most of the tritium released in a nuclear economy.

Most of the fission tritium will likely be found in the hydrosphere, as is the case with naturally produced tritium. The oceans and seas represent the largest reservoirs for dilution of tritium (Table 4.3).[27,28] Tritium is not likely to become uniformly distributed throughout these reservoirs, because only a small fraction of this total volume of

[13] J. O. Blomeke, *Management of Fission Product Tritium in Fuel Reprocessing Wastes*, ORNL-TM-851 (May 4, 1963).

[14] W. A. Haney, *Nucl. Safety* 5(4), 399–402 (Summer 1964).

[15] E. L. Albenesium and R. S. Ondrejcin, *Nucleonics* 18(9), 100 (September 1960).

[16] W. A. Haney, D. J. Brown, and A. E. Reisenauer, *Fission Product Tritium in Separations Wastes and in the Ground Water*, HW-74536 (Aug. 1, 1962).

[17] J. Y. Yang and L. H. Gevantman, *Tritium Beta-Radiation Induced Isotopic Exchange in the T_2-H_2O System*, USNRDL-TR-471 (Sept. 28, 1960).

[18] A. Doury, "Risks Presented by the Diffusion of Large Quantities of Tritium in the Atmosphere," pp. 17–26 in *Seminaire sur la Protection Contre les Dangers du Tritium*, Service Central de Protection Contre des Rayonnements Ionissants, le Vesinet, 1964.

[19] W. F. Libby, *Proc. Natl. Acad. Sci. U.S.* 44, 800–20 (August 1958).

[20] F. Begemann and W. F. Libby, *Continental Water Balance, Ground Water Inventory and Storage Times, Surface Ocean Mixing Rates and Worldwide Water Circulation Patterns from Cosmic Ray and Bomb Tritium*, OSR-TN-56-561 (Nov. 15, 1961).

[21] A. Walton *et al.*, *Studies of Nuclear Debris in Precipitation*, NYO-9532 (May 31, 1962).

[22] E. W. Barrett and L. Huebner, *Atmospheric Tritium Analysis*, AECU-4739 (Feb. 16, 1960).

[23] R. M. Brown and W. E. Grummitt, *Can. J. Chem.* 34, 220–26 (March 1956).

[24] B. Bolin, *Research in Geophysics*, vol. II, pp. 479–508, Massachusetts Institute of Technology, Cambridge, Mass., 1964.

[25] A. C. Chamberlain and A. E. J. Eggleton, *Intern. J. Air Water Pollution* 8, 135–49 (February 1964).

[26] E. Eriksson, *Tellus* 17(1), 118–30 (February 1965).

Table 4.3. Volumes of Circulating Water in the World

Data from refs. 27 and 28

	Volume of Water (m^3)	
	Total	North Latitude (30 to 50°)
Oceans and seas (surface to a depth of 75 m)	2.70×10^{16}	2.68×10^{15}
Stream channels (average)	1.17×10^{13}	2.51×10^{12}
Atmospheric moisture (average)	1.29×10^{14}	1.72×10^{13}
Subsurface water in the root zone	2.50×10^{14}	5.38×10^{13}
Total circulating water	2.74×10^{16}	2.75×10^{15}

Table 4.4. Balance of Circulating Waters

In cubic meters per year; data from ref. 28

	$\times 10^{14}$
Evaporation from the oceans	3.34
Rainfall over the oceans	2.97
Runoff into the oceans	0.37
Rainfall onto land	0.99
Evaporation from land and inland water areas	0.62

water circulates annually (Table 4.4). One would expect that concentrations in various reservoirs would approach steady-state values reflecting the turnover times of the reservoir. Because of their long turnover times, the oceans and seas would continue to have a lower tritium concentration than reservoirs such as the lower atmosphere, where the turnover times are much more rapid. This is currently the case, since rainfall over continental areas is higher than that over oceanic sites[27] due to the dilution afforded by the mixing of the ocean surface.

DISSOLUTION OF CALCIUM-STRONTIUM CARBONATE AND ITS SUBSEQUENT MOVEMENT THROUGH THE GROUND

D. G. Jacobs O. M. Sealand
Judy Varga

During a 13-year period from 1951 to 1964, a total of about 21,000,000 gal of highly basic intermediate-level liquid wastes were disposed of by discharge into open waste-seepage pits at ORNL.[29] The major portion of the ^{90}Sr in the pits is associated with sludge that has accumulated in the bottom of the pits. This sludge consists primarily of Grundite (a commercial illitic clay) and calcium carbonate from the process waste water treatment plant, and the ^{90}Sr is most likely associated with the $CaCO_3$, which makes up about 20 to 30% of the sludge. Although ^{90}Sr is known to be relatively immobile in soil under the highly basic conditions of the waste as it is discharged, there has been concern that it might be released from precipitates and move rapidly in the ground upon a sudden lowering of pH.

Estimates of the future release of ^{90}Sr from the seepage pit area were made, based on the assumption that its release would be proportionate to the dissolution and release of calcium carbonate. These calculations indicated that rapid releases of ^{90}Sr are not likely, since it would take about 1200 years of incident rainfall, assuming complete infiltration, to dissolve all of the calcium carbonate in the sludge. In order to check the validity of the assumption that ^{90}Sr release to surface streams would be proportionate to that of calcium, two series of laboratory experiments were designed.

In the first series of experiments, calcium carbonate was precipitated at the top of a hydrobiotite column from a solution tagged with ^{45}Ca and ^{85}Sr. The mixed solution was allowed to stand for an hour to allow the precipitate to form and settle. The excess solution was allowed to pass through the column and was collected in 10-ml increments. This step simulates the pit system during waste-

[27] R. L. Nace, "Water Management, Agriculture, and Groundwater Supplied," pp. 43–61 in *Water and Agriculture*, ed. by R. D. Hockensmith, American Association for the Advancement of Science, The Hornshafer Company, Baltimore, 1960.

[28] H. V. Sverdup *et al.*, *The Oceans – Their Physics, Chemistry, and General Biology*, pp. 8–46, Prentice-Hall, Englewood Cliffs, New Jersey, 1942.

[29] T. F. Lomenick, D. G. Jacobs, and E. G. Struxness, *Health Phys.* 13(8), 897–905 (August 1967).

disposal operations. Following this step, the column was leached with HCl or EDTA solution to represent subsequent leaching by groundwaters.

In the second series of experiments, the only difference in procedure was that the introduction of the ^{85}Sr tracer was delayed until after the calcium carbonate precipitate had formed and settled. At this time the ^{85}Sr was added and allowed to stand for an hour before completing the experiment. This permits one to examine the possible difference in behavior of strontium that is adsorbed onto preformed calcium carbonate with that coprecipitated with calcium carbonate.

Samples of the effluent fractions were taken for measurement of pH and for counting of ^{45}Ca and ^{85}Sr. The columns showed hydroxide ion consumption of about 0.1 meq/g when correction was made for the hydroxide ion contained in the pore volume of the column (Table 4.5). This is about the same as that measured previously for Conasauga shale from the seepage pit area.[30] The hydrogen ion consumption by both the Conasauga shale and the hy-

[30] D. G. Jacobs, Y. E. Kim, and O. M. Sealand, *Health Phys. Div. Ann. Progr. Rept. July 31, 1966*, ORNL-4007, p. 31.

Table 4.5. Hydrogen Ion and Hydroxide Ion Consumption by 20-g Vermiculite Columns

OH^- Added (meq)	H^+ Added (meq)	OH^- Adsorbed (meq)	H^+ Adsorbed			
			1 *M* HCl (meq)	0.1 *M* HCl (meq)	0.05 *M* HCl (meq)	0.01 *M* HCl (meq)
2		0.7				
4		1.4				
6		1.8				
8		1.9				
10		2.1				
12		2.2				
14		2.1				
16		2.0				
18		2.0				
20		2.3				
20	1					1
20	2					2
20	3					3
20	4			4		4
20	5			5	5	5
20	6			6	6	6
20	7			7	7	7
20	8			8	8	8
20	9			9	9	9
20	10		10	10	10	10
20	15			15	15	15
20	20		20	21	20	19.4
20	25			25	24.5	23.7
20	30		28.5	28.8	28.2	27.8
20	35			32.0	31.6	31.9
20	40		34.8	34.6	35.1	35.6
20	45			37.1	38.7	39.1
20	50		43.6	39.6	42.4	40.2
20	55			42.0	44.9	40.6
20	60		39.7	44.4	45.7	37.3

drobiotite was considerably greater than the hydroxide ion consumption. For Conasauga shale, the hydrogen ion consumption was about 2.6 meq/g,[31] while for the hydrobiotite used in this study it was about 2.2 meq/g (Table 4.5). For Conasauga shale the hydrogen ion consumption was thought to be due to the satisfying of exchange sites by hydrogen and to dissolution of calcium carbonate. In the case of the present columns, the dissolution of calcium carbonate would only account for 0.05 meq/g of hydrogen ion consumption, and satisfaction of the exchange sites would add another 0.80 to 0.85 meq/g. The remaining buffering capacity is apparently due to degradation of the hydrobiotite lattice. This was manifest in experiments where 1 *M* HCl leaches were used, because iron appeared in the effluent even though the free iron oxide had been removed. The iron apparently was freed from octahedral lattice sites in the hydrobiotite. At any rate, it seems highly unlikely, in view of this rather substantial buffering capacity, that a drastic change in pH could occur to release ^{90}Sr from the system.

Less than 1% of the ^{45}Ca and ^{85}Sr introduced into the column appeared in the effluent prior to leaching of the columns. No significant activity appeared in the effluent until breakthrough of the acid front occurred. In the case of EDTA leaches, it was necessary to add only about enough EDTA to complex the calcium in the system. There was no apparent difference in behavior whether the ^{85}Sr was added before or after precipitation of the calcium carbonate (Table 4.6). The behavior of calcium and strontium was quite similar and is directly related to the amount of acid added in the leaching process (Fig. 4.1).

[31] D. G. Jacobs and O. M. Sealand, *Health Phys. Div. Ann. Progr. Rept. July 31, 1964*, ORNL-3697, pp. 56–59.

Table 4.6. The Effect of the Concentration of the Leaching Solution on the Dissolution and Movement of $Ca(Sr)CO_3$ Through a Vermiculite Column

Leaching Solution	50% Breakthrough Volume (ml)				K_{Ca}^{Sr} [a]
	Uncorrected		Corrected for Pore Volume of Column		
	V_{Sr}	V_{Ca}	V'_{Sr}	V'_{Ca}	
Series I (Sr and Ca Carbonates Coprecipitated Together)					
1.0 *M* HCl	38.34	31.54	20.34	13.54	1.502
0.1 *M* HCl	328.2	242.9	310.2	224.9	1.379
0.05 *M* HCl	339.8	351.9	321.9	333.9	0.964
0.01 *M* HCl	2025	2198	2007	2180	0.921
0.1 *N* EDTA	46.57	39.58	28.57	21.58	1.324
0.01 *N* EDTA	125.2	135.3	107.2	117.3	0.914
				Average	1.18 ± 0.47
Series II (Sr Added After $CaCO_3$ Precipitated)					
1.0 *M* HCl	45.69	36.41	27.69	18.41	1.504
0.1 *M* HCl	277.0	310.3	259.0	292.3	0.886
0.1 *M* HCl	336.7		318.7		
0.05 *M* HCl	497	513	479	495	0.968
0.01 *M* HCl	1978	2474	1960	2461	0.796
				Average	1.13 ± 0.42

[a] $K_{Ca}^{Sr} = V'_{Sr}/V'_{Ca}$.

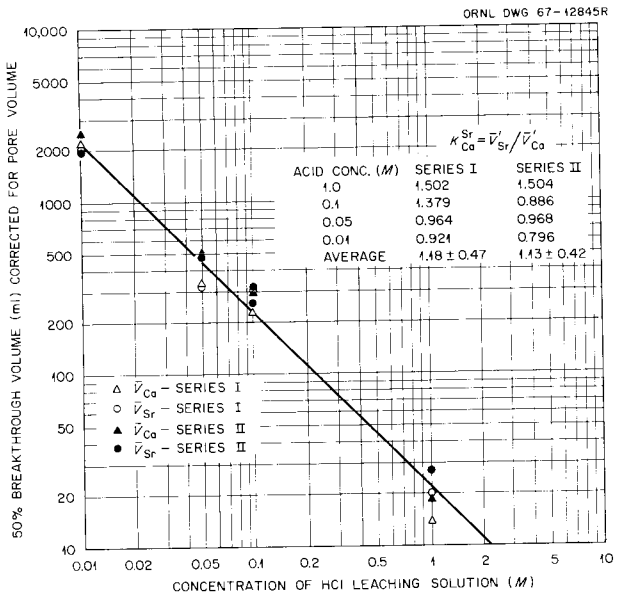

Fig. 4.1. Breakthrough Volumes of Strontium and Calcium as a Function of the Concentration of HCl Used for Leaching.

On the basis of these results, we feel that the original assumptions regarding the relative behavior of strontium and calcium in the waste seepage pit area are justified. The original calculations are somewhat conservative, because the buffering capacity of the Conasauga shale was not taken into consideration. It is quite improbable that enough acid could be added to the system to dislodge the strontium. Complexing agents, such as EDTA, might be more effective, but even then enough complexing agent would have to be added to complex all cations in the soil that have stronger complexes than strontium before substantial fractions of ^{90}Sr would be removed.

DEVELOPMENT OF CRITERIA FOR THE LONG-TERM STORAGE OF HIGH-LEVEL RADIOACTIVE SOLID WASTES

D. G. Jacobs

In the report of the Committee on Waste Disposal of the Division of Earth Sciences, National Academy of Sciences, it is recommended that disposal of highly radioactive wastes in salt is the most promising method for the near future.[32] However, they also suggest that the next most promising means of containment is the stabilization of the waste in a rather insoluble slag or ceramic material which could be placed in dry mines, surface sheds, or large cavities in salt. During the decade that has passed since these recommendations were made, the feasibility of disposal of high-level wastes in salt mines has been demonstrated, and there is little doubt that salt provides optimum characteristics for a disposal environment.

However, the question has recently been raised as to whether the permanent disposal of high-level radioactive solid wastes in salt mines offers the optimum method of waste management for all situations. In our estimation the principal criterion in determining the acceptability of any method of waste management is the probable exposure of man to radiation. Secondarily, the economics must be favorable. At this time it might be advisable to interpret a discussion of the distinction between waste storage and waste disposal. As John Frye, director of the Illinois State Geological Survey, aptly pointed out, *waste disposal* in a situation in the geologic environment implies that, should it become necessary because of a catastrophe (earthquake, war, or pestilence), surveillance at a site could be suspended and the site left unattended without causing undue concern regarding radiation exposure to man. A *waste storage* operation not fulfilling this criterion would be considered temporary and would necessitate continued surveillance. This should not imply that surveillance would not be maintained at waste-disposal facilities, only that it could be suspended with no catastrophic consequences.

In waste-management schemes currently proposed for high-level wastes, there is an initial period of on-site storage of liquid waste, followed by a solidification process and transport to a central disposal facility. One can raise the question, "If it can be considered acceptable to store liquid wastes on-site during the time when the radionuclide content is highest and the hazard potential is greatest, why cannot the wastes be stored on-site as solids for much longer times?" In light of the above discussion, one reason seems apparent: unless the situation were extremely favorable, this storage

[32] H. H. Hess (chairman), *The Disposal of Radioactive Wastes on Land*, NAS-NRC Publication 519, September 1957.

could only be considered temporary and would require continued surveillance. However, in our estimation, it seems that if suitable geologic formations were available permanent disposal on-site could be possible. For example, if salt deposits existed locally, there would seem to be little merit in transport of the wastes to some remote central disposal facility. Formations other than salt may not offer as good characteristics for permanent disposal, but their deficiencies may not result in an increase in hazards comparable with those hazards that may be encountered in waste transport through nonrestricted areas. This evaluation of relative hazard is extremely difficult to make, because in the one case we are dealing with a very long time of potential exposure compared with a second case where the potential exposure is short term.

In order to determine whether long-term on-site storage can be accomplished safely, several factors need to be considered. If, on the basis of these criteria, it seems highly improbable that unattended wastes would result in radiation exposure to man over the lifetime of the wastes, then it would seem that on-site disposal could be considered.

The first set of factors that need to be considered concern the nature of the waste material. Liquid wastes are more mobile than solid wastes and would have a higher hazard potential. The hazard potential could be reduced even more by forming solids that have low rates of dissolution, such as ceramics or glasses. The rate of release of radioactivity will be further influenced by the structural integrity and specific surface of the solid material. Also of importance is the stable salt content that would result from the leaching of the material, since this would affect the subsequent mobility of radionuclides through the ground. The thermal properties of high-level wastes are also of concern. Elevated temperatures might adversely affect the structural integrity of the disposal formation, though it would seem that most formations would rank higher than rock salt in this respect. Thermal gradients will also affect flow of water, and this factor needs some theoretical and experimental attention in order to evaluate the consequent effect on radionuclide movement. If the formation can tolerate elevated temperatures, the maximum temperature may be limited by volatility of specific radionuclides.

A second set of factors to be considered in long-term storage or disposal on-site is the nature of the container. In most cases, it is expected that the life expectancy of the container is much shorter than the life of the long-lived radionuclides. In order to be an effective barrier, the container would need to be resistant to failure at high temperature and to chemical attack, both from the outside and from within. The container should also be impermeable, so that release of radioactivity is kept to a minimum. Naturally, the integrity of the container is related to the nature of the waste; the more mobile the waste material, the greater the required integrity of the container.

Another important aspect of the container is its placement with respect to land surface, groundwater, and surface water. If the waste is placed above circulating groundwater, natural hydrologic processes will tend to move the material into the hydrosphere. Although the movement may be extremely slow, one must remember, in making a judgment concerning disposal of these high-level wastes, that the extrapolations in time are extreme. As a result, we would need to factor into our estimations several orders of magnitude to account for inexact procedures of extrapolation. The picture is not entirely hopeless, however, because in soils literature there are examples of nutrient leaching that have been followed for a few centuries.[33] For disposal operations it seems imperative that the waste be placed below circulating waters. In such a situation the geophysical properties of the disposal formation would need to be clearly defined. Some of the more important factors would include thermal properties, structural integrity (especially under elevated temperatures), and seismic activity.

For long-term storage above the water table, a much more complete description of the environment would be required. Geohydrologic and geochemical properties would need to be obtained in order to estimate rates and direction of radionuclide movement through the ground and into surface waters. A description of local demography and of water usage would be requisite for determining potential exposure from drinking water and from other food chains involving water. A study of the physical properties of the soil would be necessary to describe transport of radioactivity due to erosion or runoff. If some of the material can become airborne, meteorological conditions would require attention.

---

[33] H. Jenny, "Time as a Soil Forming Factor," Chapter III, pp. 31–51 in *Factors of Soil Formation*, McGraw-Hill, New York, 1941.

The ultimate criterion for management of radioactive wastes is the possible radiation exposure of man. If the method employed is such that there is no serious threat to man if the operation were abandoned, then the scheme can rightfully be called a disposal operation. On the basis of present information, salt offers the optimum combination of properties for a disposal formation. However, it seems possible that other formations may also be suitable.

LONG-RANGE WASTE MANAGEMENT STUDY

W. J. Boegly, Jr. J. O. Blomeke

A draft of preliminary information for the long-range waste management study has been completed and sent to the AEC for review. Since the AEC, through their Systems Analysis Task Force, is currently attempting to determine the types of reactors that will be installed between now and the year 2000, it was requested that we use one of their preliminary estimates as the basis for the draft study. The reactor mixture recommended is based on light-water reactors and fast breeder reactors (see Table 4.7).

Based on the assumed growth of nuclear power in the United States, estimates were made of the amounts of fuel to be reprocessed and the resulting waste volumes to the year 2000. Reactor types are principally light-water reactors, but fast breeder reactors assume an increasingly significant role after 1985. In estimating waste production and characteristics, the two types of reactors were considered separately and the results combined to obtain a composite reflecting the entire population.

Table 4.7. Growth of Nuclear Power in the United States, 1970–2000

Installed electrical capacity in thousands of megawatts

Calendar Year Ending –	Light-Water Reactors	Fast Breeder Reactors	Total
1970	12	0	12
1980	123	0	123
1990	294	41	335
2000	430	245	675

High-Level Waste

For the case of light-water reactors, it was assumed that the fuel was exposed to 33,000 Mwd/ton at an average power of 24.5 Mw/ton. The fuel to be processed annually rises from 300 tons in 1970 to 17,000 tons in 2000. Assuming that the fuel is processed by aqueous methods and that the resulting waste is concentrated to 100 gal per 10,000 Mwd (thermal) exposure, the annual production of waste will increase from 100,000 gal in 1970 to 5,600,000 gal in 2000. If it is stored as a liquid, 72,000,000 gal will have accumulated by the year 2000. On the other hand, if it is converted to a solid form, waste volumes may be reduced by a factor greater than 13. Fission product levels were calculated on the basis of continuous reactor operation at 24.5 Mw/ton and processing of the fuel 150 days after its discharge from the reactor.

Power generation by liquid-metal fast breeder reactors begins in 1985. For these reactors, it was assumed that all the power was generated in the core and that they operated with a specific power in the core of 113 Mw/ton, a spent fuel exposure of 80,000 Mwd/ton, and a load factor of 0.83. The quantity of fuel and blanket to be processed annually will rise from 500 tons in 1990 to 2700 tons in the year 2000. With aqueous processing of this material, it is estimated that 3,300,000 gal of liquid waste, concentrated to a volume of 100 gal per 10,000 Mwd of fuel exposure, will have accumulated by 2000. If converted to solids, 33,000 ft^3 will have been produced by 2000. Fission product levels in these wastes were calculated on the basis of continuous reactor operation at 89.3 Mw/ton and a 75-day delay between the times of fuel discharge from the reactor and fuel processing. In estimating the total fission product activities and heat-generation rates, ^{235}U thermal fission yields were used, as they have been found to give results in reasonable agreement with calculations based on fast fission yields. For individual isotopes, however, fast fission yields for ^{3}H, ^{85}Kr, ^{90}Sr, ^{137}Cs, and ^{144}Ce of 0.01, 0.6, 2.5, 6.6, and 3.9, respectively, were used.

The total fuel processing requirements, waste volumes, and fission product levels for the total projected nuclear power economy to the year 2000 are given in Table 4.8.

Table 4.8. Estimated Waste from United States Nuclear Power Economy

Aqueous processing of all fuels

	Calendar Year			
	1970	1980	1990	2000
Installed capacity, 10^3 Mw (electrical)[a]	12	123	335	675
Electricity generated, 10^9 kwhr/year[a]	89	880	2230	4295
Fuel processed, 10^3 tons/year[a]	0.3	3.5	11.5	19.7
Volume of waste produced, as liquid[b]				
Annually, 10^6 gal/year	0.10	1.2	3.7	6.1
Accumulated production, 10^6 gal	0.2	4.8	27	75
Volume of waste produced, as solid[c]				
Annually, 10^3 ft^3/year	1.0	12	37	61
Accumulated production, 10^3 ft^3	2.0	48	270	750
Accumulated fission products[d]				
Total weight, metric tons	8	490	3000	8000
Total beta activity, megacuries	1000	16,000	67,000	140,000
Total heat generation rate, 10^6 Btu/hr	11	150	700	1400
^{90}Sr, megacuries	16	790	5800	15,000
^{85}Kr, megacuries	2	90	610	1500
^{3}H, megacuries	0.07	2.7	19	45
^{144}Ce, megacuries	100	1350	6100	11,000
^{137}Cs, megacuries	16	790	5800	15,000

[a]Data from phase 2, case 3, Systems Analysis Task Force (Aug. 25, 1967).

[b]Assumes wastes concentrated to 100 gal per 10,000 Mwd (thermal).

[c]Assumes 1 ft^3 of solidified waste per 10,000 Mwd (thermal).

[d]Assumes LWR fuel continuously irradiated at 24.5 Mw/ton to 33,000 Mwd/ton and processing 150 days after reactor discharge; assumes LMFBR fuel continuously irradiated at 89.3 Mw/ton to 80,000 Mwd/ton and processing 75 days after discharge from reactor.

Low- and Intermediate-Level Liquid Wastes

For this study intermediate- and low-level liquid wastes have been estimated to be produced at rates of 200 and 10,000 gal/ton, respectively. In addition to these volumes, it can also be assumed that around 3×10^6 gal/year of low-level waste will be produced at each reprocessing plant from sources such as cell drainage, equipment decontamination, and laboratory sinks. Volumes of intermediate- and low-level waste produced are presented in Table 4.9. The volumes presented in this table do not include the estimated 3×10^6 gal/year per plant.

Table 4.9. Estimated Volumes of Low- and Intermediate-Level Wastes

Calendar Year Ending –	Gallons per Year	Accumulated Gallons
	Intermediate-Level Waste	
1970	60,000	120,000
1980	700,000	3.4×10^6
1990	2.1×10^6	18.5×10^6
2000	3.9×10^6	50.9×10^6
	Low-Level Waste	
1970	3×10^6	
1980	35×10^6	
1990	110×10^6	
2000	197×10^6	

DEEP-WELL INJECTION OF BRINE EFFLUENTS FROM INLAND DESALTING PLANTS

W. J. Boegly, Jr. D. G. Jacobs
T. F. Lomenick O. M. Sealand

Deep-well injection has been proposed as a method for disposal of brine effluents from inland desalting plants. This method has been used extensively for over 60 years for the disposal of brines from producing oil fields. In recent years, there has been increased use of deep-well injection for disposal of industrial wastes; at the end of 1966 there were 78 such wells in use. Literature pertaining to the use of deep-well injection has been reviewed in order to determine the feasibility of its use for disposing of brine effluents from inland desalting plants.[34]

A review of pertinent literature reveals that deep-well injection is technically feasible if satisfactory pretreatment is provided. Industrial waste can be disposed of in this manner for about $1.00 to $2.00 per 1000 gal. Brine disposal from oil-field operations is less costly, ranging from $0.25 to $0.70 per 1000 gal, primarily because of the magnitude of the operations and because less extensive pretreatment is required.

In order to prevent damage to the receiving formation, it will be necessary to inject waste solution without plugging the formation. This requires that the solution be free of suspended solids and be chemically stable with regard to formation of precipitates. Treatment may also be required to prevent biological growths which can plug the injection face.

A suitable site for deep-well injection requires a permeable sedimentary formation, such as sandstone or limestone, capped by an impermeable formation, such as shale, to prevent pollution of neighboring potable waters. Such sequences of formations are most likely to be situated in the closed basins, but suitable sites may be found throughout wide geographic areas of the country. Even when preliminary screening suggests that the general area is highly favorable for deep-well injection, more detailed geologic and hydrologic investigations will be required to assure that the site is satisfactory and to provide data to be used as the basis for designing an injection system.

[34] W. J. Boegly, Jr., D. G. Jacobs, T. F. Lomenick, and O. M. Sealand, "Deep-Well Injection of Brine Effluents from Inland Desalting Plants," to be published.

5. Earthquakes and Reactor Safety

T. F. Lomenick

LABORATORY STUDIES OF STRAIN ACCUMULATION IN ROCKS

Faulting is believed to be the cause of most of the shallow earthquakes in California and other tectonically related areas of the Circum-Pacific belt. This mechanism for earthquakes requires that the rock column accumulate strain until the frictional resistance of the principal fault is overcome or the elastic limits of deformation in the rocks are surpassed, and then the fault slips, or the rocks fracture, and earthquakes are generated. Thus, if the accumulation of strain in the rock column in and around faults can be measured and understood, it should be possible to determine the seismic state of a given area.

At the present time, strain accumulation in rocks is measured by geodetic surveys along triangulation nets that cross faults, etc. This method is expensive, time consuming, and, in many cases, lacks the needed precision for quantitative determinations. Another technique is the installation of strain meters at or near the surface. This technique is far more accurate than geodetic surveys but is sensitive to surface noise, etc., and has the disadvantage of measuring only the strain accumulation at the surface. It is, of course, important to measure strain accumulation at the surface but more important to measure it at depth. A promising alternative or addition to these methods of determining strain accumulation is to determine the stress and strain relationships in rocks through studies in the laboratory of core specimens or other samples taken at many places and at depths much greater than is practical with the other techniques. The method of stress determination is based on the fact that rocks such as limestone, sandstone, etc., remember the stress conditions that they have been subjected to, and this can be determined in the laboratory. On a macro scale, the stress in rocks like this may be completely elastic, and the stress is a reversible process; but on the micro scale the rocks have a memory.

Rock specimens are being obtained from selected localities that typify various stages of tectonic activity to determine fundamental relationships between the recent stress history of the area to that recorded and subsequently measured in rock sections. Lateral variations in the intensity of the recorded stress conditions adjacent to the controlling tectonic and/or structural features will be investigated, as will variations in the intensities of the recorded and measurable indicators.

6. Dose Estimation Studies Related to Peaceful Uses of Nuclear Explosives

P. S. Rohwer S. V. Kaye
K. E. Cowser W. S. Snyder
E. G. Struxness

Because there is a possibility that peaceful nuclear explosions may result in some finite radiation exposure to human populations, the methods of estimating anticipated radiation dose must be sufficiently well developed so that planning to ensure the maximum safety of all members of the population may be carried out confidently. Calculation of dose equivalents[1] for the general population requires biological data for adults, children of all ages, and even for fetuses. Age-dependent problems of this type are exceedingly more complex than when only the parameters characterizing "standard man" are used; however, when parameters that change with age are used, the resulting dose estimates may be helpful to identify the critical population group. This segment of the population probably will receive the highest dose equivalents and thus exert the most restrictive conditions on the detonation. Techniques for estimating the dose received by a population have been developed and applied. In both internal and external dosimetry we have stressed estimating the "expected" dose as accurately as possible, as opposed to the maximum dose or upper limit of dose often alluded to by other workers in this field. When dose estimates are made as realistic as possible, critical groups in the potentially exposed populations can be identified and advance remedial action taken to protect the safety of these critical population groups. This approach is highly recommended by the ICRP.[2]

This work was initiated under subcontract to Battelle Memorial Institute as part of a bioenvironmental study to determine the radiological-safety feasibility of using nuclear explosives to excavate a sea-level canal across the isthmus of Central America. Additional development and application was done with support from the AEC Division of Peaceful Nuclear Explosives.

ESSENTIAL INFORMATION FOR DOSE ESTIMATION

The information essential to estimate dose to a population may be divided into five general categories: (1) inventory and vented fractions of radionuclides produced, (2) environmental dilution or concentration factors, (3) intake and/or exposure-time factors, (4) biological parameters and habits characterizing the populations being exposed, and (5) dose-estimation equations.

Almost all data on production and venting for cratering and noncratering Plowshare devices are based on the technology developed at the National Testing Site in Nevada. After a nuclear detonation, there is an inventory of radionuclides composed of fission products, residual fissionable materials, fusion products, device activation products, and soil and rock activation products. This inventory

[1] Dose equivalent (rems) = absorbed dose (rads) × modifying factors. For the sake of convenience, "dose" is often used interchangeably with "dose equivalent" in this report.

[2] International Commission on Radiological Protection, *Principles of Environmental Monitoring Related to the Handling of Radioactive Materials* (Report by Committee 4), ICRP Publication 7, Pergamon, London, 1966.

is the source for potential radiation exposure when some of it is vented to the atmosphere or redistributed in the environment by groundwater, so that it enters a food chain or exposure pathway leading to man.

When radioactivity is vented to the environment, it is subjected to movement through pathways which might eventually lead to man. When attempting to predict radiation doses from proposed peaceful nuclear explosions, probably one of the most formidable tasks centers around anticipating for a given detonation, in a given environment, that fraction of the inventory which will expose man. A systems-analysis approach, based on coupled-compartment models of the environment, is one of the most promising methods for identifying critical pathways and eventual concentrations of radioactivity in foods consumed by man. Such an approach, utilizing a computerized sensitivity analysis of transfer coefficients, has been discussed and illustrated by Kaye and Ball.[3] The concentration of radioactivity in each exposure medium (compartment) is not easily determined when radioactivity moves through complex pathways. This concentration as a function of time may be estimated with an income and loss equation which reflects a net concentration resulting from interactions with other environmental compartments by direct or indirect coupling. The concentration of radioactivity as a function of time in a compartment of reference may be represented by

$$m_b \frac{dX_b}{dt} = \sum_{\substack{a=0 \\ a \neq b}}^{n} \lambda_{ab} m_a K_{ab} X_a - \sum_{\substack{a=0 \\ a \neq b}}^{n} \lambda_{ba} m_b K_{ba} X_b - \lambda_r m_b X_b \,, \quad (1)$$

where

b = subscript designating the compartment of reference,

a = subscript designating any donor or receptor compartment other than compartment b,

X = radionuclide concentration, μc/g,

λ = environmental transfer coefficient, [(grams transferred)/(total grams present)]/day = days^{-1}

λ_r = radioactive decay constant, days^{-1},

m = biomass per unit area, g/m^2, the subscript designation depending upon how the biomass transfer is controlled, and

K = selectivity factor (dimensionless) which adjusts the environmental transfer coefficient when it differs quantitatively from the radionuclide transfer coefficient (usually set equal to 1.0).

The output from the systems-analysis code is the input for a dose-estimation code.

THE EXREM CODE FOR ESTIMATING EXTERNAL DOSE

The three modes of exposure being given consideration for estimating external dose are: (1) submersion in the overpassing radioactive cloud, (2) submersion in contaminated water, and (3) exposure to a contaminated ground surface. Exposure to the overpassing cloud is unique because it may last only a few hours for each detonation, whereas exposures from the other two modes may persist for longer periods.

The following generalized expression is applicable to any external-exposure pathway and has been programmed for estimating dose equivalents from external exposure:

$$D_{ikq}(t_1, t_2, x) = \int_{t_1}^{t_2} \sum_{n=1}^{N'} Q_{inq} e^{-\lambda_{ri}(t-\tau_n)} P_{ikn}(x) C_{iq}(x)\, dt \,, \quad (2)$$

where

$D_{ikq}(t_1, t_2, x)$ = total external dose equivalent (rems) from beta particles or photons (identified by the index q) of radionuclide i at location k accumulated from exposure during the interval t_1 to t_2 for the mode of exposure x resulting from N' detonations,

t_1, t_2 = time (hr) entered and time left contaminated area,

x = mode of exposure,

[3] S. V. Kaye and S. J. Ball, "A Coupled Compartment Model for Radionuclide Transfer in a Tropical Environment," in *Proceedings of Second National Symposium on Radioecology* (in press).

n = detonation number,

N = number of detonations,

N' = maximum n such that $\tau_n \leqq t$ ($N' \leqq N$),

τ_n = time (hr) of the nth detonation,

Q_{inq} = quantity (μc) of the qth particle or photon of radionuclide i released from the nth detonation,

λ_{ri} = radioactive decay constant (hr^{-1}) of radionuclide i,

P_{ikn} = location correction factor (cm^{-2} or cm^{-3}) for the ith radionuclide at the kth location due to the nth detonation, and

$C_{iq}(x)$ = dose rate (rems/hr) per microcurie due to beta particles (q = 1) or photons (q = 2) of the ith radionuclide in mode of exposure x.

This code can be used to estimate the accumulated external dose resulting from any one or all of the three modes of exposure when the proper dose-rate equation is substituted for the term $C_{iq}(x)$. All of the dose-rate equations used in the EXREM code are listed and explained by Cowser *et al.*[4] The equation for estimating the dose rate above the ground surface requires that the height be specified, whereas the two submersion equations assume that the entire body surface is in contact with a large volume of contaminated air or water. The location correction factor, P_{ikn}, actually relates how much of the radionuclide production is present per square centimeter of land surface or per cubic centimeter of air or water and can be estimated with a fallout prediction model and systems-analysis techniques.

THE INREM CODE FOR ESTIMATING INTERNAL DOSE

When the rate of intake of radioactivity has been determined, this information is the primary radioactivity input for estimating the cumulative dose equivalents by the INREM code. These estimates of dose equivalents are compiled for the various body organs from inhalation or ingestion of radioactivity programmed as continuous or intermittent intakes as a function of age. The parameters in the dose equations change as a function of time as the person ages during the time of intake or during the period of interest, which may be longer than the period of intake. The model programmed for all organs except the GI tract is written:

$$D_{in}(t_1, t_2, t_b) = 51 \int_{t_1}^{t_2} I_i[(t - t_b), t] \times f_{in}(t - t_b) \left\{ \int_t^{t_2} \frac{\epsilon_{in}(s - t_b)}{m_n(s - t_b)} \times \exp\left[- \int_{t-t_b}^{s-t_b} \lambda_{in}(y)\, dy \right] ds \right\} dt, \quad (3)$$

where

$D_{in}(t_1, t_2, t_b)$ = cumulative dose equivalent (rems) received during the time interval t_1 to t_2 from the ith radionuclide in the nth organ resulting from intake during this time interval by an individual born at t_b,

t_1 = time (days) of initial intake relative to time of reference detonation,

t_2 = time (days) at end of period of interest relative to time of reference detonation,

t_b = time (days) of birth relative to time of reference detonation,

t = time (days) after reference detonation,

s = time (days) after intake relative to time of reference detonation,

$I_i(t)$ = intake (μc/day) of ith radionuclide during a unit time period t,

$m_n(t)$ = mass (g) of the nth organ at t,

$f_{in}(t)$ = fractional absorption (dimensionless) of the ith radionuclide in the nth organ at t,

$\epsilon_{in}(t)$ = effective absorbed energy (Mev) of the ith radionuclide in the nth organ at t, and

[4] K. E. Cowser *et al.*, *Dose-Estimation Studies Related to Proposed Construction of an Atlantic-Pacific Interoceanic Canal with Nuclear Explosives: Phase I*, ORNL-4101 (March 1967).

$\lambda_{in}(t)$ = effective decay constant (days^{-1}) of the ith radionuclide in the nth organ at t.

The variables t_1, t_2, t_b, t, and s are measured relative to detonation, whereas the variables $I_i(t)$, $m_n(t)$, $f_{in}(t)$, $\epsilon_{in}(t)$, and $\lambda_{in}(t)$ are functions of the age of the individual. The code uses Eq. (3) for ingestion of contaminated food and water or inhalation of contaminated air and calculates the cumulative doses to all organs except the GI tract. When the dose to the GI tract is to be calculated, the $(MPC)_a$ or $(MPC)_w$ is used in conjunction with age-dependent parameters for intake, mass, effective absorbed energy, and the unassimilated fraction of intake.

SEARCH FOR CRITICAL RADIONUCLIDES

Over 200 different radionuclides may be produced by an underground nuclear detonation. The activity of some of these radionuclides will be relatively low, and they can be considered to constitute little or no hazard, especially when the activity is diluted still further in the environment. Usually when a large number of radionuclides are evaluated for their contributions to absorbed dose, only a few will deliver most of the dose. It is necessary to identify these "critical radionuclides" because special emphasis then can be placed on obtaining more detailed information on their physical and biological behavior in a given environment. Sometimes advance knowledge of critical radionuclides can result in effective remedial action to reduce radiation exposures. For example, if ^{131}I is expected to be a critical radionuclide, certain food products can be stored or prepared in such a way that the time lag between contamination and ultimate consumption will be long enough to allow radioactive decay of ^{131}I. (The radioactive half-life for ^{131}I is 8.05 days.)

Our systematic search for critical radionuclides has been divided into the following four steps:

1. *Radionuclide Dose Equivalent List (RDEL).* – An ordered arrangement of radionuclides according to (*a*) external dose from 1 μc per cubic centimeter of water, per cubic centimeter of air, and per square centimeter of ground surface and (*b*) internal dose commitment from a 1-μc single intake by inhalation and ingestion. An RDEL does not consider production, venting, or environmental exposure pathways.

2. *Radionuclide Dose Equivalent Index (RDEI).* – An ordered arrangement of radionuclides derived from an RDEL by the incorporation of production and venting estimates. An index does not include adjustments based on fallout predictions or environmental exposure pathways.

3. *Preliminary Radionuclide Rank (PRR).* – An ordered arrangement of radionuclides derived from an RDEI by the incorporation of information on initial distribution in time and space. A PRR considers fallout predictions but does not include adjustments for environmental exposure pathways.

4. *Final Radionuclide Rank (FRR).* – An ordered arrangement of radionuclides derived from a PRR by incorporation of the best available estimates of radionuclide intakes and/or concentrations of radionuclides in the environment resulting from redistribution.

Steps 1 and 2 in the search for critical radionuclides have been completed for the canal feasibility study. The information needed to complete steps 3 and 4 is now being assembled by others. Composite analyses of the results obtained from step 2 are presented as important elements in Tables 6.1 and 6.2. Since many of the potentially critical radionuclides do not exist in the environment in sufficient quantities to be detected, it will be necessary to analyze environmental samples for stable elements. Stable-element data can then be used as an analog for the likely distribution of radionuclides in the various environmental media at the site of sampling, provided the isotopes are not fractionated and provided the chemical forms of the stable element and the radioisotopes are the same. Therefore the radionuclide lists and indexes were analyzed to identify the important elements. The potential dose for each element was estimated for each mode of exposure by summing the potential doses of its radioisotopes. The elements were then arranged in descending order of the summed percentage contribution of their radioactive isotopes to the total potential dose in each mode of exposure. Table 6.1 presents elements representing the radionuclides which together contributed approximately 99% of the total external dose when analyzed according to the RDEI's, which consider radionuclide production and venting but do not consider initial distribution and subsequent redistribution of the radionuclides. Table 6.2 presents elements representing the radionuclides which together contributed approximately 99% of the total

Table 6.1. Elements Whose Radionuclides Are of Greatest Importance for External Exposure

	Immediate Hazard[a]	Long-Term Hazard[b]	
	Submersion in Contaminated Air or Water	Submersion in Contaminated Air or Water	Exposure to a Contaminated Ground Surface
1	Lead	Hydrogen	Ruthenium-rhodium[c]
2	Sodium	Tungsten	Tungsten
3	Hydrogen	Ruthenium-rhodium	Manganese
4	Tungsten	Manganese	Strontium-yttrium
5	Manganese	Zirconium-niobium	Yttrium
6	Iodine-xenon	Beryllium	Zirconium-niobium
7	Barium-lanthanum	Cesium-barium	Cesium-barium
8	Krypton-rubidium	Strontium-yttrium	Beryllium
9	Ruthenium-rhodium	Yttrium	Promethium
10	Tellurium-iodine	Cerium	Krypton-rubidium

[a]Based on radionuclide production and venting estimates, total dose equivalent received in 13 weeks or less.

[b]Based on radionuclide production and venting estimates, dose-equivalent rate after one year of radioactive decay.

[c]This notation indicates that the dose contributions from the daughter radionuclides have been considered. In this case, for example, dose contributions from rhodium isotopes present as a result of radioactive decay of ruthenium were added to the dose estimates for the ruthenium isotopes, whereas dose estimates for the rhodium isotopes to be produced directly during the detonations were treated as a separate entity.

Table 6.2. Elements Whose Radionuclides Are of Greatest Importance for Internal Exposure

	Immediate Hazard[a]				Long-Term Hazard[b]	
	Ingestion		Inhalation		Ingestion	
	Soluble	Insoluble	Soluble	Insoluble	Soluble	Insoluble
1	Lead	Lead	Lead	Lead	Hydrogen	Hydrogen
2	Manganese	Manganese	Manganese	Manganese	Strontium	Tungsten
3	Iodine	Tungsten	Plutonium	Hydrogen	Tungsten	Ruthenium
4	Tungsten	Sodium	Iodine	Tungsten	Ruthenium	Cerium
5	Sodium	Hydrogen	Tungsten	Sodium	Plutonium	Manganese
6	Zirconium	Iodine	Sodium	Iodine	Cerium	Plutonium
7	Yttrium	Strontium	Yttrium	Strontium	Manganese	Zirconium
8	Strontium	Yttrium	Strontium	Yttrium	Calcium	Yttrium
9	Ruthenium	Ruthenium	Zirconium	Zirconium	Lead	Cesium
10	Cerium	Zirconium	Ruthenium	Ruthenium	Iron	Beryllium

[a]Based on radionuclide production and venting estimates with no radioactive decay prior to intake.

[b]Based on radionuclide production and venting estimates with one year of radioactive decay prior to intake.

internal dose. The dose estimates which led to the lists of elements in Table 6.2 were obtained using "standard man"[5] parameters in the INREM code. It seemed prudent to use "standard man" parameters in the absence of data specific for the populations living at the site of the proposed canal. The lists in Tables 6.1 and 6.2 were obtained by analysis of the element indexes for the various exposure modes and radionuclide forms (soluble and insoluble) considered in the dose-estimation study. In most cases, the appearance of an element in these tables is the result of dose contributions from more than one of its radioactive isotopes. Although the present analyses indicate that these are the elements which have radionuclides likely to be of principal importance in the feasibility study, changes and improvements in the identification of critical radionuclides or elements can be expected as more information becomes available. It is important to note that the dose calculations, which were the basis for the the lists of elements in Tables 6.1 and 6.2, made no allowance for the many factors which may lead to significant differences in biological availability of the elements.

ESTIMATING DOSE EQUIVALENTS RECEIVED BY A POPULATION EXPOSED TO TRITIUM

This example with tritium in the form of tritiated water (HTO) illustrates the use of the INREM code as well as the influence of age-dependent parameters upon the estimates of dose equivalents. Tritium is expected to be produced in large quantities by nuclear devices of the type which could be used in peaceful applications,[6] and preliminary analysis indicates that it probably would be one of the critical radionuclides. Tritium would be present primarily in the form of tritiated water,[6] and, as such, a large fraction might move rapidly in the hydrologic cycle of the environment. Tritiated water (HTO) is absorbed readily by man regardless of the mode of exposure – ingestion, inhalation, or absorption through the skin.[7,8] The dose to the body-water pool, as a result of HTO entering the body, may be estimated with the INREM code. The body-water pool consists of the intracellular fluid, the interstitial fluid, and the blood plasma. Assessment of the radiation hazard resulting from intake of HTO on the basis of the dose to the body-water pool is conservative. The body-water pool constitutes approximately two-thirds of the mass for most body organs;[9] therefore dose estimates based on total-body mass or organ mass would be lower than those based on the mass of the body-water pool. In fact, if the total body were assumed to be the critical mass absorbing radiation as a result of HTO entering the body, the dose estimates obtained would be approximately 40% lower than those presented here. On the other hand there are some tissues for which the fraction which is water is rather higher, but clearly it cannot exceed 1. The question of dose to tissue in which tritium may be found in forms other than HTO poses a more difficult question; however, a tentative, but rather speculative, treatment of the question by Snyder *et al.*[10] indicates the dose to such tissues would not be expected to be substantially larger. The INREM dose model contains several parameters which may be age-dependent: daily radionuclide intake (I_i), effective absorbed energy (ϵ_{in}), fractional absorption of the radionuclide in the organ (f_{in}), effective elimination constant of the radionuclide in the organ ($\lambda_{in} = 0.693/T_e$), and the mass of the organ (m_n). In the case of HTO, f_{in} is assumed to equal 1.0 and ϵ_{in} is assumed to equal 0.01 Mev regardless of the age of the individual. These assumptions are justified because of the ease with which the body absorbs HTO and because of the extremely low maximum energy (0.018 Mev) of the tritium beta particles.

Three parameters had to be evaluated as functions of age before the dose estimates for the population could be calculated. The size of the body-water pool was estimated from data on total-body weight and the percent of the total-body weight which is water; such information is available from various sources.[11,12] Size of the body-

[5] International Commission on Radiological Protection, *Report of Committee II on Permissible Dose for Internal Radiation*, ICRP Publication 2, Pergamon, London, 1959; *Health Phys.* 3 (June 1960).

[6] F. W. Stead, *Science* **142**, 1163 (1963).

[7] E. A. Pinson and W. H. Langham, *J. Appl. Physiol.* **10**, 108 (1957).

[8] R. V. Osborne, *Health Phys.* **12**, 1527 (1966).

[9] P. Bard, *Medical Physiology*, C. V. Mosby Co., St. Louis, 1961.

[10] W. S. Snyder *et al.*, *Health Phys. Div. Ann. Progr. Rept. July 31, 1964*, ORNL-3697, pp. 173–77.

[11] E. Boyd, *Outline of Physical Growth and Development*, Burgess, Minneapolis, Minn., 1941.

[12] P. L. Altman, *Blood and Other Body Fluids*, Fed. Am. Soc. Exptl. Biol., Washington, D.C., 1961.

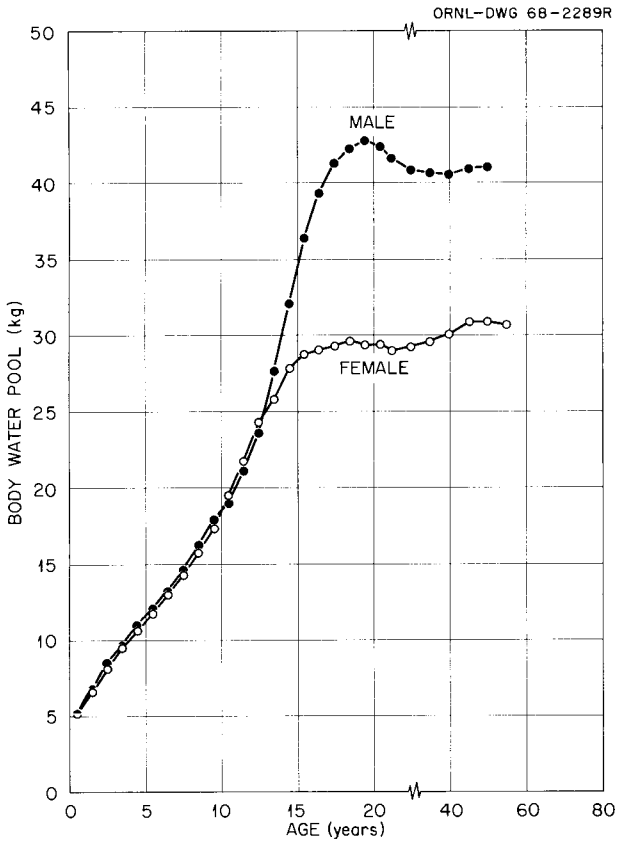

Fig. 6.1. Size of Body-Water Pool as a Function of Age.

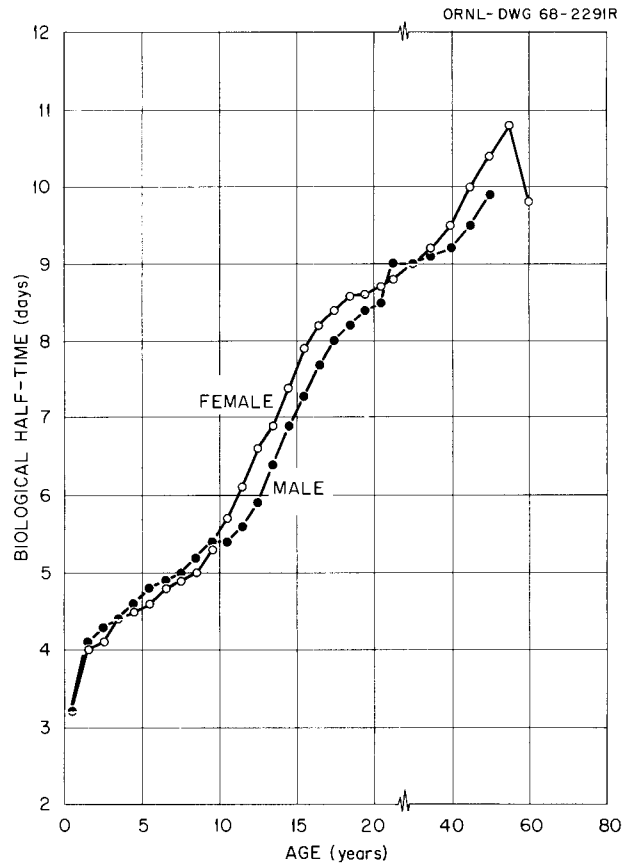

Fig. 6.2. Biological Half-Time of Water in Man as a Function of Age.

water pool is presented as a function of age in Fig. 6.1. The biological half-time (T_b) of water in the body-water pool was estimated with the following expression:

$$T_b = \frac{\ln 2}{\lambda_b} = \frac{\ln 2}{I'/m},$$

where

λ_b = biological elimination constant (days^{-1}) for turnover of the body-water pool,

I' = total daily water input (ml/day) to the body-water pool, and

m = size (ml) of the body-water pool.

The equilibrium relationship ($\lambda_b = I'/m$) may be used because HTO taken into the body is distributed uniformly throughout the body water, approximating equilibrium in less than 1 hr.[13] Total daily input to the body-water pool was estimated on the premise that 1 ml of water is required for each calorie of energy expended.[14] Figure 6.2 presents T_b as a function of age; T_e is essentially equal to T_b, in this case, because the radioactive half-life of tritium is long (12.3 years) relative to the biological half-time of water in the body-water pool (3 to 11 days). Daily tritium intake via inhalation can be estimated from data on daily air intake and the tritium concentration in the air. Figure 6.3 presents estimates of daily air intakes as a function of age. These estimates are based on age-dependent data describing daily oxygen consumption[14] and the concentration of

[13] E. A. Pinson, *Physiol. Rev.* **32**, 123 (1952).

[14] Food and Agriculture Organization, *Calorie Requirements*, FAO Nutritional Studies, No. 15 (1957).

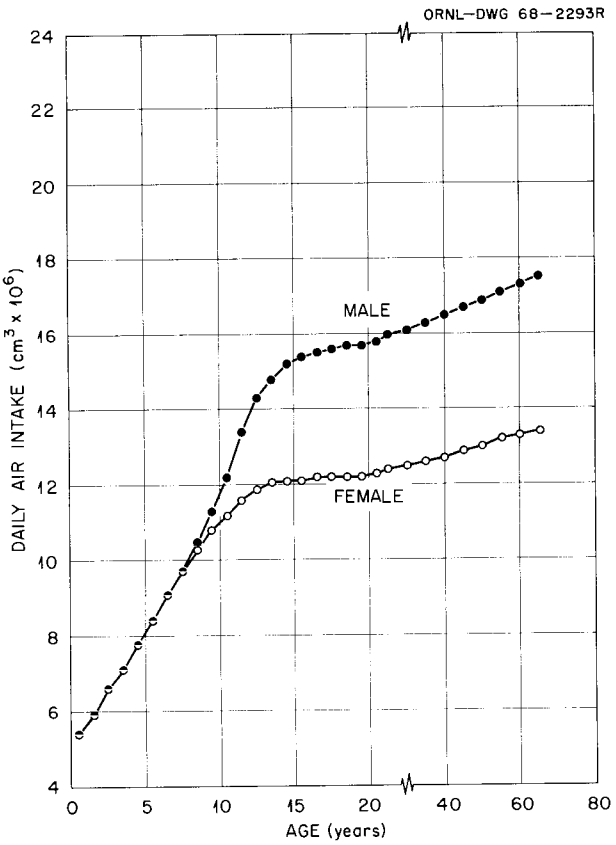

Fig. 6.3. Daily Air Intake as a Function of Age.

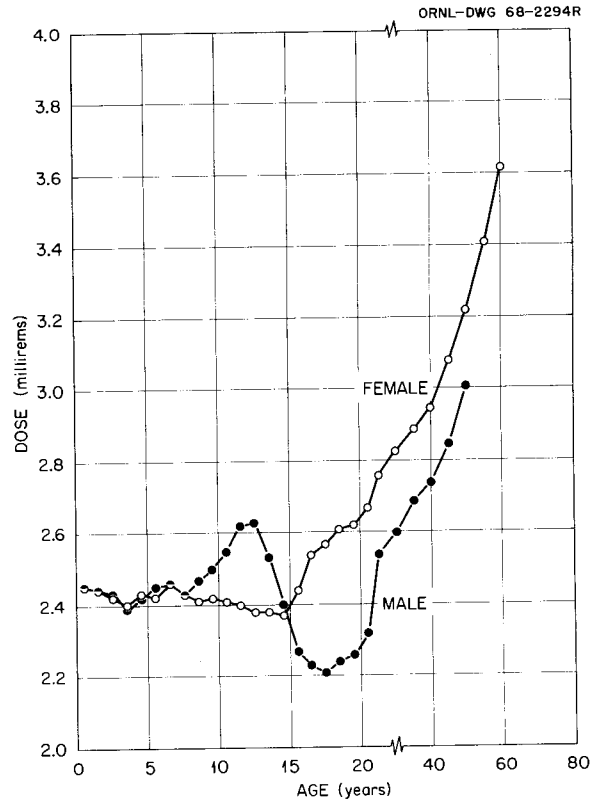

Fig. 6.4. Age-Dependent Variation of the Dose Commitment to the Body Water per Day of Intake Resulting from Inhalation of Air Containing 1 pc of HTO per cm^3.

oxygen in exhaled air,[15] with the assumption that ambient air is 20.9% oxygen. Thus it was possible to evaluate all of the age-dependent parameters in the INREM code for dose estimation.

A unit concentration (1 pc/cm^3) of HTO in air was selected for convenience, and dose estimates for the population were calculated. Age-dependent variation of the dose commitment[16] to the body water per day of intake resulting from inhalation of air containing 1 pc of HTO per cm^3 is shown in Fig. 6.4. The variation in dose commitment among the age groups is less than a factor of 1.5. The values plotted are the infinite dose equivalents (rems) resulting from 1-day intakes of air containing 1 pc of HTO per cm^3 Older members of the population receive larger dose commitments primarily because of increases in daily air intake and turnover time of the body-water pool. Since these dose equivalents are for intake via inhalation, they do not include the concomitant dose equivalents from HTO absorbed through the skin during the exposure. When HTO vapor is present in air, approximately equal amounts enter the body by inhalation and by absorption through the skin.[5] This is assumed to apply for all ages, because the ratio of daily air intake to body surface area is relatively constant as a function of age. Thus the values given in Fig. 6.4 should be doubled to more accurately estimate the total dose commitments for this hypothetical exposure. Dose equivalents for any exposure to HTO vapor may be estimated from this figure if the following information is provided:

[15] P. L. Altman, J. F. Gibson, Jr., and C. C. Wang, *Handbook of Respiration*, Saunders, Philadelphia, 1958.

[16] Dose commitment = the total dose equivalent which an individual will accrue within his lifetime as the result of a radionuclide intake.

ages of the individuals exposed (years), lengths of the exposure periods (days), and HTO concentration in the inhaled air (pc/cm^3). A primary limitation of Fig. 6.4 is its dependence on biological parameters from a Caucasian population; therefore it is best applied only when estimating dose equivalents for the population from which the basic data were drawn. A similar figure should be prepared for each population involved if one desires the most accurate dose estimates in a specific situation. Of course all modes of exposure would have to be considered when estimating the total dose equivalent received by the population.

7. Related Cooperative Projects

COOPERATION OF OTHER AGENCIES IN ORNL STUDIES

The research and development program of the Radioactive Waste Disposal Section is of special interest to various public and private agencies. Several study projects provide an opportunity for others to participate, both to supplement the Laboratory's research effort and to gain information and experience of value to the other agency. The ways in which another agency may cooperate include assignment of on-loan personnel as temporary additions to the ORNL staff, performance of specific work under cooperative agreements to augment ORNL programs, work authorized under ORNL subcontracts and performed by the contracting agency, and coordination of related work projects with ORNL projects for mutual benefit.

Disposal in Salt Formations

Agencies participating in this program during the past year have included the Carey Salt Company of Hutchinson, Kansas, an ORNL subcontractor. The results of this cooperative program are given in the section headed "Disposal in Natural Salt Formations," Chap. 3 of this report.

VISITING INVESTIGATORS FROM ABROAD

During the year, two noncitizen guests participated as temporary members of the research staff of the section.

NUCLEAR SAFETY REVIEW

One member of the section served on the staff of *Nuclear Safety* as assistant editor. During the year, several individuals in the section contributed review articles which were published under the category "Consequences of Activity Release."

PARTICIPATION IN EDUCATIONAL PROGRAMS

One member of the section participated in the cooperative program with the University of Tennessee and with Vanderbilt University. A course was presented on the Health Physics Aspects of Radionuclides Released to the Environment. A similar series of lectures was presented at a Health Physics Training Course, sponsored by ORAU, and at the preparatory course for health physics certification.

LABORATORY PROJECTS

Several members of the section served as part-time staff members of the Nuclear Safety Information Center, the Civil Defense Research Project, and the agroindustrial complex study.

Part II. Radiation Ecology

S. I. Auerbach

8. Responses of Animal Populations to Ionizing Radiation

C. E. Baker[1]
B. G. Blaylock
Gladys D. Dodson[2]
P. B. Dunaway
J. W. Gooch, Jr.
N. A. Griffith[2]
A. M. Jenkins
J. T. Kitchings
Margaret F. Miller
E. Oertel[3]
R. V. O'Neill[4]
Sue C. Purvis
J. R. Reed, Jr.[2]
D. E. Reichle[2]
A. F. Shinn[2]
J. D. Story
C. E. Styron[5]
L. E. Tucker[2]

PREDICTION OF LD_{50} IN MAMMALS

P. B. Dunaway
J. T. Kitchings III
C. E. Baker
J. D. Story
L. E. Tucker
S. C. Purvis

Estimates of $LD_{50(30-60\ days)}$ ranging from 150 to 1500 r have been reported for mammals, but no satisfactory inclusive explanations have been advanced for the differing $LD_{50(30-60)}$ estimates (hereafter called "LD_{50}") for the various species. As a consequence, it has not been possible to predict such responses as LD_{50} for an untested species. The possibility of formulating predictions of radiation effects was discussed at the inception of our studies of radiation effects in native small mammals.[6]

Data from our hematological and radiation-effects studies, as well as information from other sources, were utilized for comparisons of radiation mortality in the hemopoietic death range. An index obtained by multiplying average interphase chromosome volume (ICV) of the lymphocyte against the elimination constant of ^{59}Fe (λ_b) in each species gives close predictions of LD_{50} (rads) for the species for which data are available (Fig. 8.1). Interphase chromosome volume values for the dog were not available, but, among other relationships, we find an inverse sigmoidal dependence of lymphocyte ICV on oxygen consumption rate. The equation from 1.0 to 4.5 cc g^{-1} hr^{-1} of O_2 is $Y = 11.89 - 163X$, where Y is ICV (μ^3) and X is O_2 consumption. Lack of iron λ_b values prevented inclusion of many species with known LD_{50}'s in these calculations. However, by comparing various hematological interdependences, rough estimates of Fe λ_b and LD_{50} can be made. For example, we

[1]ORAU Graduate Fellow.

[2]Dual capacity.

[3]Consultant.

[4]NSF Postdoctoral Fellow.

[5]On loan from U.S. Army.

[6]P. B. Dunaway *et al.*, *Health Phys. Div. Ann. Progr. Rept. July 31, 1965*, ORNL-3849, p. 60.

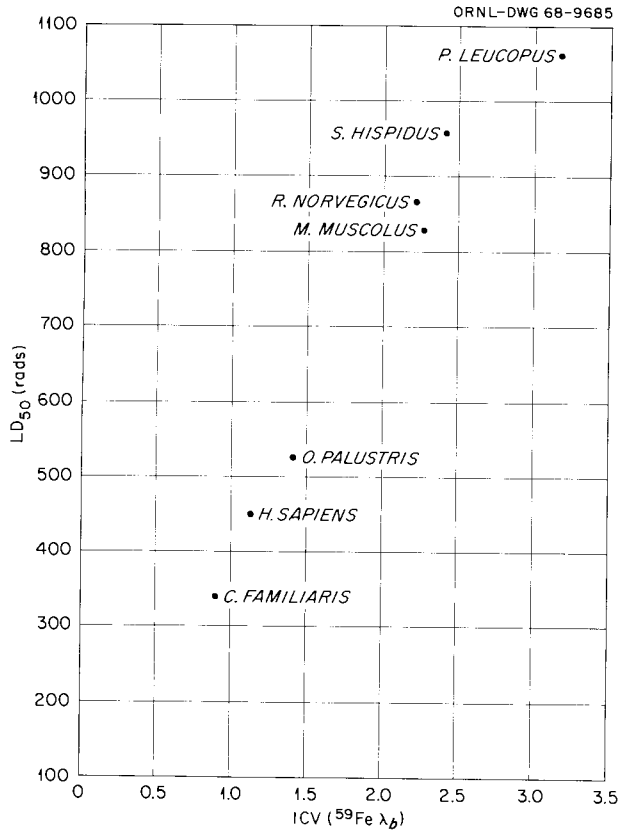

Fig. 8.1. LD_{50} vs ICV(^{59}Fe λ_b) in Several Species of Mammals.

deduced that the red squirrel (*Tamiasciurus hudsonicus*) and the grasshopper mouse (*Onychomys leucogaster*) are radiosensitive. Preliminary irradiations of red squirrels by us and grasshopper mice by T. P. O'Farrell, Battelle-Northwest Laboratories (personal communication), indicate that these rodents are, in fact, radiosensitive (LD_{50} < 600 rads). We suspect that the ICV–Fe λ_b vs LD_{50} relationship will be sigmoid rather than linear, but information on more species, particularly for extremely radiosensitive and radioresistant species, will be required for refining the first-approximation predictive equation (Fig. 8.1).

Ionizing radiation affects all tissue systems, of course, particularly those with rapid cell proliferation, but the principal cause of death in the LD_{50} range is damage to the hemopoietic tissues. For this reason, the term "hemopoietic death" is used customarily to describe mortality in this dose range. Blood responses were compared in a radioresistant rodent, the cotton rat (*Sigmodon hispidus*), and a radiosensitive species, the rice rat (*Oryzomys palustris*), after acute whole-body ^{60}Co doses of 200 and 600 rads. The hemopoietic system of the rice rat was considerably more sensitive to radiation at both radiation levels than was the hemopoietic system of the cotton rat. For brevity, only the changes in erythrocyte and leukocyte counts at 600 rads are shown in Fig. 8.2. Erythrocyte count and associated values were affected only slightly in *S. hispidus*, but RBC count, hematocrit percentage, and hemoglobin concentration decreased drastically in *O. palustris*. Similarly, total WBC counts for rice rats were below 500 cells/mm^3 from day 5 post-irradiation to day 13, but the count for cotton rats did not descend below 500, and recovery was evident by day 11. Lymphocytes of both species were particularly vulnerable to radiation. Some of the cotton rats brought in from the field were infested with a *Hepatozoon* sp. blood parasite in leukocytes; we had not found this parasite in previous years. This group of rats was given 600 rads. Surprisingly, WBC counts in the parasitized rats were higher than counts in unparasitized rats from day 11 to 24 (Fig. 8.2).

This study of radiation-induced hemopoietic effects suggests that (1) hematological parameters were logical choices for formulating predictive indexes to LD_{50} estimates and (2) *Hepatozoon* parasitism accelerated WBC recovery after irradiation.

INCORPORATION OF ^{134}Cs BY COTTON RATS

P. B. Dunaway
J. D. Story
C. E. Baker
J. T. Kitchings III
L. E. Tucker
J. W. Gooch, Jr.

Body burdens of radionuclides in mammals living in environments contaminated with radioactive fallout particles depend on three primary factors: (1) ingestion of fallout particles themselves, (2) amount of contaminated vegetative material ingested through normal feeding processes, and (3) absorption of radionuclides into tissues. One objective of a projected study in field enclosures contaminated with fallout simulant is to measure ^{137}Cs uptake and excretion rates in cotton rats. Accordingly, laboratory experiments with uptake and excretion of ^{134}Cs adsorbed from the simulant and from contaminated vegetation were completed.

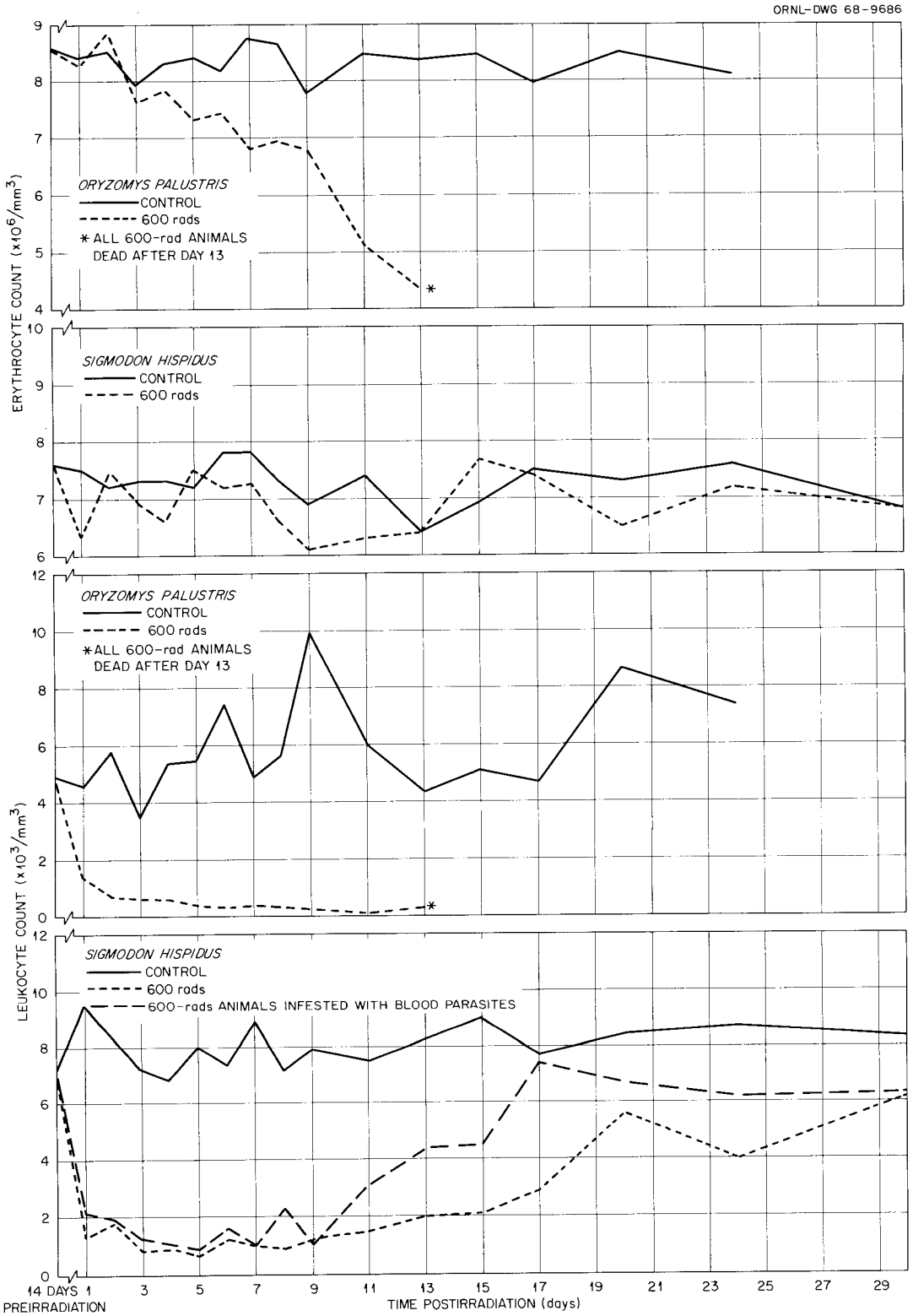

Fig. 8.2. Erythrocyte and Leukocyte Counts in Rice Rats and Cotton Rats After 600 rads.

Cesium-134-tagged simulants with varying in vitro nuclide solubilities were analyzed with respect to absorbability of the ^{134}Cs by the gastrointestinal tracts of cotton rats. Whole-body retention determinations and excretory patterns were used to discern any variation in ^{134}Cs metabolism caused by solubility differences. Transit times of the particles through the gut were determined, since particles in the GI tract will constitute internal point sources of irradiation as long as they are present.

A gavaging technique was developed to insert a single dose of simulant into the animals' stomachs. Three different simulants were used, with injected dose and in vitro solubilities as follows: (1) 0.197 μc, 60.6%; (2) 0.201 μc, 17.6%; (3) 0.209 μc, 4.3%. Whole-body, fecal, and urine samples were counted every 18 and 24 hr for 66 hr and then every 24 hr until 158 hr post injection. Analysis of fecal material showed a rapid increase in radioactivity until the 66th hour post administration. It was at this time that complete passage of the particulate matter was assumed to have occurred. Regression analysis, using percent activity remaining at 66 hr as 100% of the absorbed ^{134}Cs, gave y intercepts of 63.4%, 10.8%, and 4.0%. The elimination coefficients (λ_b) and biological half-lives (T_b) for the three groups of experimental animals were: (1) 0.008%/hr, 3.61 days; (2) 0.0084%/hr, 3.44 days; (3) 0.013%/hr, 2.21 days.

The second phase of our experimentation was to establish uptake rates and equilibrium levels of ^{134}Cs in the cotton rat during chronic ingestion of contaminated vegetation and to determine retention curves following termination of chronic ingestion. Lettuce tagged with ^{134}Cs, in doses of 0.06 μc, was given daily to groups of laboratory-born and wild-trapped cotton rats for approximately 30 days. Whole-body and excreta counts were made at various intervals over a 712-hr time span. After 712 hr, administration of the isotope was stopped, and measurements of the excretion of the absorbed cesium were begun. Serial sacrifices were made during both the accumulation phase and excretion phase of the experiment, and eight tissues were analyzed for ^{134}Cs.

The uptake curve for both groups appeared as a multicomponent curve. The first (fast) component occurred from about hour 16 to hour 208. Uptake equations for each group were as follows:

wild-trapped: $Y = 0.7727 \cdot 10^{-2}\ X\ 0.5614$;

laboratory-born: $Y = 0.7746 \cdot 10^{-2}\ X\ 0.5354$.

The second component began at about the 208th hour and ran to the 544th hour:

wild-trapped: $Y = 0.4039 \cdot 10^{-2}\ X\ 0.3448$;

laboratory-born: $Y = 0.4327 \cdot 10^{-2}\ X\ 0.3278$.

After the 544th hour the rate increase was so slight that it was considered as zero. T analysis on the wild-trapped vs laboratory-born group means showed a significant difference at the 64th hour, and a gradual increase in the divergence of the two curves was apparent throughout the uptake phase.

Using the equilibrium level as 100% absorbed dose, an elimination curve for both groups was determined. Regression equations for the elimination phase were as follows:

wild-trapped: $\log Y = 1.9751 - 0.0415X$;

laboratory-born: $\log Y = 1.9147 - 0.0458X$.

The λ_b's and T_b's for the lab group were 0.1054%/day and 6.57 days respectively. Corresponding significantly different values for the wild-trapped animals were 0.0956%/day and 7.25 days. Of the eight tissues sampled muscle had the slowest uptake.

It appears that the method of exposure, acute vs chronic ingestion, influences the metabolic kinetics of ^{134}Cs in cotton rats under laboratory conditions. Presumably, cesium T_b is shorter in animals receiving acute inputs because less cesium is incorporated in compartments with slow uptake and long retention times.

EFFECTS OF ACUTE GAMMA RADIATION ON CRICKET RESPIRATION

D. E. Reichle R. V. O'Neill

Menhinick[7] measured the effect of gamma radiation on the life-span of various stages of the cricket (*Acheta domesticus*). He noted a significant increase in life-span with low doses and postulated that this was due to a reduction in respiration rate. This hypothesis previously has been put forward to explain increased life expectancy at low radiation doses for a variety of animals. To test this hypothesis, a continuous

[7]S. I. Auerbach *et al.*, *Health Phys. Div. Ann. Progr. Rept. July 31, 1965*, ORNL-3849, p. 55.

recording electrolytic respirometer[8] was used to measure oxygen consumption of young adult crickets over a continuous period of 24 hr. Radiation doses (Table 8.1) were chosen to correspond to those used by Menhinick.

Figure 8.3 shows that there is a reduction in respiration rate following irradiation. This difference is significant at $p = 0.05$. There is no apparent shift in the daily cycle, which peaks in early evening and reaches a low point during early morning hours. Mean 24-hr respiration rates per unit weight for all doses are shown in Table 8.1. A variety of statistical tests failed to demonstrate any greater reduction in oxygen consumption at lower compared with higher radiation doses. The increased life expectancy seen at low dose levels apparently cannot be explained by reduction in respiration rate alone. It is possible that the phenomenon could result from a combination of reduced respiration at all levels, but increasing biological damage at higher doses.

[8]F. P. W. Winteringham, *Lab. Pract.* 8: 372–75 (1959).

Table 8.1. Mean Respiration Rates of Young Adult Crickets Subjected to Various Doses (8.4 rads/sec) of Gamma Radiation

The data represent an average respiration of ten individuals over 24-hour periods

Dose (kilorads)	Mean Respiration ± Standard Error (μl/hr)	Mean Weight-Corrected Respiration ± Standard Error (μl hr^{-1} g^{-1})
0	183.6 ± 11.8	454.8 ± 25.1
1	207.9 ± 13.9	342.2 ± 28.0
2	209.7 ± 15.2	420.4 ± 27.4
4	176.9 ± 12.0	379.6 ± 23.0
8	188.8 ± 15.5	389.8 ± 27.1
16	179.4 ± 6.6	339.1 ± 23.8
32	176.9 ± 8.6	359.8 ± 24.2

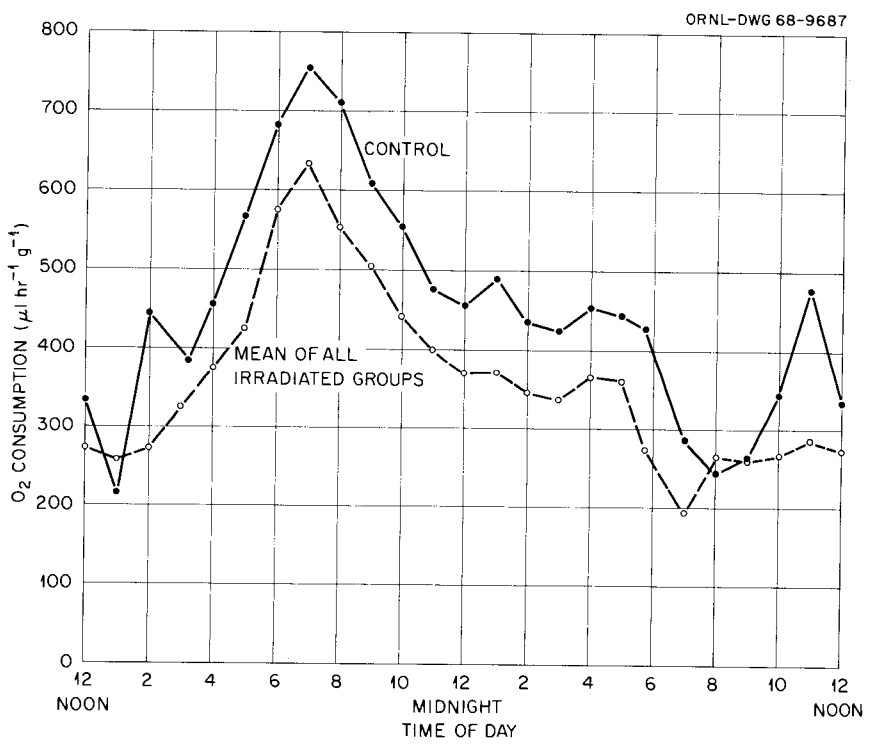

Fig. 8.3. Mean Hourly Respiration Rate of Young Adult Crickets Following Acute Irradiation. Data from all radiation doses were pooled. Measurements were taken for 24 hr with a continuous recording respirometer.

HONEYBEE IRRADIATION STUDIES

A. F. Shinn E. Oertel
A. M. Jenkins

Few studies have been made of the effects of ionizing radiation on worker honeybees.[9] However, no attempts have been made to assess the effect of various doses on their pollinating behavior, which could be an important aspect of postattack recovery of agricultural landscapes.

In the first stage of this project, queen bees of known genetic composition were substituted for the original queens in ten colonies of honeybees to convert all colonies from the Carniolan-Caucasian-Italian (CCI) strain to the same genetic constitution (Dadant hybrid GF). We investigated the effects of radiation on the longevity of laboratory-caged bees and on the daily pollen collection by irradiated colonies of bees in the field.

Four series of irradiations were conducted using samples of ~150 bees from field hives. Bees were transferred directly from the hives to cylindrical screenwire cages, irradiated, and maintained in cages until death. In series I through III (Fig. 8.4), the irradiated bees and controls were kept at 34°C (93°F) and in darkness, which are the normal conditions of the hives. The change in mean longevity from controls was statistically different for all doses except the lowest one, 50 rads of fission fast-neutron radiation. The reduction in longevity produced by 4250 rads of neutron radiation was close to that given by 5000 rads of gamma radiation. This implies an RBE of ~1 for this insect, which is similar to that obtained for vertebrates when using acute doses. Doses of 5000 and 15,000 rads (^{60}Co gamma) produced the same reduction in life-span of bees. In series IV, honeybees which were given 5000 rads of beta, gamma, or neutron radiation and which were maintained at 21°C (70°F) showed no significant reduction in life-span, but in series I and III, bees given 5000 rads of ^{60}Co gamma radiation and kept at 34°C suffered a reduction of 22% in life-span.

Five entire colonies of GF bees were given 5000 rads of ^{60}Co gamma radiation in the large animal irradiator of the UT-AEC Agricultural Research Laboratory. All irradiations were completed in less than 80 min. The weights of daily pollen collections of the five irradiated hives and of five control hives at the same site were recorded one week before and for two weeks following irradiation. On the basis of laboratory tests of longevity, a slight reduction of the lifetime of individual bees was the only expected result; we presumed that sufficient time would be available for obtaining good estimates of any changes in pollen collections. The actual result was the elimination of all the irradiated colonies as functional social units within two weeks. At the end of three weeks post irradiation only ~200 of the original 87,000 irradiated adult bees remained alive along with a few male pupae; all other individuals of all stages of development had died.

The changes in pollen collections are given in Table 8.2. The colonies to be irradiated averaged, in the week prior to irradiation, 61% as much pollen as the intended controls. However, within a week following irradiation they collected only 28% as much as the controls; within two weeks post irradiation they collected only 7%; and by the beginning of the third week, they collected none.

[9]G. Courtois and J. LeComte, *Ann. Abeille* **2**, 285–90 (1959); C. Pelerents, *Mededel. Landbouwhogeschool Opzoekingssta. Staat Gent* **27**, 896–907 (1962); C. Pelerents and J. Van Den Brande, *Bull. Inst. Agron. Sta. Rech. Gembloux* **31**, 576–83 (1963).

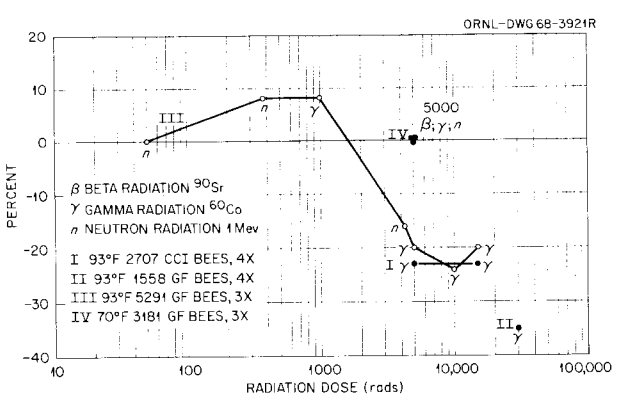

Fig. 8.4. Percent Change from Controls in Mean Longevity of Laboratory-Caged Irradiated Honeybees.

EFFECTS OF BETA AND GAMMA RADIATION ON *SINELLA CURVISETA* (COLLEMBOLA)

C. E. Styron Gladys J. Dodson

The ability of insect populations to survive a nuclear attack and to reproduce in a postattack situation is an important factor in planning post-

Table 8.2. Grams of Pollen Collected Daily by Colonies of GF Worker Honeybees Nonirradiated or Irradiated with 5000 rads on September 6, 1967

	Preirradiation	Postirradiation		
	8/28–8/31	9/9–9/15	9/19–9/20	9/21
Irradiated colonies (5)[a]	13.7	7.0	0.8	0
Nonirradiated colonies (5)[a]	22.6	24.6	11.5	5.8

[a]Number of colonies.

attack agricultural procedures. Beta radiation will likely be of great significance to insects that live in the soil and litter or pass developmental stages there. The beta dose to small insects from fallout particles may be 40 times greater than the gamma dose.[10] Collembola play an important role in the breakdown of organic material in the biological cycle of soil formation, and numerically they usually take second place only to mites in the air-breathing fauna of the soil. The objective of this study is to assess the effects of beta and gamma radiation on survival and reproductive ability of a Collembola population.

Groups of *Sinella curviseta* were exposed to $^{90}Sr(^{90}Y)$ beta radiation at 4950 rads/hr for 0.0, 0.5, 1.0, 1.5, 2.0, 4.0, and 6.0 hr. Other adults were given the same dose of ^{60}Co gamma radiation at 31,950 rads/hr. Juveniles two weeks old were exposed to the same doses of beta and gamma radiation as the adults. Following irradiation, groups were transferred to charcoal–plaster of paris culture jars and kept at 20°C. Nonirradiated adults were placed in small boxes where they laid eggs on the substrate. The adults then were removed, and the following day the eggs were exposed in situ to 0, 206, 413, 825, 1238, 1650, and 2475 rads. Eggs were allowed to hatch in these boxes, and after two weeks the young were transferred to culture jars. Each experiment consisted of three replicates.

As seen in Table 8.3, $LD_{50/30}$ values for adults suggest an RBE of 0.378 for ^{90}Sr beta radiation. The value is not a true RBE, since the dose rates differed, but it is considered to be a close approximation, since both exposures were in an acute mode. It is possible that the slightly higher RBE for juveniles, 0.432, is due to their smaller size and thinner cuticle. Of the three groups, day-old eggs showed the greatest sensitivity and the highest RBE, 0.709. The eggs of *Sinella* are 20 times more sensitive to beta radiation and 10.7 times more sensitive to gamma radiation than adults.

Table 8.3. LD_{50} and RBE Values for Beta and Gamma Irradiation of Adults, Juveniles, and Eggs

	Beta Radiation	Gamma Radiation	RBE
Adult $LD_{50/30}$	39,400	14,900	0.378
Juvenile $LD_{50/30}$	29,500	12,750	0.432
Egg LD_{50}	1,960	1,390	0.709

Figure 8.5 is a graph of fertility rates for *S. curviseta* plotted against radiation dose. Calculation of rates by month showed a significant difference between month 1 and months 2–4. Rates for months 2–4 were not significantly different from each other; therefore they were plotted together. Fertility rates generally were reduced by radiation, but recovery was observed following the first month. At the lowest dose of beta radiation (2475 rads) the fertility rate was increased 52% during the first month. The subsequent decline in fertility at this dose during months 2–4 suggests that the initial high rate was due to superovulation. Fertility rates were reduced to zero by 29,700 rads of either beta or gamma radiation. There was significant recovery during the second month at all

[10]Stephen L. Brown, "Disintegration Rate Multipliers in Beta-Emitter Dose Calculations," Stanford Research Institute Project MU-5116 (1965).

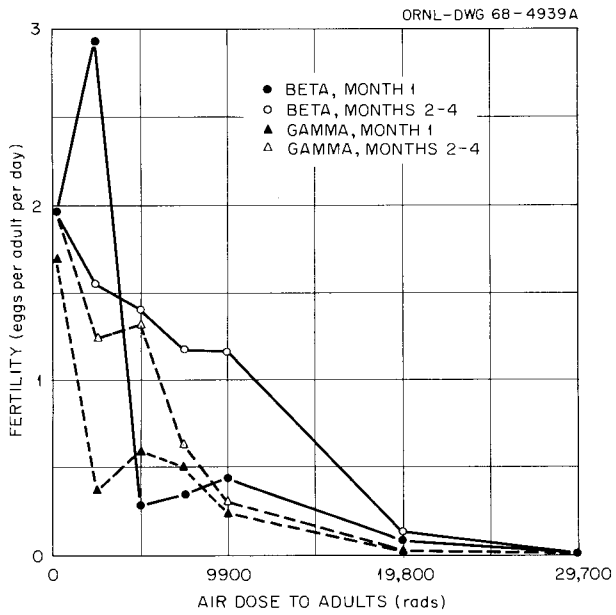

Fig. 8.5. Fertility Rates (Eggs per Adult per Day) for *Sinella curviseta* Plotted Against Air Dose (Rads) of Beta and Gamma Radiation to Adults. The rates were summed over month 1 and over months 2 to 4.

but the highest doses. Mortality of eggs from irradiated adults was high during the first month, but significant recovery occurred in months 2–4. Fertility of F_1 offspring did not vary significantly with dose.

The eggs of *Sinella* are by far the most sensitive stage for beta and gamma radiation. Because they are laid directly on the ground, their exposure to beta radiation from fallout will be greater than the other stages. The apparent superovulation induced by a low dose of beta radiation to adults could cause great increases in population densities of Collembola and shift predator-prey balances. This is an area in which we have little information.

RADIATION EFFECTS ON CARP REPRODUCTION

B. G. Blaylock J. R. Reed, Jr.
N. A. Griffith

Since the early embryonic forms are usually the most sensitive to ionizing radiation, radioactive pollution of streams and lakes by fallout or nuclear facilities could affect reproduction of aquatic populations. This is especially true of oviparous species that broadcast their eggs on the bottom sediments, where they could accumulate relatively large doses of radiation. In conjunction with a study of the hatchability of carp eggs from White Oak Lake fish, the sensitivity to irradiation of mature gametes and fertilized eggs was examined.

The hatchability of carp eggs artifically spawned in the laboratory and irradiated 30 min after fertilization was compared with eggs spawned from irradiated parent fish. A dose of 1100 rads to the fertilized eggs prevented the hatching of all eggs, and a dose of 600 rads reduced the hatchability by approximately 10 to 30%. Doses of 250 rads and less have no effect on hatchability (Table 8.4). Eggs fertilized with sperm from irradiated males had a greater hatchability than eggs irradiated 30 min after fertilization (Table 8.5). A dose of 600 rads to the male carp reduced the hatchability by about 11% and a dose of 1100 rads by 5%. Irradiating the female carp with 600 and 1100 rads had no detectable effect on egg hatchability. A chronic dose of 6.4 rads/hr of gamma radiation started immediately after fertilization and continued until hatching reduced hatchability by 10%. The embryos receiving this accumulated dose of approximately 600 rads died at different embryonic stages, and no stage appeared more sensitive to chronic radiation.

In carp the fertilized egg before the first cleavage is more sensitive to acute radiation than mature gametes. However, in comparison with other species of fish, this stage is relatively resistant. In rainbow trout an LD_{50} of 58 r has been reported for fertilized eggs prior to cleavage. Since this is considered the most sensitive stage to acute irradiation, other stages of the developing carp egg should be investigated to determine if they are relatively as resistant.

POPULATION GENETICS AND RADIATION EFFECTS STUDIES

B. G. Blaylock M. F. Miller

In evaluating the effects of radiation on future generations, the sensitivity of the germ cells to genetic changes in the different stages of the life cycle is an important factor. In relation to

Table 8.4. Hatchability of Carp Eggs Irradiated 30 min After Fertilization

Dose (rads)	Pair I		Pair II		Pair III	
	No. of Fertilized Eggs	Hatchability of Eggs (%)	No. of Fertilized Eggs	Hatchability of Eggs (%)	No. of Fertilized Eggs	Hatchability of Eggs (%)
Control	100	100.0	100	100.0	124	99.2
Control	294	100.0	60	100.0	321	99.4
50	102	100.0	45	97.8	487	99.0
100	330	98.5	45	97.8	99	98.0
250	209	98.1	76	98.7	89	99.0
500	151	70.2	38	79.0	216	91.7
1000	100	0.0	229	0.0	301	0.0
2000	298	0.0	43	0.0	265	0.0

Table 8.5. Hatchability of Carp Eggs After Irradiation of Male

	Dose to Males (rads)	No. of Fertilized Eggs	Hatchability of Eggs (%)	Probability of a Difference (P)	Death of Eggs from Radiation (%)
Pair 1	600	776	81.6	<0.001	7.2
	1100	558	85.8	<0.10	3.0
	Control	1049	88.8		
Pair 2	600	1028	82.0	<0.001	13.8
	1100	625	92.0	<0.001	3.8
	Control	1319	95.8		
Pair 3	600	774	87.3	<0.001	12.1
	1100	1100	90.7	<0.001	8.7
	Control	850	99.4		

our studies on natural and laboratory populations of *Chironomus*, the fourth instar larval and adult male stage of the life cycle of *Chironomus riparius* were tested for their radiosensitivity to the induction of chromosome aberrations into the germ cell line. Although mature gametes are found in the fourth instar larval stage of *Chironomus*, chromosome aberrations were not detected in the salivary gland chromosomes of 150 larvae whose progenitors had received a dose of 2000 rads in the fourth instar larval stage. In comparison, 41% of the progeny of irradiated males (2000 rads) mated with nonirradiated females contained at least one chromosome aberration (Table 8.6). Either the germ cells in the larval stage were more resistant to radiation than the cells in the adult males or repair or elimination of cells containing aberrations had occurred. Inversions were the most frequent type of aberration observed, which agrees with the results of most studies of this type. In comparison with other organisms such as *Drosophila*, the germ cells of the adult males of *Chironomus* are very sensitive to radiation-induced breaks.

Table 8.6. Induced Chromosome Aberrations in *Chironomus riparius* from an Acute Dose of 2000 Rads of ^{60}Co Gamma Radiation

Stage Treated	Total F_1 Larvae Examined	Total No. of Chromosome Aberrations	No. of Inversions	No. of Translocations	No. of Deletions
4th instar larvae	150	0	0	0	0
Adult males	122	54	36	16	2

Levels of radiation that have no apparent effect on a population will produce a drastic effect when the population is exposed to a stress such as competition. Although the adults of *Drosophila can* survive several kilorads of gamma radiation and populations are easily maintained while receiving an acute or chronic dose of 2000 r every generation, a dose of 1000 rads given only to the adult males is sufficient to eliminate the population when it is in competition with a closely related species. Equal numbers of *Drosophila melanogaster* and *Drosophila simulans* were used to start laboratory populations. The male *D. melanogaster* were given a dose of 1000 rads at the beginning of the study and every 3 weeks thereafter for 30 weeks. In the control population *D. melanogaster* quickly became the most abundant species, but it was eliminated in the irradiated population although the dose was reduced to 500 rads after 30 weeks (Fig. 8.6). These results illustrate the effects of an environmental stress interacting with radiation to eliminate a population. It appears that the well-known sterile-male technique used for controlling some insect species would be much more effective when employed in a competitive situation.

In evaluating the long-term effects of chronic environmental radiation on a natural population of *Gambusia affinis affinis*, the common mosquito fish, it was hypothesized that the increased fecundity in the White Oak Lake population was an adjustment to the effects of chronic radiation. Additional information collected from other populations supports this hypothesis. Gravid females were collected from three additional nonirradiated populations. These populations together with the White Oak Lake populations were sampled three times during the breeding season, and in each case the White Oak Lake fish produced more viable offspring (Fig. 8.7). This is additional data supporting our hypothesis that the exposure to chronic environmental radiation is acting as an environmental stress on the population by increasing the mortality of the embryos, but it also increases genetic variability, which speeds up the rate of evolution and allows the population to adjust to the stress.

The *Gambusia* population in White Oak Lake has been exposed to chronic environmental radiation of approximately 11 rads/day for over 100 genera-

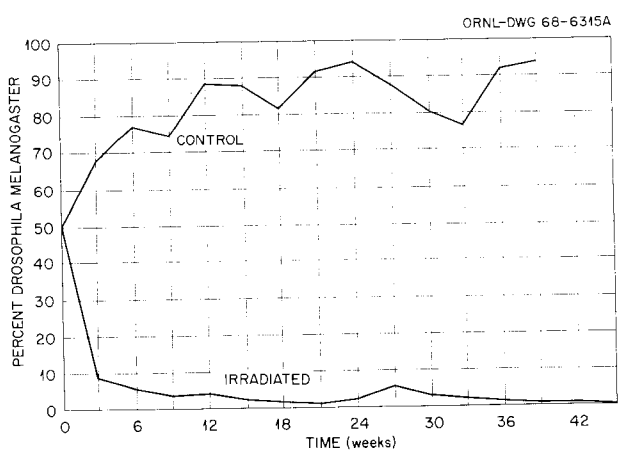

Fig. 8.6. Effect of Radiation and Competition on a Species Is Shown by the Change in Frequency of *Drosophila melanogaster* in Laboratory Populations Started with Equal Numbers of *Drosophila melanogaster* and *Drosophila simulans*. In the irradiated populations the males of *D. melanogaster* received a dose of 1000 rads at the beginning and every 3 weeks thereafter for 30 weeks.

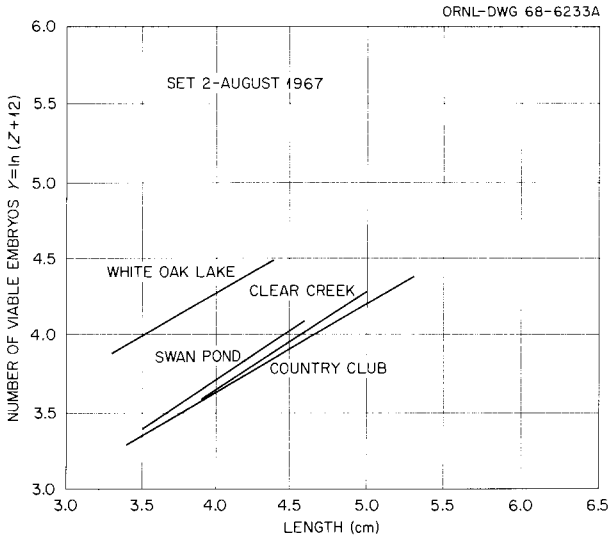

Fig. 8.7. Regressions of the Brood Size of *Gambusia affinis affinis* from White Oak Lake and Three Control Populations in Relation to the Length of the Female. The transformation $Y = \ln (Z + 12)$ was used to plot the number of viable embryos in relation to length.

tions. To determine whether fish from this population had acquired some resistance to radiation, 180 fish from White Oak Lake and an equal number from a nonirradiated population were exposed to different doses of gamma radiation from a ^{60}Co source. No significant difference was found in the $LD_{50/30}$ between the White Oak Lake population and the nonirradiated population. *Gambusia* as a species was relatively resistant to radiation, as the $LD_{50/30}$ for these fish was greater than 3000 rads.

9. Responses of Plants to Ionizing Radiation

Mary L. McPhail[1] F. G. Taylor, Jr.
H. L. Ragsdale[2] J. P. Witherspoon[3]

EFFECTS OF EXTERNAL BETA RADIATION ON HIGHER PLANTS

J. P. Witherspoon F. G. Taylor, Jr.

New studies on the effects of external beta radiation on higher plants were initiated this year. Objectives of these studies are (1) to determine radiosensitivities of important native plant species to beta radiation and (2) to provide improved estimates of the ecological effects of postattack radioactive fallout by assessing the radiological hazards of contact and beta-field exposures to plants.

In laboratory experiments simulated fallout particles consisting of albite (44 to 88 μ in diameter) containing approximately 5 nc of ^{90}Sr per particle were applied to various organs of white pine, cottonwood, cocklebur, and bean plants. These experiments were conducted in environmental growth chambers to minimize loss of particles from plants by wind and rain, thereby ensuring a constant dose rate to the tissues of interest. Dosimetric analyses have involved both consideration of models using disintegration rate multipliers with contact dose geometries and measurement of absorbed dose to tissue-equivalent volumes by scintillation extrapolation dosimetry of particles.

Although the dose rates would differ (fission product decay) in an actual fallout situation, particles of the size and initial activity of the albite simulant could be deposited on trees at distances over 100 miles downwind from nuclear weapons of the size of those detonated in the Teapot series (1955). Moreover, this particle size range (44 to 88 μ) is retained by foliage longer than larger particles.

The application of fallout simulant to plant organs for contact exposures was achieved by painting plant surfaces with particles which were coated with glycerol. This ensured retention of particles to the tissues of interest and prevented contamination of other plant parts or work areas. Control plants received a glycerol treatment only.

Figure 9.1 shows a two-year-old white pine (*Pinus strobus*) 15 days following application of particles to terminal bud clusters. In pines the particles produced a gradient of biological effects ranging from mortality of buds receiving a contact dose to growth reduction of shoots growing in "beta bath" exposures.

The appearance of a ring of dead needles around these buds at five days was unexpected. This browning of foliage appeared much earlier in the case of these "beta burns" than comparable foliar damage resulting from exposure to gamma radiation. If these particles had covered the foliage, the effect would have been a very rapid mortality of the entire plant. Complete browning and dehydration of foliage would greatly increase tree susceptibility to fire. Shoot growth from buds below contaminated terminal buds was reduced approximately 47% by 30 days. These structures were growing in a beta radiation field where dose rates varied between 70 and 200 millirads/hr. Thus, rather serious growth inhibitions were produced in a relatively low-level beta radiation field. Contaminated buds receiving contact doses of 54 to 310 rads/hr failed to grow and by ten days were dehydrated and brittle.

[1]ORAU undergraduate trainee.
[2]ORAU Predoctoral Fellow.
[3]Dual capacity.

Fig. 9.1. White Pine 15 Days Following Application of an Albite Particle Fallout Simulant Containing ^{90}Sr-^{90}Y to Terminal Bud Clusters. There is no growth from contaminated topmost buds or those on branch at upper left. "Beta burn" of foliage surrounding these contaminated buds is evidenced by the lighter color of dead needles. Note that new shoot growth from other buds increases from top to bottom of plant or with increasing distance from contaminated buds. Dose rates vary here from a contact dose of about 135 rads/hr (100 μ tissue depth) to contaminated buds to 110 millirads/hr to lower new shoots.

Table 9.1 summarizes the results of particle application to four species of plants. In all cases plant parts which received contact exposures were killed, while other plant organs survived with varying degrees of biological damage depending upon distance from the contaminated area of the plant.

An additional hazard of fallout was suggested by the presence of translocated ^{90}Sr-^{90}Y in plant parts which were not directly contaminated. Even though radiostrontium is a relatively nonmobile element and the albite particle activity has a solubility of only 4% in pH 1.0 water, the glycerol leached the particles to the extent that 0.06 to 0.1% of the tag translocated to other plant parts. In the case of the beans in Table 9.1, the fruit contained from 0.4 to 5.0 nc of ^{90}Sr per gram. Therefore rain,

Table 9.1. Effects of Beta Radiation from Albite Particles Containing ^{90}Sr-^{90}Y

Plant Species and Age	Treatment		Affected Portion of Plant	Dose Rate Range (rads/hr)	Biological Effect	Time (days)
	Microcuries	Application Site				
White pine (*Pinus strobus*), two years old	4–23	Apical bud	Apical bud	54–310[a]	100% lethality – brittle	10
	4–23	Apical bud	Apical needles	92–300[b]	Brown, dry "beta burn"	5
	4–23	Apical bud	Noncontaminated vegetative buds	0.07–0.20[b]	12–47% reduction in height growth	30
Eastern cottonwood (*Populus deltoides*), one-month-old cuttings	3.2–9.1	Apical meristem	Apical meristem	42–132[a]	100% lethality	21
	1.1–1.4	Apical meristem	Apical meristem	15–19[a]	"Beta burn" on surface of shoot	13
	1.1–1.4	Apical meristem	New foliage from contaminated meristem	?	Reduction in size and aberrant shape	10
Cocklebur (*Xanthiam pensylvanicum*), four days old	2.5–5.6	Apical meristem	Whole plant	34–76[a]	100% lethality of plants	27
	1.2–1.8	Apical meristem	Stem and foliage	16–25[a]	20–73 reduction in height growth; reduction in number and size of leaves	15
Bean (*Phaseolus vulgaris*), three weeks old	2.5–2.9	Flower buds	Flowers	34–40[a]	Wilted, dry, sterile	7
	2.5–2.9	Flower buds	Fruit from noncontaminated flowers	0.3–0.4[b]	50% reduction in size and 30% reduction in number of seed per pod	10

[a]Contact dose at 100 μ tissue depth.
[b]Beta bath dose at 100 μ tissue depth.

while serving to wash particles from plants, may also leach relatively insoluble fallout particles. If the initial contamination is high enough, translocation of a fraction of a percent may represent a hazard in the case of edible fruit or vegetables.

MINERAL UPTAKE BY IRRADIATED PLANTS

J. P. Witherspoon Mary L. McPhail

In postattack environments the efficiency with which irradiated plant populations absorb and translocate minerals may be important to their survival. Not only may ability to obtain and use nutrients affect immediate survival, but also the extent of absorption and movement of slowly available fallout products will determine internal chronic dose rates.

A study on the effects of acute sublethal radiation levels on mineral uptake and transfer in laboratory plant populations was completed this year. Rapidly growing cuttings of Eastern cottonwood (*Populus deltoides*) were exposed to 330 and 660 rads of acute fast-neutron radiation at the HPRR and, with controls, immediately tagged via foliage with ^{137}Cs. Tagging was accomplished by submerging one basal leaf in a glass vial attached to the plant stem. Each vial contained 100 μc of ^{137}Cs (10 ml of ^{137}CsCl solution, pH 3.0) and leaves were submerged for 72 hr. Plants were maintained in growth chambers (82°F day, 75°F night, 15-hr day) for the entire experiment. Plant uptake after the three-day foliar application was 1.5, 0.4, and 0.1% of the total applied for the 0-, 330-, and 660-rad treatments respectively. Up to 31 hr, total uptake rates in irradiated plants exceeded those of controls, but after this time control plant uptake rates were greatest. Treatment differences in translocation rates between plant parts also were observed. Maximum accumulation of radiocesium in new shoot growth (plant tops) occurred three to six days earlier in control plants than irradiated plants, while transfer to root systems was more rapid in irradiated plants than control plants.

From 6 to 21 days no significant treatment differences in translocation rates were observed (Table 9.2), although height growth rates were reduced by 21 and 73% in the 330- and 660-rad treatments respectively. Apparently damage to mineral transfer mechanisms, unrelated to growth rate, was induced by these sublethal radiation exposures, and repair occurred after one week.

Although treatment differences in translocation rates appeared early, then became insignificant, reduction of total ^{137}Cs uptake by factors of about 4 to 15 in the 330- and 660-rad treatment plants indicated that exposure to acute sublethal radiation levels can have an appreciable effect upon the mineral economy of plants. In the case of plants growing on sites of low fertility, a serious reduction in mineral uptake capacity may influence survival.

GENETIC MODIFICATION OF GROWTH AND RADIOSENSITIVITY OF *POPULUS DELTOIDES*

J. P. Witherspoon F. G. Taylor, Jr.

Studies on variations in growth and development of Eastern cottonwood have continued this year. These studies, which utilize asexually propagated cuttings, allow us to quantify genotypic growth

Table 9.2. Cesium-137 in Cottonwood Saplings Exposed to Sublethal Fast-Neutron Radiation 2 hr Before a Foliar Application of the Radionuclide

Values are mean percent of total ^{137}Cs in plants ±1 S.E.

Days Postirradiation	Controls			330-rad Dose			660-rad Dose		
	Leaves	Stem	Roots	Leaves	Stem	Roots	Leaves	Stem	Roots
3	33.2 ± 5.6	59.4 ± 2.7	7.4 ± 3.6	30.2 ± 2.3	53.6 ± 1.5	16.2 ± 2.3	22.4 ± 2.4	89.6 ± 20.4	10.4 ± 1.6
6	43.5 ± 7.3	41.2 ± 10.03	15.3 ± 3.2	43.0 ± 12.6	35.1 ± 14.8	21.9 ± 5.0	41.9 ± 16.6	50.0 ± 9.9	8.1 ± 2.6
12	50.5 ± 4.2	26.9 ± 4.5	22.6 ± 7.1	51.8 ± 4.3	33.1 ± 6.4	15.1 ± 3.9	45.7 ± 5.5	46.6 ± 5.6	7.7 ± 1.2
24	63.2 ± 7.6	22.1 ± 1.9	14.7 ± 2.2	54.7 ± 6.6	39.1 ± 3.1	6.3 ± 3.8	57.6 ± 19.8	30.1 ± 13.5	12.3 ± 5.2

variations which affect responses of plant populations to ionizing radiation and other environmental factors.

Field growth performance of 30 genotypes from seven states has been ascertained in our nursery for the past two years. These trees, planted as cuttings in 1966, are spaced 1 m apart. The nursery soil is Huntington silt loam, which is both cultivated and fertilized during the growing season. While the primary purpose of the nursery is to furnish experimental stock, growth data on these trees serve to illustrate variations in growth patterns of genotypes from several geographical locations. Table 9.3 shows the average shoot height, shoot weight, and number of stems for 30 clones at the end of the 1967 growing season. Ten trees from each clone were measured for growth rate during the year and harvested for biomass determinations at the end of the growing season. Height varied by a factor of 1.4 between the clones; shoot biomass, 2.3; and number of stems, 2.8. There also is as much variation between clones from one geographical location ("A" clones from a population in Alabama) as that between other widely separated locations. The Alton clone from Illinois and the W5 from Wisconsin, for example, grow relatively well in Oak Ridge.

Phenological differences, such as time of leaf emergence or root emergence, also occur between clones. These growth and developmental variations are found both in field- and laboratory-grown trees. Table 9.4 gives differences in timing of some of these phenomena in seven clones maintained in plant growth chambers under constant environmental conditions (16-hr day, 82° day, 72°F night). The table also shows changes in phenological events induced by exposure to an acute sublethal level of ^{60}Co gamma radiation (5000 r in 10 min). In this experiment dormant cuttings were irradiated and placed, with controls, in pots which were maintained in the growth chamber. Leaf and root emergence and callus formation (growth of callus tissue around the cut edge of the cuttings) were delayed about two weeks by the gamma radiation treatment. Control clones varied by factors of 1.5 for leaf emergence, 1.2 for callus and root emergence, and 3.1 in shoot-to-root biomass ratios. The variations between clones became greater following irradiation, with the greatest change in the shoot-to-root ratios (5.5). The relatively large variations in shoot-to-root ratios for both control and irradiated plants are due to genotypic differences in growth rate of root systems. The timing of root emergence was relatively constant between clones (11.3 to 13.4 days in controls and 24.0 to 29.1 days in irradiated plants), but large biomass differences existed. Genetically controlled differences in total root growth would be expected to affect responses to many environmental variables within a population of mixed genotypes.

Table 9.3. Variation in Field Growth of Cottonwood Clones – End of 1967 Growing Season

Clone	Average Height ±1 S.E. (cm)	Average Dry Weight (kg)	Average Number of Stems
A5	342 ± 20	1.02	1.6
A2	340 ± 18	1.14	2.1
K8	332 ± 11	1.09	2.2
A6	321 ± 15	0.90	1.9
A10	321 ± 25	0.96	1.8
K1	320 ± 20	1.08	3.0
A16	319 ± 14	1.26	2.0
Alton	317 ± 14	1.14	3.0
A23	314 ± 15	0.84	2.0
A17	309 ± 23	0.62	1.9
A12	307 ± 25	0.96	2.5
A8	306 ± 23	0.90	1.9
A9	303 ± 19	0.61	1.9
K4	302 ± 14	0.92	2.0
A14	296 ± 14	0.54	3.0
A3	296 ± 15	0.70	1.8
A7	292 ± 20	0.60	1.7
A21	292 ± 23	0.61	3.0
A15	283 ± 19	0.78	2.6
W5	282 ± 18	0.95	4.0
A13	282 ± 24	0.90	1.9
Rosedale	279 ± 19	1.14	2.9
A22	277 ± 16	0.60	2.0
A19	277 ± 20	0.54	2.6
Catfish	274 ± 10	1.26	1.7
A18	274 ± 22	0.67	2.0
A4	267 ± 26	0.71	1.6
A20	265 ± 16	0.78	2.7
A1	260 ± 19	0.72	1.4
A11	244 ± 12	0.66	1.9

Table 9.4. Clonal Differences in Development of Cottonwood Plants Exposed to 5000 r of ^{60}Co Gamma Radiation

Clone	Leaf Emergence (days)		Callus Formation (days)		Root Emergence (days)		Shoot Biomass[a] / Root Biomass	
	Control	Irradiated	Control	Irradiated	Control	Irradiated	Control	Irradiated
A3	9.1	27.3	12.0	27.9	12.0	26.2	5.7	5.2
A7	6.4	19.5	12.3	24.1	11.3	29.0	6.6	4.9
A8	6.0	13.3	11.9	23.0	12.3	24.0	12.9	9.1
A13	7.2	22.0	10.0	20.0	13.4	29.1	4.2	3.4
A15	6.7	17.1	11.6	24.6	11.5	26.3	10.7	27.0
A17	7.9	23.4	10.6	20.2	12.8	29.0	6.2	9.0
A21	6.6	23.8	10.3	28.4	12.3	27.0	4.4	7.5
$\bar{x}$	7.1	20.9	11.2	24.0	12.2	27.2	7.2	9.4

[a]Plants harvested at 42 days.

EFFECTS OF BIOTIC COMPLEXITY AND FAST-NEUTRON RADIATION ON CYCLING OF RADIONUCLIDES IN MICROCOSMS

H. L. Ragsdale

Aquatic microcosms consisting of various combinations of physical components (soil, water, and container surface) and biological components (*Physa heterostropha, Najas flexilis,* and *Elodea canadensis*) were used to determine the effect of increased biotic complexity on mineral cycling parameters. The stability of mineral cycling parameters was tested by stressing selected complexity levels with sublethal and lethal doses of fast-neutron radiation.

Replicate microcosms were prepared for each experiment and equilibrated in a controlled environmental chamber which was maintained at 16°C, 75 ft-c light intensity on a 12-hr light-dark cycle. One microcurie each of ^{137}Cs and ^{60}Co was added to the water component of each microcosm, and changes in compartmental activity were determined by sacrificing replicate microcosms at fixed time intervals with subsequent radiometric analysis.

Compartmental transfer rates varied among complexity levels. The transfer rate of ^{60}Co from the water and that of ^{137}Cs to the soil increased with increased complexity, while for other compartments no such linear relationship was observed. The ^{137}Cs flux patterns for most microcosm compartments were similar among complexity levels, but the ^{60}Co flux patterns of most compartments were dependent on the complexity level.

The pattern of ^{137}Cs distribution among microcosm compartments was independent of complexity and was one of flow through nonsoil compartments with rapid accumulation in the soil. In contrast to ^{137}Cs patterns, the ^{60}Co pathway patterns depended on complexity level with accumulation of ^{60}Co in nonsoil compartments in simpler microcosms and flow of ^{60}Co through nonsoil compartments to the soil in complex microcosms.

Figure 9.2 shows accumulation rates of ^{60}Co in microcosm components up to 256 hr after introduction of the radionuclide into the water. It can be noted that increasing microcosm complexity may have the effect of either increasing or decreasing initial radiocobalt uptake rates into a given component.

Microcosm components were assigned mineral cycling roles on the basis of changes in cycling parameters with increased complexity. Generally, these roles were different between radionuclides and among complexity levels for a given radionuclide.

ORNL-DWG 68-1623

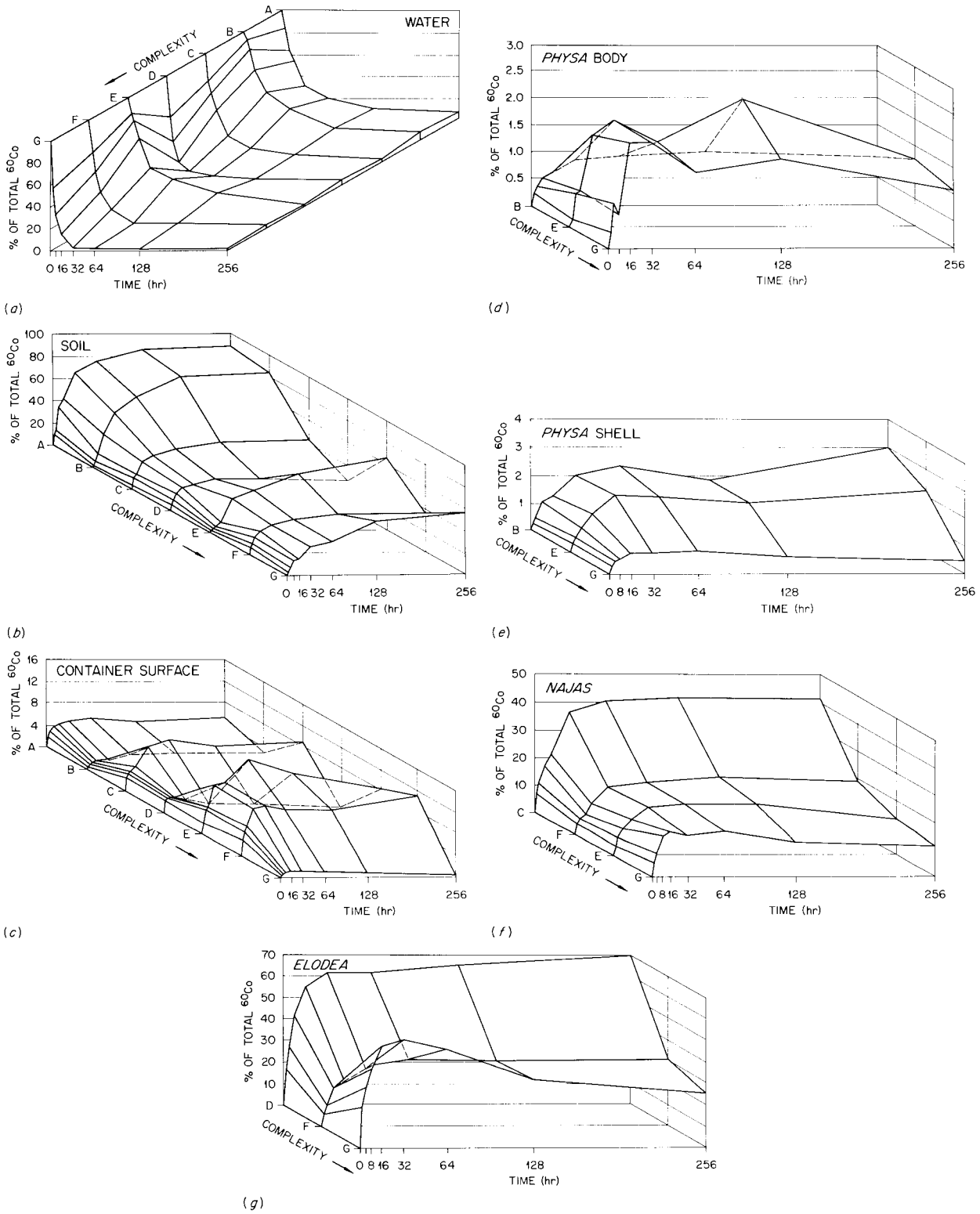

Fig. 9.2. ^{60}**Co Content of Microcosm Components as a Function of Biotic Complexity and Time.** Components: (*a*) water, (*b*) soil, (*c*) container surface, (*d*) *Physa* (snail) body, (*e*) *Physa* (snail) shell, (*f*) *Najas* (plant), and (*g*) (*g*) *Elodea* (plant). Levels of microcosm complexity: (*A*) physical components only (container surface, water, and soil), (*B*) *Elodea* + *A*, (*C*) *Najas* + *A*, (*D*) *Physa* + *A*, (*E*) *Elodea* + *Najas* + *A*, (*F*) *Physa* + *Najas* + *A*, and (*G*) *Physa* + *Najas* + *Elodea* + *A*.

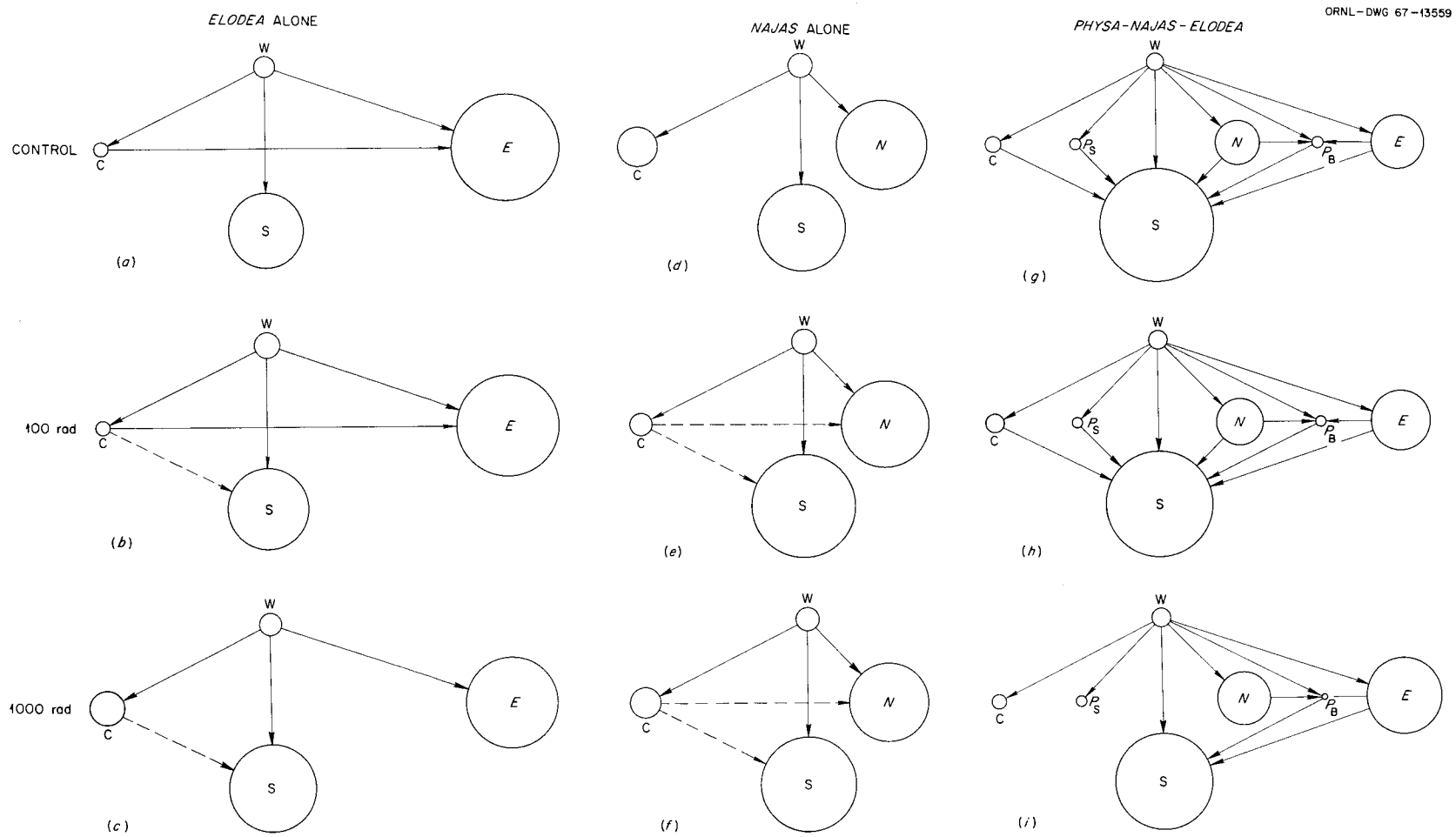

Fig. 9.3. Net Pathways and Accumulation of ^{60}Co in Microcosm Components as Influenced by Fast-Neutron Radiation and Biotic Complexity. Treatments: *a*, *d*, *g* = controls; *b*, *e*, *h* = 100 rads; and *c*, *f*, *i* = 1000 rads. Key: C = container surface, *W* = water, *S* = soil, *E* = *Elodea*, *N* = *Najas*, *PB* = *Physa* body, *PS* = *Physa* shell. Unbroken arrows indicate net pathways, broken arrows indicate pathways not present in controls, and area of circles represents relative accumulation of radiocobalt in each compartment.

Radiation stress affected ^{60}Co cycling, but no radiation effect on ^{137}Cs cycling was observed. The radiation effect on ^{60}Co cycling was dependent on the complexity level, and, in general, radiation stress decreased the cycling rate of ^{60}Co.

Figure 9.3 illustrates how both acute fast-neutron radiation (10 min irradiation by HPRR, average neutron energy of 1 Mev) and biotic complexity interact to change pathways and accumulation of radiocobalt in microcosm components. Note that increasing biotic complexity, from left to right of figure, increases the overall movement of radiocobalt through components into the soil in the case of controls. In the least complex microcosms (*a*–*c*) radiation treatments increase movement into the soil, while in the most complex microcosms (*g*–*i*) losses to the soil are decreased.

Generalizations from this study were that (1) cycling parameters for different elements (^{137}Cs and ^{60}Co) were dissimilar in less complex systems and converged toward similarity as complexity increased; (2) microcosm components had one or more mineral cycling roles, some of which changed with complexity levels; (3) increased functional complexity had the greatest effect on mineral cycling, although an increase in unifunctional species modified the mineral cycling parameters; (4) ecosystem stability was related to the sensitivity of the biological interactions and not necessarily to the sensitivity of the organisms; and (5) on the basis of mineral cycling parameters, the simpler microcosms were less stable than the complex ones to a moderate radiation stress (100 rads), but more stable than complex systems when subjected to an extreme stress (1000 rads).

10. Radionuclide Cycling in Terrestrial Ecosystems

Regina M. Anderson
D. A. Crossley, Jr.[1]
R. C. Dahlman
Gladys J. Dodson
C. A. Edwards[2]
Marilyn L. Frank
Mary P. Hoglund[2]
J. M. Kelly[3]
N. E. Kowal[4]
Virginia Merchant[5]
J. S. Olson[1]
R. V. O'Neill[4]
P. A. Opstrup[3]
L. N. Peters
D. E. Reichle[1]
M. H. Shanks[1]
Gerald Stanhill[6]
W. A. Thomas[1]
Martin Witkamp
R. I. Van Hook, Jr.[7]

SEASONAL SHOOT GROWTH IN A TAGGED LIRIODENDRON FOREST

J. S. Olson L. N. Peters
Regina M. Anderson

Previously reported results of seasonal crown sampling of the tulip poplar (*Liriodendron tulipifera*) forest tagged with ^{137}Cs in May 1962 showed that each year's flush of new foliage included a significant translocation of this long-lived isotope into materials which formed the food base of the animal food webs in the ecosystem. Since 1964, sampling of whole new growing shoots has shown how the mass of leaves (young and old), twigs, and buds and stipules have changed during each season and between seasons (Fig. 10.1).

Early in the buildup of a major population of the weevil (*Odontopus calceatus*), a fairly "normal" development of young and old leaves reached almost maximum development in early summer (4 g of oven-dry leaves per shoot by early June, the time of maximum radiocesium content). Continued unfolding during the summer slightly exceeded losses from leaf drop and consumption, so that maximum levels approached almost 5 g per shoot.

During a major increase in weevils in 1965, the early season damage by the leaf mining larvae and adults apparently slowed May foliage development and led to an actual decrease (1.75 g of leaves per shoot) in the late June collection. Even late season recovery by flushing of more new leaves made a mid-August peak value barely over half the 1964 maximum. However, twig growth was greater than in the preceding year, when there was more photosynthetic leaf "machinery." (Perhaps this excess reflects a release of growing points as a by-product of partial defoliation, including premature leaf fall. Since the new growth may well be at the expense of reserve energy stored earlier, it reminds us of limitations inherent in the estimation of productivity based on single-year analyses of growth.)

In 1966, early season suppression of growth was even more severe than before, but recovery of leaf growth continued after the main period of leaf consumption, again reaching a maximum in August, before a comparatively early period of late August and September litter fall, preceding the time in October and November when most species drop their leaves. Twig growth was lower than in the preceding years, perhaps as a carry-over of the depletion of food reserves in these dominant trees.

In 1967, many features of the seasonal growth were intermediate in character between those of

[1]Dual capacity.
[2]Consultant.
[3]University of Tennessee.
[4]NSF Advanced Science Seminar Project Participant.
[5]NSF Undergraduate Research Participant.
[6]Alien guest.
[7]ORAU Predoctoral Fellow.

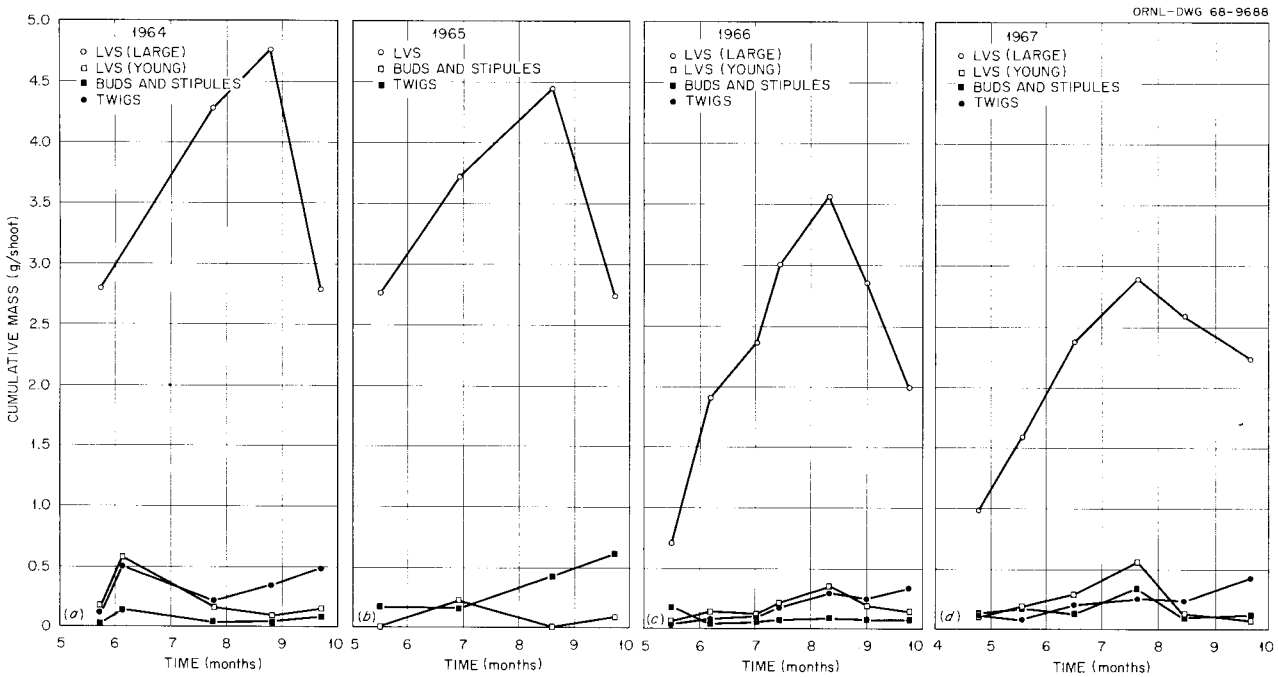

Fig. 10.1. Cumulative Growth of Leaves, Twigs, and Buds plus Stipules Through the Growing Seasons of (*a*) 1964, (*b*) 1965, (*c*) 1966, and (*d*) 1967 in Grams per New Growing Shoot.

1964 and 1966. Consumption by weevils appeared high, but high rainfall in midsummer may have started a recovery process in spite of this.

RAINFALL TRANSFERS FROM LIRIODENDRON FOREST CANOPY

J. S. Olson L. N. Peters
Regina M. Anderson

Rain leaching from tree canopies was among the earliest losses of radiocesium from the tagged forest, starting in late May 1962, as soon as the transpiration stream carried ^{137}Cs up the bole.[8,9] As expected, the quantities of leached cesium diminished in subsequent years, as the amount remaining in the canopy diminished. Relations between diminished leaf radioactivity, irregularly distributed rain, and leaching per day, which reflects a combination of both of the preceding factors, are shown in Figs. 10.2 to 10.4 respectively.

Figure 10.5 shows this very marked decline in total leached radiocesium from 1962 to 1963 and 1964.

In 1965 a lower amount of leaching was shown, as expected, in early summer, but, unexplainably, leaching increased to the preceding year's level by the end of the year. For 1966 the notable decrease was resumed again, but the 1967 rainout actually exceeded that of 1966. The latter reversal of trend may be explained partly by the unprecedented high

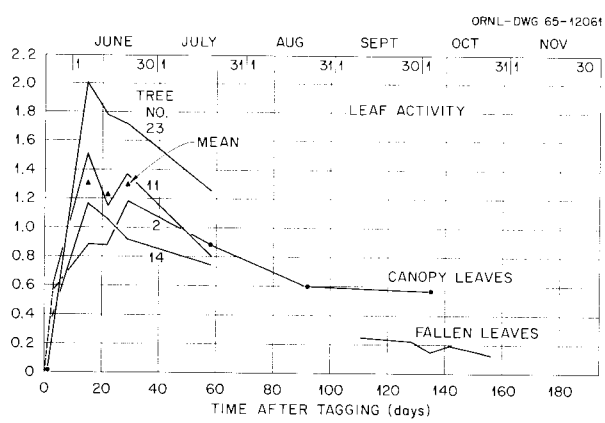

Fig. 10.2. Influence of Changing Foliage Activity.

[8]J. S. Olson, *Health Phys.* 11(12), 1385–92 (1965).

[9]H. D. Waller and J. S. Olson, *Ecology* **48**(1), 15–25 (1967).

summer rainfall in 1967. The total rate of ^{137}Cs transfer (especially in the nonfoliage season) is now very small. Nevertheless, it is still sufficient for carrying on a basic inquiry into the reasons for changes of redistribution through the ecosystem. Differential contribution of "dry fallout" (e.g., insect frass) and "rainout" may alter transfers of ^{137}Cs from the leaves.

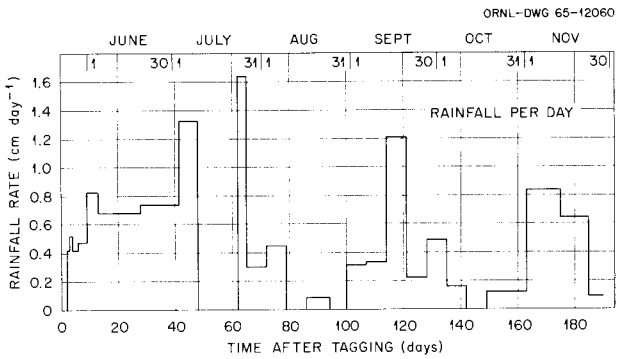

Fig. 10.3. Rainfall Distribution Through Time.

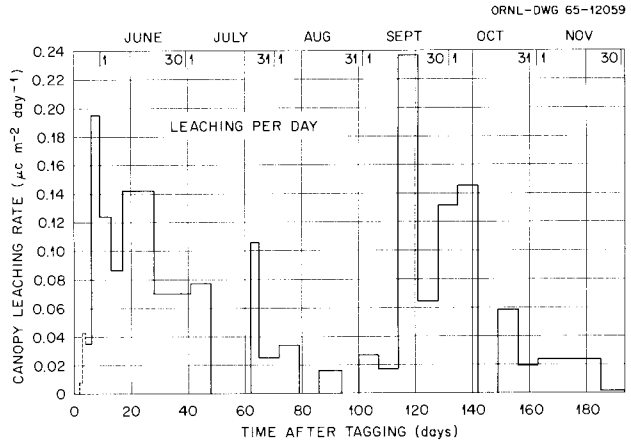

Fig. 10.4. Canopy Leaching of Radiocesium Through Time.

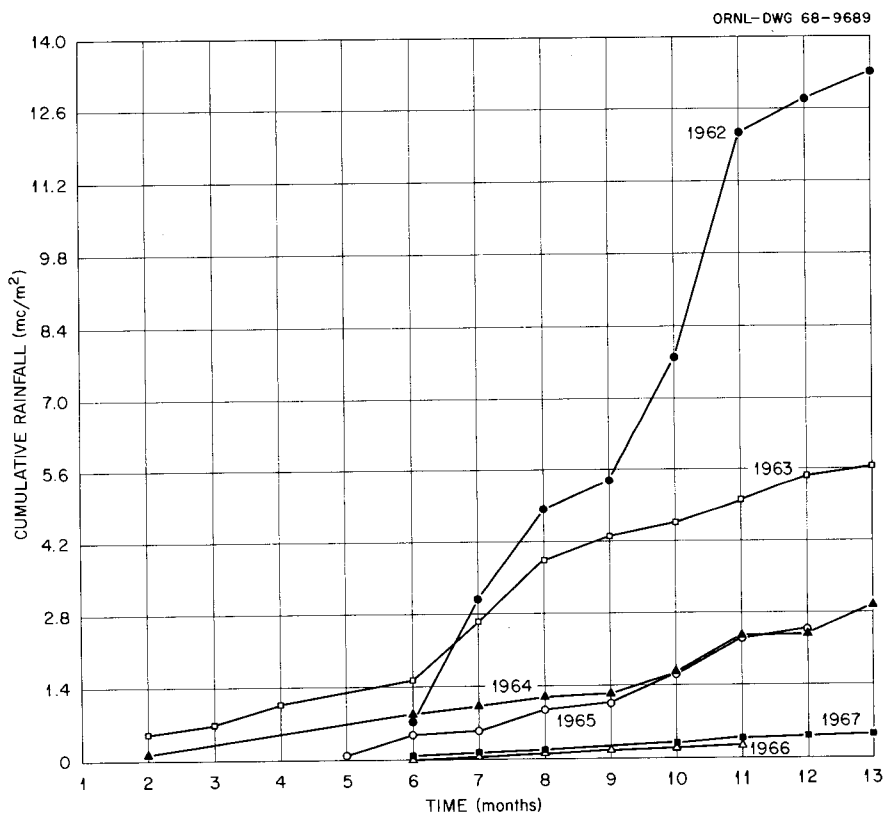

Fig. 10.5. Cumulative Leaching of Radiocesium from Leaves by Rainfall Through 1962 to 1967 Seasons.

DISPERSAL OF ^{137}Cs AROUND THE TAGGED LIRIODENDRON FOREST

J. S. Olson

Compared with the late 1965 inventory of radiocesium in the soil, there was no detectable increase in dispersal beyond 20 m outside the plot by June 1967 (Fig. 10.6). Sporadic radioactivity within this belt seems to be related primarily to dispersal of leaves from tagged trees, which had been much more radioactive in earlier years than in 1966 and 1967. Soil radioactivity continues to increase primarily within 10 m of the plot border, but the relative contribution of physical, botanical, and zoological processes to the severalfold changes here is not known yet.

Radioactivity of soil plus roots (0 to 30 cm depth) within the plot where trees were tagged in 1962 also continues to increase as the amount of ^{137}Cs in these trees decreases, by the several processes discussed in this and earlier reports.[10] The relatively large fraction of "soil" activity that was initially contained in roots continues being released to soil, so that root radioactivity is now a relatively small but variable fraction of the total. Supplementary investigations of turnover of root mass and of ^{137}Cs are being completed.

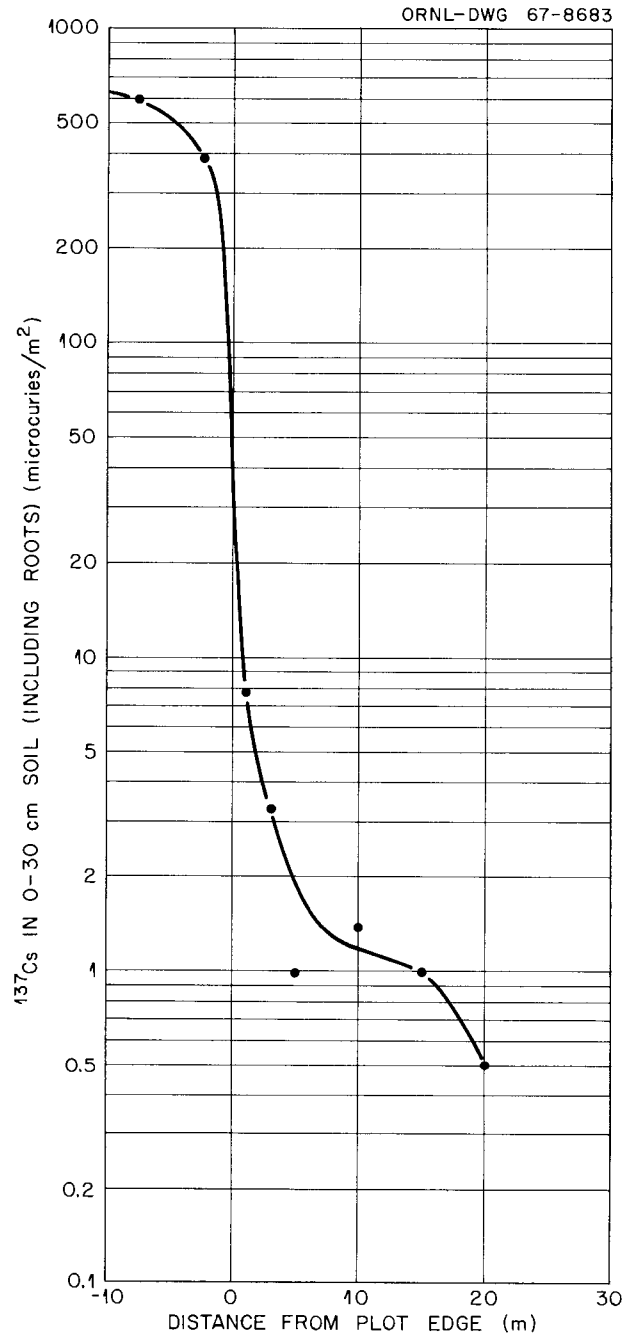

Fig. 10.6. Change of Radiocesium Concentrations Inside the Tagged *Liriodendron* Forest Plot (Left) and Successively Greater Distance Outside (Right) Between October 1965 and June 1967.

ENERGY CONTENT OF DOGWOOD TREES

W. A. Thomas

Caloric values of plants aid in understanding the energy relationships of ecosystems. After plants convert solar radiation into potential energy, this energy, in the form of plant material, may be circulated throughout the ecosystem before being utilized by other organisms or lost from the system as heat.

All samples were collected from at least eight dogwood (*Cornus florida* L.) trees (4.4 to 7.3 cm diameter at ground level; 3.3 to 6.0 m in height; 13 to 18 years old) in the understory of a loblolly pine (*Pinus taeda* L.) plantation.

Woody-tissue samples collected in November 1967, after leaf abscission, included bark, xylem, twigs, and roots; careful scraping removed all soil from roots. Mixing woody-tissue samples from four components of each of eight trees harvested during

[10] J. S. Olson, "Use of Tracer Techniques for the Study of Biogeochemical Cycles," *Functioning of Terrestrial Ecosystems at the Primary Production Level*, Proc. of Copenhagen Symposium on Ecosystems, UNESCO.

a previous study provided a "composite tree"; subsample weights were proportional to the component's contribution to total-tree oven-dry weight (stem, 45.2 g; branches, 36.8 g; roots <4 cm in diameter, 12.1 g; and roots >4 cm in diameter, 5.9 g).

Inflorescences were collected on 1 March, before spring growth commenced, and on 23 April 1968, when they had attained maximum size. Fruits with ripe pericarps were sampled on 9 September 1967.

Small green leaves (3.4 ± 0.1 cm^2 per leaf) were collected on 17 April; large green leaves (73.0 ± 1.1 cm^2) and small green leaves (7.0 ± 0.2 cm^2) were collected on 28 August 1967. Samples of green undamaged leaves and yellow senescent ones sampled on 17 September 1967 had similar areas and oven-dry weights. Each sample contained a minimum of 200 leaves or reproductive organs.

After air-drying additional yellowish-brown leaves collected on 17 September, 50 leaves (6.81 to 7.62 g, on oven-dry weight basis) were put in each of 11 nylon net litter bags. Placement of eight of these litter bags under dogwood trees in the pine plantation on 17 October 1967 permitted estimation of weight and energy losses after 4 and 26 weeks in litter. Immersion of the three remaining samples in an artificial laboratory stream for 24 hr removed water-soluble material from the leaves.

Calorific equivalents, determined for duplicate 1-g samples in an oxygen bomb calorimeter, are expressed on both the oven-dry and ash-free bases (Table 10.1). Twigs exceeded the other woody-tissue components in energy value on the ash-free basis, presumably because of higher-energy organic compounds present in the apical meristem and leaf

Table 10.1. Calorific Equivalents of Dogwood Tree Components[a]

Sample Description	Kilocalories per Gram of Oven-Dry	Percent Ash	Kilocalories per Gram of Ash-Free Oven-Dry
Woody tissue (November)			
Stem	4.63	2.4	4.74
Bark	4.33	11.2	4.87
Xylem	4.69	0.5	4.71
Twigs	4.67	5.7	4.95
Roots	4.58	1.4	4.64
Composite tree[b]	4.56	2.6	4.68
Reproductive organs			
Inflorescences (March)	4.54	9.4	5.01
Inflorescences (April)	4.37	7.2	4.71
Bracts	4.49	6.0	4.77
Receptacle plus peduncle	4.22	8.6	4.62
Fruits (September)	4.86	5.4	5.14
Pericarps	4.92	4.9	5.17
Receptacle plus peduncle	4.40	9.2	4.85
Leaves			
Small green (April)	4.41	8.5	4.82
Small green (August)	4.23	8.2	4.61
Large green (August)	4.39	8.6	4.80
Medium-sized green (September)	4.29	8.4	4.68
Medium-sized yellow (September)	4.19	8.7	4.59
After water-soluble material removed	4.64	9.0	5.09
After 4 weeks in litter	4.57	9.4	5.05
After 26 weeks in litter	4.85	9.8	5.38

[a]Mean of two duplicate samples oven-dried at 105°C and ashed at 600°C. Month of sample collection in parentheses.

[b]Explained in text.

buds. The high ash content of bark (11.2%) is to be expected, because bark typically contains a higher percentage of minerals than do other woody-tissue components. Combination of energy values with weight data presented for 28 dogwood trees of the same size in the same stand shows that bark accounted for 17.8% of the weight and 16.7% of the energy in stems. Similarly, roots contributed 23.2% of both the total weight and energy content of the total woody tissue.

The energy content per gram of oven-dry of the "composite tree" appears to be lower than anticipated, based on the other values for woody tissues in Table 10.1. Branches within the diameter range not listed as separate components in the table contribute about 20% to the total woody-tissue weight of the tree. Dilution of the energy content of the "composite tree" by these branches, especially the bark, probably accounts for the lower value compared with most of the individual components in the table.

Weight of individual inflorescences increased by a factor of 3.3 from March to April, with a slightly smaller increase in energy content of 3.2. The energy content on a unit weight basis decreased due to addition of relatively low-energy tissues to those formed the previous year. Bracts, when fully expanded, contained 54.9% of the weight and 56.4% of the energy in the inflorescences. High calorific value of the pericarps raised the energy content of the individual fruit to 14.8 times that of the inflorescence in March, while the weight increased by a factor of 13.8. Pericarps accounted for 88.8% of weight and 89.9% of the energy in fruits.

Reproductive organs can account for a sizable percentage of the total weight of nonwoody litter produced annually by dogwood trees growing in the open, with bracts contributing 3.6%, fruits 34.9%, and leaves constituting the remainder. The contributions of these components to energy supplied to the forest floor are 3.6% for bracts and 38.3% for fruits.

The calorific equivalent of the large green leaves collected in August is almost identical to that of the small leaves obtained in April. Individual leaf weight and energy content increased about 19 times between the two sampling dates. The small leaves collected in August had a markedly lower energy value, especially on ash-free basis, than either the large or other small leaves. These small leaves were newly formed in late summer, whereas leaves in the other two samples were formed the previous year and commenced growth in April. Dogwood trees produce new leaves throughout the growing season, but the leaves initiated during the previous year probably contain energy reserves which might be retained by the leaf in addition to those incorporated during the growing season. It is apparent that the newly formed leaves did not contain material with as high an energy content as did those in the other two samples.

The increase in percentage ash in the yellow leaves reflects the redistribution of organic compounds from foliage to woody tissue prior to leaf fall. Some mineral elements, notably alkali metals, also are returned to foliage, but their weight probably is exceeded by that of organic material. Senescent leaves are also subject to more efficient leaching of water-soluble material than are vigorous leaves, due to increased permeability of the cuticle to water. The reduction in energy content of senescent leaves in these samples amounted to about 2% of their energy prior to senescence. Foliage of the 28 trees studied previously contained about equal percentages of the total-tree weight (15.9 ± 0.6) and energy content (15.1 ± 0.6) in early September.

The still-intact leaf structure in all litter samples permitted careful washing of individual leaves to remove the small amount of adhering soil. The 8-cm-deep litter layer, composed primarily of pine needles, prevented serious contamination of samples with soil. No visible microorganisms, which might affect the calorific values, inhabited the samples. During the first four weeks in litter, samples lost 20.1 ± 0.5% of weight but only 12.8 ± 0.7% of their caloric value. The water-soluble fraction of leaves, as determined in the laboratory stream, constituted 23.7 ± 0.9% of the dry weight and 14.5 ± 1.0% of the energy content. These data support the conclusion that weight loss from dogwood leaves during the first four weeks in litter is caused primarily by leaching of water-soluble material, an explanation which also seems to be true for energy loss. The fact that weight loss (37.5 ± 1.7%) still significantly exceeded ($P < 0.01$) energy loss (27.7 ± 2.0%) after 26 weeks shows that the material removed from these decomposing leaves had a relatively low energy value. Energy values of litter samples increased from 4.19 to 4.85 kcal/g and from 4.59 to 5.38 kcal per gram ash-free, with a rise in ash content from 8.7 to 9.8%, during the

26 weeks in litter. Preferential leaching of water-soluble organic matter of relatively low energy content probably accounted for these increasing values.

Variation in ash content among biological materials often will obscure the true energetics of a system unless energy values are interpreted on the ash-free basis. The wide range in caloric equivalents within and among tissue groups (Table 10.1) demonstrates the magnitude of possible errors in assuming a standard value for all plant material in an investigation. Although this practice may be justified in estimating the energy content of large ecosystems, where the error in biomass estimates might surpass that from use of standard caloric values, it will often result in lost information due to misinterpretation of energy exchanges.

MICROBIOLOGY OF FOREST SOIL

Martin Witkamp Marilyn L. Frank

Because microbial turnover of minerals in forest soil is related directly to microbial respiration, rates of evolution of CO_2 from forest soils were measured in various habitats. Recent measurements using an infrared gas analyzer in the field showed that daily cycles in CO_2 evolution from soil primarily parallel the daily temperature cycle but that at night, during temperature inversions in the soil profile, a second maximum may occur. This maximum presumably is caused by thermal convection of CO_2-rich air from the warm subsoil to the cool surface and is not related to microbial activity at that time. Consequently, daily totals rather than momentary rates should be used to relate CO_2 evolution to mineral turnover by microbes.

Measurement of evolution of CO_2 from various layers of the soil profile showed that periods of rapid CO_2 generation at the surface during the afternoon may cause a downward diffusion of CO_2 into deeper layers, from where it may escape again during the night.

The rates of CO_2 evolution measured by infrared gas analysis appear to be more realistic than rates measured by previously used methods. Calculated annual evolution of carbon in CO_2 approximates the annual deposition of carbon in litter, whereas for other methods used carbon in CO_2 exceeds deposition.

Rates of CO_2 evolving from forest plots without arthropods or with different soil faunas (see Reichle *et al.*, "Effects of Pesticides on Soil Invertebrate Populations," this section) were highest in presence of added earthworms, intermediate in natural control plots, and lowest in plots without worms or arthropods. Thus soil fauna contributes significantly to soil respiration.

ACCUMULATION OF ^{137}Cs BY A SOIL FUNGUS RELATIVE TO ^{137}Cs IN ORGANIC DEBRIS AND IN SOIL SOLUTION

Martin Witkamp Marilyn L. Frank

In forest soil, remineralization of elements deposited with the litter is essential for maintenance of forest productivity. Soil fungi are the main agents in the remineralization process, by taking up minerals from the litter substrate and releasing them from their dying tissue. The minerals may be taken up directly from organic matter or via the soil solution. An experiment was designed to quantify the relationships between ^{137}Cs accumulation in a common soil fungus (*Trichoderma viride*) and ^{137}Cs concentrations in various solid litter components and their surrounding solutions. After one week, which is a realistic life span for soil fungi, ^{137}Cs concentrations in the fungus growing in soil solution were 10.4 ± 0.3 times higher than in the solutions regardless of the donor substrate. In fungus directly growing on solid substrate, ^{137}Cs concentrations over those in the substrate were proportional to the percent of ^{137}Cs lost from the substrate. Consequently, accumulation of ^{137}Cs in soil fungi without direct contact with solid donor substrate may be expected to be proportional to ^{137}Cs concentration in the soil solution. For fungi in direct contact with solid substrate, concentration appears to be proportional to ^{137}Cs availability in the substrate, where availability is a function of the decomposability of the substrate and the concentration and leachability of the ^{137}Cs in it.

TRANSIENT BEHAVIOR OF RADIOISOTOPES IN INSECT FOOD CHAINS

D. A. Crossley, Jr. D. E. Reichle
Mary P. Hoglund

Food chain transfer and the exchange of energy, nutrients, and other material among the trophic levels of communities are not instantaneous processes. Characteristically, delays or time lags

exist in the flux of materials between trophic levels. Studies with radioisotope tracers have exploited this lag time phenomenon to delineate trophic positions of mixed species populations. The following equations allow prediction of equilibrium levels of isotope in successive trophic levels and of the intervals elapsed between peak concentrations.

For arthropods feeding upon contaminated food, change in concentration is given by the income-loss balance equation

$$\frac{dC}{dt} = IA_0 e^{-k_1 t} - k_2 C , \qquad (1)$$

where C is radioisotope concentration in the consumer trophic level, I is intake rate by consumer (milligrams of food per milligram of consumer per day), A_0 is initial isotope concentration in food base, and k_1 and k_2 are isotope loss coefficients for the food base and consumer respectively. Radioisotope concentration in consumers as a function of time, $C(t)$, is the solution to the differential equation (1):

$$C(t) = \frac{IA_0}{k_2 - k_1}(e^{-k_1 t} - e^{-k_2 t}) + C_0 e^{-k_2 t} , \qquad (2)$$

where C_0 is the initial concentration of isotope in consumer arthropods. Time required for maximum concentration to occur in arthropods is obtained by setting the derivative of Eq. (2) equal to zero and solving for t_{max},

$$t_{max} = \frac{1}{k_2 - k_1} \ln \frac{k_2}{k_1} , \quad C_0 \equiv 0 . \qquad (3)$$

An example of such a transient behavior situation is given in Fig. 10.7. The 60-day time lag between peak concentrations of litter and saprovores may be substituted for t_{max}. From substitution of an independent measure of k_1 (0.02 day^{-1}) a similar value for k_2 is obtained. This estimate yields a biological half-life of about 30 days for ^{137}Cs in the saprovore trophic level. Biological half-lives approximating 30 days (at 20°C) were reported by Reichle[11] for three isopod species and by Reichle and Crossley[12] for two millipede species (at 16°C).

Such application of transient behavior analysis results in biological turnover rate estimates for radioisotopes in entire trophic levels composed of

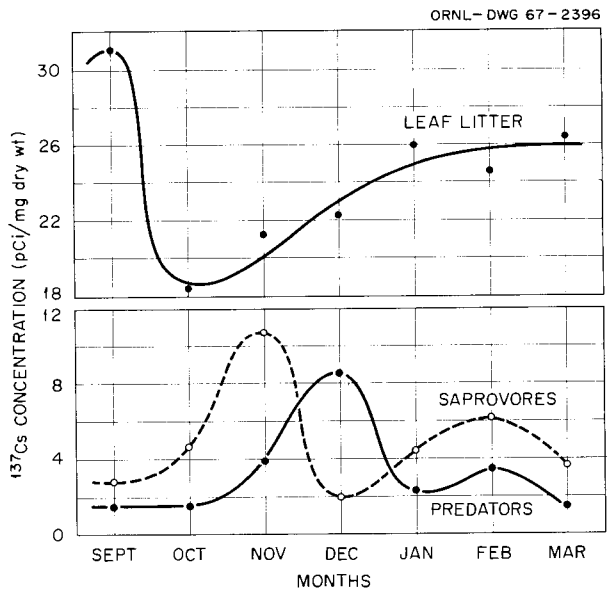

Fig. 10.7. Seasonal Fluctuation of ^{137}Cs Concentration in Leaf Litter and Saprophagous and Predaceous Arthropods in a *Liriodendron* Forest Experimentally Tagged with ^{137}Cs. Leaf litter content of radiocesium increased in September following autumnal leaf drop but then decreased due to leaching. Higher trophic levels of arthropod consumers also show changing concentrations of ^{137}Cs which reflect changes in their food bases. Relative amplitudes of the curves illustrate the decrease in ^{137}Cs concentrations through arthropod food chains.

many separate species populations. Similar applications may be made in predicting the movement and fate of nutrient elements and other environmental pollutants in food chains.

CALCIUM, POTASSIUM, AND SODIUM CONTENT OF FOREST FLOOR ARTHROPODS

D. E. Reichle M. H. Shanks
D. A. Crossley, Jr.

Whole-body nutrient composition of calcium, potassium, and sodium has been documented for 37 species of forest floor arthropods. Calcium compo-

[11] D. E. Reichle, *Ecology* **48**(3), 351–66 (1967).

[12] D. E. Reichle and D. A. Crossley, Jr., *Health Phys.* 11, 1375–84 (1965).

sition of species was highly variable, ranging from 6.4 mg per gram of ash in *Staphylinus badipes* to 328.4 mg per gram of ash for *Gyalostethus monticolens*. High calcium contents were associated with high ash composition and species characterized by well-developed exoskeletons. Ash content of millipedes averaged 48.24% of dry weight and average whole-body calcium 314.0 mg per gram of ash weight. For the remaining arthropods, these values averaged 26.87% ash and 29.50 mg of calcium per gram of ash weight. Comparisons among taxa of whole-body elemental concentrations based upon ash weights were difficult to interpret because of the variations in ash content. Therefore, results also were expressed as milligrams of element per gram of ash-free dry weight. Diplopoda averaged 327.33 mg of calcium per gram of ash-free dry weight; all other arthropods averaged only 1.89 (median = 1.6). Mean sodium concentration was 4.6 mg per gram of ash-free dry weight, with a symmetrical distribution of individual species values (median = 4.3 mg). The potassium frequency curve was positively skewed, due to occurrence of a few relatively high values for several of the diplopod species. In general, potassium and sodium concentrations were consistent within and among major taxonomic categories.

Whole-body concentrations of certain alkali metals, for example, cesium and potassium, decrease in arthropods with increase in trophic level.[12,13] Radiocesium averaged 5.95 pc per milligram of dry weight in detritus-feeders (saprovores) but only 3.00 pc/mg in predators. Similarly, potassium concentrations in the saprovore trophic level (4.42 μg/mg) were higher than in the predator trophic level (2.35 μg/mg). There are no significant differences between trophic levels in the ratio of cesium to potassium.[12,13] Sodium, in contrast, exhibited a trophic level increase from 3.57 μg per milligram of dry weight in saprovores to 5.38 μg/mg in predators. No data are available for trophic level distributions of calcium in arthropod food chains. However, in forest floor decomposer populations, where a high percentage of primary consumers (saprovores) are Diplopoda, it is probable that this primary consumer trophic level represents a "sink" in the food chain distribution of calcium.

Besides trophic level differences in elemental composition, these data also showed seasonal changes in the nutrient content of species. Three species – one predaceous, *Pachylomerides audouini* (spider), and two saprophagous, *Apheloria montana* (millipede) and *Ceuthophilus gracilipes* (cricket) – showed progressive increase in calcium concentration through the active growing seasons. Three species – *P. audouini*, *A. montana*, and the detritus-feeding *Ptyoiulus impressus* (millipede) – had highest potassium concentrations during summer months. Whole-body sodium concentrations, however, decreased from spring to summer for *C. gracilipes* and *Geotrupes* spp. (beetles). Whole-body nutrient levels may also be associated with changing seasonal composition of nutrients in food bases. Fungal mycelia, an important diet constituent of saprovores, generally contain more potassium than any other metal.[14] In years of normal temperatures and precipitation, fungus blooms in this *Liriodendron* forest during early summer.[15] Increased consumption of mycelia may explain the increased potassium content of saprophagous arthropods during the summer.

PREY PREFERENCES OF A FOREST CENTIPEDE

R. V. O'Neill Gladys J. Dodson

Preliminary to an investigation of population energy flow in the centipede *Otocryptops sexspinosus*, it was necessary to establish the sources of food for this population and the preferences of centipedes for different prey species. Potential prey available to the centipedes of *Liriodendron* forests were divided into 23 categories (Table 10.2). Prey were collected and presented to centipedes in small plastic culture dishes; after three days cultures were examined. In the table a plus sign is placed by prey species which were eaten. Because this method did not reflect natural conditions affecting search-capture behavior, a second set of experiments was performed in large 43 × 18 × 14 cm) containers which contained a layer of soil and leaf litter. The surface area presented

[13] D. E. Reichle and D. A. Crossley, Jr., "Trophic Level Concentrations of Cesium-137, Sodium and Potassium in Forest Arthropods," Proc. National Symposium on Radioecology, Ann Arbor, Mich. (in press).

[14] V. G. Lilly, "Chemical Constitute of the Fungal Cell," pp. 163–77 in *The Fungi*, ed. by G. C. Ainsworth and A. S. Sussman, Academic, New York, 1965.

[15] M. Witkamp, personal communication.

Table 10.2. Prey Preferences of the Centipede *Otocryptops sexspinosus*

Prey were presented in approximately equal standing crops. Culture dish experiments were performed in small plastic dishes; labeling experiments were performed in large containers with soil and leaf litter.

Prey Tested	Culture Dish Experiment[a]	Labeling Experiment (% of available prey consumed)	Rank of Preference
Crickets			
Nemobius maculatus, *Ceuthophilus gracilipes*	+	18.4	1
Caterpillars			
Arctiidae	+	16.7	2
Beetle larvae			
Evarthrus sp., *Scaphinotus* sp., Lampyridae	+	15.5	3
Fly larvae			
Diptera	+	12.0	4
Isopods			
Ligidium sp.	+	8.6	5
Armidillidium vulgare, *Armidillidium nasatum*, *Cylisticus convexus*	+	6.6	
Wood roach			
Parcoblatta sp.	+	8.5	5
Spiders			
Lycosa gulosa, *Lycosa avara*	+	8.5	5
Misc. small spiders	–	0	
Centipedes			
Otocryptops nigridius	+	7.0	6
Lithobiidae, Geophilidae	–	0	
Phalangids			
Leiobunum flavum, *Nemastoma kepharti*	–	0	
Collembola			
Entomobryidae	–	0	
Poduridae	–	0	
Beetle			
Evarthrus sp., *Evarthrus* sodalis, *Scaphinotus* sp.	–	0	
Annelids			
Lumbricidae	+	0	
Enchytreidae	–	0	

Table 10.2 (continued)

Prey Tested	Culture Dish Experiment[a]	Labeling Experiment (% of available prey consumed)	Rank of Preference
Snails			
Mesomphix vulgatus	–	0	
Slugs			
Unidentified	–	0	
Termites			
Unidentified	–	0.4	
Ants			
Formicidae	–	0	
Mites			
Thrombidiformes	–	0	
Millipedes			
Dixidesmus erasus, *Cambala annulatus*, *Ptyoiulus impressus*, *Apheloria montana*	–	0	

[a]"+" indicates feeding; "–" indicates no feeding.

to animals was very large compared with their size and more adequately represented natural conditions in the field. Because of culture size, it was difficult to enumerate animals remaining after the experimental period of one week. Therefore, potential prey were labeled with ^{134}Cs, and the amount of activity accumulated by the centipedes (corrected for biological turnover) was used to estimate the quantity of prey which had been consumed. These data are shown in Table 10.2 as the percentage of available prey consumed. Since prey were presented in approximately equal biomasses, these percentages can be ranked to establish the order of feeding preference by the centipede predators.

The data indicate a decided preference for crickets and various larvae, with isopods, wood roaches, large spiders, and large centipedes forming the rest of the diet. Annelid worms were eaten in the culture dishes but not in the larger containers, which contained soil in which they were concealed. This indicates that the worms will be eaten if they are exposed and discovered, but under natural conditions this would be infrequent. The small percentage consumption of termites indicates that they may be eaten on rare occasions, but they cannot be considered as common prey in the forest, where they are well protected by remaining within chambers in logs.

EFFECTS OF PESTICIDES ON SOIL INVERTEBRATE POPULATIONS

D. E. Reichle C. A. Edwards
M. H. Shanks

Soil invertebrates have long been recognized as an important factor in the decomposition of organic materials and the recycling of nutrients in natural ecosystems. Experimental studies in the field have been handicapped by the complexity of the soil fauna and inability to isolate different populations for measurement of their individual roles and synergistic interactions with other animal and microbial groups. With the use of selective pesticides, however, it is possible to manipulate the

microarthropods, earthworms, and flora of soil systems. Our technique employs a soil fumigant (dichloropropene, D-D), an insecticide (aldrin), and an earthworm extractant (formalin) for exclusion of various segments of the biota.

Earthworms were extracted using a dilute solution of formalin (75 cc of 40% formaldehyde per 6 to 12 liters of water, depending upon soil dryness) applied to the soil surface. Earthworms react to the irritant by emerging at the surface, where they may be collected. Extinction of all animal groups is accomplished by applying D-D at the rate of 170 cc/m^2 (using an injection gun delivering 5.75 cc to a depth of 15 cm at 23-cm centers). To prevent recolonization and obtain long-term suppression of microarthropods, aldrin was applied at the rate of 2.3 g of active ingredient per square meter every two months.

The results of these treatments in a *Liriodendron* forest are shown in Table 10.3 for the eight-month period following application. The D-D fumigation effectively eliminated earthworms, and recolonization was blocked by aluminum barriers sunk into the soil to a depth of 45 cm. Fumigation reduced microarthropod populations by 98.3%, when compared with control plot densities. After the transient four-week effect of D-D has dissipated, earthworms or other faunal elements may be introduced to obtain specific population combinations. With aldrin applied, recolonization by microarthropods was only 1.0% between months 2 and 4 and 0.3% between months 4 and 6.

Formalin extraction of earthworms was only 80% effective after six months and 59% after eight months, indicating that repeated treatment will be required for more substantial reduction in population number; this extraction technique was highly successful in that it had no significant effect upon soil microarthropod densities.

These experiments have provided controlled populations of soil invertebrates for studies of their roles in breakdown of organic detritus. Included within the design of these ongoing experiments is the consideration of the effects of insecticide contamination on ecological processes.

INGESTION RATE OF PINE-MOR DETRITUS BY AN ORIBATID MITE (*CULTRORIBULA JUNCTA*)

N. E. Kowal

The food web of pine mor is a relatively simple one (compared with other forest floors) that is domnated by decomposing pine litter, fungi, and microarthropods – particularly mites and collembola. Because of the absence of larger animals, the decomposing litter is unmixed with the mineral soil below. These characteristics, together with the broad geographic distribution of pine forests, suggest that pine mor might represent good experimental material for the investigation of food-web dynamics using radionuclide tracers. Since the

Table 10.3. Comparison of the Effects of Insecticides on Populations of Forest Soil Microarthropods and Earthworms

Control data expressed as number of individuals per square meter of ground surface; treatment values are percent of controls. Time scale starts at the beginning of treatment.

Months	Pesticide Treatment (percent of control populations)				Control (number of individuals per square meter)	
	D-D Fumigation		Formalin Extraction			
	Earthworms	Arthropods	Earthworms	Arthropods	Earthworms	Arthropods
2	0	1.7	36	109	10.6	75,240
4		2.7		102		88,808
6	0	3.0	20	100	31.8	66,113
8	0	6.7	41	93.1	25.1	73,668

small size of the arthropods would be the most likely limiting factor in any experimental work, I decided to try to count the radioactivity of individual microarthropods feeding upon ^{45}Ca-tagged pine needles and natural pine mor, in small containers.

Representative counts per minute (above a background of approximately 3.3 counts/min; counted for 20 min) per individual arthropod for some arthropods extracted about 20 days after inoculation follow. Pine needles: *Cultroribula juncta* (6.0–7.4); natural pine mor: spiders (20.7–107.8), protura (3.5–3.7), collembola (5.7–14.0), the predaceous mite *Labidostomma* sp. (18.8–33.9), the predaceous mite *Veigaia* sp. (12.5–17.8), and *Cultroribula juncta* (29.1–56.3). Thus, under the conditions used, individual collembola and mites count at several times background level, indicating that standard radionuclide tracer techniques are well suited to the study of the microarthropod food web in pine mor, using small containers.

The data gathered on the accumulation of ^{45}Ca by the saprovorous oribatid mite *Cultroribula juncta* allow the calculation of a crude estimate of its ingestion rate. The original data (disintegrations per minute per individual) have been normalized and converted to "equivalent micrograms of mor per individual" by dividing by the radioactivity of the respective substrates. The results are presented in Fig. 10.8.

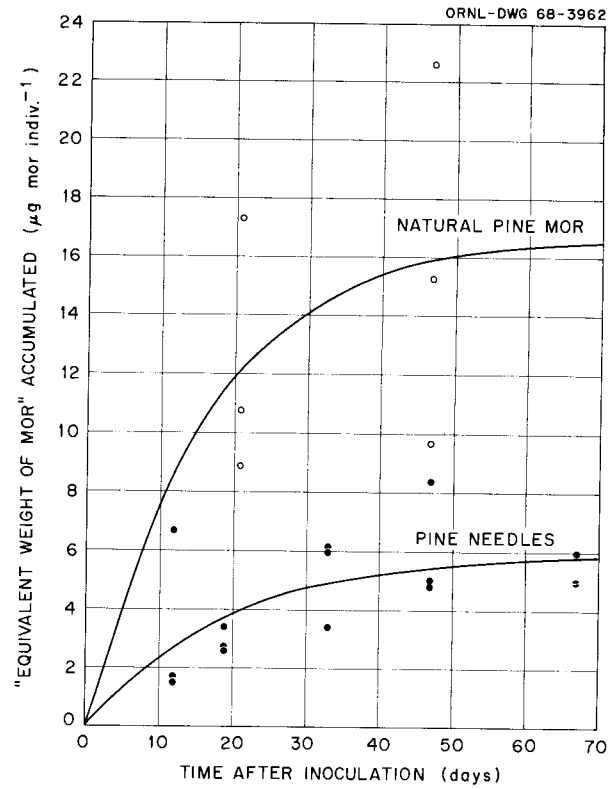

Fig. 10.8. Accumulation of "Equivalent Weight of Mor" by *Cultroribula juncta*. O = natural pine mor; ● = pine needles.

The mathematical model of accumulation used is ^{45}Ca accumulation rate = ^{45}Ca ingestion rate – ^{45}Ca elimination rate,

$$\frac{dA(t)}{dt} = I - kA(t) , \qquad (1)$$

whose particular solution is

$$A(t) = \frac{I}{k}(1 - e^{-kt}) , \qquad (2)$$

where

$A(t) \equiv$ accumulated material (body burden) at time t (micrograms of mor per individual),

$t \equiv$ time since inoculation (days),

$I \equiv$ ingestion rate (micrograms of mor per individual per day),

$k \equiv$ ^{45}Ca elimination rate coefficient (day^{-1}).

The parameters I and k can be obtained by a least-squares fit of this equation to experimental data. It should be noted that the elimination rate coefficient refers to the total elimination rate, i.e., egestion rate plus excretion rate plus exuviae-production rate plus egg-production rate. This usage differs from a common one,[16] which omits egestion rate on the grounds that the egestion component (unassimilated) can be easily separated from the other components (assimilated) in measurements of biological elimination.

At steady state the body burden does not change:

$$\frac{dA(t)}{dt} = I - kA(\infty) = 0 ,$$

[16] T. R. E. Southwood, *Ecological Methods with Particular Reference to the Study of Insect Populations*, Methuen and Co., London, 1966.

$$A(\infty) = \frac{I}{k}, \tag{3}$$

where

$A(\infty) \equiv$ steady-state value of $A(t)$.

The same model yields the standard elimination equation[17] when the ingestion rate is made equal to zero:

$$\frac{dA(t)}{dt} = -kA(t) , \tag{4}$$

$$A(t) = A(0)e^{-kt} . \tag{5}$$

Equation (2), describing the accumulation of ingested mor by mites, was fitted to the two sets of data using a nonlinear least-squares technique.[18] The resulting estimates of parameters with their confidence limits appear in Table 10.4, and the curves and data points appear in Fig. 10.8.

The very low ingestion rate of pine needles compared with that of natural pine mor is consistent with the observations of Kendrick[19] that pine needles require considerable decomposition by fungi before they are eaten by microarthropods. The fact that the tagged needles were primarily first-year needles, not yet ready to fall, must also have contributed to the low ingestion rate. Since the mean weight per individual of *Cultroribula juncta* is about 4 μg (oven dry at 65°C), the estimated ingestion rate of natural pine mor by this mite is about 0.25 μg of mor per microgram of mite per day. This agrees closely with the value of 0.40 estimated by Engelmann[20] for oribatid mites feeding on yeast. The similarity of the two estimates of the elimination rate coefficient is an indication of similar assimilation fractions of calcium in the two foodstuffs. The assimilation fraction probably approaches unity in these calcium-poor pine forests.

[17] D. A. Crossley, Jr., p. 43 in *Radiation and Radioisotopes Applied to Insects of Agricultural Importance*, IAEA, Vienna, 1963.

[18] D. W. Marquardt, *J. Soc. Ind. Appl. Math.* **11**, 431 (1963).

[19] W. B. Kendrick, *Can. J. Botany* **37**, 907 (1959); W. B. Kendrick and A. Burges, *Nova Hedwig.* **4**, 313 (1962).

[20] M. D. Engelmann, *Ecol. Monographs* **31**, 221 (1961).

BEHAVIOR OF CURIUM IN PLANTS

W. A. Thomas

Knowledge of heavy-element behavior in plants is desirable, not only to help interpret physiological phenomena, but also to evaluate the consequences of accidental release of transuranic elements to the environment. This experiment was designed to determine if plants can absorb and transport curium, the element with highest atomic number (96) available in sufficient quantities for biological investigations.

Two bean plants (*Phaseolus vulgaris* L., var. Giant Stringless) were planted in each of 12 polyethylene bottles containing 200 ml of Knop's nutrient solution tagged with ^{242}Cm (5000 dis min^{-1} ml^{-1}). Two bean plants were also grown in each of eight bottles containing a loam soil which was brought to field capacity with 200 ml of the tagged nutrient solution. The roots on each of ten bean plants growing in nutrient solution were excised 1 cm below the root collar to allow direct entry of ^{242}Cm into the transpiration stream. A common

Table 10.4. Parameters of Accumulation Model

Figures in parentheses are nonlinear 95% confidence limits

	Natural Pine Mor	Pine Needles
I, μg of mor per individual per day	1.059 (0.583, 1.535)	0.317 (0.235, 0.399)
k, day^{-1}	0.0632 (0.0535, 0.1304)	0.0531 (0.0414, 0.0784)

pasture bunch grass, tall fescue (*Festuca arundinacea* Schreb., var. Kentucky 31), was clipped to 8 cm in height and transplanted in four plastic trays (10 × 10 × 4 cm), where they grew with the root mat in 200 ml of the tagged Knop's solution.

Because of radiotoxicological hazards associated with ^{242}Cm, plants were maintained in a well-ventilated radiologically safe glove box equipped with incandescent and fluorescent lamps.

Plants were harvested after 28 days of growth in the inoculated media; bean plants in each treatment increased in dry weight by a factor of 6 during the experiment. Calculations of alpha-particle dose to roots at the start of the experiment (before isotopic decay) yielded an estimate of 0.70 rad/day, a value somewhat high because it was calculated on the assumption that the concentration of ^{242}Cm atoms within the roots equaled that in the nutrient solution. This chronic, decreasing dose evidently did not affect plant growth, since no differences existed between weight and apparent vigor of sample and control plants.

Samples of grass and of bean stem and foliage were ashed in a muffle furnace and dissolved in liquid scintillation counting solution. The near impossibility of ascertaining if heavy elements in samples of fibrous root systems had been absorbed, or only adsorbed on root surfaces, precluded analysis of root samples.

Grass, although it grew rapidly during the experiment, did not contain activity in excess of that in control samples. All bean plants grown in solution and most of them (81%) in soil exhibited significant activity in foliage and stem tissues. Absence of ^{242}Cm in grass leaves may have resulted from physiological or physical barriers to curium, although grasses do contain other heavy metals.[21]

Counting data for bean plants, expressed as percentage of total ^{242}Cm in the nutrient solution which was present in plant tissues, show significant differences ($P < 0.05$) among treatments: plants with intact roots in solution (0.030% ± 0.001), with roots in soil (0.068% ± 0.005), and with severed roots in solution (0.086% ± 0.003; $\bar{X}$ ± SE). Abrasion of roots by soil particles and activity of microorganisms in soil might result in introduction of soil solution into the transpiration stream, thus bypassing any barriers to its entry.

[21]R. P. G. Gregory and A. D. Bradshaw, *New Phytol.* **64**, 131 (1965).

On the other hand, roots in nutrient solution alone would still have most barriers intact. Formation of radiocolloids by ^{242}Cm in soil[22] should permit easier entry of this isotope into damaged roots compared with those with intact surfaces. The greater percentage uptake by plants with severed roots confirms that the transpiration stream can transport curium and indicates that the site of any "discrimination" against heavy metals is in the roots.

It is highly improbable that plants can introduce hazardous quantities of curium into food chains which lead to man unless foliage becomes contaminated after a large-scale release of this element to the atmosphere. The probability of releasing a man-made element in such quantities is practically negligible. Should such an event occur, however, the fact that curium concentrates in bone, liver, and the gastrointestinal tract[23] would greatly reduce the amount transmitted to man if other animals were between foliage and man in the food chain.

DISTRIBUTION OF RADIOCESIUM ASSIMILATED BY FESCUE FOLIAGE

R. C. Dahlman

Prior studies[24] of radiocesium movement in woody plants revealed rapid transfer of the nuclide to the roots and soil. Knowledge of radioisotope distribution patterns in grass is even more important, because this vegetation comprises the principal food substance in the grass-cattle-human food chain. Fluctuation of contaminant radioactivity in different plant parts will result in variation in radiocesium body burdens at the consumer trophic level, since insects and animals selectively graze foliage, roots, and seed. This will cause diverse internal doses to the different consumer organisms.

Foliar assimilation of radiocesium and subsequent redistribution to other parts of fescue plants was determined during vegetative and flowering phases of the growth cycle. Foliage of six-week-old fescue plants of uniform stature (9 to 12 tillers per plant and one leaf blade per tiller) was tagged by dipping in a 0.02-μc/ml ^{134}Cs solution (pH = 4;

[22]D. G. Jacobs *et al.*, *Health Phys. Div. Ann. Progr. Rept. July 31, 1967*, ORNL-4168, p. 35.

[23]P. W. Durbin, *Health Phys.* **8**, 665 (1962).

[24]H. D. Waller and J. S. Olson, *Ecology* **48**(1), 15–25 (1967).

0.01% detergent). The plants were submerged for 5 min, during which time the solution presumably permeated the stomatal aperture because of the wetting action of detergent on water. Then the plants were rinsed successively in 0.1% detergent and distilled water to remove excess radiocesium from the leaf surface. Most of the assimilated radiocesium was internal, because autoradiographs of leaves disclosed activity distributed in veins rather than concentrations in surface salt crusts. The plants were potted in gravel, and this practice minimized root weight errors which customarily are caused by mineral residues adhering to the surface of roots. Nutritional and moisture requirements were satisfied by submerging the roots and gravel media daily in a dilute nutrient solution. This soil-free system differed from the typical soil medium, but it enabled efficient recovery of roots for gravimetric radiocesium analysis. From one to four plants were harvested at various intervals following tagging, and they were separated into leaves, sheath, inflorescence, seminal roots, and nodal roots. The radiocesium content was determined from assay of three to five subsamples of each plant part. Leaching loss of the tracer was determined from daily assay of aliquots of nutrient solution that bathed the root system.

Tagging of grass by submerging foliage in an isotope solution proved successful, because the average amount of radiocesium assimilated by 18 plants was 79 ± 4 nc. Uniformity in total uptake permitted further analysis of intraplant distribution patterns (Fig. 10.9) as a function of time and phenology. The large error terms for foliage and inflorescence probably reflect considerable variation in radiocesium retention on surfaces and in extracellular spaces. Standard errors for roots were less – probably because here accumulation occurred via biological transport only, in contrast to uptake in shoots, which was a function of both metabolic assimilation and physical adsorption-diffusion phenomena.

Significant quantities of foliar-assimilated radiocesium were promptly redistributed to different plant parts, *ca.* 20% to the root system in five days and then 20% to the flower structures as they emerged from the sheath 15 days after labeling. At floral maturity the content in inflorescence increased to 45% of the total present in the plant. Redistribution of radiocesium from roots to inflorescence accounted for approximately half the initial burden in the flowering organs. Subsequent radiocesium increases in the inflorescence were the result of continuing transport from foliage. Concentration of radiocesium in floral parts has been observed by Middleton,[25] and the rapidity with which transport occurs is illustrated by these results. Approximately 15% of the label moved to the emerging fescue inflorescence in a two-day period.

Interesting radiocesium distribution patterns were observed between seminal and nodal roots of young fescue grass. The former originate from germinal tissue in the seed, and the latter develop from meristematic tissue of the stem nodes. Initially radiocesium moved from shoots to seminal roots; then after four days nearly all the basipetal movement was to the nodal roots. The quantity of activity in seminal roots was negligible relative to the total activity of the entire plant, but within two weeks even this small amount was redistributed to other parts, presumably nodal roots and inflorescence. Transfer from seminal to nodal roots corresponded to cessation of seminal root growth. Although less than 10% of the radiocesium present in the entire plant was leached from roots, this quantity reflects additional basipetal transport which would have gone undetected if the rooting media had not been examined for activity. This amount was nearly equivalent to that present in the root system. The rate of radiocesium accumulation in the total root system followed an exponential pattern during the 2- to 14-day period after uptake by foliage. Coincident with inflorescence emergence the direction of transport was reversed, and the nuclide moved back into the shoots. In the absence of this response accumulation in roots probably would have continued, but at a slower rate, such as that indicated by the total transport to roots curve of Fig. 10.9.

In the early phase of radiocesium transport from foliage the reduction in activity appeared to follow a decreasing exponential pattern, somewhat a mirror image of accumulation in roots. But the emerging inflorescence provided an additional "sink" to which the mobile nuclide moved. This caused the rate of transfer from foliage to be maintained at a relatively high level, and over 50% of the assimilated radiocesium moved out of the foliage. In the absence of inflorescence emergence

[25] L. J. Middleton, *Intern. J. Radiation Biol.* 4, 387–402 (1959).

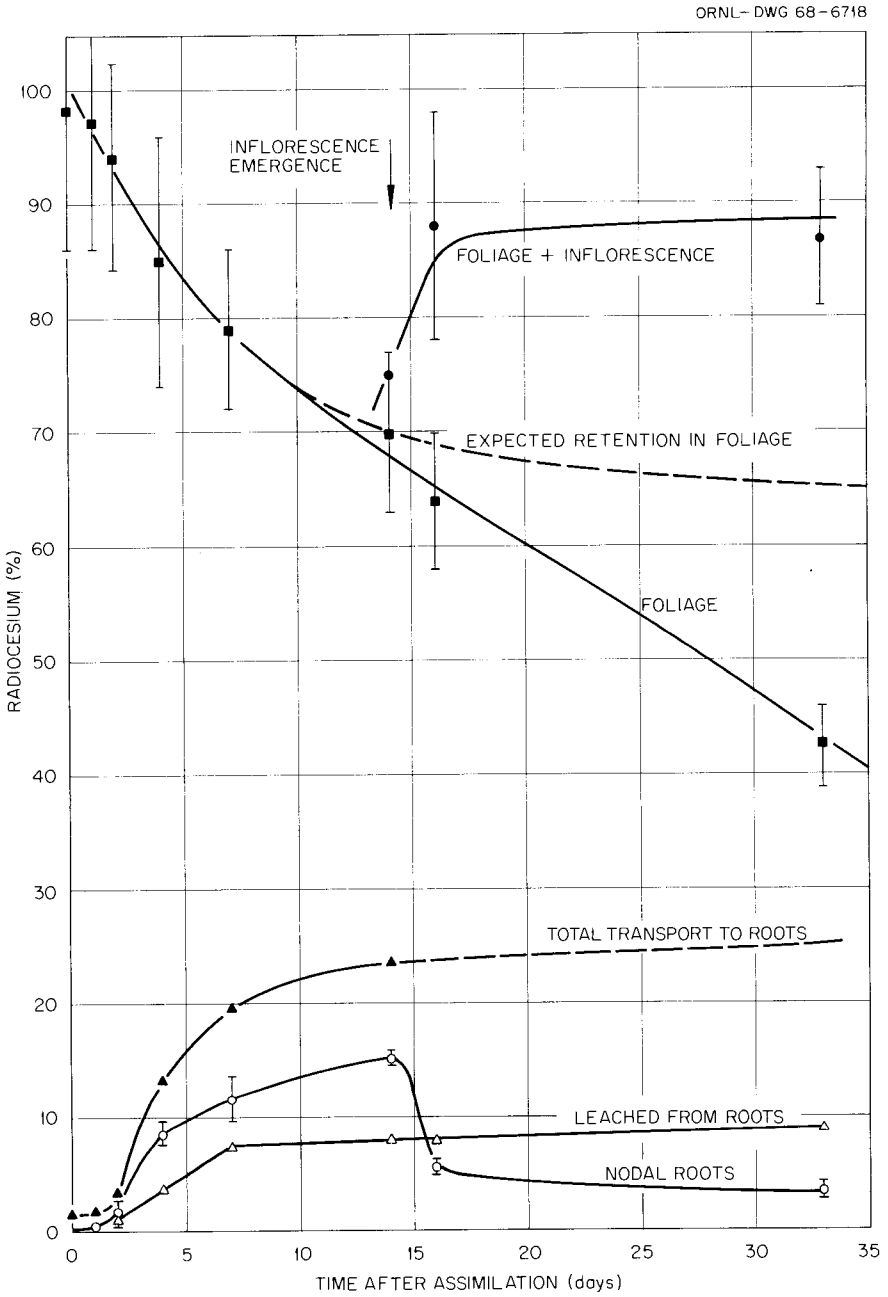

Fig. 10.9. Distribution of Radiocesium in Different Organs of Fescue Following Foliar Assimilation.

a slower rate of radiocesium transport from foliage would be expected during the late phase (two weeks) of redistribution, and the expected retention in foliage (Fig. 10.9) might be 65 to 70% of that assimilated. A two-phase rate of transport was apparent for movement from foliage. Both free and bound cesium ions probably exist in plant tissues, and the early phase (one to two weeks) of rapid decrease indicates transport of the readily available portion via the translocational stream. Then the rate diminishes, probably because of decreased availability due to physical-chemical and biological fixation of cesium in the leaf tissue.

Similar patterns of distribution in fescue plants would be expected for the radiocesium assimilated from fallout, with the exception of accumulation in soil. If the soil acts as a sink which continually absorbs cesium ions released from the roots, then transfer to the soil would be greater than that observed in this experiment. This mechanism would remove the nuclide from circulation. On the contrary, if the soil presents an optimal physical-chemical and moisture environment, these factors would modify root stress, thereby reducing root loss. However, root contribution to radiocesium accumulation in soil is not easily evaluated, because precise measurement of transfers via this route is complicated by the difficulty of separating roots from clay-mineral residues.

PRELIMINARY ESTIMATION OF EROSION AND RADIOCESIUM REDISTRIBUTION IN A FESCUE MEADOW

R. C. Dahlman

Studies of fescue vegetation contamination by close-in fallout debris (fine sand) are in progress at the 0800 Ecology Research Area. One aspect of the investigation concerns the retention of the contaminant inside the study enclosures subject to the precipitation regime of eastern United States. Local rainfall averages 50 in./year, which occasionally occurs as intense storms, and redistribution of the simulant via erosion may create public hazards or affect the radiation dose to experimental organisms. Potential radioactivity redistribution was evaluated for observed and hypothetical conditions of precipitation prior to introducing the fallout simulant. The results of the analysis are compared with other locally observed losses and with predicted erosion based on a soil-loss equation used for cultivated systems.

Radiocesium removal from the experimental area will be a function of (1) the quantity of water and eroded solids in runoff and (2) the quantity of ^{137}Cs dissolved in water and sorbed on solids. Runoff collecting and measuring devices have been installed on two of four plots which will be contaminated with fallout simulant. The apparatus measures quantitatively the total runoff, and it collects subsamples of solids and solution for assay of radioactivity. In this way the materials carried from the plots in runoff will be monitored in order to evaluate ^{137}Cs transfer to the natural drainage system outside the experimental area. Before the runoff exits from the plot, it passes through a basin in which sand-size particles settle; therefore the simulant sand will not erode from the area.

Surface water runoff from plot 2 has been observed since October 1967 and from plot 7 since February 1968. Runoff was related to soil moisture recharge and rainfall intensity, and generally the soil system had the capacity to absorb approximately 4 in. of rain, after which it became saturated and runoff occurred. This observed 4-in. recharge correlates well with the calculated water storage capacity based on available pore space [25% when soil water was 25% (field capacity is 28%)] assuming recharge of the top 15 to 20 in. of the profile. For these specified conditions the sandy-loam soil could absorb 3.7 to 5 in. of water if the rate of precipitation is less than the rate of percolation. Indeed the soil system absorbed the precipitation input, because runoff was inconsequential, and the maximum observed was 2% of the total input. Six of nine runoff events yielded less than 1% of the input.

The splitter apparatus has capacity to measure 28×10^3 liters of runoff per day. This is equivalent to 5.5 in. of rainfall if runoff conforms to the observed patterns and if it consists of 5% (2.5 times the observed) of the precipitation input. Add 4 in. of soil recharge to the 5.5 in. of rainfall equivalent runoff; then the experimental design (plant-soil system and apparatus) will accommodate a 9.5-in. event in a 24-hr period, a highly unlikely occurrence. Although readily infiltrated by water, the soil probably could not absorb completely the input from a high-intensity rainfall (10 in. in 24 hr), and the collectors would be overloaded by the increased runoff. Therefore, during periods of con-

tinuous rainfall the installation will be serviced at least twice daily to assure that runoff does not exceed the measuring capacity of the apparatus.

Eroded solids were almost absent in the runoff water. Apparently the dense cover of grass and litter filtered and removed most of the soil from surface runoff. Small quantities (<1 g per 5 liters of runoff) of mineral sediments were adsorbed on the inside of the polyethylene collectors, but more than 25 liters of runoff was necessary to deposit a collectable quantity of solid material. Obviously, erosion of surface soil should not be a serious problem in this experiment; however, we plan to examine the mineral solids for sorbed radiocesium.

The important factors determining the initial distribution of ^{137}Cs will be sorption on soil and movement of dissolved and solid materials in water. From laboratory tests it was determined that the simulant will release 10% of the fixed ^{137}Cs following contact with water for 24 hr, and 24% of the radiocesium will transfer to clay in a 1:1:10 simulant:clay:water slurry. Equilibration occurs rapidly, because only 26% transfer was observed after seven days. However, the slurry preparation would represent an unrealistic situation relative to the field situation, and the actual release of ^{137}Cs from the simulant should be less than that observed in laboratory tests.

For these solubility (10%) and exchange (20%) parameters a model (Fig. 10.10) was constructed to show the expected behavior of the contaminant under circumstances of a heavy rain (> 4.0 in.) immediately following application to the plots. The absolute quantity of ^{137}Cs in water and soil would be 200 and 400 mc per plot respectively. Because of the high K_d of cesium reaction with illitic clays, the water would be desorbed quickly by the clay; thus, most of the ^{137}Cs in solution would transfer to the soil. Another input to the soil would involve a 20% transfer of ^{137}Cs directly to clay via the exchange mechanism, constituting a total of 0.6 curie in the soil compartment of the system. Initially, it was assumed that only the top centimeter of soil would fix cesium.

Observed runoff has not exceeded 2% of the precipitation input, especially when the soil recharge potential will accommodate a 4-in. rain. However, if we consider the most extreme case of 5% (2.5 times the observed) runoff, then 0.1 mc per plot will be transferred in 400 liters of runoff. Linear extrapolation probably would hold for rainfall of greater magnitude.

Based on the observed average rate of soil erosion (1 g per 5 liters), the quantity of soil contained in 400 liters of runoff would be 80 g. This quantity represented 6.65×10^{-3}% of the surface centimeter of soil (1.2×10^6 g) in contact with the simulant. The estimated radiocesium that could be removed in the solid phase is calculated as 0.04 mc per plot. Although the greatest quantity of radioactivity is carried by solid materials, the total loss in this phase will be negligible (0.92 mc/year from all plots) because the vegetative cover effectively prevents soil erosion. The radioactivity movement from plots with collectors and without collectors has been estimated as 480 and 1200 mc/

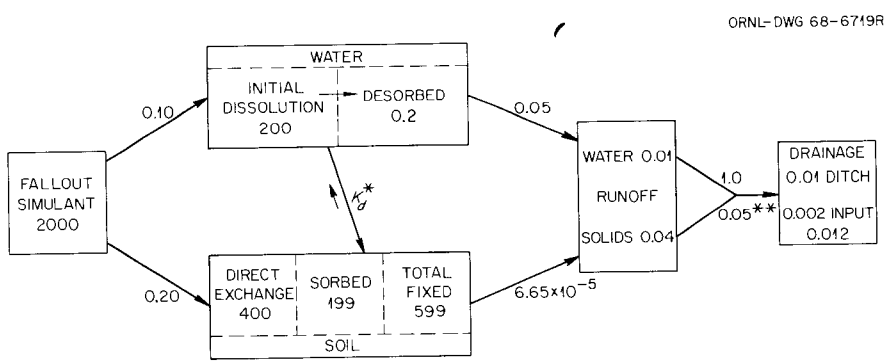

$*K_d = \frac{Cs\ soil}{Cs\ sol'n} = 1000$

**FRACTIONAL TRANSFER BECAUSE SEDIMENTS WILL BE COLLECTED FOR RADIOASSAY.

Fig. 10.10. Predicted Movement of Radiocesium from One Runoff Shortly After Application of Fallout Simulant. Numbers in compartments represent millicuries of ^{137}Cs per plot, and other values indicate fractional transfer between compartments.

year respectively. Although the loss from plots having no collectors would be greater by a factor of 4, there is no cause for alarm, because the predicted losses via runoff would constitute only 0.021% of the 8 curies of contaminant in the four plots. Thus, only a minor quantity of radiocesium (1.7 mc/year) will be released to the outside drainage system, and considering the high sorptive capacity of local soil for cesium, the contaminant probably will be retained in the drainage ditch, and will not be carried to the Clinch River.

The results from two local experiments (small-plot radionuclide movement studies conducted at area 0807 and simulant-plot radiation effects studies located at area 0800) permit a comparison of predicted and observed soil loss. The Wischmeier and Smith[26] soil-loss equation independently predicts erosion for these plots. The terms used in their equation were based on the physical and biological characteristics of small and simulant plots, and the predictions are compared against measured erosion (Table 10.5). For the simulant plots, preliminary runoff data were collected for six months, during which time the rate of soil loss was approximately 1 g per 5 liters, which constitutes 0.5 g/m^2 and extrapolates to 1 $g\ m^{-2}\ year^{-1}$. For anticipated conditions of severe runoff, annual soil loss is predicted on the basis of 20 rainfall events, each producing 400 liters of runoff; then, we would expect 16 $g\ m^{-2}\ year^{-1}$ [(400 liters/event) (20 events)/(5 liters/g) (100 m^2)]. Using the Wischmeier and Smith model the predicted value (12 g/m^2) is more than ten times greater than the observed to date, but under very severe conditions the expected (16 g/m^2) would be slightly greater than that predicted from the model. Agreement between observed and predicted erosion loss is reasonably good considering that the soil-loss model was derived for cultivated systems. Also it is emphasized that topographic features of the simulant plots approach the lower limits for which the model is applicable.

Continuous observation of erosion from tall meadow small plots[27,28] over a two-year period provides additional results for correlating predicted and observed soil loss. After one year the observed soil loss from the vegetated system was 72 g/m^2, compared with predicted losses of 42 g/m^2. For the next year the observed loss was only 13 g/m^2, an appreciable reduction in erosion. Averaging both years gives 43 g/m^2, a quantity closely correlated with predicted losses. The energy-intensity (EI) values were nearly equivalent for both periods of measurement. The discrepancy in soil loss during these periods of nearly constant rainfall erosivity probably is related to other factors, such as changes in vegetation cover and latent effects of plot construction. We can only speculate about disturbances to the vegetation-soil system during small-plot construction, but from our observation of fence and drain installation in the simulant plots, at least one growing season (6 to 12 months) was required for stabilization of the disturbed areas. In any small-plot design, exposed soil inside the fence perimeter would be susceptible to erosion, and losses would be magnified, especially under circumstances of a large perimeter-to-area ratio (1.85 for small plots vs 0.4 for simulant plots).

A comparison of predicted and observed results serves to test the model and the choice of terms used in an evaluation. Long-term evaluation is desirable because of variability in erosion responses associated with individual rainfall events. Despite the limited duration of observation, there was some agreement between predicted and observed erosion from both simulant and small plots. Correlation appeared better when predicted erosion was compared with the maximum expected assuming extreme conditions of rainfall erosivity. For normal conditions, however, the Wischmeier and Smith model overestimates erosion from a heavily vegetated sod (three times greater for second-year results from small plots; ten times greater for simulant plots). This suggests that the management factor term of their model needs downward revision because of the overriding influence of dense vegetation in reducing erosion. We would recommend a value of 0.001 or less for the coefficient C in connection with established grass communities.

[26] W. H. Wischmeier and D. D. Smith, *Predicting Rainfall Erosion Losses from Cropland East of the Rocky Mountains: Guide for Selection of Practices for Soil and Water Conservation*, U.S. Dept. Agr., Agr. Handbook No. 282 (1965).

[27] A. S. Rogowski and Tsuneo Tamura, *Health Phys.* 11, 1333–40 (1965).

[28] Tsuneo Tamura and A. S. Rogowski, "Movement of ^{137}Cs by Runoff, Erosion and Infiltration from a Soil Under Cover Conditions," presented at Symposium on Postattack Recovery, Nov. 6–19, 1967, Fort Monroe, Va. (unpublished).

Table 10.5. Comparison of Terms Used in Soil-Loss Model and Predicted vs Observed Erosion from Simulant and Small Plots

	Rainfall (R) (EI in ft-tons acre^{-1} year^{-1})	Erodibility (K) (tons/acre)/(100 ft-tons/acre) (in./hr)	Slope Length Gradient (LS)	Cover Correction (C)	Erosion		
					Predicted		Observed (g m^{-2} year^{-1})
					(tons acre^{-1} year^{-1})	(g m^{-2} year^{-1})	
Simulant plots (100 m^2)	200	0.30 (Lindside)	0.18	0.005	0.054	12.1	1 (16)[a]
Small plots[b] (5.5 m^2)	300	0.40 (Captina)	0.26	0.006	0.187	41.5	72 (1st year) 13 (2d year) 43 (av)

[a]Maximum expected under extreme conditions of rainfall input and erosion.

[b]Terms were calculated from data presented by Rogowski and Tamura (1965)[27] and by Tamura and Rogowski (1967).[28]

SEASONAL CHANGE IN ROOTS, TOPS, AND DEAD BIOMASS OF *ANDROPOGON* AND *FESTUCA* FIELDS

J. M. Kelly P. A. Opstrup

Two grassland communities were sampled periodically through 1967 with 40 meter-square plots on each sampling date, a total of 560 plots. A $\frac{1}{4}$-m-square plot taken from the meter-square plot was separated to species, living and dead. Twenty root biomass samples to a depth of 60 cm were taken by hydraulic core sections and washed at each sampling date in conjunction with the meter-square plots. In addition 100 unclipped plots were read with a capacitance meter and ranked by species.

Estimates of production in the *Andropogon* and *Festuca* communities, as measured by positive biomass increase, were 892 and 1001 g m^{-2} $year^{-1}$ (Tables 10.6 and 10.7 respectively). The standing crop of litter in each community remained relatively constant at approximately 181 and 114 g/m^2. The trends in standing dead biomass differ in both communities. The maximum value for the *Andropogon* community standing dead (824 g/m^2) occurs at the time of frost, when most of the live material is transferred to the standing dead. The maximum value for the *Festuca* community standing dead is 408 g/m^2; this value is recorded in the early growing season. Apparent daily mean production rates vary from 1.05 (March 10–June 7) to 3.34 g m^{-2} day^{-1} (June 7–August 7) for aboveground production in the *Andropogon* community and from 1.21 (March 1–April 28) to 3.29 g m^{-2} day^{-1} (April 27–May 15) for the *Festuca* community. Estimated rates for belowground biomass increase ranged from 0.55 (August 7–September 7) to 1.31 g m^{-2} day^{-1} (June 7–August 7) for the *Andropogon* community and 1.38 (March 1–April 28) to at least 4.02 g m^{-2} day^{-1} (April 28–May 18) for the *Festuca* community.

This study considers refinements of technique or results in several aspects of grassland study: (1) Minimal limits on net production from biomass change in *Festuca* and *Andropogon* old-field communities appear to be closer estimates of total community net production than most values found in the literature because (*a*) the sampling was sufficiently frequent to be close to peak biomass for each significant taxon, (*b*) the samples were separated into living and dead biomass for each species, (c) the standing crop of litter as well as litter input and decomposition were measured closely, and (*d*) root biomass was needed for quantification of this compartment and gives a way of obtaining indirect limits on translocation to and from root storage. (2) Estimation of input to and loss from standing dead for the present year is confounded by previous year's standing dead material in both communities; so many studies neglect or underestimate both transfers. A satisfactory

Table 10.6. *Andropogon* **Community Biomass Means in Grams of Organic Material per Meter Square**

Sample Period	Depth (cm)				Live Aboveground Biomass	Standing Dead Biomass	Litter
	0–20	20–40	40–60	0–60			
Early April	377 (45)[a]	58 (40)	11 (40)	446	13	824	218
Early June	384 (52)	113 (105)	26 (85)	523	96	591	161
Early August	437 (46)	128 (202)	38 (110)	603	300	519	162
Mid-September	507 (34)	71 (50)	42 (154)	620	373	527	198
Late October	659 (86)			804[b]	313	633	184
Late December	519 (24)			633	20	806	163
Total positive increase				358	534	1143	

[a]Coefficients of variability.

[b]These values are estimates of total biomass.

Table 10.7. *Festuca* Community Biomass Means in Grams of Organic Material per Meter Square

Sample Period	Depth (cm)				Live Aboveground Biomass	Standing Dead Biomass	Litter
	0–20	20–40	40–60	0–60			
Mid-January	202 (32)[a]	60 (40)	16 (71)	278	75	300	105
Mid-March	377 (31)	90 (45)	22 (53)	489	52	245	107
Mid-April	436 (22)	99 (44)	34 (110)	569	122	354	119
Mid-May	476 (48)	135 (122)	42 (40)	653	194	408	121
Mid-June	492 (32)	90 (41)	106 (155)	688	199	335	108
Late July	551 (52)	118 (87)	96 (119)	765	257	333	117
Late September	598 (28)	81 (54)	27 (57)	706	302	356	100
Late November	659 (49)	96 (90)	39 (59)	794	258	309	132
Total positive increase				575	426	538	

[a]Coefficients of variability.

method of identification, such as a more permanent dye, needs to be developed to better quantify both income and loss for age classes in this compartment. (3) Input and decomposition of litter appear to be balanced; so amounts are relatively stabilized in both communities. (4) Total live community biomass is still increasing in the *Festuca elatior* community, while total biomass appears to have stabilized in the *Andropogon virginicus* community. (5) There was not an increase in root biomass of a proportional magnitude below 20 cm compared with the great seasonal changes of roots in the top 20 cm (202 to 659 and 377 to 659 g/m^2 respectively). (6) Due to an unusually wet July the expected summer depression in *Festuca* production did not occur. (7) The estimates of compartmental transfer rates need to be further quantified, especially the losses due to consumption and respiration, as well as values for translocation of soluble carbohydrates.

A NEW INSTRUMENT FOR THE AERODYNAMIC MEASUREMENT OF WATER VAPOR FLUX FROM AND CARBON DIOXIDE FLUX TO UNDISTURBED VEGETATION UNDER FIELD CONDITIONS

Gerald Stanhill

In ecological studies there is a great need for a simple field instrument capable of measuring the fluxes of water vapor and carbon dioxide above undisturbed vegetation. Aerodynamic methods possess the important advantage of being nondestructive and applicable to any surface, including heterogeneous vegetation associations; moreover, they are capable of yielding mean values for large areas, thus avoiding sampling problems. However, the complexity and cost of the apparatus at present available is such as to render the method unsuitable for field use over periods long enough to be of ecological or agricultural interest.

Under adiabatic conditions the flux of water from an aerodynamically rough surface is given by Rider's modification of the Thornthwaite-Holzmann equation,[29]

$$E = \frac{pk^2(u_2 - u_1)(q_1 - q_2)}{\ln\left[(z_2 - d)/(z_1 - d)\right]^2}, \qquad (1)$$

where E is the water vapor flux (g cm^{-2} sec^{-1}), p is air density (g/cm^3), k is van Karman's constant = 0.41, u is wind speed (cm/sec) at the two heights of measurement z_2 and z_1 (cm), q is the specific humidity of the air, and d is the displacement level of the vegetation (cm).

[29]N. E. Rider, *Quart. J. Roy. Meterol. Soc.* **83**, 181–93 (1957).

Taking pk^2 as a constant, a, and $\ln [(z_2 - d)/(z_1 - d)]^2$ as a second constant, b, dependent on the heights of measurement and the height of vegetation, the equation can be rewritten

$$(u_2 - u_1)q_1 - (u_2 - u_1)q_2 = \frac{Eb}{a}. \qquad (2)$$

This equation forms the basis of the instrument developed. Two airstreams are pumped at a constant flow rate from heights z_2 and z_1 above the evaporating surface of interest. These airstreams are passed separately through desiccant tubes for a sampling time whose duration is proportional to $u_2 - u_1$. This wind speed difference is measured by a pair of matched anemometers mounted at heights z_2 and z_1. Providing that these heights are within the internal atmospheric boundary layer of the surface whose flux is of interest (i.e., providing that the length of fetch $x \geqq 100(z_2 - d)$, then the water flux will be simply proportional to the difference in the weight of water absorbed in the two desiccant tubes. The flux of carbon dioxide can be measured by adding two tubes of a suitable absorbent. In principle, the flux of any other substance which can be quantitatively absorbed and which moves by turbulent diffusion also can be measured with the same instrument.

In certain situations, when the distance between the two heights of measurement and the distance between the top of the evaporating surface and the lower level of measurement become too great, then correction for nonadiabatic conditions may be necessary. These can be incorporated automatically by including temperature sensors at the heights z_2 and z_1, so that the duration of sampling time is corrected according to the Richardson number stability parameter.

When water-use efficiency (i.e., water flux per unit carbon dioxide flux) is of interest rather than the absolute values of either flux, then errors due to nonadiabatic stability conditions or to uncertainties in the exact value of the displacement level to be used will cancel out and may be ignored.

The instrument described is being tested in the old-field vegetation site (Ecology Area 0800) at Oak Ridge, and the measurements are being compared with independent estimates of water loss and dry matter increment. A more critical evaluation of its accuracy will be made by comparison with readings at an accurate weighing lysimeter installation.

TRANSFER OF ^{137}Cs, ^{54}Mn, AND ^{32}P IN TERRESTRIAL MICROCOSMS

Martin Witkamp Marilyn L. Frank
Virginia Merchant

In previous reports[30,31] our microcosms contained consumer-decomposer subsystems with dead plant material as the donor compartment. In a new series of experiments rye grass was used as primary producer, grasshoppers as consumers, and natural microflora as decomposer. A sixfold increase in light influx as well as a temperature increase from 16 to 25°C enhanced consumption by grasshoppers more than it did growth of grass. The subsequent decrease in standing crop resulted in significantly less ^{137}Cs and ^{54}Mn in grass at higher than at lower light and temperature values. In contrast, addition of fertilizer increased ^{137}Cs and ^{54}Mn accumulation in grass significantly without greatly influencing isotope content of the grasshoppers. Increased light and temperature also decreased rates of isotope accumulation in grass sooner than at lower light and temperature values, presumably because of earlier maturation of the grass at the higher values. These experiments provide a first quantitative insight in the ecology of mineral flow in our "closed" systems.

Rye grass grown at deficient nutrient concentrations on glass fiber with tap water accumulated significantly more ^{32}P than when grown on glass fiber with Knop's nutrient solution. Similarly, rye grass on substrate deficient in nutrients accumulated more ^{32}P when competing for food with dense microbial populations. These differences are statistically significant ($P < 1\%$), but thus far they lack an ecological explanation, and further study will be required.

Experiments and analog computer simulation of consumer-decomposer microcosms of increasing complexity were continued. The results showed that the effect of a compartment on mineral transfer into another compartment was not related to the accumulation of minerals in the first compartment. For instance, microflora turned over only 10% of the litter but contained one-third of the ^{137}Cs of the system. In contrast, millipedes turned over

[30] S. I. Auerbach *et al.*, *Health Phys. Div. Ann. Progr. Rept. July 31, 1966*, ORNL-4007, pp. 43–120.

[31] S. I. Auerbach *et al.*, *Health Phys. Div. Ann. Progr. Rept. July 31, 1967*, ORNL-4168, pp. 68-118.

one-third of the litter and contained less than 1% of the ^{137}Cs. Thus the effects by microbes and millipedes on net ^{137}Cs kinetics relative to their ^{137}Cs contents differed by two orders of magnitude.

The simulations also indicated rapid exchange of the isotope back and forth between two compartments of various systems. For example, in a sterile leaf-soil system, each month 19% of ^{137}Cs in the leaves moved to the soil while 34% of the soil ^{137}Cs moved back into the leaves. In systems consisting of leaves, microflora, millipedes, snails, and soil, the millipedes and snails transferred 13% of their ^{137}Cs content each day (almost their entire content each week) to the organic part of the soil. The ^{137}Cs in organic soil matter moved into the soil and back again at rates of near 13 and 10%/day. Thus computer simulations give an insight in the rapid mutual exchange rates between compartments that cannot be obtained from the usually reported net transfer rates.

The computer simulations also showed that in systems with five or more compartments, several alternate pathways may yield identical results, that for choosing the right pathway, close daily contact between investigator and the experiment as well as the simulation is required, and that additional experimentation may be necessary to clear up uncertainties in subsystems.

Our present experiments comparing transfer of different elements in systems of different complexity, in closed and open systems, in aquatic and terrestrial systems, and under different environmental conditions are designed to give a first broad understanding of the mechanism, pathways, kinetics, and ecology of mineral cycling and probably of the basics of the interrelationships of the ecosystem network structure.

ASSIMILATION AND BIOLOGICAL TURNOVER OF ^{134}Cs, ^{131}I, AND ^{51}Cr BY *ACHETA DOMESTICUS*

R. I. Van Hook, Jr. D. A. Crossley, Jr.

Understanding of radionuclide accumulation by insects requires careful assessment of assimilation and turnover rates. The present study was undertaken to compare the biological turnover of three radionuclides (^{134}Cs, ^{131}I, and ^{51}Cr) in the brown cricket *Acheta domesticus* (L.). Each radioisotope was administered via food pellets prepared from ground cricket meal and water. One-half gram of meal combined with 1 ml of water containing radioisotope (10 μc/ml) produced a solid pellet when dried in an oven at 105°C for 24 hr.

Retention of ^{134}Cs, ^{131}I, and ^{51}Cr following multiple feeding experiments is illustrated in Fig. 10.11 (solid lines). Dashed lines illustrate the retention predicted for a single ingestion of radioisotope. These lines were prepared from the slope ($=k_2$) of the solid lines and from a_2 of single feeding experiments, where $a_2 = p_2$ (digestive assimilation).

These curves may be described by a two-component model of the form

$$A_t = 100A_0(a_1 e^{-k_1 t} + a_2 e^{-k_2 t}),$$

where A_t is the whole-body radioactivity at time t, A_0 is initial whole-body radioactivity, and a_1 and a_2 are proportions of whole-body radioactivity lost at rates e^{k_1} and e^{k_2} by gut and tissue components respectively ($a_1 + a_2 = 1$).

The rapid decrease in whole-body radioactivity which occurred during the first day for all three radionuclides was due to gut clearance. Rates for each radioisotope yield nearly identical biological half-lives and elimination coefficients (^{134}Cs: $T_b = 4.9$ hr, ^{131}I: $T_b = 4.3$ hr, ^{51}Cr: $T_b = 4.3$ hr). Differences between values obtained for the rates k_1 (Fig. 10.11) are not significant statistically. Turnover time, which is the time required for 100% turnover of the gut contents, may be estimated from the reciprocal of k_1 (i.e., $1/k_1$). For *Acheta* the turnover time is approximately 6.7 hr.

Since k_1 represents the rate of loss for unassimilated material from the gut, the proportion p_2 must represent the fraction of the ingested material assimilated into body tissues.[32] Assimilation fractions are widely different for the three radioisotopes. The value obtained for radiocesium (65%) agrees closely with 73% reported by Reichle and Crossley.[33] A value of 21% was attained for radioiodine. McGinnis and Kasting[34] reported no assim-

[32] D. E. Reichle, *Ecology* **48**(3), 351–66 (1967).

[33] D. E. Reichle and D. A. Crossley, Jr., "Trophic Level Concentrations of Cesium-137, Sodium and Potassium in Forest Arthropods," Proc. National Symposium on Radioecology, Ann Arbor, Mich. (in press).

[34] A. J. McGinnis and R. Kasting, *Science* **144**, 1464–65 (1964).

ilation of stable chromic oxide by the pale western cutworm *Agrotis orthogonia*. Our value of 5.7% for *Acheta* probably indicates greater sensitivity of radiotracers for assimilation studies.

The rates k_2 and the half-times T_{b_2} represent the quantities usually designated as "elimination rates" or "biological half-lives." They indicate the rates at which radionuclides incorporated into tissues are excreted. Radiocesium had the most rapid excretion rate (T_{b_2} = 62 hr); chromium was somewhat slower (83 hr). Radioiodine was excreted very slowly if at all (T_{b_2} = 4299 hr). The excretion rate found for ^{134}Cs is similar to that reported for *Acheta* by Reichle and Crossley.[33] The extremely slow excretion of radioiodine may be due to its concentration in the insect integument and the slow turnover from that tissue. Chromium has not been reported to occur in insect tissues.

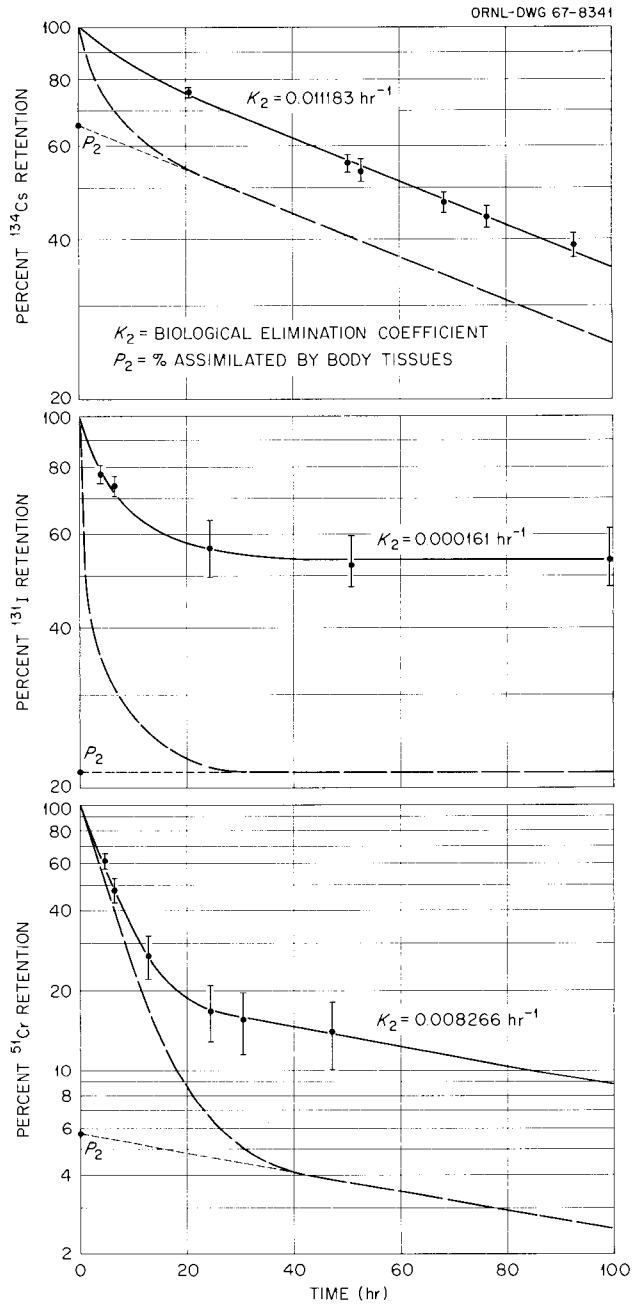

Fig. 10.11. Retention of Radionuclides by Crickets (*Acheta domesticus*). Solid line shows retention following multiple ingestion (six days); points include one standard error. Dashed lines illustrate the retention predicted for a single ingestion of radioisotope. These lines were prepared from the slope ($=k_2$) of the solid lines and a_2 of the single feeding experiments.

11. Radionuclide Cycling in Aquatic Ecosystems

C. H. Courtney[1]
N. A. Griffith
S. E. Kolehmainen[2]
C. R. Malone[3]
D. J. Nelson[4]
B. C. Patten
J. R. Reed, Jr.
Sue A. Rucker
J. Standaert[1]

WHITE OAK LAKE STUDIES

S. E. Kolehmainen

White Oak Lake fish are being sampled to determine body burdens of ^{137}Cs, ^{106}Ru, and ^{60}Co as well as the distribution of radionuclides among the fish species. Most emphasis is being placed on ^{137}Cs in bluegills (*Lepomis macrochirus*) and the comparative metabolism of ^{137}Cs and potassium by this species. A study of movement of ^{137}Cs and potassium in aquatic food chains is an important part of the investigation.

Bluegills are being collected at monthly intervals until sufficient fish for ten samples are obtained. Flesh samples and the residue (bone, fins, internal organs, etc.) are analyzed for radionuclide content with a multichannel analyzer. Since bluegills are rather small, it is necessary to composite several fish to obtain a sample for consistent counting geometry. Other species of fish are analyzed as they become available for comparative purposes.

Cesium-137 concentrations in White Oak Lake fish are shown in Table 11.1. The concentrations of shad, bluegill, and bass were similar to those observed in these species in 1965.[5] There was no significant trophic level increase in the ^{137}Cs concentrations among these fish, although the largemouth bass had a slightly higher concentration than the other species. Concentrations of ^{137}Cs varied among a few individual bluegills by

[1]ORAU-NSF Undergraduate Research Participant.
[2]Alien guest.
[3]AEC Postdoctoral Fellow.
[4]Dual capacity.

[5]S. I. Auerbach *et al.*, *Health Phys. Div. Ann. Progr. Rept. July 31, 1966*, ORNL-4007, p. 88.

Table 11.1. ^{137}Cs in White Oak Lake Fish

Species	Number of Samples	^{137}Cs (μc per gram of wet weight)	Standard Deviation
Bluegill (*Lepomis macrochirus*)	24	38.99	16.74
Redear (*Lepomis microloplus*)	4	23.68	2.22
Warmouth (*Chaenobryttus gulosus*)	9	29.15	10.04
Largemouth bass (*Micropterus salmoides*)	2	58.55	6.53
Goldfish (*Carassius auratus*)	6	29.23	7.18
Gizzard shad (*Dorosoma cepedianum*)	4	42.89	2.15

a factor of 4, which is greater than the indicated variation among all species (Table 11.1).

The T_b of ^{137}Cs in bluegills from White Oak Lake is being determined by repeated measurements of fish maintained in the laboratory. These fish presumably are at equilibrium with ^{137}Cs, since they have spent their entire lives in the White Oak Lake environment. The T_b of ^{137}Cs in 60- to 80-g bluegills held at 12°C was 115 days, and that of 10-g fish was 80 days. These experiments are being continued. The excretion curves obtained are essentially linear and do not show the rapid initial elimination of ^{137}Cs ordinarily found in acutely tagged fish. These data suggest that most of the ^{137}Cs in the bluegills is associated with the long component of T_b curves. Comparative studies of the turnover of potassium are being done with ^{42}K. Preliminary results with bluegills held at 22°C showed a T_b of about 16 days. This is somewhat shorter than the T_b indicated from potassium balance studies with bluegills.

The food habits of bluegills are being determined in order to measure feeding rates of fish in the lake. Stomach analyses showed that 70.9% of their food is comprised of chironomid larvae and pupae, 13% other insects, tubificids, and fish, and 16.1% detritus and algae. Bluegills were fed ^{137}Cs-tagged chironomids in the laboratory, and they assimilated about 70% of the ingested radionuclide. These data will be used for the feeding rate study.

UPTAKE AND EXCRETION OF ^{60}Co BY BLACK BULLHEADS (*ICTALURUS MELAS*)

J. R. Reed, Jr. N. A. Griffith
C. H. Courtney

Black bullheads (*Ictalurus melas*) in White Oak Lake, a 10-hectare impoundment near ORNL, were found to have a higher whole-body concentration of ^{60}Co than other fish species living in the same water.[6] Since the trace element cobalt is known to be essential in the metabolism of many animals, it was of interest to study the biological pathways of cobalt in fishes, especially in black bullheads.

The objectives of the study were to determine the rates of uptake, sites of deposition, and the biological half-life of ^{60}Co in this species and to compare the results obtained under laboratory conditions with those obtained from fish in the natural environment. Uncontaminated fish were used in three laboratory studies – ^{60}Co uptake from water, excretion of ^{60}Co after uptake from water, and excretion of ^{60}Co after uptake from tagged food.

In the studies on ^{60}Co uptake from water, three fish were held in isotope solution for seven days. After one, two, three, six, and seven days the fish were removed and counted in a small-animal whole-body counter. Near-maximum levels of activity were reached in one day (Fig. 11.1). Following the initial rapid uptake, the whole-body activity increased slowly to a maximum after three days in solution and remained nearly constant for the remainder of the test period.

In a second uptake experiment four fish were placed in each of three tubs of isotope solution with the same activity. Dissection of fish daily during the first three days of isotope uptake from water showed that individual tissues varied in their uptake rates and in the amount of radiocobalt accumulated. The gills, gut, and stomach had the most rapid uptake rates, reaching their maximum activity ratios (tissue dis min^{-1} g^{-1} to whole body dis min^{-1} g^{-1}) of 6, 25, and 5, respectively, in two days or less (Fig. 11.2). Other tissues generally reached their peak activities after three days. The liver, bone, and flesh were low in radiocobalt activity ratios (0.57, 0.58, and 0.22) (Table 11.2).

The greater activity in the gills was not surprising in view of their large surface area and rich blood supply (Table 11.2). The high activity in the gut and stomach probably was due to isotope that was swallowed by the fish, although freshwater species generally do not drink large quantities of water as do marine species. After two days the other tissues reached their maximum activities, and the flesh, while low in activity per gram, probably constituted a major source of the whole-body activity, since flesh constitutes about 60% of the body weight in bullheads.[7]

Whole-body elimination and tissue excretion of ^{60}Co were measured in the excretion study following radiocobalt uptake from water. Three fish which had been in isotope solution for three days were allowed to excrete in a tank of uncontaminated water. The fish were removed daily during

[6] S. I. Auerbach *et al.*, *Health Phys. Div. Ann. Progr. Rept. July 31, 1966*, ORNL-4007, p. 88.

[7] L. Krumholz, *Bull. Am. Museum Nat. Hist.* 110(4), 330 (1956).

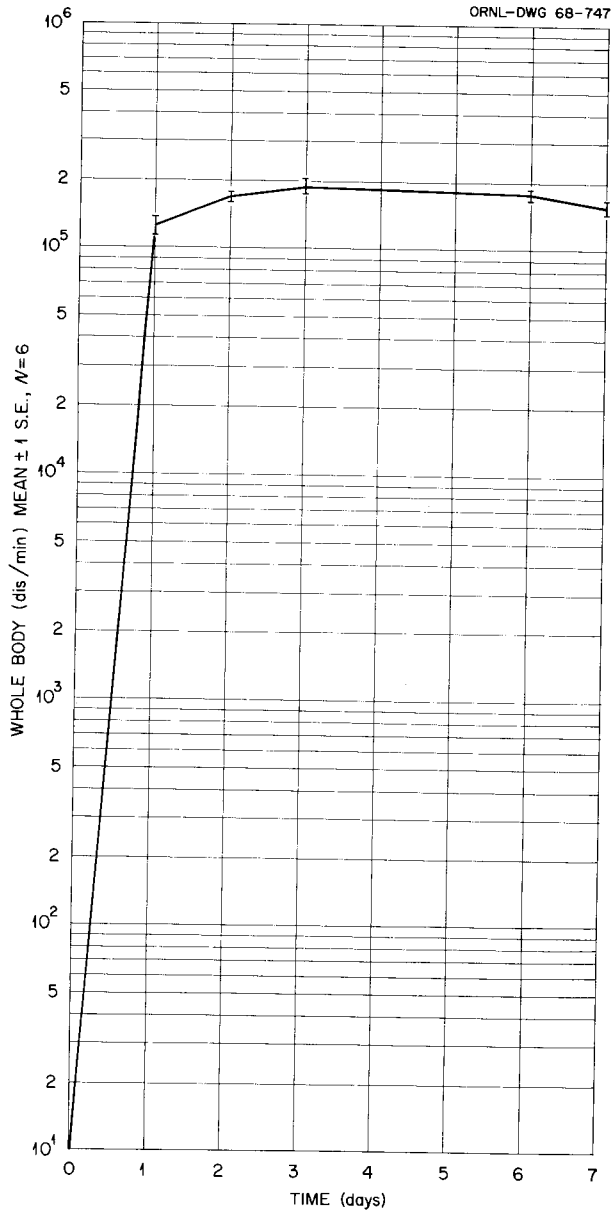

Fig. 11.1. Whole-Body Uptake of ^{60}Co from Water by Black Bullheads.

the first four days and counted in a small-animal whole-body counter. In the second experiment 18 fish which had been in isotope solution for three days were allowed to excrete in a large tank of springwater. Three fish were removed and sacrificed after excretion periods of 1, 2, 4, 8, 16, and 32 days.

A similar excretion study was performed with the bullheads following radiocobalt uptake from food. Individual fish were fed a nightcrawler that had been tagged with ^{60}Co. The fish were allowed to digest the worm for 3 hr before counting began. Whole-body counting was done daily for five days and weekly thereafter.

The rate of ^{60}Co elimination varied somewhat with the form of uptake. The fish that received radiocobalt via the water lost 28% of the initial activity in the first day of excretion, probably through the gut (Fig. 11.3). The remaining 72% was excreted in three components, the first two having biological half-lives of 4 and 35 days respectively. The third component had a long but undetermined biological half-life. Fish that received radiocobalt in a single feeding lost 95.5% of the initial activity during the first day of excretion. The remaining 4.5% of the activity also showed three components of excretion, the first two having biological half-lives of 1.5 and 48 days and the third component a long but undetermined biological half-life.

There was considerable variation in the excretion of radiocobalt among the separate tissues following uptake from water (Fig. 11.2). The gills, gut, and stomach lost activity rapidly during the first day of excretion, and these losses probably represented the initial loss in whole-body activity discussed above. With the exception of the kidney and the blood, other tissues eliminated radiocobalt steadily over a 32-day excretion period. The activity in the blood and kidney remained high during that period (Table 11.3).

Dissection of bullheads from White Oak Lake showed that the skin and bone were similar in radiocobalt content to the skin and bone of laboratory fish after three days of isotope uptake from water (Table 11.2). The blood, liver, and kidney of White Oak Lake bullheads had greater concentrations of ^{60}Co than the same tissues in laboratory fish after three days in isotope solution. The gills, gut, and stomach were greater in activity in laboratory fish than in White Oak Lake fish. Stable and radiochemistry showed that the kidney retained more cobalt per gram than any tissue examined and that in an equilibrium situation it might constitute a major sink for cobalt (Table 11.4). The reasons for these greater levels of cobalt in the kidney of bullheads are not known, but Kasenen *et al.*[8] suggested that in rats cobalt may function in kidney tubular metabolism.

[8] A. Kasenen, I. Lindgren, and H. A. Salmi, *Acta Physiol. Scand.* **61**, 376–79 (1964).

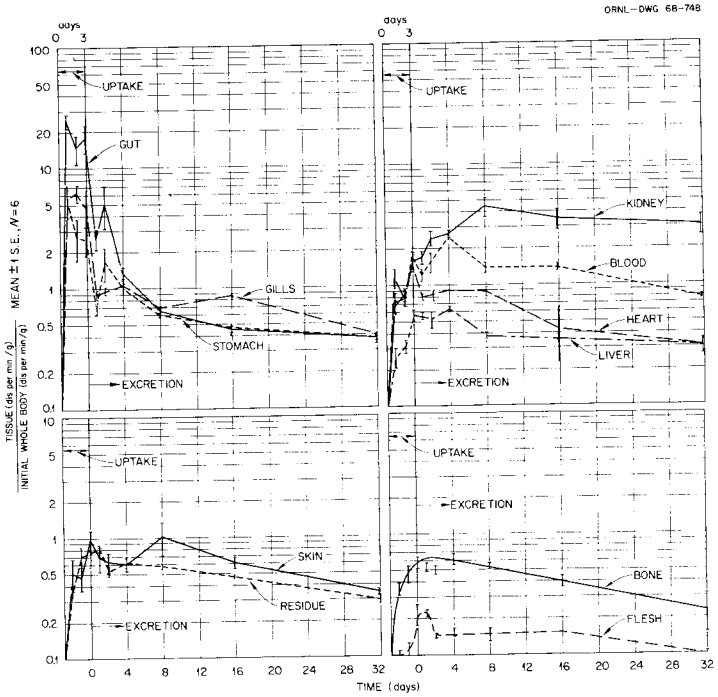

Fig. 11.2. Uptake of ^{60}Co in Black Bullhead Tissues During Three Days in Isotope Solution and Excretion of ^{60}Co from Tissues After Three Days of Uptake.

Table 11.2. ^{60}Co Uptake from Water by Bullhead Tissues

$$\frac{\text{Tissue dis min}^{-1}\ \text{g}^{-1}}{\text{Whole body dis min}^{-1}\ \text{g}^{-1}}, \text{ mean} \pm 1 \text{ SE}, N = 6$$

Tissue	Uptake Period (days)			White Oak Lake, $N = 5$
	1	2	3	
Blood	0.73 ± 0.07	0.78 ± 0.07	1.68 ± 0.09	4.02 ± 1.09
Skin	0.51 ± 0.07	0.47 ± 0.05	0.95 ± 0.11	0.85 ± 0.20
Flesh	0.09 ± 0.00	0.12 ± 0.01	0.22 ± 0.02	0.70 ± 0.21
Liver	0.26 ± 0.02	0.31 ± 0.02	0.57 ± 0.03	2.46 ± 0.69
Stomach	5.31 ± 0.71	2.64 ± 0.48	2.54 ± 0.37	1.54 ± 1.15
Gut	24.75 ± 1.68	14.73 ± 1.80	17.76 ± 2.28	5.90 ± 1.23
Kidney	0.68 ± 0.04	0.83 ± 0.05	1.56 ± 0.13	31.31 ± 7.99
Heart	1.16 ± 0.11	0.78 ± 0.05	1.59 ± 0.11	0.00
Gills	5.62 ± 0.79	6.21 ± 0.53	4.62 ± 0.91	1.16 ± 0.58
Bone	0.35 ± 0.02	0.46 ± 0.04	0.58 ± 0.04	0.43 ± 0.26
Bile and bladder	0.73 ± 0.00	0.50 ± 0.03	1.91 ± 0.23	
Spleen	2.40 ± 0.18	0.92 ± 0.05	3.08 ± 0.19	
Residue	0.37 ± 0.02	0.70 ± 0.07	0.66 ± 0.05	0.81 ± 0.19

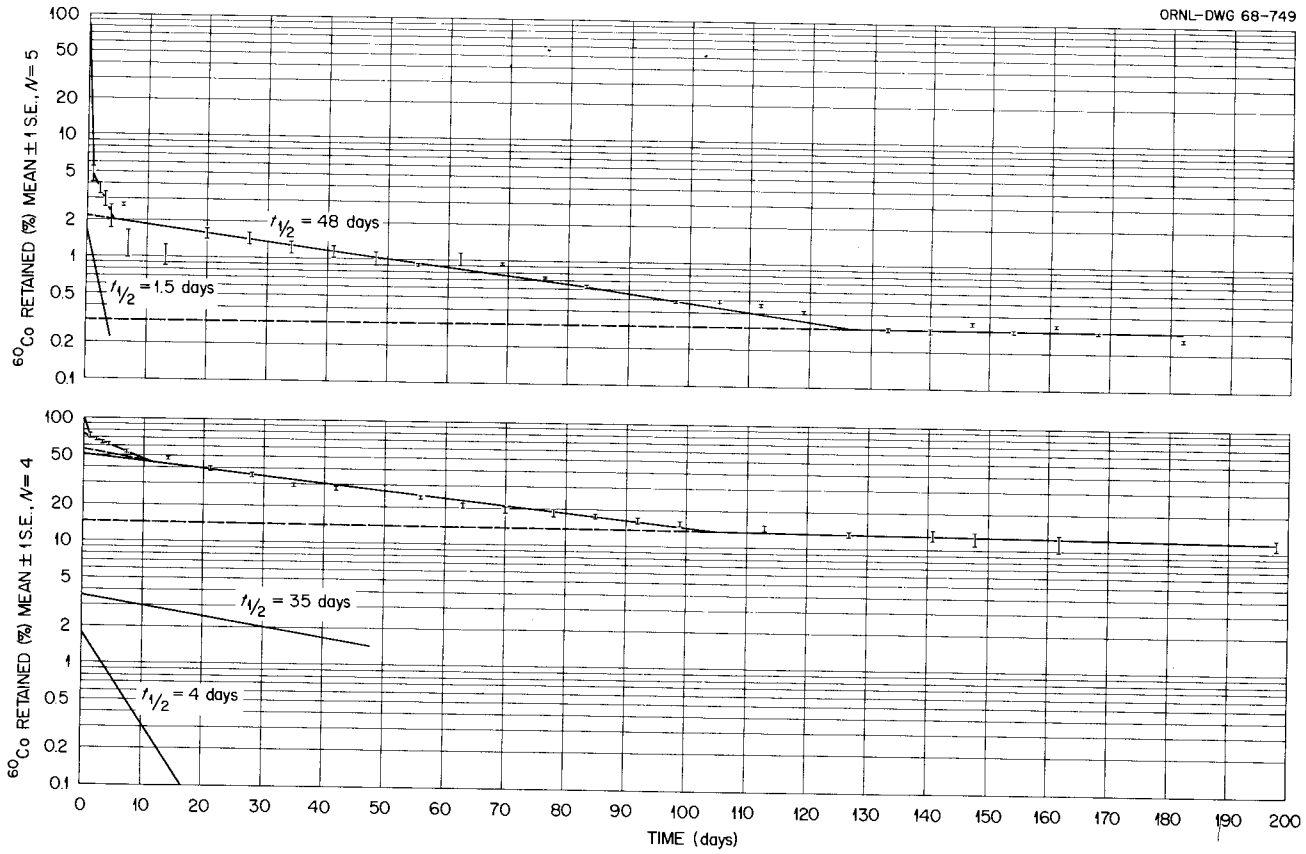

Fig. 11.3. Whole-Body Elimination of ^{60}Co by Black Bullheads After Uptake via Tagged Food (Top) and Uptake via Tagged Water (Bottom).

Table 11.3. ^{60}Co Excretion by Bullhead Tissues After Uptake from Water

$$\frac{\text{Tissue dis min}^{-1}\ \text{g}^{-1}}{\text{Initial whole body dis min}^{-1}\ \text{g}^{-1}}, \text{ mean} \pm 1 \text{ SE}, N = 6$$

Tissue	Excretion Period (days)					
	1	2	4	8	16	32
Blood	1.21 ± 0.07	1.58 ± 0.15	2.43 ± 0.02	1.37 ± 0.07	1.39 ± 0.04	0.78 ± 0.02
Skin	0.68 ± 0.45	0.63 ± 0.03	0.62 ± 0.02	1.02 ± 0.17	0.61 ± 0.08	0.35 ± 0.01
Flesh	0.22 ± 0.01	0.14 ± 0.01	0.16 ± 0.01	0.15 ± 0.01	0.15 ± 0.00	0.09 ± 0.01
Liver	0.56 ± 0.02	0.52 ± 0.04	0.63 ± 0.01	0.38 ± 0.01	0.37 ± 0.01	0.31 ± 0.02
Stomach	0.67 ± 0.04	1.68 ± 0.25	1.00 ± 0.11	0.61 ± 0.01	0.47 ± 0.05	0.38 ± 0.01
Gut	2.58 ± 0.23	5.12 ± 0.99	1.32 ± 0.07	0.65 ± 0.01	0.46 ± 0.02	0.38 ± 0.02
Kidney	1.67 ± 0.11	2.43 ± 0.17	2.65 ± 0.08	4.40 ± 0.47	3.47 ± 0.34	3.08 ± 0.30
Heart	0.79 ± 0.02	0.81 ± 0.04	0.91 ± 0.00	0.88 ± 0.05	0.43 ± 0.11	0.31 ± 0.30
Gills	0.88 ± 0.04	0.95 ± 0.04	1.06 ± 0.01	0.68 ± 0.01	0.81 ± 0.01	0.40 ± 0.00
Bone	0.53 ± 0.02	0.51 ± 0.03	0.61 ± 0.03	0.54 ± 0.02	0.41 ± 0.02	0.24 ± 0.04
Residue	0.82 ± 0.00	0.53 ± 0.03	0.62 ± 0.00	0.58 ± 0.03	0.47 ± 0.01	0.30 ± 0.01

Table 11.4. Stable Cobalt in Black Bullhead Tissues

Mean micrograms of Co per gram of fresh weight, $N = 4$

	Springwater Fish	White Oak Lake Fish
Blood	0.305	0.025
Flesh	0.030	0.010
Liver	0.116	0.034
Kidney	1.068	0.510
Bone	0.083	0.026

RADIOTUNGSTEN UPTAKE AND ELIMINATION IN BLACK BULLHEADS (*ICTALURUS MELAS*)

J. R. Reed, Jr. N. A. Griffith

Little is known concerning the metabolism of the trace element tungsten in fishes. Because the radioisotopes of tungsten are prevalent radionuclides produced by Plowshare-type nuclear explosives and because fish is a major diet constituent of humans in many parts of the world, a study was initiated to determine the rates of uptake and turnover of radiotungsten by freshwater fish.

Black bullheads (*Ictalurus melas*) were selected as a representative freshwater species. Preliminary studies consisted of three types of experiments in the laboratory. One dealt with whole-body uptake of radiotungsten from water and another with whole-body excretion of radiotungsten after uptake from water. The average ($N = 6$) whole-body uptake of ^{187}W from water with a concentration of 4.8×10^5 dis min^{-1} ml^{-1} reached a maximum level after the fish were in isotope solution for four days. Whole-body elimination of ^{187}W after four days of uptake from water followed a two-component curve. The initial rapid loss of 24% of the activity in 6 hr was followed by a longer, linear component with a biological half-life of 2.75 days. After seven days of excretion the bullheads retained 13% of the initial radiotungsten activity. A third experiment was performed to determine the radiotungsten losses following a single feeding. Each of six fish was fed a nightcrawler which had been injected with 73 μc of ^{187}W. Radiotungsten was excreted at two different rates following feeding. The initial rapid component had a biological half-life of 18 hr, probably representing gut elimination and accounting for 71% of the initial activity. The second component, representing the remaining 29%, had a biological half-life of seven days. At the end of seven days of excretion the fish retained 12.5% of the initial whole-body activity.

Experiments are being continued to determine the rates of turnover of radiotungsten by individual tissues.

FEEDING RATES OF SNAILS DETERMINED WITH ^{60}Co

D. J. Nelson C. R. Malone

Introduction

Freshwater snails frequently comprise an obvious component of the macrofauna of small streams. In the Oak Ridge area, *Goniobasis clavaeformis* is one of the most abundant snails in the spring-fed streams. These snails continually graze over rock surfaces and may contribute significantly to energy flow and mineralization of organic materials in the stream bottom. Since there is no general method to quantify the feeding rates of snails, the purpose of this research was to develop and test such a method using food tagged with ^{60}Co. Additional objectives were to determine the rate of food passage through the digestive tract of snails, the biological half-life (T_b) of ^{60}Co in snails, and the assimilation efficiency of ^{60}Co by snails.

Materials and Methods

Snails were collected from a small, rocky stream adjacent to the Laboratory site. The source of the stream is a spring which is tapped to provide a running springwater supply inside the laboratory. Snails were placed in flowing springwater, as were rocks from the stream bottom. Aufwuchs on the rocks provided food for the snails prior to experimental feeding.

Rocks with aufwuchs from the creek were tagged with ^{60}Co by placing them in a tub containing from 2 to 7×10^4 dis min^{-1} ml^{-1} for periods of 1 to 3 hr. The rocks were removed from the solution, rinsed in springwater, placed in shallow pans, and covered with springwater. Snails were placed on the rocks, and timing of the feeding started immediately. Snails usually righted themselves within a few minutes and started moving over the rock sur-

faces. The timed feeding experiments lasted 1 hr, and 30 snails were used in each of ten experiments. Water temperatures were from 14 to 17°C.

Following the timed experiments the snails were counted in a well-type scintillation crystal for ^{60}Co activity. An aufwuchs sample was removed by rubbing the rocks with a rubber policeman. The removed material was washed into a previously tared aluminum weighing dish, dried, weighed, ashed, weighed, and then counted for ^{60}Co. Thus, ^{60}Co activity was determined for total dry weight and ash-free weight. The quantity of food eaten was determined by the relationship

$$\frac{\text{disintegrations of } ^{60}\text{Co per minute per snail}}{\text{disintegrations of } ^{60}\text{Co per minute per milligram of aufwuchs}} = \frac{\text{milligrams of aufwuchs}}{\text{snails}}.$$

Since feeding experiments lasted 1 hr, quantities of food ingested per hour were obtained directly. Results were expressed either as dry weight or as ash-free weight.

Some additional snails fed on tagged rocks were placed in containers both with and without food to determine the clearance rate of an ingested food mass. Feces were collected at intervals and counted for their ^{60}Co activity. In another phase of the work the snails were allowed to feed for 24 hr, and their excretion of ^{60}Co was determined for 64 days to obtain a T_b. Snails used for the ^{60}Co excretion experiment were marked individually with model paint.

In some of the experiments, snails were retained in screened containers which excluded them from the tagged aufwuchs. These snails were used to evaluate the adsorption of ^{60}Co directly from water. Concentrations of ^{60}Co in the water during feeding experiments were usually low, and activity in the snails exposed to water was usually less than 10% of that in snails feeding on the rocks.

Results and Discussion

Feeding rates of snails weighing about 250 mg, determined in several experiments (Fig. 11.4), varied from 0.004 to 0.08 mg of ash-free dry weight per hour. The variation may be attributed to the date when the experiments were run and the time of day when the 1-hr experiments started. Reasons for the variation introduced by the date of the experiments were not definitely known, but one possibility was the quantity of food available on the rock surfaces. This quantity could have varied

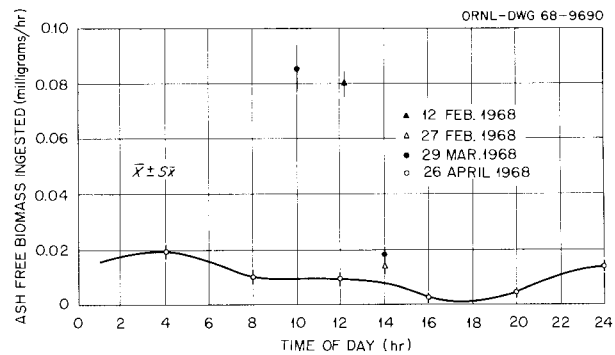

Fig. 11.4. Feeding Rates of *Goniobasis clavaeformis* Determined on Four Different Dates. Two separate feeding rates were measured on March 29, 1968, and on April 26 feeding rates were measured at 4-hr intervals for 24 hr.

because of changes in spring discharge or because of greater leaf cover from trees or from the emergent watercress (*Nasturtium officinale*).

A significant difference in feeding rates was observed between the first two experiments, which were conducted in a morning and an afternoon on different days. The next two experiments were run morning and afternoon of the same day, and the afternoon feeding rate was about one-fourth that observed in the morning. Because of these apparent consistent differences in feeding rates, a series of experiments was run every 4 hr for a 24-hr period. This series of experiments showed that the snails ingested food most actively at about 4:00 AM and that they ingested the least food in the experiment starting at 4:00 PM. All other feeding rates fell quite evenly between the high and low rates (Fig. 11.4). While snails crawl over the rocks at all times, these experiments suggest that they do not feed uniformly during a 24-hr period.

The rate of movement of food through the gut of snails was studied by feeding snails ^{60}Co-tagged aufwuchs and then collecting feces at 30-min intervals for 3 hr. At $\frac{1}{2}$ hr the ^{60}Co activity in the feces was slightly above background and noticeably so at 1 hr (Fig. 11.5). Peak activity was reached at 2 hr with a rapid decrease by 3 hr. This phase of the study showed that the 1-hr test feeding periods were appropriate for snails and that only small proportions of food would pass through the gut of the snail during the 1-hr feeding experiments.

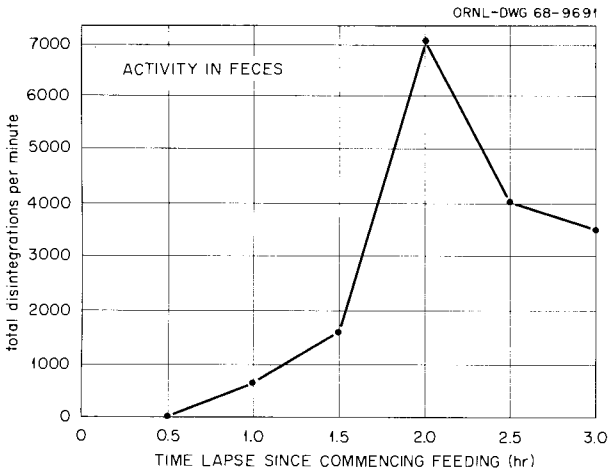

Fig. 11.5. Rate of Passage of ^{60}Co-Tagged Food Through the Digestive Tract of *Goniobasis clavaeformis*. Feces were collected at 30-min intervals for a 3-hr period.

The T_b of ^{60}Co in the snails was estimated by counting 30 tagged snails for 64 days. One compartment, consisting of about 25% of the ingested ^{60}Co, was excreted with a T_b of about 320 days, and an additional compartment of 25% was excreted with a T_b of 4.5 days. The remaining 50% was considered unassimilated and represented excretion during the first day.

This study suggests that tagging food with ^{60}Co and then allowing snails to eat the food for a short period of time is a suitable technique for the indirect determination of food consumption rates in a nonequilibrium situation. The T_b of ^{60}Co in *Goniobasis* is relatively long, and it appears that the equilibrium equation ordinarily used to measure feeding rates would be applicable only in situations where the snails had been exposed to ^{60}Co their entire lives. Also, the short tagging technique can be used to determine feeding chronologies over short time periods such as a 24-hr cycle.

AQUARIUM EXPERIMENTS

B. C. Patten
N. A. Griffith
Sue A. Rucker
D. J. Nelson

Radionuclide cycling studies in simple aquaria ecosystems were initiated to provide precise replicated data suitable for systems analysis. Six 50-gal aquaria were set up in the laboratory to study the movement of ^{137}Cs, ^{85}Sr, ^{54}Mn, ^{65}Zn, and ^{60}Co. The defined biotic components included snails (*Helisoma*), newts (*Diemictylus viridescens*), *Vallisneria*, *Najas*, *Ceratophyllum demersum*, and *Elodea*. The nonliving components sampled included water, sand, and glass slides. Three of the aquaria were tagged with ^{137}Cs, ^{85}Sr, and ^{65}Zn, and the other three contained ^{137}Cs, ^{54}Mn, and ^{60}Co. The isotopes were introduced into the water. Aquaria were sampled through time in a geometric progression, so that the earlier sampling periods were at shorter intervals. Since samples from the uptake phase of this experiment are still being analyzed for their radionuclide content, results from this portion of the experiment will be reported later.

At the termination of the uptake phase of the experiment, several of the biotic components remained in the aquaria after having been exposed to the radionuclides for approximately five months. Since these organisms had been exposed chronically to several radionuclides, we removed them to flowing springwater and counted them at intervals with a multichannel analyzer system to follow radionuclide excretion.

A linear least-squares regression model was used to calculate the excretion rate of radionuclides by snails and newts. The percent of radionuclide retained was transformed to logarithms for the calculations. Data obtained from these experiments are different from results observed in biological half-life experiments with acutely tagged organisms in two significant ways (Fig. 11.6). First, the early excretory patterns do not show rapid loss rates, which are usually associated with the passage of food through the gut. Accordingly, the loss rate is linear on semilog paper. Second, a much higher fraction (over 90% in most cases) of the isotope is associated with the component having a long T_b. These results are in agreement with previous dissection experiments[9] which showed that 90% of the strontium in bluegill flesh was excreted very slowly (see the section "White Oak Lake Studies," this report). Thus it appears that the single long-term component observed in excretion curves is, quantitatively, the most important.

[9]S. I. Auerbach *et al.*, *Health Phys. Div. Ann. Progr. Rept. July 31, 1967*, ORNL-4168, pp. 93–97.

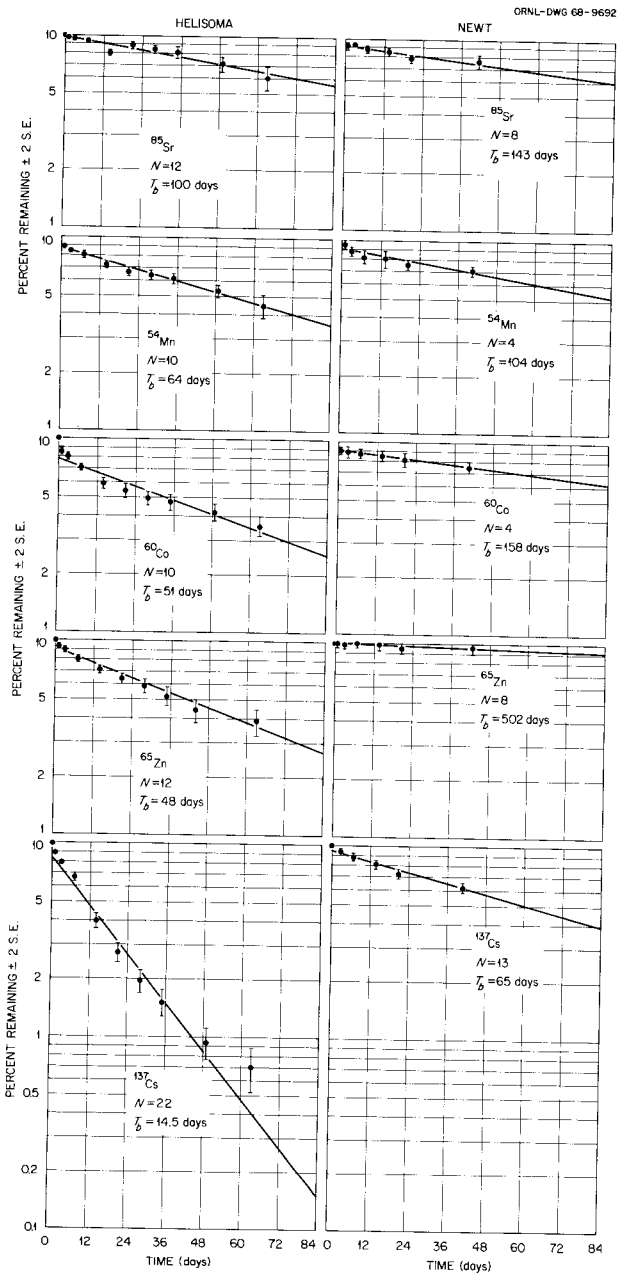

Fig. 11.6. Excretion of Five Radionuclides by Snails and Newts After Chronic Exposure. A large proportion of the radionuclide is associated with the long-term component of the biological half-life.

WHITE OAK LAKE PERIPHYTON

B. C. Patten Sue A. Rucker
J. Standaert

Study of periphyton development on artificial substrates suspended in the water column of White Oak Lake was continued. The substrate material was Plexiglas.

Figure 11.7 shows the temporal sequence of biomass development during the summer of 1967. The vertical pattern is similar to that observed in an earlier study.[10,11] Here the biomass was resolved into ash and ash-free components. In general, the organic matter has a relatively more uniform vertical distribution than the inorganic (Fig. 11.7), and the ash/ash-free ratio increases in the time series, particularly in the upper water layers.

Methanol extractions of phytopigments were incomplete with higher quantities of periphytic mass, accounting for the greater variation toward the right in Fig. 11.8. Nevertheless, over the biomass range represented and independent of lake depth or time, a generally linear relation was observed in all samples lumped together between chlorophyll A concentration and ash-free dry weight (Fig. 11.8).

---

[10] E. C. Neal, B. C. Patten, and C. E. DePoe, *Ecology* **48**(*b*), 918–24 (1967).

[11] S. I. Auerbach *et al.*, *Health Phys. Div. Ann. Progr. Rept. July 31, 1967*, ORNL-4168, p. 99.

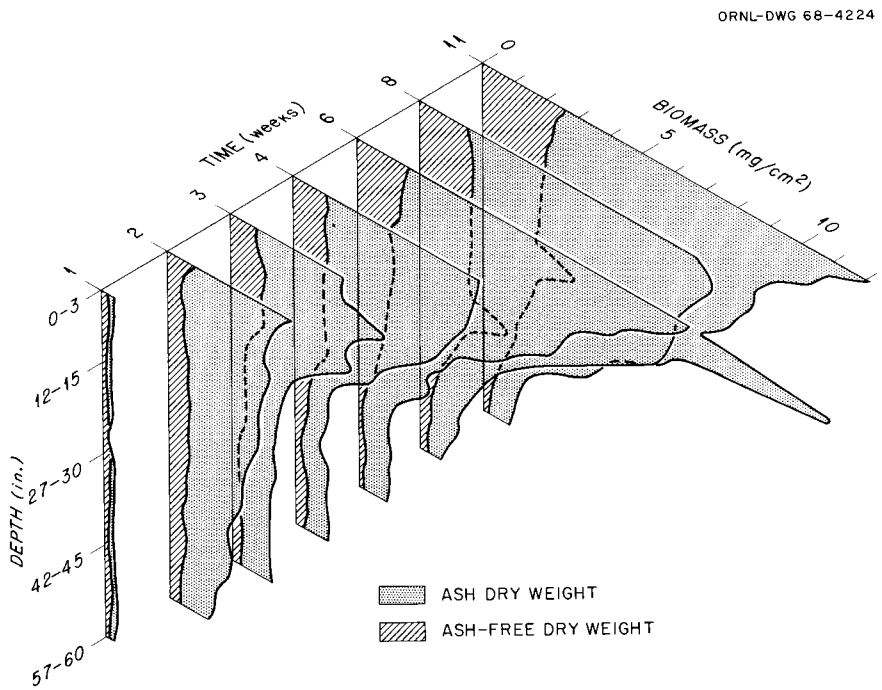

Fig. 11.7. Ash Dry Weights and Ash-Free Dry Weights of Periphyton Growing on Plexiglas Strips in White Oak Lake for an 11-week Period.

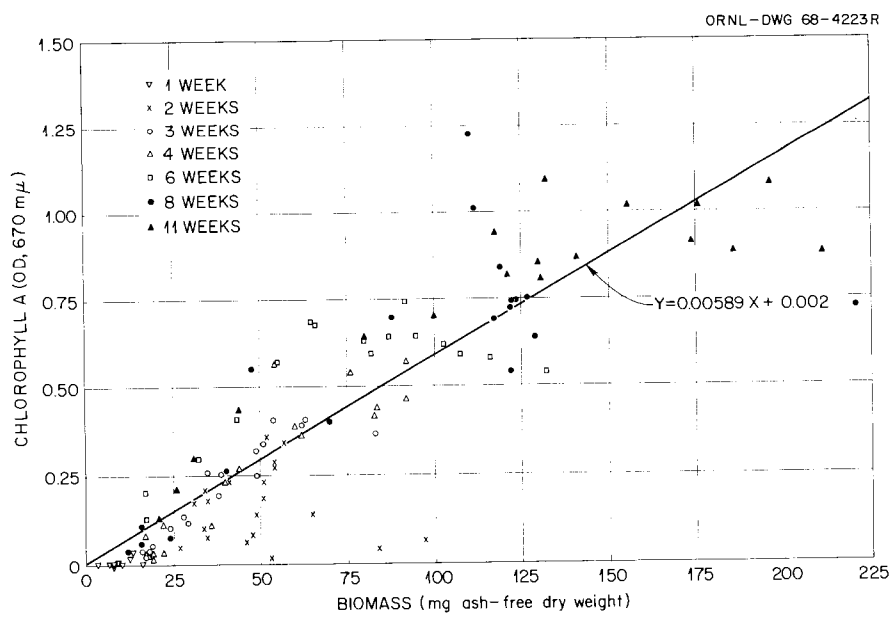

Fig. 11.8. Relationship Between Chlorophyll A and Periphyton Biomass on Plexiglas Strips Suspended in White Oak Lake for an 11-week Period.

12. Watershed Aquatic Habitat Interactions

C. H. Abner[1]
W. P. Bonner[2]
J. H. Burris[3]
J. W. Curlin[2]
Tom Grizzard[2]
W. F. Johnson[1]
R. H. Moneymaker[4]
D. J. Nelson[2]
L. N. Peters[2]
W. M. Snyder[5]
Gerald Stanhill[6]
T. Tamura[2]
F. G. Taylor, Jr.[2]
W. A. Thomas, Jr.[2]

WALKER BRANCH WATERSHED PROJECT

J. W. Curlin
D. J. Nelson
Tom Grizzard
F. G. Taylor, Jr.
L. N. Peters
W. A. Thomas, Jr.
T. Tamura
W. P. Bonner
C. H. Abner
W. F. Johnson
J. H. Burris
W. M. Snyder
R. H. Moneymaker
Gerald Stanhill

Objectives

This project is designed to evaluate the impact of man's use or misuse of the landscape upon water quality and biotic productivity of the water which flows from that landscape. It will contribute to the understanding of biogeochemical relationships between aquatic habitats and their watersheds through the synthesis of an empirical watershed model which will (1) relate the water quality and productivity of the stream to the adjacent terrestrial ecosystem, (2) equate the net loss of chemical elements to the rate of mineral cycling, (3) establish the relationship between the hydrologic cycle and the mineral cycle, and (4) provide bench-mark information of natural terrestrial-aquatic ecosystems for comparison with those modified by man's cultural practices.

The project is organized on the paired-watershed principle, which allows measurement of treatment effects on the treated watershed to be compared with control values on the untreated watershed after adjustment for inherent response differences established during a three- to five-year cross-calibration period. During the interim, important information on precipitation, stream flow, mineral income, mineral loss, water movement, vegetational characteristics, soil characteristics, and stream ecology is being assembled which will be used to establish interwatershed correlations. Such data will also provide an insight into the stability and dynamic equilibrium conditions on relatively undisturbed forested watersheds of this region.

Stream Gages and Environmental Monitors

Construction was completed this year on two streamflow gages which form the nucleus of the Walker Branch facility (Fig. 12.1). The weirs have 120° V-notch cross sections capable of measuring volume rates up to 63 cfs and as low as 0.001 cfs. Stage height above the apex of the V is recorded at 5-min intervals by automatic binary-coded punched-tape recorders to the nearest 0.001 ft.

Automatic water samplers continuously siphon a sample proportional to streamflow (Fig. 12.2). A unique feature of the sampling system is the provision for a fast sampling mode which fractionates the sample over time. Under normally stable conditions the water is composited in 27-liter polyethylene bottles. Upon sensing an increase in streamflow which exceeds a preset differential

[1]ORNL engineering support.
[2]Dual capacity.
[3]Computer Technology Center.
[4]Consultant, U.S. Soil Conservation Service.
[5]Consultant, Georgia Institute of Technology.
[6]Alien guest.

Fig. 12.1. Weir on the West Fork of Walker Branch.

threshold, the instrument fractionates the sample into 250 samples of up to 250 ml each at fixed intervals through the duration of a storm. Air and water temperature at the weir sites are continually recorded with a strip-chart recorder.

Five automatic digital recording precipitation gages provide a continuous rainfall record within a triangular network superimposed over the watershed. These records are synchronized with the streamflow recorders.

Modified Wong rainfall collectors sample precipitation and dry fallout separately for chemical analysis. From these data area-volume estimates of chemical income will be estimated.

Hydrologic Analyses

A unified data reduction-processing package is being programmed for the computer. Figure 12.3 shows the flow of data and analytical summaries produced. A computer plotting routine will give parallel graphic output of the continuous stream hydrograph and associated hyetograph as well as an isohyetal map of the precipitation pattern over the watershed.

Some original innovations are included in the hydrograph analysis routine. Storm events are identified from the concomitant precipitation record on the basis of rainfall intensity-duration rather than by the conventional method of using the stream hydrograph. We expect this approach to improve the sensitivity of detecting precipitation-streamflow lags, since rainfall is actually the causal agent and streamflow the response.

Detailed analysis of flow separation and flow time delay phenomena will be performed on the storm hydrograph using least-squares solution and a soil infiltration model.

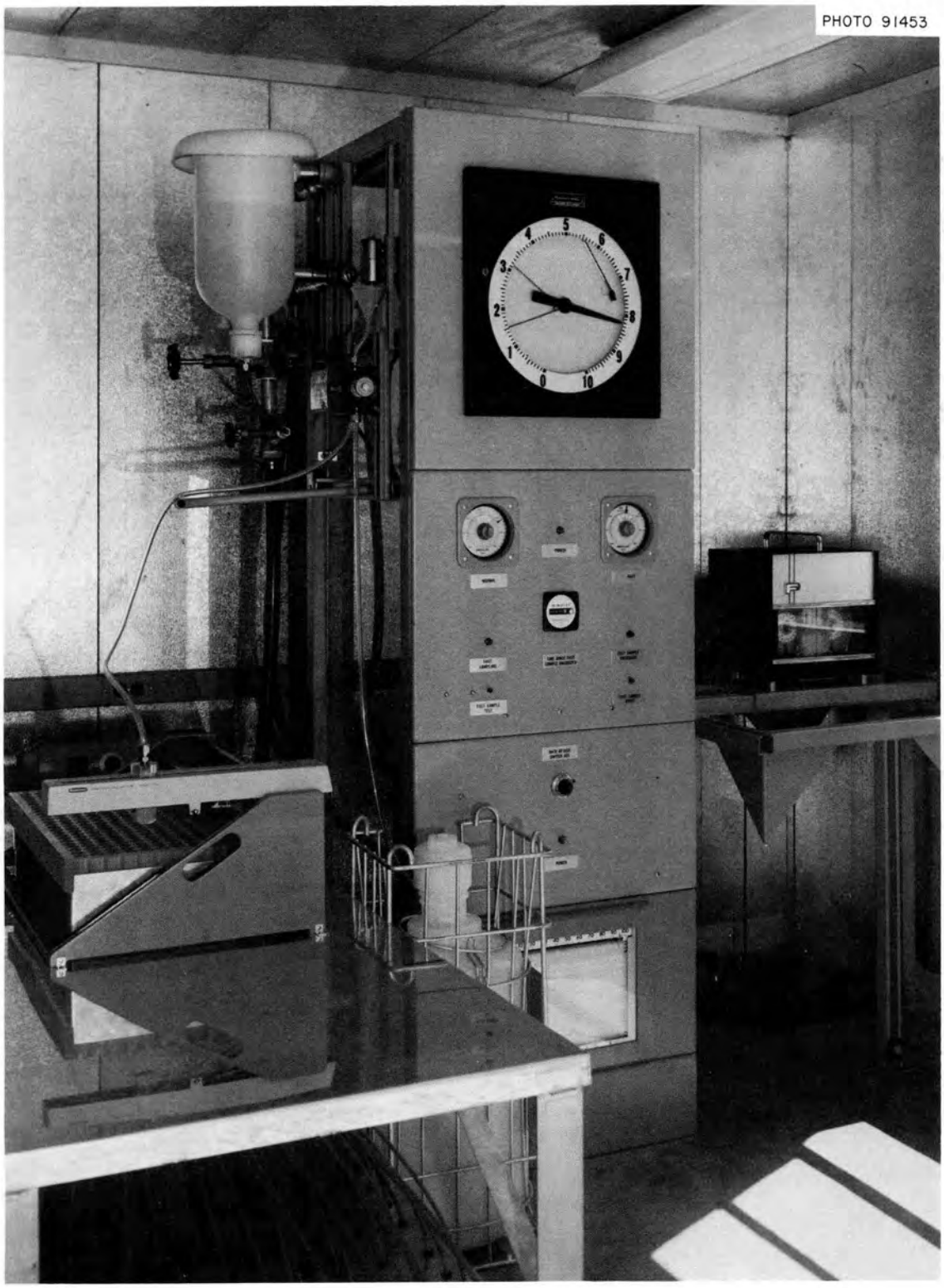

Fig. 12.2. Instrumentation Installed in Gage House. Continuous water sampler on left, stage height recorder.

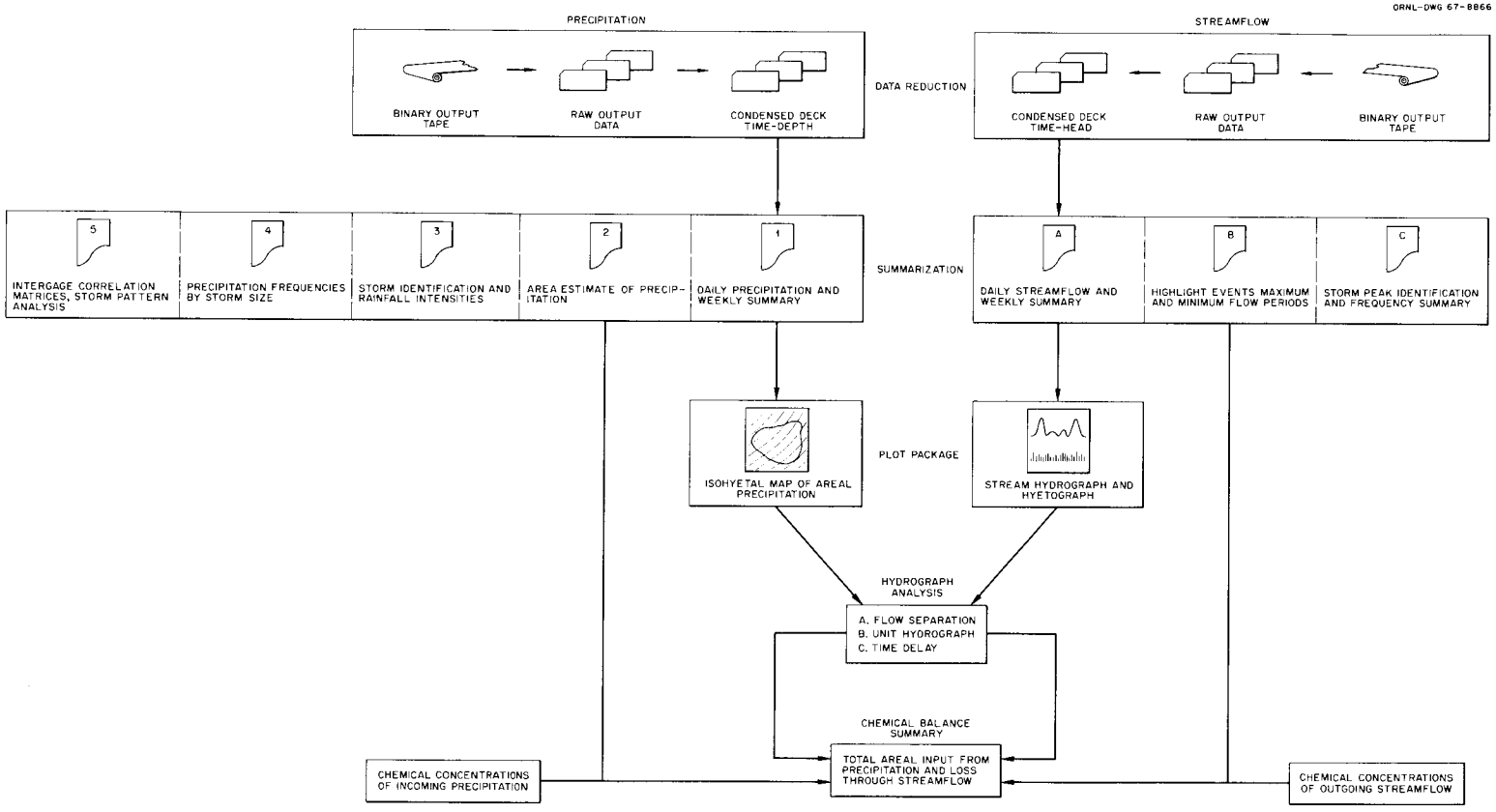

Fig. 12.3. Flow Diagram of Hydrologic Analyses.

The final step in data processing merges the chemical concentration data from precipitation and stream-water samples with the volume expansion derived from total areal precipitation income and total streamflow loss. Coupled with the estimates of dry particulate fallout, these data represent the gain and loss of chemical elements to the nutrient budget of the watershed.

Meteorological Input

The input of selected mineral elements by dry fallout and rain scavenging to the watershed are being sampled by modified Wong precipitation collectors (Fig. 12.4). Collectors were modified by the addition of a bracket to hold a second polyethylene collector, which serves to catch dry fallout (collector open in the figure). The rainfall collector is under the metal cover. When raindrops fall on the moisture-sensing switch, the metal cover swings over the dry fallout collector. With this slight modification the Wong precipitation collector serves as a differential collector of dry fallout and rain-scavenged materials. About 1 in. of liquid (0.1 *N* HCl) is maintained in the bottom of the dry collector to prevent resuspension of deposited material. Wetfall catches of mineral elements are related to rainfall measured by the Fischer and Porter rain gages at the same sites. Thus evaporation of rainfall does not introduce an error in concentrations of elements observed in rainwater.

Analyses showing quantitative inputs of rain-scavenged material and dry fallout for February 1968 are in Table 12.1. Rainfall for February 1968

Fig. 12.4. Wong Precipitation Collector Modified to also Sample Dry Fallout. Rainfall collector is covered in this picture.

Table 12.1. Input of Chemical Elements to Walker Branch Watershed as Rain-Scavenged Material and Dry Fallout in February 1968

		Input ($\mu g/cm^2$)						Rainfall (cm)
		Na	Ca	K	SO_4	NO_3	PO_4	
Rain-scavenged rain gage	1	0.32	0.50	0.11	6.9	2.4	0.13	1.78
	2	1.9	1.6	0.52	1.5	0.60	0.23	2.54
	3	2.0	0.83	0.42	*a*	0.61	0.30	2.79
	4	0.75	2.0	0.33	24.0	0.61	0.20	2.50
	5				partial rainfall record			
Dry fallout rain gage	1	0.33	5.7	0.91	8.6	4.5	0.63	
	2	0.74	4.8	0.57	4.05	3.2	0.44	
	3	0.31	6.5	0.83	37.0	4.7	0.48	
	4	1.4	6.6	1.2	15.0	4.5	0.72	
	5	0.70	6.8	0.94	12.0	4.6	0.63	

[a]Below limits of detection.

was about 1 in., in contrast with the normally expected precipitation of about 5.5 in. The abnormally low rainfall may have decreased the input of rain-scavenged chemical elements. However, dry fallout constituted a significant input to the watershed, particularly with respect to calcium, SO_4^{2-}, and NO_3^-.

Water Quality

Sampling of water from both forks of Walker Branch was initiated in July 1967 to determine the chemical characteristics of various segments of each stream and to identify the differences in each as water travels downstream. Anomalies noted in initial samplings were confirmed through more complete samplings in September 1967 and March 1968 which included water from both springs and streams (Table 12.2). Although the data cannot be quantified due to the lack of flow measurements, the data show that water ranges from low to intermediate hardness, with the calcium and magnesium existing primarily as HCO_3^-. The concentration of other ions is normal for an unpolluted stream contacting limestone formation.

Changes in the chemical characteristics of the water in the west fork generally follow the expected changes in water quality as the different springs contribute ions. Observed changes in the east fork, however, could not be predicted on the basis of inputs from known springs in the area. A factor of importance in interpreting the data is that the stream flows underground for approximately 39% of the distance from the limit of perennial flow (2500 ft) to the weir site (0 ft) during much of the year (Fig. 12.5).

The two reaches showing the greatest changes in chemical characteristics are between 2500 and 1430 ft, a reach where the water flows over the surface of the ground, and between 1430 and 980 ft, where the water flows underground during periods of low discharge. The threefold increase in the concentration of calcium and magnesium between 2500 and 1430 ft cannot be explained on the basis of inputs from known springs in the area, although visual observations suggest that the flow increases as the water flows downstream between these two points. Dye tracers show that at least some of the water entering the ground at 1430 ft reappears in spring S1E, which is located at approximately 965 ft.

Values for free CO_2 obtained in September 1967 are lower than those calculated from chemical equilibria. Similar differences have been observed in other locations and were attributed to the presence

Table 12.2. Chemical Characteristics of Walker Branch Waters

Location	Date of Sampling	Constituent (mg/liter)				pH
		Ca	Mg	HCO_3	CO_2	
West Fork						
S6W	Sept. 26, 1967	26.6	8.4	122	15.8	6.50
S5W	Sept. 26, 1967	23.8	10.0	128	4.8	7.01
S3W	July 26, 1967	32.0	15.4	172	*a*	7.60
	Sept. 26, 1967	34.4	14.3	177	7.3	7.15
S1W	Sept. 26, 1967	31.8	11.8	158	6.8	7.05
50 ft	July 26, 1967	26.0	11.2	133		7.70
	Sept. 26, 1967	33.3	12.9	167	3.1	7.60
East Fork						
S4E	July 26, 1967	4.6	0.7	15		6.30
	Sept. 26, 1967	8.0	3.0	37	6.5	6.58
S3E	Sept. 26, 1967	38.4	15.6	195	2.8	7.72
2300 ft	Sept. 26, 1967	14.9	5.9	75	6.8	6.72
1430 ft	Sept. 26, 1967	22.1	9.5	117	4.5	7.38
	Mar. 8, 1968	13.8	8.2	79	1.8	7.75
980 ft	July 26, 1967	15.0	6.8	78		6.90
	Sept. 26, 1967	26.3	10.6	134	11.3	6.79
	Mar. 8, 1968	16.8	5.8	85	11.0	7.25
S1E	July 26, 1967	15.0	6.8	78		6.90
	Sept. 26, 1967	26.3	10.2	134	12.4	6.63
	Mar. 8, 1968	16.8	7.3	94	12.0	7.15
710 ft	Sept. 26, 1967	27.0	10.0	134	10.1	7.24
125 ft	July 26, 1967	18.0	6.8	86		7.35
	Sept. 26, 1967	26.9	12.0	143	6.5	6.92

[a]Not determined.

of organic or strong mineral acids. Values for CO_2 obtained in March 1968 agree more closely with calculated values. These results possibly reflect the seasonal variation in physical and biological parameters.

A more complete understanding of the observed changes in water quality will be obtained by correlating flow data and chemical analyses with both physical and biological parameters. One possible explanation is given in the section on soil characteristics.

Soil Characteristics and Investigations

The soil survey of the watershed was completed, and a map (Fig. 12.6) detailing the series distribution in the area was prepared. The predominant series are the Bodine and Fullerton soils, which are derived from cherty limestone and dolomitic material and cover about 90+% of the area. Associated with these two soils is the Claiborne series. The primary difference among the three soils is the texture of the B horizon, which is heaviest (clayey)

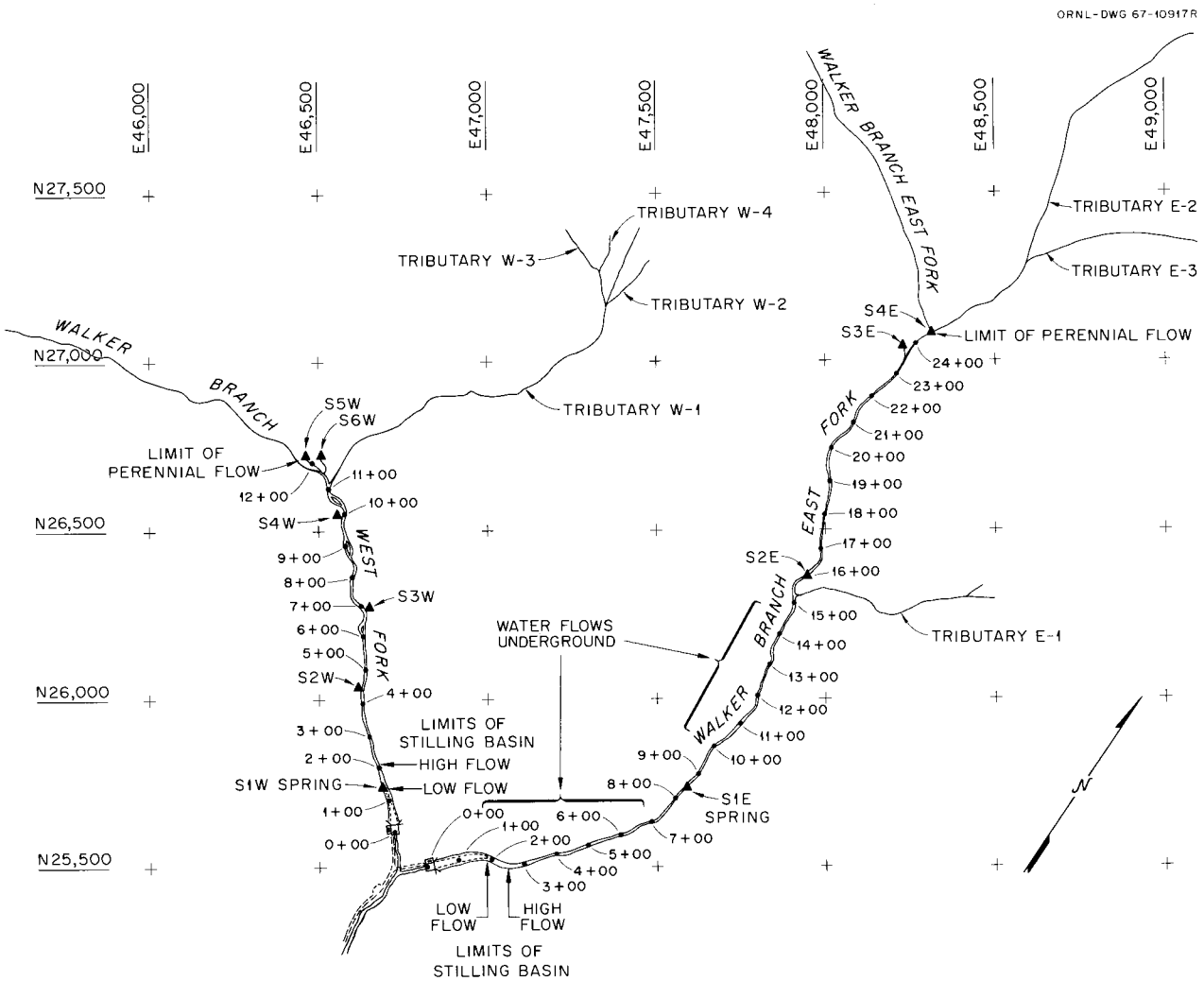

Fig. 12.5. Horizontal Traverse of Walker Branch Watershed Showing Reference Stations and Spring Locations.

in the Fullerton and lightest in the Bodine (silt or clay loam). Small areas of Tarklin and Lindside series also were mapped. The latter two soils, though limited in area, are noteworthy because of their geographic distribution. They are found principally along the east fork of Walker Branch draining the watershed, and their occurrence helps to explain the anomalies of the preliminary observations made of water quality over the pathway of the stream. The Tarklin soil has a fragipan zone between 18 and 60 in. This compact zone in soils is known to impede vertical drainage and to foster lateral movement of water. The soft water at spring S4E (Fig. 12.5) possibly has a small amount of dissolved ions because the spring emerging at that point drains an area predominantly occupied by the Tarklin soil. It is hypothesized that rain falling on this soil percolates through the profile down to the fragipan zone and then flows laterally and emerges without contacting limestone material at the spring. Nearby S4E is spring S3E, of relatively hard water. This spring occurs beyond the boundary of the Tarklin soils and emerges in the Bodine soil area. Since the Bodine soil has no fragipan and is extremely permeable, the water penetrates deeper and flows in limestone strata prior to emerging as a spring at the point S3E. The hard water then could result from contact with the limestone

ORNL-DWG 67-10914

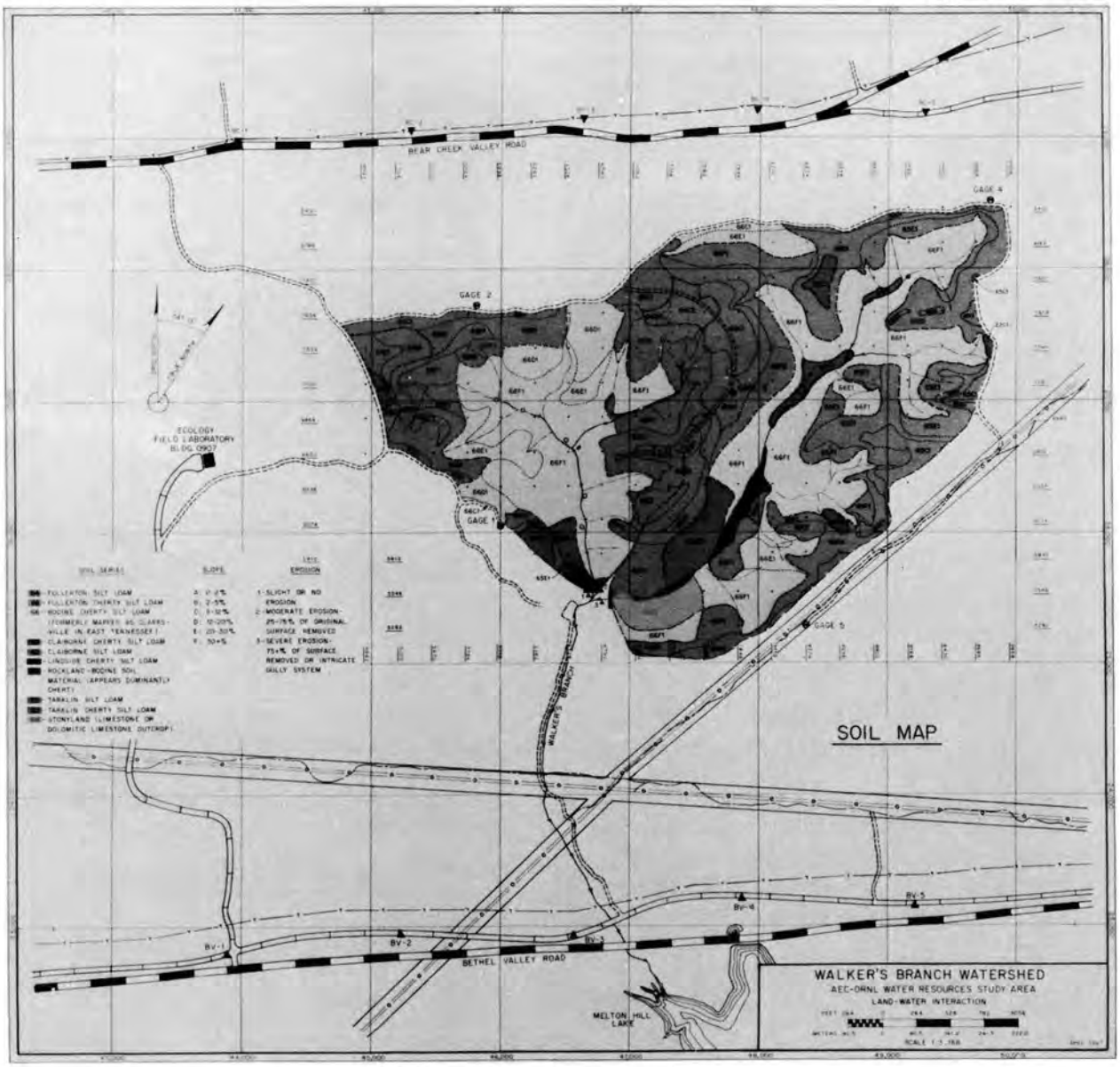

Fig. 12.6. Soil Map of Walker Branch Watershed.

material. The types of soil in the drainage area may be a factor in determining the different characteristics of water quality coming from springs within a relatively small area.

At approximately 1430 ft, the stream in the east fork goes underground and appears at approximately 980 ft, then disappears at 710 ft to reappear at 125 ft. In the traverse where the stream is underground, the soil is mapped as Lindside. This soil is of alluvial origin, deriving its material from the adjacent upland area. It is possible that the stream once flowed at the surface throughout the reach, but as coarse material was deposited from higher elevations, the stream maintained its level, and a porous colluvial mantle developed above it.

In contrast to the east fork, the water quality in west fork was found to follow expected changes as the different springs contributed ions to the

stream. The soils adjoining the stream and draining the area are exclusively Bodine and Fullerton. The uniform distribution of these soils with no evidence of fragipan helps to explain the predictable changes of the quality of water.

Initial soil sampling for characterization included the Bodine and Fullerton soils since they made up over 90% of the soils in the watershed. Results of the laboratory tests of pH, ion exchange capacity, and particle size distribution are shown in Table 12.3. With the exception of the leaf litter (A_{00}) of the typical Bodine, all the horizons are acidic in reaction. Even the high clay zone of the Fullerton soils is acidic, showing that the limestone has been leached from the profile to depths greater than 45 in. The ion exchange capacity measurements show that the leaf litter (A_{00}) and the partially decomposed litter (A_0) show highest cation exchange capacity, which is characteristic of humus. In the mineral portions (A_1 through B_2) the exchange capacity is closely related to clay content in the horizon. Hence in the deeper zones which show higher clay contents, the exchange capacity is higher than the shallow zones of mineral soil. The low capacity of the mineral soil is consistent with the clay mineral analyses, which revealed that kaolinite is predominant in the zones with high clay content. The exchange capacity of kaolinite is generally <10 meq/100 g.

The particle size analysis also shows agreement with field textural estimates. Fullerton and the associated transition soils show high clay content in the B horizon; the typical Bodine soil shows a lower clay content in the B horizon as compared with the Fullerton series. The lower clay content in the B of the Bodine soils as compared with the Fullerton soils gives the former better permeability and faster drainage.

Aquatic Organisms

The aquatic organisms in both forks of Walker Branch were sampled during July and August 1967 to determine the biotic resources available for study. Several sampling techniques were tried, but quantitative methods such as the Surber sampler or removal of an area of the substrate with subsequent elutriation were not overly successful. Since the major objective was a survey, random picking of rocks, leaves, or branches was used as the most effective method for obtaining organisms to be identified.

Approximately 60 different species of aquatic invertebrates were collected, and preliminary identifications were made. The species collected, particularly caddis flies (Trichoptera), stoneflies (Plecoptera), and mayflies (Ephemeroptera), are typical of small rocky creeks. Diptera larvae and Coleoptera larvae were not collected in large numbers, although limited light trap collections suggested the presence of many small chironomids. Gerridae (water striders) were obvious in pool areas, and crayfish were represented by at least one species of *Cambarus*. Snails (*Goniobasis clavaeformis*) are one of the most obvious components of the biota of both forks.

Vertebrates included four species of salamanders and three species of fish. The most abundant fish were blacknose dace (*Rhinichthys atratulus*) with smaller numbers of creek chubs (*Semotilus atromaculatus*) and sculpins (*Cottus carolinae*).

The fauna of the two forks is quite similar, with 20 of the commonly collected species occurring in both streams. The west fork contains 19 additional species, while the east fork contains 17 additional forms. Many of the latter species were found only in one collection, and future studies probably will show an even greater commonality among the biota of the two forks.

Table 12.3. Mechanical Analysis, pH, and Cation Exchange Capacity of Fullerton and Bodine Soils

Horizon	Depth (in.)	Percent Content			Recovery Total	pH	Cation Exchange Capacity (meq/100 g)
		Sand	Silt	Clay			
Coordinates: N7335 E6262 – Fullerton Cherty Silt Loam (Transition to Bodine)							
A_{00}						5.82	74.64
A_0		31.13	49.05	7.96	88.14	5.51	24.36
A_1	0–3	35.23	51.76	9.46	96.45	4.82	5.69
A_2	3–8½	37.97	54.39	8.89	101.25	4.74	3.85
AB	8½–22	34.11	52.53	11.38	99.02	4.80	3.65
B_2	22–45	19.53	35.62	44.26	99.41	4.94	8.44
Coordinates: N7300 E7148 – Fullerton Cherty Loam (Typical)							
A_{00}						5.23	54.48
A_0						5.82	29.04
A_1	0–4	33.26	51.52	10.36	95.14	5.40	5.37
A_2	4–11	30.78	56.61	11.35	98.74	4.95	3.48
A_3	11–16½	29.92	58.30	13.35	101.57	4.60	4.62
B_1	16½–21	22.11	50.70	25.48	98.79	4.72	6.55
B_{21t}	21–29	20.99	37.78	40.14	98.91	4.89	7.26
B_{22t}	29–40	28.73	28.56	41.20	98.49	5.01	8.43
Coordinates: N7060 E5550 – Bodine Cherty Silt Loam (Typical)							
A_{00}		57.02	13.44	7.81	78.27	7.33	55.76
A_0		36.77	49.43	4.62	90.82	6.70	22.40
A_1	0–3	31.24	55.32	8.60	95.16	6.27	12.74
A_{21}	3–12½	27.13	56.25	13.69	97.07	5.46	7.91
A_{22}	12½–15	25.34	56.47	16.24	98.05	5.48	6.48
B_{1t}	15–18½	29.62	55.09	14.00	98.71	5.46	6.34
B_{21t}	18½–31	36.85	48.73	13.30	98.88	5.20	5.36
B_{22t}	31–43	35.56	48.26	14.96	98.78	5.02	5.47
Coordinates: N8153 E9253 – Bodine Cherty Silt Loam (Transition to Fullerton)							
A_{00}		52.99	13.49	14.12	80.60	5.78	52.29
A_0		27.11	51.24	7.29	85.64	6.54	44.48
A_1	0–2	22.37	61.07	11.72	95.16	5.85	13.02
A_2	2–9	20.50	66.33	10.71	97.54	5.90	6.82
AB	9–24½	19.12	63.62	15.73	98.47	6.26	4.88
B_2	24½–40	12.94	49.84	35.90	98.68	6.43	7.27

13. Systems Ecology

E. E. C. Clebsch[1]
A. M. Craig, Jr.[2]
R. C. Dahlman[3]
Kenneth Doxtader[4]
Ann W. Freeman[5]
A. J. P. Gore[6]
G. R. Hoffman[7]
J. S. Olson[3]
R. V. O'Neill[7]
P. A. Opstrup[5]
J. D. Ovington[8]
Philip Sollins[7]
C. E. Styron[3,9]
Harry Vardis[5]
R. B. Williams[10]

INDIRECT ESTIMATION OF ENERGY FLUXES IN ANIMAL FOOD WEBS

R. V. O'Neill

One of the most important factors which has limited the application of systems techniques to real ecosystems has been the difficulty of directly measuring energy fluxes when they approach the degree of complexity shown in Fig. 13.1. It is possible to measure the standing crop (x_i) and respiration loss (R_i), but direct measurement of the energy flux between compartments becomes extremely difficult when more than one prey species is being eaten. Outlined here is a technique for indirectly estimating the energy fluxes or transfer between compartments derived from data which involves far less time and difficulty than would be necessary for direct measurement.

The probability that a predator will feed upon one prey rather than another is directly proportional to the standing crop of that prey (x_i). The more prey available, the more likely that an encounter will occur. Predation is also dependent on factors such as prey preference and defense mechanisms of the prey. These factors are combined into a single parameter, w_{ij}. In essence, w_{ij} expresses the relative frequency or ratio in which the various prey are consumed when they are available in equal standing crops. The probability that population j will feed upon population i then becomes

$$p_{ij} = \frac{x_i w_{ij}}{\sum_{i=1}^{n} x_i w_{ij}} .$$

This probability then expresses the fraction of the total diet of that predator composed of species i. At steady state the total energy income must equal energy loss (R_j), and the energy flux from i to j is $p_{ij}R_j$.

It is now possible to quantify the energy dynamics of the example given in Fig. 13.1. The w_{ij}'s are shown on the arrows between compartments. The calculations for the top predator (x_{10}) are done as discussed above. For each nonterminal compartment we redefine the energy loss as

$$E_i = R_i + \sum_{j=1}^{n} p_{ij}E_j ,$$

since at steady state the population must take in sufficient energy to satisfy its respiratory loss

[1]Consultant, The University of Tennessee.
[2]Mathematics Division.
[3]Dual capacity.
[4]Colorado State University.
[5]The University of Tennessee.
[6]Nuffield Scholar, The Nature Conservancy, England.
[7]NSF Advanced Science Seminar Project Participant.
[8]Consultant, Australian National University, Canberra.
[9]On loan from U.S. Army.
[10]On leave from Radiobiological Laboratory, Bureau of Commercial Fisheries.

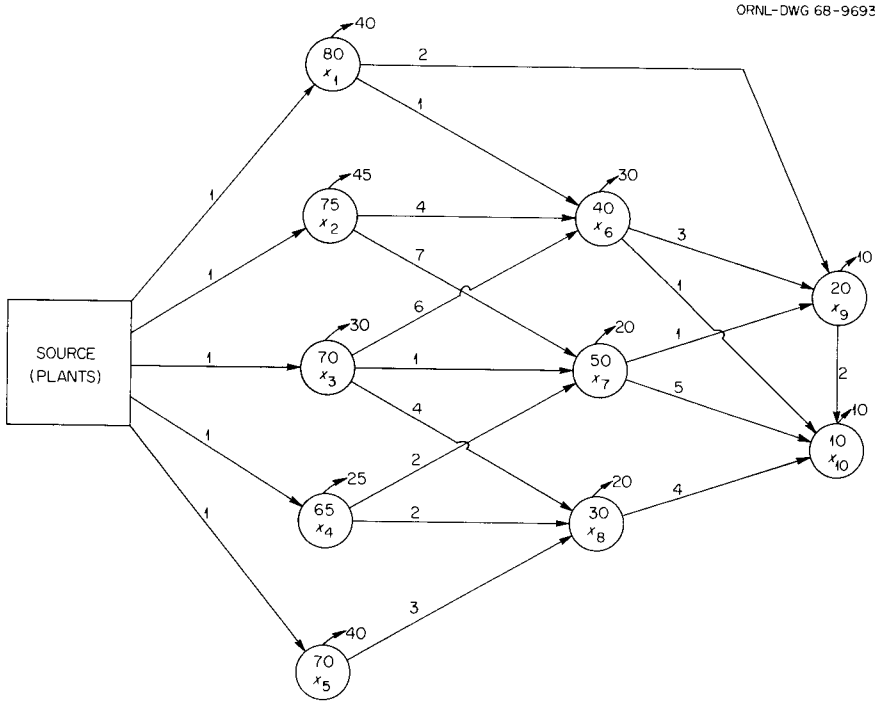

Fig. 13.1. Diagram of a Hypothetical Food Web. Standing crop, in calories per square meter, is shown within compartments; respiration loss, in calories per square meter per year, is shown on vertical arrows leaving each compartment. Numbers on arrows connecting compartments represent estimates of w_{ij}.

Table 13.1. Calculation of Energy Fluxes for the Food Web Shown in Fig. 13.1

Numbers indicate calories per square meter per year being exchanged from the compartment at the end of the row to the compartment at the head of the column

0	1	2	3	4	5	6	7	8	9	10	
0.0	48.7	78.0	61.0	34.6	47.7	0.0	0.0	0.0	0.0	0.0	0
	0.0	0.0	0.0	0.0	0.0	3.5	0.0	0.0	5.2	0.0	1
		0.0	0.0	0.0	0.0	13.3	19.7	0.0	0.0	0.0	2
			0.0	0.0	0.0	18.1	2.7	10.2	0.0	0.0	3
				0.0	0.0	0.0	4.9	4.7	0.0	0.0	4
					0.0	0.0	0.0	7.7	0.0	0.0	5
						0.0	0.0	0.0	4.0	0.9	6
							0.0	0.0	1.7	5.6	7
								0.0	0.0	2.6	8
									0.0	0.9	9
										0.0	10

plus the loss to mortality. Calculated energy fluxes for the example in Fig. 13.1 are shown in Table 13.1.

In systems where the animals are small and natural conditions can be reasonably approximated in laboratory cultures or field enclosures, an estimate of w_{ij} can be obtained simply by presenting the predator with the available prey in equal standing crops. Other estimates could be made from scat or gut analyses where these are appropriate. Where a reasonable estimate of w_{ij} can be made, this technique provides a simple method for calculating energy fluxes. It is hoped that this method will make possible quantification of many complex ecological systems which cannot be approached by established techniques of direct measurement.

APPLICATIONS OF COMPARTMENT MODELING TO POPULATION DYNAMICS

R. V. O'Neill C. E. Styron

King and Paulik[11] have shown the feasibility of adapting compartment modeling techniques to population studies. This is accomplished by regarding each day of the life cycle as a separate compartment and defining the size of that compartment (X_i) at time t as

$$X_i(t) = X_{i-1}(t-1) - b\,X_{i-1}(t-1)\,, \qquad (1)$$

where b is mortality rate in animals per animal per day. Thus, each day a mortality is imposed on all age groups, and the individuals are transferred to the next older group. The number of individuals in the youngest age group (X_e) is defined by

$$X_e(t) = a\,X_a(t-1)\,, \qquad (2)$$

where a is fecundity rate in eggs per adult per day and X_a is the number of adults. The number of adults is defined by

$$X_a(t) = X_a(t-1) - c\,X_a(t-1) + (X_i - bX_i)\,, \qquad (3)$$

where c is mortality in adults per adult per day and X_i is the oldest juvenile group.

This technique was used to model the Collembola population data presented by Styron and Dodson earlier in this report. Because of the impossibility of counting more than a few hundred Collembola in each culture and because excretory products accumulated in the cultures, the actual experiments could only be continued for about a month. This was sufficient to calculate the various parameters of population growth, but it was not possible to predict the long-range effects of acute radiation on population size and structure. Therefore the measured population statistics were used in a model of the type discussed above to extrapolate results for longer periods of time.

Figure 13.2 shows the predicted number of adults for 20 weeks following irradiation. Over a range from 4.95 to 9.90 kilorads (beta), the effect of a unit increase in dose is far less than for intervals above or below this range. This indicates that response is relatively independent of dose. This result is implied in the data, but because of the complexity of the system it is impossible to predict from simple examination of the measured parameters.

In order to predict radiation effects on the ability of the population to increase under natural conditions, it was necessary to incorporate into the model parameters which limit the population's ability to increase in the field. These parameters were assembled from the literature, and the resulting population dynamics can be considered as those of a hypothetical population with characteristics common to many Collembola species.

Self-inhibition was introduced so that a maximum of 1000 adults could survive in the hypothetical unit area under consideration. To accomplish this, formula (3) was modified to

$$X_a(t) = X_a(t-1) - c\,X_a(t-1) + (X_i - bX_i)\frac{1000 - X_a(t-1)}{1000}\,. \qquad (4)$$

A sinusoidal temperature function with a period of one year and a range from 0 to 25°C was generated. Laboratory measurements indicated that no reproduction occurred below 10°C. Above this temperature there was a linear relationship between reproduction and temperature of the environment

[11] C. E. King and G. J. Paulik, *J. Theoret. Biol.* **16**, 251–67 (1967).

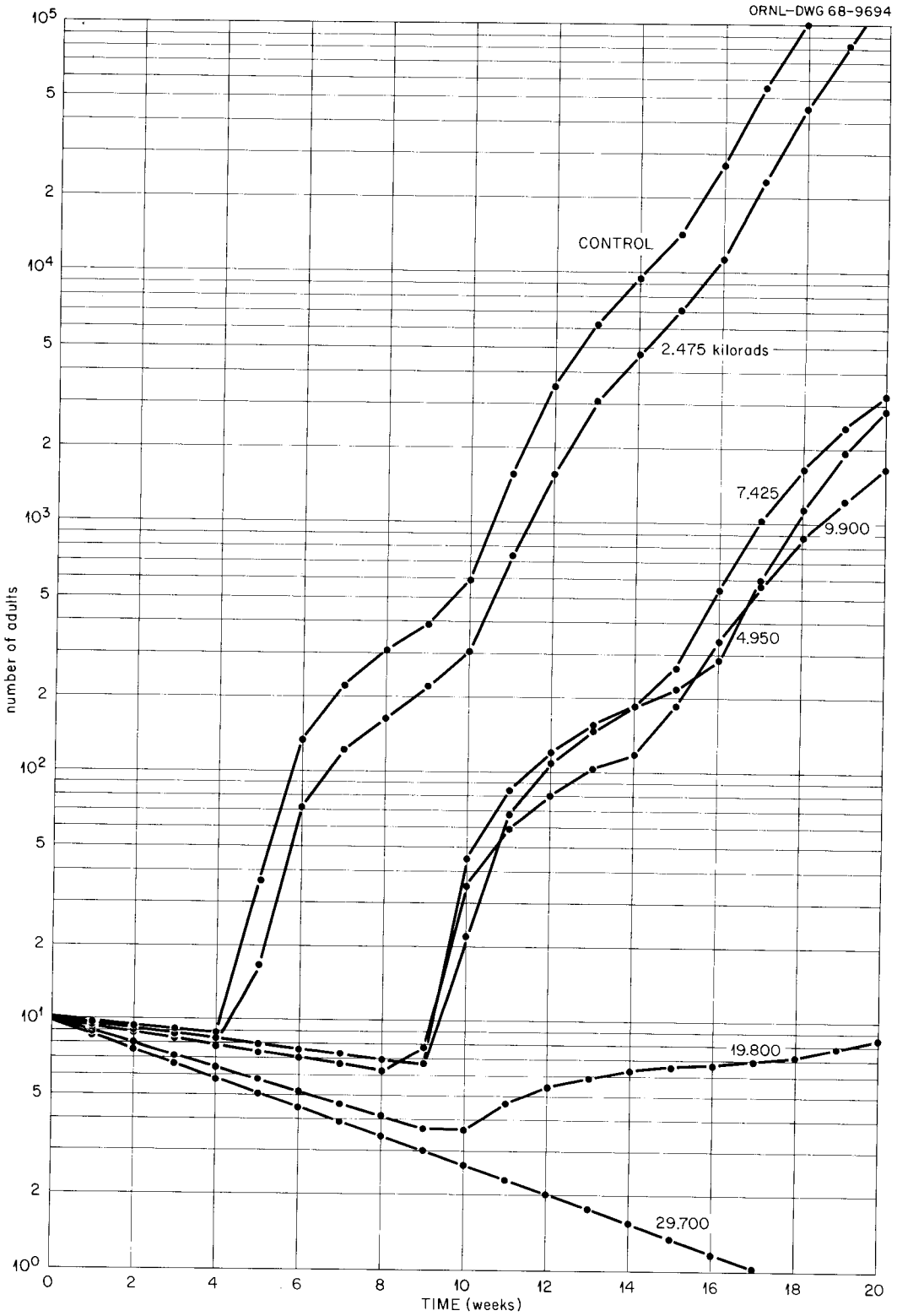

Fig. 13.2. Potential Increase by Ten Adult Collembola Following Irradiation. The numbers of adults, predicted by modeling based on information from laboratory studies, increase under conditions of infinite space and optimal food supply.

with a slope of 0.1844 up to 25°C. This information was used to modify the constant *a* in formula (2) so that it became a variable dependent on the generated temperature function.

Food availability is probably never a factor influencing mortality in Collembola but might be important in determining the energy available for reproduction. Therefore, a function was generated which goes to unity in September and falls to a minimum of 0.5 in August to simulate available litter. The fecundity parameter [*a* in formula (2)] is then multiplied by the values generated by this function to simulate the limitation due to lack of available food.

Finally, a predator function is generated as a sine wave with a period of one year and a range from 0 to 0.04. This function is generated so that its peak follows the temperature peak by one month. In this way we have simulated the effects of a group of predator species which reach maximum density in late summer and minimal density during the winter. The values generated by this function are added to the mortality rates [constant *b* in formula (1) and constant *c* in formula (3)] to obtain the total mortality. The control values shown in Fig. 13.3 represent the effect of these natural parameters on 1000 adults introduced into this simulated natural system. The results show ability to colonize hypothetical unit area and reach equilibrium in about six months and show an annual summer peak which is common for Collembola. The other curves in Fig. 13.3 show the effect of superimposing on this population the postirradiation rates and recovery measured in the laboratory. At lower doses, where complete recovery is possible within a reasonable length of time, the population quickly reaches control values. At higher doses the population is eliminated without recovery.

Such studies demonstrate the practical application of modeling techniques for revealing implications within experimental data and arriving at preliminary but quantitative predictions of potential population increase under natural conditions.

FORD FOUNDATION REPORT ON SYSTEMS ECOLOGY

J. S. Olson R. B. Williams

Systems ecology is not yet an organized body of knowledge but is rather a way of thinking, a holistic approach to ecology. In one kind of analysis, an ecosystem is envisioned as a group of compartments joined by flows of energy and materials. The value of this abstraction is that it can be analyzed by the techniques of mathematics and engineering, and thus with systems of differential equations, and/or simulated with electronic computer programs. Simulation implies an ability to reconstruct the history of ecosystems and forecast

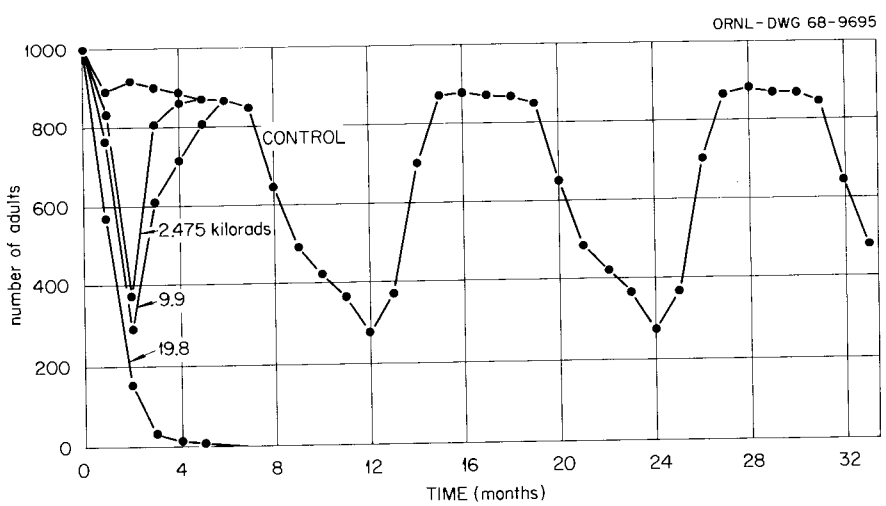

Fig. 13.3. Effect of Radiation on Survival Under Hypothetical Natural Conditions. Numbers of adults are shown following the release of 1000 adults during January. The figure shows the effect of radiation on the ability of this group to achieve and maintain the population levels shown by the controls.

their future states. A present study supported by a grant from the Ford Foundation undertakes a synthesis of current ecological knowledge relevant to these techniques of systems analysis. The grant to the Oak Ridge Associated Universities (ORAU) led to an agreement between ORAU and the Union Carbide Nuclear Division authorizing the use of personnel and facilities of the Radiation Ecology Section. The study will (1) summarize a considerable body of data already available on the state of selected ecosystems (e.g., tables or matrices of important constituents in selected compartments: plant, animal, inorganic). Part of this effort involves evaluation and summarization of estimates of transfer of selected constituents (nutrients) between compartments of an ecosystem. Such summaries are being developed in terms of fractional transfer rates or transition probabilities where relevant. (2) A closely related phase is use of compartment model analyses or simulations to infer the consequences that are implied by a given set of assumptions. It is by a matching of the model system's behavior with empirical information about nature and with auxiliary knowledge about the parts or subsystems of the landscape that the ecologists judge the usefulness of theory or the need to change models in successive approximations. (3) A third phase of work will seek answers to several difficult questions concerning future applications and potential use of model methodology.

The prime requirement for analysis of ecosystems is knowledge of transfer coefficients between compartments and of the factors which control transfer coefficients. A transfer coefficient is the quotient of a flux between adjacent compartments (mass per unit area per unit time) divided by the content of one of the compartments, usually the donor compartment (mass per unit area). It is thus dimensioned as a ratio: fraction transferred per unit time or $[t^{-1}]$. Similar definitions apply to energy flow. Transfer coefficients generally cannot be measured directly, but rather require measuring both flux and standing crop. Sometimes they can only be estimated indirectly in the process of modeling an ecosystem.

Most current research in quantitative ecology does not contain the data needed to compute transfer coefficients, because investigators in general have studied either the size of one or a few compartments or the flux into or out of a single compartment. Only a few measured both the size of a compartment and one flux rate for it; still fewer, the size of a compartment and all the fluxes into and out of it. Particular parts of each ecosystem [e.g., stem volume (and mass) in forests; large phytoplankton and zooplankton in aquatic systems] receive much attention; equally important parts (e.g., bacteria, small plankton, and benthic plants) are ignored or await improved technique. Those few published ecosystem studies which contain considerable information on standing crops and transfer coefficients to permit compartmental analysis mostly have large gaps which are bridged only by guesswork even though information in related literature often provides upper and lower bounds for the missing values.

A second approach to the analysis of actual ecosystems is the synthesis of models for particular geographic units where a large amount of research has been done, for example, Lake Mendota, Wisconsin, the North Sea, the Black Sea, etc. Several of the ecosystem studies are of this type. The disadvantages of this approach are: (1) Because studies on parts of an ecosystem often were done at widely separated times, a synthesis of the studies may not depict the ecosystem as it ever existed. (2) Because the studies were not designed for systems analysis, much interpolation and extrapolation will doubtless be necessary, and the model will reflect the preconceived ideas of its maker on how an ecosystem is structured. The gain from this approach is motivation of additional studies planned from the outset as suitable for systems analysis.

A third approach is the construction and analysis of hypothetical ecosystems representing abstractions such as a temperate eutrophic dimictic lake or a tropical lowland rainforest. Information is available in the literature for modeling many such abstractions. This approach also should yield insight into how the rates and compartment sizes of actual ecosystems must interact and will focus attention on discrepancies between particular cases and broad classes. Both the "case study" and "class" approaches are related in topics to follow.

COMPARTMENTAL ANALYSIS OF PRODUCTION AND DECAY OF *JUNCUS ROEMERIANUS*

R. B. Williams

Juncus roemerianus, or needle rush, grows in the upper intertidal zone and covers extensive areas

along the shore of North Carolina and elsewhere on the Atlantic coast. *Juncus* culms grow from perennial rhizomes and occasionally reach a height of 2 m. The mature culms persist green and alive for some period after reaching their full height, then slowly die – downward from tip to base, remain standing although dead for some period, and ultimately fall to the ground and decay. All three types of culms, live, dying, and dead, are present throughout the year.

As part of a study of total plant production in the estuarine area near Beaufort, North Carolina, rate of production of *Juncus* was measured. The standing crop of *Juncus* was measured at five-week intervals for a year. The sample, consisting of all the aboveground material from two 1-m squares, was collected, sorted into live, dying, and dead, and these dried and weighed. Most of the biomass was dead, indicating that the turnover of dead *Juncus* and of the total *Juncus* biomass was slow. It was assumed that the average total biomass, 2454 g/m^2, was present throughout the year and that the distribution of this average biomass into live, dying, and dead was proportionate to that in the samples. The results (Fig. 13.4) suggested that the live material has a seasonal cycle with higher values in summer and fall, the dying has a seasonal cycle with higher values in spring and summer, and dead material has a seasonal cycle with higher values in winter and spring.

These data on standing crop were summarized in a simple compartmental model. The three compartments, live, dying, and dead, were defined by the following equations:

$$\frac{d\,(\text{live})}{dt} = \text{growth} - \text{rate of transfer to dying compartment} \times \text{standing crop live } (344\ g/m^2),$$

$$\frac{d\,(\text{dying})}{dt} = \text{rate of transfer to dying compartment} \times \text{standing crop live} - \text{rate of transfer to dead compartment} \times \text{standing crop dying } (504\ g/m^2),$$

$$\frac{d\,(\text{dead})}{dt} = \text{rate of transfer to dead compartment} \times \text{standing crop dying} - \text{rate of transfer out of dead compartment} \times \text{standing crop dead } (1604\ g/m^2).$$

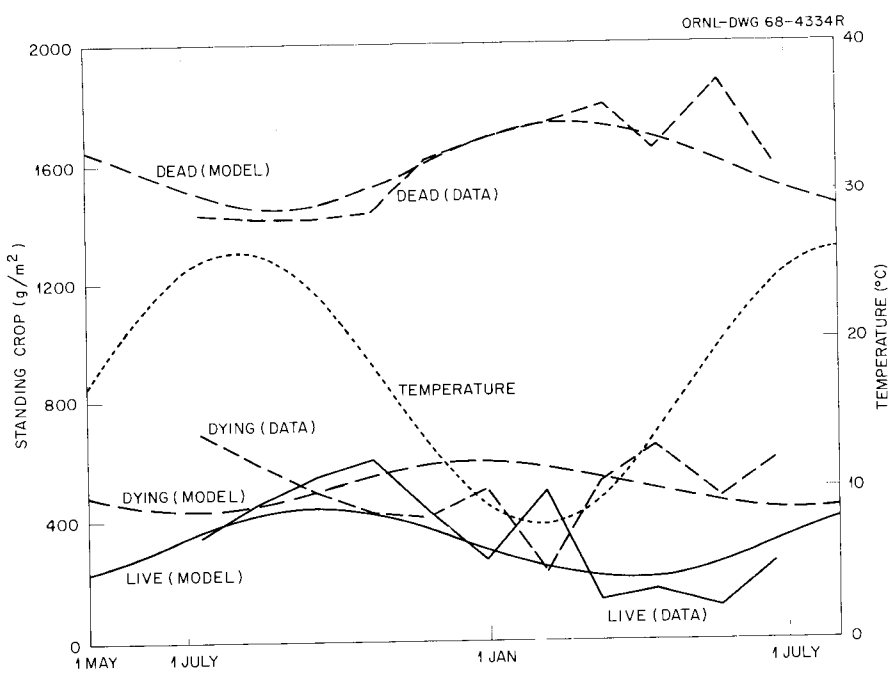

Fig. 13.4. Comparison of the Behavior of the Mathematical Model (Smoothly Curved Lines) with the Data (Straight Line Segments) on Which It Was Based.

The rates of transfer needed to complete the model were obtained from measurements of growth rate and longevity of 92 individual culms followed throughout their life history. The model thus obtained had an input (growth) of 735 g m^{-2} $year^{-1}$ and annual rates of transfer (out) for live, dying, and dead compartments of 2.137, 1.458, and 0.458 respectively.

The actual rate of input to the live compartment fluctuated around its annual mean because growth rate was correlated significantly with air temperature. Temperature at Beaufort, North Carolina, was approximated with a sine curve, in which the start of the cycle (the date equivalent to zero radians) was May 1 (Fig. 13.4). Equations for air temperature as a function of season and growth rate as a function of air temperature were combined into an equation of growth rate as a function of season. The rate of transfer from the live compartment to the dying compartment was greatest in the fall and was significantly correlated with minus cosine in the seasonal cycle starting May 1. This transfer rate was therefore made a function of cosine. The solution of the set of differential equations representing the model was completed with an analog computer. The equations thus obtained were:

$$\frac{d\,(\text{live})}{dt} = 735[1 + \sin(2\pi \times \text{years})] - 2.0[1 - 0.436 \times \cos(2\pi \times \text{years})] \times \text{live},$$

$$\frac{d\,(\text{dying})}{dt} = 2.0[1 - 0.436 \times \cos(2\pi \times \text{years})] \times \text{live} - 1.458 \times \text{dying},$$

$$\frac{d\,(\text{dead})}{dt} = 1.458 \times \text{dying} - 0.458 \times \text{dead}.$$

Figure 13.4 compares the computer output (i.e., the behavior of the model) with the data on which the model was based. There is reasonable agreement between the observed and computed values for the live and the dead compartments and poor agreement between observed and computed values for the dying compartment. The reason for this poor agreement is unknown. This compartmental model of *Juncus* production does, however, explain some of the observed seasonal cycles in standing crop and suggests that observations on standing crop and on growth and longevity form a coherent body of data.

COMPUTER SIMULATION OF PHOSPHORUS CYCLING IN A DOUGLAS FIR FOREST ECOSYSTEM IN WESTERN WASHINGTON

G. R. Hoffman

Phosphorus cycling in a Douglas fir [*Pseudotsuga menziesii* (Mirb.) Franco] ecosystem was simulated on a digital computer.[12] Data were obtained from Riekerk,[13] whose research was done at Fern Lake, western Washington, in a 35-year-old stand of Douglas fir on very poor sandy soil. Model compartments were (1) forest floor, (2) surface soil, (3) tree bases, (4) tree boles, and (5) tree crowns. In stages, the model was set up to illustrate both linear and nonlinear transfers between compartments. The striking result from the computer simulation was the deterioration of the system. Riekerk did not treat phosphorus input from precipitation explicitly, but his values for phosphorus in crownwash presumably included phosphorus from precipitation. Cole *et al.*[14] reported only a trace of phosphorus in precipitation at their study site in western Washington, so the input from precipitation is very small and would hardly prevent the running down of the system. Figure 13.5 shows graphically the compartment values over a simulated 280 years. In one simulation the system was run for a simulated 1120 years, and, though losses from compartments slowed considerably, steady state was never attained.

The surface soil represents a rather large pool of phosphorus (353 kg/hectare) at initial conditions, while the forest floor contains only 26.8 kg/hectare. Tracer studies indicated, however, that the trees absorb 87% of their phosphorus from the forest floor and 13% from the surface soil. This depletes the forest floor rapidly at first and then more slowly but constantly over the entire simulation times. Obviously the transfer coefficients must change with time if the system is to maintain itself indefinitely. Alternatively there may be significant

[12] L. J. Bledsoe and J. S. Olson, *COMSYS1: A Stepwise Compartmental Simulation Program*, ORNL-TM report (in press).

[13] H. Riekerk, "The Movement of Phosphorus, Potassium, and Calcium in a Douglas Fir Forest Ecosystem," Ph.D. dissertation, University of Washington, Seattle, 1967.

[14] D. W. Cole *et al.*, "Distribution and Cycling of Nitrogen, Phosphorus, Potassium, and Calcium in a Second-Growth Douglas-Fir Ecosystem," University of Washington, Seattle, mimeo., 1967, 35 pp.

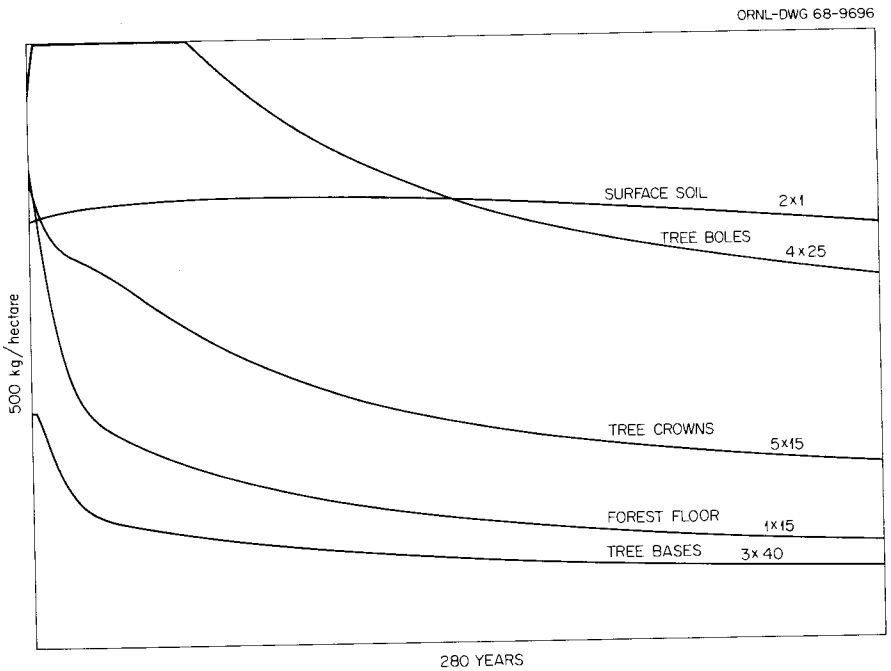

Fig. 13.5. Cycling of Phosphorus in Douglas Fir Ecosystem. Compartment model, linear.

undetected input of phosphorus, perhaps from weathering or deep seepage. As indicated, the stand is only 35 years old, and changes in nutrient cycling with successional changes of the habitat have not been considered. The author is currently working on a computer simulation of forest succession in the Pacific Northwest, and nutrient cycling changes concurrent with successional changes may possibly be worked out for certain areas of the economically and ecologically important Douglas fir region.

NITROGEN EQUATIONS OF GRASSLAND AND DUNE SOILS

R. C. Dahlman J. S. Olson
Kenneth Doxtader

Quantitative formulation of nitrogen cycles is important because so many aspects of production and nutrition are limited by some step in the economy of this element. In areas of intensive agriculture, it is now economically feasible to provide most of the crop's nitrogen demand in the form of artificially produced fertilizer input. In other native and managed systems the total nitrogen and the organic matter are functions of many ecosystem variables and climatic factors; shortage of available nitrogen commonly occurs because of low rates of turnover of nitrogen from organic residues. To understand the natural or modified balance and manipulate it, or perhaps to design for an "optimum ecosystem output" from basic principles, calls for a systems analysis. The historic foundation for such an analysis of grassland soil economy was therefore reviewed. Pedological equations of state discussed in detail by Jenny[15–17] show surprising geographic regularities in accumulations and equilibria under native prairie conditions of the central United States. These functional relationships between soil properties (*s*), biological components (*b*), and the ecological system's microenvironment (*a*) are *state variables* which in

[15]H. Jenny, *J. Phys. Chem.* **34**, 1053–57 (1930).

[16]H. Jenny, *Factors of Soil Formation. A System of Quantitative Pedology*, McGraw-Hill, New York, 1941, 281 pp.

[17]H. Jenny, *Comparison of Soil Nitrogen and Carbon in Tropical and Temperate Regions*, Missouri Agr. Expt. Sta. Res. Bull. 765, pp. 5–31, 1961.

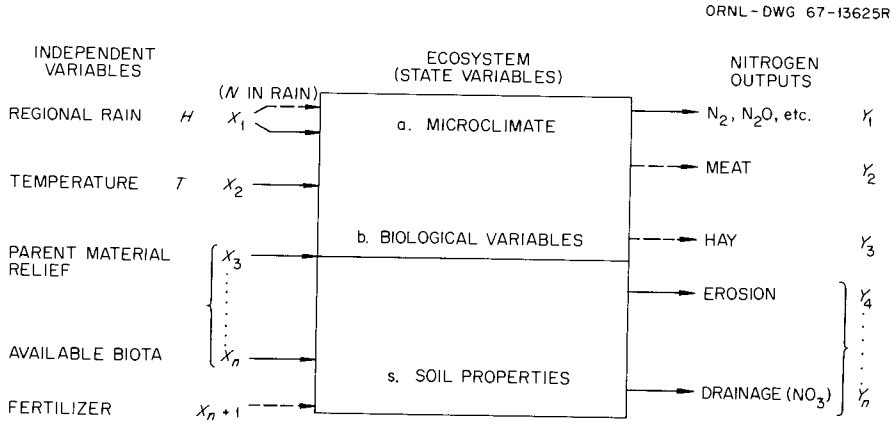

Fig. 13.6. Relationships Among Ecosystem Properties, Independent Variables (Inputs), and Nitrogen Outputs.

turn are influenced by regional climate – including appropriate measures of moisture (H) and temperature (T) – and other *exogenous variables*, including inputs and others (here called X_i in Fig. 13.6).

The influence of the two main climatic variables (temperature and moisture) can be restated by the function

$$N = f(T, H \mid \text{given other soil-forming factors nearly constant}) . \quad (1)$$

Deviations (dN) from any standard condition are (to a first-order Taylor series approximation) a sum of contributions due to each relevant independent variable:

$$dN = \left(\frac{\partial N}{\partial T}\right)_H dT + \left(\frac{\partial N}{\partial H}\right)_T dH + \sum_{i_{3\ldots n}} \left(\frac{\partial N}{\partial X_i}\right)_{T,H} dX_i + \text{extra terms.} \quad (2)$$

Here the summation sign includes influences of factors *other than* temperature and moisture, multiplied by the differentials of these other factors from the chosen "standard" reference condition. The condition described in the case study below is for near-native grassland biotic factors, moderate drainage and exposure, potentially loamy substrate, and sufficient time for ecological succession and soil formation to equilibrate through developmental processes like those discussed below for dunes.

The "extra terms" may represent quadratic and higher-order terms in a Taylor series expansion of the function f, plus a sum of random variables inherent in either the inputs to the ecosystem or the sampling properties of the system. Jenny's three-dimensional plot of the functional dependence of N on H and T is shown in Fig. 13.7.

Unfortunately, good long sequences of grassland soils of known age are rare. The age sequence described by Olson[18] includes early grass stages of succession followed by forest on dunes. It happens to be based on much sandier soils than those of Jenny – probably even less silty than the Sand Hills of Nebraska and other Great Plains States. That paper's argument follows earlier examples of Jenny *et al.*[19] in suggesting a formula for nitrogen buildup as a function of *time t*. The increase toward a limiting value N_{lim} is:

$$N = N_{\text{lim}}\,(1 - Ge^{-K_3 t}) = 0.087(1 - 0.997e^{-0.003t}). \quad (3)$$

Both the turnover fraction –0.003 and the asymptotic value for soil nitrogen (here for 0-to-10-cm soil only) were expected to vary, even locally, as a function of topographic and parent material factors (including siltiness due to residual loess in the oldest dune soils) and, of course, as a

[18] J. S. Olson, *Botan. Gaz.* **119**(3), 125–70 (1958).

[19] H. Jenny, S. P. Gessel, and F. T. Bingham, *Soil Sci.* **68**, 419–32 (1949).

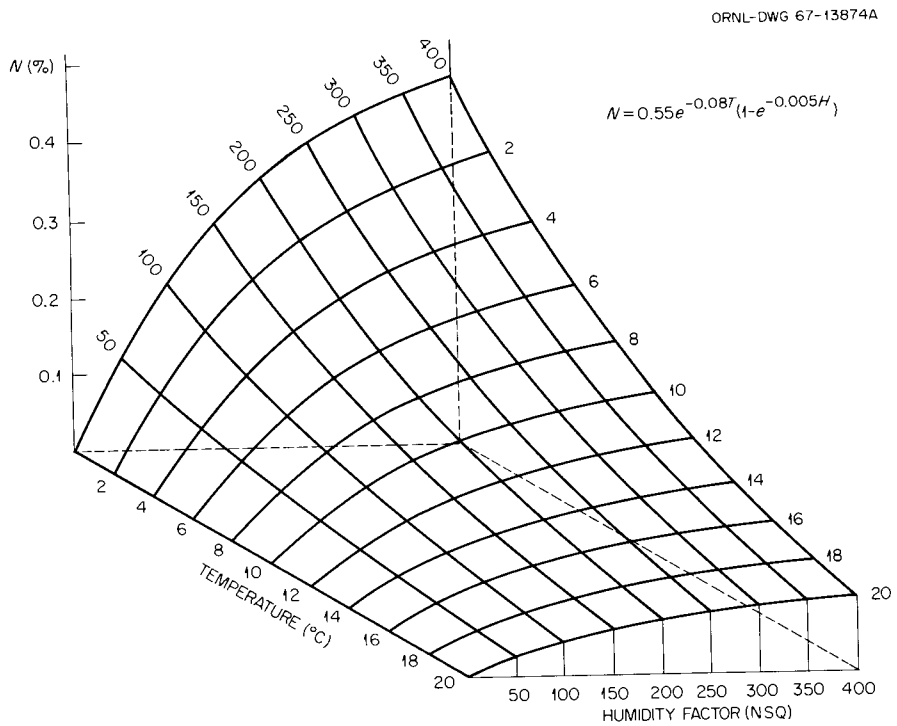

Fig. 13.7. Nitrogen Content of Loamy Grassland Soils in the United States as a Function of Annual Temperature and Annual Humidity Factor H = (Precipitation/Absolute Saturation Deficit) or "N.S.Q." of Jenny.

function of input rates of nitrogen. Here $G = 1 -$ fraction of the equilibrium value which is already present in parent material or in the preexisting soil which was entering a new system of management. If $G > 1$, Eq. (3) describes *decrease* from an *initial value* to a lower limiting value and describes a widespread decline in nitrogen and organic reserves under cultivation. We suggest that a term like that in parentheses in Eq. (3) could simply be multiplied by the equation in Fig. 13.7 to give a still more general expression encompassing changes in the nitrogen accumulation through time (in nature) or its depletion under conditions of cultivation (if insufficient crop residues are left in the soil):

$$N = ce^{-k_1 T}(1 - e^{-k_2 H})(1 - Ge^{-k_3 t}) . \qquad (4)$$

Additional terms like those in Eq. (2) could be added to account for any significant soil-forming factors besides climate and time and for stochastic variation which is not merely an artifact of sampling.

Soil development on sand dunes of approximately known age at the south tip of Lake Michigan seems compatible with the following simple hypothesis:

1. *Income* indicated by the early accumulation rates in 0-to-10-cm soil[20] is only 4 kg/hectare (0.4 g/m^2), which seems compatible with commonly cited estimates of rainfall income, 4.6 to 9.2 kg/hectare.
2. *Fractional loss rate* [the exponential coefficient of time in Eq. (4)] is near −0.003 per year, which implies loss equal to income after equilibration toward N_{lim}.
3. *Lag time* during the accumulation can be expressed in various ways, but $3/k = 1000$ years approximates the time to 95% of equilibration in the overall process.

Equations (3) and (4), or their elaborations, illustrate solutions which could be deduced from income-loss equations if pertinent terms were

[20] J. S. Olson, *Botan. Gaz.* 119(3), 159 (1958), Fig. 17B.

known.[18,19] For several forms of N denoted by either j or $k = 1, 2, \ldots, m$, the net rate of change of the kth compartment simply equals the sum of all income rates minus total loss rate:

$$\frac{dN_k}{dt} = \text{income} - \text{loss}$$

$$= \sum_{\substack{j=1 \\ j \neq k}}^{m} N_j f_{jk} - \left(-N_k f_{\substack{jk \\ j=k}}\right) = \sum_{j=1}^{m} N_j f_{jk} , \quad (5)$$

where the total loss rate, expressed as a turnover fraction per (short) unit time, is conveniently defined as:

$$f_{\substack{jk \\ k=j}} = f_{jj} = f_{kk} = -\sum_{\substack{k=1 \\ k \neq j}}^{m} f_{jk} , \quad (6)$$

which equals $-k$ in the terminology of Olson[18] and Jenny *et al.*[19]

A major difference between grassland soils and those of cultivated land is that the former are always occupied by vegetation, which tends to hold natural income, while the latter are periodically disturbed by cultivation alternating with periods of cropping, whose output of N normally requires replenishments.

By conducting the experiments in lysimeters, it has been possible to compile a balance sheet showing nitrogen gains, losses,[21] and distribution in different components of the cropping system. Deficits occur in most instances and suggest that denitrification can be important even in fairly aerated soils. The recovery of fertilizer nitrogen applied to grassland systems is seldom more than 60%. Woldendorp[22] concluded that nitrogen losses were the result of the action of denitrifying bacteria in the rhizosphere of plants. Considerable quantities of gaseous products ($N_2 + N_2O$) were formed when rye grass and pea roots were incubated with nitrate. With ammonium nitrogen or in the presence of killed roots, nitrogen losses were slight. Complementary to the regional analysis approach of Jenny, we have analyzed the nitrogen cycle of a native grassland near Columbia, Missouri. The nitrogen content of peak standing crop of shoots (3.6 g/m^2) and roots (6 to 12 g/m^2) is shown in Fig. 13.8. A comparison of the nitrogen distribution in plant biomass, litter, and soil compartments indicates that the major portion is present in the soil humus. Only a small part of the total ecosystem budget is associated with recent organic production (plant parts and microorganisms). Because most of the nitrogen is in the reserve category and only a small fraction is present in biological parts, it is possible that the transfer rates, residence time, and the interrelationships among the different components contribute greatly to the economy of the ecosystem. New production is supported by the available-nitrogen pool, much of which arises from rapid turnover of fresh biological materials (weekly for microorganisms[23] and four years for roots[24] and shoots.[25] Field studies with ^{15}N would reveal more precisely the major source of the nitrogen assimilated into the new biomass. Appreciable aboveground growth (at least 500 g/m^2) and only negligible consumption (in areas reserved from grazing) produces a sizable pool of standing dead grass and litter.

Utilization of available nitrogen by higher plants was at least 6 g/m^2, based on the inventory of the season's root and shoot growth. This value agrees well with the estimated annual available-nitrogen pool. Although nitrogen demand of microorganisms is unknown, it is often considered as great as the requirement of higher plants. Under steady-state conditions it is likely that the microorganisms maintain the pool at a relatively constant level because of the equilibria established between immobilization and mineralization. For the most part microbial inputs to the pool would be compensated by corresponding utilization. Consequently, the nitrogen demand of higher plants would largely be satisfied by nitrogen released from mineralized organic inputs (roots and shoots), assuming negligible input from other sources. Information was unavailable concerning the nitrogen inventory and transfer rates related to the microorganism compartment of the system.

---

[21] M. A. Brown, *Leaching Losses of Nitrogen*, Soils and Fertilizer Research Branch, TVA, Wilson, Ala., T65-1SF (1965).

[22] J. W. Woldendorp, *Mededel. Landbouwhogeschool Wageningen* **63**(13), 1 (1963).

[23] S. L. Jansson, *Kgl. Lantbruks-högskol. Ann.* **24**, 101–361 (1958).

[24] R. C. Dahlman and C. L. Kucera, *Ecol.* **46**(1 and 2), 84–89 (1965).

[25] M. Koelling and C. L. Kucera, *Ecol.* **46**(4), 529–32 (1965).

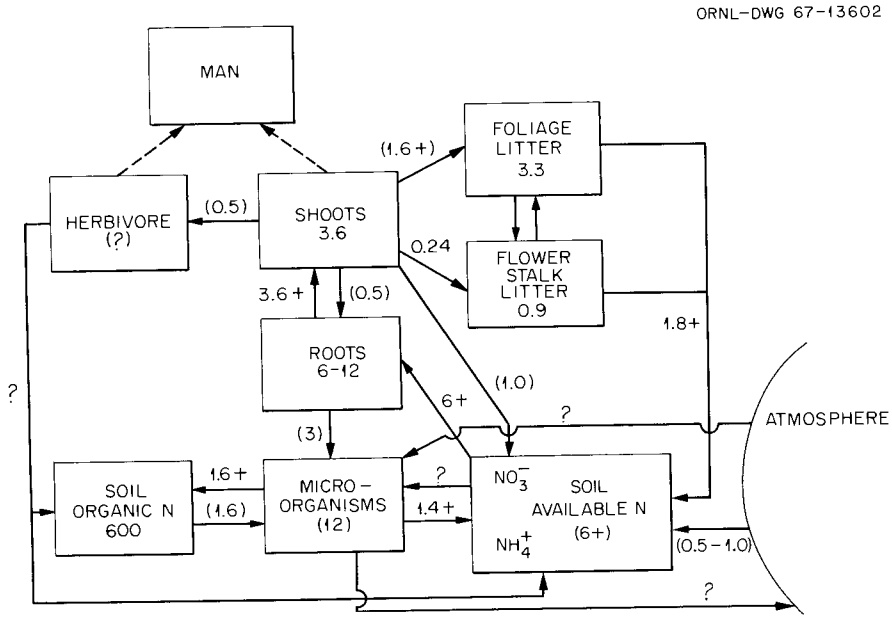

Fig. 13.8. Preliminary Estimates of Nitrogen Inventory and Transfer Relationships for Different Compartments of a Native Prairie Ecosystem. Contents and rates are expressed in grams per square meter per year, and the numbers in parentheses are first-order approximations.

DRY WEIGHT RANK METHOD FOR GRASSLAND STUDIES

P. A. Opstrup

There is an obvious need for a quick, accurate method of biomass estimation of grassland on a dry-weight basis. The approach used here is based on the methods of De Vries[26] and Mannetje and Haydock.[27] A computer program has been written for the analysis of the biomass estimation technique and is discussed herein.

Program RANKER is based on the premise that a more precise estimate overall of the total biomass of an area may be obtained by ranking a large number of plots rather than by ranking and clipping a smaller number. This requires a sufficient number of plots be clipped to get a good estimation of the correlation between observed values (dry weight grams per square meter) and predicted values. The method of determining the relationship between a matrix of species ranks, W, and the percent of the total weight each species accounted for, C, is obtained by minimizing the function Q,

$$Q = \sum_i (C_i - \sum_j W_{ij} P_j) , \qquad (1)$$

where P_j is the vector of correction coefficients for the jth rank and W_{ij} is the proportion of times the ith species was given the jth rank such that $\Sigma_j W_{ij} = 1.0$ for all i and $0 \leqq W_{ij} \leqq 1.0$ and $0 \leqq C_j \leqq 1.0$ (ref. 28).

This method was used in the summer of 1967 on two old-field communities dominated by *Festuca elatior* and *Andropogon virginicus* respectively. The multiple correlation values between the actual (clipped) and predicted values were very high, ranging from 0.94 to 0.99. The vector of correction coefficients, P, was then applied to a series of plots in which the species only had been ranked.

[26] D. M. De Vries, *Verslag. Landbouwk. Onderzoek.* No. 39 A, 1–24 (1933).

[27] L. 't Mannetje and K. P. Haydock, *J. Brit. Grassland Soc.* 18(4) (1963).

[28] S. I. Auerbach *et al.*, *Health Phys. Div. Ann. Progr. Rept. July 31, 1966*, ORNL-4007, p. 109.

Table 13.2. Relationships Between Clipped (*C*) and Estimated (*E*) Proportions of Total Biomass Oven-Dry Weight as Determined by the Rank Method in the *Andropogon* Community

Species	August		September		October		December	
	C	*E*	*C*	*E*	*C*	*E*	*C*	*E*
				Replication 1				
Andropogon virginicus	0.80	0.61	0.79	0.82	0.88	0.84	0.93	0.93
Aster pilosus	0.02	0.09	0.10	0.07	0.03	0.04	0.03	0.01
Panicum latifolium	0.02	0.01						
Campsis radicans	0.02	0.01	0.01	0.01	0.01	0.01	0.01	
Carex frankii	0.02	0.03					0.01	0.01
Eupatorium fistulosum	0.02	0.07	0.01	0.01				
Rubus allegheniensis	0.01	0.05				0.03		
Solidago altissima	0.06	0.03	0.03	0.04	0.02	0.01		
Panicum commutatum	0.01		0.01		0.05	0.02		
Rosa sp.		0.01						
Oenothera biennis	0.02	0.03						
Senecio smallii	0.01		0.01			0.01		
Erigeron canadensis			0.02	0.01				
Eulalia viminea				0.01				
Panicum anceps						0.03	0.01	
Galium tinctorium						0.01		
				Replication 2				
Andropogon virginicus	0.66	0.59	0.68	0.55	0.78	0.78	0.85	0.81
Aster pilosus	0.14	0.11	0.09	0.13	0.05	0.05	0.05	0.05
Panicum latifolium	0.01	0.06						0.03
Campsis radicans	0.03		0.01	0.02		0.01		0.04
Eupatorium fistulosum		0.04	0.01	0.02				
Rubus allegheniensis		0.05	0.03	0.03		0.02		
Carex frankii	0.01						0.02	
Solidago altissima	0.04	0.03	0.04	0.03	0.02		0.01	0.02
Panicum nitidum			0.01	0.01	0.01	0.01	0.01	
Oenothera biennis	0.01	0.02	0.01	0.01				
Diodia virginiana	0.05	0.05	0.02		0.01	0.01	0.01	
Acalypha rhomboidea				0.02				
Rosa sp.	0.01		0.01	0.04		0.01		
Panicum commutatum	0.02	0.03	0.03	0.08	0.03	0.02		
Solanum carolinense		0.01		0.01				
Senecio smallii	0.03					0.01		
Panicum anceps			0.01		0.04	0.03	0.04	0.04
Erigeron canadensis			0.01		0.01			
Cirsium arvense					0.03	0.01		
Oxalis stricta					0.01			
Ganaphalium purpureum					0.01			
Vernonia altissima								0.02

Table 13.3. Relationships Between Actual (*A*) and Estimated (*E*) Proportions of Total Biomass Oven-Dry Weight as Determined by the Rank Method in the *Festuco* Community

Species	June		July		August		September	
	A	*E*	*A*	*E*	*A*	*E*	*A*	*E*
Replication 1								
Festuca elatior	0.91	0.91	0.88	0.87	0.90	0.90	0.95	0.94
Aster pilosus		0.01	0.03	0.03	0.01	0.02		0.01
Solidago altissima	0.03	0.03	0.01	0.01	0.03	0.02	0.01	0.01
Andropogon virginicus			0.01	0.02			0.01	
Campsis radicans	0.01	0.01	0.05	0.03	0.01	0.01		
Rubus allegheniensis	0.01		0.01	0.01	0.02	0.03	0.01	0.03
Eupatorium fistulosum					0.02	0.01		
Sorgum halepense							0.01	
Daucus carota							0.01	
Ipomoea hederacea	0.01	0.01	0.01	0.01				
Oenothera biennis	0.01							
Solanum carolinense				0.01				
Replication 2								
Festuca elatior	0.88	0.88	0.89	0.88	0.90	0.90	0.88	0.88
Aster pilosus	0.01	0.01	0.01	0.01	0.01	0.02	0.01	0.01
Solidago altissima				0.01	0.01	0.02	0.02	0.02
Andropogon virginicus		0.01			0.01		0.05	0.03
Campsis radicans	0.02	0.02	0.01					
Rubus allegheniensis	0.01	0.01	0.02	0.04	0.05	0.03		0.04
Ipomoea hederacea	0.03	0.03	0.04	0.03				
Plantago major	0.01	0.01	0.01					
Trifolium repense	0.01	0.01		0.01				
Panicum nitidum	0.01							
Lespedeza cuspidata	0.01		0.01			0.01	0.03	0.01
Solanum carolinense	0.01							
Eupatorium fistulosum					0.01	0.01	0.01	
Carex frankii					0.01			

The results are summarized in Tables 13.2 and 13.3, in which only the dominant species are listed. Any species that accounted for at least 1% of the total weight in any given sample period was included in the dominant taxa list.

Festuca elatior accounted for a minimum of 87% of the estimated herbage weight in the *Festuca* community (Table 13.3). Relatively little change is noted between the observed and the estimated values. This agrees with the species composition of that community. *Festuca* uniformly dominated the field for the entire year. It was ranked first in all the clipped and estimated plots and never accounted for less than 88% of the total clipped biomass.

The *Andropogon* community was not as uniformly distributed over the sample area as was *Festuca*. *Andropogon virginicus* accounted for a minimum of 55% of the estimated herbage weight (September *E*, replication 2) in the *Andropogon* community (Table 13.2). This field contained "pockets" of various species that completely dominated small areas. These species include *Oenothera biennis, Aster pilosus, Solidago altissima, Eupatorium fistulosum,* and *Rubus allegheniensis.* The increase in the actual over the predicted weight composition for

such species was usually between 1 and 4%, though higher changes did occur. The dominance of these "pockets" can be seen particularly well in the first *Andropogon* sample, where the change in the composition of *Andropogon virginicus* between the observed (*C*) and estimated (*E*) values was a negative 13% (September, replication 2). The difference was not as great later in the season when *Andropogon* growth was at a maximum.

The advantages of this rapid sampling technique are twofold. First, it reduces the amount of laboratory work (weighing, sorting, and drying). This is desirable when storage space is limited or drying facilities are at a minimum or taxed. Second, this method allows for the optimum usage of time for obtaining the largest representative sample possible. This is especially desirable when working in irradiated areas, where samples cannot be taken and the amount of time spent in the area is critical. The rapid sample method allows for quick sampling without the clipping of plots within the area.

MODEL OF PEAT, STANDING DEAD, AND LIVE ORGANIC CONTRIBUTIONS TO SUBARCTIC BLANKET BOG

J. S. Olson A. J. P. Gore

In the terminology of Schwarz and Friedland[29] three broad classes of system variables (x, q, and Y), listed on the left of Table 13.4, correspond with the "compartments" chosen (Fig. 13.9) by Gore and Olson[30] for a preliminary model of primary production of a blanket bog near Moor House in the Pennine Mountains, England, where ecosystem studies have continued since 1958. The normal export of migratory animals (sheep) was not relevant to the fenced areas under study but would be very important in a management-oriented model. Digital computer simulation of the ecosystem's behavior therefore deals with yearly steps (Fig. 13.10) which become relatively fine when considered relative to a time scale of thousands of years for the slow accumulation of anaerobic peat substrate (Fig. 13.11).

We assumed no variation over the years in the solar energy source, and 10,000 was taken as the constant input variable v_1 or x_1. Net primary production, however, was not assumed constant during recovery from clearing by clipping at the surface of aerobic peat, but increased from the initial rate of 100 g m^{-2} year^{-1} to 420 g m^{-2} year^{-1}, according to the following formula (where Δt = one-year steps):

$$\frac{\Delta v_2}{\Delta t} = v_1 f_{12} + f_{22} v_2$$

$$= 0.1021 \times 10{,}000 - 0.5 v_2 \,. \qquad (1)$$

[29] R. J. Schwarz and B. Friedland, *Linear Systems*, McGraw-Hill, New York, 1965.

[30] A. J. P. Gore and J. S. Olson, *Aquilo, Ser. Botan.* 6, 297–313 (1967).

Table 13.4. Classes of System Variables and Ecological Examples of Compartments

Numerical examples from Fig. 13.9, after A. J. P. Gore and J. S. Olson, *Aquilo, Ser. Botan.* 6, 297–313 (1967); from Fig. 4 after Fig. 3 of Olson, 1964*a*.

Variable		Ecological Examples (Compartments)	Fig. 13.9
Inputs (x)	x_1	solar energy (atmospheric CO_2)	1
	x_2	primary production (net or gross)	2
State variables (q)	q_1	green plants (high or low)	3
	q_2	dead organic material (standing or mat)	4
	q_3	substrate (shallow, deep, etc.)	5, 6
	q_4		
	⋮	animals (plant, detritus, or animal feeders)	
		migratory animals	
Outputs (Y)	Y_1	respiration and gas loss (CO_2, CH_4)	7
	⋮	other exports	

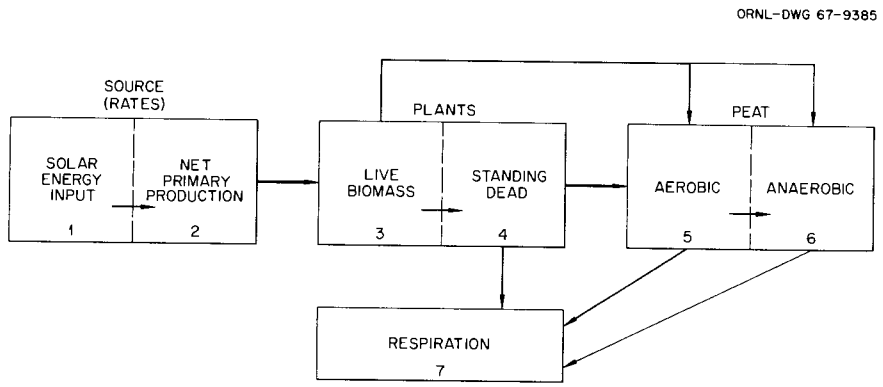

Fig. 13.9. Compartment Model for the Transfer of Organic Matter Through a Blanket Bog Ecosystem at Moor House, Pennine Hills, England. Data from A. J. P. Gore and J. S. Olson, *Aquilo, Ser. Botan.* 6, 297–313 (1967). The thicker arrows outside the boxes indicate the main pathways; compartment 1, "solar energy input," is an input limiting *potential* production rate, while net primary production reflects the gross production minus respiration of *live* higher plants. (Hence there is no arrow of additional gas loss from "live plant biomass" to "respiration.") Not shown here is a production input to sphagnum, which is enmeshed with aerobic peat.

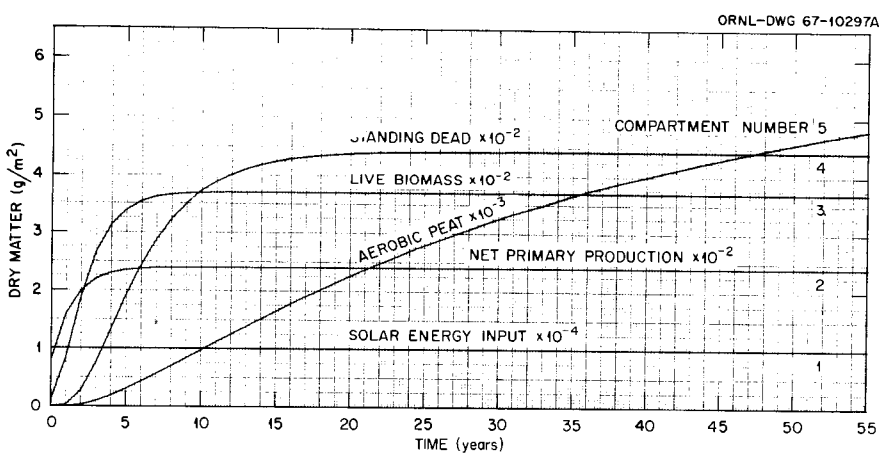

Fig. 13.10. Computer-Simulated Behavior of Five Compartments of Model of *Eriophorum vaginatum* Contribution to Subarctic Blanket Bog. The model curves rise quickly for net primary production *rate* and accumulation of live and standing dead material. Aerobic peat (compartment 5 here refers only to that fraction derived from *Eriophorum*) illustrates the relatively slow accumulation rate due to slow annual turnover, taken as –0.0676. Alternative estimates of –0.0534 and –0.0895 are suggested for depths of 15 and 12 cm.

ORNL-DWG 67-10462

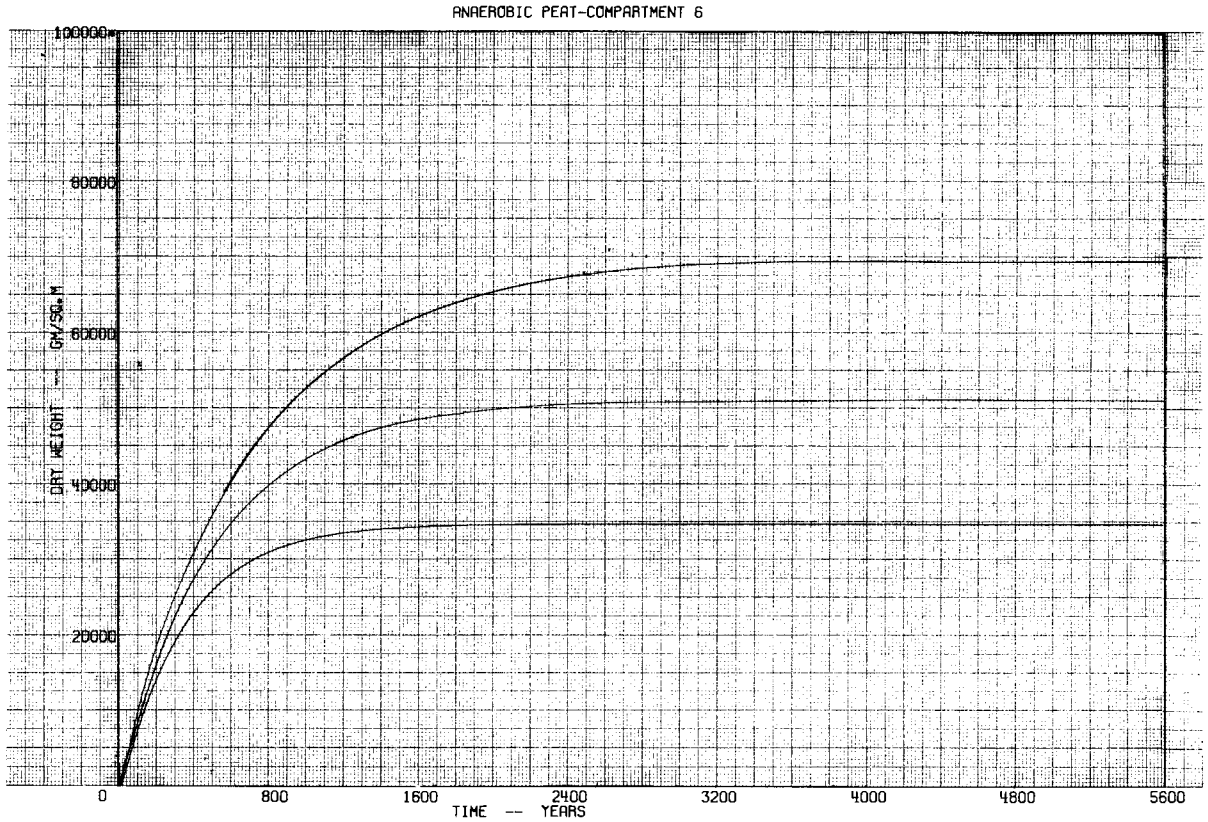

Fig. 13.11. Graphic Output from the Computer, Illustrating the Times Required to Reach Steady-State Masses Corresponding with Depths of 60, 80, and 100 cm (Each Including 12 cm of Aerobic Peat). Model assumptions here imply a constant input of 97 g m^{-2} $year^{-1}$ and turnover rates of –0.0028, –0.0019, and –0.0014 respectively. Gore and Olson [*Aquilo, Ser. Botan.* 6, 297–313 (1967)] allow the alternative possibility of Clymo (1965) that decay rates vary less than this, while input fractions from aerobic peat may vary with depth of water table (as shown in Fig. 13.10).

This approaches a steady state [when $\Delta v_2 = 0$ in Eq. (1)] of

$$v_2 = \frac{210}{0.5} = 420 \text{ g m}^{-2} \text{ year}^{-1} = x_2 . \qquad (2)$$

The approach to this balanced condition between positive and negative terms of Eq. (1) is rather quick, because $f_{22} = 0.5$ means that half the difference between the current production and this stationary-state level is erased each year.

Variables $v_3 \ldots v_6$ represent grossly "lumped" state variables (labeled $q_1 \ldots q_4$ in the linear systems notation of Schwarz and Friedland[29]). Data available in 1967 suggested that about f_{23} = 0.76 of the net primary production went into higher plants (initially cottongrass, *Eriophorum*, gradually replaced by heather, *Calluna vulgaris*, with few minor species). Since much of this material lies under the sphagnum surface as roots and shoot bases, slightly less than half (–0.49) turned out to be the effective annual turnover for higher plants. (Provisional allocations are $f_{34} = 0.2$ to standing dead, $f_{35} = 0.27$ to aerobic peat, and $f_{36} = 0.0175$ to deep, anaerobic peat – that is, below 9 to 15 cm from the peat surface.)

Sphagnum varies locally, and no feasible separation of it from the surface, aerobic peat could be attempted yet, but $f_{25} = 0.238$ was the typical fraction of net primary production allocated to these lower plants "lumped" in this substrate layer. "Standing dead" organic material therefore

refers to higher plant debris: before snow packing and partial decay completes the process of adding it to the surface peat. Data on accumulation in early stages, dominated by *Eriophorum*, suggested fractional loss of −0.24 per year, which was provisionally taken to contribute about equally to aerobic peat and to export (releasing CO_2 and heat energy, by microbial respiration). In summary, then, live and dead organic materials were taken to change by yearly increments:

$$\frac{\Delta v_3}{\Delta t} = v_2 f_{23} + v_3 f_{33} = v_2 \times 0.762 - v_3 \times 0.49 \,, \quad (3)$$

$$\frac{\Delta v_4}{\Delta t} = v_3 f_{34} + v_4 f_{44} = v_3 \times 0.2 - v_4 \times 0.24 \,. \quad (4)$$

The sphagnum fraction of net primary production plus fractions of both live and dead higher plants are all taken as inputs to the aerobic peat layer. The loss or turnover fraction, taken as −0.068, is slightly less than Clymo's recent direct measurement of fresh sphagnum (−0.088, personal communication), but this may be appropriate if old residues are more resistant to decay than average. Approximately 0.017 of live biomass (see above) and also of aerobic peat were inferred as inputs to anaerobic peat, while its annual loss varied, apparently in the range −0.0014 to −0.0028, over the rolling hilltop and swale topography of the blanket bog (−0.0019 for average peat depth of 80 cm). Thus equations for annual change of the two substrate (peat) layers were:

$$\frac{\Delta v_5}{\Delta t} = v_2 f_{25} + v_3 f_{35} + v_4 f_{45} + v_5 f_{55}$$

$$= 0.238 v_2 + 0.0272 v_3 + 0.210 v_4 - 0.068 \,, \quad (5)$$

$$\frac{\Delta v_6}{\Delta t} = v_3 f_{36} + v_5 f_{56} + v_6 f_{66}$$

$$= 0.0175 v_3 + 0.0169 v_5 - 0.0019 v_6 \quad (6)$$

for the intermediate peat depths. For very wet valley or lake bogs the anaerobic peat losses (through methane primarily) may become less than −0.0001, so this layer becomes essentially an "output" buried by the local system, rather than a part of its recirculation, and for these cases estimates of 72 to 100 g m^{-2} $year^{-1}$ of net peat accumulation (based on palynologic-climatic zones and radiocarbon dating) may approximate the input to this "sink" – because the loss term f_{66} is negligible. On the other hand, for the blanket bog, Fig. 13.11 suggests even the fairly slow turnover rates given in the last terms of Eq. (5) and (6) provide plenty of time for the anaerobic part of the blanket bog to approximate a kind of stationary state. Possibly peat depths there fluctuate around such a stationary state, as climates and regional conditions fluctuate over the centuries of millenia.

The cumulative output "account" of dry matter for the bog ecosystem includes that released as CO_2 from aerobic respiration from standing dead materials and mostly CH_4 from peat decay. The rate of export is

$$\frac{\Delta v_7}{\Delta t} = v_4 f_{47} + v_5 f_{57} + v_6 f_{67} + v_7 f_{77}$$

$$= 0.12 v_4 + 0.051 v_5 + 0.002 v_6 - 0 \,. \quad (7)$$

By putting loss equal to zero, v_7 (or Y_1 in Table 13.4) thus gives a summation of all these gaseous exports. This total excludes respiration from live plants, because these were already deducted from organic matter fixation by defining v_2 (x_2) as *net* primary production: gross production *minus* respiration.

FORSTAN: A COMPUTER PROGRAM FOR ESTIMATING FOREST STAND DRY WEIGHT AND MINERAL CONTENT

E. E. C. Clebsch
A. M. Craig, Jr.
Harry Vardis
A. W. Freeman

The development and testing of mathematical models of the circulation of organic matter and mineral elements in forest stands require inventories of amounts of organic matter and mineral elements in several compartments in those forests. Equations for estimating such quantities have been derived from over 600 felled trees of about 40 species which grow on the ORNL reservation, in the Great Smoky Mountains, and in nearby physiographic provinces. Harvesting of the trees and

the processing of samples were carried out by personnel of ORNL and The University of Tennessee working separately or cooperatively in several different forest ecosystems of the region. A computer program, FORSTAN (FORest STand ANalysis) has been developed for the processing and analysis of the data.

FORSTAN uses detailed sample data from tree boles, branches, and leaves to predict parameters such as total mineral content (Ca, Mg, K, P), dry weight, height, volume, etc., of felled trees on which a minimum amount of data has been taken. Derived estimating equations are then used to find these same parameters for forest stands from measurement of the breast height diameter of the individual trees.

FORSTAN has six main subroutines: Dry Weight, Branch Weight, Bole Weight, Weight-Height, Growth, and Mineral. REGRESS 2[31] is called as a subroutine approximately 30 times from the main subroutines. Its output includes a printed table with statistical information on the input data, characteristics of the derived regressions generated by CALCOMP, and graphs based on ln-ln relationships.

Subroutine Dry Weight computes for each sample branch of a given basal diameter the calcium, magnesium, potassium, and phosphorus contents in addition to dry weight for both branch wood and leaves. Output includes tables, CALCOMP graphs relating basal diameters to each of these parameters, and statistical information from REGRESS 2. This subroutine requires card input.

Subroutine Branch Weight calculates the dry weight of wood in branches per felled tree by either multiplying fresh weight by dry percent or from regression coefficients from subroutine Dry Weight, using basal diameter of branches as a predictor. This subroutine calls subroutine Blowup, which uses other regression coefficients from Dry Weight to calculate the mineral content of the branches and leaves of these felled trees. Subroutine Branch Weight also computes the mean branch diameter and mean branch weight. Both of these subroutines have tabular output and call REGRESS 2 to relate DBH (diameter 1.37 m above ground) to total branch and leaf dry weight and total branch and leaf mineral content. Branch Weight requires card input.

[31]G. M. Van Dyne, *REGRESS — a Multiple Regression and Correlation Program with Graphic Output for Model Evaluation*, ORNL-TM-1288 (1965).

Subroutine Bole Weight uses card input which includes diameters, lengths, and, when available, fresh weights of cut sections of felled trees to calculate volume, length, and density of these sections. The volume equations of a neiloid estimates the volume of the base of a tree, a paraboloid for the sections between the base and tip, and a cone for the tip of the tree. These parameters are summed to obtain total tree volume, tree height, and calculated density per tree. REGRESS 2 relates DBH to total bole dry weight and height. Tabular output includes length, volume, and density per section and volume, density, dry weight, and height per bole.

Subroutine Weight-Height sums information from Branch Weight and Bole Weight to get total tree dry weight and relates it to DBH with REGRESS 2. Total tree height is included in the tabular output. REGRESS 2 relates DBH and height and performs a multiple regression on DBH and height against total tree dry weight. No card input is necessary. An example of tabular and graphic output is found in Fig. 13.12.

Subroutine Growth uses the regression coefficients from Weight-Height and breast height diameters based on growth rings to estimate the present dry weight of the tree and the dry weight ten years ago. These values are used in a derived estimating equation to obtain average annual

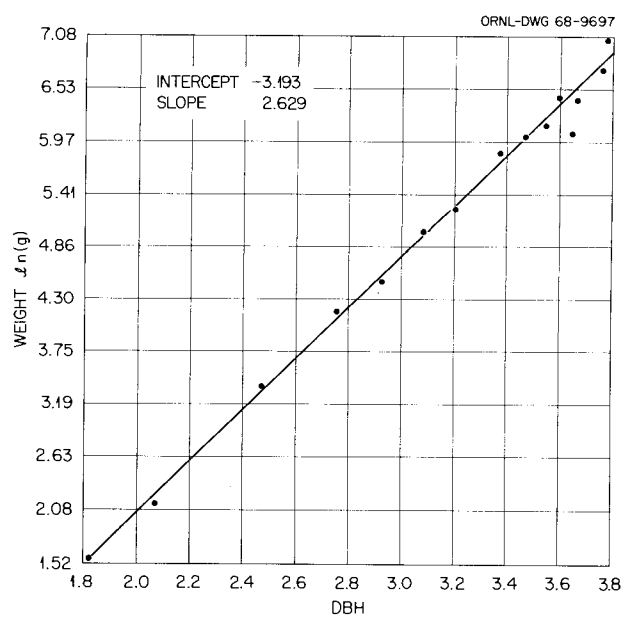

Fig. 13.12. ln (DBH) vs ln (Total Tree Dry Mass), Great Smoky Mountains Fraser Fir.

growth increment in percent. Card input is necessary for this subroutine.

Subroutine Mineral uses card input with diameters and mineral concentrations of three representative wafers cut from the lower, middle, and upper parts of the tree. These data are used in an equation to calculate the average concentration over the whole bole. These concentrations are multiplied by the total bole dry weight as found in subroutine Bole Weight to get element weights in the bole. These weights are added to branch element weights from subroutine Blowup to get total tree element weights.

To get forest stand information, one would measure the breast height diameters of all individuals by species in a sample plot of known area and apply the regression coefficients from subroutine Mineral for total tree mineral content and Weight-Height for total tree dry weight. For a more detailed description, DBH could be used as a predictor of branch or leaf mineral content and weight from Blowup and Branch Weight regression coefficients, and bole weight from Bole Weight regression coefficients. If specific branch information is desired, basal diameters would predict single branch and leaf parameters from Dry Weight regression coefficients.

ESTIMATED BIOMASS OF LEAF, BRANCH, BOLE, AND ROOTS OF TROPICAL LOWER MONTANE RAIN FOREST, EL VERDE, PUERTO RICO

J. S. Olson J. D. Ovington
Philip Sollins

The analysis of forest growth noted in several previous progress reports, and similar to steps described in FORSTAN, was carried further with data from the AEC rain-forest project of the Puerto Rico Nuclear Center (PRNC). Regression equations based on species groups *A*, *B*, and *C* reported by Olson and Bledsoe[32] were further tested and then applied to stand data that had been rechecked by PRNC and U.S. Army personnel with U.S. Forest Service aid in three rain-forest stands. These are: (1) North Experimental Area (later irradiated by a ^{137}Cs source; Vicksburg stand V0093), (2) South Experimental Area (unirradiated "control"; V0092), and (3) an area later opened by cutting instead of by gamma radiation (V0093A). Almost all of the biomass is represented in the dicotyledonous plants (i.e., excluding palms) represented in Table 13.5. Exact numbers could be improved if there had been time for more harvest data and separate regressions for certain major and minor species. Root data here exclude the small but metabolically active category of roots less than 0.5 cm in diameter. These were incompletely recovered by harvest technique but can be estimated by a combination of these methods and soil coring.

Subtotals of the inner circle of 20 m diameter and four quadrants (of an annulus, 20 m wide) are given so the reader can judge the general similarity and certain variations to be expected in such a tropical forest. These stands lie on fairly steep slopes, modified in some degree by removal of choice trees and some natural blowdown earlier in this century. Individual species show further irregularities in local distribution which have indicator value for local variations of the environment. Nevertheless there is a remarkable consistency in trend among many species and areas in proportions of major plant parts. Such relations should be very helpful in carrying the analysis of tropical woodlands toward further understanding of production *rates* (as distinct from static inventory of biomass and nutrient budgets). Data on all these aspects of an ecosystem need to be combined in order to develop and test predictive models of system behavior. Such models in turn should help judge the wisdom of conflicting resource policies and managerial decisions affecting vast areas of tropical landscape which will respond in quite diverse ways, in different areas, to their impending clearing for agriculture or management for forestry.

[32] S. I. Auerbach *et al.*, *Health Phys. Div. Ann. Progr. Rept. July 31, 1967*, ORNL-4168, p. 91.

Table 13.5. Biomass of Major Living Components of the El Verde Lower Montane Rain Forest, Puerto Rico[a]

Average grams per square meter or tons per square kilometer predicted from regression for dicotyledon species groups *A*, *B*, and *C*

Area and Subdivision	Leaves	Branches	Bole	Roots (>0.5 cm)	Total
Irradiated area (V0093)					
0–10 m radius	1018	6017	29,364	12,422	48,821
10–30 m					
Northeast	1134	6145	26,799	10,448	44,526
Southeast	921	3644	15,364	6,190	26,119
Southwest	948	4428	18,275	8,155	31,806
Northwest	639	3062	11,113	4,158	18,972
0–30 m total	922	4508	19,162	7,813	32,405
"Control" area (V0092)					
0–10 m radius	235	826	3,536	1,636	6,233
10–30 m					
Northeast	304	1140	4,838	2,133	8,415
Southeast	737	3093	12,413	5,743	21,986
Southwest	518	2487	10,238	4,851	18,094
Northwest	723	4989	20,446	11,217	39,375
0–30 m total	533	2693	11,045	5,502	19,773
"Cut" area (V0093A)					
0–20 m radius	1024	3924	16,173	5,807	26,928

[a]Excludes monocotyledons (palms), tree fern, epiphytes, individuals less than 1 cm in diameter at 1.3 m, and some unidentified minor and unidentified species of larger size. Since the latter were more common on the "Control" area, these figures may underestimate actual biomass by more for it than for the other area.

14. Forest Management

W. C. Cate
J. W. Curlin[1]
G. L. Gilreath[2]
E. H. Rosenbalm

FOREST MANAGEMENT

W. C. Cate
E. H. Rosenbalm
J. W. Curlin
G. L. Gilreath

The forest management program entered its fourth year of operation this year, during which we reached the scheduled mean annual cutting budget of 1,500,000 bd ft of sawtimber for the first time. An additional 3300 cords of pulpwood and fence posts were cut as thinning products from the extensive loblolly and shortleaf pine plantations planted 20 years ago by the AEC. Gross revenue from these sales was in excess of $45,000.

The coordination of the forest management program with the ecological research objectives has proven effective. Compatibility between the programs has exceeded expectations, and the programs have developed into a symbiotic relationship extending to other Laboratory organizations as well.

Negotiations for a long-term timber sale contract are in their final phase between AEC and a wood-using industrial organization. This is the culmination of a five-year effort by TVA to attract a stable, progressive integrated wood-using production plant in the Oak Ridge area. Four federal, private, and municipal landowners have pledged their annual cut for ten years to assure the industry of sufficient raw material during its early years of establishment. The advantages accruing to ORNL's forest management program and the local economy are (1) assurance of a stable continuing timber market, (2) stumpage prices tied to a national price index, (3) diversification of the local industrial economy, and (4) creation of a number of new jobs.

Southern pine beetle (*Dendroctonus frontalis*) activity increased slightly in the spring of 1968; however, the brood density and extent of infestation indicate that effective control can be maintained by selective timber salvaging during the summer with subsequent chemical control in the winter months when population expansion is minimal.

---

[1]Dual capacity.

[2]Temporary employee.

Part III. Radiation Physics

R. D. Birkhoff R. H. Ritchie

15. Theoretical Radiation Physics

Jacob Neufeld R. H. Ritchie

V. E. Anderson[1]
J. C. Ashley
Julian Crowell[2]
Mary Feezell[1]
Kenneth Fox[2]
W. R. Garrett
Duncan Grant[3]
R. N. Hamm
Larry Johnson[3]
Betty McGill
J. W. McKeever[4]
H. C. Schweinler
W. S. Snyder
J. E. Turner
R. E. Wilems[5]
H. A. Wright

NEW EVALUATION OF MEAN EXCITATION ENERGIES FOR USE IN RADIATION DOSIMETRY

Atomic mean excitation energies (the quantity I in the Bethe stopping-power formula) were obtained from the stopping-power and range data reported in 12 sets of experiments in the literature.[6] The analysis incorporated shell corrections that include contributions made from electrons in all shells. Except for one set of data the values of I obtained in the new analysis are consistent with those suggested for the elements in the NAS-NRC report 1133.[7] Some disagreements were found in a comparison with the older NBS Handbook 79.[8] The following formulas were found to give a reasonable fit to the mean excitation energy of an element of atomic number Z:

$$I\,(\text{ev}) = 11.2 + 11.7Z\,, \qquad Z \leqq 13\,, \qquad (1)$$

$$I\,(\text{ev}) = 52.8 + 8.71Z\,, \qquad Z > 13\,. \qquad (2)$$

Mean excitation energies for some 36 compounds and mixtures of particular importance in radiation dosimetry were calculated.[6]

[1]On loan from Central Data Processing Facility (ORGDP).

[2]Consultant.

[3]Research participant.

[4]Graduate student, University of Tennessee.

[5]Oak Ridge Graduate Fellow.

[6]Patricia Dalton and J. E. Turner, "New Evaluation of Mean Excitation Energies for Use in Radiation Dosimetry," *Health Phys.* (in press).

[7]*National Academy of Sciences–National Research Council Report 1133*, U. Fano, ed. (1964).

[8]*National Bureau of Standards Handbook 79* (1961).

EFFECT OF DELTA-RAY BUILDUP IN HIGH-ENERGY DOSE CALCULATIONS

Dose buildup due to delta rays in a soft-tissue slab bombarded by normally incident protons was studied to assess its effect in high-energy dose calculations.[9] Based on calculated energy and angular distribution of delta rays from 2-Gev protons and on experimental data for electron energy dissipation in water, it was estimated that a delta-ray buildup in absorbed dose of ~8 to 9% occurs in the first 3 cm of depth in the slab before electronic equilibrium is reached. With 400-Mev protons only a small buildup occurs in the first few millimeters, and the effect of delta rays is negligible when absorbed dose is averaged over thicknesses of the order of 1 cm.

[9] R. B. Vora, M. A. Prasad, and J. E. Turner, "Effect of Delta-Ray Buildup in High-Energy Dose Calculations," *Health Phys.* (in press).

HIGH-ENERGY DOSIMETRY

A simplified model for nuclear interactions has been used to obtain estimates of dose and dose equivalent for neutrons and protons in the energy range from 400 Mev to 2 Gev incident normally or isotropically upon a soft-tissue slab. The Monte Carlo calculations, based on a simplified model for nuclear interactions, take into account the production of pions as well as nucleons in nuclear interactions. The results are presented in the form of graphs showing the distribution of absorbed dose and dose equivalent with depth within the tissue phantom. Depth-dose curves obtained for 2000-Mev protons and neutrons incident normally on one surface of a 30-cm-thick infinite slab of soft tissue are shown in Figs. 15.1 and 15.2. The total absorbed dose is broken down to show the contribution due to ionization by primary particles (in the case of incident protons), ionization by secondary

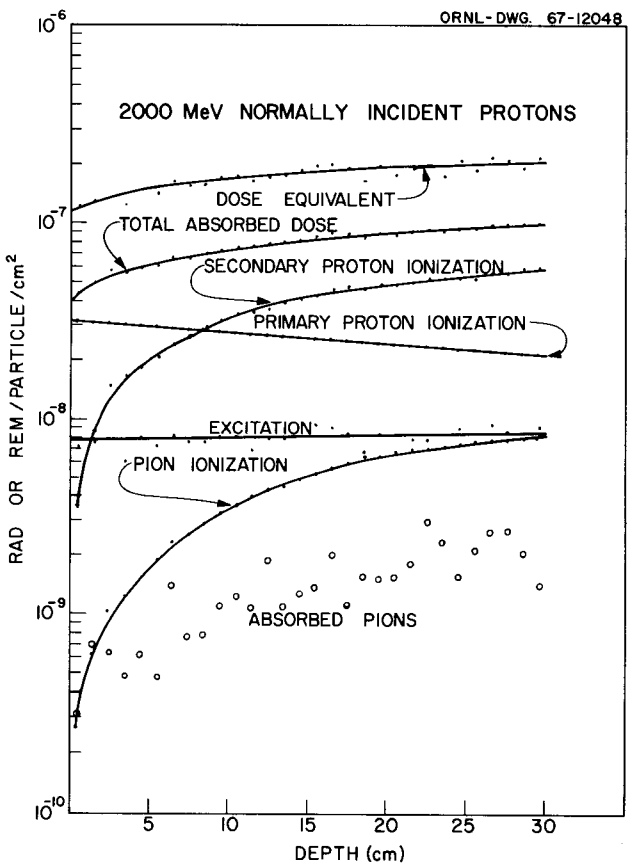

Fig. 15.1. Absorbed Dose and Dose Equivalent as a Function of Depth for 2000-Mev Normally Incident Protons.

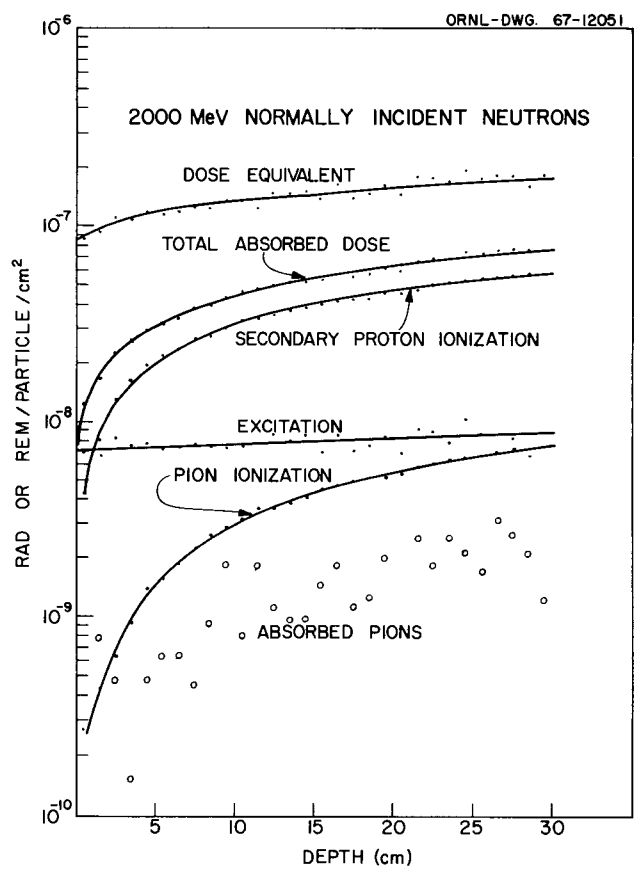

Fig. 15.2. Absorbed Dose and Dose Equivalent as a Function of Depth for 2000-Mev Normally Incident Neutrons.

particles, ionization by pions, excitation and recoil energy of residual nuclei following cascades, and the contribution from pions that stop within the tissue.

Some observations which can be made from these calculations include the following. For normally incident protons the maximum absorbed dose and dose equivalent occur near the back of the 30-cm tissue phantom. The buildup of the dose due to secondary particles increases with incident proton energy. For 600 Mev incident energy the buildup is approximately 12% within the first centimeter of tissue and 60% within 30 cm. For 2000 Mev incident energy the buildup is approximately 17% within the first centimeter and almost 150% within 30 cm. The absorbed dose near the surface is approximately the same for 600-Mev protons as for 2-Gev protons, but near the back of the phantom the dose from 2-Gev protons is almost 50% higher than that for 600-Mev protons. The quality factor also increases with incident proton energy, from approximately 1.5 for 600-Mev protons to approximately 2 for 2-Gev protons. Pions contribute less than 10% of the absorbed dose for 2-Gev incident protons.

For normally incident neutrons the dose also increases with incident particle energy as well as with depth within the tissue phantom. However, since the primary particles do not lose energy by ionization, the buildup of the dose is much more significant than for incident protons. The buildup is of the order of a factor of 10 within the thickness of the phantom. Furthermore, the character of the absorbed dose is significantly different near the surface than near the back of the slab. Near the surface the absorbed dose is almost entirely due to the high-LET evaporation products and recoils. Near the back of the phantom the major contribution to the dose is from ionization by secondary protons, and the quality factor for this radiation is approximately 1. Consequently, the quality factor decreases from almost 10 near the surface to approximately 2.5 near the back of the phantom. Pions contribute less than 15% to the absorbed dose for 2-Gev incident neutrons.

The contribution to the absorbed dose from second- and higher-order collisions (i.e., nuclear interactions initiated by secondary nucleons) is significant. For 600-Mev normally incident protons, neglecting second- and higher-order collisions would result in an error of approximately 10% in the absorbed dose. This error would be even more for higher incident energies because the number of secondary cascade nucleons increases with incident energy.

In spite of the approximations used in this simplified model, the results seem to be in reasonable agreement with available experimental measurements.

Studies of the effects of the presence of bone in a soft-tissue target were completed for 100-, 250-, and 400-Mev incident protons and neutrons. With protons, which deliver most of the absorbed dose directly by ionization, the presence of bone apparently makes little difference at these energies. With neutrons, however, a reduction in quality factor in the bone regions (compared with the quality factor when the target was homogeneous soft tissue) occurred. While this reduction was slight at 100 Mev, it amounted to almost 20% (i.e., from 8.4 to 6.8) at 400 Mev. Detailed analysis showed that the lower quality factor was a result of the relatively smaller contribution of heavy evaporation particles and recoil nuclei to the absorbed energy per unit mass in bone. These contributions to the absorbed dose were assigned a quality factor of 20 in the calculations. While the use of detailed data obtained from the statistical nuclear models used in the calculations is very uncertain, the smaller quality factor in bone appears reasonable from the physical standpoint. Compared with the relatively lighter nuclei in soft tissue, the heavier nuclei in bone present a higher Coulomb barrier to the evaporation of heavy fragments, and, also, they do not have as high an average recoil energy.

GROUND-STATE ENERGY EIGENVALUES AND EIGENFUNCTIONS FOR AN ELECTRON IN THE FIELD OF A STATIONARY ELECTRIC DIPOLE

The trial function

$$\psi(\xi, \eta) = e^{-(\alpha/2)\xi t} \sum_{p,q=0}^{\infty} C_{pq} \xi^p \eta^q \qquad (3)$$

has been used to calculate ground-state energy eigenvalues for an electron moving in the field of a stationary electric dipole. Here ξ, η are the elliptic-hyperbolic coordinates defined in Fig. 15.3. The electron is separated by distances r_1 and r_2 from the dipole charges $\pm q$, the dipole moment being $D = qR$. A function of the form (3) was used

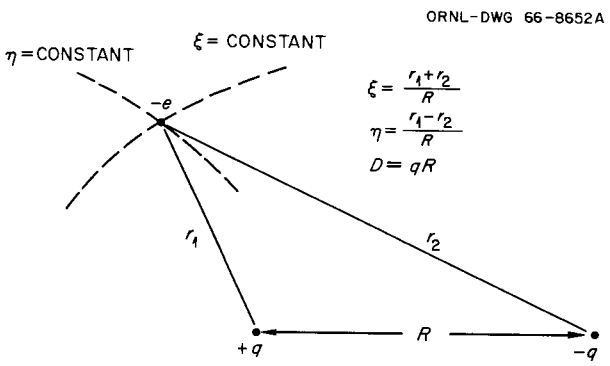

Fig. 15.3. Electron-Dipole System.

earlier to calculate the value of the minimum dipole moment needed to bind an electron, $D_{min} = 0.6393ea_0$ (atomic units). This functional form was found to be appropriate for the calculation of ground-state binding energies when the dipole moment is not too large, that is, when $D \lesssim 1.65ea_0$. For larger moments a function of the form

$$\psi(\xi, \eta) = e^{-(\alpha/2)(\xi+\eta)} \sum_{p,q=0}^{\infty} C_{pq}\xi^p\eta^q , \quad (4)$$

in which the exponential term depends only on the distance of the electron from the positive charge $+q$ of the dipole, was used. This hydrogenic trial function gave good convergence in calculations when $D \gtrsim 1.65ea_0$. Some of the resulting ground-state eigenvalues as a function of dipole moment when $q = e$ are given in Table 15.1. Only a few values are included in the range $0.84 \leqq D \leqq 30$ covered by an earlier, independent calculation.[10]

The ground-state energy eigenfunctions for the electron were also calculated, and the resulting electron probability densities are shown by the contour maps of ψ^2 in Figs. 15.4 through 15.7. Here the Z axis is that of the dipole, and ρ is the distance from the Z axis. With $D = 10ea_0$ in Fig. 15.4, it is seen that the electron cloud is hydrogenic in character, being concentrated symmetrically about the positive charge. With $D = 3ea_0$, ψ^2 spreads out to greater distances and shows a definite asymmetry due to the presence of the negative dipole charge. At still smaller dipole moments the probability density becomes spread out over very great distances in the upper half of space as the critical value $D_{min} = 0.6393ea_0$ is approached. A profile of ψ^2 along the Z axis for the entire range of dipole moments is shown in Fig. 15.8. For large D the function approaches the correct hydrogenic maximum value $\psi^2 = 1/\pi$ at the position of the positive charge. For $D \gtrsim D_{min}$, the values of ψ^2 (and the binding energy) drop precipitously with only a small decrease in dipole moment.

Mean values of powers of the distances of the electron from the dipole charges in the ground state are given in Table 15.2. Further details of this work are given elsewhere.[11,12]

Table 15.1. Ground-State Energy Eigenvalues as a Function of Dipole Moment

Dipole Moment (atomic units, ea_0)	Binding Energy (rydbergs, $e/2a_0$)
0.639315	0
0.6670	8.973×10^{-20}
0.67465	8.7779×10^{-16}
0.69272	8.3346×10^{-12}
0.72365	7.6350×10^{-9}
0.74099	7.2849×10^{-8}
0.76449	6.8437×10^{-7}
0.797368	6.29117×10^{-6}
0.840374	4.64096×10^{-5}
0.902195	3.13853×10^{-4}
1.00002	2.04928×10^{-3}
30	0.933338
40	0.950003
50	0.960000
100	0.980000
250	0.992
400	0.995

[10] R. F. Wallis, R. Herman, and H. W. Milnes, *J. Mol. Spectry.* 4, 51 (1960).

[11] J. E. Turner, V. E. Anderson, and K. Fox, *Ground-State Energy Eigenvalues and Eigenfunctions for an Electron in an Electric-Dipole Field*, ORNL-4297 (1968).

[12] J. E. Turner, V. E. Anderson, and K. Fox, "Ground-State Energy Eigenvalues and Eigenfunctions for an Electron in an Electric-Dipole Field," *Phys. Rev.* (in press).

ORNL-DWG 68-2266

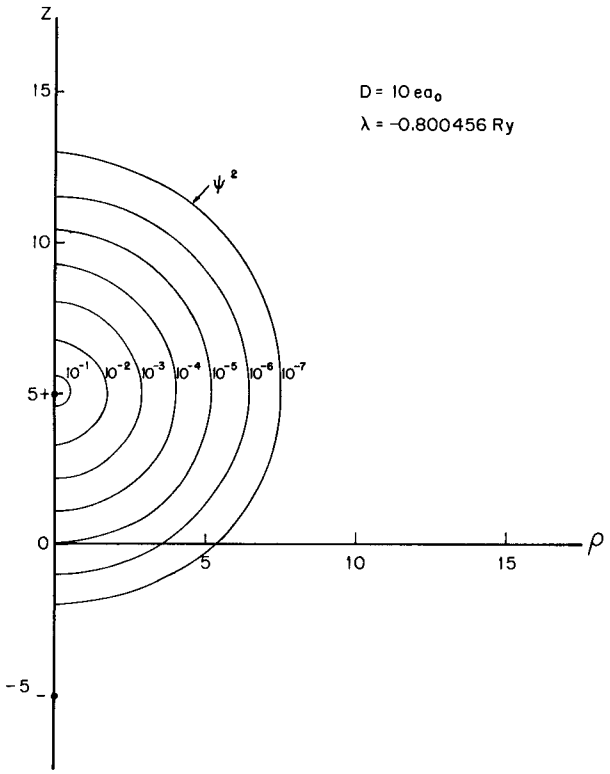

Fig. 15.4. Probability Density Contours for $D = 10ea_0$. The dipole has charges $\pm e$. Distances are in units of a_0.

ORNL-DWG 68-2267

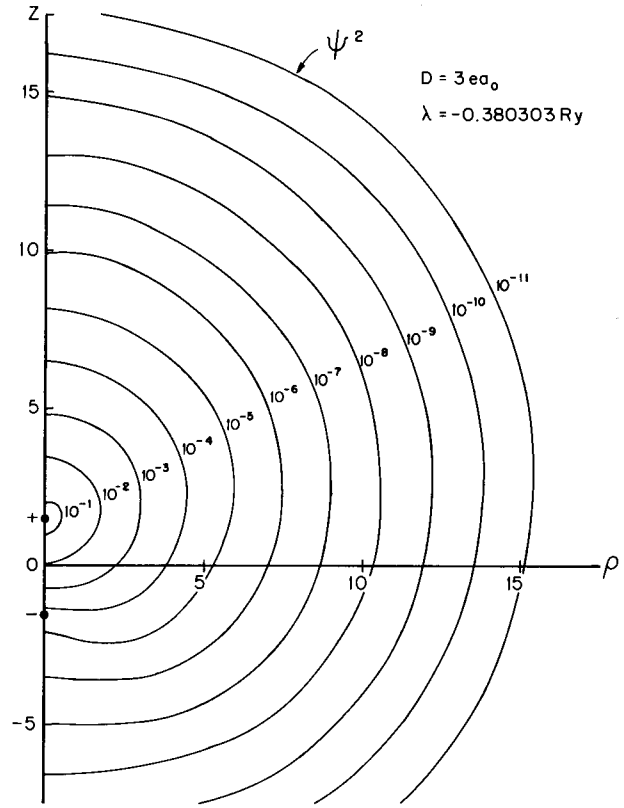

Fig. 15.5. Probability Density Contours for $D = 3ea_0$. The dipole has charges $\pm e$. Distances are in units of a_0.

QUANTUM THEORY OF THE PLASMA RESONANCE EMISSION PROCESS

In a very interesting experiment, Brambring and Raether[13] observed light emission from photon bombardment of thin silver foils.[14] Bösenberg and Raether[15] have recently observed this same phenomenon using potassium foils. These authors explain their results qualitatively in terms of the excitation and decay of plasmons.

This process has been studied in the framework of a nonrelativistic quantum theory of an imperfect plasma. One finds the normal modes of electronic motion in a plane plasma slab of thickness a from the Bloch hydrodynamical equations for a degenerate electron gas. One quantizes the plasmon field assuming that in first approximation the equilibrium plasma has uniform electron density n_0 inside the boundaries. Deviations from uniformity are codified in a density function $\delta n(\mathbf{r})$ which may represent the effects of structural irregularities, phonons, impurities, etc., as a function of position in a real foil. We may refer to this function as describing static density fluctuations (SDF) in the system. The Hamiltonian of the system is divided into a part representing noninteracting photons and plasmons plus interaction terms, which are treated by perturbation-theoretic techniques. Some of the interactions of interest are depicted in Fig. 15.9. One needs to consider here only photons, denoted by dashed lines, and radiative surface plasmons, shown as wavy lines. Figure 15.9*a* shows a vertex

[13] J. Brambring and H. Raether, *Phys. Rev. Letters* 15, 882 (1965).

[14] W. Steinmann, J. Hofmann, and K. Stettmaier, *Phys. Letters* 23, 234 (1966).

[15] J. Bösenberg and H. Raether, *Phys. Rev. Letters* 18, 397 (1967).

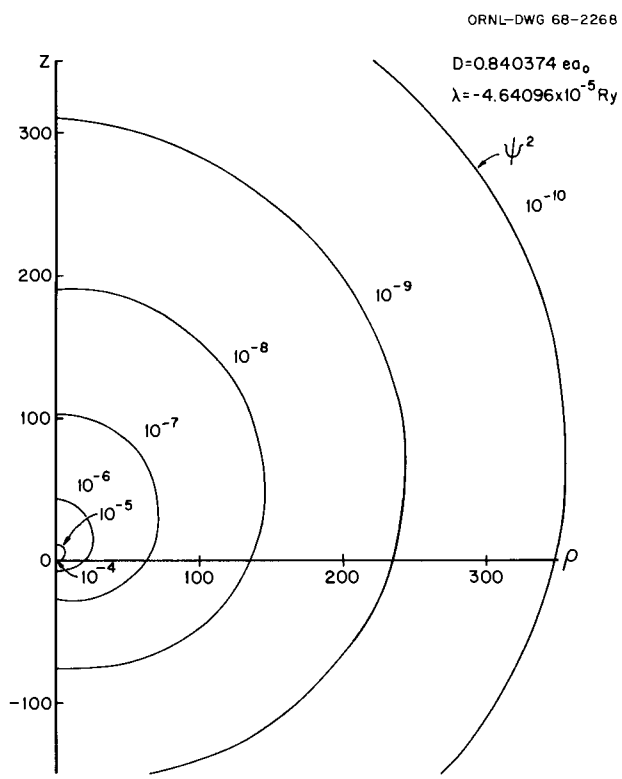

Fig. 15.6. Probability Density Contours for $D = 0.840374ea_0$. The dipole has charges $\pm e$. Distances are in units of a_0.

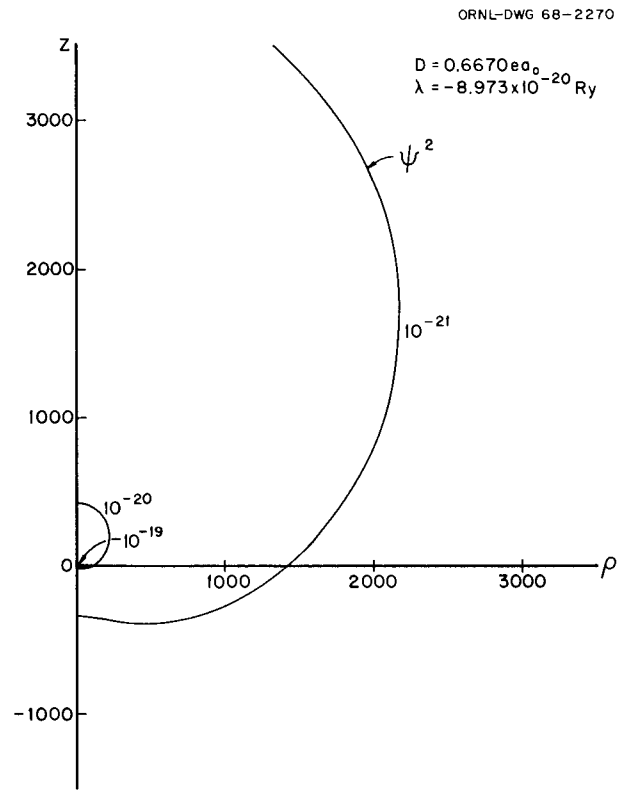

Fig. 15.7. Probability Density Contours for $D = 0.6670ea_0$. The dipole has charges $\pm e$. Distances are in units of a_0.

representing photon-plasmon interactions, neglecting SDF. This process conserves momentum parallel with the slab surfaces. Figures 15.9*b*–15.9*d* depict various possible interactions involving SDF which do not conserve momentum.

The probability that a photon shall be emitted from a plasma slab which is bombarded by *p*-polarized photons may be determined for the processes shown graphically in Figs. 15.9*e*–15.9*i*. Treating the ratio $a\omega_p/c$ as an expansion parameter, we find the differential emission probability per unit solid angle to be

$$\frac{dP_p}{d\Omega_f} = \frac{a^2\omega_p^6}{256\pi^2c^4}\,\frac{\sin^2\theta_0\sin^2\theta_f}{|\cos\theta_0|}$$

$$\times\frac{\omega_p^2 + 49(\gamma_0+\gamma_f)^2/16}{[(\omega_0-\omega_p)^2+(\gamma_0/2)^2][\omega_0-\omega_p)^2+(\gamma_f/2)^2]}$$

$$\times\, G(\mathbf{k}_{0\perp} - \mathbf{k}_{f\perp})\,, \qquad (5)$$

where $\gamma_0 = \gamma_d + a\tan\theta_0\sin\theta_0$ and $\gamma_f = \gamma_d + a\tan\theta_f\sin\theta_f$. Here γ_d is the electronic damping rate of the plasmon, $a = \omega_p^2 a/2c$, and (θ_0, θ_f) is the angle of the (incident, emitted) photon relative to the foil normal. The vector $(\mathbf{k}_{0\perp}, \mathbf{k}_{f\perp})$ represents the component of the wave vector of the (incident, emitted) photon parallel with the foil surface.

The quantity $G(\mathbf{k}) = L^{-2}|\int d\boldsymbol{\rho}\,\exp(i\mathbf{k}\cdot\boldsymbol{\rho})\,\bar{f}(\boldsymbol{\rho})|^2$ is related to the autocorrelation function for SDF in the plasma; $\bar{f}(\boldsymbol{\rho})$ is the average of $[\delta n(\mathbf{r}) - \langle\delta n\rangle]n_0$ over the depth of the slab, and $\langle\delta n\rangle$ is the average of $\delta n(\mathbf{r})$ over the whole slab interior. The two-dimensional vector $\boldsymbol{\rho}$ is parallel with the slab surfaces, and L^2 is the slab area. If one assumes that the SDF are random with Gaussian correlation characterized by σ, the mean distance between density fluctuations measured parallel with the surfaces, one may write $G(\mathbf{k}) = \pi\sigma^2\langle\bar{f}^2\rangle \times e^{-k^2\sigma^2/4}$, where $\langle\bar{f}^2\rangle$ is the mean square value of $\bar{f}(\boldsymbol{\rho})$.

ORNL-DWG 68-2892

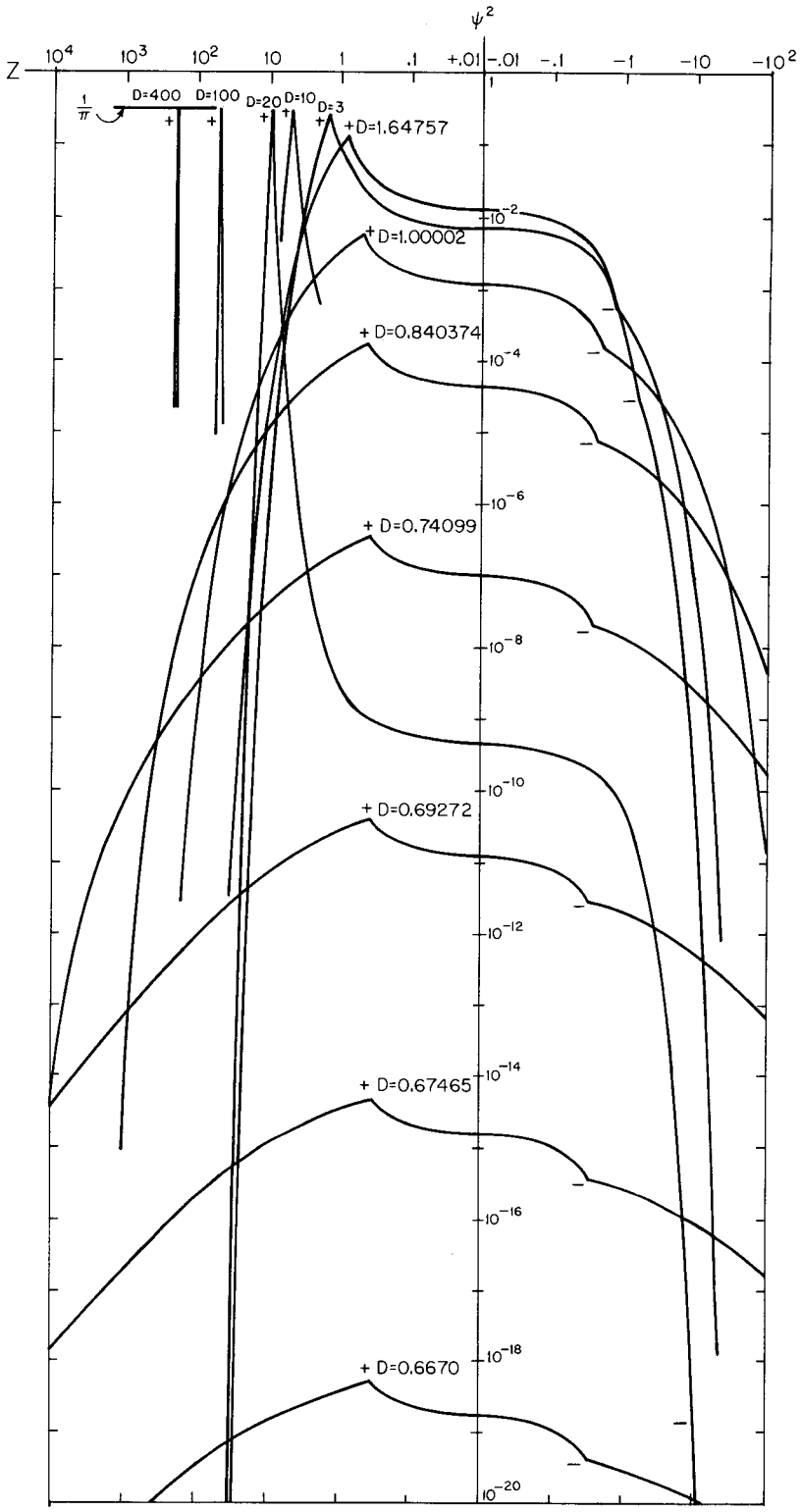

Fig. 15.8. Profiles of Probability Density Along Dipole Axis for a Number of Values of Dipole Moment.

Table 15.2. Mean Value of Powers of r_1 and r_2 in Atomic Units

Multiplicative powers of 10 are indicated; e.g., 1.98844 −09 means 1.98844×10^{-9}

D (ea_0)	$\langle 1/r_1 \rangle$	$\langle 1/r_2 \rangle$	$\langle r_1 \rangle$	$\langle r_2 \rangle$	$\langle r_1^2 \rangle$	$\langle r_2^2 \rangle$
0.6670	1.98844 −09	1.98844 −09	1.68090 +09	1.68090 +09	6.02533 +18	6.02533 +18
0.67465	1.63175 −07	1.63175 −07	1.85435 +07	1.85435 +07	6.84169 +14	6.84169 +14
0.69272	1.27693 −05	1.27684 −05	2.23186 +05	2.23186 +05	9.42090 +10	9.42091 +10
0.72365	3.60140 −04	3.59719 −04	7.36761 +03	7.36789 +03	9.54085 +07	9.54127 +07
0.74099	1.07428 −03	1.07119 −03	2.40522 +03	2.40552 +03	9.96340 +06	9.96483 +06
0.76449	3.15358 −03	3.13170 −03	7.94704 +02	7.95017 +02	1.06992 +06	1.07041 +06
0.797368	9.05608 −03	8.90868 −03	2.66808 +02	2.67143 +02	1.19161 +05	1.19340 +05
0.840374	2.31083 −02	2.23124 −02	1.00355 +02	1.00720 +02	1.66592 +04	1.67327 +04
0.902195	5.56899 −02	5.18451 −02	3.97801 +01	4.01895 +01	2.60299 +03	2.63573 +03
1.00002	1.29228 −01	1.12049 −01	1.61723 +01	1.66527 +01	4.17762 +02	4.33551 +02
1.18800	2.96508 −01	2.21946 −01	6.54633 +00	7.16579 +00	6.65705 +01	7.51094 +01
1.64757	6.18481 −01	3.40537 −01	2.82110 +00	3.78665 +00	1.18349 +01	1.83059 +01
2	7.59162 −01	3.48599 −01	2.19131 +00	3.42882 +00	6.96332 +00	1.40346 +01
3	9.23567 −01	2.91830 −01	1.68937 +00	3.74003 +00	3.96064 +00	1.52578 +01
4	9.70378 −01	2.34766 −01	1.57229 +00	4.49226 +00	3.36059 +00	2.12598 +01
5	9.86674 −01	1.93294 −01	1.53266 +00	5.36238 +00	3.16292 +00	2.97772 +01
6	9.93276 −01	1.63313 −01	1.51658 +00	6.28301 +00	3.08302 +00	4.04787 +01
7	9.96285 −01	1.41012 −01	1.50922 +00	7.23014 +00	3.04653 +00	5.32706 +01
8	9.97800 −01	1.23907 −01	1.50544 +00	8.19278 +00	3.02817 +00	6.81153 +01
9	9.98619 −01	1.10425 −01	1.50342 +00	9.16515 +00	3.01782 +00	8.49932 +01
10	9.99092 −01	9.95488 −02	1.50225 +00	1.01441 +01	3.01180 +00	1.03895 +02
15	9.99821 −01	6.65773 −02	1.50044 +00	1.50865 +01	3.00240 +00	2.28599 +02
20	9.99943 −01	4.99718 −02	1.50014 +00	2.00612 +01	3.00078 +00	4.03450 +02
25	9.99979 −01	3.99896 −02	1.49989 +00	2.50465 +01	2.99925 +00	6.28325 +02
30	9.99990 −01	3.33283 −02	1.49992 +00	3.00378 +01	2.99949 +00	9.03270 +02
40	9.99997 −01	2.49984 −02	1.49998 +00	4.00275 +01	2.99988 +00	1.60320 +03
50	1.00000 +00	2.00000 −02	1.50000 +00	5.00200 +01	3.00000 +00	2.50300 +03
100	1.00000 +00	1.00000 −02	1.50000 +00	1.00010 +02	3.00000 +00	1.00030 +04

ORNL-DWG 67-11064

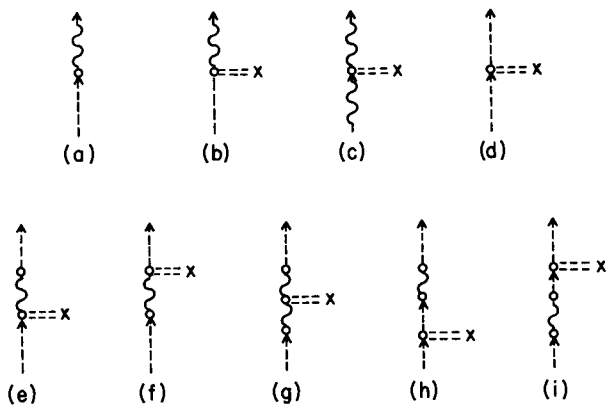

Fig. 15.9. Some Possible Interactions in an Imperfect Plasma. (*a*) Vertex at which a photon may generate a radiative plasmon; (*b*) vertex at which a photon is destroyed and a plasmon is created through interaction with SDF; (*c*) vertex at which a plasmon scatters elastically on SDF; (*d*) a vertex representing elastic scatter of a photon by SDF; (*e*)–(*i*) representative possible processes in which a photon is absorbed and another photon emitted through first-order interactions with SDF. It is necessary to consider various time orderings of the three vertices shown in (*g*).

One may easily obtain the probability for elastic scatter of *s*-polarized photons on SDF. Here we need consider only the diagram of Fig. 15.9*d*. We find

$$\frac{dP_s}{d\Omega_f} = \frac{a^2\omega_p^4 \cos^2\theta_{0f}}{16\pi^2 c^4 |\cos\theta_0|} G(\mathbf{k}_{0\perp} - \mathbf{k}_{f\perp}) , \qquad (6)$$

where θ_{0f} is the angle between the unit polarization vectors of the incident and emitted photons.

The ratio of Eqs. (5) and (6) is independent of the SDF. It should be quite interesting to compare this ratio with detailed experimental data. Equation (5) predicts the shape of curve 1, Fig. 2 of ref. 8 fairly well, if one assumes $a = 400$ A and uses data for γ_d from the paper of Brambring.[16] A careful comparison for both polarizations may require some effort toward reducing experimental background and evaluating the efficiency of the experimental system as a function of wavelength and polarization of the emitted light.

It is interesting to note that the present formalism is apropos not only to SDF which are associated with structural irregularities in plasmas but is directly applicable to SDF consisting of regular variations in the plasma density. Such variations might exist in a thin metal foil deposited on a replica grating transparent to light of wavelength λ_p. The present results may be transcribed directly to this "grating foil" case.

One finds that the probability for photon emission in the *n*th-order diffraction direction for photons incident in a plane perpendicular to the grating rulings has a form quite similar to Eqs. (5) and (6); photons which are *p* polarized are capable of exciting radiative surface plasmons in the "grating foil," and the probability for this process has the same double Lorentzian dependence on ω as does Eq. (5). On the other hand, *s*-polarized photons are diffracted in the usual way without exciting plasmons.

The probability of photon emission in an *n*th-order diffraction direction due to *p*-polarized incident photons is given by

$$P_{pn} = \frac{a^2\omega_p^4}{64c^2} \frac{\sin^2\theta_0 \sin^2\theta_f}{|\cos\theta_0 \cos\theta_f|}$$

$$\times \frac{\omega_p^2 + 49(\gamma_0 + \gamma_f)^2/16}{[(\omega - \omega_p)^2 + \gamma_0^2/4][(\omega - \omega_p)^2 + \gamma_f^2/4]} \bar{f}_n^2 , \qquad (7)$$

and for *s*-polarized photons incident on the grating foil,

$$P_{sn} = \frac{a^2\omega_p^2}{4c^2} \frac{\cos^2\theta_{0f}}{|\cos\theta_0 \cos\theta_f|} \bar{f}_n^2 . \qquad (8)$$

In both of these formulas the angle of observation θ_f satisfies the *n*th order of diffraction condition $\sin\theta_0 + (c/\omega_p)2\pi n/\delta$. In obtaining these results we have assumed that $\bar{f}(\rho)$ may be expanded in a Fourier series according to

$$\bar{f}(\rho) = \bar{f}(x) = \sum_{n=-\infty}^{\infty} \bar{f}_n e^{+2\pi i n x/\delta} , \qquad (9)$$

where δ is the repeat distance of the grating. The rulings are taken parallel with the *y* axis, and

[16] J. Brambring, *Z. Physik* 200, 186 (1967).

$$\bar{f}_n = \frac{1}{\delta} \int_{-\delta/2}^{\delta/2} \bar{f}(x)\, e^{-2\pi i n x/\delta}\, dx \,. \qquad (10)$$

One concludes that the probability of observing the resonance process in diffraction should be appreciably larger than in the systems studied by Raether and co-workers, since (1) SDF in "grating foils" should be much larger than in foils evaporated on flat surfaces and (2) diffraction of a given order concentrates the emitted light in narrow wedges of directions, while in the Raether arrangement light is emitted into a whole sphere of directions.

RADIATIVE DECAY OF COULOMB-STIMULATED PLASMONS IN SPHERES

The excitation by energetic electrons and the subsequent radiative decay of plasmons in small plasma spheres have been investigated using a quantum-theoretic approach. The cross section for dipole plasmon creation in a sphere of radius R by an energetic nonrelativistic electron with speed v is found to be

$$\sigma = \frac{36\pi e^2 R^2}{\hbar v} I(\omega_r R/v) \,, \qquad (11)$$

where $I(x) = x^{-1} \int_1^\infty dy\, y^{-3}\, j_1^2(xy)$, ω_r is the dipole plasmon eigenfrequency, and $j_1(z)$ is the spherical Bessel function of order 1. The distribution of radiation from the decay of a plasmon created by electron bombardment has been considered in detail. It is estimated that plasma decay light from electron bombardment of small, randomly distributed metal spheres suspended in a dielectric medium may be emitted with intensity comparable with that found in experiments on plasmon decay light from metal slabs. A detailed account of this work will appear in the *Physical Review*.

QUANTUM TREATMENT OF MULTIPLE REAL TRANSITIONS

A quantum mechanical derivation of the probability that an energetic particle, interacting with an extended many-particle system which possesses a large number of eigenstates lying close together in energy, will excite n of these states during an interaction time t has been completed. Transcribed into terms appropriate to a classical point particle, the result is the same as the familiar Poisson distribution. To our knowledge this is the first calculation of this distribution based on a quantum mechanical treatment.

ELECTRON MEAN FREE PATHS IN A FREE-ELECTRON GAS

The mean free path of low-energy electrons in a free-electron gas has been calculated using a many-body perturbation theory approach in which the effect of the exclusion principle in intermediate states is explicitly included. Results have been obtained for the case of a screened Coulomb potential for electron densities corresponding to real metals. It is found that although the correction for the operation of the exclusion principle in intermediate states acts to reduce the cross section, when the effect of the exclusion principle in final states is taken into account, the intermediate states correction is small. Thus it is found that the calculated mean free paths in metals are still considerably shorter than experimental values.

A more detailed account of this work is given in ORNL-TM-2072.

SURFACE PLASMON RESONANCE EFFECT IN GRATING DIFFRACTION

Recently, very precise data relevant to the Wood grating anomalies have been obtained by members of the Radiation Physics of Solids Group. They have studied the polarization of light by concave diffraction gratings in the wavelength region 4000 to 16,000 A. Representative data are shown on p. 189.

An explanation of these anomalies in terms of surface plasmon resonance is presented. One assumes that the surface plasmon is only slightly perturbed by the presence of density variations due to the grating structure. For example, the dispersion curve of the plasmon on a grating surface does not seem to be greatly different from that of a plasmon on a plane surface of the same material at least in the long-wavelength region. In this view, the resonances observed in first-order diffraction may be discussed in terms of the graph shown in Fig. 15.10, in which we depict a simple

ORNL-DWG 68-9698

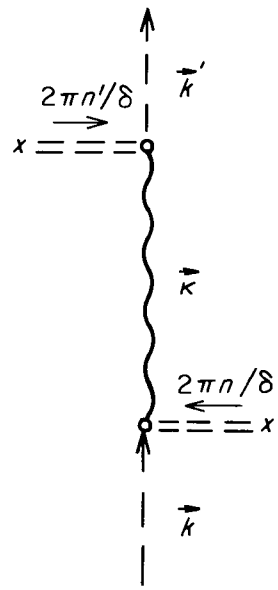

Fig. 15.10. Feynman Diagram for Second-Order Process Involving Grating Diffraction Through a Surface Plasmon Intermediate State.

second-order process. Here a photon of wave vector **k** in the region outside of the grating is incident upon the grating surface, which if perfectly plane would only specularly reflect the photon; a surface plasmon could not be excited under these conditions. Because there is a periodic density variation in the region of the surface, the grating may absorb momentum in a direction normal to the rulings and in multiples of $2\pi\hbar/\delta$, where δ is the distance between rulings. One assumes that the average grating surface lies in the x-y plane, that the gratings are parallel with the y axis, and that the wave vector **k** lies in the x-z plane. Thus at the lower vertex in the graph of Fig. 15.10, a surface plasmon with x momentum equal to $2\pi\hbar n/\delta$ plus the x component of the momentum of the incident photon may be created. The interaction Hamiltonian giving rise to this process may be written

$$H' = \frac{en_0}{c} \int \hat{\mathbf{A}} \cdot \hat{\mathbf{v}}\, f(\mathbf{r})\, d\tau\,, \qquad (12)$$

where $\hat{\mathbf{A}}$ is the vector potential operator of the photon, $\hat{\mathbf{v}}$ is the velocity operator of the surface plasmon, and $f(\mathbf{r})$ is the fractional variation of the grating electronic density from its value n_0 deep in the metal. In order for its effect to be observed in a first-order diffraction direction, the plasmon must in general get rid of some of the x momentum which it acquired from the grating by making a second encounter, indicated by the top vertex, in which a photon of wave vector $\mathbf{k}'$ is emitted. The compound process proceeds through an intermediate surface plasmon state; it is well known that when the energy of an intermediate quantum state is nearly the same as that of the initial state a resonance in the cross section for the compound process will occur. Thus, from the theory of quantum resonant intermediate states, one could expect that P_n, the probability for the process under discussion, might have the typical Lorentzian form,

$$P_n \sim \frac{|F_n F_{n\pm 1}|^2}{[\omega_k - \Omega(\kappa_n)]^2 + [\gamma(\kappa_n)/2]^2}\,, \qquad (13)$$

valid in the neighborhood of the frequency for which the denominator has its minimum. Interference with the first-order diffracted beam has been neglected here. In this expression $\kappa_n = k_x + 2\pi n/\delta$, $\omega_k = c|\mathbf{k}|$, $\Omega(|\kappa|)$ and $\gamma|\kappa|$ are the eigenfrequency and damping rate, respectively, of a surface plasmon with wave vector κ, and F_n is proportional to the average value of the nth Fourier coefficient of the electronic density in the neighborhood of the grating surface. Possible higher-order processes giving rise to a probability function containing a product of several resonance denominators may also be important in this connection.

The condition for intermediate state resonance is that the energy of the virtual surface plasmon should be equal to the energy of the incoming photon, that is, $\omega_\kappa = \Omega(\kappa_n)$; dropping the subscript on ω_k,

$$\omega = \Omega\left(\left|\frac{\omega}{c}\sin\alpha + \frac{2\pi n}{\delta}\right|\right)\,, \qquad (14)$$

where α is the angle between **k** and the normal to the grating surface. Thus if the wavelength corresponding to the center of a resonance of given order n is measured as a function of the angle of incidence α, one may construct the $\Omega(\kappa)$ curve by graphical methods. Such a construction has been carried out and yields the surface plasmon dispersion curves for aluminum and gold graphed in Fig. 15.11.

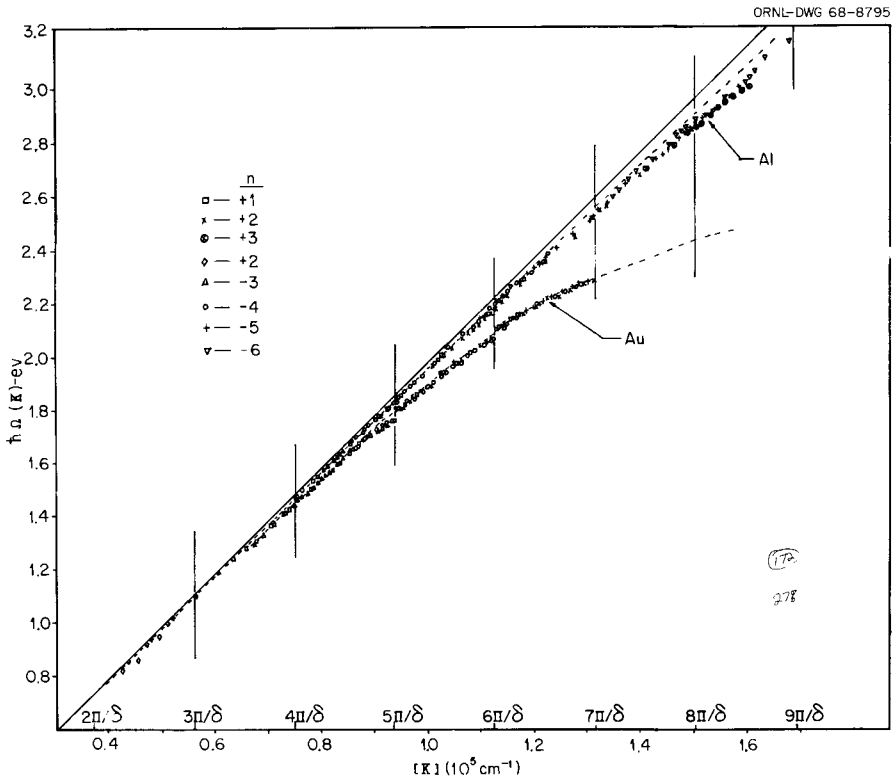

Fig. 15.11. Surface Plasmon Dispersion Relation for an Aluminum Grating Surface Inferred from Data on Grating Anomalies.

ELECTRON PENETRATION IN METALS

In solids our understanding of the various modes of energy loss by low-energy electrons (0 to 10 kev) is only semiquantitative at present. To improve this understanding, probabilities for the interaction of electrons with electrons and ions in aluminum metal have been estimated using simple theoretical models for volume and surface plasmon excitation, single-electron excitation, etc. These interactions give rise to large numbers of secondary, tertiary, and higher-order electrons, each of which has similar possibilities for interaction. Preliminary calculations of the attenuation of an electron beam in foils a few hundred atoms thick compare favorably with experimental results. Calculations made originally for 0- to 1.5-kev electrons are currently being extended to higher energies. Such multiple-collision calculations are necessary in order to obtain a better understanding of single-collision cross sections in this range of energies, because single-collision experiments are extremely difficult to perform. The mechanisms of these interactions are of interest in assessing human exposure.

SECONDARY ELECTRON EMISSION DUE TO THE DECAY OF COULOMB-STIMULATED SURFACE PLASMONS

The effect of surface plasmon decay in the spectrum of electrons ejected from a metal by energetic charged-particle bombardment has been investigated theoretically. The probability of secondary electron emission through the intermediary of a surface plasmon is obtained by treating the surface plasmon as a virtually excited quantum state. The decay probability of the plasmon is computed by expanding the wave function for metal electrons in terms of products of eigenfunctions of the momentum parallel to the surface and eigenfunctions of a simple static potential barrier at the surface. Analytical expressions have been obtained for the de-

cay rate to (1) electron states outside the metal, (2) bound states in the metal, and (3) free states in the metal. The yield of surface plasmon decay electrons for the case of 235-ev electrons normally incident on a magnesium surface is found to be ~ 0.2 electron per incident electron. The spectrum of these electrons should exhibit a maximum at an energy approximately equal to the surface plasmon energy in magnesium minus the work function of the same metal.

POTENTIAL ENERGY CURVES FOR DIATOMIC MOLECULES

Klein's semiclassical method for obtaining the potential energy U_e as a function of internuclear distance R had previously been programmed for high-speed computer. Other programs have been written and tested to calculate from the Schrödinger equation the vibrational wave functions and energy eigenvalues (Fig. 15.12). The energies, as functions of vibrational quantum number v and rotational quantum number J, agree with the experimental values (from which the potential energy was computed) to within 0.0001 ev. The energy E_0 and angular momentum quantum number J_0 at which "orbiting" occurs have been computed from the theoretical relations $E_0 = U_e(R_0) + \frac{1}{2}R_0\, U_e'(R_0)$ and $J_0(J_0 + 1)\hbar^2 = \mu R_0^3\, U_e'(R_0)$, where R_0 is the orbiting radius, $\hbar$ is Dirac's constant, and μ is the reduced mass of the two nuclei.

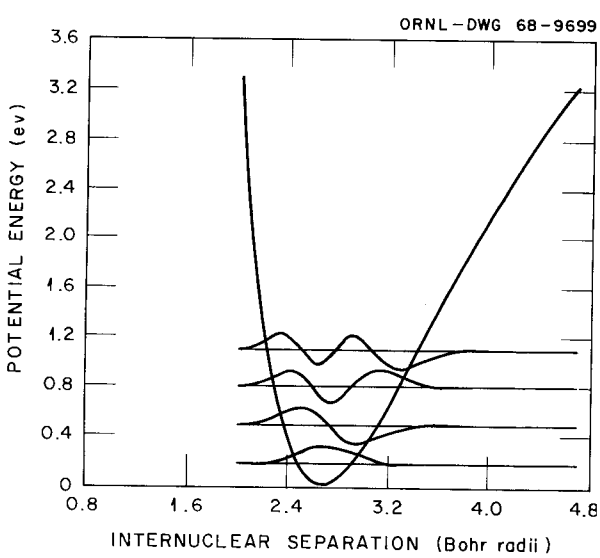

Fig. 15.12. Wave Functions for the (v, J) Energy States (0, 0), (1, 0), (2, 0), and (3, 0) Superposed on the Corrected Rydberg-Klein Potential Energy Curve of $H^{81}Br$.

EXCHANGE AND NONADIABATIC POLARIZATION EFFECTS IN LOW-ENERGY ELECTRON SCATTERING

The treatment of low-energy electron scattering by atomic and molecular systems is complicated by the simultaneous effects of the distortion of the scattering system by the incident electron and the exchange of the incident electron with those of the target. A method for treating the former energy-dependent target distortion problem has been developed and reported previously.[17] The method was first applied in the case of positron scattering, where no exchange effects are encountered. A successful treatment of both polarization and exchange in the electron scattering problem has been developed and applied to simple and more complicated atomic systems.

Dynamic Exchange

We consider electron-hydrogen scattering and investigate exchange and polarization by a perturbation method. A further extension is then made to many electron systems.

The Hamiltonian for the electron-hydrogen problem in Rydberg atomic units is

$$H = -\nabla_1^2 - \frac{2}{r_1} - \nabla_2^2 - \frac{2}{r_2} + W(r_1, r_2)\,, \qquad (15)$$

where $W(r_1, r_2) = 2/r_{12}$ and r_{12} is the separation of electrons 1 and 2. The isolated target system satisfies

$$H_0\phi_n = \epsilon_n\phi_n\,, \qquad (16)$$

and the wave function for the scattering system is written as

$$\Psi(\mathbf{r}_1, \mathbf{r}_2) = \psi(\mathbf{r}_2)[\phi_0(\mathbf{r}_1) + \chi(\mathbf{r}_1, \mathbf{r}_2)] \pm \psi(\mathbf{r}_1)[\phi_0(\mathbf{r}_2) + \chi(\mathbf{r}_1, \mathbf{r}_2)]\,, \qquad (17)$$

[17] *Health Phys. Div. Ann. Progr. Rept. July 31, 1967*, ORNL-4168, p. 124.

where the spin functions have been omitted and the $\pm$ refers to the singlet and triplet states of the two-electron system. The Schrödinger equation for the scattering problem takes the form:

$$\left(-\nabla_1^2 - \frac{2}{r_1} - \nabla_2^2 - \frac{2}{r_2} + W\right)\{\psi(r_2)[\phi_0(r_1) + \chi(r_1, r_2)] \pm \psi(r_1)[\phi_0(r_2) + \chi(r_1, r_2)]\}$$
$$= E\{\psi(r_2)[\phi_0(r_1) + \chi(r_1, r_2)] \pm \psi(r_1)[\phi_0(r_2) + \chi(r_1, r_2)]\}, \quad (18)$$

where $E = E_0 + k^2$ is the total energy, E_0 being the ground energy of hydrogen and k^2 the kinetic energy of the scattered particle. The boundary conditions

$$\langle \phi_0, \chi \rangle = 0 ; \quad \langle \phi_0, \phi_0 \rangle = 1 ,$$
$$\psi(r) \underset{r\to\infty}{\to} \frac{\sin(kr - l\pi/2 + \delta_l)}{kr} \quad (19)$$

are imposed on the solutions to Eq. (18). We employ the variational method in order to obtain the scattering equation for ψ. Thus,

$$\delta \int \Psi^*(\mathbf{r}_1, \mathbf{r}_2)(H - E)\Psi(\mathbf{r}_1, \mathbf{r}_2)\, d\tau = 0 . \quad (20)$$

We first note from the form of ψ in Eq. (7) and the Schrödinger equation (18) that the direct terms in the integral (20) are identical to those of the corresponding positron equations investigated earlier (except for a change in sign of W). Thus, the analysis of these terms has been completed, and the dynamic polarization potential defined previously[17] appears in the scattering equation in the same form. However, in addition we have here the exchange terms, which make the scattering equation considerably more complicated. Proceeding through the perturbation method whereby terms of second order in W and χ are ignored, making use of the orthogonality relation (19) and Eq. (16), and having utilized the previous analysis for the direct terms, the scattering equation becomes

$$-\nabla_2^2 \psi(\mathbf{r}_2) - \left\langle \phi_0 \left| \frac{2}{r_2} - W \right| \phi_0 \right\rangle \psi(\mathbf{r}_2)$$
$$+ [V_p(\mathbf{r}_2) - k^2]\psi(\mathbf{r}_2) = \mp\Big\{(E_0 - k^2) \int \phi_0(\mathbf{r}_1)\psi(\mathbf{r}_1)d\mathbf{r}_1$$
$$\times \phi_0(\mathbf{r}_2) - k^2[\int \phi_0(\mathbf{r}_1)\psi(\mathbf{r}_1)\chi(\mathbf{r}_1, \mathbf{r}_2)d\mathbf{r}_1$$
$$+ \int \chi(\mathbf{r}_1, \mathbf{r}_2)\psi(\mathbf{r}_1)\, d\mathbf{r}_1 \cdot \phi_0(\mathbf{r}_2)]$$
$$+ \int \chi(\mathbf{r}_1, \mathbf{r}_2)\left(-\nabla_1^2 - \frac{2}{r_1}\right)\psi(\mathbf{r}_1)\, d\mathbf{r}_1 \cdot \phi_0(\mathbf{r}_2)$$
$$+ \int \phi_0(\mathbf{r}_1)\left(-\nabla_2^2 - \frac{2}{r_2}\right)\psi(\mathbf{r}_1)\chi(\mathbf{r}_1, \mathbf{r}_2)\, d\mathbf{r}_1$$
$$+ \phi_0(\mathbf{r}_2) \int \phi_0(\mathbf{r}_1)W(\mathbf{r}_1, \mathbf{r}_2)\psi(\mathbf{r}_1)\, d\mathbf{r}_1\Big\} . \quad (21)$$

In this equation $V_p(r_2)$ is the dynamic polarization potential derived previously,[17] and the $\mp$ signs go with the singlet/triplet states, respectively.

The scattering equation (21) is excessively complicated as it now stands. The difficulties arise in the exchange terms on the right-hand side containing the perturbation χ. However, within the approximation made in the perturbation calculation of χ, these exchange polarization terms are negligible. Thus we shall drop the members on the right-hand side containing integrals over χ. Decomposing the differential equation by the usual partial wave analysis yields the radial equations,

$$\frac{d^2}{dr_2^2} f_l(r_2) + \left[\frac{2}{r_2} - V_c(r_2) - V_p(r_2) + k^2\right] f_l(r_2)$$
$$= \pm P_{1s}(r_2)\Big\{(E_0 - k^2)\delta_{l0} \int_0^\infty f_l(\rho) P_{1s}(\rho)\, d\rho$$
$$+ \frac{2}{2l+1}\Big[r^l \int_0^\infty f_l(\rho)P_{1s}(\rho)\rho^{-(l+1)}\, d\rho$$
$$+ r^{-(l+1)} \int_0^r f_l(\rho) P_{1s}(\rho)\, \rho^l\, d\rho$$
$$- r^2 \int_0^r f_l(\rho) P_{1s}(\rho)\, \rho^{-(l+1)}\, d\rho\Big]\Big\} . \quad (22)$$

Here f_l is the lth partial wave, and P_{1s} is the reduced ground-state radial function of hydrogen; $V_c(r_2) = \langle \phi_0 W \phi_0 \rangle$. This equation is of the form of the adiabatic exchange equation previously investigated in electron scattering by alkali atoms[18] with the difference that $V_p(r_2)$ is now the dynamic polarization potential.

[18] W. R. Garrett, *Phys. Rev.* **140**, A705 (1965).

The equations for electron-hydrogen scattering have been solved, and results for singlet and triplet phase shifts are shown in Table 15.3. Comparison is made in Table 15.3 with the very elaborate variational calculation of Schwartz[19] and with the nonadiabatic method of Temkin.[20] It is seen that the agreement between the calculations is very good. However, the value of the present analysis lies not in its ability to yield a reliable cross section for low-energy electron-hydrogen scattering but in the fact that the analysis may be extended to more complicated systems, whereas other methods, for example, the variation method of Schwartz, cannot.

Nonadiabatic Distortion of a Many-Electron System

We consider electron scattering from a system of N electrons whose Hamiltonian is

$$H^{(\mathrm{tar})} = \sum_{i=1}^{N} -\nabla_i^2 - \sum_{i=1}^{N} \frac{2Z}{r_i} + \sum_{i>j}^{N}\sum \frac{2}{r_{ij}} \qquad (23)$$

and whose unperturbed wave function is a Slater determinant

$$\Phi_0 = \frac{1}{\sqrt{N!}} \det(\phi_1 \ldots \phi_i \ldots \phi_n) , \qquad (24)$$

with

$$\langle \phi_i, \phi_j \rangle = \delta_{ij} , \qquad (25)$$

where $\phi_i(r_i)$ is a single-electron spin orbital.

The total Hamiltonian can then be written

$$H = -\nabla_f^2 - \frac{2Z}{r_f} + \sum_{j=1}^{N} \frac{2}{r_{ij}} + H^{(\mathrm{tar})} , \qquad (26)$$

where $\mathbf{r}_f$ is the coordinate of the free electron.

Now we consider the motion of the incoming electron to be coupled with that of the bound electrons, producing new orbitals

$$\phi_i' \equiv \phi_i'(\mathbf{r}_1, \mathbf{r}_f) = \phi_i(\mathbf{r}_i) + \chi_i(\mathbf{r}_i, \mathbf{r}_f) . \qquad (27)$$

Table 15.3. Electron-Hydrogen Phase Shifts, $l = 0$ and $l = 1$

Results are compared with those of Temkin[a] and of Schwartz;[b] $k = \sqrt{E}$, where E is electron energy in rydbergs (13.6 ev)

Singlet				
	$l = 0; n_0^+$			$l = 1; n_1^+$
k	Temkin	Variational (Schwartz)	Present, Nonadiabatic	Present, P-wave
0.0	5.6	5.95		
0.1	2.59	2.553	2.612	+0.0071
0.2	2.11	2.067	2.141	0.0181
0.3	1.74	1.696	1.751	0.020
0.4	1.45	1.415	1.452	0.0095
0.5	1.23	1.202	1.215	−0.0080
0.6		1.041	1.029	−0.0277
0.7		0.930	0.887	−0.043
0.8	0.87	0.886	0.786	−0.052
Triplet				
	$l = 0; n_0^-$			$l = 1; n_1^-$
k	Temkin	Variational (Schwartz)	Present, Nonadiabatic	Present, P-wave
0.0	1.76	1.77		
0.1	2.942	2.939	2.955	0.0118
0.2	2.723	2.717	2.733	0.0523
0.3	2.516	2.500	2.529	0.122
0.4	2.301	2.294	2.321	0.207
0.5	2.112	2.105	2.129	0.288
0.6		1.933	1.956	0.351
0.7		1.780	1.800	0.398
0.8	1.647	1.643	1.662	0.423

[a]See ref. 20.
[b]See ref. 19.

[19]C. Schwartz, *Phys. Rev.* **124**, 1468 (1961).
[20]A. Temkin, *Phys. Rev.* **126**, 130 (1962).

We now take the total wave functions to be

$$\Psi(r_1, r_2, \ldots r_N, r_f)$$

$$= \psi(r_f) \frac{1}{\sqrt{N!}} \det [\phi'_1(r_1, r_f) \ldots \phi'_N(r_N, r_f)] . \quad (28)$$

We now determine equations for the perturbed orbitals by application of

$$\delta \int \Psi^* (H - E) \Psi \, d\tau = 0 , \quad (29)$$

where we apply a limited variation $\delta\phi_i$ for each bound orbital but omitting $\psi(r_f)$.

Proceeding as in the single-electron problem, where use is made of the orthogonality properties; where $2/r_{if}$, the interaction between bound and free electrons, is considered as a perturbation; and where second-order terms are omitted, we get, after a horrendous amount of algebra, the following equation for the perturbation $\psi_i(r_i)$ of the ith spin orbital:

$$\psi(r_f) \left[-\nabla_i^2 - \frac{2Z}{r_i} + \sum_{j=1}^{N} \int \phi_j^*(r_2) \frac{2}{r_{i2}} \phi_j(r_2) \, d\mathbf{r}_2 \right.$$

$$\left. - \epsilon_i^0 - \nabla_f^2 \right] \chi_i(r_i, r_f) - 2\nabla_f \chi_i(r_i, r_f) \cdot \nabla_f \psi_f(r_f)$$

$$= \phi_i(r_i) \left\{ \sum_{\substack{j=1 \\ j \neq i}}^{N} \left[\int \phi_j^*(r_2) \frac{2}{r_{2f}} \phi_i(r_2) \chi_j(r_i, r_f) \, d\mathbf{r}_2 \right. \right.$$

$$\left. - \int \phi_j^*(r_2) \frac{2}{r_{2f}} \phi_j(r_2) \chi_i(r_i, r_f) \, d\mathbf{r}_2 \right]$$

$$\left. - \frac{2}{r_{if}} \right\} \psi(r_f) + V_{\text{exch}}^{\text{perturbed}} (r_i, r_f) . \quad (30)$$

This equation is the Hartree-Fock equation for the perturbation χ_i of the ith spin orbital and is analogous to the perturbation equation for the single-electron orbital of hydrogen in the same way that the ordinary Hartree-Fock equation for the unperturbed orbital ϕ_i is analogous to the corresponding bound-state hydrogen-like equation. We again drop the perturbation exchange terms in these equations, indicated by $V_{\text{exch}}^{\text{perturbed}} (r_i, r_f)$ in Eq. (30).

The remaining considerations are the dynamic terms ∇_f and ∇_f^2 in Eq. (20), these being the momentum operator and kinetic energy operator for the incident electron. We can now treat these exactly as in the one-electron case, that is, through the "asymptotic approximation" introduced in ref. 17, Eq. (13). This leads to the perturbation equation

$$\left[-\nabla_i^2 - \frac{2Z}{r_i} + V_a(r_i) - \epsilon_0^i + 3k^2 \right] \chi_i(\mathbf{r}_i, \mathbf{r}_f)$$

$$= \left[V_{\text{exch}}(r_f) + V_a(r_f) - \frac{2}{r_{if}} \right] \phi_i(\mathbf{r}_i) , \quad (31)$$

where $V_a(r_i)$ is the sum on the left of Eq. (20) and $V_{\text{exch}}(r_f)$ and $V_a(r_f)$ are the two sums on the right side of Eq. (20). This is a perturbed Hartree-Fock orbital equation which can be solved in the usual Hartree-Fock procedure. Solutions for $\chi_i(r_i, r_f)$ yield the dynamic polarization potential

$$V_p(r_f) = \sum_i \int \phi_i^*(r_i) \frac{2}{r_{if}} \chi_i(r_i, r_f) \, d\mathbf{r}_i , \quad (32)$$

which can then be used in describing the electron scattering problem.

The set of equations (31) is being programmed for solution, and application to electron scattering on alkali atoms and noble-gas atoms is anticipated.

16. Interaction of Radiation with Liquids and Solids

E. T. Arakawa R. D. Birkhoff

J. J. Cowan[1]
L. C. Emerson
R. N. Hamm
J. A. Harter
J. D. Hayes[2]
A. G. Kenerly[3]
R. A. MacRae[4]
M. Y. Nakai[5]
S. J. Nalley[1]
Linda R. Painter[2]
Margaret S. Riedinger[2]
L. H. Toburen[6]
R. C. Vehse[2]
Mary W. Williams[4]

OPTICAL PROPERTIES OF ALUMINUM OXIDE

Studies of the optical properties of insulating materials[7] have been extended to include Al_2O_3. Transmittance measurements on anodized Al_2O_3 films have been made for incident photon energies from 5 to 18 ev and the imaginary part, $k(E)$, of the refractive index calculated. The results for $k(E)$ as a function of incident photon energy are presented in Fig. 16.1. Reflectance measurements on single-crystal corundum (α-alumina) have been made at four angles of incidence from 8.5 to 28.5 ev. In addition, transmittance measurements have been obtained from 7.7 to 8.6 ev in the vicinity of the main absorption edge. The measured transmittance and reflectance for crystalline Al_2O_3 are presented in Fig. 16.2.

Below 8 ev Al_2O_3 is transmitting, and the near-normal reflectance yields $n(E)$, the real part of the refractive index, directly. Above 23 ev an analysis of the measured reflectance as a function of the angle of incidence gives reasonably consistent values of $n(E)$ and $k(E)$. Using these values of $n(E)$ and $k(E)$ in the energy ranges 0 to 8 ev and 23 to 28.5 ev, the optical constants in the energy range 8 to 23 ev were obtained from the reflectance at 20° angle of incidence by means of a Kramers-Kronig analysis.[8] The dielectric constants, $\epsilon_1(E)$ and $\epsilon_2(E)$, where $\epsilon_1 = n^2 - k^2$ and $\epsilon_2 = 2nk$, are

[1]Radiological Health Physics Fellow.

[2]USAEC Special Health Physics Fellow.

[3]On loan from Instrumentation and Controls Division.

[4]Consultant.

[5]On loan from Thermonuclear Division.

[6]Oak Ridge Graduate Fellow.

[7]E. T. Arakawa *et al.*, *Health Phys. Div. Ann. Progr. Rept. July 31, 1967*, ORNL-4168, pp. 137–40.

[8]E. T. Arakawa *et al.*, *Health Phys. Div. Ann. Progr. Rept. July 31, 1967*, ORNL-4168, pp. 140–41.

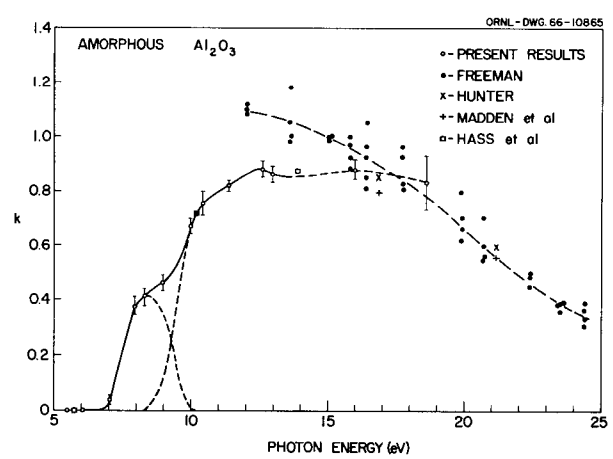

Fig. 16.1. Extinction Coefficient of Anodized Al_2O_3 Films vs Incident Photon Energy.

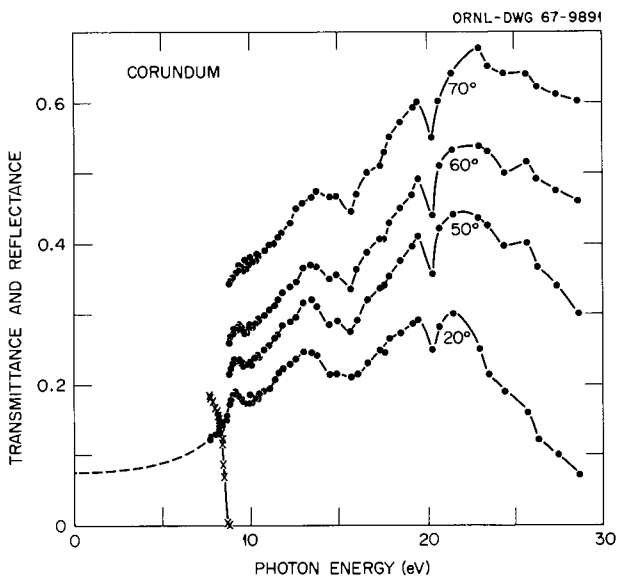

Fig. 16.2. Transmittance and Reflectance of Single-Crystal Al_2O_3 vs Incident Photon Energy. X, transmittance; ●, reflectance at 20, 50, 60, and 70° angles of incidence; ---, calculated normal incidence reflectance.

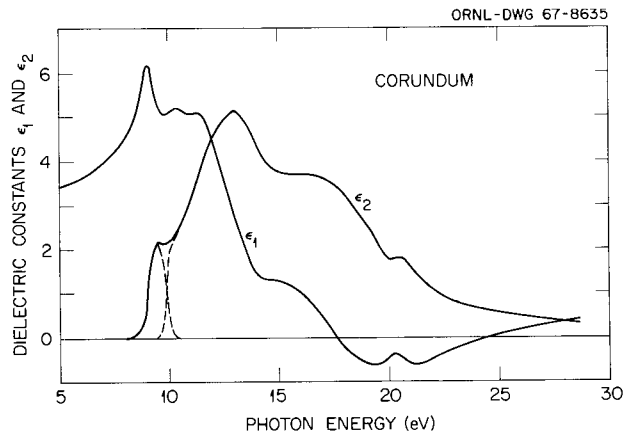

Fig. 16.3. Dielectric Constants of Single-Crystal Al_2O_3 vs Incident Photon Energy.

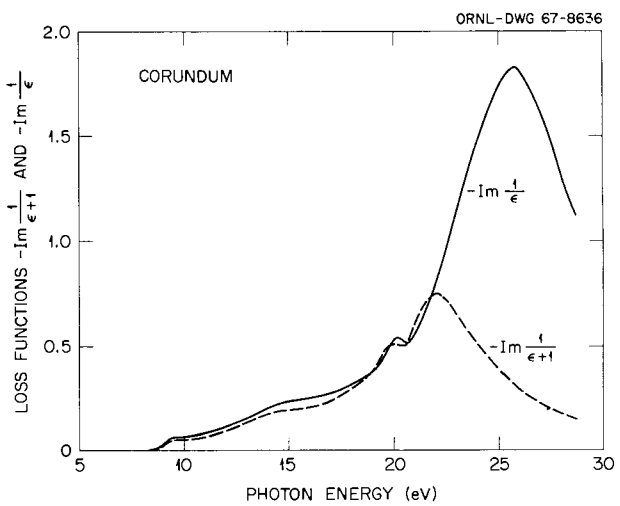

Fig. 16.4. Energy-Loss Functions of Single-Crystal Al_2O_3 vs Incident Photon Energy.

shown in Fig. 16.3. The energy-loss functions $-\mathrm{Im}\,(\epsilon+1)^{-1}$ and $-\mathrm{Im}\,(\epsilon)^{-1}$, calculated from the experimentally determined values of $\epsilon = \epsilon_1 + i\epsilon_2$, are shown in Fig. 16.4.

The main absorption edge is seen to occur at 6.8 ev for anodized Al_2O_3 films and at (8.55 ± 0.05) ev for single-crystal Al_2O_3. Structure in k (Fig. 16.1) or ϵ_2 (Fig. 16.3) above the absorption edge can be interpreted in terms of an exciton, a band-to-band absorption edge, and interband transitions for both anodized and single-crystal Al_2O_3. For the anodized films the exciton is estimated to be at (8.4 ± 0.3) ev and the band-to-band transition edge at (9.4 ± 0.4) ev as indicated in Fig. 16.1. Broad structure in k indicates possible interband transitions at 12.5 and 16 ev. For the single-crystal Al_2O_3 the exciton is estimated to be at (9.5 ± 0.1) ev and the band-to-band transition edge at (9.9 ± 0.1) ev as indicated in Fig. 16.3. Interband transitions occur at about 13.0, 16.5, and 20.5 ev. It is seen that the band-to-band transition edge is the same for anodized films as for single-crystal Al_2O_3 to within the experimental accuracies indicated. It is not known why the transmission cutoff and the exciton energy should be different in the two forms of Al_2O_3. The interband transitions at 12.5 and 16 ev in the anodized films appear to correspond to those at 13 and 16.5 ev in the corundum.

The total number of valence electrons per Al_2O_3 molecule is 24, which yields a theoretical free-electron plasma energy,[7] assuming an effective electron mass equal to the free-electron mass, of 27.8 ev. It is seen in Fig. 16.4 that $-\mathrm{Im}\,(\epsilon)^{-1}$ for single-crystal Al_2O_3 has a maximum at 25.8 ev. This corresponds to a plasma resonance, since all

of the conditions for a plasma resonance[9] are satisfied. Thus we would expect that high-energy electrons on traversing single-crystal Al_2O_3 (corundum) would lose 25.8 ev, or integral multiples of this energy, in creating volume plasma oscillations. This plasma resonance would involve all 24 valence electrons per Al_2O_3 molecule, but its value would be shifted from the free-electron value because of the existence of interband transitions. In the same way the observed peak in $-\mathrm{Im}\,(\epsilon + 1)^{-1}$ at 22.0 ev implies that high-energy electrons would lose integral multiples of this energy in creating surface plasma oscillations. Unfortunately, at this time, characteristic electron energy-loss measurements are unavailable for corundum.

As with the other insulators studied previously,[7] sum rule calculations for single-crystal Al_2O_3 explain the close proximity of the theoretical free-electron plasma energy and the experimental plasma energy given by the peak in $-\mathrm{Im}\,(\epsilon)^{-1}$.

OPTICAL PROPERTIES OF VACUUM-EVAPORATED FILMS OF POLYCRYSTALLINE TELLURIUM

The room-temperature optical constants $n(E)$ and $k(E)$ of polycrystalline films of tellurium evaporated in situ have been determined in the energy range from 3 to 38 ev. The films used were of high quality, having reflectances significantly higher than previously reported in the literature. Various experimental procedures were used in order to obtain the optical constants as accurately as possible over different energy ranges. Reflectance measurements were made at angles of incidence of 20, 45, and 70° from 3 to 25 ev, transmission measurements from 18 to 26 ev, and critical-angle measurements from 28 to 38 ev. Values of $n(E)$ and $k(E)$ from 3 to 14 ev were obtained by a Kramers-Kronig[8,10] analysis of the 20° reflectance data, values of $n(E)$ above 14 ev were determined from the critical-angle measurements and from a least-squares fit of Fresnel's equations to the multiangle reflectances, and values of $k(E)$ above 18 ev were obtained from transmission measurements. The optical constants are shown in Fig. 16.5. The real and imaginary parts of the complex dielectric constant, $\epsilon(E) = \epsilon_1(E) + i\epsilon_2(E)$, and the energy-loss functions $-\mathrm{Im}\,(\epsilon + 1)^{-1}$ and $-\mathrm{Im}\,(\epsilon)^{-1}$ were calculated from $n(E)$ and $k(E)$. These are shown in Figs. 16.6 and 16.7.

The optical properties of tellurium are very similar to those of selenium.[11] Structure in $\epsilon_2(E)$ between 7 and 9 ev is attributed to interband transitions. The main structure in the energy-loss function $-\mathrm{Im}\,(\epsilon + 1)^{-1}$ occurs at 11.3 ev and in $-\mathrm{Im}\,(\epsilon)^{-1}$ at 5.6 and 17.2 ev. This is in good agreement with the characteristic electron energy losses observed by Robins[12] at 5.2, 11.8, and 17.0 ev. From our optical data the 11.8-ev electron energy loss is identified with the creation of surface plasma oscillations and the 17.0 ev loss with the creation of volume plasma oscillations involving all six valence electrons per Te atom in the $5s^2 5p^4$ electron configuration. The optical data do not allow positive identification of the 5.2 ev electron energy loss.

OPTICAL AND PHOTOEMISSION MEASUREMENTS FOR COPPER, NICKEL, AND PALLADIUM

Photoelectric emission measurements[13] have been extended to include copper and the results correlated with published optical data for this material. Additional photoelectric emission data have been obtained for nickel and palladium, as well as measurements of the optical properties. These data have resulted in a more definite interpretation of the photoelectric effect in nickel and palladium than was previously possible.

Photoelectron current vs retarding voltage measurements were obtained as previously, but these data have been reduced to photoelectron energy distribution curves more efficiently and with some increase in accuracy. The number of electrons emitted with a given energy Ve is given by

$$\lim_{\Delta V \to 0} \left(\frac{\Delta I}{\Delta V} \right),$$

[9] H. Ehrenreich and H. R. Philipp, *Proc. Intern. Conf. Phys. Semiconductors*, p. 367, Institute of Physics, London, 1962.

[10] R. A. MacRae, E. T. Arakawa, and M. W. Williams, *Phys. Rev.* **162**, 615 (1967).

[11] E. T. Arakawa *et al.*, *Health Phys. Div. Ann. Progr. Rept. July 31, 1967*, ORNL-4168, pp. 141–42.

[12] J. L. Robins, *Proc. Phys. Soc. (London)* **79**, 119 (1962).

[13] E. T. Arakawa *et al.*, *Health Phys. Div. Ann. Progr. Rept. July 31, 1967*, ORNL-4168, pp. 146–48.

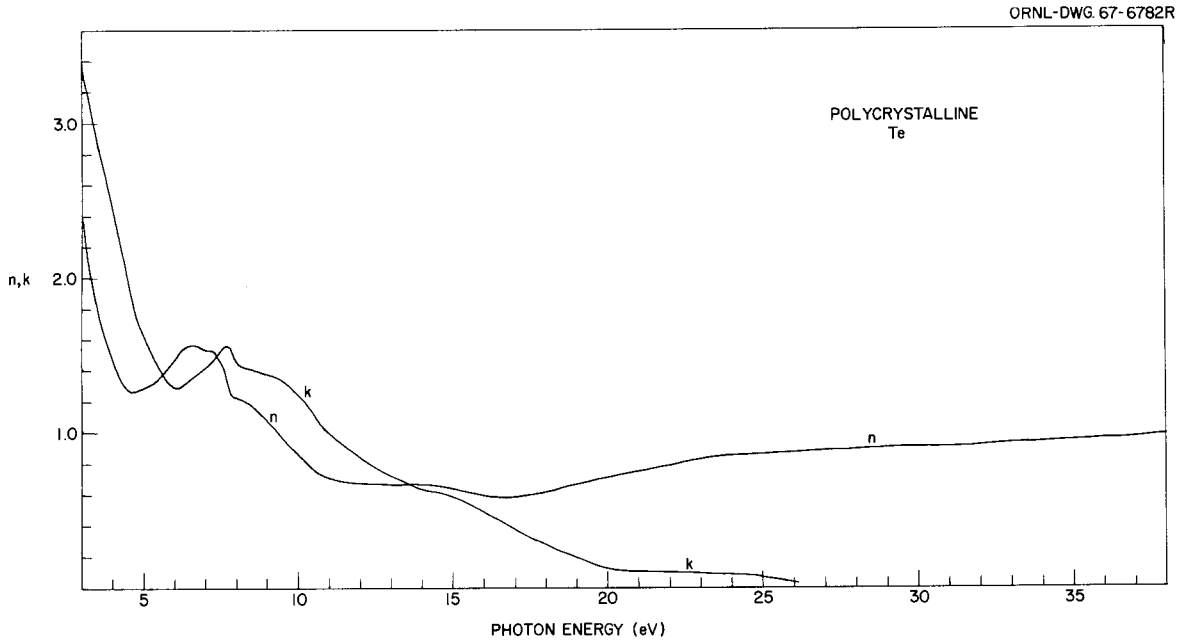

Fig. 16.5. Optical Constants of Vacuum-Evaporated Tellurium vs Incident Photon Energy.

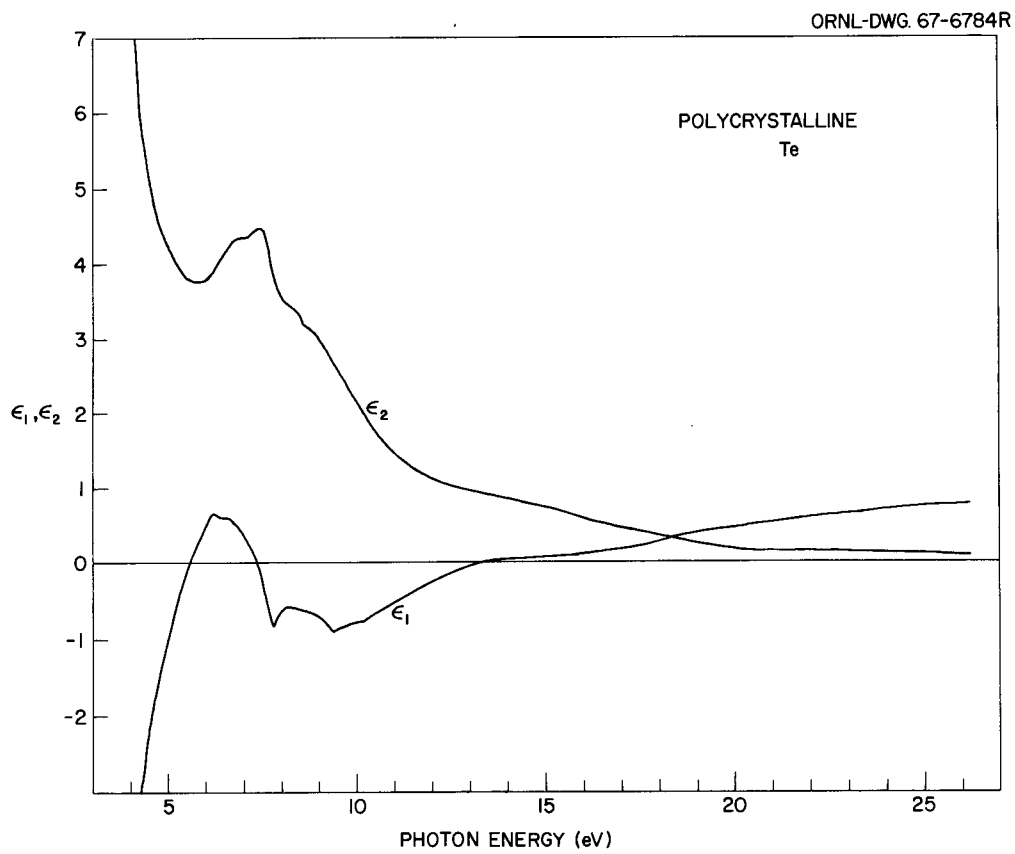

Fig. 16.6. Dielectric Constants of Vacuum-Evaporated Tellurium vs Incident Photon Energy.

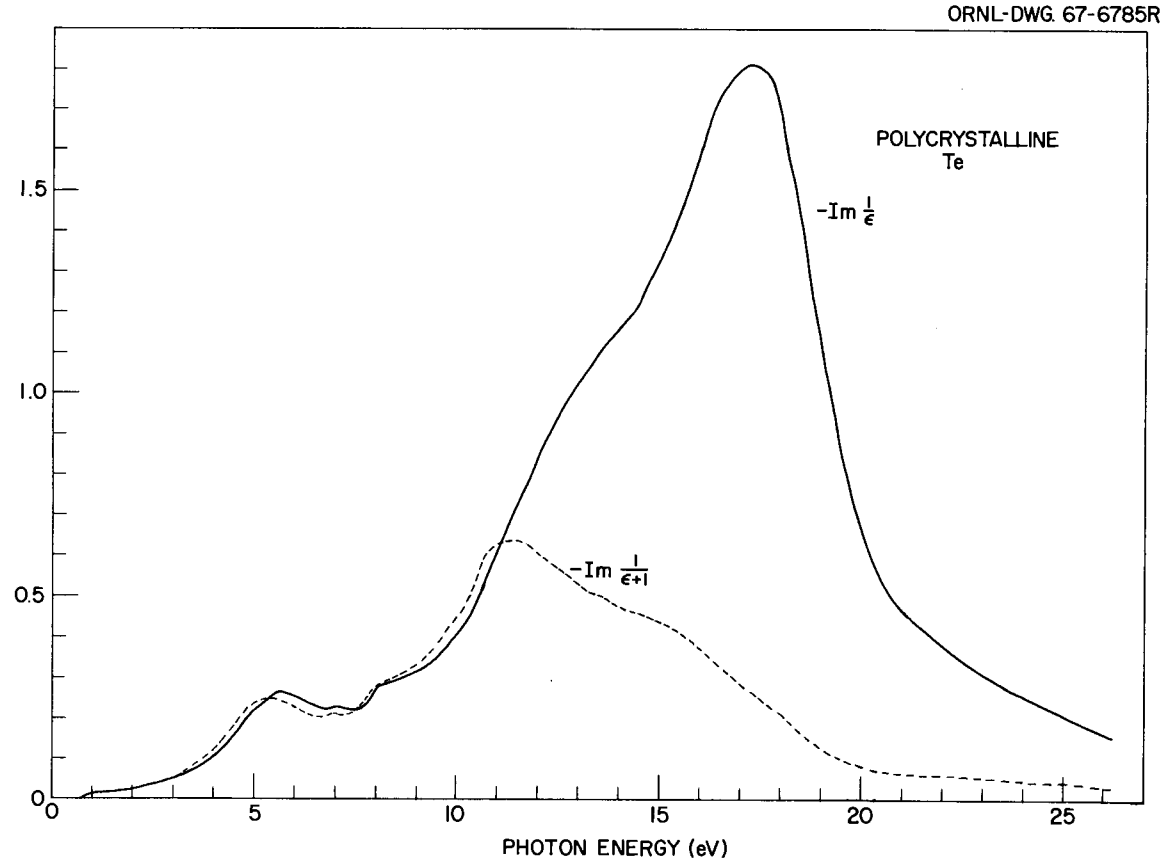

Fig. 16.7. Energy-Loss Functions of Vacuum-Evaporated Tellurium vs Incident Photon Energy.

where I is the photoelectric current and V the retarding potential difference. This quantity was determined by numerical differentiation using a computer program which fitted seven successive points to a second-degree polynomial. The normalized energy distribution curves were then plotted using Calcomp plotting equipment. Typical data and the analysis obtained are shown in Fig. 16.8.

Photoelectron energy distribution curves for copper in the photon energy region 10.2 to 20.4 ev are shown in Fig. 16.9. The curves are plotted so that the energy scale is relative to the Fermi level; that is, $E^* = E - h\nu + \phi$, where E is the energy of the emitted electron, $h\nu$ is the energy of the incident photon, and ϕ is the work function, which is 4.4 ev for copper. Persistent structure appears for values of E^* of −2.6, −4.0, −6.8, −8.6, and −12.0 ev, and published optical data[14–16] for copper enable identification to be made of some of this structure in the photoelectron energy distribution curves. The sharp structure at $E^* = -2.6$ ev is due to the d-band peak in the density of states of the valence band of copper. Structure at $E^* = -4.0$ ev and at $E^* = -6.8$ ev has not been positively identified. The structure at $E^* = -8.6$ ev appears to be due to photoelectron excitation of a 6-ev interband transition, while the structure at −12.0 ev is consistent with the interpretation that 9.4-ev volume plasma oscillations are excited by the photoelectrons prior to emission.

In Fig. 16.10 photoelectron energy distributions for palladium are compared with measured optical constants and calculated energy-loss functions.

[14]B. R. Cooper, H. Ehrenreich, and H. R. Philipp, *Phys. Rev.* **138A**, 494 (1965).

[15]D. Beaglehole, *Proc. Phys. Soc. (London)* **85**, 1007 (1965).

[16]L. R. Canfield and G. Hass, *J. Opt. Soc. Am.* **55**, 61 (1965).

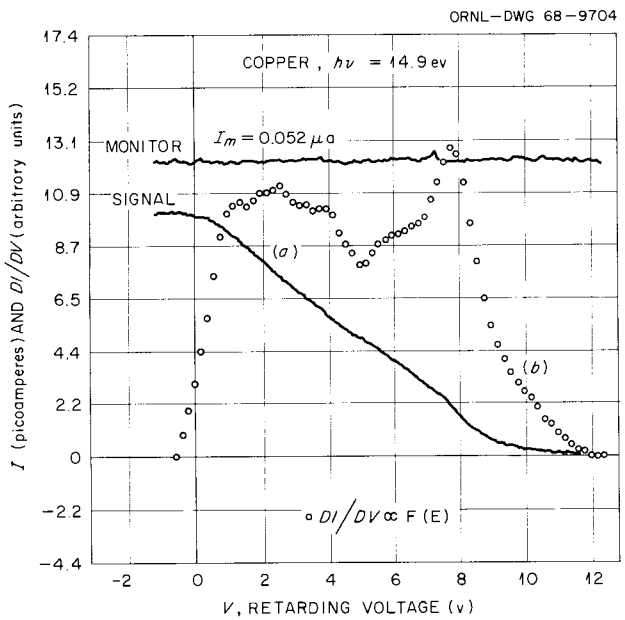

Fig. 16.8. Typical Photoemission Data. (*a*) Electron emission current as a function of the retarding voltage; (*b*) computed slope of the emission current curve for a copper sample with $h\nu = 14.9$ ev.

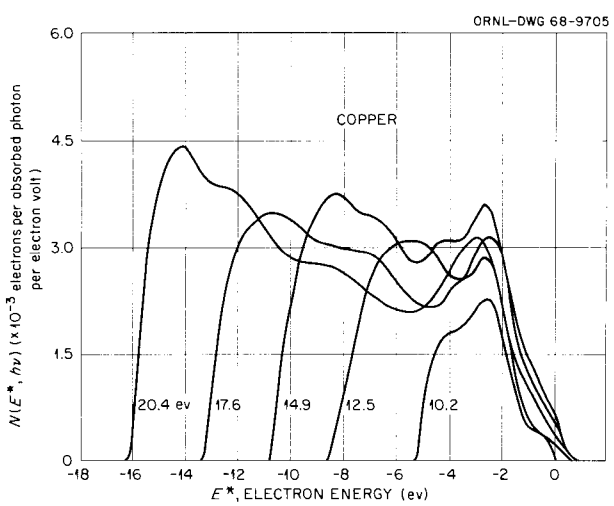

Fig. 16.9. Photoelectron Energy Distribution Curves for Copper in the Vacuum Ultraviolet.

The work function for palladium is assumed to be 4.8 ev, as determined from the maximum photoelectron energy. The optical data confirm the identifications made previously of the discrete losses of

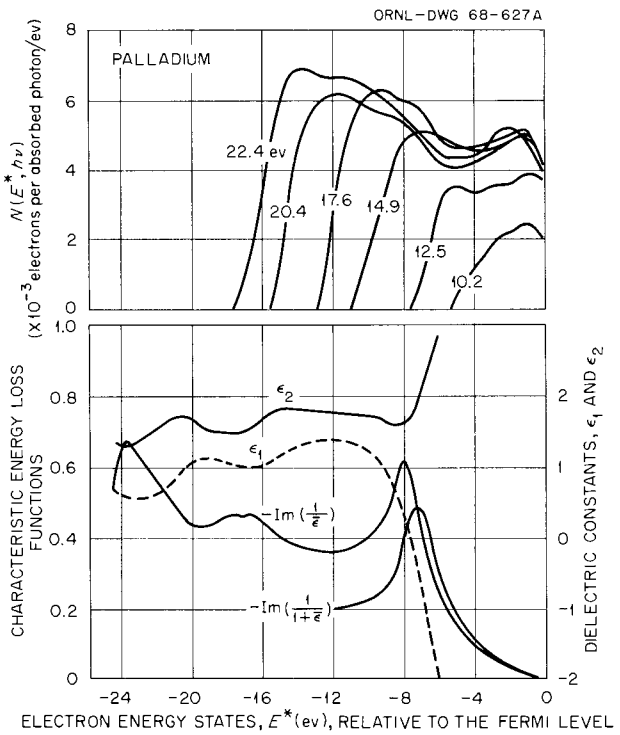

Fig. 16.10. Photoelectron Energy Distribution Curves and Optical Constants of Palladium in the Vacuum Ultraviolet.

7.0 and 10.5 ev, which appear as structure at $E^* = -7.5$ and -11.0 ev. The structure at $E^* = -7.5$ ev lies 7.0 ev below the peak in the *d* states at -0.5 ev and can be associated with the peak in the energy-loss function $-\mathrm{Im}\,(\epsilon)^{-1}$ at 8 ev, since no structure appears in ϵ_2 at this energy to suggest an interband effect. Thus this 7.0 ev discrete loss is due to photoelectron excitation of volume plasmons. On the other hand, the structure at $E^* = -11.0$ ev in the energy distribution curves corresponds to broad structure in ϵ_2, indicating that this structure corresponds to a discrete loss of 10.5 ev due to excitation of an interband transition. No structure appears in the energy-loss functions that would suggest a discrete energy loss of the correct amount.

The electron energy distribution curves for copper, palladium, and nickel were measured as a function of time for an incident photon energy of 10.2 ev. All showed a similar response to surface effects caused by the adsorption of impurity gases,

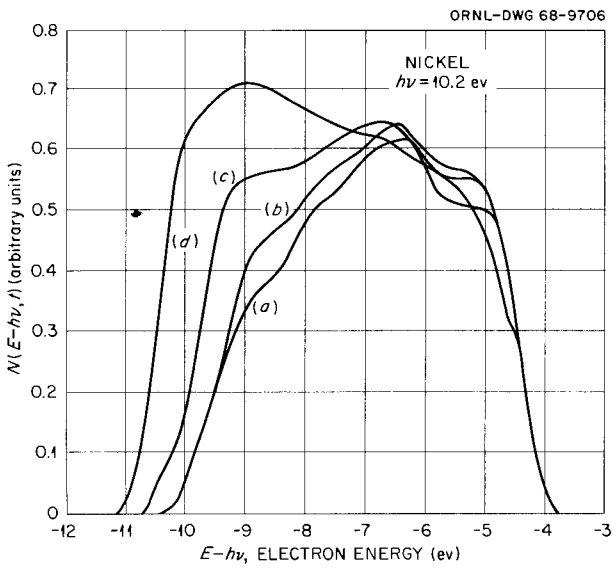

Fig. 16.11. Photoelectron Energy Distribution Curves of Nickel at $h\nu = 10.2$ ev as a Function of Sample Age. (*a*) $t = 8$ min, (*b*) $t = 25$ min, (*c*) $t = 2$ hr, and (*d*) $t = 5$ hr after evaporation.

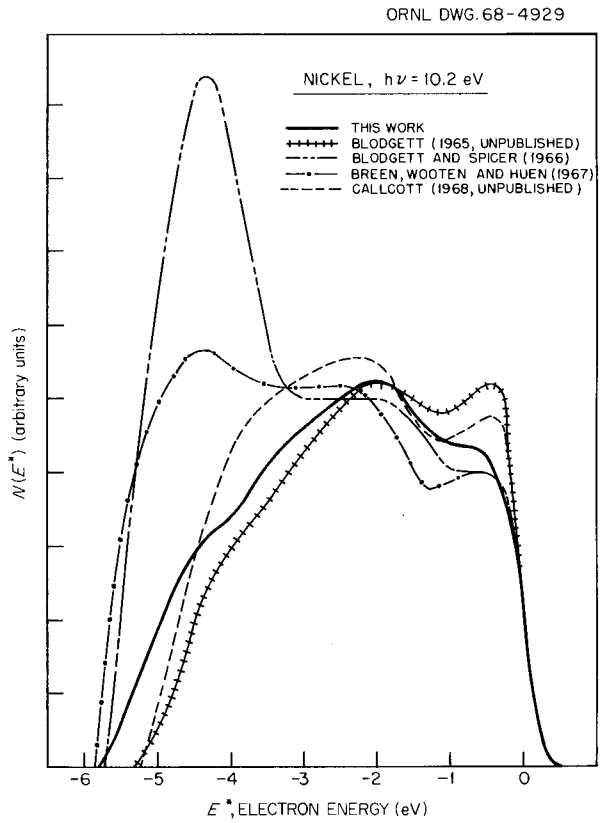

Fig. 16.12. Comparison of Photoelectron Energy Distribution Curves from Various Authors for Nickel at $h\nu = 10.2$ ev.

with the total yield per absorbed photon increasing with time after deposition of the metal film. Figure 16.11 shows the results of the temporal studies on nickel. As with copper and palladium, the shape of the distribution was not distorted appreciably in the first half-hour after deposition. Thus all photoemission data reported here were obtained within a half-hour of film evaporation. The deviation of the low-energy electron peak with time is probably due to changes in the photoemitting properties of the adsorbed surface layer. The data for nickel of Blodgett,[17] Blodgett and Spicer,[18] Breen, Wooten, and Huen,[19] and Callcott[20] are shown together with the results of this work in Fig. 16.12. The data reported by Blodgett[17] as "anomalous" show the same general characteristics as the evaporated film data reported here, while Blodgett's data for the "normal" form of nickel reveal structure suggestive of the surface effects observed for aged samples (Fig. 16.11).

In Fig. 16.13 photoelectron energy distributions are compared with measured optical constants and calculated energy-loss functions for nickel. The work function for nickel is assumed to be 4.5 ev. The *d*-band peak in the density of states lies at $E^* = -0.5$ ev, and there are additional persistent structures at E^* equal to -1.6, -5.0, and -10.5 ev. These structures, identified in terms of the measured optical properties, are due to photoelectron excitation of 1.1- and 4.5-ev interband transitions and 10.0-ev volume plasma oscillations. In contrast, Blodgett and Spicer[18] associate the structure at $E^* = -5.0$ ev with anomalous structure in the density of electronic states of nickel.

These data support the basic conclusion that relatively low-energy photoelectrons, excited within the metal, may lose discrete amounts of energy in

[17] A. J. Blodgett, Jr., "Band Structure and Ferromagnetism in Nickel, Iron, and Gadolinium Photoemissive Studies," in Stanford University, Stanford Electronics Laboratories Technical Report No. 5205-2, (1965) (unpublished).

[18] A. J. Blodgett, Jr., and W. E. Spicer, *Phys. Rev.* **146**, 390 (1966).

[19] W. M. Breen, F. Wooten, and T. Huen, *Phys. Rev.* **159**, 475 (1967).

[20] T. A. Callcott, private communication, 1968.

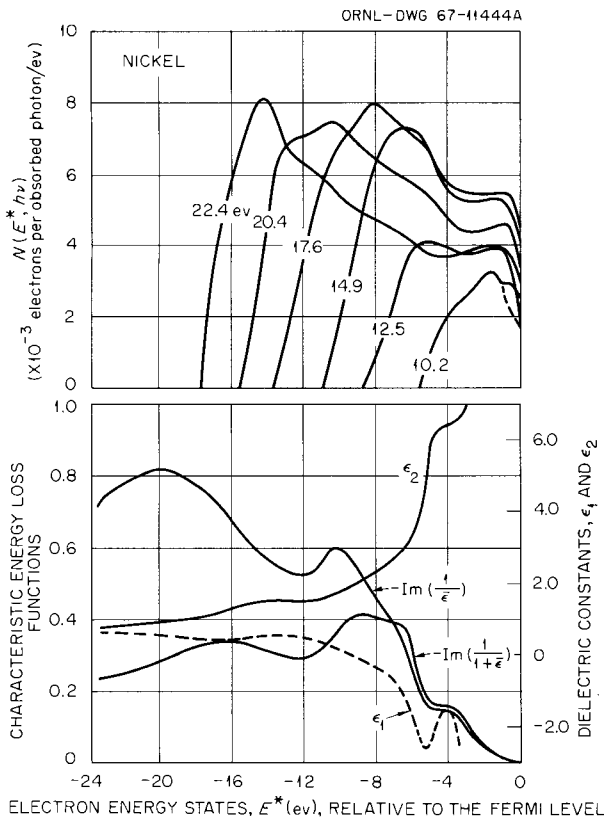

Fig. 16.13. Photoelectron Energy Distribution Curves and Optical Constants of Nickel in the Vacuum Ultraviolet.

the same way that high-energy electrons can lose energy on traversing the metal. In fact it appears that the inelastic scattering of photoelectrons generated by incident photons from 10 to 24 ev can be interpreted in terms of the same theoretical functions derived for the inelastic scattering of electrons of much higher energies.

ULTRAHIGH VACUUM ELLIPSOMETRY

In general, when light is reflected from a plane surface, the amplitude ratio of the light polarized parallel to the plane of incidence to that polarized perpendicular to this plane is changed. Additionally, a phase change is introduced by the reflection process between these two components. Thus, light linearly polarized at an arbitrary angle of incidence is generally reflected as elliptically polarized light, with the eccentricity and the azimuth of the polarization ellipse completely determined by the optical properties of the reflecting surface.

The change in polarization can be measured with a polarizing spectrometer, or ellipsometer, thus permitting the determination of the optical properties of the reflecting surface. With this method, sensitivity to the presence of very thin films on the surface is high, and the optical constants of both the surface film and the substrate, particularly the real part of the index of refraction, can be determined with great accuracy.

An ellipsometer which features an ultrahigh-vacuum sample chamber was constructed and is shown in Fig. 16.14. Light from the monochromator is elliptically polarized by the prism polarizer and Babinet-Soleil compensator prior to reflection from the metal surface within the sample chamber. When the proper ellipticity has been achieved, the reflection process converts the light to linearly polarized light, which is then analyzed by the second prism and photon detector. All three optical elements are mounted in divided circles which are accurate to 1′ of arc. The light beam enters and leaves the sample chamber through special Pyrex windows mounted on Kovar seals welded to the metal flanges such that their surfaces are normal to the beam. These windows have been carefully annealed to remove as much of the residual strain birefringence as possible.

To maintain a high level of chamber cleanliness, it was considered necessary to eliminate oil pumps from the system. The roughing pump is a zeolite adsorption pump equipped with an external bakeout mantle. This is preceded by a combination titanium getter pump and a 25-liter/sec differential ion pump. Following a three-day bakeout cycle, chamber pressures of 6×10^{-11} torr have been obtained.

The detector used depends upon the wavelength region under study. The initial measurements were made between 3500 and 6000 A using an EMI 9524S photomultiplier and between 8500 and 15,000 A using an IRI Tl-SA16 lead sulfide detector. Recent measurements on palladium between 6000 and 8000 A using an EMI 9558QC photomultiplier have supplemented the palladium data reported earlier.[21] The previous measurements have also been redone using new Pyrex windows to reduce the errors in-

[21] R. D. Birkhoff *et al.*, *Health Phys. Div. Ann. Progr. Rept. July 31, 1967*, ORNL-4168, p. 144.

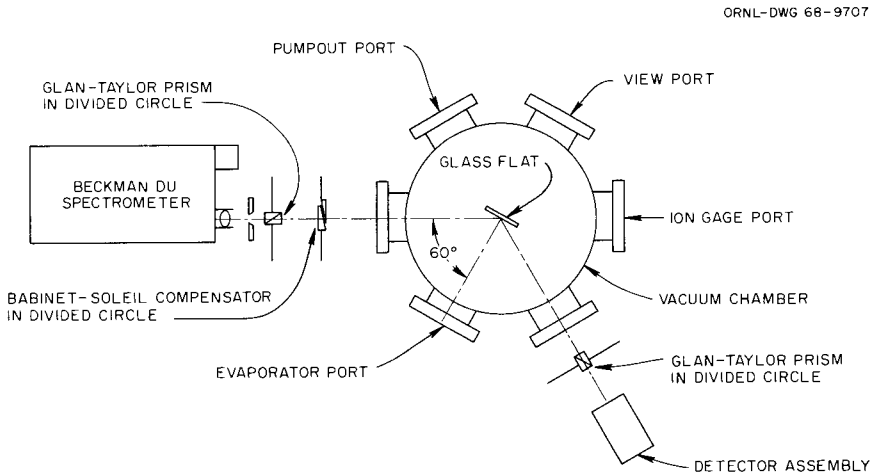

Fig. 16.14. Apparatus Used to Study the Ellipticity of Light Reflected from Metal Surfaces in Ultrahigh Vacuums.

troduced by the strain birefringence in the original windows.

Two new strain-free fused quartz windows will be installed in the near future. This will extend the short-wavelength range from its present position at the Pyrex cutoff down to 2240 A, at which wavelength the prism polarizers become opaque. This will then provide an overlapping spectral region accessible to both the polarimetric and photometric methods of studying the optical properties of surfaces.

EVALUATION OF A REFLECTION-TYPE POLARIZER FOR USE IN THE ULTRAVIOLET

Previous studies[22] of reflection-type polarizers have been continued, using triple-reflection polarizers with gold surfaces. Gold films provide an excellent surface for use in a reflection-type polarizer since gold is stable, doesn't oxidize easily, and can be used in the ultraviolet region.

In order to compare the observed polarization with the theoretical value the optical constants of gold must be known. Gold films were obtained by vacuum evaporation at a pressure of 10^{-5} torr. After exposure to the atmosphere the room-temperature reflectance, R_V, where V refers to a vertical axis of rotation for the sample, was measured as a function of angle of incidence from 400 to 3000 A. Light is partially polarized by the monochromator; to eliminate this variable, reflectance measurements, R_H, at the same angles of incidence were made with the gold film rotated through 90° so that the axis of rotation of the sample is horizontal. The average of the two reflectances for a given angle of incidence gives the reflectance, R, for unpolarized light at that angle of incidence. Figure 16.15 shows R_V and R_H for an angle of incidence of 70° obtained using a 1500-A blaze grating in the wavelength range 1100 to 3000 A. The structure in R_V and R_H in the region of 1250 A results from the fact that the radiation incident on the gold film has been polarized by the grating. It is seen that a single observation of reflectance at a given angle of incidence, if uncorrected for the polarization of the incident radiation, could lead to large errors in the optical constants.

The real and imaginary parts, $n(\lambda)$ and $k(\lambda)$, of the complex index of refraction of gold were determined as a function of wavelength from Fresnel's equations using a least-squares-fit method. The resulting values of n and k are shown in Fig. 16.16, compared with previous values obtained by Canfield, Hass, and Hunter[23] and Philip.[24] The bars on the curves for n and k indicate the variations of the optical constants, for different gold films, obtained in this laboratory. For any given gold film the optical

[22]R. D. Birkhoff *et al.*, *Health Phys. Div. Ann. Progr. Rept. July 31, 1965*, ORNL-3849, p. 133–35.

[23]L. R. Canfield, G. Hass, and W. R. Hunter, *Le Journal de Physique* **25**, 124 (1964).

[24]R. Philip, *Opt. Acta* **7**, 47 (1960).

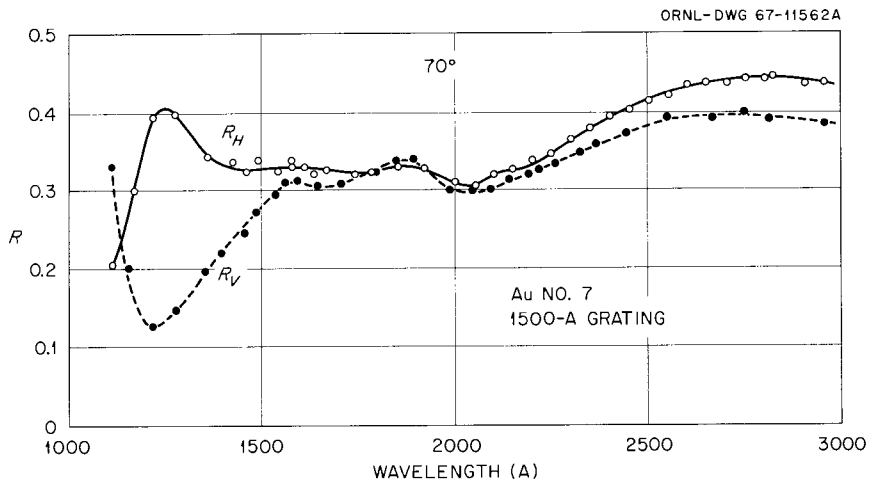

Fig. 16.15. Reflectances for Two Orientations of the Gold Film at Right Angles to Each Other and for an Angle of Incidence of 70° vs Wavelength.

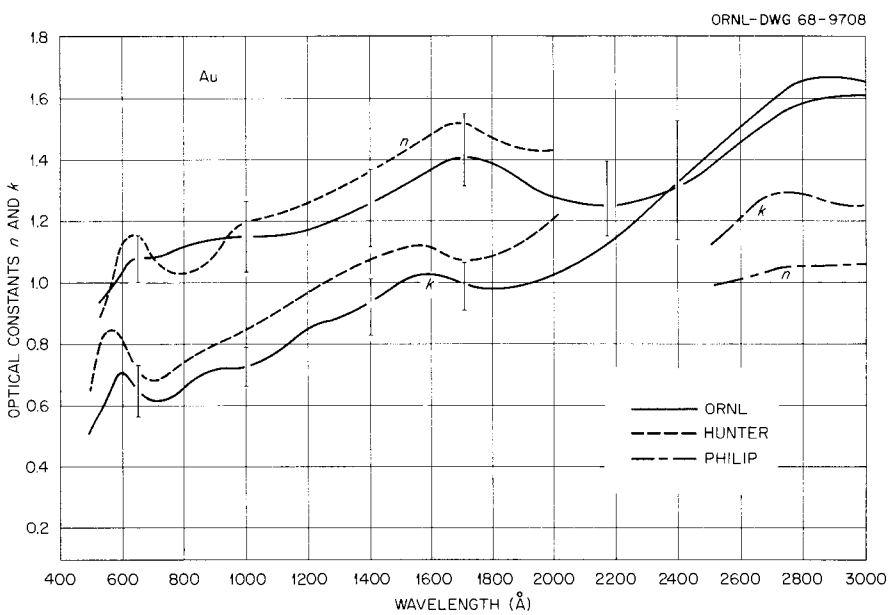

Fig. 16.16. Optical Properties of Gold vs Wavelength.

constants remain constant with time after deposition. The reproducibility of the optical constants for different gold films influences the reproducibility of the polarization produced by a triple-reflection polarizer with a given geometry. It is suggested, in view of the differences observed between different gold films, even when made in the same laboratory, that measurements should be made of the optical constants of the gold each time that a reflection-type polarizer is constructed. The relevant constants can then be used in the calibration of the polarizer.

Knowing the optical constants of the gold surfaces, a triple-reflection polarizer can be evalu-

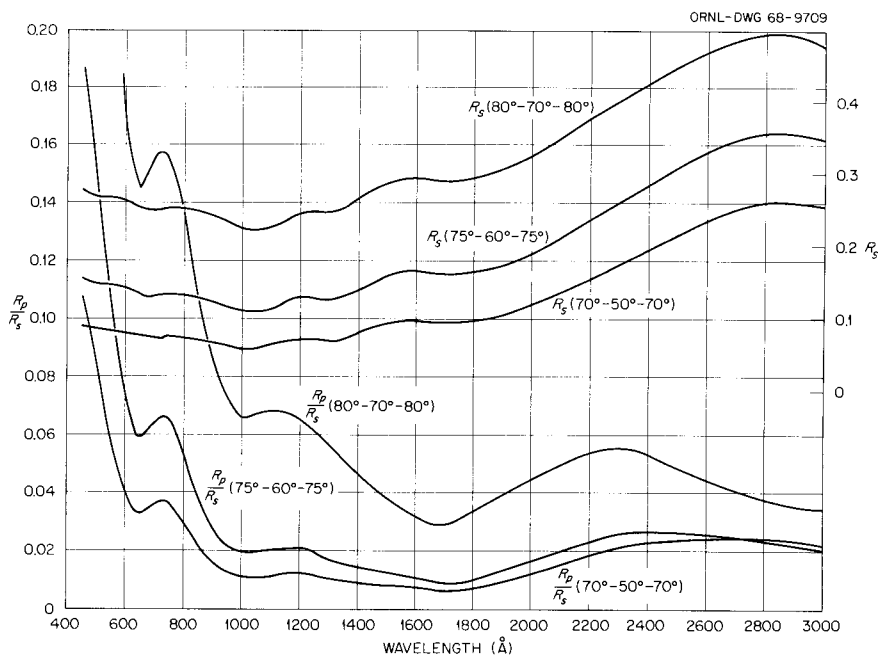

Fig. 16.17. Calculated Polarization, R_p/R_s, and Reflectance, R_s, for Triple-Reflection Polarizers of Different Geometries.

ated. For specified angles of the three surfaces[22] the polarization, R_p/R_s, produced by the system and the reflectance, R_s, for the transmitted beam can be calculated. Figure 16.17 shows the polarization, R_p/R_s, and the reflectance, R_s, calculated for three possible combinations of incident angles, using the optical constants for a single gold film. From such calculations the most suitable geometry may be chosen for a particular polarizer. For example, the middle combination (75°-60°-75°) would be a good choice for almost complete polarization combined with high transmission for the region 800 to 3000 A, whereas the first combination (70°-50°-70°) would be better for wavelengths less than 800 A. In certain wavelength regions it is seen that it is possible to obtain 99% polarization with approximately 20% transmission of the polarized beam.

Direct measurements of the polarization produced by a triple-reflection polarizer of given geometry, using a polarizer-analyzer combination, are found to agree with the calculated values presented in Fig. 16.17 over the wavelength range 500 to 5000 A.

TIME STUDIES OF THE POLARIZATION DUE TO GRATINGS

A triple-reflection polarizer was used to study the polarization of the radiation emerging from a Seya-Namioka monochromator. This polarization is introduced by the presence of the grating.

Representative time studies are shown in Figs. 16.18 and 16.19 for two 1500-A blaze gratings. For the grating associated with Fig. 16.18, measurements were made over a period of approximately one month and for that in Fig. 16.19, over a period of approximately four months. It is seen that the polarization and the time dependence are different for the two gratings. The change in polarization with time is more rapid with a new grating than after it has been in use for some time. These studies indicate that, particularly with a new grating, polarization measurements of the radiation exiting from the monochromator should be made each time the instrument is used and the value of the polarization is required.

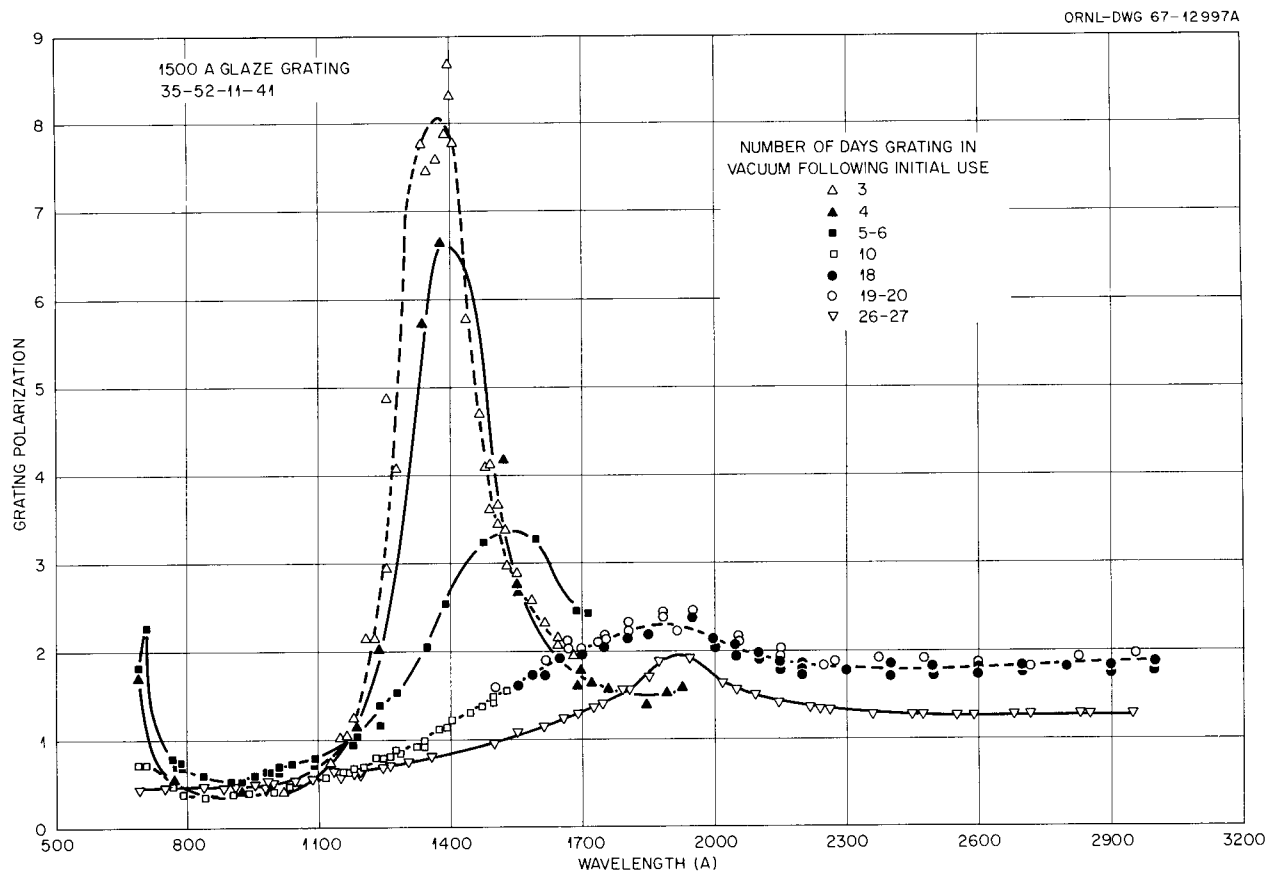

Fig. 16.18. Polarization of 1500-A Blaze Grating as a Function of Wavelength and Time.

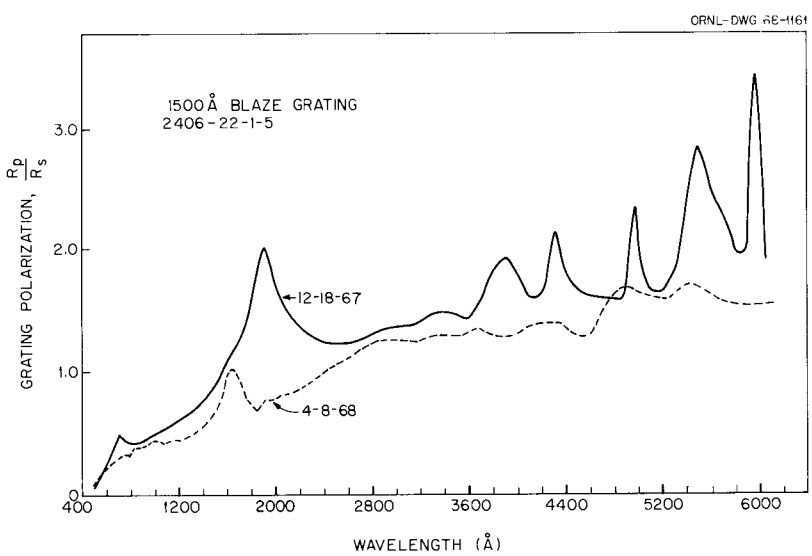

Fig. 16.19. Polarization of 1500-A Blaze Grating as a Function of Wavelength and Time.

GRATING ANOMALIES

Anomalies in the intensity of light diffracted from a diffraction grating were first observed by Wood[25] in 1902. These anomalies, which occur for light polarized with its E vector in the plane of incidence (perpendicular to the grating rulings), have been studied both experimentally and theoretically by many workers. Recent treatments have been given by Hessel and Oliner[26] and Hägglund and Sellberg.[27]

We have measured the intensity of the diffracted light from concave diffraction gratings for light polarized with its E vector parallel and perpendicular to the plane of incidence. These measurements were made on a Bausch and Lomb replica grating ruled with 600 lines per millimeter and having a blaze angle of 2°35′. The grating was coated with a vacuum-evaporated layer of aluminum. Measurements were made using a Polaroid analyzer and with a fixed angle between entrance and exit slits as the spectrum was scanned. The measurements were then repeated with other angles between entrance and exit slits. Data were taken in the wavelength region 3000 to 8000 A using an EMI 9558 phototube. These data are shown in Fig. 16.20. The angles θ shown are half the angle between the incident and diffracted beam. The intensity of p-polarized light (E vector in the plane of incidence) exhibits peaks that shift in wavelength as the angle is varied. The s component varies smoothly with wavelength for all angles of incidence. These data, along with data taken in the region 8000 to 16,000 A using a PbS detector, are shown in Fig. 16.21. The position of the peaks in wavelength is plotted as a function of the angle θ, half the angle between the incident and diffracted beam.

An explanation of these anomalies in terms of a surface plasmon resonance has been formulated and is presented in the theory section of this report.

[25] R. W. Wood, *Phil. Mag.* **4**, 396 (1902).

[26] A. Hessel and A. A. Oliner, *Appl. Opt.* **4**, 1275 (1965).

[27] J. Hägglund and F. Sellberg, *J. Opt. Soc. Am.* **56**, 1031 (1966).

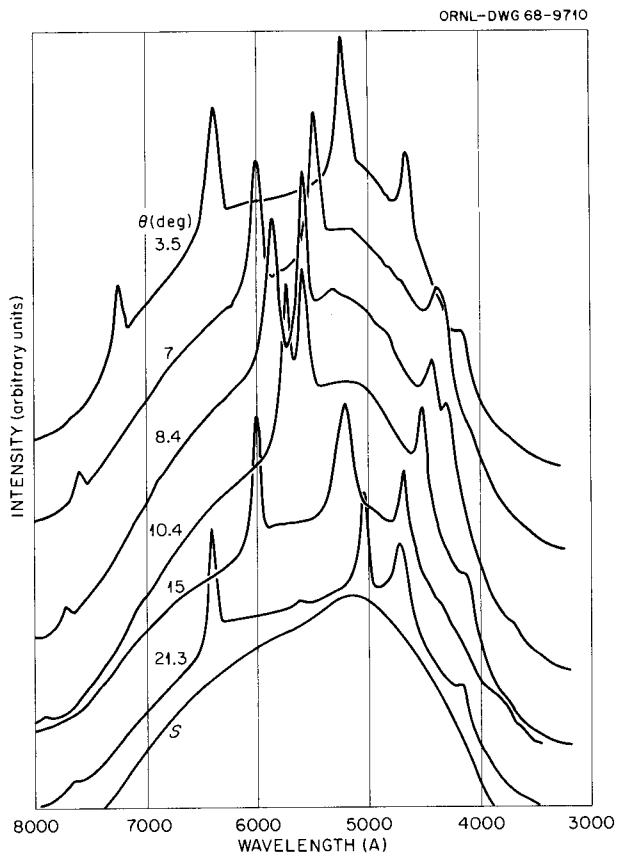

Fig. 16.20. Intensity of Diffracted Light for Various Angles, 2θ, Between Entrance and Exit Slits.

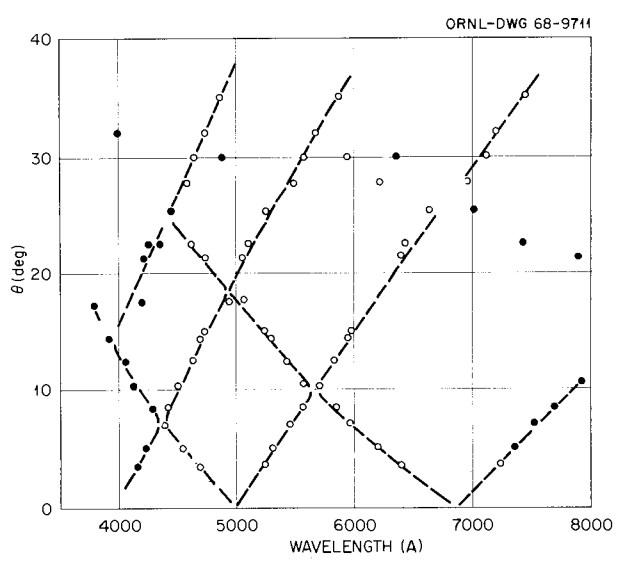

Fig. 16.21. Position of Peaks in p-Polarized Diffracted Light as a Function of Wavelength and Angle 2θ Between Entrance and Exit Slits.

17. Atomic and Molecular Radiation Physics

L. G. Christophorou

M-E. M. Abu-Zeid[1]
V. E. Anderson[2]
J. B. Birks[3]
R. P. Blaunstein[4]
D. Q. Brown[3]
J. G. Carter
E. L. Chaney[5]
A. A. Christodoulides[6]
J. T. Cox
J. A. Harter
R. H. Huebner[4]
A. G. Kenerly[7]
C. E. Klots
DeVaughn Pittman
J. A. Stockdale

SCATTERING OF THERMAL ELECTRONS BY POLAR MOLECULES

Drift velocities for a large number (30) of pure polar molecules have been measured, and a number of these are shown in Fig. 17.1. The electric dipole moment μ for these molecules ranges from 0 to $\sim$4.1 Debye units (D.u.). The data on pure polar molecules and those on four other polar molecules in mixtures with ethylene have been analyzed,[8] and mean scattering cross sections $\langle \sigma_m(v) \rangle$ have been obtained. The mean scattering cross sections, defined by

$$\langle \sigma_m(v) \rangle = \int_0^\infty \sigma_m(v)\, f_0(v)\, v^2\, dv\,, \qquad (1)$$

where $\sigma_m(v) = \int d\sigma(v)\,(1 - \cos\theta) = A/v^2$ and $4\pi f_0(v)v^2$ is the normalized Maxwellian distribution function, are plotted in Fig. 17.2 as a function of μ. For comparison, the theoretical predictions of Altshuler[9] and Mittleman and von Holdt,[10] as well as the position of the critical moment, μ_{min}, are shown on the figure. The general conclusion is that the point dipole Born approximation calculation of Altshuler is in better agreement with experiment than the exact calculation of Mittleman and von Holdt. When $\mu > 0.6$ D.u. the Altshuler theory agrees with experiment within less than a factor of 2, while for $0.6 \leqq \mu \leqq 4.1$ D.u. the agreement is within 50% in most cases.

Further, the experimental cross sections are higher than those predicted by Altshuler for all $\mu \lesssim 2.4$ D.u. and smaller when $\mu \gtrsim 2.4$ D.u. This finding, added to the fact that at and around the minimum dipole moment, μ_{min}, required to bind an electron to a dipole the cross sections are enhanced, indicates the possible effect of the binding of an electron to a molecule (when $\mu > \mu_{min}$) and is consistent with the existence of a potential resonance as predicted by Takayanagi and Itikawa.[11]

DIPOLE AND NONDIPOLE CONTRIBUTIONS TO THE CROSS SECTION FOR SCATTERING OF SLOW ELECTRONS FROM POLAR MOLECULES

The effect on the scattering cross section of nondipole terms in the potential when slow electrons are scattered from polar molecules is being

[1]Student from the University of Tennessee, Knoxville.

[2]On loan from Central Data Processing Facility (ORGDP).

[3]Consultant.

[4]Radiological Health Physics Fellow.

[5]USAEC Health Physics Fellow.

[6]Graduate Assistant, The University of Tennessee, Knoxville.

[7]On loan from Instrumentation and Controls Division.

[8]L. G. Christophorou and A. A. Christodoulides, *Proc. Phys. Soc.* (submitted for publication).

[9]S. Altshuler, *Phys. Rev.* **107**, 114 (1957).

[10]M. H. Mittleman and R. E. von Holdt, *Phys. Rev.* **140A**, 726 (1965).

[11]K. Takayanagi and Y. Itikawa, *Proc. Phys. Soc. Japan* **24**, 160 (1968).

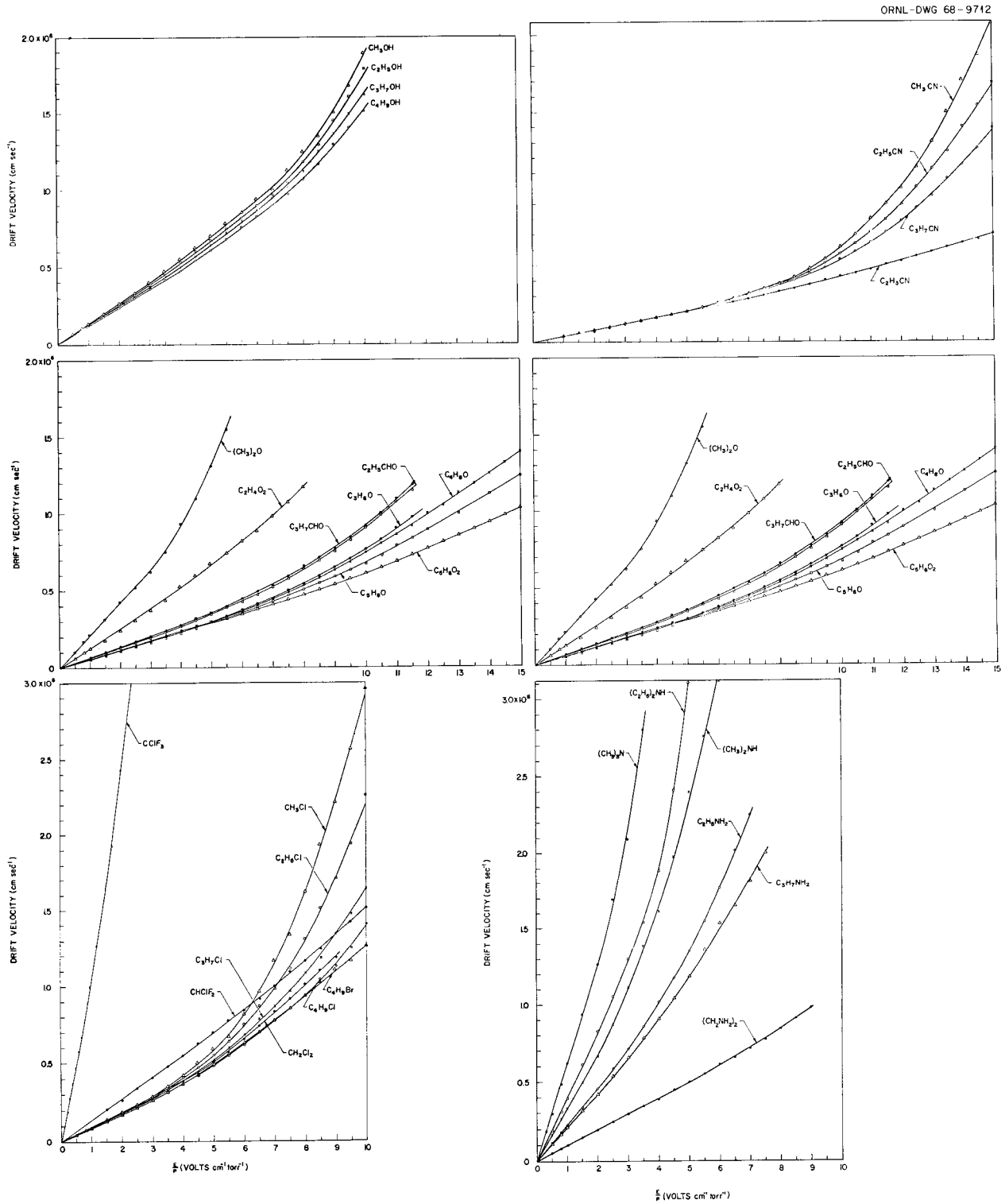

Fig. 17.1. Electron Swarm Drift Velocities in Polar Gases.

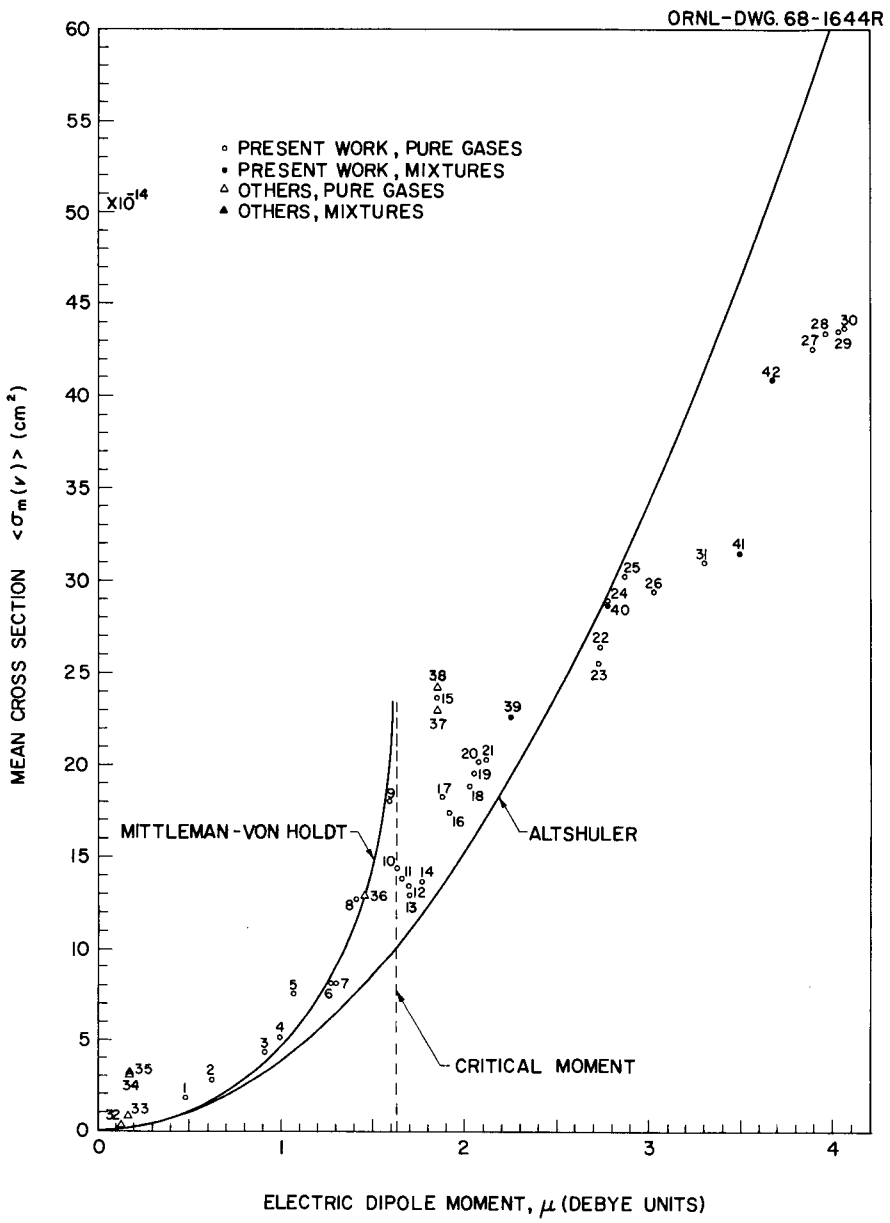

Fig. 17.2. Mean Cross Section $\langle \sigma_m(v) \rangle$ vs Electric Dipole Moment μ.

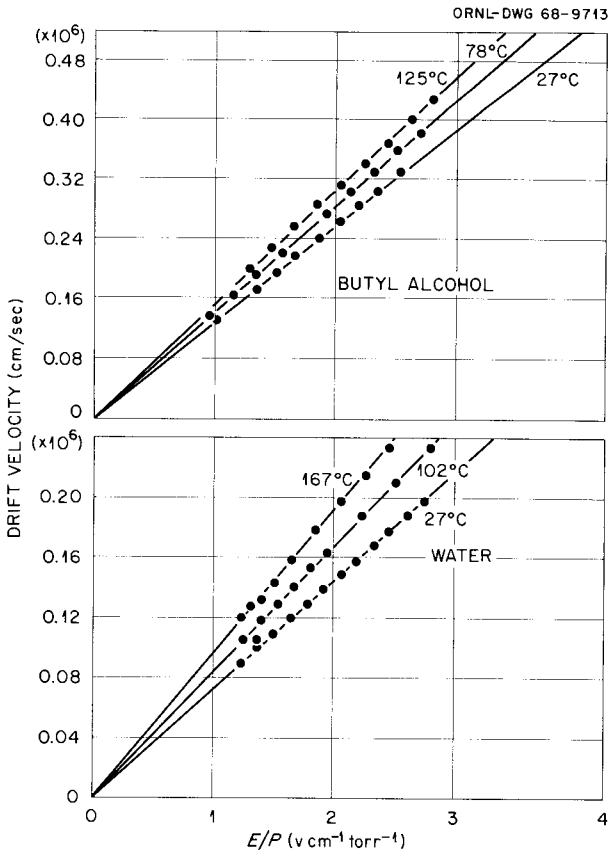

Fig. 17.3. Temperature Dependence of the Drift Velocity of Thermal Electrons in Butyl Alcohol and Water.

investigated. Drift velocities for pure polar molecules are measured as a function of temperature, and a representative set of data is shown in Fig. 17.3. An analysis of these data is being made, using various forms for the scattering cross section which are appropriate to specific (assumed) scattering potentials.

ELECTRON ATTACHMENT TO HALOGENATED ALIPHATIC HYDROCARBONS

Dissociative electron attachment to a large number of halogenated toxic aliphatic hydrocarbons has been studied. Small amounts of these compounds have been mixed (in less than one part per thousand) with N_2. Thus the distributions of energies in the electron swarm, $f(\epsilon, E/P)$, were characteristic of N_2 itself, and such distributions are known.

A mean attachment cross section has been defined as

$$\langle \sigma_a(\epsilon) \rangle_v \equiv \frac{\int_0^\infty \sigma_a(\epsilon)\epsilon^{1/2} f(\epsilon,E/P)\, d\epsilon}{\int_0^\infty \epsilon^{1/2} f(\epsilon, E/P)\, d\epsilon}, \qquad (2)$$

where $\sigma_a(\epsilon)$ is the attachment cross section as a function of electron energy ϵ.

The absolute rate of electron attachment, αw, where α is the probability of electron attachment per centimeter traveled in the field direction per torr of electron-attaching gas and w is the electron swarm drift velocity, is a function of E/P and is related to $\sigma_a(\epsilon)$ and $f(\epsilon, E/P)$ by

$$\alpha\, w(E/P) = N(2/m)^{1/2} \int_0^\infty \sigma_a(\epsilon)\epsilon^{1/2} f(\epsilon, E/P)\, d\epsilon\,, \qquad (3)$$

where N is the number density and m is the electron mass.

From Eqs. (2) and (3) we have

$$\langle \sigma_a(\epsilon) \rangle_v = \frac{\alpha w}{N(2/m)^{1/2}} \frac{1}{\int_0^\infty \epsilon^{1/2} f(\epsilon, E/P)\, d\epsilon} = \frac{\alpha w}{N(2/m)^{1/2} \langle \epsilon^{1/2} \rangle}\,, \qquad (4)$$

where $\langle \sigma_a(\epsilon) \rangle_v$ can appropriately be called the "mean velocity-weighted attachment cross section."

From the known distribution functions in N_2, $\langle \epsilon^{1/2} \rangle$ has been calculated for those E/P for which αw has been measured. Thus $\langle \sigma_a(\epsilon) \rangle_v$ was determined. The difference between $\langle \sigma_a(\epsilon) \rangle_v$ and $\sigma_a(\epsilon)$ becomes smaller with decreasing peak energy of the dissociative attachment resonance. This is illustrated in Fig. 17.4, where $\sigma_a(\epsilon)$ for Br^-/HBr, Cl^-/HCl, and H^-/H_2O are compared with $\langle \sigma_a(\epsilon) \rangle_v$.

In addition, the "mean energy-weighted,"

$$\langle \sigma_a(\epsilon) \rangle_{v^2} \equiv \frac{\int_0^\infty \sigma_a(\epsilon)\, \epsilon\, f(\epsilon, E/P)\, d\epsilon}{\int_0^\infty \epsilon\, f(\epsilon, E/P)\, d\epsilon}, \qquad (5)$$

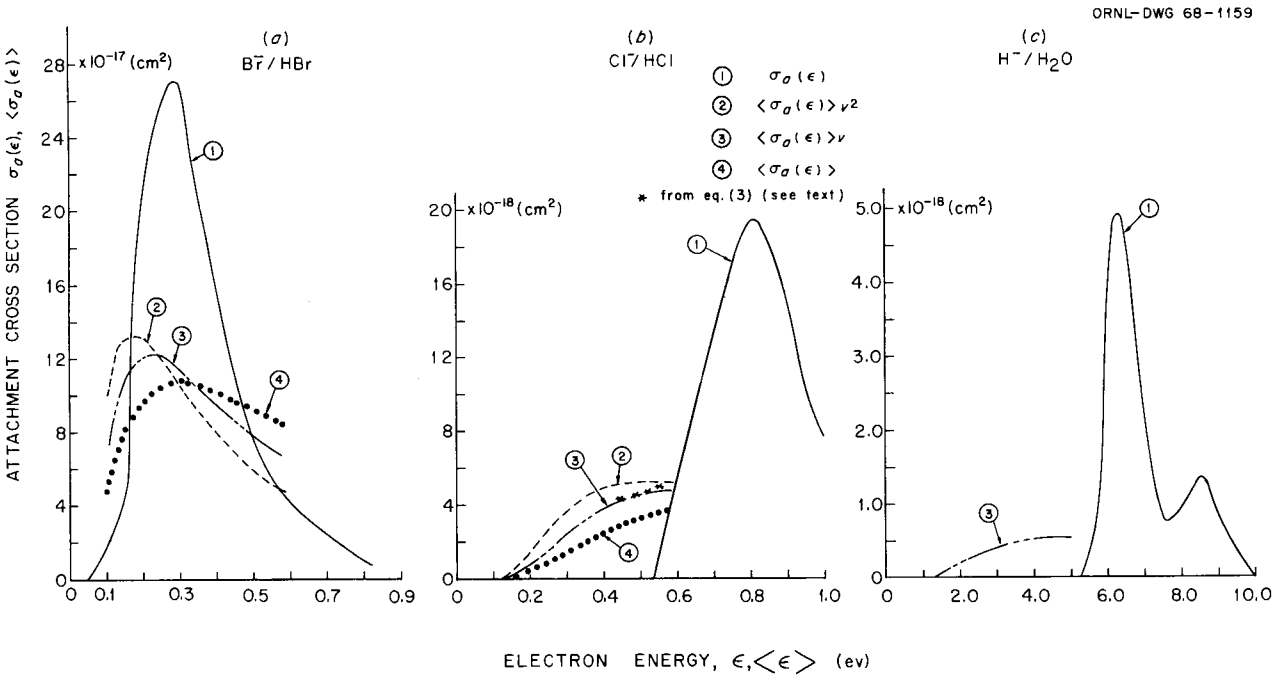

Fig. 17.4. Attachment Cross Section as a Function of Electron Energy.

and the "mean attachment cross section,"

$$\left\langle \sigma_a(\epsilon) \right\rangle \equiv \frac{\int_0^\infty \sigma_a(\epsilon)\, f(\epsilon, E/P)\, d\epsilon}{\int_0^\infty f(\epsilon, E/P)\, d\epsilon}, \qquad (6)$$

are given in Fig. 17.4. For low enough energies and precise forms of $f(\epsilon, E/P)$, as in the present experiments of mixtures with N_2, $\left\langle \sigma_a(\epsilon) \right\rangle_v$ becomes very close to $\sigma_a(\epsilon)$. From Fig. 17.4 it is seen that for energies <1.0 ev, the mean electron attachment cross section as a function of mean electron energy derived from swarm experiments alone will yield accurate values of the electron attachment cross section as a function of electron energy.

Figures 17.5 and 17.6 show the mean dissociative electron attachment cross sections calculated using Eq. (4) as a function of mean electron energy for 22 aliphatic hydrocarbons. The electron attachment rates were measured by us or deduced from the literature.[12]

[12]T. G. Lee, *J. Phys. Chem.* **67**, 360 (1963).

An effort has also been made to relate the measured cross sections to the toxic action of these compounds. Although it was found that toxicity increases with increasing attachment cross section, lack of reliable toxicity data did not allow a complete evaluation of the data.

ELECTRON ATTACHMENT TO AROMATIC HYDROCARBONS

The construction of an apparatus designed for the measurement of the rates of electron attachment to molecules in the gas phase in the temperature range from 25 to 210°C has been completed. The design, construction, and pressure-measuring devices associated with this apparatus have been modified with respect to those used in previous experiments of this type. These modifications allowed the present attachment studies for molecules which are in the crystalline form at 25°C and thus exhibit low vapor pressures.

Mean nondissociative electron attachment cross sections have been calculated from the measured electron attachment rates for the aromatic hydrocarbons benzene, naphthalene, phenanthrene, tri-

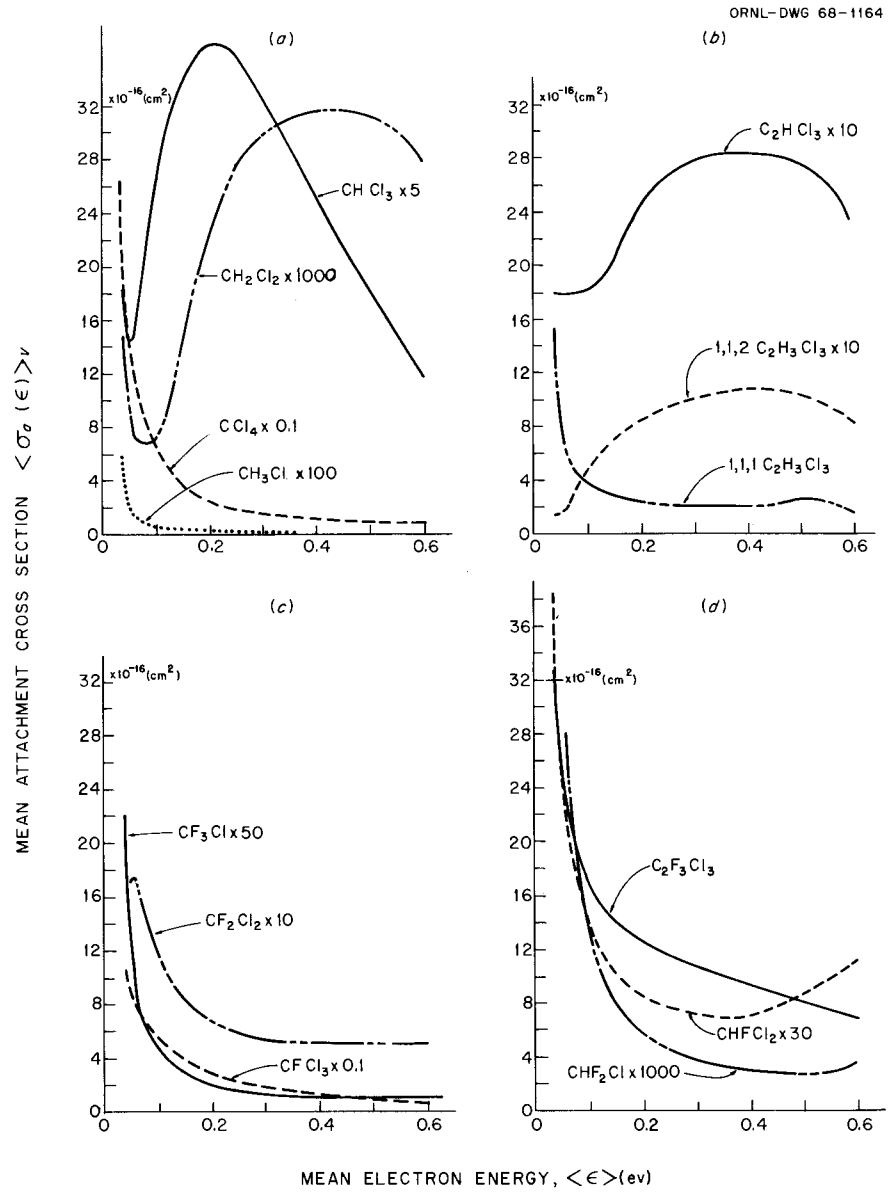

Fig. 17.5. Mean Attachment Cross Sections as a Function of Mean Electron Energy for Halogenated Aliphatic Hydrocarbons.

phenylene, chrysene, pyrene, anthracene, perylene, and 1,2-benzanthracene. All these hydrocarbon molecules exhibit sharp attachment cross sections peaking at thermal energies. The peak attachment cross sections vary from $<10^{-20}$ cm^2 for the single-ring benzene molecule to a maximum of 1.93×10^{-15} cm^2 for the slightly carcinogenic molecule 1,2-benzanthracene.

Figure 17.7 shows the mean electron attachment cross section as a function of mean electron energy for anthracene and 1,2-benzanthracene. A study of the temperature dependence of the electron attachment rate yields a v^{-1} velocity dependence for the thermal electron attachment cross section for pyrene, anthracene, and 1,2-benzanthracene.

Of all the compounds studied the highest value of the electron attachment cross section was exhibited by the slightly carcinogenic 1,2-benzanthracene, while perylene, which has a higher

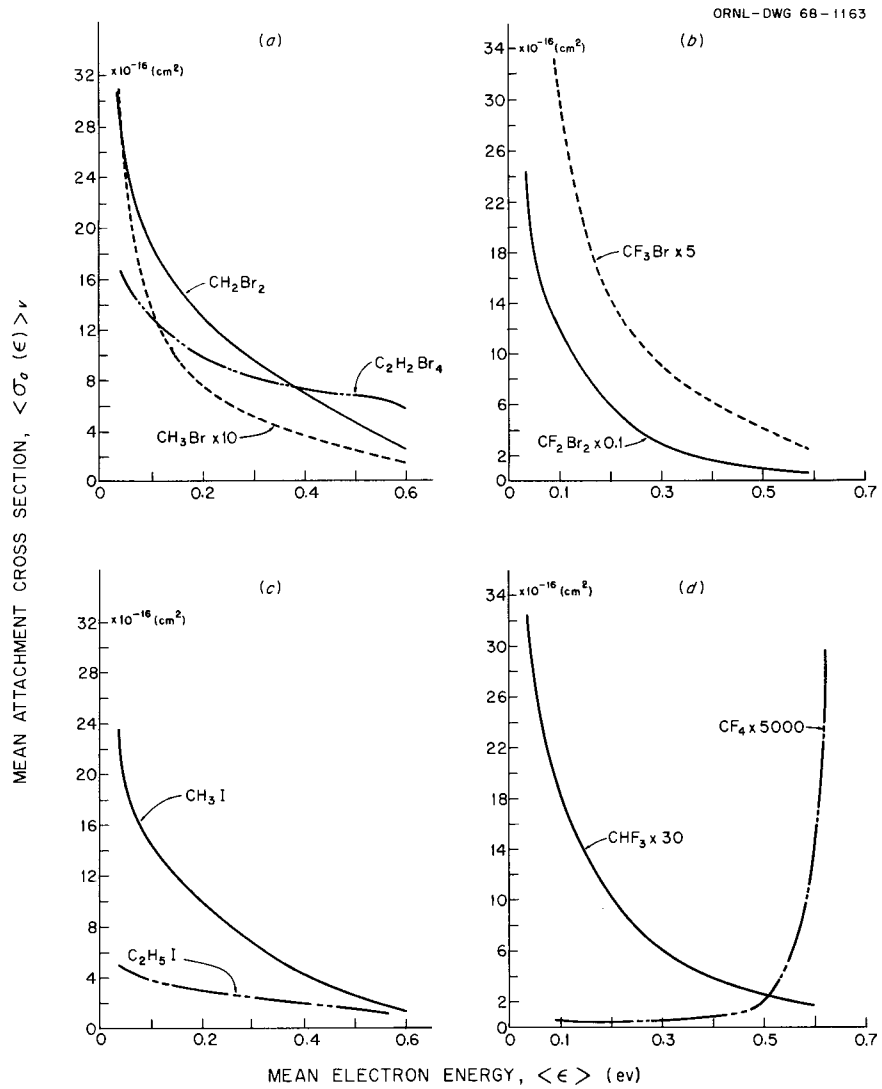

Fig. 17.6. Mean Attachment Cross Sections as a Function of Mean Electron Energy for Halogenated Aliphatic Hydrocarbons.

value of the electron affinity, exhibited a lower attachment cross section. This behavior suggests that although a correlation between chemical carcinogenicity and electron attachment remains speculative, continuation of investigations of this nature may prove helpful in elucidating the biological mechanisms.

The measured cross sections have been related to other molecular parameters such as the energy of the first excited π-singlet state and the molecular electron affinity. The attachment cross sections increase with increasing electron affinity and decreasing energy of the first excited π-singlet state.

DISSOCIATIVE ELECTRON ATTACHMENT TO MOLECULES[13]

Dissociative electron attachment cross sections, $\sigma_a(\epsilon)$, for 30 molecules have been summarized,

[13] L. G. Christophorou and J. A. Stockdale, *J. Chem. Phys.* 48, 1956 (1968).

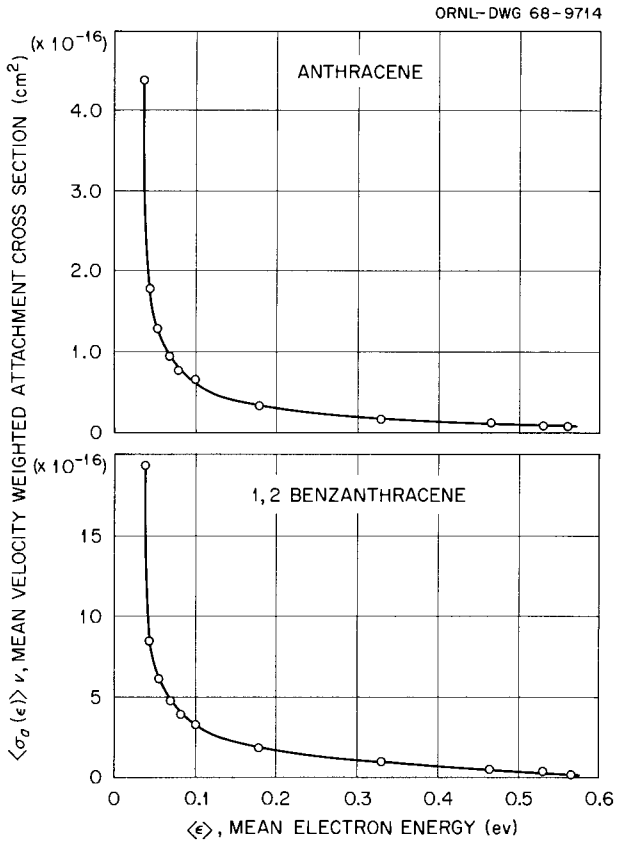

Fig. 17.7. Mean Attachment Cross Section as a Function of Mean Electron Energy for Anthracene and 1,2-Benzanthracene.

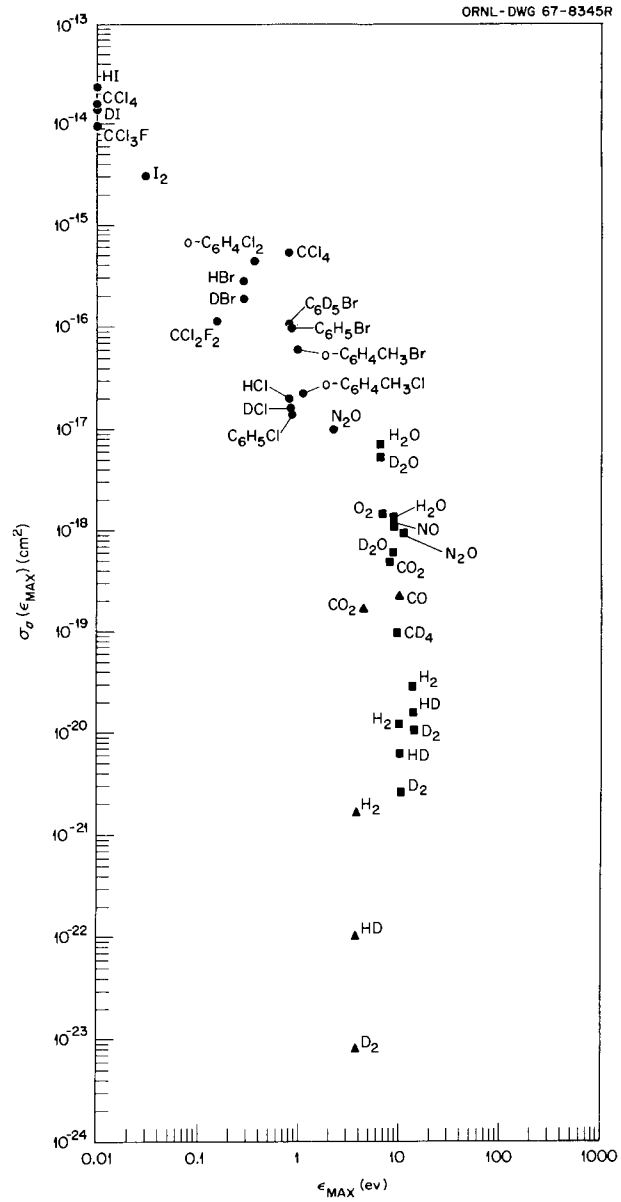

Fig. 17.8. Peak Values $\sigma_a(\epsilon_{max})$ of Dissociative Electron Attachment Cross Section as a Function of the Peak (Resonance) Energy ϵ_{max} for Polyatomic Molecules.

evaluated, and discussed within the framework of the resonance scattering theory. The peak values, $\sigma_a(\epsilon_{max})$, of the dissociative attachment cross section are plotted in Fig. 17.8 as a function of the peak energy, ϵ_{max}, of the dissociative attachment resonance. It is seen that the dissociative attachment peak cross section, $\sigma_a(\epsilon_{max})$, is a strong function of the peak (resonance) energy, ϵ_{max}, with a break in this dependence at the energy where electronic excitation of the neutral molecule begins to occur. Based on the experimental data, three groups of molecules have been distinguished.

Group I: Those where ϵ_{max} is less than the energy, ϵ_N, of known excited electronic states of the neutral molecule and the negative-ion state is purely repulsive in the Franck-Condon region.

Group II: Those where $\epsilon_{max} \geqq \epsilon_N$ and decay of the excited negative ion AX^{-*} to an electronically excited neutral molecule, AX*, is possible and also very probable due to the overlap of the wave function of the resonance electron state with the electronically excited molecular state AX*.

Group III: Those with exceptionally small $\sigma_a(\epsilon_{max})$ for which a vertical onset for dissociative attachment occurs. For the molecules in group I, $\sigma_a(\epsilon_{max})$ varies almost as $(\epsilon_{max})^{-1}$,

while for group II $\sigma_a(\epsilon_{max})$ is a much stronger decreasing function of the resonance energy ϵ_{max}. For group I the effect of autoionization on $\sigma_a(\epsilon_{max})$ is small, and isotopic effects on $\sigma_a(\epsilon_{max})$ are contained within the square root of the inverse ratio of the reduced masses of the products. For group II and especially group III the effect of autoionization on $\sigma_a(\epsilon_{max})$ is large, and so are the isotopic effects on $\sigma_a(\epsilon_{max})$ (see details in ref. 13).

EXCITED ELECTRONIC STATES OF BENZENE AND NAPHTHALENE[14]

Pariser[15] has characterized the ground and the singly excited π-electronic states of aromatic hydrocarbon molecules by three properties: *multiplicity* (singlet or triplet); *symmetry* (benzene: A_{1g}, E_{2g}, B_{1u}, B_{2u}, or E_{2u}; naphthalene: A_g, B_{1g}, B_{2u}, or B_{3u}); and *sign* (plus or minus in the linear combination of the molecular orbital configurations). The corresponding selection rules for electric dipole transitions are

(*a*) multiplicity: $1 \longleftrightarrow 1$; $3 \longleftrightarrow 3$; $1 \leftarrow\|\rightarrow 3$

(*b*) symmetry: $g \longleftrightarrow u$; $g \leftarrow\|\rightarrow g$; $u \leftarrow\|\rightarrow u$

(c) sign: $- \longleftrightarrow +$; $- \leftarrow\|\rightarrow -$; $+ \leftarrow\|\rightarrow +$

An investigation of the singlet and triplet π-electronic states of benzene and naphthalene in the light of recent experimental results obtained by electrons and photons led to the following conclusions concerning the above selection rules.

1. Selection rule *a* is violated with electron excitation, especially when the electron energy is close to the excitation threshold.
2. Selection rule c is violated with electron excitation and is not a stringent rule, probably due to vibrational interaction (it is violated under photon excitation also).
3. Selection rule *b* is valid with both high-energy electron and photon excitation. For low-energy electrons, however, *g-g* or *u-u* transitions may be weakly observed because of the impacting electron's form factor, although no such transitions have been observed with threshold electron excitation.[16]

This analysis also led to the identification of the new electronic transition observed[16] in the threshold electron excitation spectrum of naphthalene at 5.4 ev as the second $^3B^+_{2u}$ state.

EMISSION FROM LIQUID BENZENE AND LIQUID BENZENE AND NAPHTHALENE DERIVATIVES EXCITED BY ELECTRON IMPACT

In Fig. 17.9 the emission from liquid benzene, toluene, and ethylbenzene excited by electron impact is compared with that under ultraviolet excitation. Both emissions were taken at room temperature. From the ultraviolet-induced spectra, the excimer and monomer components can be separated[17] and compared with the electron-impact-induced spectra. This is shown in Fig. 17.9 by the broken line. The emission spectrum of singlet-state excimers, $^1M_2^*$, for toluene and ethylbenzene was obtained from the ultraviolet-induced spectra at $-77°C$, where the excimer emission intensity is enhanced compared with that at room temperature. From Fig. 17.9 it is seen that the emission under electron impact coincides with that of $^1M_2^*$ induced by ultraviolet light. This is also clearly shown in Fig. 17.10, where the emission from the three liquid naphthalene derivatives under ultraviolet excitation is almost entirely due to $^1M_2^*$ and coincides with that under electron impact (note, however, the slight difference in the position of the 1,6-dimethylnaphthalene spectra). Results similar to those shown in Figs. 17.9 and 17.10 have been obtained for a large number of benzene and naphthalene derivatives.[18]

From the data presented in Figs. 17.9 and 17.10 and a detailed comparison of the spectral characteristics of the electron-impact-induced emission with those of $^1M_2^*$, it has been concluded that the structureless emission observed under electron bombardment is due to singlet-state excimers, $^1M_2^*$. Further support for this interpretation is provided from the lifetime measurements discussed in the next section. It might be noted that other excimeric species such as triplet,

[14] J. B. Birks, L. G. Christophorou, and R. H. Huebner, *Nature* **217**, 809 (1968).

[15] R. Pariser, *J. Chem. Phys.* **24**, 250 (1956).

[16] R. N. Compton *et al.*, *J. Chem. Phys.* **48**, 901 (1968).

[17] J. B. Birks and L. G. Christophorou, *Proc. Roy. Soc. (London)* **274A**, 552 (1963); **277A**, 571 (1964).

[18] M-E. M. Abu-Zeid, L. G. Christophorou, and J. G. Carter, *Emission and Decay of Organic Liquids Under Electron Impact*, ORNL-TM-2219 (1968).

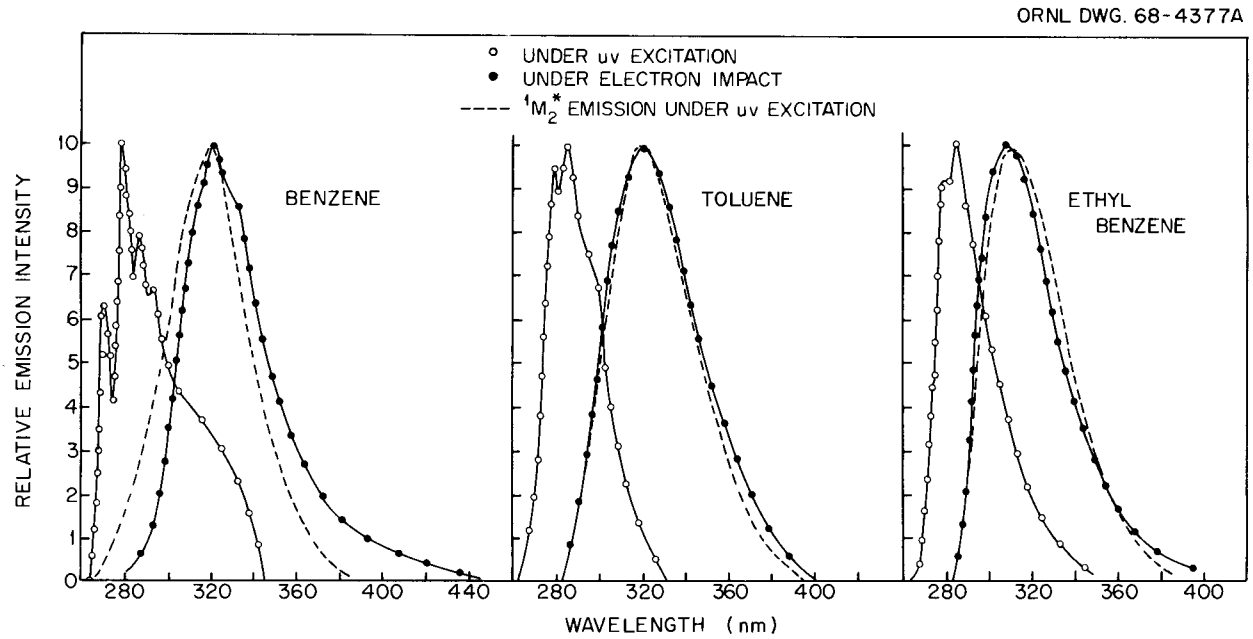

Fig. 17.9. Emission from Liquid Benzene, Toluene, and Ethylbenzene Under uv Excitation, Under Electron Impact, and $^1M_2^*$ Emission Deduced from uv-Induced Emission in Concentrated Solutions. All spectra under electron impact were taken at room temperature.

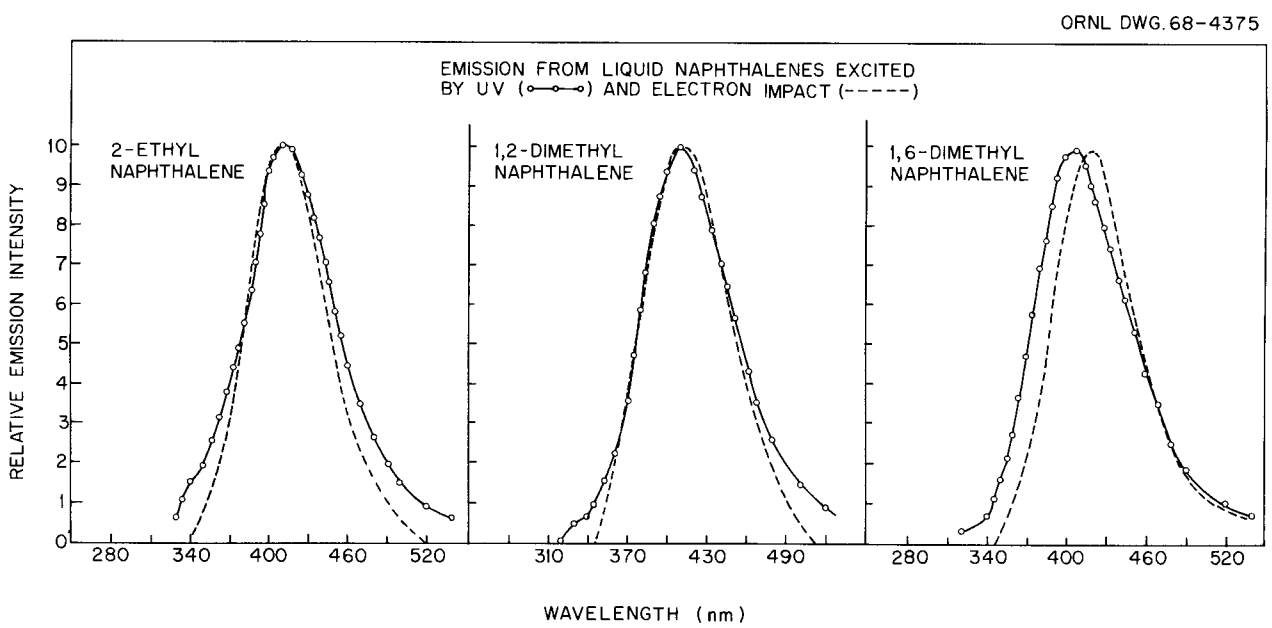

Fig. 17.10. Emission from Liquid 2-Ethylnaphthalene, 1,2-Dimethylnaphthalene, and 1,6-Dimethylnaphthalene Under uv Excitation and Under Electron Impact.

$^3M_2^*$, and possibly quintet, $^5M_2^*$, state excimers are known to form and may emit.[19–22]

The production of $^1M_2^*$ under electron impact is believed[23] to be via a one-step (or a sequential two-step) ion-recombination process, that is,

$$M_1^+ + e + {}^1M_1 \longrightarrow {}^{1,3}M_2^{**} \xrightarrow{?} {}^{1,3}M_2^* \begin{cases} \nearrow {}^1M_1 + {}^1M_1 + h\nu \text{ (excimer)} \\ \searrow {}^1M_1^* + {}^1M_1 \longrightarrow {}^1M_1 + {}^1M_1 + h\nu \text{ (monomer)} \end{cases} \quad . \quad (7)$$

The absence of monomer, $^1M_1^*$, emission has been attributed[23] to strong monomer quenching. As we have reported earlier,[23] a dose rate of 10^7 rads/sec is estimated in our emission work with electrons, although much higher dose rates are possibly involved in the region close to the liquid surface at the entrance of the electron beam.

On the basis of process (7), $^3M_2^*$ species are also formed in our electron impact experiments. Although the observed emission is entirely (or predominantly) characteristic of the $^1M_2^*$ species, for the compounds 1,4-diethyl benzene, 1,4-dimethyl-2-ethyl benzene, 1,3-dimethyl-4-ethyl benzene, 1,2,3,5-tetramethylbenzene, isobutylbenzene, and *n*-pentylbenzene a weak emission band, shifted to longer wavelengths with respect to the $^1M_2^*$ band, has been observed at ~500 nm. Figure 17.11 shows the emission from four of these compounds (the purity of all four compounds was

[19] G. Castro and R. M. Hochstrasser, *J. Chem. Phys.* **45**, 4352 (1966).

[20] J. B. Birks, *Phys. Letters* **24A**, 479 (1967).

[21] E. C. Lim and S. K. Chakrabarti, *Mol. Phys.* **13**, 293 (1967).

[22] J. Langelaar, R. P. H. Rettschnick, A. M. F. Lambooy, and G. J. Hoytink, *Chem. Phys. Letters* **1**, 609 (1968).

[23] J. G. Carter, L. G. Christophorou, and M-E. M. Abu-Zeid, *J. Chem. Phys.* **47**, 3879 (1967).

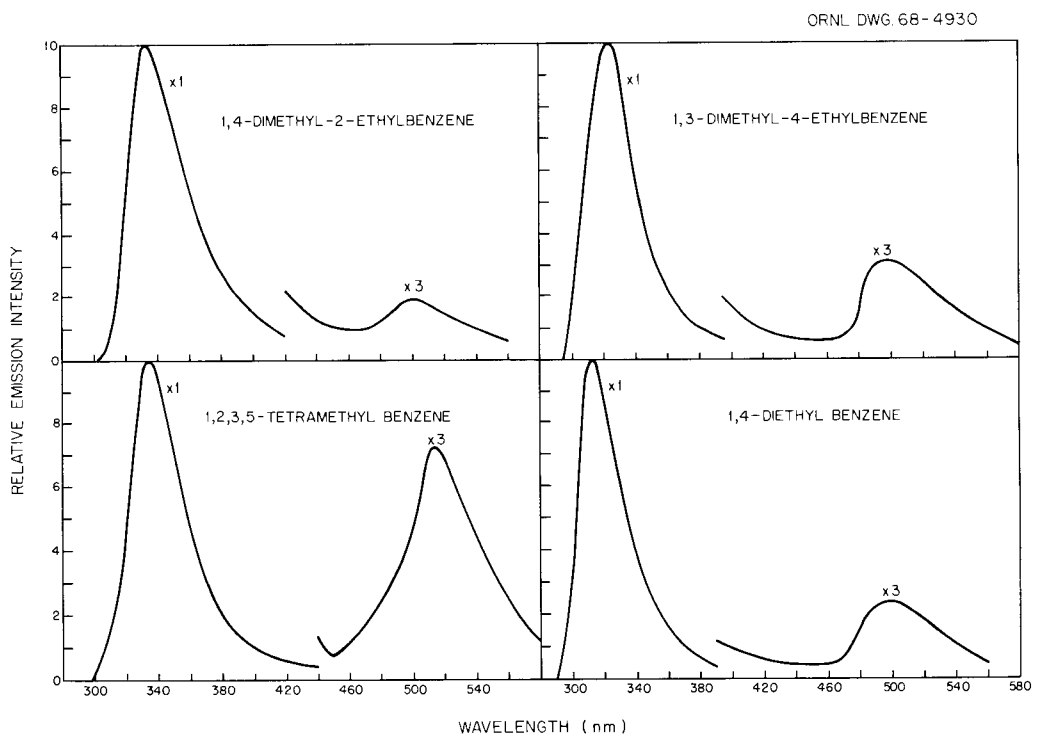

Fig. 17.11. Emission Spectra from Liquid 1,4-Diethylbenzene, 1,4-Dimethyl-2-ethylbenzene, 1,3-Dimethyl-4-ethylbenzene, and 1,2,3,5-Tetramethylbenzene Under Electron Impact, Showing, in Addition to the $^1M_2^*$ Band, a Peak at ~500 nm Attributed to $^3M_2^*$.

greater than 99%). Excluding the possibility of emission from photoproducts, the weak bands at ~500 nm can be attributed to emission from triplet-state excimers, $^3M_2^*$. A structureless emission in the same wavelength region observed[21] in studies of halogenated benzenes in organic glasses has been similarly attributed[21] to triplet-state excimers.

LIFETIMES OF LIQUID BENZENE AND LIQUID BENZENE AND NAPHTHALENE DERIVATIVES EXCITED BY ELECTRON IMPACT

We have described earlier[24] the principle of a nanosecond pulsed electron source for the measurement of the lifetimes of luminescent species excited by electron impact. The development of the method has been completed, and lifetimes for 13 organic molecules excited by electron impact have been measured.

The decay curves obtained by this pulsed sampling technique represent the combined effect of the instrumental response function and the true time course of the rise and decay of the sample scintillation emission. Letting the response function of the system be $I(t)$ and the true time course of the scintillation emission be $f(t)$, the total response function, $F(t)$, is given by the convolution integral,

$$F(t) = \int_0^t I(t')\, f(t - t')\, dt' . \tag{8}$$

Assuming that

$$f(t) = \frac{N}{\tau}\, e^{-t/\tau} , \tag{9}$$

where N is a normalizing constant and τ is the scintillation decay time, we have

$$\tau \frac{dF(t)}{dt} + F(t) = N\, I(t) . \tag{10}$$

Equation (10) was used to determine the response function of the system. Although a number of workers[25] have used anthracene crystals (as a standard) to determine $I(t)$, liquid standards (Nuclear Enterprises Nos. 213, 215, 223, 225, 227, and 317)[26] have been used in the present study.[27] It was found that the response function of the equipment (which depends on several factors)[25] is a Gaussian whose width is predominantly determined by the phototube voltage (decreasing with increasing phototube voltage). For phototube voltages above 1800 v the width became <2 nsec. Typical $I(t)$ functions are shown in Fig. 17.12 for a number of phototube voltages. It is seen that $I(t)$ approaches zero intensity within 5 to 10 nsec, depending on the phototube voltage.

Representing $I(t)$ by $e^{-(t/\tau_i)^2}$, where τ_i is a parameter characteristic of the width of the Gaussian function, we have

$$F(t) \cong \text{constant}\; e^{-t/\tau} \tag{11}$$

for large values of t. Equation (11) was applied to determine τ from $F(t)$ directly.

A representative set of data on the decay of emission from the organic liquids studied by electron impact is shown in Fig. 17.13. Curve *a* gives the response of the equipment, while curve *b* shows the rise and decay of the benzene luminescence. From the decay portion of *b* we obtained Fig. 17.13c, the inverse of the slope of which yields the mean lifetime of the emitting species. The average of nine independent measurements gave a mean lifetime of 12.25 nsec. Similar measurements were made for a number of other liquids, and the results are summarized in Table 17.1. No change in the measured lifetime was detected in any of the compounds listed in the table when the electron current was changed by a factor of ~5 at constant electron energy (56 kev). For 2-ethylnaphthalene no change in the measured lifetime was observed when the elec-

[24] *Health Phys. Div. Ann. Progr. Rept. July 31, 1967*, ORNL-4168, p. 161.

[25] See, for example, R. K. Swank, H. B. Phylips, W. L. Buck, and L. J. Basile, *IRE Trans. Nucl. Sci.* **NS-5**, 183–87 (December 1958); D. F. McDonald, B. J. Dunn, and J. V. Braddock, *IRE Trans. Nucl. Sci.* **INS-7**, 17–22 (June–September 1960).

[26] The lifetimes of these standards have been measured by E. A. Yates, D. G. Crandall, and J. Kirkbride, *Scintillation Time Response Measurements*, Technical Note No. S-60,2104, EGG 1183-2104, August 1966 (Santa Barbara Division).

[27] For problems arising when anthracene crystals are used as standards, see J. B. Birks, *The Theory and Practice of Scintillation Counting*, The Macmillan Co., New York, 1964.

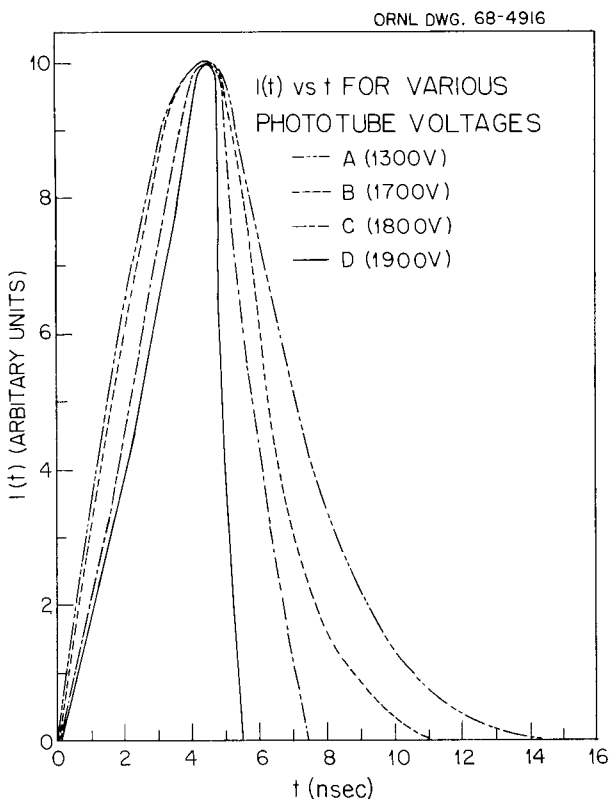

Fig. 17.12. Typical Response Functions for the Equipment at Various Phototube Voltages.

Table 17.1. Lifetimes of the Emitting Species in Liquid Benzene and Liquid Benzene and Naphthalene Derivatives Under Electron Impact

Compound[a]	Lifetime[b] (nsec)	Purity[c] (%)
Benzene	12.25 ± 0.2	99.99
Toluene	15.65 ± 0.2	99.66
Ethylbenzene	8.56 ± 0.1	99.9
i-Propylbenzene	8.73 ± 0.1	99.9
n-Propylbenzene	12.56 ± 0.2	99.99
o-Xylene	11.71 ± 0.14	99.9
m-Xylene	11.13 ± 0.24	99.9
p-Xylene	11.9 ± 0.3	99.99
Mesitylene	22.86 ± 0.3	99.8
1-Methylnaphthalene	68.67 ± 0.2	99.3
2-Ethylnaphthalene	25.39 ± 0.1	99.99
1,2-Dimethylnaphthalene	48.45 ± 0.36	99.77
1,6-Dimethylnaphthalene	35.4 ± 1	99.96

[a]Oxygen-free liquids.

[b]Average of 4 to 5 runs; these values must be considered as lower limit since traces of oxygen may affect the measured life time.

[c]Estimated by gas chromatography.

tron beam intensity was decreased from 1.3×10^{-8} to 9×10^{-10} amp at constant beam energy (56 kev).

Birks *et al.*[28] analyzed the results of Ivanova *et al.*[29] on the variation with concentration of the decay time of benzene, toluene, and *p*-xylene in deoxygenated hexane solutions (under ultraviolet excitation) and obtained 12, 16, and 12 nsec for the lifetime of ${}^1M_2^*$ in benzene, toluene, and *p*-xylene respectively. The almost exact agreement of these values with our measurements in Table 17.1 supports our spectroscopic data and our interpretation that the main emission under electron impact originates from ${}^1M_2^*$. The finding that

$$\tau\left({}^1M_2^*\right)_{uv} \cong \tau\left({}^1M_2^*\right)_e \qquad (12)$$

suggests that ${}^1M_2^*$ is resistant to ionization quenching. This indicates a drastic difference in the ionization quenching probabilities of ${}^1M_1^*$ and ${}^1M_2^*$. Further, it has been reported by Christophorou and Carter[30,31] that ${}^1M_2^*$ in 2-ethylnaphthalene is more resistant to collisional quenching than ${}^1M_1^*$. This finding is supported by the present experiments, where the lifetime of ${}^1M_2^*$ is found to be the same in oxygen-free and oxygen-saturated liquid benzene, although the lifetime of ${}^1M_1^*$ was reported[29] to have decreased from 26 nsec for benzene in oxygen-free solutions in hexane to 5.7 nsec in the corresponding oxygen-saturated solution.

In view of (12) the present lifetime measurements have been used in connection with the quantum ef-

[28]J. B. Birks, C. L. Braga, and M. D. Lumb, *Proc. Roy. Soc. (London)* **283A**, 83 (1965).

[29]T. V. Ivanova, G. A. Mokeeva, and B. Ya Sveshnikov, *Opt. Spectry.* **12**, 325 (1962).

[30]L. G. Christophorou and J. G. Carter, *Nature* **212**, 816 (1966).

[31]J. G. Carter and L. G. Christophorou, *J. Chem. Phys.* **46**, 1883 (1967).

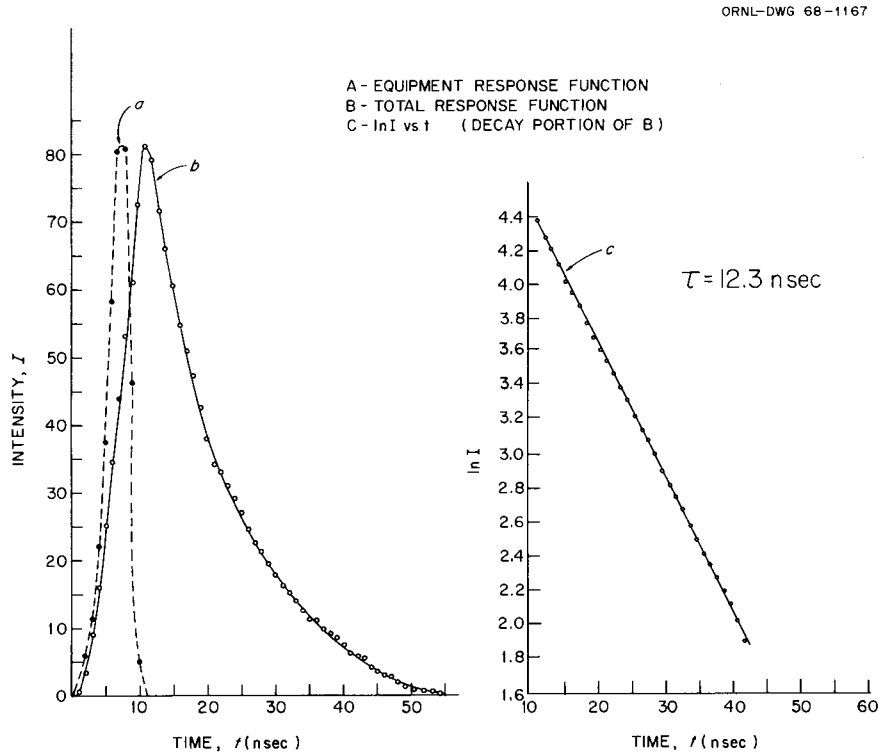

Fig. 17.13. Decay of Liquid Benzene Under Electron Impact.

ficiency data for $^1M_2^*$ reported by Lumb and Weyl[32] to determine the radiative rate constant $k_f(^1M_2^*)$ of $^1M_2^*$ for a number of benzene derivatives.

IONIZATION EFFICIENCIES OF MOLECULES

The greatly enhanced ionization yield obtained when impurity molecules are present in an irradiated rare gas (the so-called Jesse effect) has been attributed first to the role of metastable states and, more recently,[33] to the discharge of resonance excited states of the rare-gas atoms. A positive identification of the responsible agents is fundamental to an understanding of radiation action. An earlier analysis has given the quantity $G_n\eta_i$, where G_n is the 100-ev yield of the sensitizing states in argon and η_i is the ionization efficiency of the sensitized impurity.

Using a standard ionization chamber and vacuum ultraviolet monochromator, we have measured the photoionization efficiency of a number of molecules at wavelengths of 1067 and 1048 A; these wavelengths correspond to the energies of the resonance states suspected to be precursors to the Jesse effect in argon. Figure 17.14 shows the good correlation between $G_n\eta_i$ and the η_i(photons), strongly supporting the notion that the resonance states are indeed the active agents. The slope then yields a unique measure of G_n for these states.

Implicit in this comparison is the notion that the ionization efficiency of a molecule excited by photons is identical with that pertinent to sensitization by an excited atom of like energy. This remarkable equality is supported by the correlation in Fig. 17.14 and may be rationalized in terms of standard theories of energy transfer.

TRANSITION YIELDS IN IRRADIATED GASES

As interpretations of the action of high-energy radiation on matter become more refined, approach-

[32] M. D. Lumb and D. A. Weyl, *J. Mol. Spectry.* **23**, 365 (1967).

[33] G. S. Hurst, T. E. Bortner, and R. E. Glick, *J. Chem. Phys.* **42**, 713 (1965).

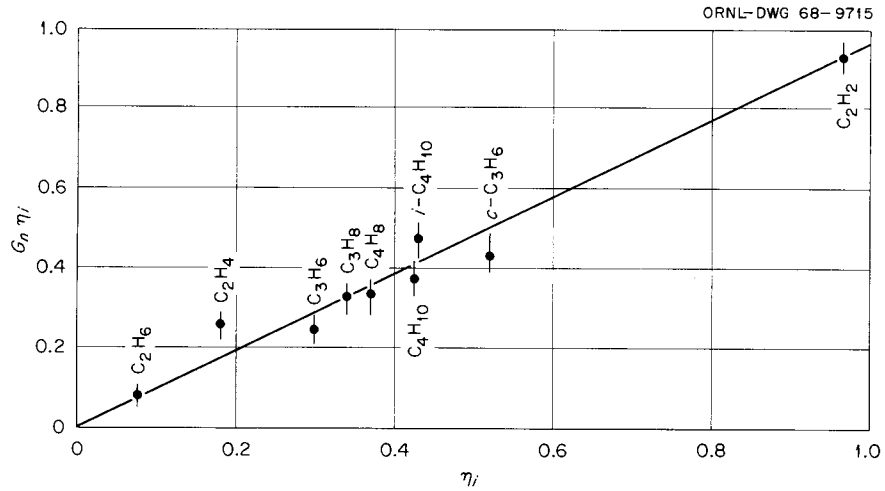

Fig. 17.14. Correlation Between the Observed Sensitized Ionization in Irradiated Argon and the Photoionization Efficiency for Several "Impurity" Molecules.

ing, as they now are, discussion in terms of the primary quantum transitions involved, it becomes timely to investigate methods for predicting the nature and yields of such transitions. This is especially true as both microscopic excitation cross-section data and experimental yield measurements become increasingly available.

Earlier work from this laboratory involving experimental and theoretical investigations of degradation spectra may be viewed as an important first step toward the desired understanding. One phase of this work involves the theoretical construction of approximate degradation spectra accompanying the slowing down of characteristic radiations in representative gaseous media. These spectra, obtained at several levels of approximation, are then used in conjunction with cross-section data from the literature to compute yields of several types of electronic transitions. The degree of consistency in the computed yields may then be taken as a measure of the sensitivity of such results to the assumptions inherent in the calculations.

Table 17.2 illustrates the nature of the results obtained. The degradation spectra employed are pertinent to 5-Mev alpha particles slowing down in the several gases and were computed both with and without neglect of the binding of the K-shell electrons. Yields were obtained with experimental cross-section data and, when possible, with cross sections obtained from the Born approximation. They are seen to be, indeed, quite insensitive to the origin of $y(T)$, the degradation spectrum assumed.

Of particular interest in each case are the yields of a transition predicted by the optical approximation. These yields may be obtained from simple optical data and are thought to be appropriate to a projectile of extremely high initial velocity. The discrepancies then presumably reflect the finite velocity of the alpha particle and hence the nonequivalence of high-energy radiations.

Table 17.2. Transition Yields from 5-Mev Alpha Particles

Cross Sections	$y(T)$							Optical	Observed Yield
	He	N_2		CH_4		O_2			
		Free	Born	Free	Born	Free	Born		
He 2^1P									
Born	0.70	0.75	0.74	0.65	0.66	0.81	0.81	0.68	1.01
Expt.	0.53	0.56	0.56	0.51	0.52	0.58	0.58		
He 3^1P									
Born	0.19	0.21	0.21	0.185	0.185	0.225	0.225	0.17	0.43
Expt.	0.16	0.17	0.17	0.16	0.16	0.17	0.17		
He 2^1S									
Born	0.11	0.125	0.12	0.091	0.096	0.14	0.14	0.0	
Expt.	0.059	0.065	0.066	0.052	0.053	0.073	0.072		
O_2, 8.44 ev (Born)	1.37	1.29	1.30	0.87	0.95	1.39	1.40	0.24	
N_2^+, $B^2\Sigma_u^+$, $v' = 0$ (expt.)	0.092	0.090	0.090	0.093	0.093	0.089	0.089	0.124	0.15

18. Electron and Ion Collision Physics

R. N. Compton

V. E. Anderson[1]
J. F. Burns[2]
Ada Carter
C. D. Cooper[2]
F. J. Davis
J. A. Harter
R. H. Huebner[3]
G. S. Hurst[2]
A. G. Kenerly[4]
W. T. Naff[5]
D. R. Nelson
P. W. Reinhardt
H. C. Schweinler
J. A. Stockdale

DETERMINATION OF DIFFUSION COEFFICIENTS OF THERMAL ELECTRON SWARMS IN GASES

Thermal electron diffusion coefficients were determined in nine gases. A time-of-flight method was modified so that the diffusion of electron swarms could be studied in an electric-field-free region.[6] Thermal electron diffusion was investigated by switching off the electric field when the swarm had drifted to the center of the chamber, allowing the swarm to diffuse for varying periods of dwell time (DwT), and then reapplying the drift field to sweep the electrons to the detector. The increasing width of the swarm time-of-arrival distribution with DwT provided a measure of the thermal diffusion coefficient. The drifting of the swarm to and dwelling at the center of the chamber followed by drifting to the detector produced a drift-dwell-drift (DDD) movement of the swarm; from this arose the name "DDD technique."

The coefficients of diffusion were determined from two measured quantities t_m and δt, where t_m corresponds to the peak drift time (DrT) and δt to the $1/e$ full width of the time-of-arrival distribution. However, t_m and δt generally had to be corrected for three types of distortion caused by (1) nonrandom sampling of the swarm, (2) a convolution of the experimental fluctuation distribution with the true diffusion distribution, and (3) the non-Gaussian shape of the time-of-arrival distribution due to the swarm being sampled in time instead of in space. Since several diffusion processes occur in the DDD technique, a simple unfolding of the distorted experimental data to obtain the drift velocity w and diffusion coefficient D was not possible. Instead, a correction-factor method was devised and verified whereby the measured values of t_m and δt are corrected to the true drift time t_0 and ideal full width δt_0 such that w and D can be calculated, respectively, from the relations

$$w = L/t_0 \tag{1}$$

and

$$D = \frac{w^2 (\delta t_0)^2}{16 t_0} . \tag{2}$$

The mean thermal diffusion-pressure ($D_t P$) values determined were 0.213, 2.08, 0.883, 0.132, 0.293, 0.177, 0.015, 0.251, and 0.278 $cm^2\ \mu sec^{-1}$ torr for He, Ne, Ar, H_2, N_2, CO, CO_2, CH_4, and C_2H_4 respectively. These values, except for Ne, have been compared in Fig. 18.1 with the DP vs E/P

[1]On loan from Central Data Processing Facility (ORGDP).

[2]Consultant.

[3]Radiological Health Physics Fellow.

[4]On loan from Instrumentation and Controls Division.

[5]Graduate Student, University of Georgia.

[6]*Health Phys. Div. Ann. Progr. Rept. July 31, 1967*, ORNL-4168, p. 156.

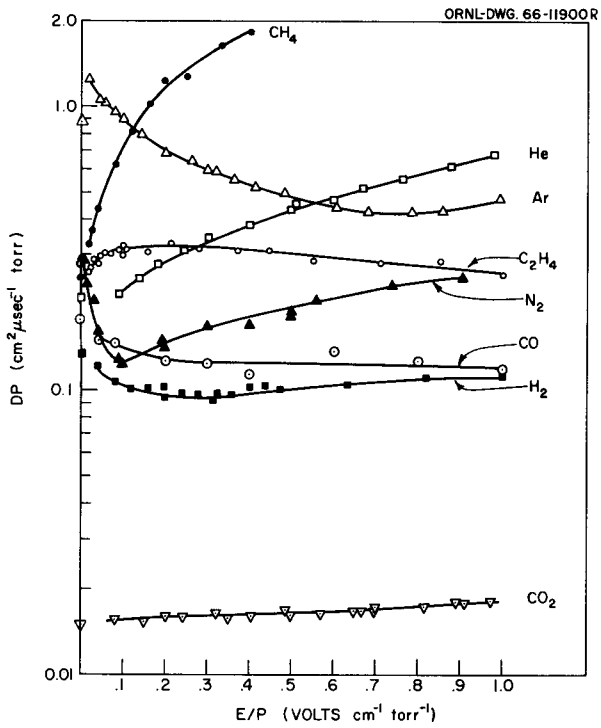

Fig. 18.1. Variation of *DP* as a Function of *E/P* for Indicated Gases. Present thermal *DP* values are found on the ordinate for $E/P = 0$. The data of E.B. Wagner, F. J. Davis, and G. S. Hurst, *J. Chem. Phys.* **47**, 3138 (1967) (WDH) are shown for increasing *E/P* and are connected by solid lines.

data of Wagner, Davis, and Hurst (WDH).[7] An extrapolation of the WDH data to $E/P = 0.0$ gives good agreement with the present thermal diffusion values except for Ar and C_2H_4. The thermal *DP* value found for Ar is lower than a WDH extrapolated value because of the increased scattering cross section near zero energy. The discrepancy between the thermal *DP* value found for C_2H_4 and a reasonable extrapolation of the WDH data is not understood. It has been suggested that this discrepancy arises from a temporary negative ion of C_2H_4.[8] A refined and more exact data analysis is presently being developed which should help to resolve the problem.

[7]E. B. Wagner, F. J. Davis, and G. S. Hurst, *J. Chem. Phys.* **47**, 3138 (1967).

[8]G. S. Hurst and J. E. Parks, *J. Chem. Phys.* **45**, 282 (1966).

EQUILIBRATION OF ELECTRON SWARMS IN ARGON TO A THERMAL ENERGY DISTRIBUTION

The necessity of allotting some period of time for an electron swarm to equilibrate to a thermal energy distribution from that distribution it had during its drift to the center of the chamber was dramatically demonstrated for the case of argon. A set of $(\delta t_0)^2$ for 100-torr argon vs [drift time, DrT, plus drift dwell time, DwT] data is shown in Fig. 18.2. Referring to Fig. 18.2, the first set of data points corresponds to the straight diffusion with no DwT. The second set of points is separated from the first set by a period of time referred to as the equilibration period. The slope of the line between the second and the third sets of data points provides the value of $16D/w^2$ for diffusion of the thermally equilibrated swarm (where D is the diffusion coefficient and w the drift velocity). The sharp discontinuity between the first and

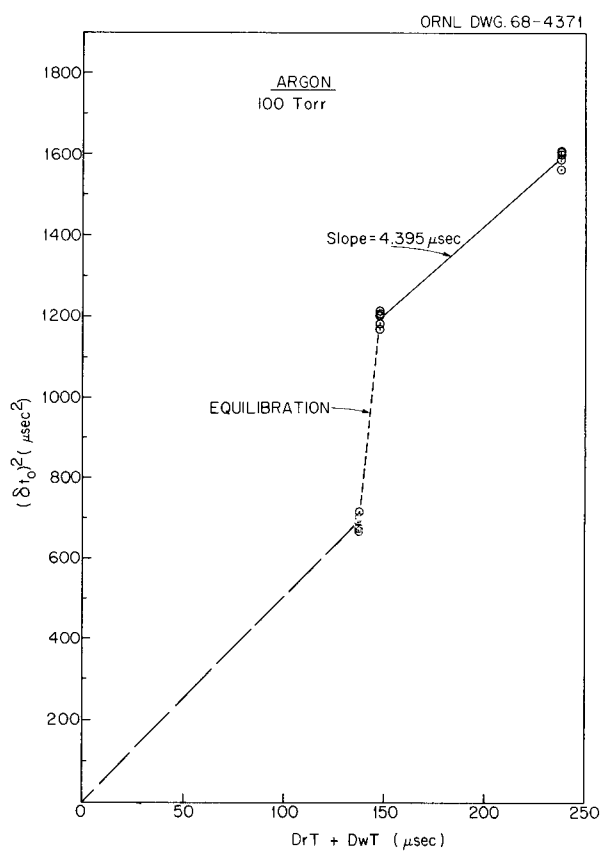

Fig. 18.2. Argon Diffusion Data.

second set of data points was only observed for the argon data because of two commensurate factors: (1) the sharp change in the e^--Ar scattering cross section near the Ramsauer-Townsend (R-T) window and (2) the unusually small fractional energy loss per elastic collision of an electron with Ar molecules.

The equilibration process in argon was studied in greater detail at a pressure of 50 torrs for two E/P distributions. The $(\delta t_0)^2$ vs DwT data for energy distributions corresponding to $E/P = 0.05$ and 0.07 v cm^{-1} torr^{-1} are shown in Figs. 18.3 and 18.4. The total time required for these two E/P electron swarms to equilibrate to a thermal energy distribution was $\sim$10 and 15 μsec respectively.

The equilibration process is further elucidated in Fig. 18.5, where the total e^--Ar scattering cross section of Golden and Bandel[9] is shown with the electron energy distributions corresponding to values of $E/P = 0.00$, 0.05, and 0.07. It is evident that the majority of electrons of the distributions for $E/P = 0.05$ and 0.07 lie above the 0.285-ev R-T window and will eventually "see" the window before reaching the thermal energy distribution. For the period of time that the electrons are in the vicinity of the window, their probability of collision is small, which increases their mean free path and results in a large coefficient of diffusion. Because the electrons have a low mean fractional energy loss ($\Delta \sim 2m/M \sim 2.7 \times 10^{-5}$) for elastic collisions, many collisions (and a large amount of diffusion) of the electrons occur before they pass through the R-T window. In contrast to argon, methane has a total scattering cross section that is closely similar to argon in both magnitude and shape at energies below 10 ev;[10] however, rotational and vibrational modes of excitation in methane allow large fractional energy losses through inelastic-type collisions. Thus, electron scattering through the R-T window of methane is so rapid that very little diffusion

[9] D. E. Golden and H. W. Bandel, *Phys. Rev.* **149**, 58 (1966).

[10] H. S. W. Massey and E. H. S. Burhop, *Electronic and Ionic Impact Phenomena*, Oxford University Press, London, 1952.

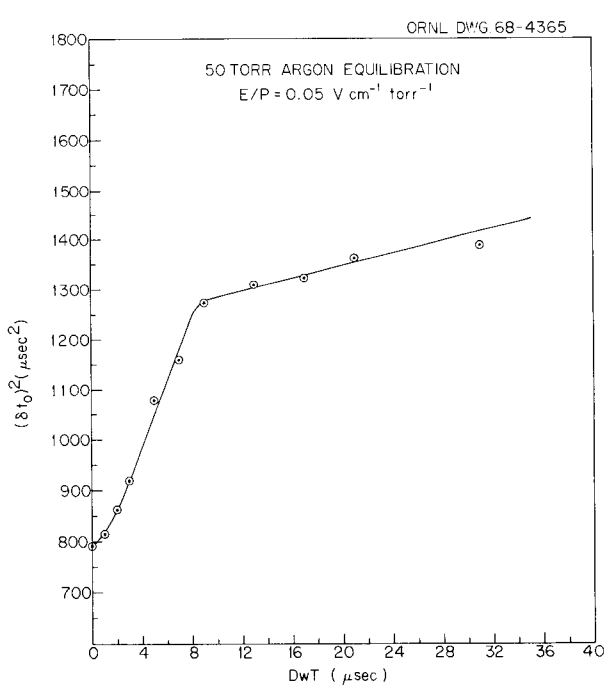

Fig. 18.3. Argon Equilibration for $E/P \cong 0.05$ v cm^{-1} torr^{-1} at 50 Torrs.

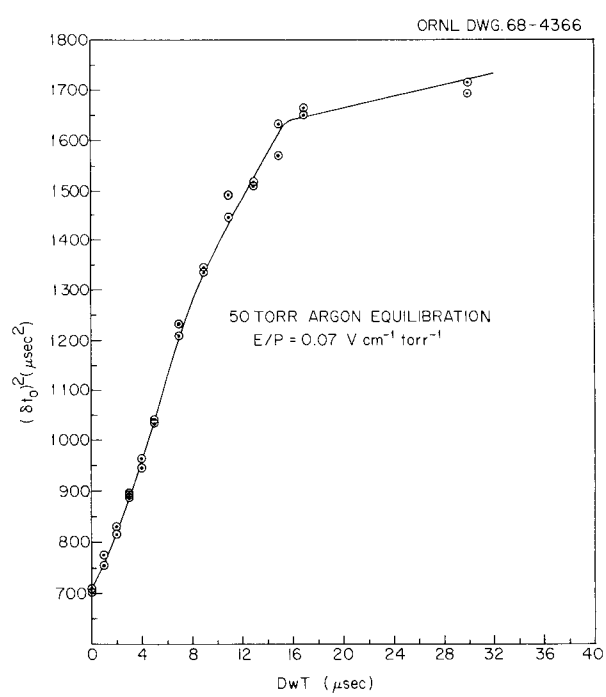

Fig. 18.4. Argon Equilibration for $E/P \cong 0.07$ v cm^{-1} torr^{-1} at 50 Torrs.

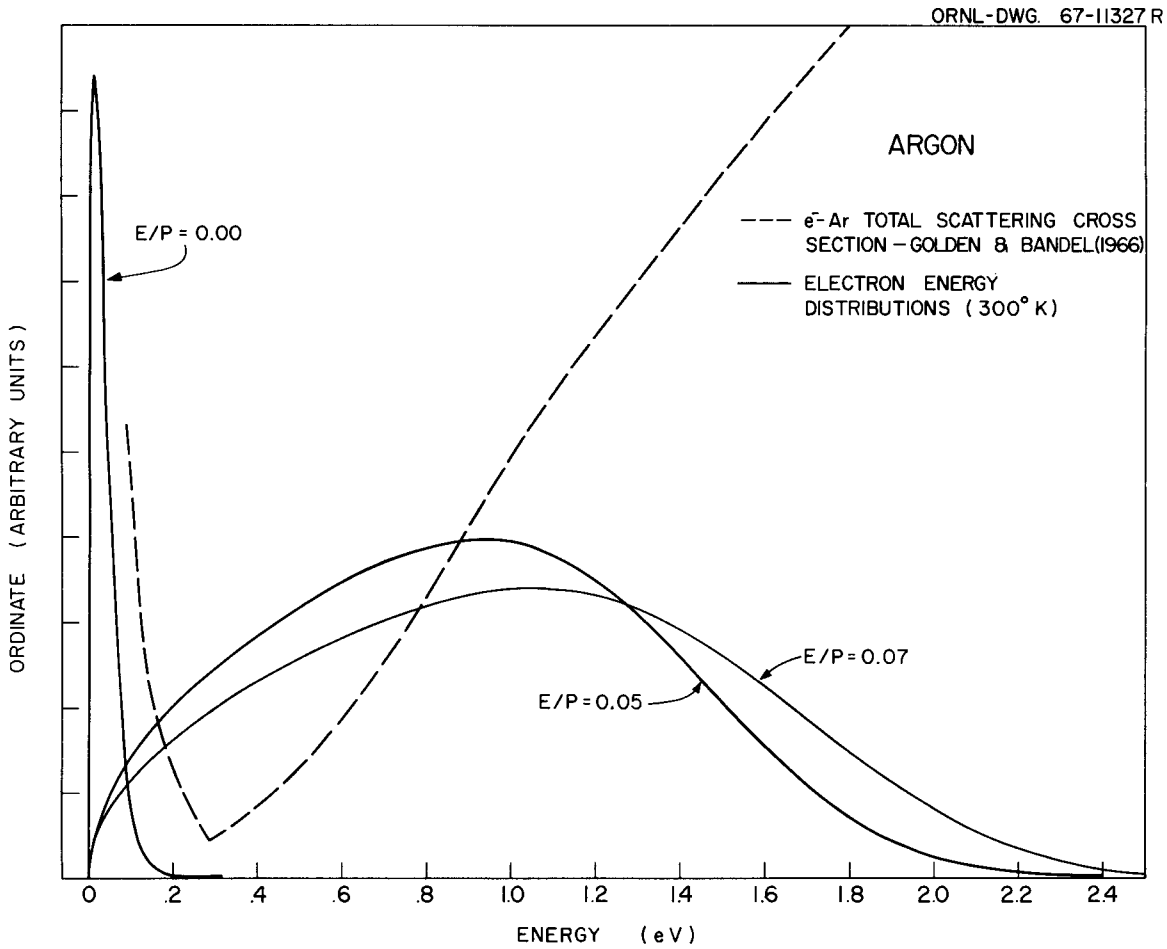

Fig. 18.5. Equilibration of Electron Swarms Through the Ramsauer-Townsend Window in Argon.

occurs in the vicinity of the window, thereby making it difficult to observe any discontinuity in the $(\delta t_0)^2$ vs DwT diffusion data of methane.

EXCITATION OF ATOMS AND MOLECULES BY ELECTRON IMPACT

Threshold electron impact excitation spectra obtained with the SF_6 "scavenger" technique have been presented for a number of molecules.[11] Electrons with energy very close to the excitation threshold of a molecule AB are thermalized by inelastic scattering and subsequently captured by SF_6, that is,

$$e_{fast} + AB \longrightarrow AB^* + e_{thermal},$$

$$e_{thermal} + SF_6 \longrightarrow SF_6^- .$$

The energy-loss spectrum obtained by recording the SF_6^- current as a function of energy (in the presence of a sample gas) is therefore called a "threshold" excitation spectrum. The method has shown a remarkable sensitivity for the detection of optically forbidden transitions and temporary negative ion resonances, because such transitions are allowed under electron impact and are strongly peaked near their thresholds. Previous studies over the past two years have included helium, mercury, hydrogen, nitrogen, hydrogen chloride, water, heavy water, diacetyl, glyoxal, benzene, nitrobenzene, and naphthalene. More recently, excitation spectra have been obtained

[11] R. N. Compton *et al.*, *J. Chem. Phys.* **48**, 901 (1968).

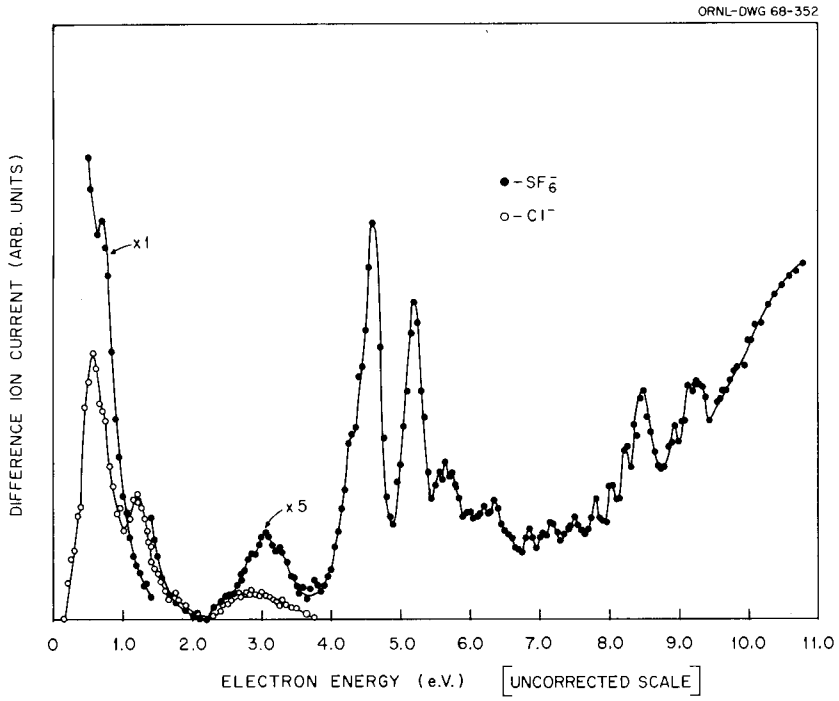

Fig. 18.6. Threshold Electran Impact Excitation Spectrum of 1-Chloronaphthalene.

for 1-chloronaphthalene, 1-bromonaphthalene, xenon hexafluoride, pyridine, and azulene. Figure 18.6 shows the excitation spectrum of chloronaphthalene. The SF_6^- ion current (closed circles) shows a slight peak at ~0.6 ev, which corresponds to the Cl^- peak at 0.55 ev, indicating that some electrons with ~0.0 ev are autoionized from the lowest negative ion state in competition with dissociation of the Cl^- ion. The spectral features are quite similar to those of naphthalene and further substantiate the previous optically observed peak in the naphthalene spectrum at 5.4 ev.

The excitation spectrum of azulene, shown in Fig. 18.7, may be the most important excitation spectrum studied thus far. Azulene has long been known to violate the general rule that the primary emitting level of a molecule is the lowest level of a given multiplicity (i.e., S_1 or T_1). Azulene, however, shows a unique emission from the second singlet state only (i.e., $S_2 \rightarrow S_0$), and no phosphorescence has been detected. Various possible explanations for this phenomenon have been proposed, among them the suggestion[12] that if a triplet level lay close to S_2, then $S_2 \rightarrow T_2$ may be fast compared with $S_2 \rightarrow S_1$, explaining the absence of any observed fluorescence from S_1. The subsequent energy transfer to a low-lying triplet

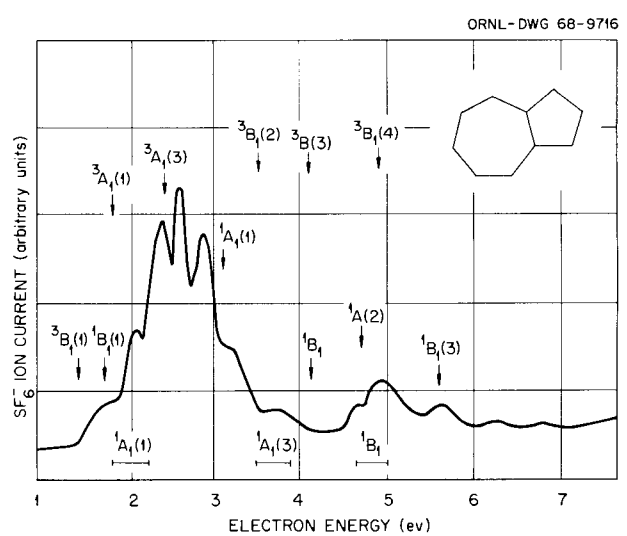

Fig. 18.7. Threshold Electron Impact Excitation Spectrum of Azulene.

[12]N. J. Turro, *Molecular Photochemistry*, p. 61, W. A. Benjamin, Inc., New York, 1965.

state ($T_2 \rightarrow T_1$) which then undergoes a radiationless transition to the ground state would account for the apparent lack of phosphorescence. All direct attempts to observe the triplet states of azulene have failed, so that this explanation is at best tentative. Figure 18.7 shows support for this suggestion if the three well-defined peaks between the first and second singlet states are attributed to triplet states lying above the lowest triplet at ~1.6 ev.

The electron impact excitation spectrum of xenon hexafluoride has also been studied and shows three well-resolved electronic states above 3 ev. Studies of xenon difluoride and xenon tetrafluoride are in progress. Information concerning the position of the electronic states will increase the understanding of the structure of these rare-gas molecules.

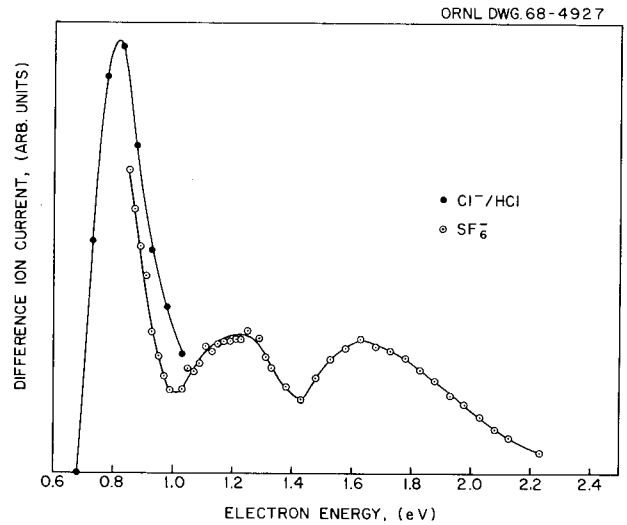

Fig. 18.8. Threshold Negative Ion Resonances in Pyridine.

TRANSIENT NEGATIVE ION RESONANCES IN MOLECULES

Short-lived negative ion states in molecules are known to give rise to unusually large energy-loss resonances in inelastic electron scattering cross sections.[13] Recently the SF_6 scavenger technique has been employed to observe temporary negative ion resonances in benzene, naphthalene, and seven benzene derivatives. The benzene resonance occurred as a single resonance peaking at 1.55 ev, which is consistent with theoretical electron affinity values ranging from −1.4 to −1.63 ev. Pyridine, which is isoelectronic with benzene (C-H is replaced by a nitrogen atom), however, shows a doublet negative ion state: one peaking at the energy of the benzene resonance (1.55 ev) and another ~0.4 ev lower in energy (see Fig. 18.8). This splitting is attributed to a removal of the degeneracy of the benzene negative ion due to the presence of a more electronegative atom (nitrogen) present in the ring.

The SF_6 scavenger technique was also employed to detect transient negative ion states in a series of fluorinated benzenes, and the peak of the resonance occurred at 1.35 ev for C_6H_5F, 0.6 ev for 1,3-$C_6H_4F_2$, 0.3 ev for 1,3,5-$C_6H_3F_3$, and ~0 ev for 1,2,3,4-$C_6H_2F_4$ and C_6HF_5. The peak energies of the resonances shown in Fig. 18.9 decrease approximately linearly with the number of fluorines added to the benzene ring. A plot of resonance energy vs number of fluorine substituents added to the benzene ring gives a straight line with a slope of 0.4 ev/fluorine, which loosely implies that each fluorine added to the benzene ring increases the electron affinity by ~0.4 ev.

A new high-resolution electron transmission apparatus employing a 127° electrostatic analyzer has been constructed to determine the total scattering cross sections and to search for structure in the temporary negative ion resonances. Figure 18.10 shows the temporary negative ion resonance in ethylene determined from the transmission experiment (*B*) together with the SF_6 scavenger (*C*) and the trapped electron results (*D*). Also shown are the transmission studies of Boness and Hasted (*A*). Aside from the "dip" in the electron transmission at 1.8 ev, there was no further structure detected. The resonance apparent in the transmission (*B*) and SF_6 scavenger studies at 1.8 ev occur very close to the theoretical electron affinity calculations (*E*, *F*). No vibrational structure was observed in the ethylene resonance, although electron energy resolution was sufficient to observe eight vibrational levels in the N_2^- resonance. The cross section for the ethylene resonance was determined by comparison with the measured value for nitrogen to be $1.0 \pm 0.5 \times 10^{-15}$ cm^2.

[13] G. J. Schulz, *Phys. Rev.* 116, 1141 (1959).

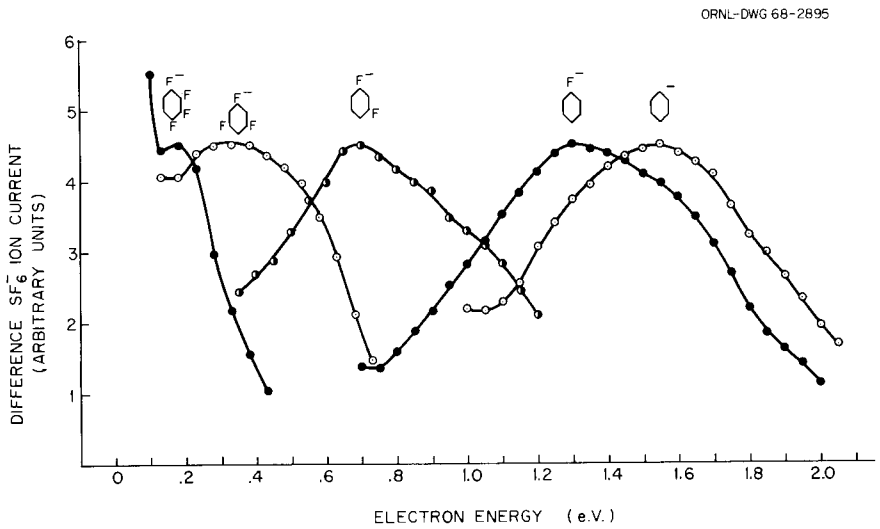

Fig. 18.9. Electron Energy Loss Resonances Due to Temporary Negative Ion States for a Series of Fluorinated Benzenes.

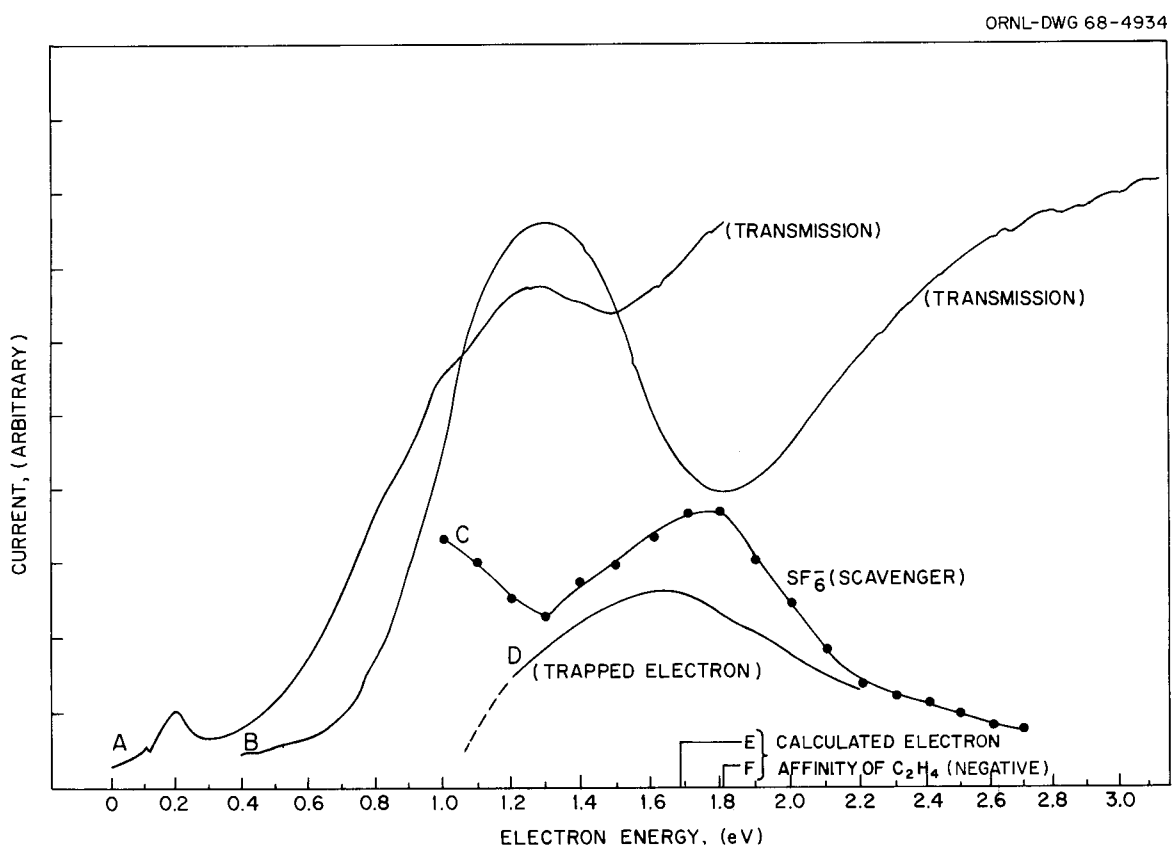

Fig. 18.10. Temporary Negative Ion Resonances in Ethylene.

TEMPORARY NEGATIVE ION LIFETIMES

Previous studies have shown that certain complex molecules which possess positive electron affinities can attach electrons into negative ion states whose lifetimes against autoionization vary from ~1 to ~50 μsec.[14,15] A semitheoretical treatment accounting for these surprisingly long lifetimes was presented which represented the molecular negative ion as a collection of weakly coupled harmonic oscillators. The principle of detailed balance was invoked to relate the attachment rate and autoionization lifetime. The experimental measurements for SF_6 were shown to be reasonably consistent with the equation relating lifetime, cross section, and electron affinity. The attaching electron was envisioned as sharing its energy with the many internal degrees of freedom of the molecule, allowing the ion to exist for some time before autoionization occurs. This treatment predicts a general increase of negative ion lifetime as the number of atoms in the molecule becomes larger. In this connection negative ion lifetimes have been carefully measured for eight alicyclic and aromatic fluorocarbon molecules. Figure 18.11 shows a plot of the logarithm of the lifetime, τ, vs the number of vibrational degrees of freedom, N, which indeed exhibits a remarkable increase of τ with N. To a first approximation the semiempirical theory of ref. 14 predicts a linear increase of $\ln \tau$ vs N. An extremely good straight line can be fitted to all of the data points in Fig. 18.11 with the exception of $C_7F_8^-$ and $C_7F_{14}^-$. These two molecules are the only ones in which a perfluoromethyl group (CF_3) extends from the ring instead of a fluorine atom, suggesting that internal vibrations of the CF_3 group are not excited. This would effectively reduce the number of degrees of freedom by 9, which puts $C_7F_8^-$ and $C_7F_{14}^-$ on a line with the other data points.

[14] R. N. Compton *et al.*, *J. Chem. Phys.* **45**, 4634 (1966).

[15] R. N. Compton and L. Bouby, *Compt. Rend.* **264**, 1153 (1967).

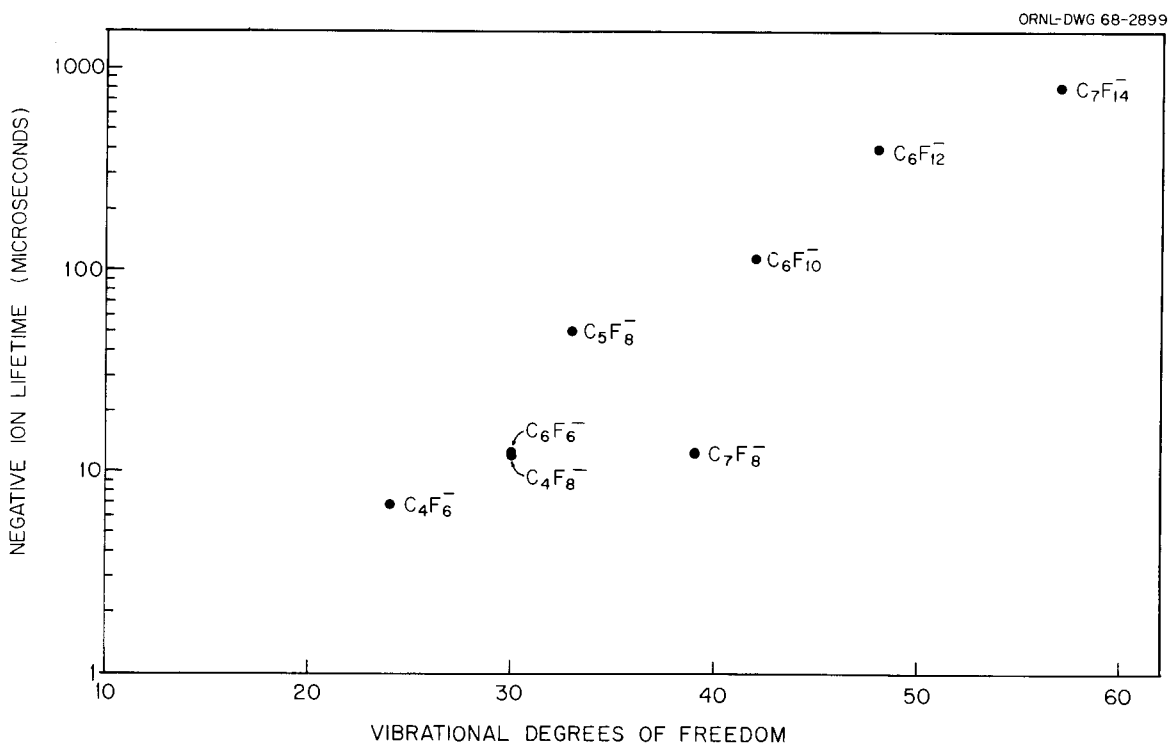

Fig. 18.11. Logarithm of Negative Ion Lifetimes for a Series of Alicyclic and Aromatic Fluorocarbon Negative Ions as a Function of the Number of Variational Degrees of Freedom.

All of the long-lived ions have a maximum attachment cross section at some energy less than 0.05 ev, and the widths of the resonances observed in the beam experiments were instrumental with the exception of $C_7F_{14}^-$, whose width at one-half maximum was approximately 0.2 ev.

Azulene is also found to attach thermal energy electrons into a negative ion state with a lifetime of 9.3 μsec. Lifetime measurements will also be performed on deuterated azulene in order to study the isotope effects on autoionization.

STUDIES OF DISSOCIATIVE ELECTRON ATTACHMENT

The swarm-beam technique has previously been employed to study isotope effects on the dissociative electron attachment cross sections for H_2O and D_2O^{16} and for the hydrogen halides and their deuterated analogs.[17] The experimental measurements of the attachment cross sections for the hydrogen halides were hampered somewhat by the occurrence of a low-energy attachment process which was presumably due to a secondary reaction occurring in the high-pressure swarm experiments. This has prompted the construction of a low-pressure single-collision total ionization chamber employed to determine cross sections for the production of negative ions. The electron energy scale for the attachment cross sections is determined to within 50 mv by the use of the helium negative ion resonance at 19.31 ev. The He^- transmission resonance shown in Fig. 18.12 indicates an electron beam energy resolution of 0.1 ev. The data recording procedure has been completely automated by using an automatic retarding potential difference technique and a continuous electron energy scan. Cross-section measurements for the much-studied O_2 molecule are in excellent agreement with previous values. Preliminary measurements on the dissociative attachment cross section in ammonia and deuterated ammonia have been made. Very precise measurements of the energy of the peak of the cross sections showed that the ND_3 resonance occurs at 0.20 ± 0.02 ev higher energy than the NH_3 peak, which is approximately equal to the difference in zero-point vibrational energy of the two molecules. The peak in the total negative ion cross section for NH_3 and ND_3 occurred at 5.65 and 5.85 ev respectively. Also, the width of the ND_3 cross section was 0.30 ev narrower than that for NH_3. Kinetic energy measurements of the ions resulting from the peak in NH_3 and ND_3 at $\sim$6 ev as a function of the electron energy have also been obtained by retarding the ions arriving at the ion collector. Provided there is no excited energy of the ion or neutral product, the ion kinetic energy, E_i, is related to the electron energy, E_e, by

$$E_i = (1 - m_i/M)\,[E_e - (D - A)]\ , \qquad (3)$$

where m_i is the mass of the ion, M is the mass of the molecule before dissociation, D is the dissociation energy of the broken bond, and A is the electron affinity of the atom or molecule which becomes negatively charged. Thus for H^- from NH_3 (or D^- from ND_3), a plot of E_i vs E_e should be a straight line of slope 0.94 (0.9) whose extrapolation of $E_i \to 0$ gives the value $D - A$. Figure 18.13 shows excellent agreement with Eq. (3) for NH_3 and ND_3. This procedure will be used in the future to determine either unknown bond dissociation energies or electron affinities for polyatomic molecules to within 0.1 ev. Mass spectra measurements of individual ions from NH_3 as a function of energy, found by employing the automatic retarding potential difference technique and using HCl as a calibration gas, show that NH_2^- peaks at the same energy as the peak in the cross section and that H^- occurs at $\sim$0.2 ev lower energy; NH^-, NH_2^-, and H^- also peak at the $\sim$10- to 11-ev secondary maximum in the total cross section. Preliminary measurements also show that NH_3^- is formed at approximately thermal energies and rises again at higher energies ($\sim$10 ev). Tentative results show that the NH_3^- ion current is linear with the pressure of NH_3. The interpretation of the mechanism of formation of NH_3^- is only speculative; however, the data indicate a radiative attachment process.

Studies of the collisions of monoenergetic electrons with NO_2 have provided important new lower limits to the electron affinities of O_2 and NO. The fragment ions O^-, NO^-, and O_2^- produced by dissociative attachment of electrons to NO_2 have been recorded as a function of the electron energy from 0 to 12 ev (see Fig. 18.14). The electron

[16] R. N. Compton and L. G. Christophorou, *Phys. Rev.* **154**, 110 (1967).

[17] L. G. Christophorou, R. N. Compton, and H. W. Dickson, *J. Chem. Phys.* **48**, 1949 (1968).

ORNL DWG 68-6253

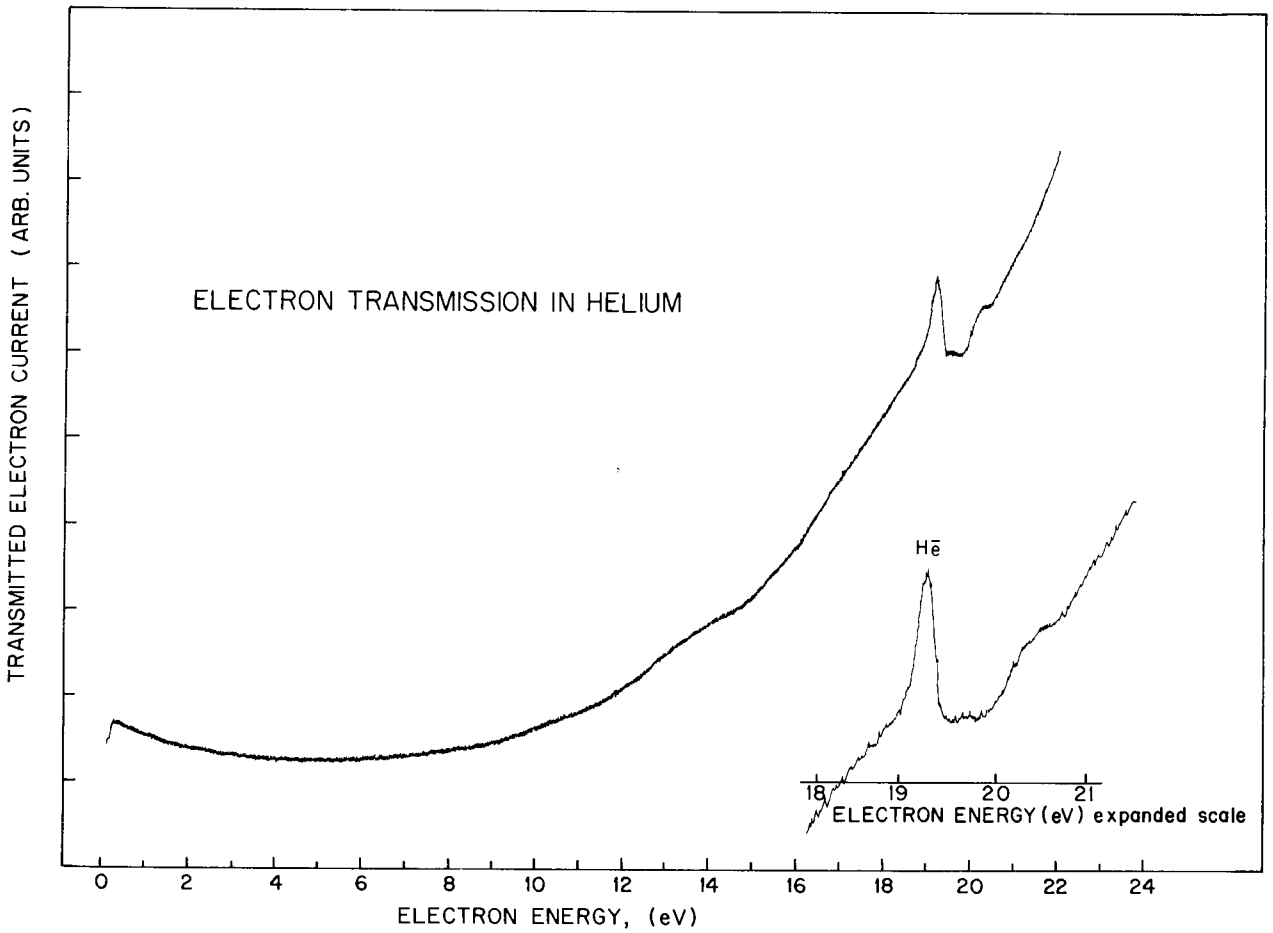

Fig. 18.12. Electron Transmission in Helium.

energy scale was determined by using five independent calibrating ions: O^-/NO_2, Cl^-/HCl, O^-/CO, O^-/CO_2, and H^-/H_2O. From the appearance potentials of NO^- and O_2^- the electron affinity of NO is found to be $\geq 0.60 \pm 0.15$ ev and the electron affinity of O_2 $\geq 0.95 \pm 0.15$ ev. Table 18.1 shows good agreement in the case of NO; however, the range of values for O_2 is perplexing. The evidence presented here suggests that the older value for the electron affinity of O_2, 0.95 ± 0.07 ev, obtained from lattice energies, is presently to be preferred.

LOW-ENERGY NEGATIVE ION MOLECULE REACTIONS

Very few low-energy negative ion molecule reactions have been studied. In particular the important low-energy region from 0 to 2 ev is almost completely unexplored, due mainly to the difficulty of obtaining adequate energy resolution with negative ion beams at such low energies. Atmospheric negative ions (e.g., those of the ionospheric *D* region) react chiefly in this low-energy region, and negative ion reactions of possible biological interest take place here. Further, measurements in this region should permit sensitive tests of theory, since cross sections are predicted to change rapidly at low ion energies.

Negative ions produced through dissociative electron attachment $e + XY \rightarrow X^- + Y$ have kinetic energies in the range 0 to 2 ev. Where excitation of the fragments X^- and Y does not take place, the energy E_i of the negative ion X^- is given by

$$E_i = (1 - \beta)\,[E_e - (D - A)]\,, \qquad (4)$$

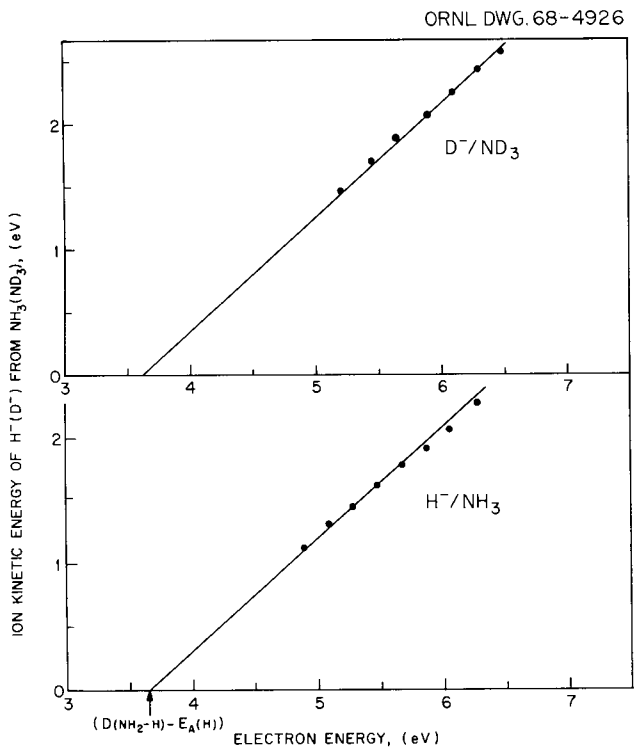

Fig. 18.13. Ion Kinetic Energy vs Electron Kinetic Energy for Negative Ions from Ammonia and Deuterated Ammonia.

where E_e is the electron energy, β is the ratio of the mass of the negative ion X^- to the mass of the parent molecule XY, D is the dissociation energy of the parent molecule into X and Y, and A is the electron affinity of X. Energy distributions of negative ions formed in dissociative attachment are presently being measured by a retarding analysis in an electron-beam transmission experiment.[18]

H^- and D^- ions have been produced by dissociative attachment $e + H_2O \rightarrow H^- + OH$ and $e + D_2O \rightarrow D^- + OD$ in the ion source region of a time-of-flight mass spectrometer, and the intensities of the OH^- and OD^- ions produced in the succeeding negative-ion–molecule reactions:

$$H^- + H_2O \rightarrow OH^- + H_2 \,, \tag{1}$$

$$O^- + D_2O \rightarrow OD^- + D_2O \,, \tag{2}$$

were monitored as functions of the delay time between the electron gate pulse and the ion extraction pulse.[19] Figure 18.15 illustrates the

[18]See previous section, "Studies of Dissociative Electron Attachment."

[19]*Health Phys. Div. Ann. Progr. Rept. July 31, 1967*, ORNL-4168, p. 166; R. N. Compton and L. G. Christophorou, *Phys. Rev.* **154**, 110 (1967).

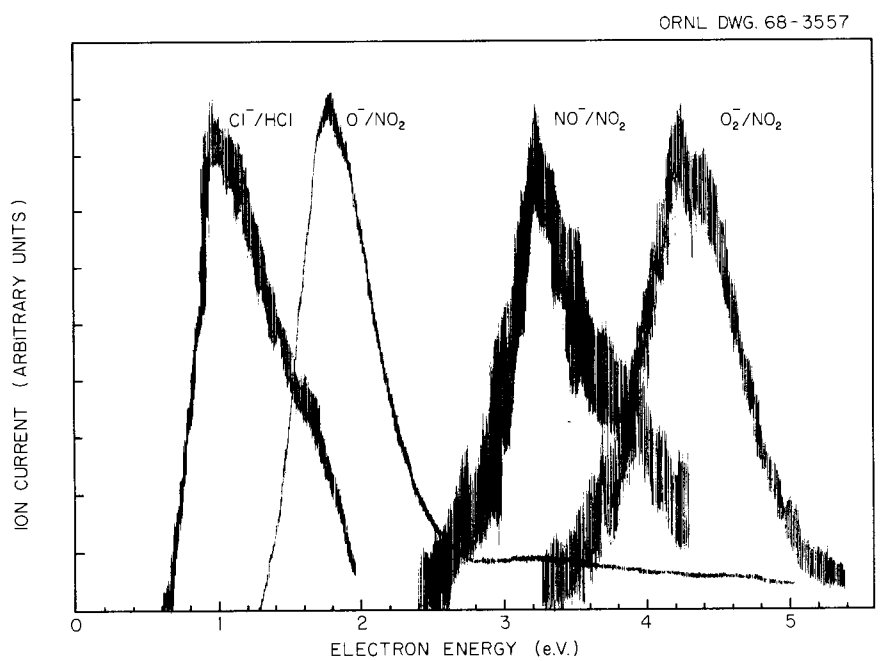

Fig. 18.14. Negative Ions of Atomic Oxygen, Nitric Oxide, and Molecular Oxygen from Nitrogen Dioxide as a Function of Electron Energy. Electron energy calibration was obtained from Cl^-/HCl.

Table 18.1. Electron Affinity of O_2

Electron Affinity	Method	Reference
0.15 ± 0.05	Photodetachment	D. S. Burch, S. J. Smith, and L. M. Branscomb, *Phys. Rev.* **114**, 1652 (1959)
0.7	Lattice energies	M. G. Evans, N. S. Hush, and N. Uri, *Quart. Rev. (London)* **6**, 186 (1952)
0.9	Lattice energies	M. Kazarnovskii, *Dokl. Akad. Nauk SSSR* **59**, 67 (1948)
0.46 ± 0.02	Detailed balancing	A. B. Phelps and J. L. Pack, *Phys. Rev. Letters* **6**, 111 (1961)
≧0.58	Electron impact	R. K. Curran, *J. Chem. Phys.* **35**, 1849 (1961)
≧0.95 ± 0.15	Electron impact	Present work

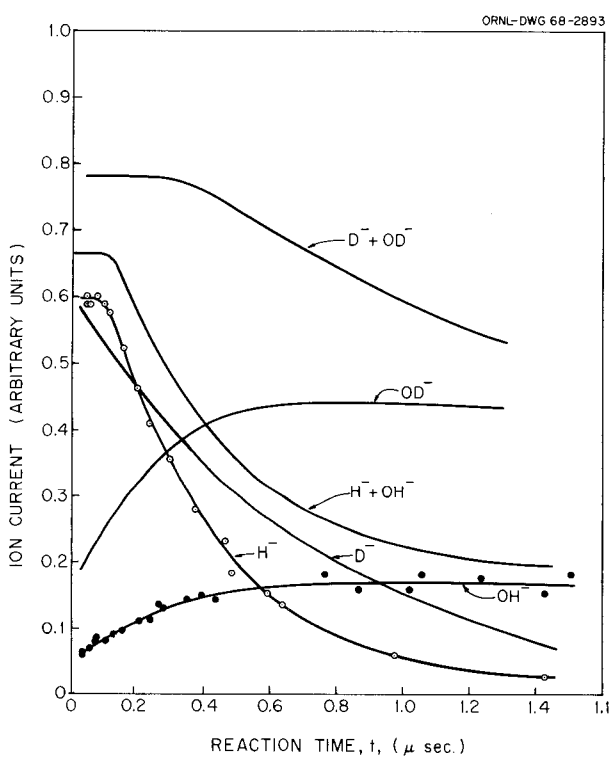

Fig. 18.15. H^- and OH^- and D^- and OD^- Ion Currents as a Function of Reaction Time t for the Negative-Ion–Molecule Reactions $H^- + H_2O \rightarrow OH^- + H_2$ and $D^- + D_2O \rightarrow OD^- + D_2$. H_2O pressure, 7.0×10^{-4} torr; D_2O pressure, 4.8×10^{-4} torr.

results for the case where the electron energy was set at the peak of the dissociative attachment resonance at 6.4 ev in H_2O and 6.5 ev in D_2O. It is interesting to note that for delay times less than 0.4 μsec the sum of the D^- and OD^- currents is constant, indicating that the ion currents in this time region are not depleted by drift losses of ions from the source. Figure 18.16 shows plots of $\ln (1 - [OH^-]_t/[H^-]_{t=0})$ and $\ln (1 - [OD^-]_t/[D^-]_{t=0})$ against delay time t for the reactions (1) and (2). These yield cross sections of $1.6 \pm 0.3 \times 10^{-14}$ cm^2 at an H^- energy of 1.93 ± 0.37 ev and $5.8 \pm 1.2 \times 10^{-14}$ cm^2 at a D^- energy of 1.84 ± 0.27 ev for reactions (1) and (2), respectively. These very large cross sections show the importance of high angular momenta in such reactions. The ratio of the cross sections (2)/(1) = 3.6 is also very large, for reasons not yet understood.

Figure 18.17 shows a plot of O^- and NO_2^- ion currents for the charge-exchange reaction

$$O^- + NO_2 \rightarrow NO_2^- + O \,, \qquad (3)$$

where O^- is produced from the dissociative attachment reaction $e + NO_2 \rightarrow O^- + NO$. A modulated retarding potential difference applied to the electron beam was coupled with phase-sensitive ion detection, permitting electron (and therefore ion) energy resolution of better than ±0.1 ev.

Detailed studies of reactions (1) and (3) as functions of ion energy are being made in the 0- to 2-ev region.

In addition to the negative ion charge-transfer studies described above, an apparatus has been designed and constructed to investigate low-energy neutral-neutral charge-transfer processes. For example, the electron affinity of NO_2 is slightly larger than the ionization potential of cesium. Thus collisions of cesium and NO_2 at low energy may result in the following reaction:

$$Cs + NO_2 \longrightarrow Cs^+ + NO_2^- \,. \qquad (4)$$

Reaction (4) will have considerable theoretical and practical importance.

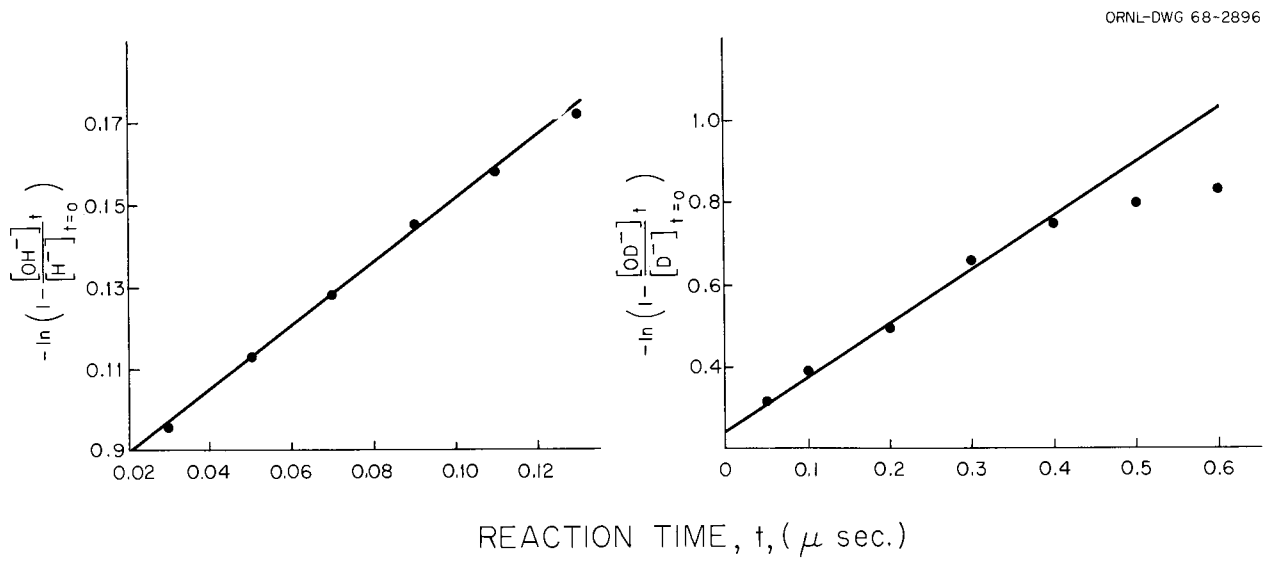

Fig. 18.16. $-\ln(1 - [\text{Secondary Ion}]_t/[\text{Primary Ion}]_{t=0})$ as a Function of Reaction Time t for the Reactions $H^- + H_2O \rightarrow OH^- + H_2$ and $D^- + D_2O \rightarrow OD^- + D_2$. H_2O pressure, 7.0×10^{-4} torr; D_2O pressure, 4.8×10^{-4} torr.

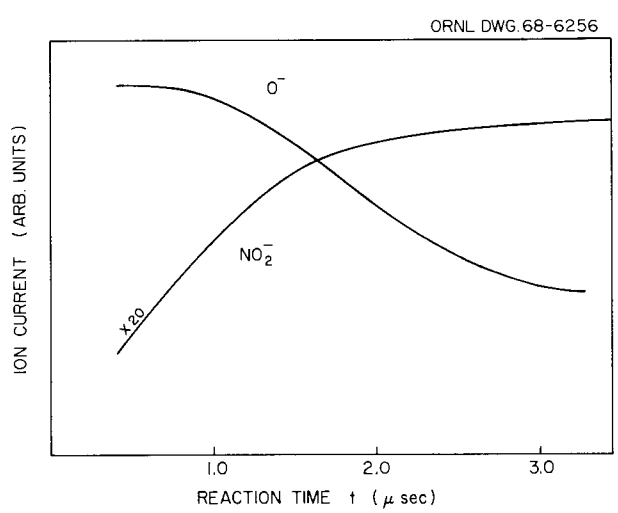

Fig. 18.17. O^- and NO_2^- Ion Currents as a Function of Reaction Time t for the Negative-Ion Charge-Exchange Reaction $O^- + NO_2 \rightarrow NO_2^- + O$. NO_2 pressure, 1.9×10^{-4} torr.

19. Graduate Education and Vocational Training

K. Z. Morgan
M. F. Fair

J. C. Ashley
R. D. Birkhoff
L. G. Christophorou
L. C. Emerson
W. R. Garrett
C. E. Klots
R. H. Ritchie
H. C. Schweinler
J. E. Turner

GRADUATE EDUCATION AND VOCATIONAL TRAINING

Five USAEC Fellows in Health Physics reported to the Division in June for summer training. Two came from the University of Rochester and one each from the Universities of California, Illinois, and Vanderbilt. Thirteen Fellows participated in the summer training program during July and August 1967. The summer program is open to Fellows from all participating universities. The first week was spent in the ORAU Special Training Division doing health physics experiments. The second week was spent at ORNL in a program of orientation. The remainder of the training period included five weeks with the research groups and five weeks in applied health physics.

In the applied health physics training, the student gains practical experience in all phases of radiation protection under the supervision of a senior health physicist. The student learns the radiation protection services that are provided for the Physics Division, Reactor Chemistry Division, Metals and Ceramics Division, Solid State Division, Chemical Technology Division, Rolling Mill, Tracer Facilities, High Level Radiochemical Development Laboratory, Fission Products Pilot Plant, Waste Disposal Group, Isolation Laboratory, Pilot Plant Operations, transuranium facilities, and the Ecology Research Group. In addition, he learns of personnel monitoring, instrument calibration, counting facilities, bioassay techniques, and whole-body counters.

In health physics research, the students are first given a brief summary of all the research projects which are in progress in the Division. They then choose the group in which they will remain for the five-week period of basic research under senior scientist supervision. The fields of investigation include: interaction of radiation with gases, solids, and matter; theoretical radiation physics; Health Physics Research Reactor; dosimetry; radioactive waste disposal; and radiation ecology.

The summer program gives the student sufficient experience in applied health physics to enable him to take a position in this field. Also, he learns of the tremendous breadth in research health physics and is made aware of the diverse problems available for thesis work should he decide to continue his education for the M.S. or Ph.D. degree under the fellowship.

Seven students were enrolled in the course in General Health Physics (Physics 4710-20-30) taught by Division members at The University of Tennessee. This was a three-quarter course which met 3 hr/week. A course in Applied Radiation Physics (Physics 234) at Vanderbilt University was taken by three AEC Fellows and four physics majors. This was a one-semester course which met 4 hr/week. Students were selected for the 1968–69 Fellowship Program.

The book *Principles of Radiation Protection: A Textbook in Health Physics* was published in December 1967. This book should be widely used in health physics education and particularly in the UT and Vanderbilt courses listed above.

Universities and colleges at which ORNL health physics research and educational activities were discussed are listed below:

Arkansas College
Bradley University
Bucknell University
Carson-Newman College
Florida A & M University
Florida State University
Georgia Institute of Technology
Glenville State College
Indiana State University
Kyoto University, Japan
Louisiana State University (New Orleans)
Madison College
Medical College of Virginia
Muskingum College
Northwestern University
Roanoke College
State College of Arkansas
Stout State University
Tennessee Technological University
Tokyo Institute of Technology, Japan
Tokyo University, Japan
University College, Dublin, Ireland
University College, London
University of Arizona
University of Aston, Birmingham, England
University of Bombay, India
University of Kentucky
University of Louisville
University of Missouri
University of Tennessee
Vanderbilt University
West Virginia University
Winthrop College
Wisconsin State University (River Falls)
Wisconsin State University (Superior)

Many of these visits were made under the Traveling Lecture Program. As an added bonus the Division staff members who visited these schools were able to acquaint the staff members with the work and facilities of this Division.

There were a number of Oak Ridge Graduate Fellows, AEC Fellows, and USPHS students in the Division working on theses as partial requirements for advanced degrees. Their thesis titles and universities are listed below.

1. M-E. M. Abu-Zeid, "Optical Emission and Lifetimes of Organic Molecules Excited by Electron Impact" (Tennessee)
2. R. P. Blaunstein, "Electron Transport in Carcinogens" (Tennessee)
3. A. A. Christodoulides, "Scattering of Thermal Electrons from Polar Molecules" (Tennessee)
4. Patricia Dalton, "Mean Excitation Energies Calculated from Stopping Power and Range Data" (Vanderbilt)
5. H. W. Dickson, "Measurement of Electron Attachment Coefficients in Hydrogen Halides and Water-Bromobenzene Mixtures" (Tennessee)
6. F. W. Garber, "Transmission of Low-Energy Electrons Through Thin Alkali Metal Films" (Tennessee)
7. R. N. Hamm, "The Mean Free Path of Low Energy Electrons in an Electron Gas" (Tennessee)
8. J. D. Hayes, "Optical Properties of Selenium and Tellurium in the Vacuum Ultraviolet" (Vanderbilt)
9. R. H. Huebner, "Electron Impact Investigation of Aromatic Hydrocarbons and Other Complex Molecules" (Tennessee)
10. W. T. Naff, "Transient Negative Ion States in Alicyclic and Aromatic Fluorocarbon Molecules" (Georgia)
11. S. J. Nalley, "Low-Energy Electron Studies on Thin Metallic Films" (Tennessee)
12. D. R. Nelson, "Lifetime of Electrons on Polyatomic Molecules" (Tennessee)
13. Linda R. Painter, "Optical Reflectivity of Water in the Vacuum Ultraviolet" (Tennessee)
14. Margaret S. Riedinger, "Determination of Optical Constants of Palladium by Ellipsometry" (Vanderbilt)
15. J. A. Stockdale, "Negative Ion Molecule Reactions in the Energy Range from 0 to 2 eV" (Tennessee)
16. L. H. Toburen, "Charge Exchange Cross Sections for MeV Protons in Various Gases" (Vanderbilt)
17. R. C. Vehse, "Reflectance of Evaporated Al Films in the Wavelength Region 800 to 2000 Å" (Tennessee)
18. R. E. Wilems, "Collective Interactions in Solids" (Tennessee)
19. H. A. Wright, "Differentiability of Set Functions" (Tennessee)

Four research participants, eight ORAU undergraduate students, and ten undergraduate research participants in ecology worked with the Division during the summer. At the same time, three summer

technical students and two students from the Youth Opportunity Program assisted the Division.

Ricardo G. Leon, a citizen of Mexico, completed a three-month training period in applied health physics.

The Division provided assistance to the staff at the University of Tennessee in updating and revising its graduate curriculum in health physics. This includes courses in General Health Physics, Radiation Chemical Physics, Radiation Biology, Physics of Polyatomic Molecules, Interaction of Electrons with Gases, Interaction of Electrons with Solids, and Interaction of Radiation with Matter. This curriculum has attracted Fellows who desire education to the master's level and also those who wish to pursue the Ph.D. degree. A great deal of help was provided to the University of Tennessee in establishing a co-op type program with ORNL leading to the B.S. degree in Health Physics. This type of assistance and consultation is available to any school desiring to set up a Health Physics program or institute courses in this field. For example, queries have been received from Georgia Institute of Technology, Lenoir-Rhyne College, University of Alabama at Birmingham, University of Kentucky, and University of Southern Mississippi with regard to setting up courses in Health Physics. Assistance was given to the University of Tennessee and Vanderbilt University in the preparation of qualifying examinations in Health Physics. Visits to ORNL with lectures and tours were provided for classes in Health Physics from the University of Arkansas and the University of North Carolina.

Several Health Physics Division staff members assisted members of the University of Tennessee Physics Department in preparing a proposal for research support to the Division of Biology and Medicine of the Atomic Energy Commission. This proposal, entitled "Electronic Properties of Liquid Water," is an outgrowth of research initiated at ORNL and will establish a liaison between UT and ORNL in this important new research area. Several staff members of the Radiation Physics Section of the Health Physics Division worked with the University of Tennessee faculty in preparing the preliminary examinations for the Ph.D. degree and in grading these examinations. Two of our staff hold Ford Foundation appointments at the University and in this capacity participated in student advising on matters of curricula and research. They were also active on the University Committee on Graduate Education. Several of the staff attended thesis examinations for master's and Ph.D. students at the University of Tennessee, Georgia Institute of Technology, and Vanderbilt University. Our staff played prominent roles in the Faculty Meetings of the University of Tennessee Physics Department staff.

In an informal cooperative program with the University of Georgia Physics Department, this department supplied and purified fluorinated benzene compounds which were then studied at ORNL in order to determine lifetimes for negative ion states and to search for new negative ion species. Also, a cooperative study of the absorption of light in water vapor was carried on informally with this university. Again on an informal basis, we have worked with Florida State University (the Radiation Chemistry Group) on studies of electron impact excitation of pyridine and searched for triplet states in this molecule. Also with this university we have engaged in research of mutual interest on ionization in gas mixtures. With the University of Tennessee we have worked on autoionizing states in helium and have had many informal discussions with various members of the Chemistry Department on problems in radiation chemistry. We worked with the University of Kentucky on studies of mutual interest in the area of electron interactions with molecules. This work is culminating in a book chapter by Compton of our staff and Hurst of theirs in the *Advances in Radiation Chemistry*, edited by Magee and Burton. With the University of British Columbia we have had extensive correspondence on the subject of the sulfur hexafluoride scavenger technique, and we believe this information has been of considerable assistance to the staff there. A paper has appeared in which this help has been acknowledged. With the University of Houston we have had many conversations on setting up an experiment to measure the ionization in gas mixtures due to beta particles. This work has culminated in a government contract to this institution. The vacuum ultraviolet grating calibration facility at ORNL has been made available to interested universities, and we have calibrated gratings for physicists at the University of Kentucky. We have reviewed a draft of a research proposal from the University of Kentucky and have supplied drawings of much vacuum ultraviolet equipment to the

Georgia Institute of Technology, including light sources and polarizers. Some equipment has been loaned to the latter to help them set up a research and education program in measurement of optical properties of solids, particularly in the region below 1000 A. With the former we have had many discussions regarding setting up a radiation physics curriculum and research program. Considerable correspondence has been exchanged with the University of Manchester (England) with regard to the training and research of the group there which studies electron excitation of luminescence in organics. The University of Puerto Rico sent us for review their research proposal on electron excitation of polyatomic molecules – the support, if awarded, to be used in graduate education and research. Also we have had much correspondence with the staff at California Institute of Technology and the University of Athens (Greece) on electron impact studies of molecules in the gaseous phase.

Several members of the Radiation Physics Section assisted in the preparation of a proposal to the National Science Foundation for a Center of Excellence award in the previous fiscal year (1967). One member (Birkhoff) and a University of Tennessee professor (Bugg) helped Dr. Alvin H. Neilsen, Dean of the Liberal Arts College, host the site visit of the NSF representatives. In late March of 1968 word was received that the Center of Excellence award had been made to the University Physics Department. These funds and matching state funds will be used to complete the physics building on the campus and to set up research programs and hire staff. Some of these research programs will be established according to our plans in the original proposal and will bring about an increased involvement of the staff of the Radiation Physics Section with the University Physics Department.

Three members of the Radiation Physics Section of the Health Physics Division, ORNL, helped in the screening of applicants for the 1967–68 USAEC Fellowship Program. This work was done at the Oak Ridge Associated Universities. Assistance was also given to ORAU in the presentation of a ten-week Health Physics course and several courses for medical personnel entitled "Medical Radioisotopes."

The Division cooperated with ORAU in presenting an eight-week course in Health Physics for college teachers during the summer of 1967.

One member of the Division (Turner) spent six weeks in Bombay, India, giving an extensive series of lectures on health physics and radiation physics at the Bhabha Research Center.

The demands for education in health physics have continued to rise. Emphasis will be on education to the Ph.D. level to provide personnel for positions of leadership in industrial, academic, and medical institutions. Although the advanced program will be emphasized, education will continue to be offered during the summer at the master's level to provide vocational training which includes a knowledge of health physics principles and procedures. The needs of the reactor industry must be met.

20. Physics of Tissue Damage

E. T. Arakawa
R. D. Birkhoff
F. W. Garber[1]
R. N. Hamm
W. J. McConnell
L. R. Painter[2]

ELECTRONIC PROPERTIES OF LIQUID WATER IN THE VACUUM ULTRAVIOLET

In order to determine the optical properties of water in the vacuum ultraviolet, two general methods were used. In the first the reflectance of water in equilibrium with its vapor at 1°C was measured in the spectral region 1050 to 3000 A for three angles of incidence. Light from a Seya-Namioka monochromator was reflected from a gold mirror onto either the water surface or a gold reference surface at the various angles and reflected specularly onto a coronene-coated photomultiplier. The optical constants were then obtained from a solution of Fresnel's equations. This method gave reliable values of n, but the reflectances measured in this way were not accurate enough to give good values of k. These values of n are labeled "free surface" in Fig. 20.1.

The second method involved placing water against the plane surface of a transparent semicylinder which formed one side of a sealed cell. Light is incident normally on the curved surface, reflects from the water-semicylinder interface, and exits, again normally. A quartz semicylinder was used down to 1680 A, where it becomes opaque, and a CaF_2 semicylinder from 1680 A down to 1250 A. The reflectance was measured as a function of angle of incidence for angles between 13 and 87° using an angle-doubling scanning device.[3] From 1250 to 1720 A the optical constants n and k were determined from a least-squares fit of the measured reflectances to Fresnel's equations. Above 1720 A the absorption of water becomes weak, and a critical angle may be measured, from which the index of refraction n was determined. Values of k were determined from the shape of the reflectance curve just above the critical angle, since the reflectance in this region is very sensitive to k.[4] This method of determining k was applicable for k values between about 0.02 and 0.0005. The optical constants as determined using a semicylinder are relative to the index of refraction of the semicylinder and must be multiplied by the semicylinder index to be compared with vacuum-water constants.

The values obtained by the various experimental methods in the present work are shown in Fig. 20.1. Values of k obtained elsewhere using an absorption cell[5–10] are also shown. The ORNL

[1]Oak Ridge Graduate Fellow.

[2]Consultant.

[3]R. C. Vehse, J. C. Sutherland, and E. T. Arakawa, *Rev. Sci. Instr.* **39**, 268 (1968).

[4]J. Fahrenfort, p. 437 in *Proceedings of the Xth Colloquium Spectroscopicum Internationale*, ed. by E. R. Lippincott and M. Margoshes, Spartan, Washington, D.C., 1963.

[5]J. L. Weeks, G. M. A. C. Meaburn, and S. Gordon, *Radiation Res.* **19**, 559 (1963).

[6]M. Halmann and I. Platzner, *J. Phys. Chem.* **70**, 580 (1966).

[7]C. D. Hodgman, *J. Opt. Soc. Am.* **23**, 426 (1933).

[8]K. Tsukamoto, *Rev. Optique* **7**, 89 (1928).

[9]J. Barrett and A. L. Mansell, *Nature* **187**, 138 (1960).

[10]W. C. Price, P. V. Harris, G. H. Beaven, and E. A. Johnson, *Nature* **188**, 45 (1960).

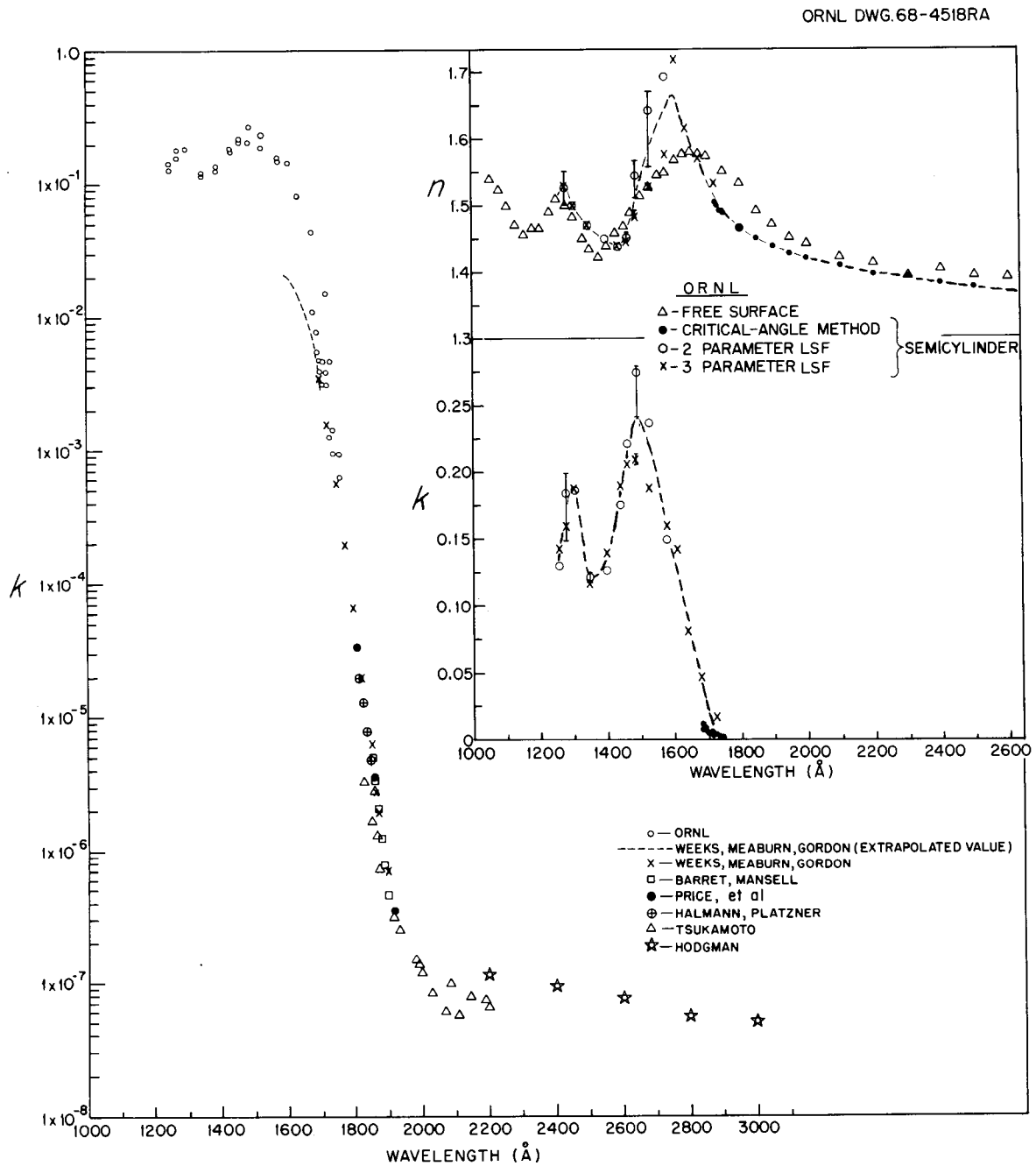

Fig. 20.1 Optical Constants n and k of Liquid Water.

values are in good agreement with those of Weeks, Meaburn, and Gordon[5] in the region of overlap from 1700 to 1750 A. The long-wavelength values of n are consistent with dispersion measurements.[11–13]

Figure 20.2 shows the real and imaginary parts of the complex dielectric constant, $\epsilon = (\tilde{n})^2 = \epsilon_1 + i\epsilon_2$, where $\epsilon_1 = n^2 - k^2$ and $\epsilon_2 = 2nk$, and the energy-loss function, $-\mathrm{Im}\,(1/\epsilon)$, for volume plasmons.[14]

[11]E. Flatow, *Ann. Physik* **12**, 85 (1903).

[12]R. W. Roberts, *Phil. Mag.* **9**, 361 (1930).

[13]J. Duclaux and P. Jeantet, *J. Phys.* **2**, 346 (1921); **5**, 92 (1924).

[14]R. H. Ritchie, *Phys. Rev.* **106**, 874 (1957).

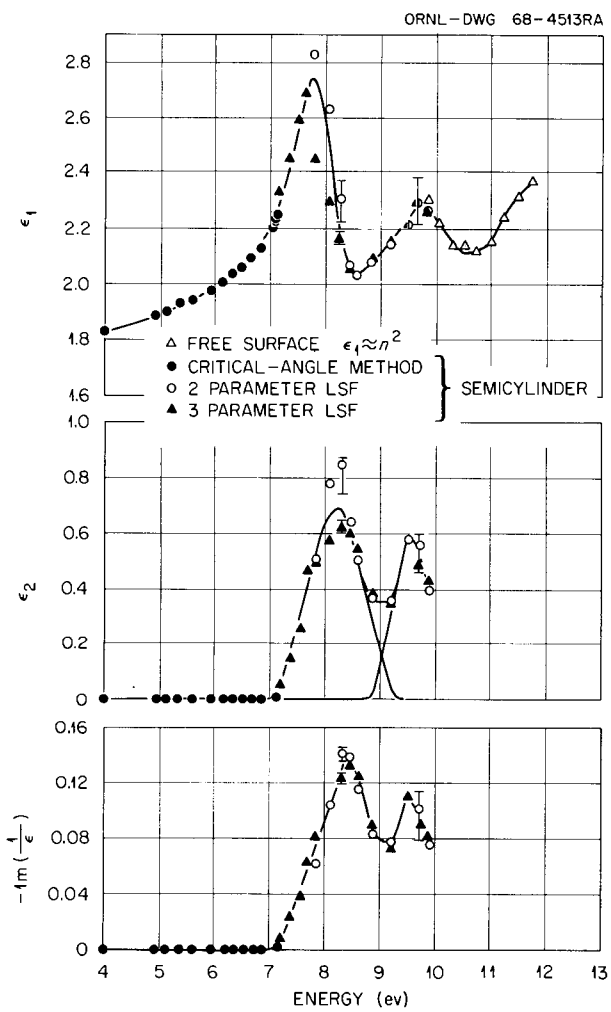

Fig. 20.2. Real and Imaginary Parts of the Complex Dielectric Constant and Energy-Loss Function of Liquid Water.

Unambiguous identification of the ultraviolet spectrum would require a knowledge of the band structure of liquid water. The positions of the two peaks in k for the liquid state are not the same as in the vapor,[15,16] suggesting that either the same absorption processes are occurring at different energies in the liquid and vapor or possibly that other processes are involved in the condensed state. Structure in the ultraviolet spectra of insulators in the solid state has been interpreted primarily in terms of exciton transitions, interband transitions, and volume plasma resonances.[17,18] Although the shape alone does not permit positive identification of the process, one possible interpretation is that the sharp oscillator-like structure in the dielectric constants near 8.3 ev is due to an exciton transition, while the structure at 9.6 ev is due to an interband transition. According to this interpretation, the exciton transition obscures the position of the absorption edge for band-to-band transitions, estimated to be at approximately 9 ev (see Fig. 20.2).

Attempts are being made to extend the measurements to the spectral region below 1050 A, where absorption in the water vapor surrounding the sample is more intense.

SLOWING-DOWN SPECTRA

Previously measured electron-flux spectra[19–21] in irradiated media were in good agreement with the Spencer-Fano theory above 10 kev but were much larger than theory below this energy. One possible explanation for this discrepancy might be a spurious response of the spectrometer. To check this, an electron gun which simulated the radioactive sources over a small azimuthal angle was built and calibrated. Figure 20.3 shows the

[15]K. Watanabe and M. Zelikoff, *J. Opt. Soc. Am.* **43**, 753 (1953).

[16]R. L. Platzman, pp. 20–42 in *Radiation Research*, ed. by G. Silini, North-Holland, Amsterdam, 1967.

[17]J. C. Phillips, *Phys. Rev.* **133**, A452 (1964).

[18]R. S. Knox, *Solid State Physics*, suppl. 5, ed. by F. Seitz and D. Turnbull, Academic, New York, 1963.

[19]W. J. McConnell *et al.*, *Phys. Rev.* **138**, A1377 (1965).

[20]W. J. McConnell, H. H. Hubbell, Jr., and R. D. Birkhoff, *Health Phys.* **12**, 693 (1966).

[21]W. J. McConnell *et al.*, *Radiation Res.* **33**, 216 (1968).

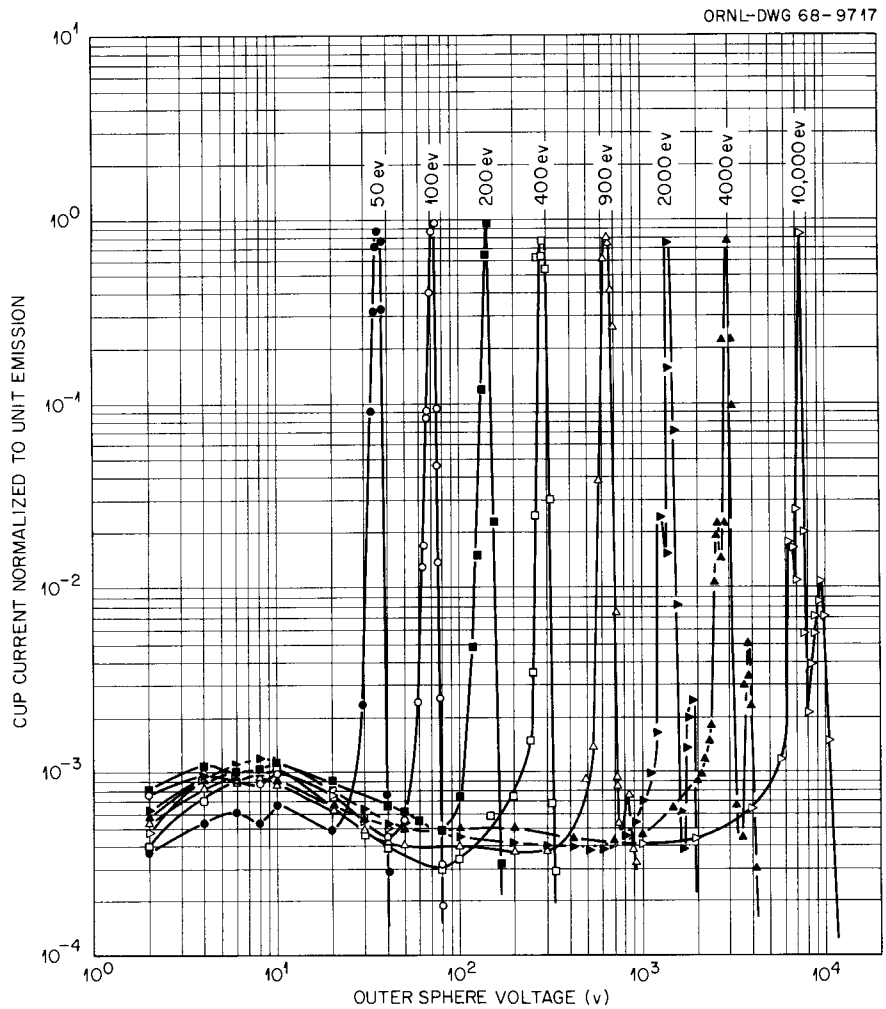

Fig. 20.3. Keplertron Line Profiles.

data obtained with this gun. The maxima approach 1 instead of the 0.25 transmission of the spectrometer because the electrons emitted from the gun were limited to the acceptance angle of the spectrometer. The small peaks on the low-energy sides of the main peaks are produced by electrons scattering from the edges of the exit slit. The higher-energy small peaks shown are envelopes drawn around a number of very sharp peaks. These are caused by scattering from the tops of the anti-scatter ridges on the inner sphere of the spectrometer. The low-energy tails have an average height of about 0.05% of the height of the main peaks. This is a factor of 3 lower than the 0.15%[22] found earlier using another electron gun. The data taken with the current electron gun show again that the spectrometer operates properly and furthermore that the spurious response correction (based on the 0.15% figure) applied to the slowing-down spectra was an overestimate. Thus the discrepancy between theory and experiment is not due to spectrometer response, and the discrepancy is larger than previously reported.

[22]H. H. Hubbell, Jr., W. J. McConnell, and R. D. Birkhoff, *Nucl. Instr. Methods* 31, 18 (1964).

LOW-ENERGY ELECTRON TRANSMISSION IN SOLIDS

The previously reported[23] electron gun and ultrahigh-vacuum system have been used to study the thickness dependence of electron transmission in solids. The target used in these experiments is a sandwich made by vacuum evaporating an aluminum foil on a glass slide and then oxidizing the surface of the foil to a depth of approximately 75 A. A top foil is then vacuum evaporated onto the oxide after placing the target in the vacuum system and pumping down to a pressure of approximately 10^{-9} torr. The electron beam from the gun is directed onto the target sandwich normally. The currents to the top layer and bottom layer are measured by Leeds and Northrup light-beam galvanometers. The ratio of the top current to the total beam current is related to the absorption in the top foil. The experiments described here differ from those already reported[23,24] in that complete suppression of secondary emission from the top foil into the vacuum has been accomplished. This was not the case in the previously reported data.

Figure 20.4 shows data taken using the same bottom foil and oxide layer with a top foil that is increased by further evaporation after each run. The thickness range covered in this manner is from 75 to 200 A. It is seen that for primary electron energies between 1 and 15 ev the absorption in the top foil is nearly constant and independent of foil thickness. In the energy range of 15 to 50 ev the absorption in the top foil increases rapidly due to the increase in the volume plasmon cross section and inelastic electron scattering. It is also to be noted that the absorption is independent of foil thickness, within experimental error, in this energy region also. Above 50 ev the absorption in the top foil exhibits a dependence upon foil thickness. As the primary-electron energy is increased above 50 ev, the absorption is approximately constant before sharply falling to zero current in the top foil at an energy which is dependent upon foil thickness.

A Monte Carlo code has been written[25] to study electron transmissions theoretically. Results of the Monte Carlo calculation are also shown in Fig. 20.4. It is seen that the general features of the experimental data and the Monte Carlo calculations are in agreement. The main disagreement is in the energy region below 50 ev. At the present time the theoretical model is being revised, and it is hoped that this will improve the agreement between theory and experiment.

If the primary-electron energy is increased past the point where the top-foil current falls to zero it is found that the top foil suffers a loss of electrons, as shown by the negative electron currents in the top foil in Fig. 20.5. It is seen that the negative absorption in the top foil goes through a minimum value, which is dependent upon the foil thickness. The energy at which the minimum in the curve occurs is also a function of the top-foil thickness. As the energy is further increased, the curves rise again and appear to approach a common curve independent of foil thickness. This rise in the curve is probably due to a decrease in secondary-electron production and the start of *K*-shell ionization in the top foil. Further study using the Monte Carlo code is under way at this time in order to obtain a better understanding of the absorption in this high-energy region. One may wonder what the absorbed dose is in a layer which *loses* electrons, if dose is defined as the number of electrons liberated per unit volume (as in the definition of the roentgen).

---

[23] S. J. Nally *et al.*, *Low Energy Electron Studies in Aluminum*, ORNL-TM-2030 (January 1968).

[24] F. W. Garber, *Low Energy Electron and Proton Transmission in Aluminum and Silver*, ORNL-TM-1153 (August 1965).

[25] R. H. Ritchie and V. E. Anderson, unpublished.

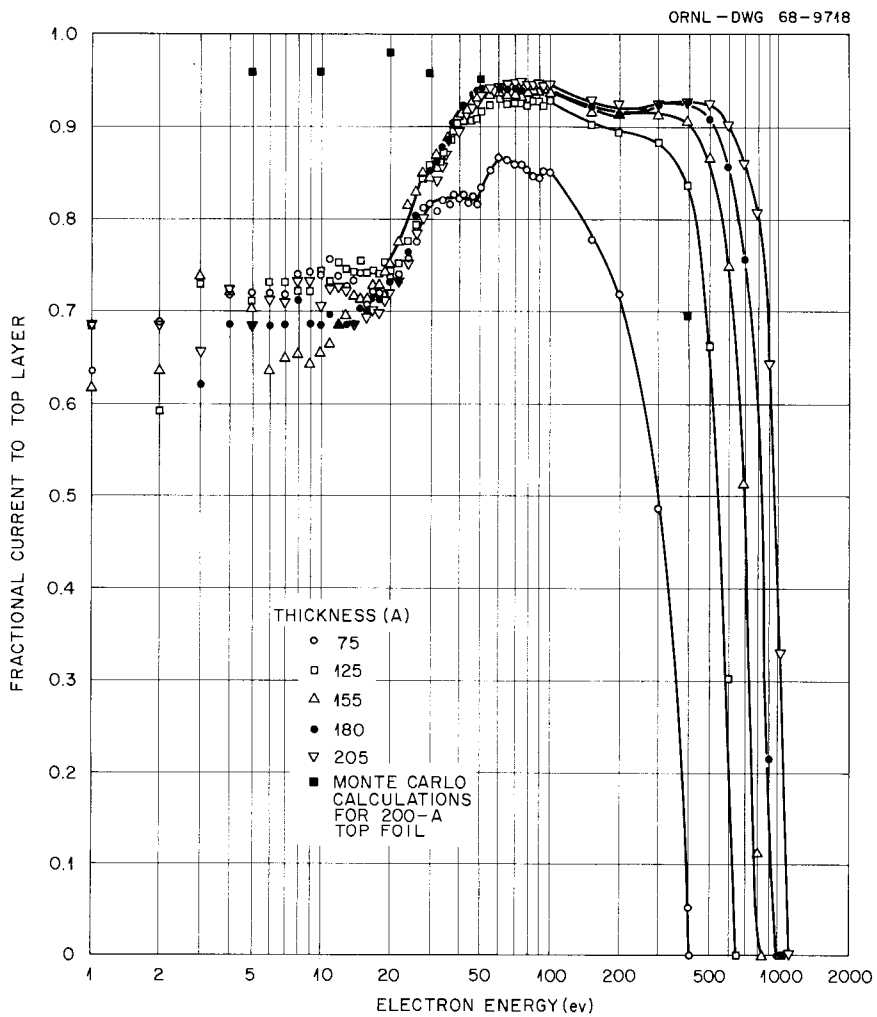

Fig. 20.4. Fractional Current to Top Layer for Several Thicknesses vs Incident-Electron Energy. Also shown are the results of the Monte Carlo calculations for a 200-A top layer.

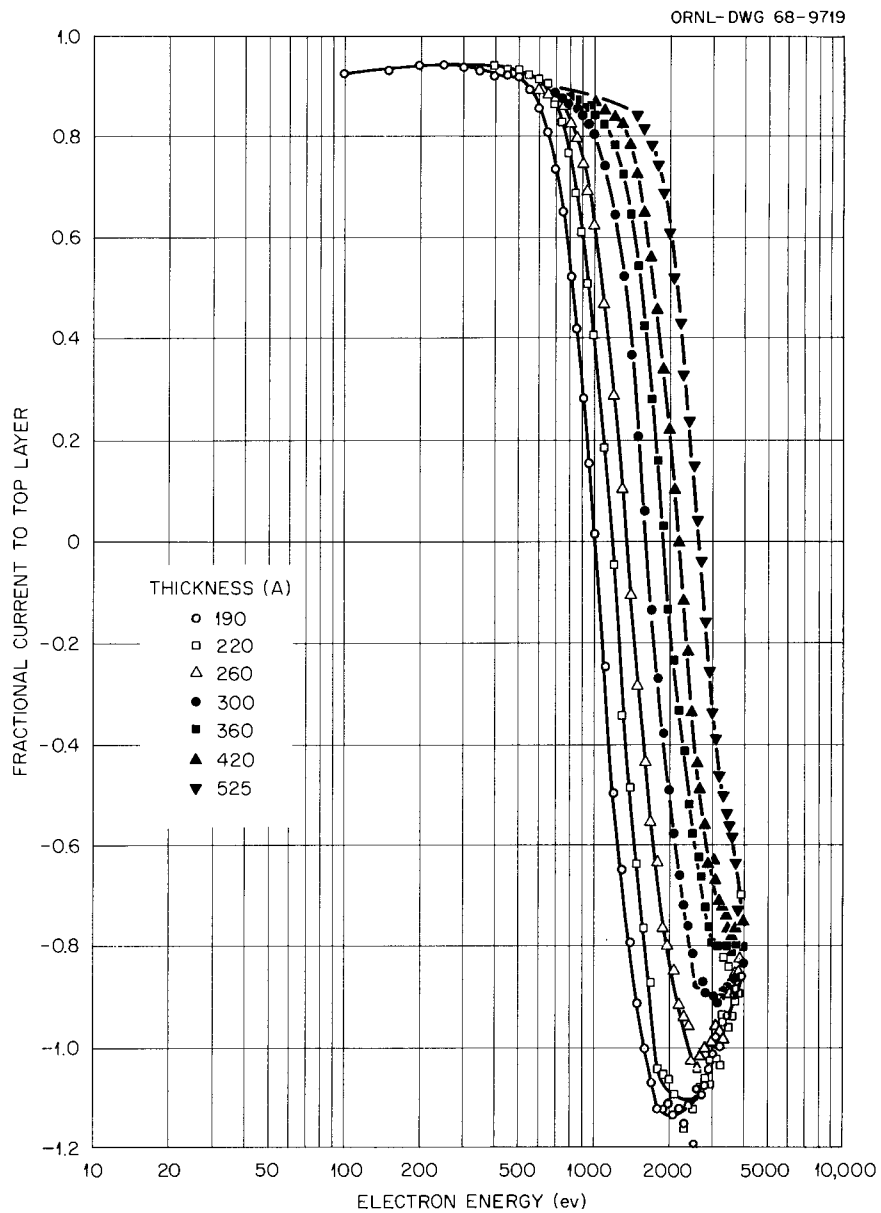

Fig. 20.5. Fractional Current to Top Layer for Various Thicknesses vs Incident-Electron Energy.

Part IV. Radiation Dosimetry Research

J. A. Auxier

21. Dosimetry for Human Exposures and Radiobiology

J. A. Auxier

J. S. Cheka
F. F. Haywood
H. H. Hubbell, Jr.
J. E. Jackson
D. R. Johnson[1]
T. D. Jones
G. D. Kerr[1]
W. H. Shinpaugh
D. R. Stone
E. B. Wagner

JAPANESE DOSIMETRY PROGRAM

Analysis of Cases for Which Calculated Doses Exceed 800 Rads

The Atomic Bomb Casualty Commission in Japan (ABCC) has calculated radiation doses to over 90% of the survivors of the wartime bombings of Hiroshima and Nagasaki. The methods and air-dose curves used were those developed by ORNL personnel. About 200 calculated doses were over 800 rads. The shielding histories and other information on these cases were obtained from ABCC and studied at ORNL. All but about 100 cases were eliminated, or lower dose figures obtained, because of errors or contradictions in the histories and calculations.

Most persons surviving the nuclear explosions inside cave-type air-raid shelters were sufficiently far from the hypocenter and shielded by large enough thicknesses of earth so that the exposure level was thought to be nearly zero. Although the exposures were quite low, four patients of the 108 shelter survivors became victims of leukemia. These 4 histories plus an additional 50 histories were chosen as a sample for study. Of the 50 nonleukemia cases, 5 were shielded but by less than 0.75 m of earth and other shielding material; 3 were shielded by more than 0.75 m but less than 1.5 m; 13 were shielded by more than 1.5 m but less than 3 m; 21 were shielded by more than 3 m of earth; and 8 were in shelters which were open in the direction of the hypocenter. Leukemia patient No. 1 was at a ground distance of 1218 m, shielded by a hill, and had 1.5 m of earth over the top of his shelters; and although he became a patient suffering from leukemia, he was still alive in 1959 (at which time the shielding history was updated). Leukemia patient No. 2 was exposed at a ground distance of 1378 m, and although he lived until 1952, his shielding configuration is unknown. Leukemia patients 3 and 4 were exposed at distances of 1088 and 1257 m, respectively, and were heavily shielded except in one

[1]On leave of absence.

lateral direction. They both died from leukemia (No. 3 in 1950 and No. 4 in 1956).

There are about 50 cases (35 of them in Hiroshima) for which we can find no reason (except high doses) to reject the estimates. About 50 more (28 of them in Hiroshima) consisted for the most part of survivors inside typical Japanese houses shielded by many other Japanese houses. With such shielding, one would still expect a high dose level, so the dose estimates are probably reasonable.

Bomb Yields

A primary datum in calculating the open-air-dose curves, and hence the dose to each survivor in Japan, is the yield or total energy release of each bomb.

When the T65D calculation procedure was set up at ABCC in 1965, the yield of the Nagasaki device was given[2] as 22 ± 1 kilotons (ref. 3) because devices of nearly identical design had been tested several times with reproducible results in this range. The Hiroshima device has never been tested, so the yield was estimated by calculation and indirect evidence as 12.5 ± 2.5 kilotons.

Recent restudies of old data indicate that this figure is a lot better than there was reason to expect. Lord Penney reexamined his original data on blast effects, which he collected in Hiroshima and Nagasaki in 1945, using recent results on the location of the burst point. He stated that the best estimate of the Hiroshima yield was 12.5 kilotons.[4]

Two Japanese scientists, Kimura and Tajima of Tokyo University, in 1945 estimated the thermal yield in Hiroshima from the depth of charring of a piece of cypress found there and the charring produced by an electric heater on the same piece. Taking 35% as a fraction of the yield appearing as thermal radiation, one obtains 13 kilotons as the total yield from their figures.

Caudle,[5] of the Naval Ordnance Laboratory, recalculated the Hiroshima yield from the pressure traces recorded by the observing plane from canisters dropped on parachutes simultaneously with the bomb. He used a computer code on the propagation of blast waves and obtained a yield of 15 ± 2 kilotons. The largest uncertainty is in the exact location of the canisters when the blast wave struck them. He assumed a head wind at bombing and canister altitude of 35 mph. However, the only upper air sounding that has been found for that time and date (Tokyo) gives the wind at 9000 m as from the south at 5 to 7 m/sec (11 to 16 mph). Another weak bit of evidence indicating that the winds might have been from south to southeast is the fact that the canister was found by the Japanese near the village of Kameyama-Mura, which is north of Hiroshima and northwest of the drop point.

The bomb run was made at a heading of 260°, or nearly west. Assuming a crosswind of this speed reduces the slant range from Caudle's figure of 34,565 ft to between 32,000 and 33,000 ft. Caudle's curves then give a yield of between 12.5 and 13.5 kilotons. Unfortunately, the distance where a given blast wave pressure occurred varies with the cube root of the yield,[6] so any error in distance produces three times the error in calculated yield.

Many other estimates of the yield in Hiroshima can be calculated from the relative distances for the same effects in Hiroshima and Nagasaki, if the yield in Nagasaki is assumed to have been 22 kilotons.

Some of these results are shown in Table 21.1. For this the curves have been used which Bowen of Lovelace Foundation calculated for a 22-kiloton yield in Nagasaki at 500 m burst height and 12.5 kilotons in Hiroshima at 570 m. For blast effects the distance for the same degree of damage of various types permits finding from the curves the overpressure in each city. Ideally the pressures should be the same for the same effect if the yields are correct. The table indicates that they do not differ more than 5 or 6%. Notice that the discrepancies are not always in the same direction – sometimes the figure for Hiroshima is higher, sometimes that for Nagasaki.

---

[2] J. A. Auxier *et al.*, *Health Phys.* 12, 425–29 (1966).

[3] 1 kt or kiloton of TNT equivalent is defined as a total energy release of 10^{12} cal.

[4] Lord Penney *et al.*, *The Explosive Yields at Hiroshima and Nagasaki*, United Kingdom Atomic Energy Authority (February 1968).

[5] K. F. Caudle, *Yield of the Hiroshima Weapon*, NOLTR-65-143 (February 1966).

[6] S. Glasstone, *The Effects of Nuclear Weapons*, rev. ed. 1962, p. 128, published by USAEC.

Table 21.1. Comparative Effects of Hiroshima and Nagasaki Atomic Bombs

Assuming Hiroshima yield 12.5 kilotons at 570 m height and Nagasaki yield 22 kilotons at 500 m

A. Blast Effects (British Data)

Effect	Hiroshima		Nagasaki	
	Distance from Hypocenter (ft)	Incident Overpressure (psi)	Distance from Hypocenter (ft)	Incident Overpressure (psi)
Collapse of typical houses	6,750	3.10	7,450	3.20
Structural damage	7,900	2.42	8,600	2.55
Serious nonstructural damage	7,900	2.42	9,000	2.37

B. Thermal Effects

Effect	Hiroshima		Nagasaki	
	Distance from Hypocenter (ft)	Radiation (cal/cm^2)	Distance from Hypocenter (ft)	Radiation (cal/cm^2)
Roughening of polished granite				
British estimate	1,500	53.5	2,000	77
Japanese estimate	2,000	44	3,000	49.5
USSBS estimate	1,300	59		
S. Nagaoka estimate	3,450	21.3	5,250	15.5
Flash burns on wood				
British estimate	9,000	2.93	10,000	4.0
W. G. Penney estimate	9,500	2.60	11,000	3.45
USSBS estimate	13,000	1.37	9,200	4.9
Flash burns on roof tiles				
Melting (Nagaoka)	1,970	45	3,200	45

C. Human Mortality and Injury

Effect	Hiroshima		Nagasaki	
	Distance from Hypocenter (ft)	Radiation (cal/cm^2)	Distance from Hypocenter (ft)	Radiation (cal/cm^2)
Mortality (Dikewood data)				
Outside unshielded				
10% mortality	4,750	10.5	6,120	11.4
1% mortality	6,100	6.6	9,000	5.3
Thermal injury to survivor (Dikewood data)				
Outside unshielded				
10% injured	11,500	1.75	14,000	2.0
1% injured	12,800	1.40	17,700	1.12
Total burns (Oughterson-Warren data)				
Outside unshielded				
20% injured	13,200	1.3	15,100	1.7
10% injured	14,500	1.05	17,400	1.15
1% injured	20,300	0.65	23,400	0.6

The second part of the table shows similar results for thermal effects. One should compare only the same observer's estimates in the two cities, since observers seemed to differ on the qualitative effects noted. Again the number of calories per square centimeter seems to be about the same for the two cities, and the figures are not consistently higher in one city.

The last part of the table shows similar effects for human mortality or injury. It is assumed here that death or thermal injury at long distances from the hypocenter is due solely to flash burns. On this assumption, the heat received for a given effect is again about the same in the two cities.

Incidentally, the average of the ratios of blast pressure and thermal radiation to produce the same effect in the two cities is 0.98 ± 0.07, which is fortuitously good.

Table 21.2 shows some of the better estimates of the bomb yields. The conclusion is that at present all the data are consistent with an assumed yield of 22 kilotons in Nagasaki and 12.5 kilotons in Hiroshima and that the original hope of being able to compute most of the radiation doses to survivors within 10 to 15% is within sight of fulfillment.

Table 21.2. Bomb Yield Estimates for Japan

In kilotons TNT equivalent

Estimate	Hiroshima	Nagasaki
T65D	12.5 ± 2.5	22 ± 2
Penney (1968)	12.5	
Kimura and Tajima (1945)	13	
Caudle (N.O.L. 1965)	15 ± 2	
Caudle (revised)	13 ± 2	
Ratio of effects in two cities	12.7 ± 1	

Dose to Fetuses in Utero

For many purposes in health physics, especially in internal dose calculations, it is necessary to know the dose to individual body organs and the physiological effects of such doses. Therefore, preliminary studies are under way to calculate the depth dose and organ dose values for the survivors and to correlate these figures with the ABCC medical findings, especially for fetuses in utero at the time of the bomb.

With the assistance of ABCC, data were obtained from several gynecologists in Hiroshima and Nagasaki which should permit the estimation of the location of the fetus in a Japanese mother at various times during pregnancy and the thicknesses of shielding tissue surrounding it. Monte Carlo calculations of the absorbed dose in such cases are planned.

Epicenters

The epicenters, or locations where the atomic bombs exploded, are essential data for the calculation of the doses to survivors. An extensive study has been completed of all the data that could be found for determining these locations. A paper has been submitted to ABCC for publication as a technical report[7] summarizing these findings.

The recommended values for the coordinates of the epicenters, in terms of the U.S. Army maps in use at ABCC, are as follows: Hiroshima: 744.298 × 1261.707, height of burst 580 m; and Nagasaki: 1293.626 × 1065.932, height of burst 504 m.

The recommended values for Hiroshima differ from those used in the T65D calculations by only about 15 m, so no dose recalculations are needed. For Nagasaki the recommended point is about 35 m from the one used in the T65D calculations, so a recalculation of the doses would seem desirable.

OPERATION HENRE

ORNL participation in Operation HENRE was completed in September 1967. Specific objectives of this experiment and a description of facilities have been reported earlier.[8–10] Targets utilized

[7] H. H. Hubbell, Jr., *et al.*, *The Epicenters of the Atomic Bombs in Japan. Part II. Reevaluation of All Available Data and Our Recommended Values* (submitted to ABCC February 1968 for publication in their Technical Report series).

[8] T. G. Provenzano *et al.*, *Feasibility Study: Intense 14-Mev Neutron Source for Operation HENRE*, CEX-65.01 (May 1966).

[9] F. F. Haywood and J. A. Auxier, *Technical Concept – Operation HENRE*, CEX-65.02 (March 1965).

[10] F. F. Haywood, T. G. Provenzano, and J. A. Auxier, *Operations Plan – Operation HENRE*, CEX-65.03 (September 1965).

during this phase of the program at heights of 500 and 1125 ft provided neutrons in the range of 3×10^{12} to 9×10^{12} neutrons/sec for 4-hr periods.

Neutron and Gamma-Ray Air-Dose Curves

In September 1967, a spectrum-modifying shield (Fig. 21.1) of depleted uranium and steel was placed around the target in order to produce a degraded fission spectrum similar in shape to the spectrum of the weapon dropped over Hiroshima. This shield was constructed of 12 concentric cylindrical cans with 1-in.-thick walls and bottoms. The inner six cans were fabricated of depleted uranium and the outer six of steel.

Prior to Operation BREN in 1962, it was known that the neutron leakage from an unshielded metal reactor (HPRR) was similar to the spectrum leaking from a typical weapon of nominal yield. However, the results of an experiment at Los Alamos in 1964 revealed the neutron energy spectrum from the weapon dropped over Hiroshima to be much softer than that from a typical weapon; about half of the neutron absorbed dose in tissue would have

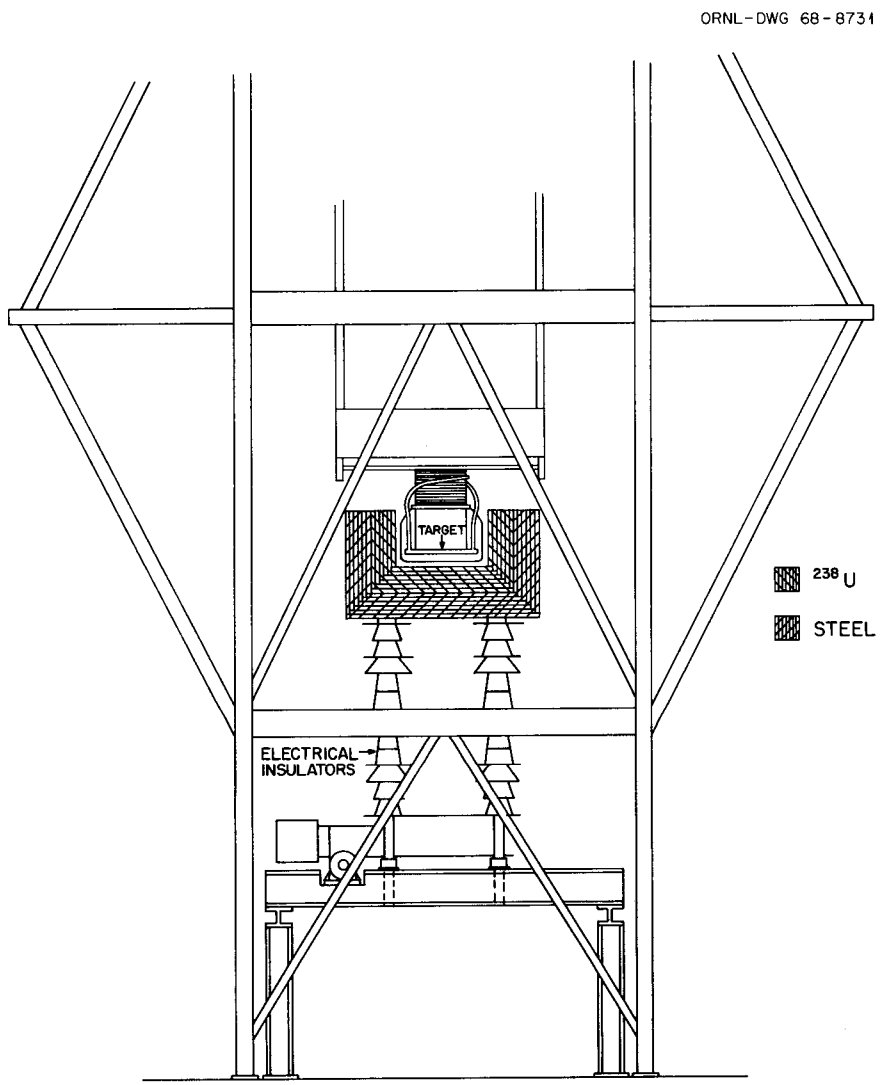

Fig. 21.1. Diagram of Spectrum-Modifying Shield Mounted at Base of BREN Tower, Indicating Position of Uranium and Steel with Respect to the Accelerator Target. The maximum diameter of the shield is 58 in.

been deposited by neutrons having an initial energy of less than 300 kev if the target tissue had been within a few meters of the bomb (or if the initial spectrum and the equilibrium spectrum were identical). Therefore, the purpose in using this spectrum shifter and 14-Mev neutron source arrangement was to compare neutron and gamma-ray air-dose curves from the spectrum simulator and those from Operation BREN.[11] Good agreement between these distributions would indicate that there was no serious problem in the estimates of dose vs distance which have been given for Hiroshima. A comparison between these two cases is given in Fig. 21.2. Measurements in the radiation field of the spectrum simulator are normalized to air-dose curves determined during Operation BREN. These normalized data do not have accompanying limits of accuracy, but it is seen for both neutrons and gamma rays that the data are in good agreement with the previously reported air-dose curves.

Air-dose distributions for gamma rays and neutrons from the 14-Mev neutron source are presented in Figs. 21.3 and 21.4 respectively.[12] These data represent refinements of information presented earlier.[13] Data are presented for a source height of 1125 ft and detector height of 1000 ft, and a detector height of 3 ft with the source at heights of 27, 300, and 1125 ft.

[11] F. F. Haywood, J. A. Auxier, and E. T. Loy, *An Experimental Investigation of the Spatial Distribution of Dose in an Air-over-Ground Geometry*, CEX-62.14 (1964).

[12] Z. G. Burson, EG&G Inc., private communication.

[13] F. F. Haywood, *Health Phys. Div. Ann. Progr. Rept. July 31, 1967*, ORNL-4168, p. 189.

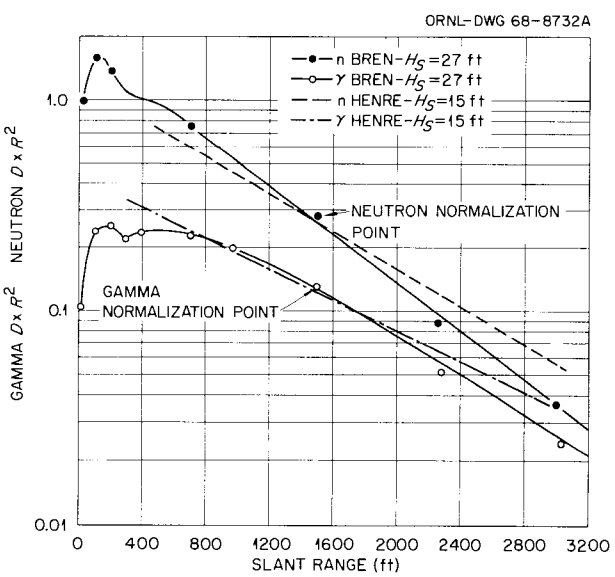

Fig. 21.2. Comparison of Measured Neutron and Gamma-Ray Air-Dose Curves for HPRR and for the Spectrum-Modifying Shield. In both cases, the source was mounted near the base of BREN tower.

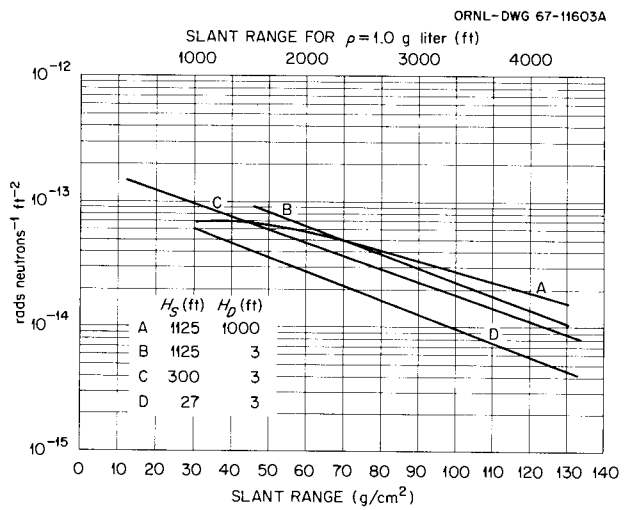

Fig. 21.3. Gamma-Ray Air-Dose Curves for Detector Heights of 3 and 1000 ft and Accelerator Heights of 1125, 300, and 27 ft as a Function of Slant Range.

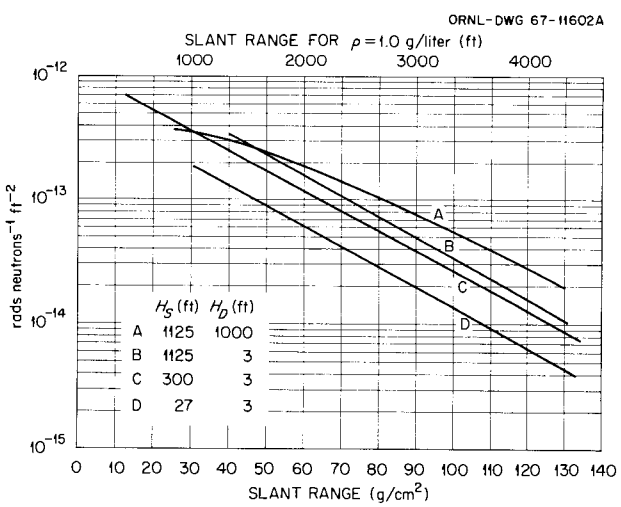

Fig. 21.4. Neutron Air-Dose Curves for Detector Heights of 3 and 1000 ft and Accelerator Heights of 1125, 300, and 27 ft as a Function of Slant Range.

For purposes of computing neutron dose along an air-ground interface, it is necessary to consider two media, infinite and finite. An infinite medium may exist if its boundaries are more than one relaxation length away from the point of interest for any particular type of radiation. A finite medium, on the other hand, is represented by two media whose densities vary greatly and which share a common boundary. Neutron dose in an infinite medium may be computed by the relation:

$$D_{\infty} = \frac{G \cdot Be^{-R/L}}{4\pi R^2} ,$$

where G is a term describing the neutron source output, B is dose buildup factor, R is slant distance (range) between source and point of interest, and L is the relaxation length in air for neutron dose. If one desired to compute the neutron dose along the boundary of the finite medium for various source heights above the boundary, the following relation may be used:

$$D_{\text{finite}} = \frac{G \cdot Be^{-R/L} \cdot K}{4\pi R^2} ,$$

where all terms are the same as above and K is a boundary correction factor: the ratio of dose in a finite medium to dose in an infinite medium for a given slant range. Infinite air measurements were made during HENRE with the 14-Mev source 1125 ft high and detectors suspended below a helicopter 1000 ft high. K for neutron dose is presented in Fig. 21.5 for three source heights. Other tables of K values are being prepared.

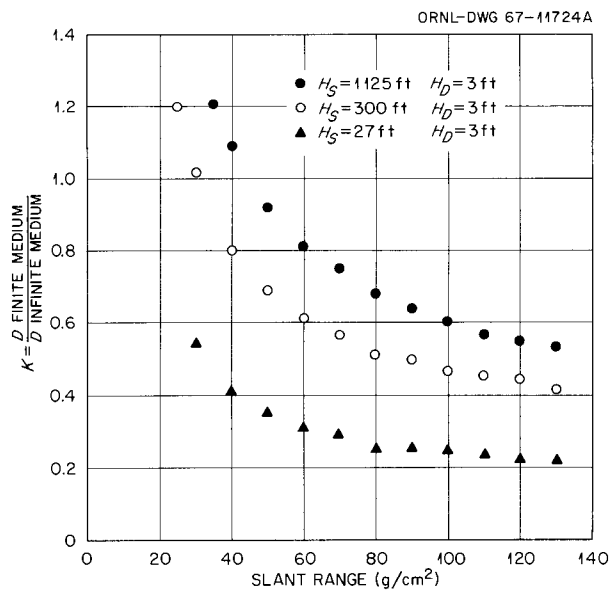

Fig. 21.5. Neutron Dose Boundary Correction Factor, K, for Source Heights of 1125, 300, and 27 ft as a Function of Slant Range.

Neutron and Gamma-Ray Angular Distributions

Even though unexpectedly low neutron yields limited the success of the experiment, certain programs produced good results. Among these were the measurements of neutron and gamma-ray dose as a function of angle, high-energy gamma-ray spectrum as a function of angle, and fast-neutron spectrum at various distances from the source.

Results obtained during HENRE for the dose incident at angles of 0, 30, 60, and 90° with respect to the source-detector line are shown in Table 21.3. These data represent the dose accepted by a unit solid angle set by a cone of 30° full angle with the measurements normalized to the zero direction dose value. The table also shows the values obtained during Operation BREN,[14] typical weapons test[15] data, and the calculations of Straker.[16] Data are given for both neutron and gamma-ray dose, and comparison of the data sets indicates reasonable agreement in the neutron dose values but poorer agreement in the gamma dose values. The considerable variations in the sources involved are no doubt responsible for these variations. Dose values were not measured at larger angles due to the low dose rates at 750 yd from the base of the tower.

Spectrum Measurements

Before HENRE, gamma-ray spectra had not been successfully measured during a field experiment. For HENRE a pair spectrometer was set up at 500

[14] J. H. Thorngate *et al.*, *Energy and Angular Distribution of Neutrons and Gamma Rays — Operation BREN*, CEX-62.12 (February 1967).

[15] R. H. Ritchie and G. S. Hurst, *Health Phys.* 1, 390–404 (1959).

[16] E. Straker, private communication.

Table 21.3. Angular Dose Normalized to 0° for HENRE, BREN, Weapons Test, and Calculated for HENRE

Angle (deg)	HENRE	BREN	Weapons Test	Calculated
		Neutron		
0	1.000 ± 0.137	1.000 ± 0.225	1.00	1.000
30	0.413 ± 0.094	0.454 ± 0.121	0.53	0.481
60	0.277 ± 0.069	0.289 ± 0.105	0.28	0.176
90	0.159 ± 0.082	0.147 ± 0.085	0.17	0.085
		Gamma		
0	1.000 ± 0.040	1.000 ± 0.027	1.00	1.000
30	0.301 ± 0.020	0.475 ± 0.028	0.20	0.286
60	0.087 ± 0.013	0.324 ± 0.040	0.05	0.047
90	0.056 ± 0.012	0.216 ± 0.050	0.03	0.015

yd from the base of the tower in a movable collimator with a 30° acceptance cone. The pair production cross section limited successful spectrum measurements to energies above 1.5 Mev. Figure 21.6 gives the response of the spectrometer when the accelerator was at 1125 ft and the collimator aimed at 0, 45, and 90° with respect to the source-detector line. A simple stripping program was used to remove the spectrometer response from the data. Most of the remaining peaks may be identified with gamma rays emitted from excited ^{16}O, which occurs from the n,p reaction in ^{16}O and the resulting beta decay of the ^{16}N produced, and from excited states of ^{13}C, which result from the $^{16}O(n,\alpha)^{13}C$ reaction. A line at 4.4 Mev is typical of ^{12}C and may be the result of the second reaction if the ^{13}C produced decays by neutron emission. Data taken at 0° with a source height of 500 ft give similar results as the 0°, 1125 ft run except that a greater amount of the 4.4-Mev gamma ray is observed. Calculations by Straker give a spectrum having the same general shape as those shown. Typical results for the neutron spectra have already been reported.[17]

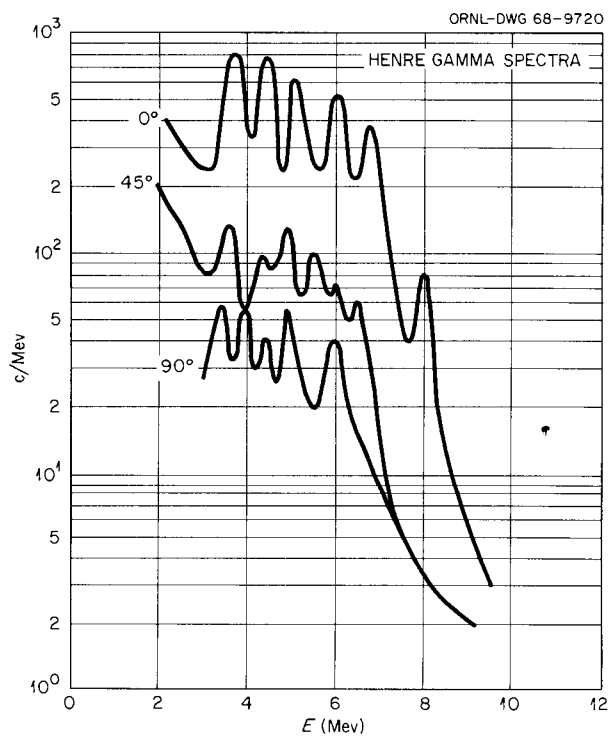

Fig. 21.6. HENRE Gamma Spectra as a Function of Angle at a Distance of 500 yd.

NUCLEAR ACCIDENT DOSIMETRY INTERCOMPARISONS

During the week December 4 through 8, 1967, the fourth in a series of intercomparisons in nuclear accident dosimetry (NAD) systems was conducted at the ORNL Health Physics Research Reactor (HPRR). In addition to members of the DOSAR staff, there were representatives from five other AEC contractors.

[17] J. H. Thorngate, *Health Phys. Div. Ann. Progr. Rept. July 31, 1967*, ORNL-4168, p. 191.

During this study, there was one moderated and one unmoderated burst. Dosimeter stations were positioned along the circumference of a 3-m radius circle (see Fig. 21.7), placing the dosimeter center line 3 m from core center of the HPRR. For the moderated burst, a 23-cm-thick plastic shield was placed, between HPRR and dosimeters, at 2 m (see Fig. 21.8). As an aid in the use of badge dosimeters and blood sodium activation dosimetry, a Bomab phantom filled with a 3.2-mg/ml saline solution was positioned at 3 m for both bursts. Reactor height (H_R) and dosimeter height (H_D) were 1.5 m for both experiments. A critique was held on Friday, December 8, for the purpose of presenting preliminary results. Final results were received about one month later and are given in detail in Tables 21.4 and 21.5. A brief recap, including a statistical treatment, is given in Table 21.6. Agreement between systems is found to be better for the moderated spectrum than for the bare spectrum. This is true both for neutron and gamma-ray dose. However, in the critique it was pointed out that some of the dosimeters (in particular, threshold detectors) which were near either edge of the plastic shield exhibited higher values than similar detectors centered behind the plastic array. Because of this, an additional experiment was conducted to describe the angular neutron fluence distribution at the 3-m station. Results of this experiment are shown in Fig. 21.9. One can see that this variation as a function of angle is quite significant and probably influenced measurements behind the array accordingly. Two things can be pointed out as probable causes for variations in this distribution: (1) the fitting together of the sections of the shield (large, open cracks between sections permitted streaming) and (2) an increase in the scattered component near edges of the shield.

The fifth in this series of intercomparison studies was conducted from July 8 through 26, 1968. As in the case of No. 3, this one was on an international scale. Participants ranged from several national laboratories and from England, Japan, and France.

The actual intercomparison of nuclear accident dosimetry systems was conducted during the first two weeks. In addition to the regular experiments, a series of informal lectures and discussions were given by scientists known and respected the world over. Final results of the intercomparison of NAD systems are expected in mid-August. A symposium was added to this study and was conducted during the third week. The primary topic of this series of lectures was "Etch-Pit Determination of Tracks in Solid-State Detectors." Lab exercises were conducted in addition to lectures and discussions.

X RADIATION HAZARDS ASSOCIATED WITH THE USE OF VACUUM ELECTRICAL COMPONENTS

During the last several years, there has been a significant increase in the application of vacuum electrical components[18,19] in the scientific community and an even larger application in the electrical power and communications industry. Unknown to most users of these products (such as switches, relays, contactors, and variable and fixed capacitors), intense x-ray fields are frequently encountered at distances of several meters. More important is the fact that manufacturers of these products do not print hazard warnings in their literature or on the product containers.

For purposes of this discussion, only one type of component, the high-voltage–high-current switch, will be considered. Vacuum switches, such as the one shown in Fig. 21.10, have the following characteristics:

Application: dc switching under load, capacitor discharging, 60 hertz power switching

Test voltage: 70 kv (50 kv, 60 hertz)

Maximum recommended operating voltage: 60 kv

Continuous current: 100 to 200 amp dc

Dc interruption: 100 kw

The tungsten electrodes (one stationary and one movable) may be obtained in either normally open or closed configurations. When the contacts are separated by a few millimeters, and when a high potential (0 to 60 kv) exists between them, the switch acts much like a cold-cathode x-ray tube.

[18]Norman Peach, *Power* 111(9), 189–96 (September 1967).

[19]Hugh C. Ross, "Vacuum Switch Properties for Power Switching Applications" in *Power Apparatus and Systems*, American Institute of Electrical Engineers, April 1958.

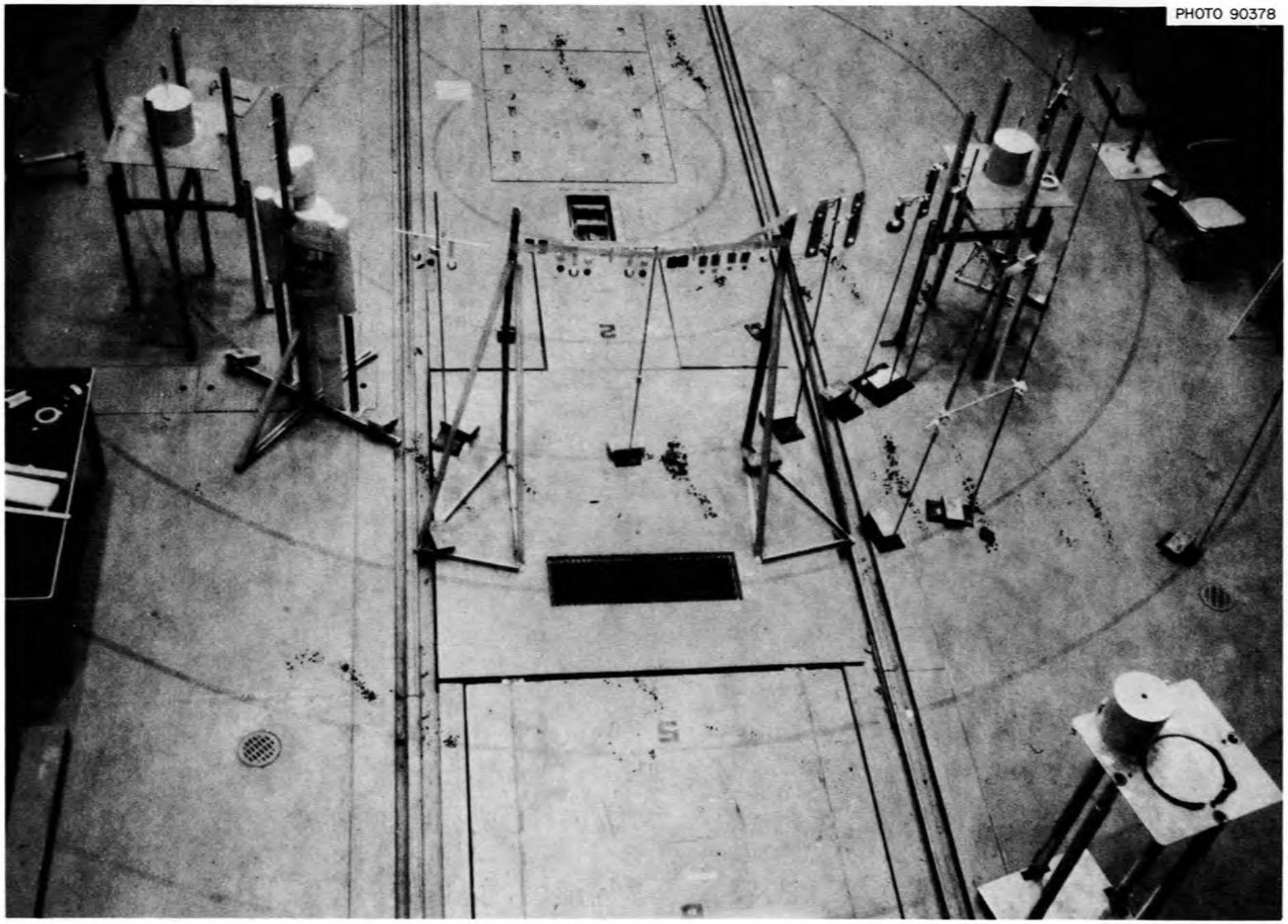

Fig. 21.7. Dosimeter Array for Unshielded HPRR Pulse.

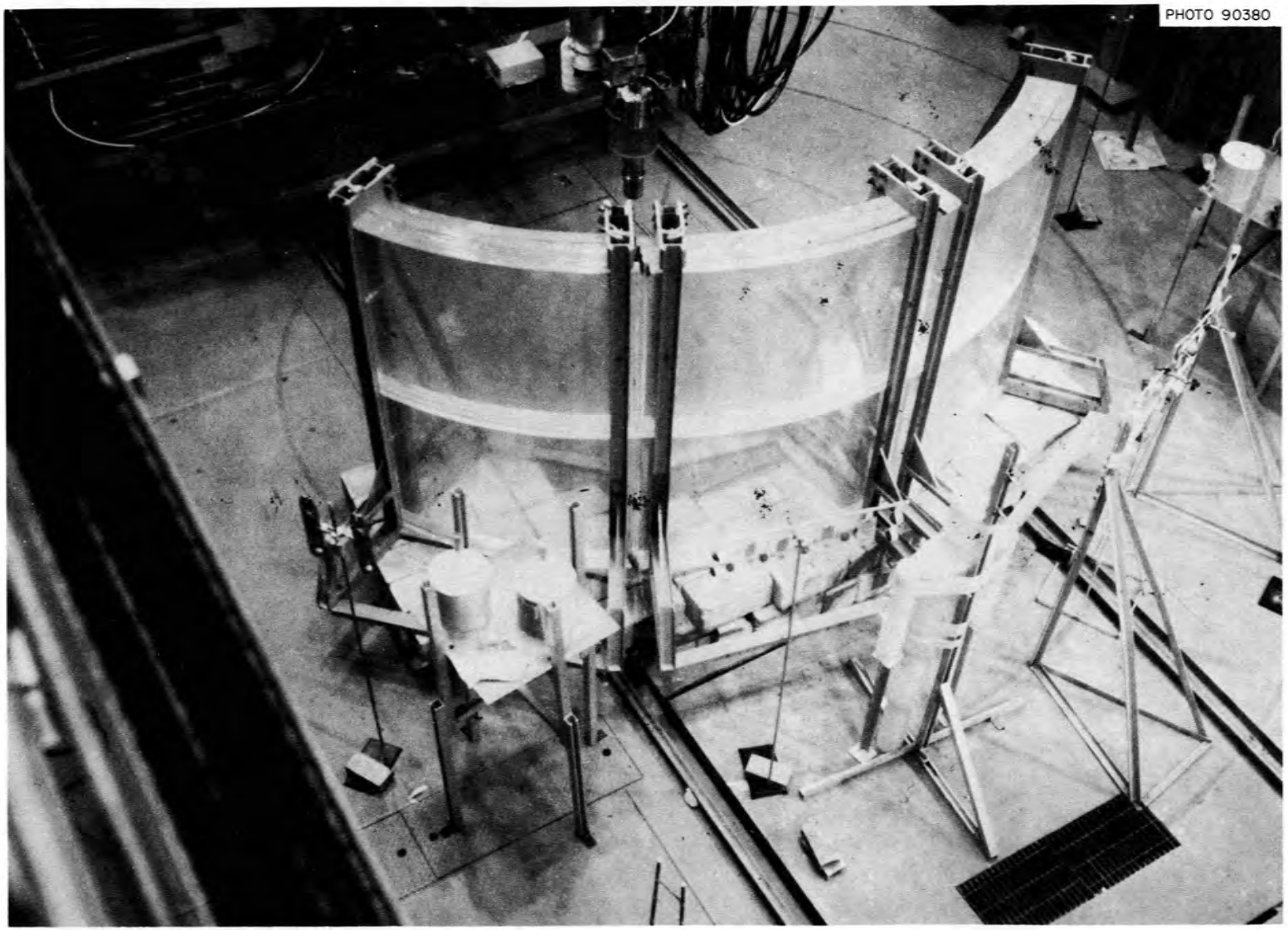

Fig. 21.8. Dosimeter Array for HPRR Pulse Shielded by 23-cm Plastic Shield.

Table 21.4. Nuclear Accident Dosimetry Intercomparison

Unmoderated burst
December 5, 1967
Yield, 1.17×10^{17} fissions

Study Group	D_n (rads)	D_γ[a] (rads)	D_n/D_γ[b]	Neutron Fluence (neutrons/cm²) Au, ϕ Thermal	Pu, $\phi > 0.001$ Mev	Np, $\phi > 0.75$ Mev	U, $\phi > 1.5$ Mev	S, $\phi > 2.5$ Mev	Cu ϕ	In ϕ	Bomab ^{24}Na (μc/ml)	Bomab D_n (rads), Surface	Bomab D_γ (rads), Surface	Neutron Dosimetry System	Gamma-Ray Dosimetry System
				$\times 10^{10}$	$\times 10^{10}$	$\times 10^{10}$	$\times 10^{10}$	$\times 10^{10}$	$\times 10^{10}$	$\times 10^{10}$	$\times 10^{-3}$				
PNL	577	71.7	8.0	0.9	25			3.9	7.0[c]	13[d]				Moderated foil	Film
														Activation foils	TLD
IDO	351			1.1[e]				3.08	11.05[f]	2.17[g]				PNTD	TLD
				11.0[h]											
SRL	462	68	6.8	0.81	18[i]			2.7[j]	8.2[k]	6.3[l]	4.6	537	125	SRL	TLD
ORGDP	571[m]	66	8.7	0.99	18	13	6.0	3.6		5.3	3.9	560[m]	165	ORGDP	BADGE with RPL and Li
	454[n]		6.9									676[n]		TDU	
Y-12	493	59	8.4	0.87	21	15	6.7	3.8			3.7	668		TDU	RPL and film
DOSAR-1	441	66	6.7	0.6	18	13	6.4	3.7			3.0			TDU	RPL
DOSAR-2	489			0.7	20	14	6.8	3.6						TDU LEXAN	
DOSAR-3	490	66	7.4											Prop. Ctr.[o]	Phil[p]

[a] 0.87 rad/r.
[b] Neutron dose/gamma dose.
[c] 1.4×10^{-9} rad neutron^{-1} cm^2.
[d] 2.9×10^{-9} rad neutron^{-1} cm^2.
[e] 0–0.4 ev.
[f] 1.22×10^{-9} rad neutron^{-1} cm^2.
[g] 2.87×10^{-9} rad neutron^{-1} cm^2.
[h] 0.4–2 ev.
[i] ϕ > thermal energy.
[j] >3 Mev.
[k] 1.3×10^{-9} rad neutron^{-1} cm^2.
[l] 2.9×10^{-9} rad neutron^{-1} cm^2.
[m] ORGDP dosimeter.
[n] TDU.
[o] Hurst proportional counter.
[p] Phil gamma-ray dosimeter.

Table 21.5. Nuclear Accident Dosimetry Intercomparison

Moderated burst
December 6, 1967
Yield, 8.28×10^{16} fissions

Study Group	D_n (rads)	D_γ[a] (rads)	D_n/D_γ[b]	Neutron Fluence (neutrons/cm²) Au, ϕ Thermal	Pu, $\phi > 0.001$ Mev	Np, $\phi > 0.75$ Mev	U, $\phi > 1.5$ Mev	S, $\phi > 2.5$ Mev	Cu ϕ	In ϕ	Bomab ^{24}Na (μc/ml)	Bomab D_n (rads), Surface	Bomab D_γ (rads), Surface	Neutron Dosimetry System	Gamma-Ray Dosimetry System
				$\times 10^{10}$	$\times 10^{10}$	$\times 10^{10}$	$\times 10^{10}$	$\times 10^{10}$	$\times 10^{10}$	$\times 10^{10}$	$\times 10^{-4}$				
PNL	29	34.5	0.84	0.7	1.7			0.2	1.1[c]	0.4[d]				Moderated foil	Film
	35	33.1	1.05											Activation foils	TLD
IDO	48			0.44[e]				0.14	1.2[f]	0.9[g]				PNTD	TLD
				0.04[h]											
SRL	24	32	0.75	0.76	3.0[i]			0.15[j]	2.0[k]	0.45[l]	2.4	19	48[m]	SRL	TLD
													37[n]		
ORGDP	23	31	0.75	0.55	0.86	0.28	0.24	0.15		0.34	2.2	19[o]	45[m]	ORGDP	BADGE
	18		0.58									25[p]	22[n]	TDU	RPL and Li
Y-12	21	34	0.62	0.45	1.04	0.55	0.26	0.16			2.4	28		TDU	
DOSAR-1	32	30	1.05	0.48	1.5	0.81	0.35	0.18			1.6			TDU	
DOSAR-2	30			0.43	1.4	0.52	0.33	0.14						TDU LEXAN	

[a] 0.87 rad/r.
[b] Neutron dose/gamma dose.
[c] 1.4×10^{-9} rad neutron^{-1} cm^2.
[d] 2.9×10^{-9} rad neutron^{-1} cm^2.
[e] 0–0.4 ev.
[f] 1.22×10^{-9} rad neutron^{-1} cm^2.
[g] 2.87×10^{-9} rad neutron^{-1} cm^2.
[h] 0.4–2 ev.
[i] ϕ > thermal energy.
[j] > 3 Mev.
[k] 1.3×10^{-9} rad neutron^{-1} cm^2.
[l] 2.9×10^{-9} rad neutron^{-1} cm^2.
[m] Front.
[n] Midpoint.
[o] ORGDP dosimeter.
[p] TDU.

The resulting x-ray field is influenced by the previous history of the tube. One which has undergone many make-and-break operations under load is apt to be more hazardous than a new tube.

Recently, a variety of vacuum components, including several switches like the one described above, were tested to demonstrate the x-ray hazard and to collect data in preparation for a more extensive study of these components.

During this test, measurements of exposure rate were made with a thin-walled portable ionization chamber. High voltage was provided by a 200-kv, 6-ma dc power supply.

It was noted in the test of one switch (described above) that at 4 m, the exposure rates for 50, 55, and 60 kv were 82, 200, and 360 mr/hr respectively. The voltages in this case were either at or below the rated continuous operating voltage. At 75 kv, which is just 8% greater than the test voltage, the exposure rate at 4.0 m was found to be 490 mr/hr.

During the coming year, it is expected that more exhaustive tests will be performed on a great variety of components.

Table 21.6. Neutron and Gamma-Ray Dose Results

Burst No.	Fission Yield	Neutron Dose (rads)		Gamma Dose (rads)	
		Range	Average[a]	Range	Average[a]
B 309	1.17×10^{17}	351–577	481 ± 68	59–71.7	66.1 ± 4.1
B 310	8.28×10^{16}	18–48	28.9 ± 9.0	30–34.5	32.4 ± 1.8

[a] $\sigma = [\Sigma(x_i - x)^2/(n-1)]^{1/2}$.

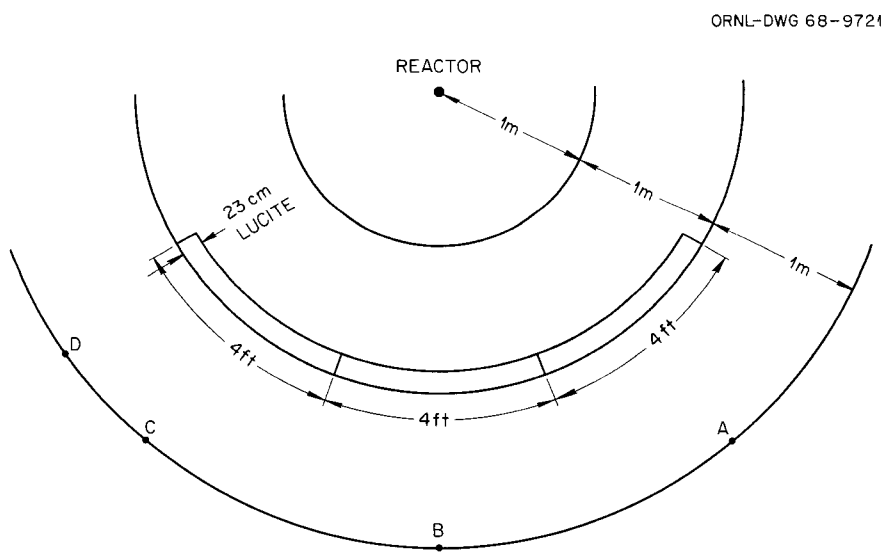

POINT	DOSE (rads)
A	27
B	21.9
C	31.1
D	44.6

Fig. 21.9. Angular Distribution of Neutron Dose from HPRR Behind 23-cm-thick Plastic Shield.

ORNL-DWG 68-8733

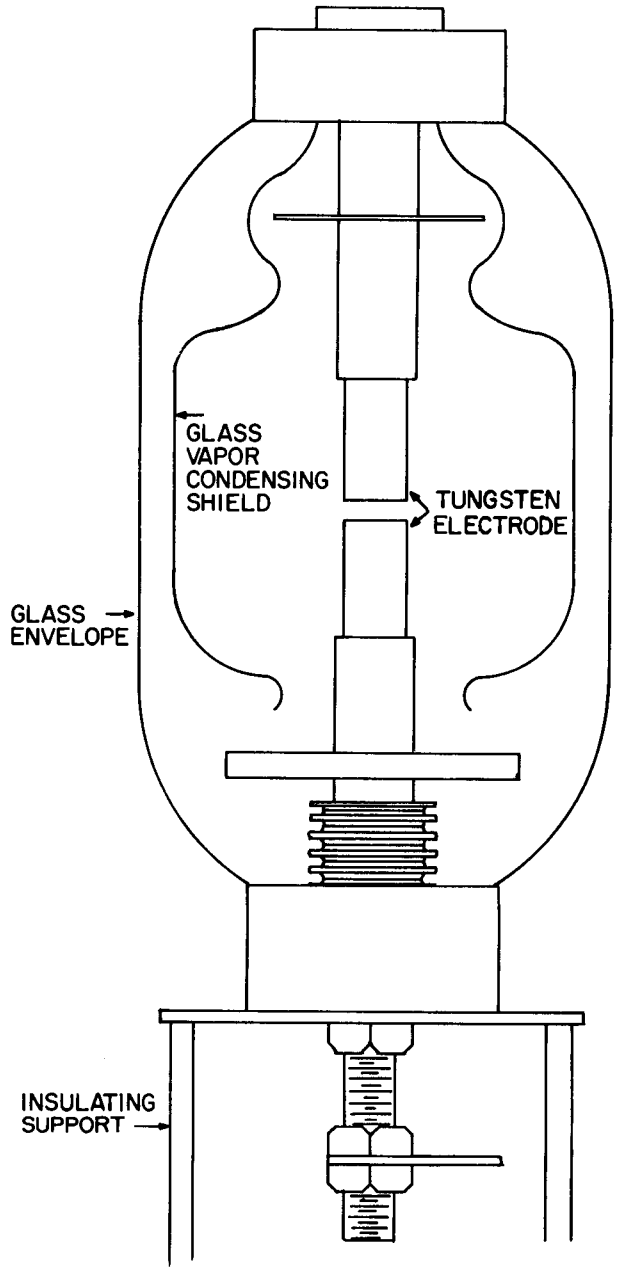

Fig. 21.10. Diagram of Typical High-Voltage Vacuum Switch.

22. Applied Research

K. Becker

C. D. Bopp[1] T. D. Jones
R. H. Boyett W. W. Parkinson[1]
J. S. Cheka E. M. Robinson

D. R. Sears[1]

The main goal of the Applied Research Group, which was newly formed in September 1967, has been to start some programs related to the better understanding of the principles of several promising new methods in solid-state dosimetry and to develop improved detectors for routine health physics and for research. In particular, studies have been carried out on (1) thermally stimulated exoelectron (after)emission from irradiated solids, (2) radiophotoluminescence in silver-activated lithium borate glasses with low energy dependence, and (3) the mechanism and application of the registration of alpha-particle tracks in organic polymers. None of these programs have been completed; only some typical results which have been obtained so far are briefly reported.

DOSIMETRY BY THERMALLY STIMULATED EXOELECTRON EMISSION (TSEE)

The counting of low-energy electrons, which are emitted from the surface of irradiated ionic crystals during optical or thermal stimulation, can be used as a sensitive method of integrating radiation dosimetry.[2] The principle and dosimetric potentials of this method are similar to those of thermoluminescence dosimetry (TLD). It offers, however, some advantages over TLD such as higher sensitivity, simpler preparation of the (unactivated) detectors, extremely thin sensitive volumes (<100 A), etc. A program has been started to investigate the physical principles and dosimetric possibilities of TSEE detectors.

A reader has been built based on a gas-flow G-M counter (Fig. 22.1), with a heating element inside the counting volume onto which a disk-shaped carrier with the detector material can be placed (for details of the design see ref. 3). Heating rate and maximum temperature can be varied by an automatic temperature controller and indicator. Besides the integral count, the "glow curves" (e.g., the count rate as a function of heating time or temperature) can be directly recorded. As detector holders, low-Z conducting materials such as graphite or beryllium disks have been used. It is, however, also possible to hot-press the detector substance mixed with a conducting material into pellets which are used as dosimeters.

A pellet 2.5 cm in diameter consisting of 50% BeO powder and 50% graphite, for example, is quite sensitive (~30,000 counts/r; 1 mr doubles the background count of the unshielded G-M counter), has little energy dependence down to a few kiloelectron volts (the lower sensitivity below 100 kev can be compensated by the addition of small amounts of high-Z materials), and shows no fading at room temperature.

[1]Reactor Chemistry Division.

[2]J. Kramer, *Z. Angew. Phys.* 15, 20 (1963); 20, 411 (1967).

[3]K. Becker and E. M. Robinson, *Health Phys.*, in press.

Fig. 22.1. G-M Counter Used for the Detection of Thermally Released Exoelectrons, with Detector Planchet Placed on the Heater Element for Insertion into the Counting Volume.

Of many substances that exhibit TSEE, LiF and BeO have been studied in more detail because of their flat energy response. Typical glow curves as obtained at a relatively high heating rate (100°C/min) are given in Fig. 22.2. Of several LiF samples, a very pure unactivated material ("suprapur," E. Merck, Darmstadt, Germany) was most sensitive. Other LiF preparations such as commercial TLD phosphors are less sensitive. The LiF peak at 130 to 150°C, depending on the heating rate, and the BeO peak at 260°C are well reproducible. Other TSEE materials such as $CaSO_4$, $SrSO_4$, and $BaSO_4$ exhibit more complex TSEE spectra having two or three peaks between 150 and 300°C.

Pure detector materials plated on the carrier produced erratic results. Reproducible results could be obtained by mixing of the finely powdered detector with graphite powder and plating of a thin layer of this mixture on the carrier. The sensitivity is a supralinear function of the detector-to-graphite ratio (Fig. 22.3). Up to 75% LiF the response is linear (Fig. 22.4). For an effective detector surface of 3.15 cm^2, the sensitivity of LiF (75%) is 2100 counts/r.[4] With the unshielded counter, 10 mr can be detected.

The sensitivity can be increased by (1) the increase of the detector surface (the sensitivity is a linear function of the effective surface of the detector, Fig. 22.5; the whole inside of a sealed G-M counter tube can, for instance, be plated with the detector material and heated for the reading) or (2) by reduction of the background of the G-M counter by shielding or anticoincidence techniques.

At high doses, the high count rate tends to block the G-M counter. A reduction in sensitivity for extending the dose range is possible by "dilution" of the detector, reduction of its effective surface size, and a very slow heating rate (slow release of

[4]K. Becker, *Health Phys.*, in press.

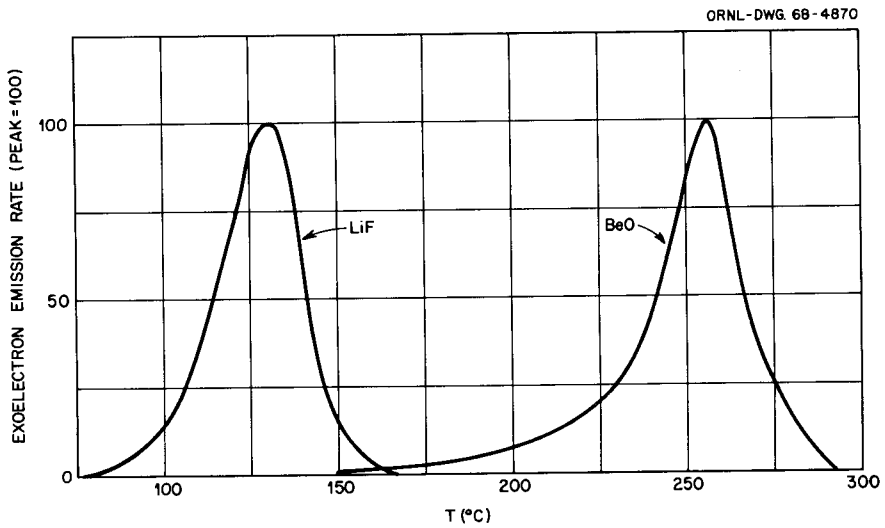

Fig. 22.2. Thermally Stimulated Exoelectron Emission Rate in Gamma-Irradiated Mixtures of 50% BeO and LiF ("Analyzed Reagent," J. T. Baker Chemical Company) and 50% Graphite Powder as a Function of Temperature, Normalized for Peak Emission = 100. Heating rate 100°C/min.

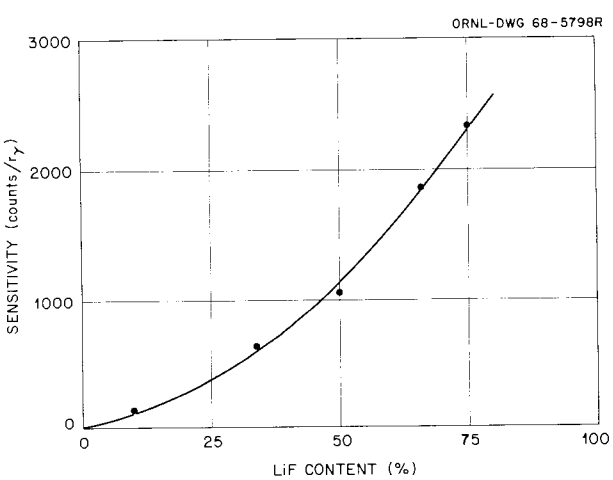

Fig. 22.3. Sensitivity of LiF/Graphite Mixtures Plated on a Graphite Disk (3.14 cm^2 Sensitive Area) as a Function of LiF Content.

exoelectrons), as well as by the use of an ionization chamber instead of the G-M counter for the exoelectron measurement. Another method which in addition permits repeated readings of the same sample is based on a partial release of the exoelectrons at lower temperature. In a BeO detector, for example, reading at maximum temperature of 255°C instead of 300°C leads to a marked decrease in the count during repeated 5-min heating cycles (Fig. 22.6).

Because of the clear separation of the LiF and BeO glow peaks, both substances can be mixed together with graphite. The two peaks remain so well separated (Fig. 22.7) that a repeated measurement of the dose information stored in the LiF is possible without affecting the dose integration in the BeO. Because the fading in the LiF is small and in the BeO is negligible at room temperature, this offers an interesting possibility for personnel dosimetry.

The samples can be annealed many times at temperatures above the glow peaks. All TSEE detectors are light sensitive. A short time in direct sunlight completely anneals the radiation effect but does not affect the intrinsic sensitivity and background. Low-intensity artificial light does not disturb the measurements.

Thermal neutrons can be measured by the use of ^{6}LiF/^{7}LiF dosimeter pairs, and fast neutrons by the use of hydrogenous radiators in front of the recoil-proton-sensitive detector layer. It has been found that in some TSEE materials having a multipeak emission spectrum such as $CaSO_4$, $SrSO_4$, and $BaSO_4$ the peak ratio depends on the LET of the radiation. High-LET particles tend to increase

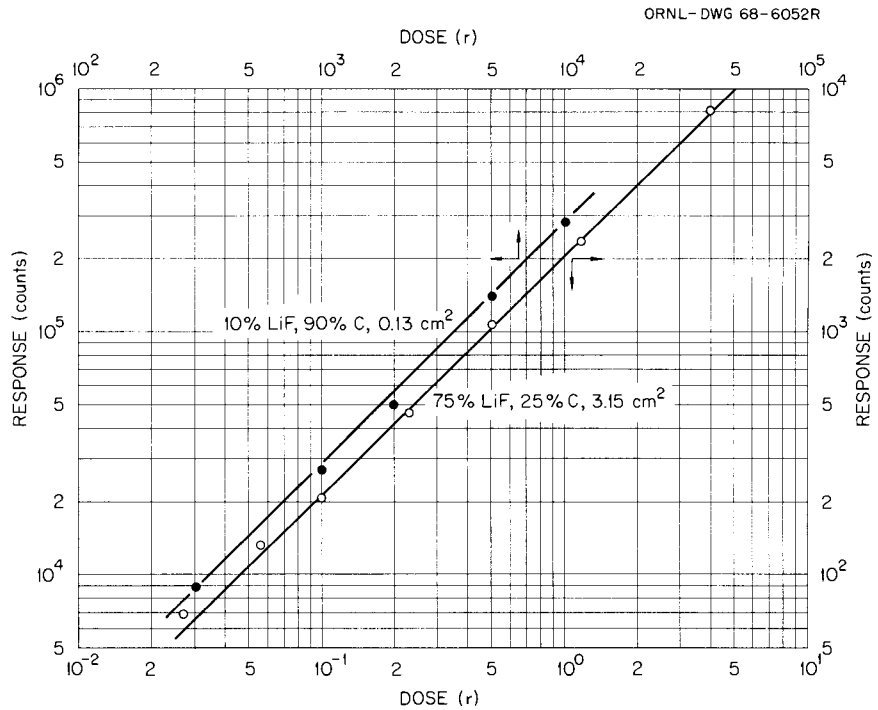

Fig. 22.4. Detector Response in Total Counts as a Function of ^{60}Co Gamma Radiation Dose. (*a*) For a detector of medium sensitivity (75% LiF, 25% C, 3.14 cm^2 sensitive surface), (*b*) for a detector of low sensitivity (10% LiF, 90% C, 0.13 cm^2 sensitive surface).

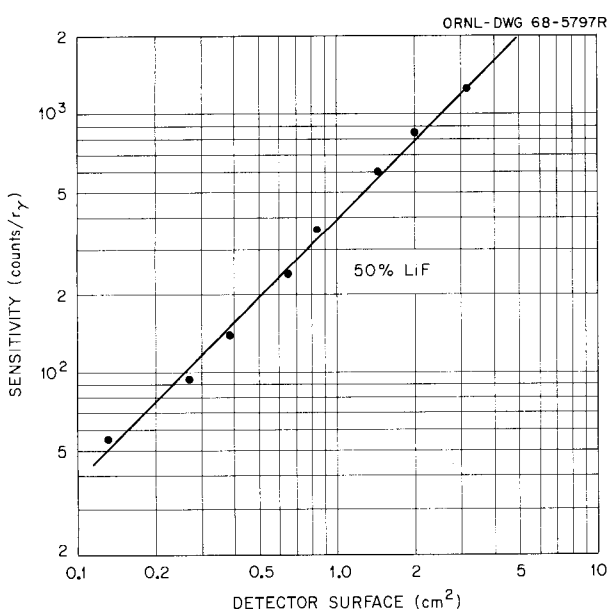

Fig. 22.5. Sensitivity of a 50% LiF/50% C Detector Material as a Function of the Effective Detector Surface.

the low-temperature peak. Partial annealing of the low-temperature peaks can, therefore, be used as an effective method of discrimination against the gamma radiation effect in mixed fast-neutron and photon radiation fields.

Further work on TSEE detectors, for example, on their fading kinetics, their fast-neutron response, the energy distribution of the emitted electrons, the relation between thermoluminescence and TSEE, and their use as solid-state "microdosimeters," is in progress.

LITHIUM BORATE GLASSES AS RADIOPHOTOLUMINESCENCE (RPL) DOSIMETERS

A basic disadvantage of all commercial radiophotoluminescent metaphosphate glass dosimeters is their considerable energy dependence. By replacing the metaphosphate glass base by an ($Li_2O \cdot xB_2O_3$) glass system and by reduction of

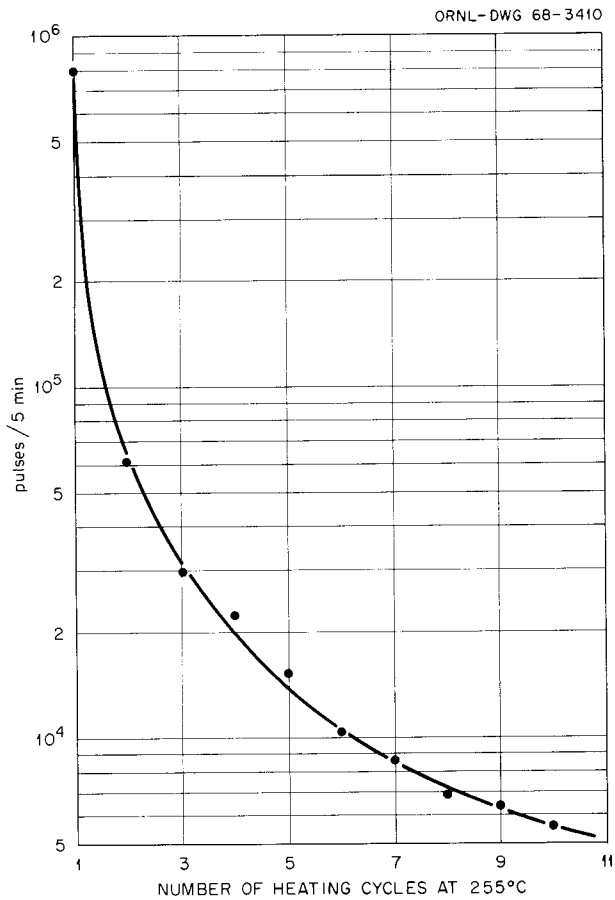

Fig. 22.6. Pulses per Heating Cycle at 255°C for Consecutive Readings of the Same Irradiated BeO Detector at a Temperature Not Sufficient for a Complete Release of the Exoelectrons.

the silver content, it became possible to prepare glasses whose energy dependence is within ±10 to 20% between several keV and several MeV (Fig. 22.8).

The new glasses have been prepared by melting a mixture of Li_2CO_3 or $LiNO_3$, B_2O_3, and $AgPO_3$, corresponding to a final glass composition of ($Li_2O \cdot 2\text{–}4\ B_2O_3$) with variable additions of silver phosphate, in a platinum crucible at 900 to 950°C for 30 to 60 min and pouring the viscous liquid in a stainless steel mold. The resulting glass blocks of 8 × 8 × 4.7 mm can be read in the commercial fluorimetric RPL readers. The glasses are stable in normal laboratory air, but they soften at high humidity and dissolve in water.[5]

[5]K. Becker and J. S. Cheka, *Health Phys.*, in press.

Because of their low silver content, the RPL buildup and fading are slow processes in such glasses. In order to obtain the maximum RPL, a heat treatment of the glass prior to the reading is required. One to two hours at 320°C usually leads to optimum RPL (Fig. 22.9). Annealing of the RPL is possible at temperatures above 400°C.

The "absolute" RPL spectra (corrected for the photomultiplier response characteristics) of the lithium borate glasses are only little dependent on the silver concentration but quite different from the symmetrical RPL spectra usually obtained in phosphate glasses, peaking at approximately 610 to 630 nm (Fig. 22.10). The commercial RPL readers are, therefore, not optimal for the reading of borate glasses. The "predose" corresponds to approximately 1 r. Less than 1 r can be measured with good accuracy.

At high dose levels, phosphate glasses develop an absorption peak at 313 nm whose shape does not change during annealing at increased temperature (Fig. 22.11). Unlike this, a rather complex absorption spectrum is observed in the borate glass (Fig. 22.12). The thermal stability of the different absorption centers is quite different, as is indicated by the shift in the spectral shape during annealing. The absorption is generally more stable than in the phosphate glass. At 150°C, for example, some absorption peaks of a borate glass even show a buildup (Fig. 22.13). These glasses can, therefore, be used as high-level dosimeters with low energy response and high stability. Their dose range (Fig. 22.14) can be extended to higher values by the use of thin glass plates (for details, see ref. 6).

LET EFFECTS IN RADIOPHOTOLUMINESCENCE GLASSES

It has been found that the type of centers formed in RPL glasses depends on the LET of the radiation. In particular, the RPL and absorption spectra as well as the buildup and fading kinetics of different glasses have been compared after gamma and thermal-neutron radiation, the latter interacting with the glasses mainly by (n,α) reactions with the Li and B of the glass base.

[6]J. S. Cheka and K. Becker, to be published in *Nuclear Applications*.

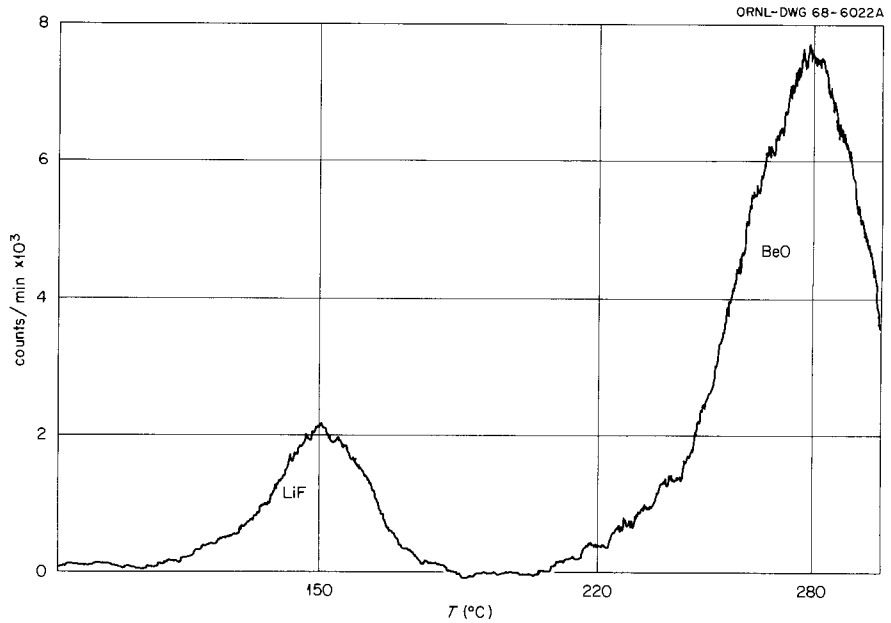

Fig. 22.7. TSEE "Glow Spectrum" of a Detector Consisting of 8% BeO, 67% LiF, and 25% C, After Exposure to Gamma Radiation.

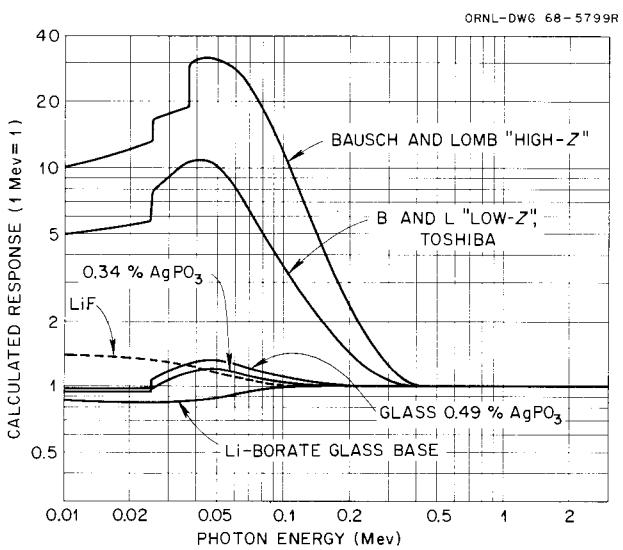

Fig. 22.8. Energy Dependence of Several Commercially Available Metaphosphate Glasses (High-Z and Low-Z Glasses Made by Bausch & Lomb, Rochester, New York; P-1 Made by Toshiba, Tokyo, Japan) in Comparison with the New Lithium Barate Glasses. Calculated from the mass absorption coefficients of the constituents and normalized for the response at 1 Mev = 1. The dotted line indicates the energy dependence of lithium fluoride.

The difference in the RPL spectra after thermal-neutron and gamma exposure is usually less pronounced in phosphate (Fig. 22.15) than in borate glasses (Fig. 22.16). During thermal stabilization, the thermal-neutron-induced RPL spectrum becomes more similar to the gamma-induced spectrum. In both glass types, the gamma-induced RPL is initially thermally considerably more stable than the thermal-neutron-induced RPL (Fig. 22.17). Figure 22.17 also illustrates the generally higher stability of RPL in borate glasses. After extended thermal annealing, however, the "residual" RPL is higher in thermal-neutron-exposed glasses (Fig. 22.18).

In the radiation-induced changes of the ultraviolet absorption spectra of phosphate glasses, only small differences between thermal-neutron and gamma exposures have been observed. As in the RPL spectra, those differences are much more pronounced in the borate glasses (Fig. 22.19) (for details, see ref. 7).

[7]K. Becker and J. S. Cheka, to be presented at the Second International Conference on Luminescence Dosimetry, Gatlinburg, Tenn., 1968.

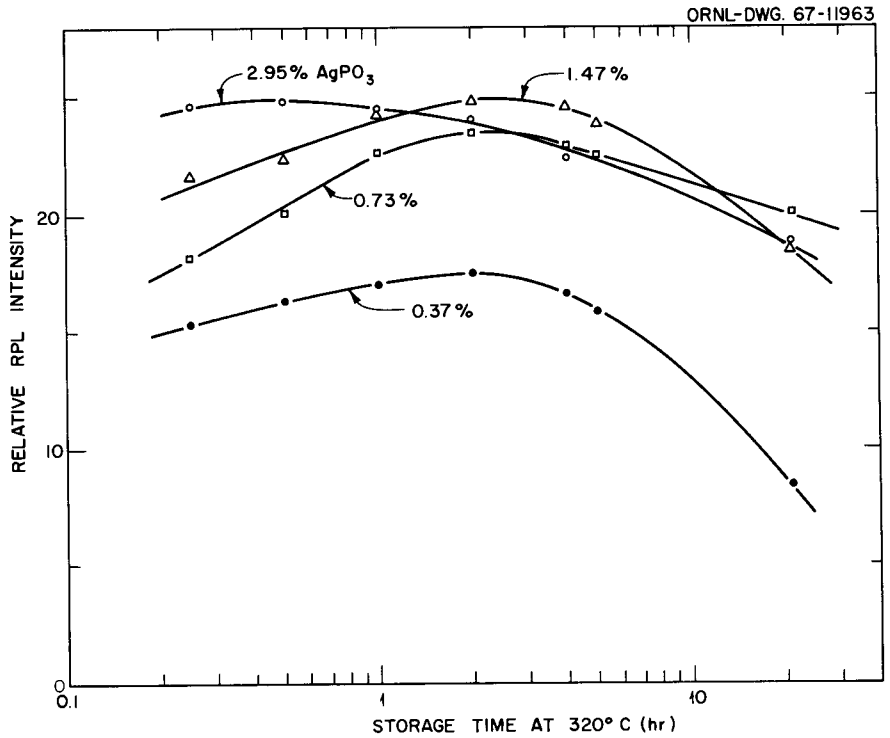

Fig. 22.9. Relative RPL Intensity of ($Li_2O \cdot 4B_2O_3$) Glass Blocks Containing Different Amounts of $AgPO_3$ and Exposed to the Same Gamma Radiation Dose as a Function of Storage Time at 320°C.

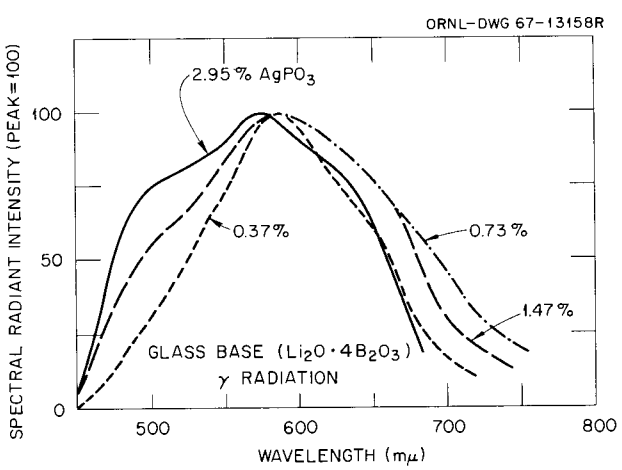

Fig. 22.10. "Absolute" (Corrected for Detector Response Characteristics) RPL Spectra of Borate Glass with Different $AgPO_3$ Content for 365 mμ Excitation. Normalized for ~580 mμ peak intensity = 100.

LONG-TERM STABILITY OF RADIOPHOTOLUMINESCENCE IN PHOSPHATE GLASSES

Since 1962, the long-term stability of RPL in three different commercial phosphate glasses (Toshiba FD-R1-1 and Bausch and Lomb high-*Z* and low-*Z* fluorods) has been compared for storage of unstabilized glasses exposed at different dose levels in the dark at room temperature. The results are summarized in Fig. 22.20. In one of the three glass types (Toshiba), the reading after five years is still within a few percent of the initial reading taken 24 hr after exposure (for details, see ref. 8). Evidently, such glasses can be used for extended periods, probably even as a lifetime dosimeter, and offer a remeasurable legal evidence of a radiation exposure.

[8] J. S. Cheka, *Health Phys.*, in press.

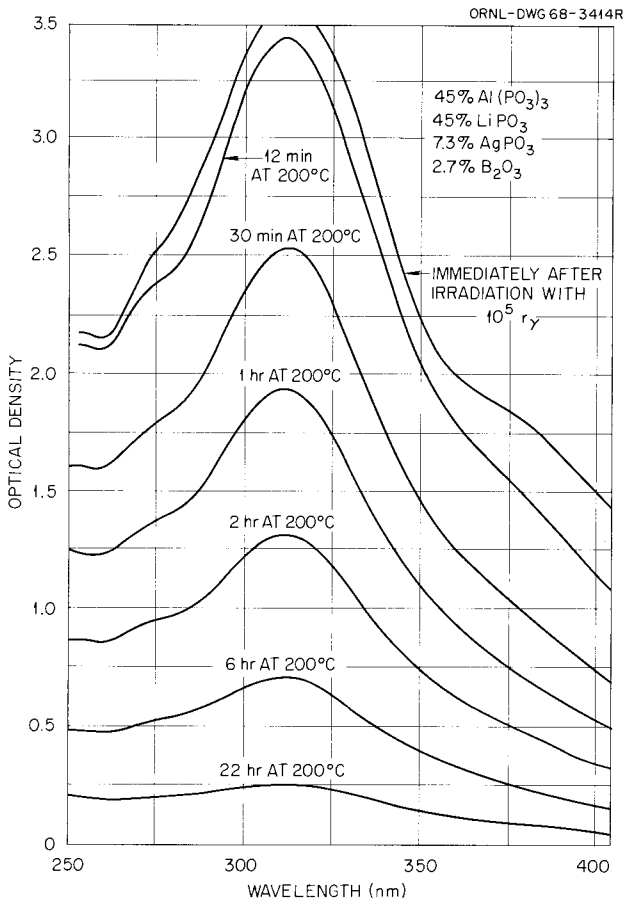

Fig. 22.11. The UV Absorption Spectrum of a Silver-Activated Phosphate Glass Block (Toshiba, Tokyo) of 4.7 mm Thickness Immediately After Exposure to 10^5 r of ^{60}Co Radiation and During Different Phases of Thermal Annealing at 200°C. Measured relative to an identical unexposed glass block.

DOSIMETRY AT THE UT-AEC AGRICULTURAL RESEARCH LABORATORY VARIABLE DOSE-RATE FACILITY

Members of the Applied Research Group acted as consultants to the UT-AEC Agricultural Research Laboratory in the design and calibration of an animal exposure facility, containing six sources of approximately 13,000 curies each of ^{60}Co and permitting the exposure of one to seven large animals to dose rates of 0.5 to 65 r/min.

The uniformity of source loading was checked with an ionization chamber; the maximum deviation from the average dose values at the seven exposure stations was found to be within ±6% at source elevations above 350 mm and detector elevations from 40 to 200 cm.

Toshiba FD-R1-1 radiophotoluminescence (glass) dosimeters, encapsulated in 0.5 mm Ta and 0.42 mm Teflon as energy compensation filters and to be evaluated in a Turner 110 fluorimeter, have been calibrated in the 100-to-1000-r dose range for use as a dosimetry system at the facility (for details, see ref. 9).

RADON AND RADON DAUGHTER PERSONNEL DOSIMETRY WITH SOLID-STATE ALPHA-PARTICLE DETECTORS

Alpha-particle tracks can be made visible in certain organic polymers such as cellulose nitrate or acetate by a proper etching technique. This method can be used for the personnel dosimetry of uranium miners for radon and radon daughters. It is superior to a similar technique using photographic emulsions[10] because the solid-state detectors are insensitive to light and other disturbing environmental effects and exhibit no fading of the "latent" radiation effect even at high humidity and temperature.

A simple apparatus (Fig. 22.21), consisting of a diluted radium solution from which the radon can be continuously extracted by bubbling air through it at a known flow rate and an exposure volume of sufficient size, have been used for testing a cellulose triacetate (Triafol T made by Bayer AG., Germany) foil detector. Its sensitivity was found to be approximately 30 tracks cm^{-2} pc^{-1} hr^{-1} ml. In a detector with a sensitive area of 3 cm^2, a weekly MPC causes 100 tracks, corresponding to a statistical accuracy of ±10% (for details, see ref. 11).

In order to simplify the tedious and time-consuming visual counting procedure, a flying-spot-type automatic scanning microscope (Fig. 22.22) has been used. The field size can be varied between 6×10^{-4} and 1 mm^2. This area is scanned in 7 sec.

---

[9] E. M. Robinson and J. S. Cheka, *UT-AEC Agricultural Research Laboratory Variable Dose-Rate Gamma Facility*, ORNL report, in preparation.

[10] E. L. Geiger, *Health Phys.* 13, 407 (1967).

[11] K. Becker, *Health Phys.*, in press.

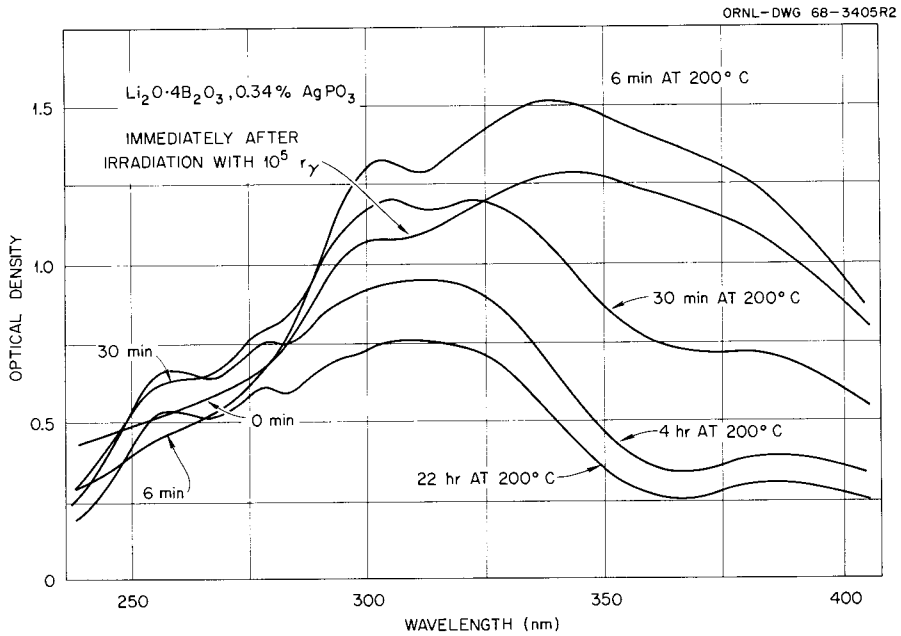

Fig. 22.12. The UV Absorption Spectrum of Glass ($Li_2O \cdot 4B_2O_3$, 0.34% $AgPO_3$) Immediately After Exposure to 10^5 r of ^{60}Co Radiation and After Different Heat Treatment.

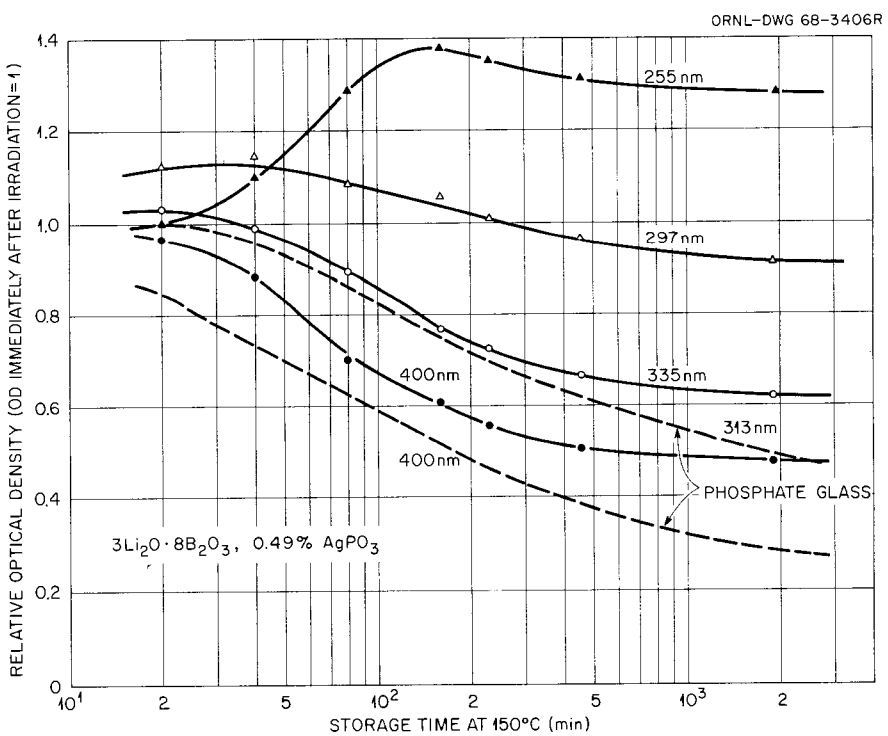

Fig. 22.13. Comparison of the Stabilities of the Optical Densities at Different Wavelengths in Phosphate and a Lithium Borate Glass at 150°C. Normalized to the density immediately after exposure.

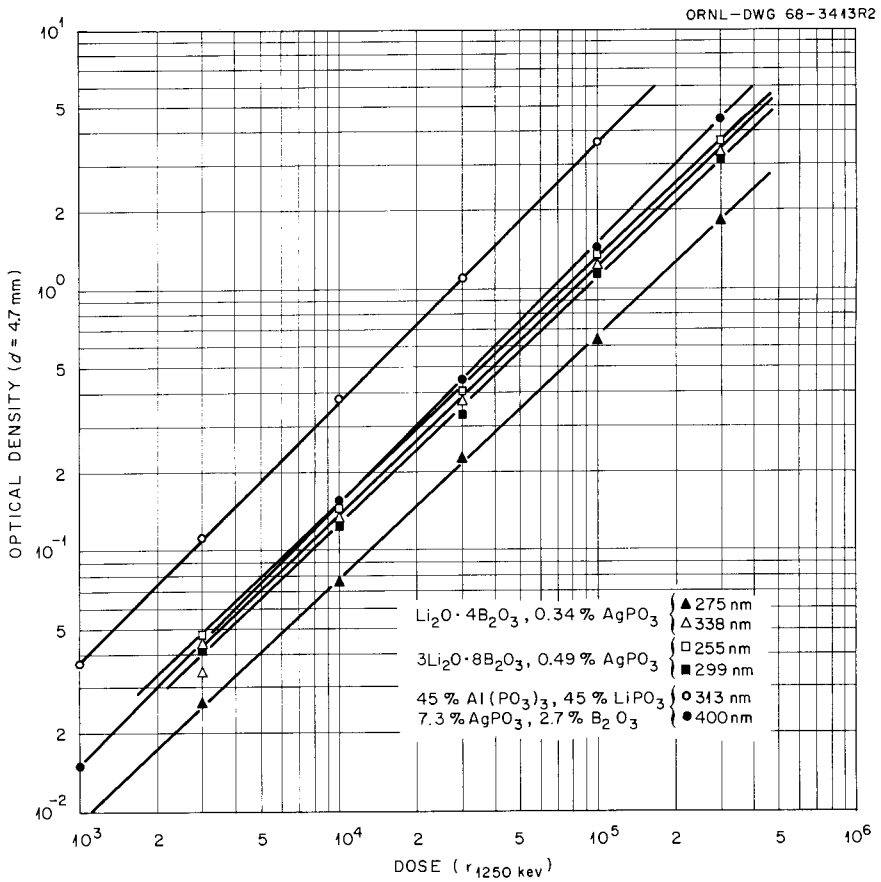

Fig. 22.14. Optical Density at Different Wavelengths in Phosphate and Borate Glasses of 4.7 mm Thickness as a Function of ^{60}Co Gamma Radiation Dose. Measured immediately after exposure at room temperature.

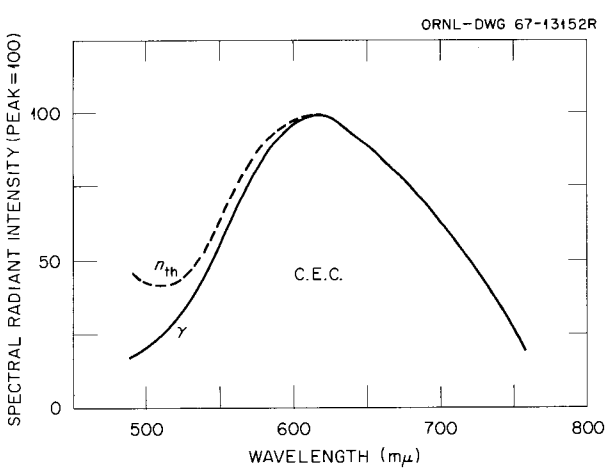

Fig. 22.15. Thermal-Neutron- and Gamma-Radiation-Induced "Absolute" RPL Spectra in a French Dosimeter Glass (C.E.C., Montrouge) Containing 2.4% Ag, 3.5% Al, 2.5% Li, 4.7% Na, 0.5% Be, 33.8% P, and 52.5% O.

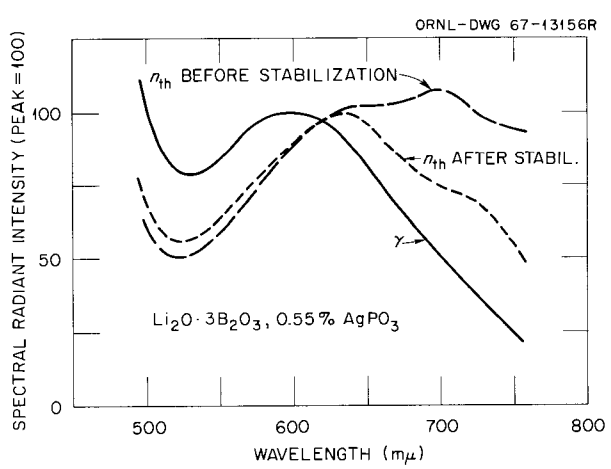

Fig. 22.16. Thermal-Neutron- and Gamma-Radiation-Induced RPL Spectra in Experimental Lithium Borate Glass Before and After a 1-hr 350°C Heat Treatment.

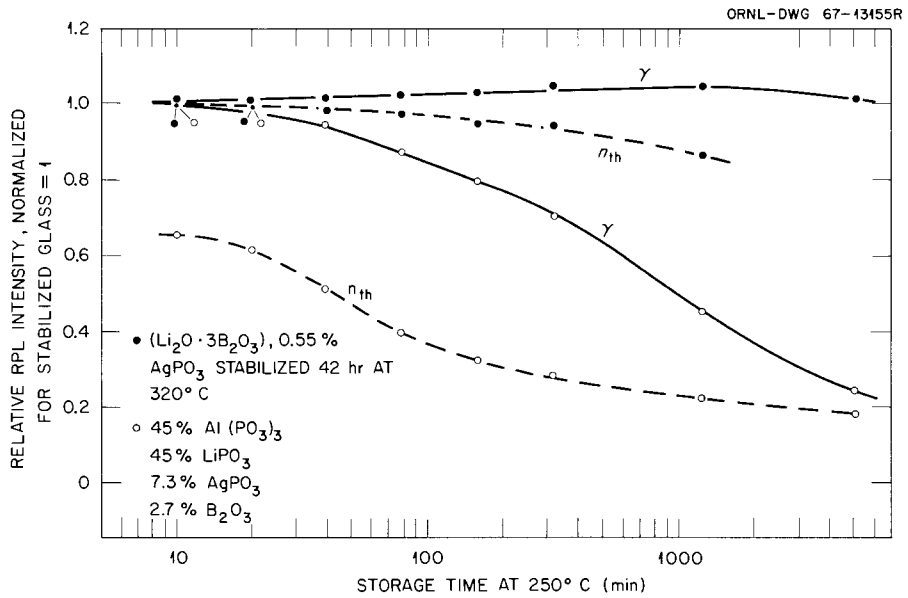

Fig. 22.17. Relative Thermal-Neutron- and Gamma-Radiation-Induced RPL Intensity in a Commercial Dosimeter Glass (Toshiba P-1) and a Lithium Borate Glass, Stabilized 42 hr at 320°C, as a Function of Storage Time at 250°C. Normalized to reading after stabilization = 1.

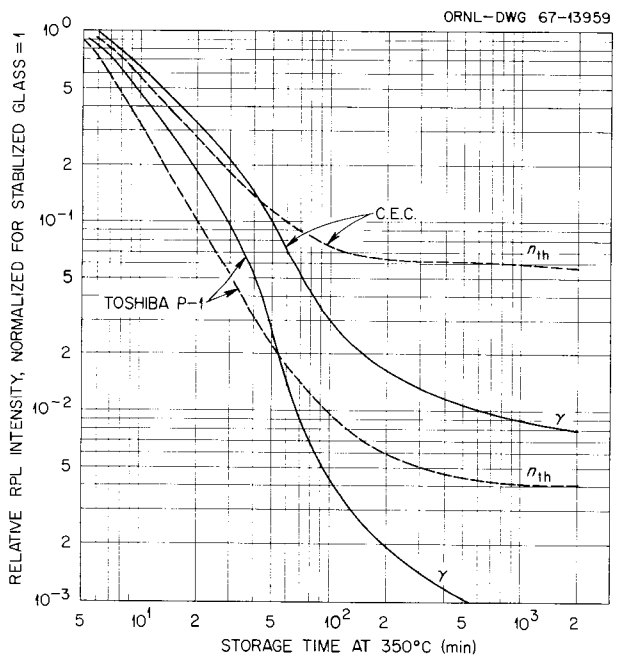

Fig. 22.18. Relative Thermal-Neutron- and Gamma-Radiation-Induced RPL Intensity in Two Commercial Glasses (C.E.C. and Toshiba P-1) as a Function of Storage Time at 350°C. Normalized to reading after stabilization = 1.

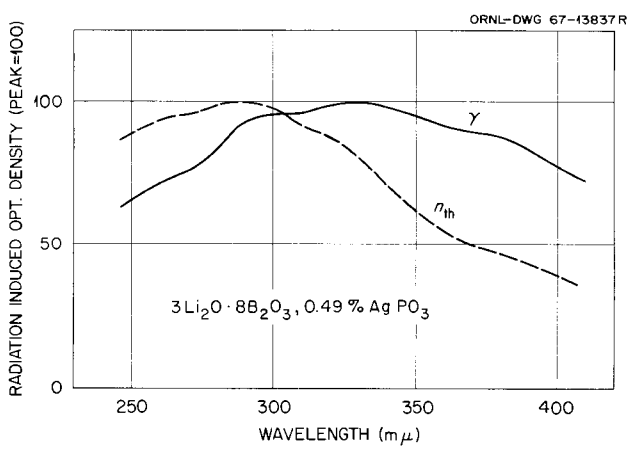

Fig. 22.19. Radiation-Induced Optical Density, Normalized for Peak Density = 100, as a Function of Wavelength for Borate Glasses Exposed to Thermal Neutrons and to Gamma Radiation. Unstabilized.

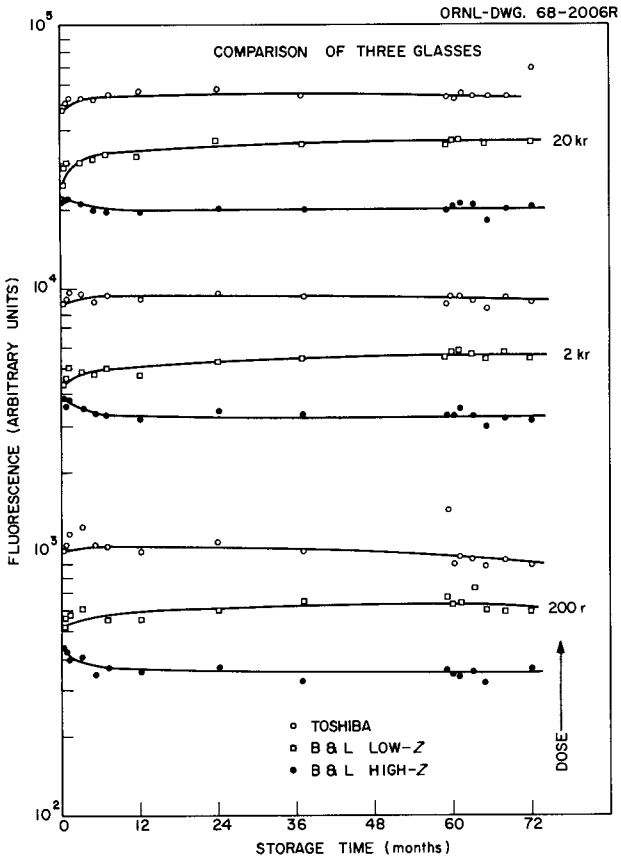

Fig. 22.20. Relative RPL Intensity of Three Commercial Dosimeter Glasses as a Function of Time post Exposure to Different Dose Levels.

An enhancement of the detector sensitivity would be desirable. Electrostatic deposition of the radon daughters which are attached to aerosol particles is impractical at the high humidity in mines. Thermal precipitation also did not result in a significant increase in the detector's sensitivity, mainly because increased temperature creates some fading problems.

CALCULATION OF PROBABILITY OF OVERLAPPING TRACKS IN SOLIDS

In connection with studies on nuclear track registration in solids by the etching technique, it seemed likely that in some less sensitive organic polymers low-LET tracks produced by particles with the LET of alpha particles or less can only be registered if the regions of damaged material caused by two or more particles overlap. If at least two damaged channels have to overlap and the track density as well as the observed etch pit density are known, the average diameter of the damaged region can be calculated.

If it is necessary that at least two tracks intersect in the fraction ϵ before an etchable track occurs, then to a first approximation the size of an incident track may be computed by considering areas a, a', and A, where $a' = a$ and A is the size of the area of observation.

Let a/A be the probability that a point P lies in area a all inside total area A. Likewise let a'/A be the probability that P lies inside a'. Now the probability that P is inside both a and a' is $(a/A)(a'/A)$, and if they must intersect in the fraction ϵ or greater to leave a track, then $P_{\text{eff}} = (1-\epsilon)(a/A)(a'/A)$. If n targets (previous hits) are present, the probability of an etchable track is

$$P_{an} = \frac{(1-\epsilon)na^2}{A^2},$$

and it is noted that this probability function is dimensionless if n is dimensionless.

The total number of etchable tracks is

$$N_{tr} = \int_0^n P_{an}\, dn$$

$$= \frac{(1-\epsilon)a^2}{A^2}\,\frac{n^2}{2}.$$

Solving for a^2 the result is

$$a^2 = \frac{2A^2N_{tr}}{(1-\epsilon)n^2} = (\pi r^2)^2,$$

so finally

$$r = \left[\frac{2A^2N_{tr}}{(1-\epsilon)\pi^2n^2}\right]^{1/4}.$$

CHEMICAL PROCESSES INVOLVED IN LATENT TRACK FORMATION IN PLASTICS

Little is known about the basic mechanism of the charged-particle interaction with organic dielectrics which is responsible for the preferential etching

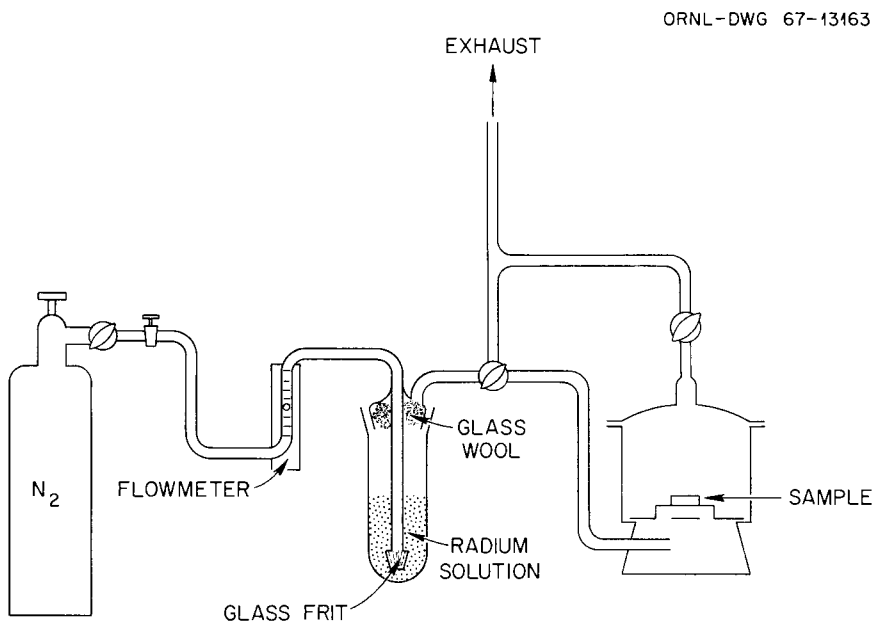

Fig. 22.21. Experimental Setup for Exposure of Different Polymer Alpha-Particle Detector Foils to Known Amounts of Radon and Radon Daughters.

along the track. One theory[12] explains the damage on the basis of an electrophysical "ion explosion spike" mechanism. There is, however, increasing evidence that radiochemical processes which lead to chemical reaction products in a cylindrical zone along the track and so create a higher solubility and reactivity of the material in this zone are more important for the latent track formation in plastics. In order to understand better the processes involved, a program has been initiated in cooperation with the Reactor Chemistry Division for studying the chemistry of the radiation interaction with plastics under different conditions. In particular, experiments have been carried out to identify the chemical decomposition products in cellulose and cellulose derivates after exposure to high- and low-LET radiations.

For example, the decomposition products resulting from gamma irradiation of regenerated viscose cellulose film have been examined by infrared spectrometry. The infrared spectra before and after irradiation (Fig. 22.23) show the formation of carbonyl groups in high yield as indicated by the band at 1740 cm^{-1}. Carbonyl groups would be expected to increase the dissociation constant of nearby acid-forming groups, thereby increasing the rate of dissolution in alkali etching reagents. The band at 2340 cm^{-1}, which may be dissolved CO_2, although other bands of this compound are unresolved, is not produced in films containing residual sulfur from the viscose treatment. The effect of oxygen and other radical-scavenging atmospheres (e.g., N_2O) is being followed presently by analysis of gaseous and low-boiling products. The dependence of the yields of these products on the LET of the incident radiation or particles will be studied after development of the analytical techniques.

In another series of experiments, the sharp reduction in molecular weight of polytetrafluoroethylene (Teflon) is being studied as a possible new means of registering tracks through the dependence of recrystallization on molecular weight. Films of Teflon have been bombarded with alpha particles and fission fragments and heat-treated to produce recrystallization. The crystalline structure has been examined microscopically, and tracklike patterns have been observed. The microscopic structure depends on the conditions of heat treatment, and the various factors are being optimized to prove whether the patterns are tracks or artifacts whose formation is enhanced by radiation.

[12] R. L. Fleischer, P. B. Price, and R. M. Walker, *J. Appl. Phys.* **36**, 3645 (1965); *Phys. Rev.* **156**, 353 (1967).

Fig. 22.22. Flying-Spot Scanner for the Automatic Counting of Particle Tracks in Solids.

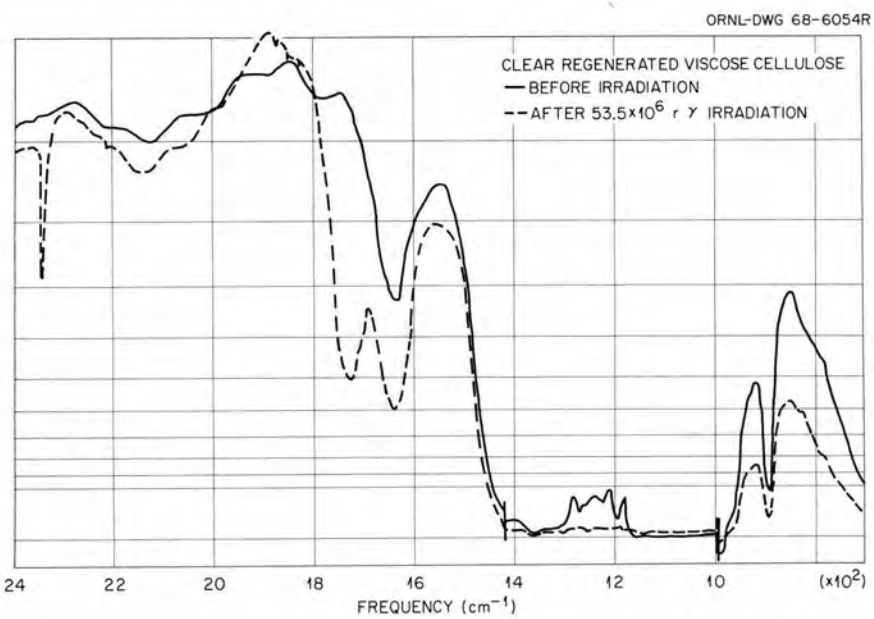

Fig. 22.23. Infrared Spectra Before and After Irradiation of Regenerated Viscose Cellulose Film.

OXYGEN AND HUMIDITY EFFECTS ON THE SENSITIVITY OF ORGANIC NUCLEAR TRACK DETECTORS

Radiation effects on many organic materials and organisms are enhanced by the presence of oxygen. It was found that in some organic foils such as cellulose triacetate (Triafol T), which have been exposed to alpha particles from a thick ^{238}U foil, the appearance of the alpha etch pits also depends on the absence or presence of oxygen during irradiation. The maximum etch-pit diameter in the oxygen-free foils is smaller (Fig. 22.24) and the number of visible etch pits considerably less (Fig. 22.25). The apparent decrease of visible etch pits after more than 100 min of etching is due to "overetching" (e.g., etch pits became less well defined if too large).

No oxygen effect has been observed in cellulose nitrate, a material which is, unlike cellulose acetate, rich in loosely bound radical scavengers. Quite small amounts of oxygen caused a considerable difference in sensitivity in cellulose acetate; replacement of air by pure oxygen did not further increase the sensitivity. Also a pretreatment of this foil in an H_2O_2 solution just increased the etching speed but did not significantly affect the sensitivity.

The etching speed (e.g., the increase of the etch-pit diameter as a function of the etching time) is also affected by the humidity of the cellulose acetate foil (Fig. 22.26). Unlike the oxygen effect, it makes no difference whether the foil has been "softened" with water or H_2O_2 prior to or after irradiation. Despite a considerable difference in the etching speed in dry and humid foils, the sensitivity (e.g., the maximum number of visible etch pits) depends only little on the foil treatment (Fig. 22.27).

The latent alpha-particle tracks are quite stable even at increased temperature. In a cellulose acetobutyrate foil, for example, no fading has been observed at room temperature. Up to 100°C, little fading occurs within one day (Fig. 22.28). Only at a temperature close to the softening point of the polymer considerable fading has been found. Even then, however, some invisible tracks "reappear" after extended etching (for details, see ref. 11).

FAST-NEUTRON DOSIMETRY BY DIRECT INTERACTION WITH ORGANIC POLYMERS

The registration of fission fragments in solid-state detectors which have been combined with foils of fissionable materials recently became a standard technique for fast-neutron dosimetry.

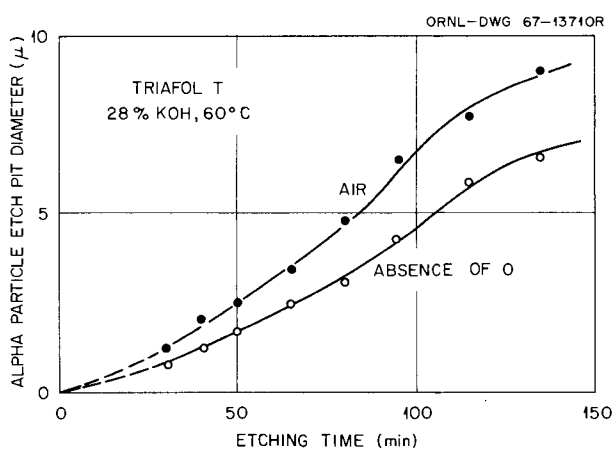

Fig. 22.24. Maximum Alpha-Particle Etch Pit Diameter in Triafol T as a Function of Etching Time in a Foil Kept and Exposed in Dry Air and in a Foil Kept and Exposed in Nitrogen.

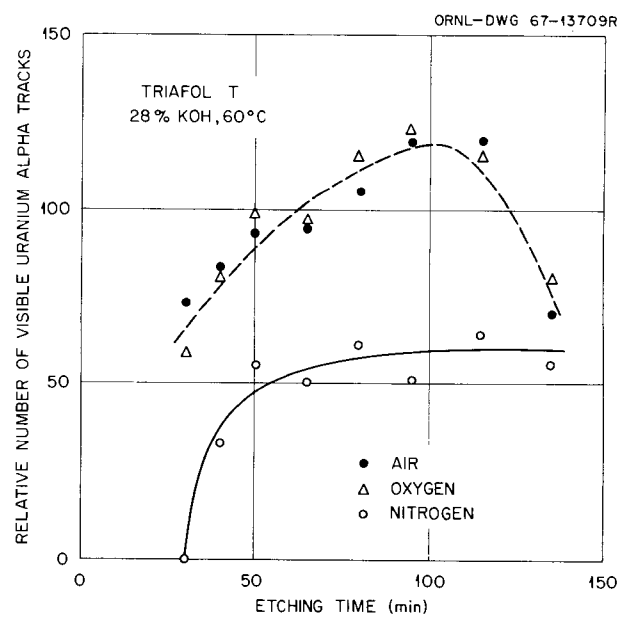

Fig. 22.25. Relative Number of Visible Alpha-Particle Tracks as a Function of Etching Time of Triafol T Kept for 20 hr Prior to Exposure and Exposed (*a*) in Dry Air, (*b*) in Dry Oxygen, and (*c*) in Dry Nitrogen.

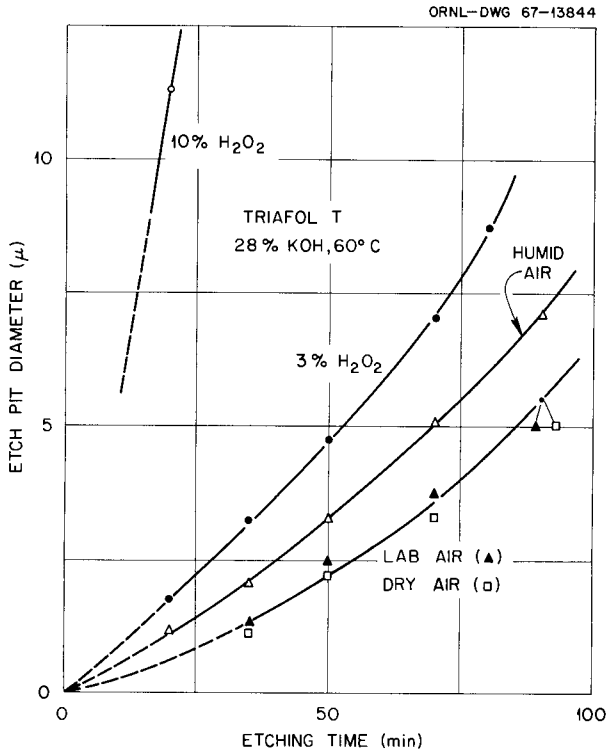

Fig. 22.26. Maximum Alpha-Particle Etch Pit Diameter as a Function of Etching Time in a Triafol T Foil Exposed to Uranium in Dry Air and Kept 20 hr in Laboratory Air, Dry Air, Air of 100% Relative Humidity, and in 3 and 10% H_2O_2 Solution Between Exposure and Etching.

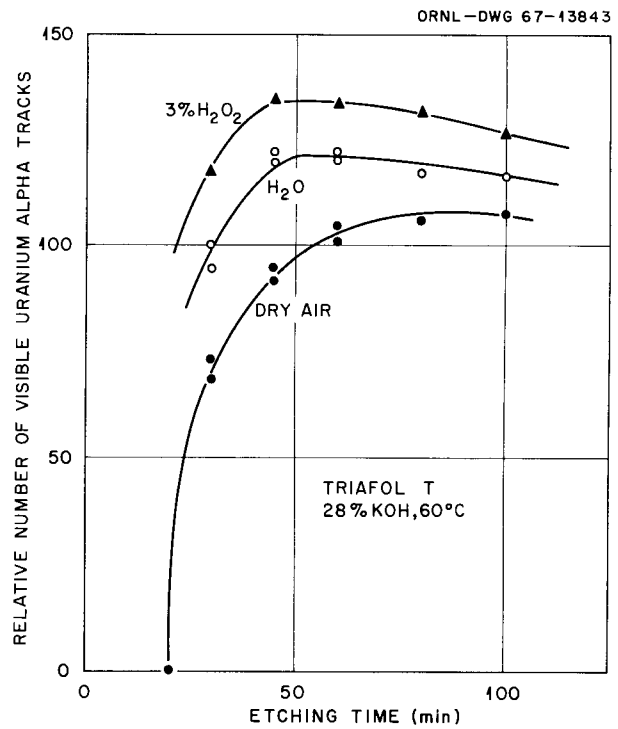

Fig. 22.27. Relative Number of Visible Alpho-Particle Tracks as a Function of Etching Time of Triafol T Kept for 20 hr Prior to Exposure (*a*) in Dry Air, (*b*) in H_2O, and (*c*) in 3% H_2O_2 Solution. Etching immediately after exposure.

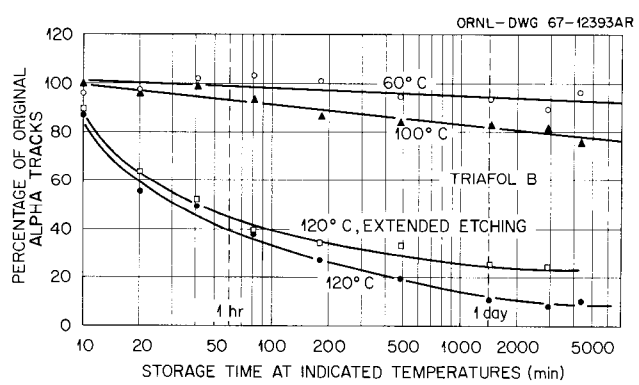

Fig. 22.28. Fading of "Latent" Alpha-Particle Tracks from a Uranium Foil as a Function of Storage Time at Different Temperatures in Triafol B.

Some disadvantages of fissionable materials (background increase because of spontaneous fission, possible alpha-radiation damage in the detector foil surface, safety problems, and costs) make it, however, desirable to avoid their use.

One possibility to do this is the visualization of recoil nuclei and alpha-particle tracks produced by the direct interaction of fast neutrons with the constituents of organic foils (Fig. 22.29). The number of visible tracks after optimized etching has been found to be usually higher than the fission fragments from a uranium foil. For example, at 14 Mev between 1.2 and 2.8 tracks/neutron $\times 10^{-5}$ can be found caused by direct interaction with different organic foils (cellulose nitrate, acetate, acetobutyrate, and polycarbonates) as compared with 1.2×10^{-5} fission-fragment tracks in a combination of a thick natural uranium foil and a fission-fragment detector.

Because of anisotropic scattering of the recoil nuclei, a directional dependence up to –30% of the frontal neutron incidence sensitivity has been ob-

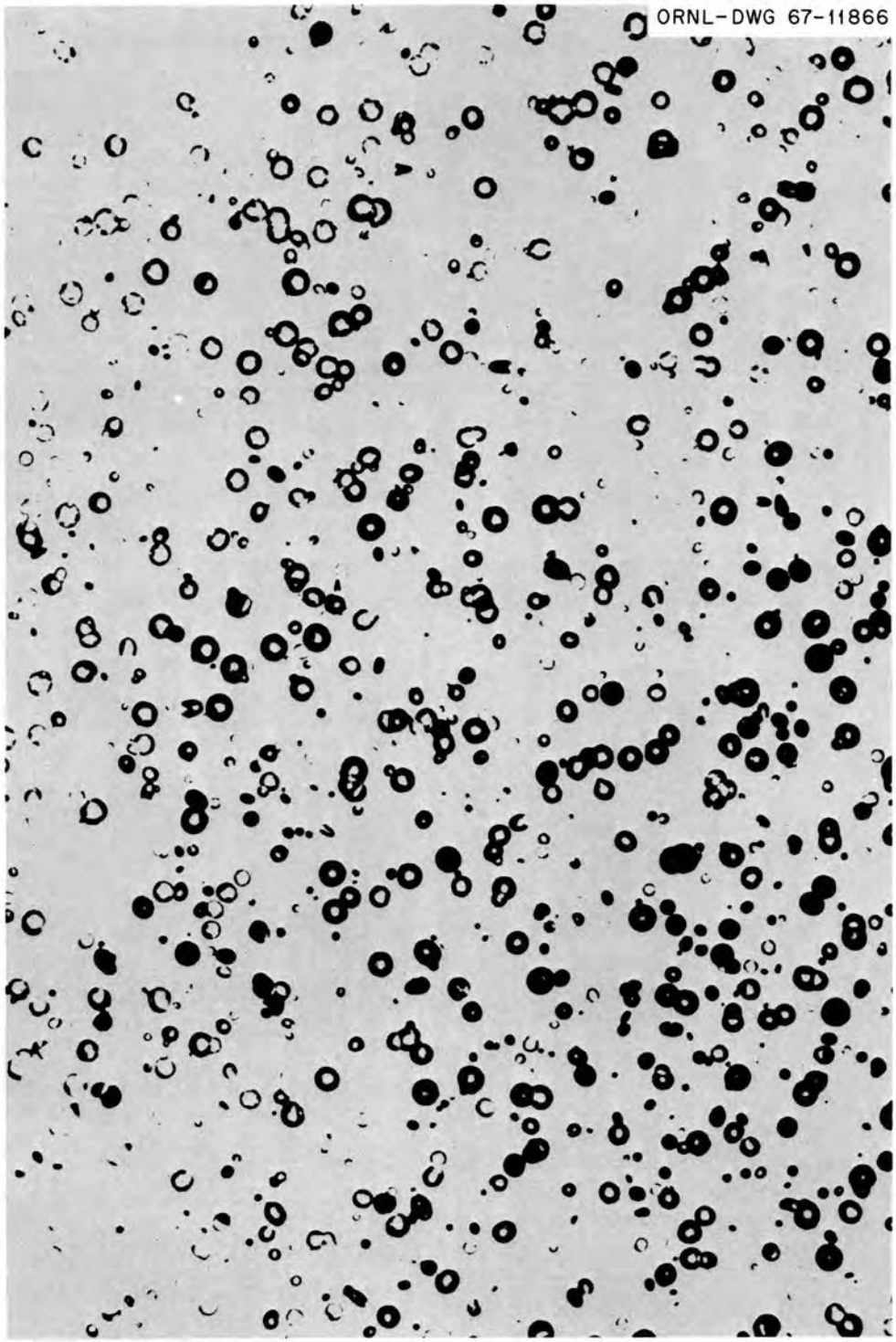

Fig. 22.29. Makrofol E Foil After Exposure to 14-Mev Neutrons Without Additional External Radiators. Etched 2 hr in 30% KOH at 60°C.

served for 14-Mev neutrons (Fig. 22.30). The stability of the latent recoil and alpha-particle tracks caused by fast neutrons is similar to that of alpha-particle tracks from external sources. No fading occurs at 60°C, but considerable fading occurs close to the softening point of the foils (Fig. 22.31).

The direct-interaction detection method has been used for some neutron depth-dose measurements in a polyethylene cylinder. Some preliminary results with 14 Mev and Am/Be neutrons are given in Fig. 22.32.

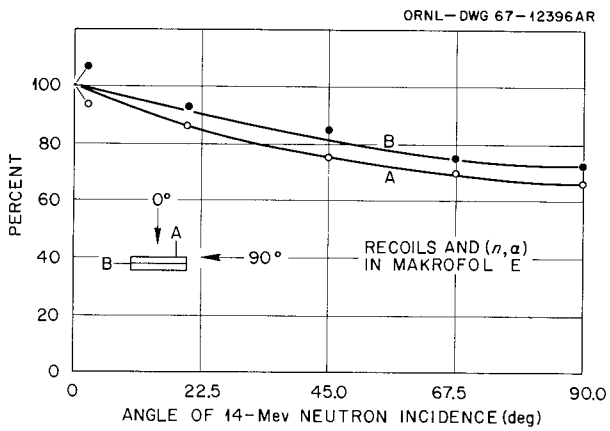

Fig. 22.30. Directional Dependence of Direct Neutron Effects on Makrofol E for 14-Mev Neutrons.

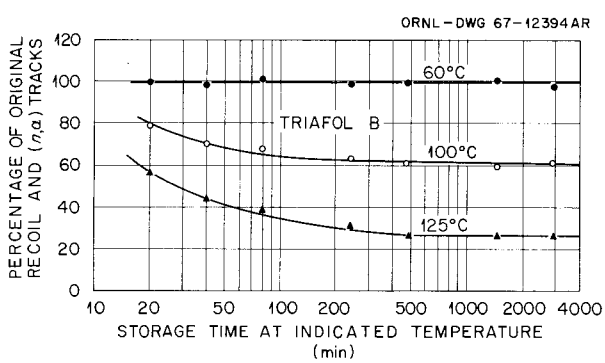

Fig. 22.31. Fading of Recoil Nuclei and Alpha-Particle Tracks from 14-Mev Neutron Interaction in Triafol B.

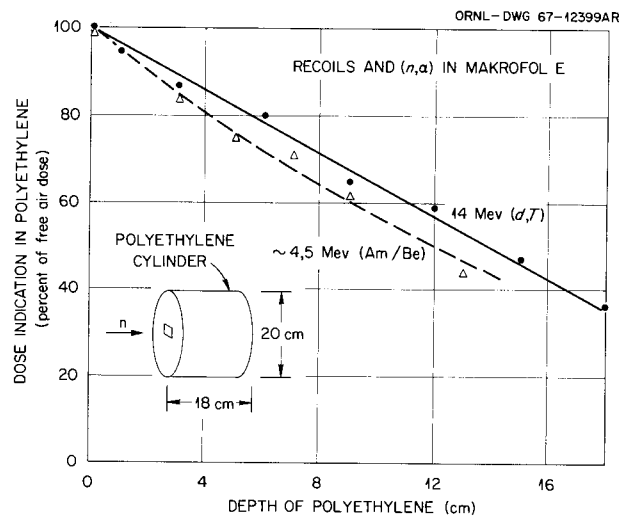

Fig. 22.32. Number of Visible Alpha- and Recoil-Particle Tracks in Makrofol E Foils Exposed to 14-Mev and Am/Be Neutrons in Different Depths of a Cylindrical Polyethylene Phantom. Relative to the track count in foils exposed at corresponding distances in air.

23. Spectrometry Development and Research

J. H. Thorngate

M. D. Brown[1] P. T. Perdue

T. Saigusa[2]

VAN DE GRAAFF OPERATIONS

During the period from July 1, 1967, to July 1, 1968, the ORNL Physics Division's 3-Mv Van de Graaff positive-ion accelerator was available to the Radiation Dosimetry Research Section for a total of four months. A wide variety of runs were made using the monoenergetic ion beams available from the machine. Monoenergetic neutrons from the $^{3}H(p,n)^{3}He$, $^{2}H(D,n)^{3}He$, $^{3}H(D,n)^{4}He$, and $^{51}V(p,n)^{51}Cr$ reactions were used to obtain response as a function of neutron energy for: (1) the HENRE neutron telescope,[3] (2) the HENRE ^{6}LiI scintillation neutron spectrometer,[4] (3) the proportional counter fast-neutron dosimeter system used at the DOSAR, and (4) new types of radiophotoluminescent glass gamma-ray dosimeters. Monoenergetic gamma rays from a variety of resonance (p,γ) reactions were used to determine the shape of the response of a pair spectrometer used to measure high-energy gamma rays during Operation HENRE. In addition, visitors from several installations, including one French laboratory, were accommodated during these periods and provided with known fluences of monoenergetic neutrons.

The Van de Graaff program has been an important addition to the work of this section and will continue with an increasingly heavy use of the available time forecast.

INVESTIGATION OF ORGANIC SCINTILLATORS

Organic scintillators have been the subject of research over the past several years at the DOSAR primarily due to the neutron response of these materials. *p*-Quaterphenyl, first mentioned by Sangster,[5] has been of particular interest because it has a light output as a function of particle energy that is similar to anthracene and pulse-shape qualities similar to *trans*-stilbene. Further, *p*-quaterphenyl has a melting point of 315°C and is quite stable.

Scintillation-grade *trans*-stilbene, anthracene, and *p*-quaterphenyl are synthetic materials and as organic chemicals are quite pure. However, the publication of research on the zone refining of anthracene[6–8] led to the investigation of zone-refining of *trans*-stilbene, anthracene, and *p*-quaterphenyl. Construction of an experimental zone refiner was completed, and zone refining of anthracene has begun using the method of Lacey and Lyons.[9]

---

[1]Part time.

[2]Alien guest.

[3]J. H. Thorngate, *Health Phys. Div. Ann. Progr. Rept. July 31, 1966*, ORNL-4007, p. 175.

[4]J. H. Thorngate, *Health Phys. Div. Ann. Progr. Rept. July 31, 1967*, ORNL-4168, p. 191.

[5]R. C. Sangster, *MIT Technical Report No. 55* (1952).

[6]B. S. Alehsandrov *et al.*, "Zone Purification of Materials to Use in Monocrystal Scintillators," pp. 239–42 in *Growth of Crystals*, vol. 3, 1962.

[7]M. J. Joncich and D. R. Bailey, *Anal. Chem.* 32(12), 1578–81.

[8]P. W. Alexander, A. R. Lacey, and L. E. Lyons, *J. Chem. Phys.* 34, 2200–2201 (1961).

[9]A. R. Lacey and L. E. Lyons, *Rev. Sci. Instr.* 34(3), 309–10 (1963).

Studies of the zone-refined scintillators using an ultraviolet light have been encouraging, and a detailed investigation is under way to determine light output as a function of purification for gamma rays and neutrons. An evaluation of the pulse-shape discrimination qualities will also be made using the method of Peele and Love.[10]

CALCULATION OF SPECTRA OF RECOIL HEAVY PARTICLES

Experimentally determined energy spectra of recoil particles produced in tissue-equivalent material by 3- and 15-Mev neutrons were reported last year.[11] A Monte Carlo calculation has been completed for 15.09-Mev neutrons for similar conditions. For the calculations, 1.5-mm silicon-cube detectors were placed at 12 points within the phantom (Fig. 23.1). It was assumed that the direction and energy of a neutron after scattering are determined only from the scattering collision with an element of tissue: H, C, N, or O.

A larger detector model was used to improve economy of calculation. In the calculation, if the flight path of a neutron ends in this quasi-detector, the probabilities that the neutron interacts with tissue-equivalent material and silicon detector, respectively, are calculated. Recoil energies are further calculated for proton and alpha particles in tissue and for various kinds of recoil particles in silicon. The position where the reaction occurs in the volume around the real detector is randomly chosen according to a uniform distribution over the volume, the thickness of which is assumed to be the maximum range of a 15.09-Mev proton, 2.51 mm, and defined by the distance x centimeters from the surface of the real detector. The energy of the recoil particle to be observed is determined by the range-energy relation from the residual range $(R - x)$, where R (cm) is the initial range of the recoil particle. The detection efficiency ϵ with which the recoil particle is observed is defined by the expression

$$\epsilon = \frac{1}{2}\left(1 - \frac{x}{d}\right),$$

where d (cm) is the maximum distance which the recoil particle can travel to the detector and be registered in the same energy group. The particle can be assigned to other energy groups if it can travel farther than this distance d. Detection efficiencies for such cases are also given by similar expressions. The above calculation of detection efficiency is restricted to the detector with infinite half surface. Since a side of a real detector is 1.5 mm in length and just equal to the range in silicon of a 15.09-Mev proton, a portion of energy from some energetic protons is not deposited in the detector, and such particles must be assigned to the groups of lower energies. The magnitude of this effect for protons is evaluated by dividing the solid angle subtended at the surface of the detector into several smaller angles and taking account of the range in silicon of the particles. The conversion factor by which the quasi-detector is converted to the real volume of the detector or that of tissue-equivalent material around it is given by the ratio of their volumes.

The calculation was done for 42 energy groups ranging from 1 kev to 15.09 Mev for a total of 50,000 neutrons. Contributions to the energy spectra are obtained from the detector and the tissue-equivalent material around it and recorded as (1) energy spectra contribution from the silicon detector, (2) energy spectra contribution from the tissue-equivalent material around the detector, and (3) the sum of contributions 1 and 2.

The calculated energy spectrum (3) of recoil particles assigned to detector No. 1 is shown in Fig. 23.2. The ordinate is the number of recoil particles per 64-kev energy interval per neutron incident upon the phantom. Some deviations from the experimental data are found in the region of energy less than 8 Mev; the calculated values are within factors of 2 to 3 for the most part, but range up to 8 for two groups of energy of the measured values. Standard deviations of the numbers of recoil particles are about 10% or less, except 20% at the highest energy group. This large deviation results from the small number of the highest-energy protons.

---

[10] R. W. Peele and T. A. Love, National Research Council Publication 1184, *Nucl. Sci. Series Report No. 40*, 1964.

[11] G. F. Stone and J. H. Thorngate, ORNL-TM-1927 (1967).

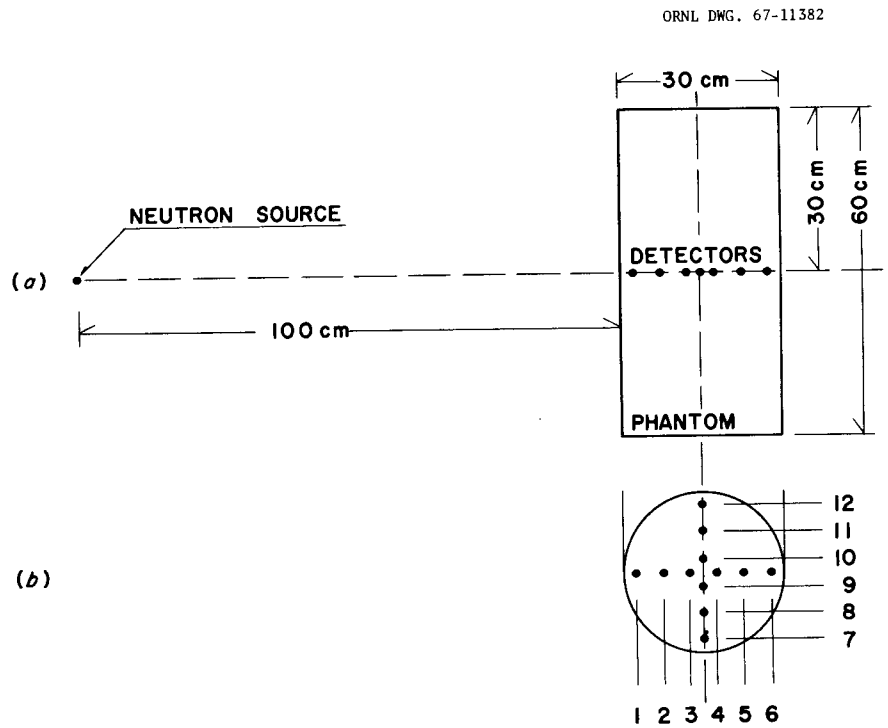

Fig. 23.1. Geometrical Arrangement on Which Calculations of Energy Spectra Were Based. (a) Source, phantom, and detectors; (b) plane view of arrangement of detectors.

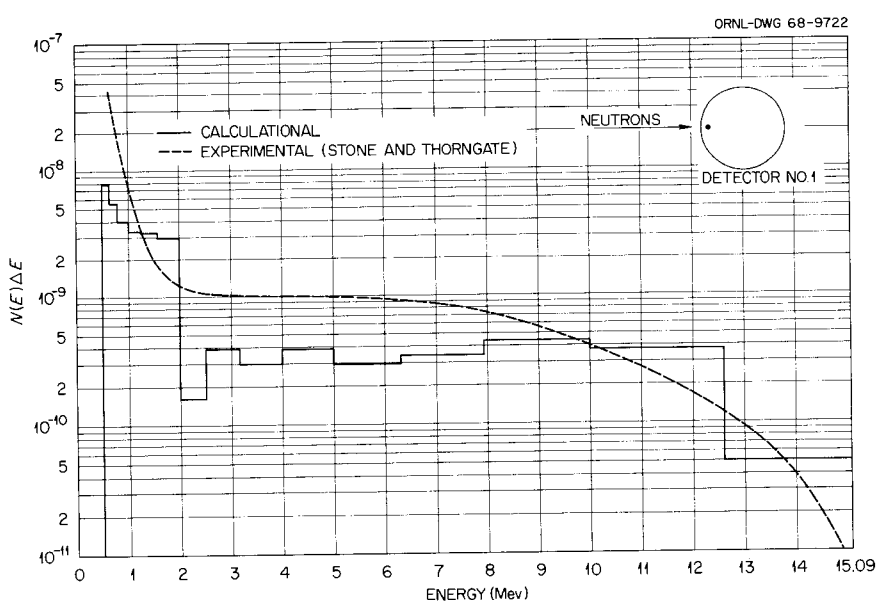

Fig. 23.2. Energy Spectrum of Charged Particles Recoiling in Detector No. 1 and the Tissue Around It.

24. HPRR and DLEA Operations

D. R. Ward[1]

F. F. Haywood
R. L. Francis[2]
L. W. Gilley[1]
J. W. Poston[3]

HEALTH PHYSICS RESEARCH REACTOR

During this report period, there was a significant decrease in large animal exposures. However, there was a large number of operations for experiments involving irradiation of seed, plants, small animals, and dosimetry systems. In addition, the fourth and fifth intercomparisons of nuclear accident dosimetry systems were conducted in December 1967 and July 1968. A large number of operations was done in support of dosimetry development, in particular, to development as relates to track registration in insulating solids.

The Health Physics Research Reactor (HPRR) was used on two occasions by Oak Ridge Associated Universities for criticality monitoring exercises. This was in conjunction with two ten-week special training courses in Health Physics.

Servo control during extended runs is made possible through the use of the original regulating rod, whose reactivity worth is 83 cents. During long runs at low to intermediate power, this rod overcompensated when reactivity insert and withdrawal commands were given by the servo amplifier. In order to have more flexibility during operations, a new regulating rod was fabricated. The outer part was made of aluminum and is the same physical size as the original rod; however, a $\frac{1}{4}$-in.-diam hole through the center allows the insertion of a fuel (U-Mo) bolt insert. The aluminum rod and insert have a reactivity worth of 34 cents. Critical experiments indicate the aluminum rod alone is worth 18 cents. At the present time, the aluminum rod is used for servo control of the reactor and has provided a more stable power level during extended power runs.

There were several notable modifications in reactor-related instrumentation. Flux mapping experiments near the core indicated that the ionization chambers which are used for power level determination were positioned in such a way as to cause a slight depression of the neutron level in the experimental area. These chambers were raised several inches, hence removing this shadow. New transistorized scalers were installed for readout of the two fission chamber startup channels (for monitoring small changes in neutron multiplication). These replaced the original tube-type scalers, thereby removing a heat source which sometimes influenced the gain of the amplifiers used with these channels. In addition, a transistorized master timer was installed to operate these scalers automatically, so that precisely timed counts were available for reactor period measurements preceding bursts. Another timer was installed. This was connected to the reactor scram circuit for automatic shutdown at a predetermined time; it is started at $1/e$ of power level as the reactor approaches the desired power level.

A significant amount of effort has been put into the following items; however, at this writing work is not complete. A new electronic criticality monitoring system has been designed and is being installed in the reactor building. The system is composed of three detectors placed in the experimental area. A two-out-of-three coincidence

[1]On loan from Neutron Physics Division.

[2]On loan from Instrumentation and Controls Division.

[3]On leave of absence.

is required for alarm, which may be due to either a preset level alarm or to a rapidly increasing pulse, as in the case of a criticality. The main purpose of this instrument is to provide neutron monitoring during periods that the reactor is not operating (i.e., maintenance, experimental setup, core changes, etc.).

In the six years of operation of HPRR, there has not been an instance in which facility personnel were unaccountable at startup of the reactor. This achievement is very gratifying, but in order for the present muster system to function properly, another person must be on duty at the personnel checking station to issue and pick up muster badges and to read off, to the operator, numbers of all badges issued when this information is required. A new badge rollcall system has been studied, and a working model has been fabricated. The muster badges of this new system would contain a tiny key to be inserted into a slot in one of several conveniently located control centers when a roll call was requested. Neon lamps would be used to indicate the status of each person in the facility.

At the present time, the reactor can be operated about 8.5 min at 10 kw; this limitation is due to temperature rise. There are more and more instances where operations at this power level are required but for longer periods. Therefore, arrangements have been made to evaluate methods of drawing large quantities of air across the core. It is expected that the operating time at 10 kw will be increased between 30 and 75%. Air used to cool the core would be drawn over the outer surface and over the inner annulus surface and surface of the safety block. The air would then be exhausted through a set of absolute filters.

An exhaustive study is currently under way to evaluate all factors which influence the neutron yield during bursts. This includes careful measurements of reactivity changes with corresponding changes in rod settings, ambient temperature, and with various misplacements of the safety block relative to the burst rod. It is felt that there may as yet be some bursts which are preignited because the neutron source is not farther away from the core. A new shield and source drive have been designed so that the source would be placed several feet from the core and its shield would have thicker walls. This action should produce longer wait times between insertion of burst rod and burst, hence elimination of preinitiated bursts.

DOSAR LOW-ENERGY ACCELERATOR ANALYZING MAGNET

In fiscal year 1967, a surplus magnet was acquired from the Electronuclear Division. During this report period, a power supply for this magnet was fabricated, and the units (see Fig. 24.1) were used as an analyzing magnet for the DOSAR Low-Energy Accelerator (DLEA). The power supply will provide a current to 480 amp with adequate regulation for the operation of the analyzing magnet. A vacuum chamber was constructed to fit around the pole pieces of this magnet. The completed assembly has been installed, providing a uniform magnetic field of 130 to 13,000 gauss. A proton beam has been accelerated through the vacuum chamber, and work is in progress on adjusting the strong focus and beam tubes.

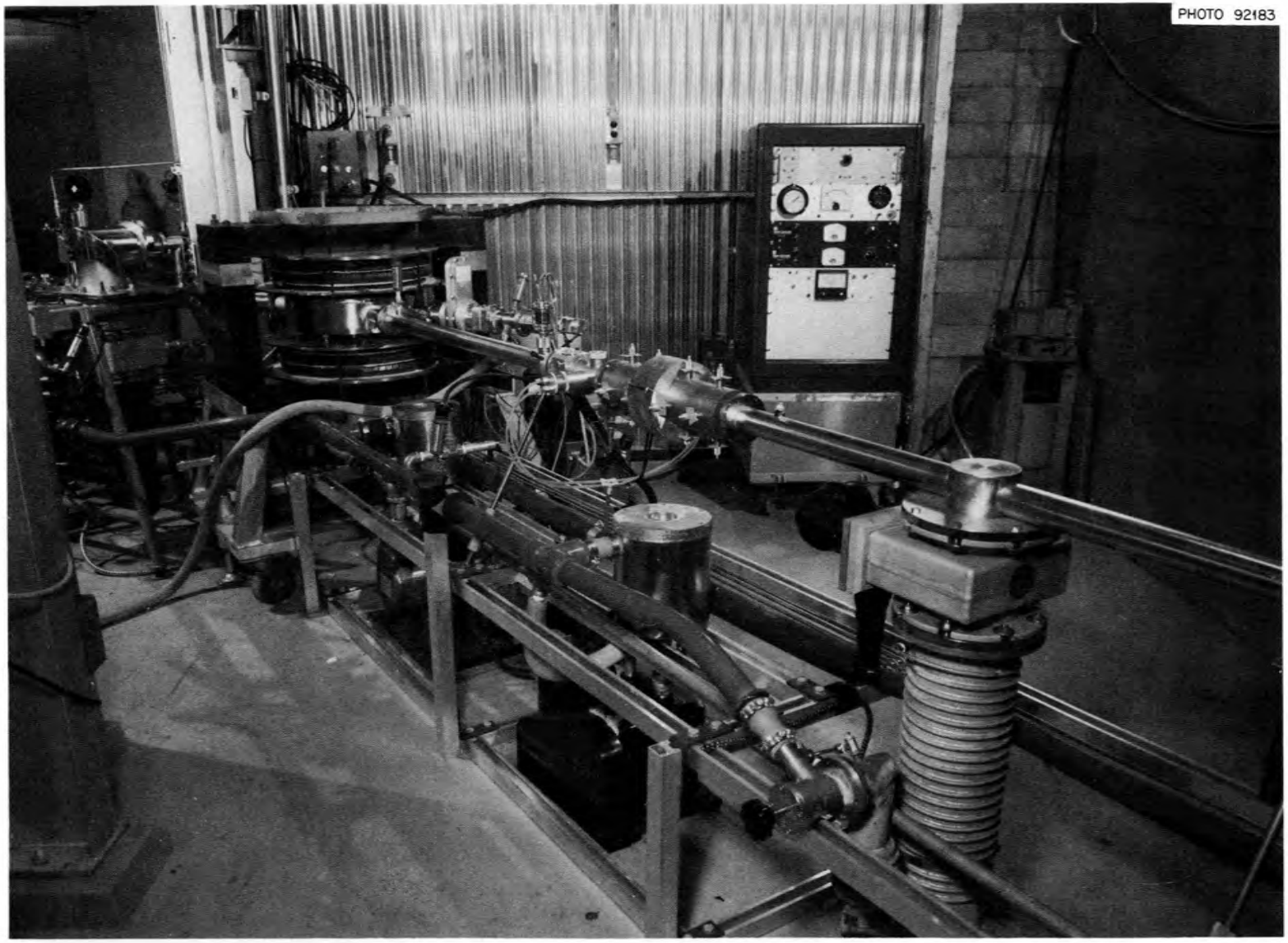

Fig. 24.1. Modified DLEA Drift Tube Assembly with Analyzing Magnet and Power Supply in Background.

Part V. Internal Dosimetry

W. S. Snyder

25. Internal Dose Estimation

W. S. Snyder
S. R. Bernard
T. G. Clark
Mary Jane Cook
B. R. Fish
Mary R. Ford
J. P. Hickey
C. F. Holoway
K. Z. Morgan
Isabel H. Tipton[1]
J. L. Thompson

AN ESTIMATE OF THE SYSTEMIC BODY BURDEN OF ^{239}Pu RESULTING FROM A CONTAMINATED WOUND

W. S. Snyder Mary R. Ford
G. G. Warner[2]

Knowledge of the retention and toxicology of plutonium in the human body is very limited, and techniques of total-body counting are not available for detecting a permissible body burden. Thus when exposure from an internal source of plutonium occurs at levels near or below the limiting organ burdens, it must be evaluated on the basis of an interpretation of excretion data. Excretion data, however, from intakes of known amounts of plutonium on which such an interpretation can be based are scarce and, in fact, are confined almost exclusively to data reported by Langham[3] on hospital patients who received intravenous injections of plutonium citrate. A method of analysis based on these data is used here to evaluate the body burden for a case of contamination via a wound.

The excretion data of the subject as made available for this study are shown in Fig. 25.1. The data are incomplete in that no fecal data are available, the exact time and amount of the first urinary sample are not known, and the urinary data extend only to 150 days after the injury. Also the interpretation is complicated by the use of DTPA (diethylenetriaminepentaacetic acid) treatment, for which neither the times nor amounts of the DTPA administered are known precisely.

A computer code reported in ref. 4 is used to estimate intake to blood. It is based on a power function model of excretion fitted to the urinary excretion data of the hospital patient.[3] The effect of

[1]Physics Department, University of Tennessee.

[2]Mathematics Division.

[3]W. H. Langham *et al.*, *Distribution and Excretion of Plutonium Administered Intravenously to Man*, LA-1151 (1950).

[4]W. S. Snyder, M. R. Ford, and G. Warner, "A Study of Individual Variation of Excretion of Plutonium by Man and Its Significance in Estimating the Systemic Burden," Proceedings of Thirteenth Annual Bioassay and Analytical Chemistry Meeting, Oct. 12–13, 1967, Berkeley, Calif. (in press).

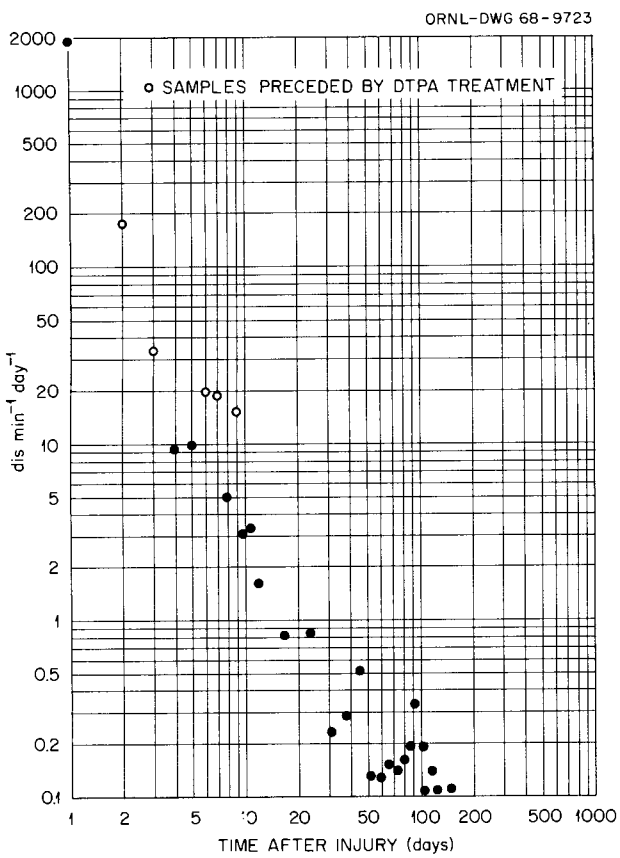

Fig. 25.1. Urinary Excretion Data of Subject.

DTPA treatment on rate of excretion is not allowed for in the computer program. There are conflicting accounts of the enhancement to be expected from treatment with DTPA, practically no enhancement[5] to enhancement by a large factor, perhaps 100-fold.[6] In the absence of information on the level of treatment, it does not seem possible to posit any quantitative correction for the effect of treatment in this case. Consequently, judgment concerning the effect of treatment has been based on the internal evidence of the data on this case.

The trend of the subject data is different in the early period, say days 1 to 10, than at later times, say days 20 to 150. This difference is confirmed by fitting power functions to the two portions separately by two methods (see Table 25.1): (1) the Point Fit method, minimizing the sum of absolute deviations, and (2) the Area Fit method, also minimizing the sum of absolute deviations, but which considers excretion as a continuous process. The curves fitted to the excretion data beginning at day 1 or day 17 produce steeper slopes and larger coefficients than do those fitted at later times. It is of some interest to establish the cause of steeper slope, for example, whether it indicates leaching of plutonium from the wound site or changing enhancement of the excretion due to the treatment. Leaching of plutonium from the wound site would be expected to increase the excretion rate, but it does not seem likely that this could account for a steeper slope of the excretion curve. If the power function correctly indicates the slope of the excretion curve of a single intake, this would plot as a straight line on log-log paper. No superposition of such lines at different times can produce a steeper slope for the curve which represents the sum of the

[5] J. R. Mann and R. A. Kirchner, *Health Phys.* 13(8), 877–82 (1967).

[6] C. R. Lagerquist, I. B. Allen, and K. L. Holman, *Health Phys.* 13(1), 1–4 (1967).

Table 25.1. Power Functions $at^{-\alpha}$ Fitted to Excretion Data of the Subject over Certain Periods of Time

Days post Exposure Included	By Point Fit—Least Deviations		By Area Fit—Least Deviations	
	Coefficient a (dis min^{-1} day^{-1})	Exponent α	Coefficient a (dis min^{-1} day^{-1})	Exponent α
1–10	1909	3.47	95.5	0.95
17–150	16.7	1.06	15.8	1.05
24–150	5.32	0.80	5.08	0.79
38–150	5.32	0.80	5.08	0.79
45–150	0.707	0.37	1.12	0.37

intakes. Thus, we ascribe the increased slope as an effect of treatment. There is no significant change detected whether one begins the fitting at day 24 or day 38, and the value of 0.8 obtained here for the exponent is well within the range of values reported for the hospital patients and is quite close to the value of 0.77 obtained by Langham.[3] The much lower exponent and coefficient when the fitting begins at day 45 is attributable to the fact that most of the measured values are close to the limit of detection. As the excretion levels approach background values, that is, the levels found to occur in "blanks" from "unexposed" individuals, the curve would be expected to become flatter. It seems reasonable that a value of about 0.1 dis min^{-1} day^{-1} (which is about the amount excreted per day by the subject after day 45) be taken as this level, the counting statistics as well as reported levels in "blanks" both making this plausible.

Analysis by methods described in ref. 4 of the day-to-day fluctuations of the excretion data provides another indication that leaching from the wound site during the period from 17 to 150 days is not sufficient to alter the excretion pattern significantly and probably is small compared with the amount entering blood in the early period. The distribution of "high" daily urine outputs is not in excess of that predicted by the methods of ref. 4, as is indicated by the data in Table 25.2. While the procedure used here does not constitute a "proof" that no additional intake occurs after the

Table 25.2. Number of Intakes and Total Intake Estimated by Various Power Function Formulas

Model	Sample Days Used	k, Number of Samples	Fluctuation Allowance (%)	N^a	n^b	Total Intake (μc)
Subject's own formula[c] =	24–150	16	0		12	6.8×10^{-4}
$2.3 \times 10^{-3} t^{-0.80}$,	38–150	14	0		10	6.6×10^{-4}
PF-ALD[d]	24–150	16	10	1.5	2	3.8×10^{-4}
	38–150	14	10	1.3	1	4.2×10^{-4}
	24–150	16	20	3.0	4	5.1×10^{-4}
	38–150	14	20	2.6	3	5.1×10^{-4}
"Typical" formula =	24–150	16	0		13	7.7×10^{-4}
$3.2 \times 10^{-3} t^{-0.93}$,	38–150	14	0		11	7.6×10^{-4}
PF-ALD[d]	24–150	16	10	1.5	3	4.7×10^{-4}
	38–150	14	10	1.3	1	4.6×10^{-4}
	24–150	16	20	3.0	4	5.5×10^{-4}
	38–150	14	20	2.6	3	5.3×10^{-4}
Subject's own formula[c] =	24–150	16	0		13	3.0×10^{-3}
$4.8 \times 10^{-4} t^{0.79}$,	38–150	14	0		11	2.9×10^{-3}
AF-ALD[e]	24–150	16	10	1.5	3	1.9×10^{-3}
	38–150	14	10	1.3	2	1.9×10^{-3}
	24–150	16	20	3.0	5	2.0×10^{-3}
	38–150	14	20	2.6	3	2.1×10^{-3}
"Typical" formula =	24–150	16	0		13	5.8×10^{-4}
$1.5 \times 10^{-3} t^{-0.65}$,	38–150	14	0		11	5.5×10^{-4}
AF-ALD[e]	24–150	16	10	1.5	3	4.1×10^{-4}
	38–150	14	10	1.3	2	3.3×10^{-4}
	24–150	16	20	3.0	4	4.0×10^{-4}
	38–150	14	20	2.6	3	4.4×10^{-4}

[a]Expected number of intakes due to fluctuations = $(k - 1)$ times fluctuation allowance.

[b]Number of intakes found after first intake.

[c]The constant is normalized to Langham's power function fit to the data of the hospital patients.

[d]Point fit—absolute least deviations.

[e]Area fit—absolute least deviations.

first week or two, it does indicate that the excretion data are distributed in value as one might expect following a single or short-term intake to blood. Thus, we consider that the high values of the exponent seen when the early portion of the data is used for fitting are due to treatment, and the lowest values seen when only the late portion of the data is analyzed are due to an approach to background. We consider the value of 0.8 for the exponent as being the best estimate of the slope of the excretion curve for this individual.

The urinary excretion curves fitted to the data of all the hospital patients by the above methods, as reported in ref. 4, are $3.2 \times 10^{-3} t^{-0.93}$ and $1.5 \times 10^{-3} t^{-0.65}$ respectively. These formulas represent a fraction of the injected dose excreted per day. These formulas can be used, therefore, to make a first estimate of the intake of the subject under study. The excretion data of the subject are in units of disintegrations per minute per 24-hr sample. By comparing the formulas of the hospital patients mentioned above and those of the subject, one estimates the subject's intake to be $5.32/3.2 \times 10^{-3}$ dis/min $= 7.6 \times 10^{-4}$ μc using the "point fit" formulas and $5.08/1.5 \times 10^{-3} = 1.5 \times 10^{-3}$ μc if the "area fit" formulas are compared. Since elimination of a systemic body burden is negligibly small when uninfluenced by treatment, the total intake to blood may be taken as the estimate of the systemic burden on day 160 exclusive of any insoluble material which may remain at the wound site or which may be present in the lungs.

EFFECT OF SIZE, SHAPE, COMPOSITION, AND DENSITY OF BODY ORGANS ON THE ABSORPTION OF GAMMA RAYS FROM A UNIFORM SOURCE IN AN ORGAN

W. S. Snyder Mary R. Ford
G. G. Warner[7]

A code has been reported previously by Fisher and Snyder[8] for estimation of dose due to a source of photons within the human body. The phantom used in this code has approximately the form of the human body with a head and a leg region, and a trunk which is an elliptical cylinder. Twenty-two internal organs are mathematically defined as regions within the phantom, and they have approximately the right shape and size. In previous results reported from the use of this phantom, the phantom was taken as homogeneous. The present paper reports results obtained by modifying the code and the phantom in such a way that differences in density and composition of human tissues can be taken into account. The skeletal region is taken with a density of 1.5 g/cm^3 and with approximately the following composition by weight: 40% O, 23% C, 10% Ca, 7% H, 7% P, and 4% N. The lung region is given a density of 0.3 g/cm^3, with a composition as follows: 76% O, 10% H, 10% C, and 3% N. The remaining portion of the phantom is given a density of near 1 g/cm^3 and a composition of 63% O, 23% C, 11% H, and 2% N.

The code uses a modified sampling technique which permits one to estimate the path of a photon originating at an arbitrary point in the phantom but without determining entrance and exit points from the various regions. This avoids time-consuming checks for crossing of boundaries and therefore permits one to use substantially the sample size available previously. Sources distributed uniformly in the skeletal region and in the lungs have been programmed for initial photon energies of 0.01, 0.015, 0.02, 0.03, 0.05, 0.1, 0.2, 0.5, 1, 1.5, 2, and 4 Mev, and a sample size of 30,000 photons was used in each case.

Results obtained with the modified code, that is, using the nonhomogeneous phantom, are compared in Figs. 25.2 and 25.3 with values reported by Fisher and Snyder[8] and with values obtained by the first-collision effective radius method of ICRP Publication 2.[9] It will be noted that the absorbed fractions estimated by the Monte Carlo codes are significantly lower than those obtained by the methods used by the ICRP except for the skeleton and at photon energies below 0.1 Mev, where the increased importance of the photoelectric effect for bone as opposed to soft tissue generally produces higher estimates in the present calculation.

Comparing the two Monte Carlo calculations: at energies above 0.2 Mev the absorbed fractions change approximately in proportion to mass, and

[7]Mathematics Division.

[8]H. L. Fisher, Jr., and W. S. Snyder, "Distribution of Dose in the Body from a Source of Gamma Rays Distributed Uniformly in an Organ," to be published in *Proceedings of International Congress on Radiation Protection, Rome, Italy, September 5–10, 1966.*

[9]*Recommendations of the International Commission on Radiological Protection*, ICRP Publication 2, Pergamon, 1959.

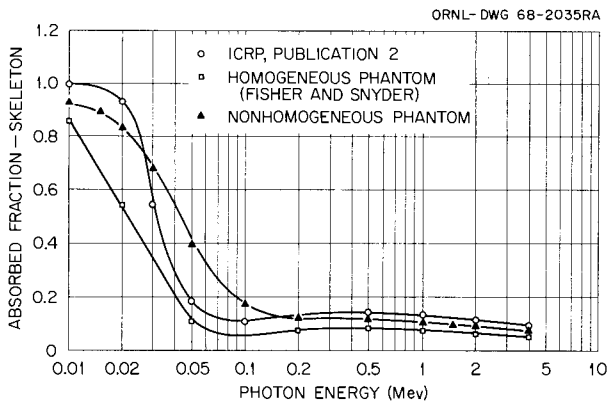

Fig. 25.2. Estimates by Various Methods of Absorbed Fractions of Photon Energy in the Skeleton. Source uniform in the skeleton.

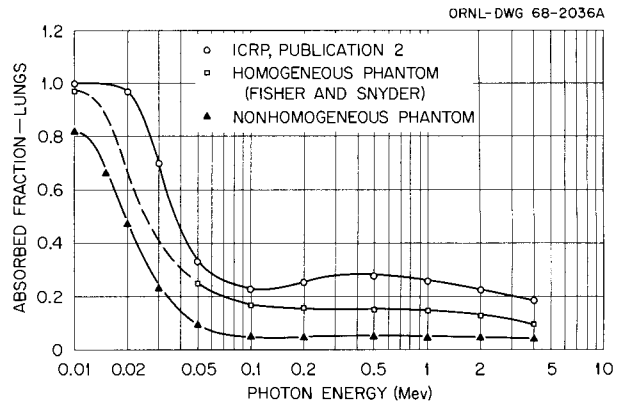

Fig. 25.3. Estimates by Various Methods of Absorbed Fractions of Photon Energy in the Lungs. Source uniform in the lungs.

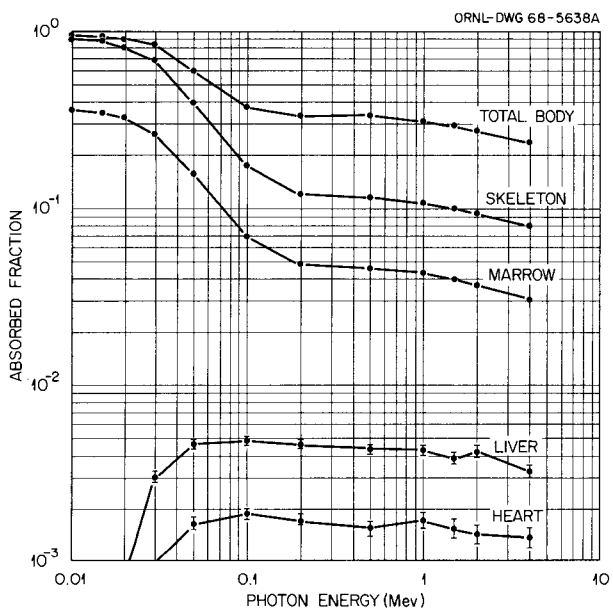

Fig. 25.4. Absorbed Fractions of Photon Energy in Various Organs. Source in the skeleton.

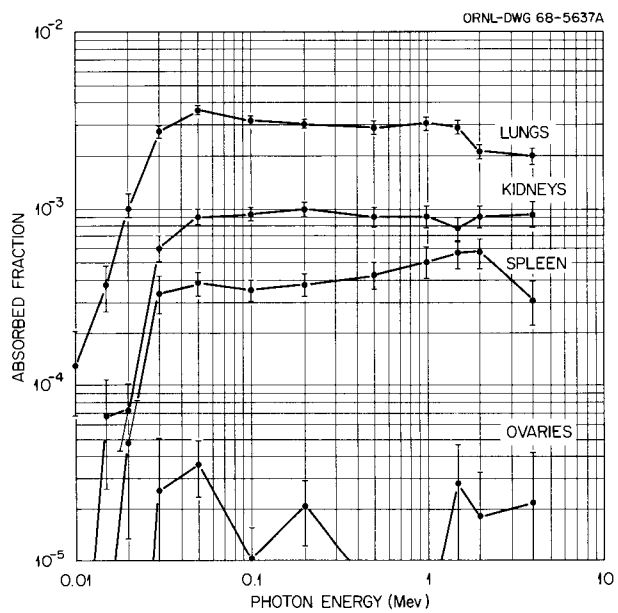

Fig. 25.5. Absorbed Fractions of Photon Energy in Various Organs. Source in the skeleton.

thus the doses are essentially the same; at photon energies below 0.2 Mev no detailed comparison with the earlier calculation for the source in the lungs is possible, because only a few cases were run with the homogeneous phantom. Results with the source in the skeleton are generally higher for the nonhomogeneous phantom than for the homogeneous. This is as would be expected, since not only is there greater mass in the nonhomogeneous case, but also the absorption coefficients are greater for bone than for tissue.

Figures 25.4 and 25.5 show the absorbed fraction in some organs other than those in which the source was located. The computed points have

been connected by straight lines, and the bars on the points represent one standard deviation on either side of the mean. Where no bars appear the deviations are less than 2% of the mean. These results illustrate what is, perhaps, the most novel feature of this code and mode of calculation in that it provides estimates of the absorbed fraction for all the 22 organ systems as well as for the whole body. Only the absorbed fractions considered to be statistically significant are shown in Fig. 25.4. In some cases, where the organ region is very small or located at a great distance from the source or both, the absorbed fraction is so small and the number of photon interactions occurring in the region is so small that the estimates are unreliable. Such a case is illustrated in Fig. 25.5, where for the absorbed fraction with the source located in the skeleton, one standard deviation is 30 to 95% of the mean. This could be remedied by running a larger sample of photons, but machine time becomes the limiting factor.

The estimates of absorbed fraction or, equivalently, of dose obtained by the method of this paper are sufficiently accurate to obtain the average dose in the organs represented here in all those cases where the statistics are sufficiently accurate, and we are trying, at present, various means of obtaining more reliable results for small organs located rather far from the source.

THE RELATIVE IMPORTANCE OF ^{137}Cs CONTAMINATION IN VARIOUS FOODSTUFFS IN TERMS OF TOTAL DOSE FOR VARIOUS AGE GROUPS OF A POPULATION

Mary Jane Cook W. S. Snyder

If a particular foodstuff, symbolized by the index i, is contaminated with ^{137}Cs, the total dose received by an organ of an individual consuming foodstuff i is the product of four factors – namely, $C_i \times I_i \times D \times T_b/0.693$, where C_i is the concentration of ^{137}Cs in the foodstuff, I_i is the daily intake of the foodstuff, T_b is the half-time for biological elimination from the body, and D is the dose rate to the organ in rems per day due to the presence of unit activity in the body. This is equivalent to assuming 100% absorption of ^{137}Cs into the blood and using a single-exponential model for elimination of ^{137}Cs from the body. Taking D as a constant amounts to assuming the distribution of ^{137}Cs in the body does not change much with time, and this seems to be the case for the forms of ^{137}Cs commonly encountered in the diet. Each of these four factors varies somewhat with age and other characteristics of the individual, and thus in determining the critical group of an exposed population, one must consider the variation of each factor. It is the product of the four factors which is proportional to the dose commitment per day of exposure and which will be indicative of the critical group so far as dose commitment is concerned. The variation of each of these factors with age will be discussed here briefly as an example of how this criterion can be applied in assessing the significance of exposure of a population to environmental ^{137}Cs.

The dose rate D due to unit activity in the body has been studied by Fisher and Snyder,[10] who give values of D appropriate for individuals of different sizes and for organs located at different positions in the body. A Monte-Carlo-type code was used to estimate the dose rate within the body due to a uniform distribution of ^{137}Cs within the body. Six phantoms corresponding to the newborn, to 1, 5, 10, and 15 year olds, and to an adult have been designed, and dose rate estimates are available for each of them. Fisher and Snyder assumed that 1 μc of ^{137}Cs was distributed uniformly within the phantom, and the absorbed fraction of energy for the whole body is presented in Fig. 25.6. A difference of about a factor of 2 is found in the fraction of energy absorbed when the same concentration of ^{137}Cs is present in the infant and in the adult. This applies only to the gamma dose rate, as the dose rate due to the beta radiation present does not vary significantly with body size if the concentration remains constant. It happens that the doses due to gammas and betas are approximately equal; so the total dose rate would only be about half as sensitive to changes in body size as is this gamma dose rate. The variation of the gamma dose rate within the phantom is shown in Fig. 25.7. There is approximately a difference of a factor of 2 in the gamma dose rate distribution as one proceeds from the central axis to the lateral surface of the phantom. The difference is more like a factor of 4 as one goes from the central axis to the head or feet.

We consider next the second factor, the biological turnover time, and its possible variation with age

[10] H. L. Fisher, Jr., and W. S. Snyder, *Health Phys. Div. Ann. Progr. Rept. July 31, 1966*, ORNL-4007, p. 221.

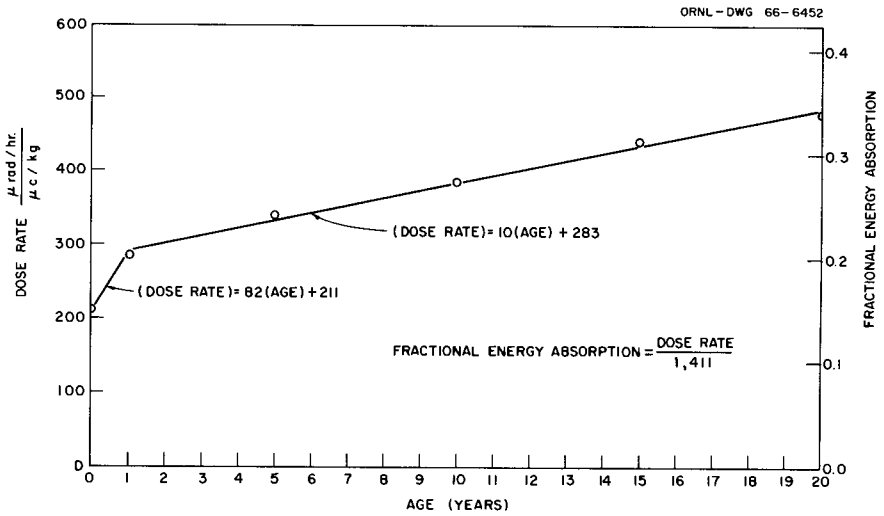

Fig. 25.6. Average Total-Body Gamma Dose Rate from a Uniformly Distributed ^{137}Cs Source.

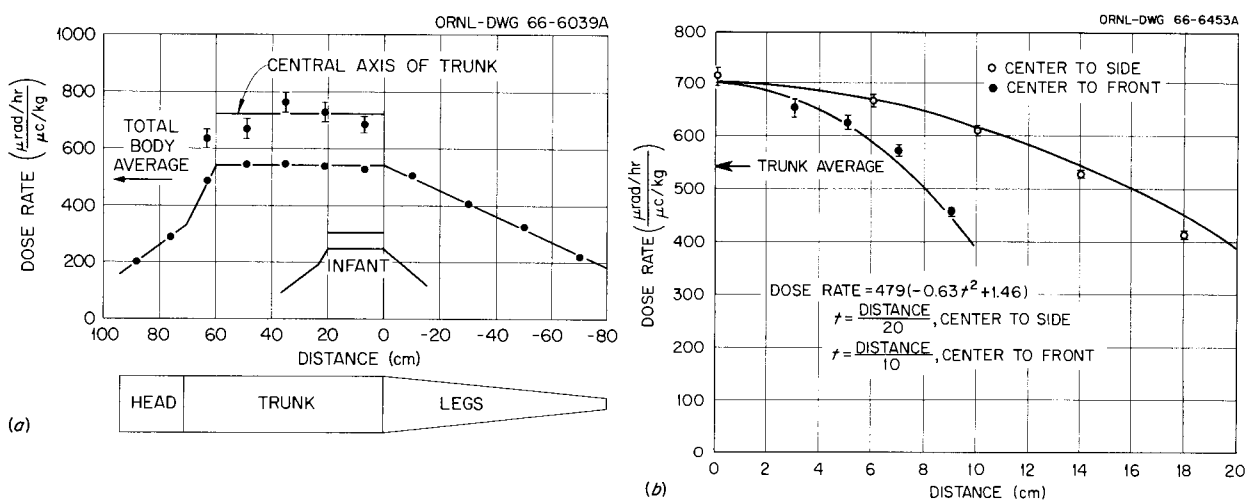

Fig. 25.7. Variation of Gamma Dose Rate in Phantom. (*a*) Average gamma dose rote in horizontal layers in the adult phantom from uniformly distributed ^{137}Cs source; (*b*) gamma dose rate from center to surface of adult phantom from a uniform ^{137}Cs source.

which is shown in Fig. 25.8. Several investigators have discussed the biological half-life of ^{137}Cs for different age groups, and various models have been proposed. Snyder and Cook[11] have offered one model (the dashed curve) based on stable cesium in the diet and the human body; the solid curve is obtained by Fisher and Snyder,[12] who observed that the experimental values of T_b were roughly proportional to body mass and thus related to age. For illustrating the use of age-dependent

[11]M. J. Cook and W. S. Snyder, *Health Phys. Div. Ann. Progr. Rept. July 31, 1965*, ORNL-3849, p. 190.

[12]H. L. Fisher, Jr., and W. S. Snyder, *Health Phys. Div. Ann. Progr. Rept. July 31, 1967*, ORNL-4168, p. 261.

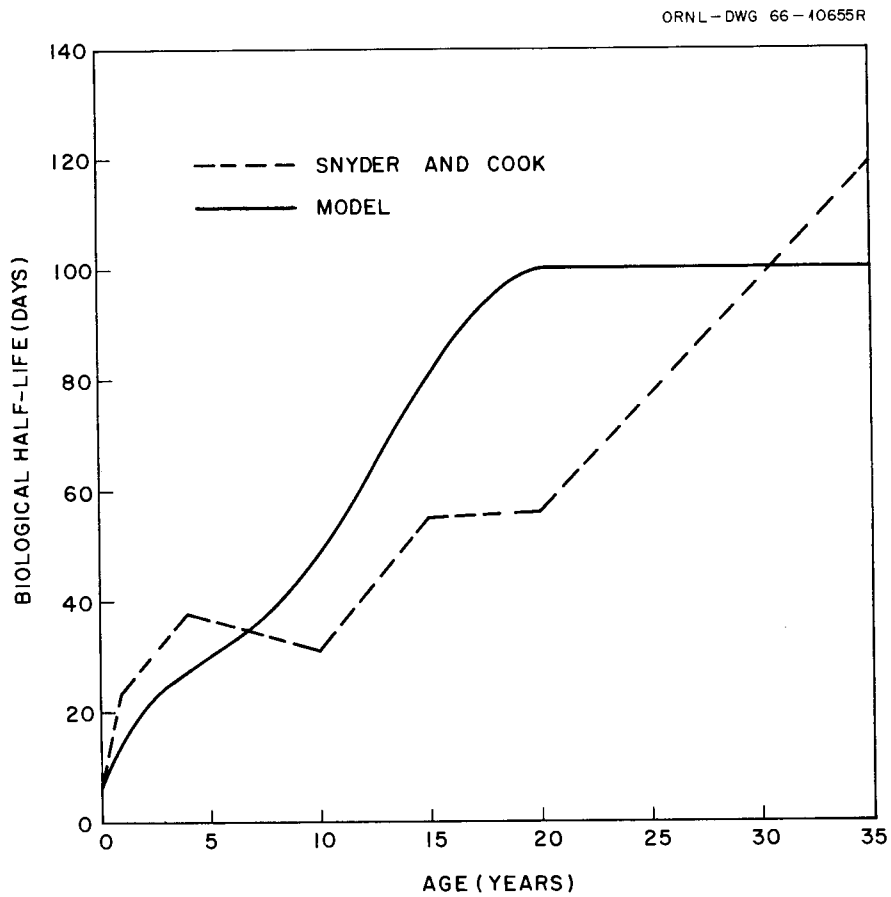

Fig. 25.8. Variation of the Biological Half-Life of Cesium with Age.

data, we have selected the model of Fisher and Snyder.

The third factor, I_i, of the original expression is the daily intake of foodstuff i, which is also a function of age. As an illustration, the intake of milk, meat, fresh vegetables, and fresh fruits has been considered. The data of Fig. 25.9 corresponding to diets consumed after the first year of life were obtained from ref. 13 and represent a moderate-cost family food plan of 1964. It will be noted that intake is significantly different for different ages as well as for males and females. The diet for the infant during the first year was taken from Klein.[14] The infant of one year or less presumably eats mainly cooked, strained, and canned meats, fruits, and vegetables. Because such an infant probably consumes quite small quantities of fresh fruits and vegetables, we have substituted intake of the cooked, strained, and canned fruits and vegetables for the fresh during the first year of life in calculating dose commitment for our illustrative cases. The estimated diets for the first year of life are from a different source than those for older individuals, and we have not attempted to reconcile the difference of the estimates at one year of age.

We have studied the product of these four factors – C_i, concentration of ^{137}Cs in the foodstuff; I_i, daily intake of foodstuff as a function of age; T_b, the biological half-life as a function of age; and D, the dose rate in rems per day due to the presence of unit activity in the body. In Fig. 25.10 we have

[13]Agricultural Research Service, *United States Department of Agriculture Family Economics Review*, Consumer and Food Economics Research Division, October 1964.

[14]S. Klein, *Health and Safety Laboratory Fallout Program Quart. Summary Rept. July 1, 1960*, HASL-88, p. 231.

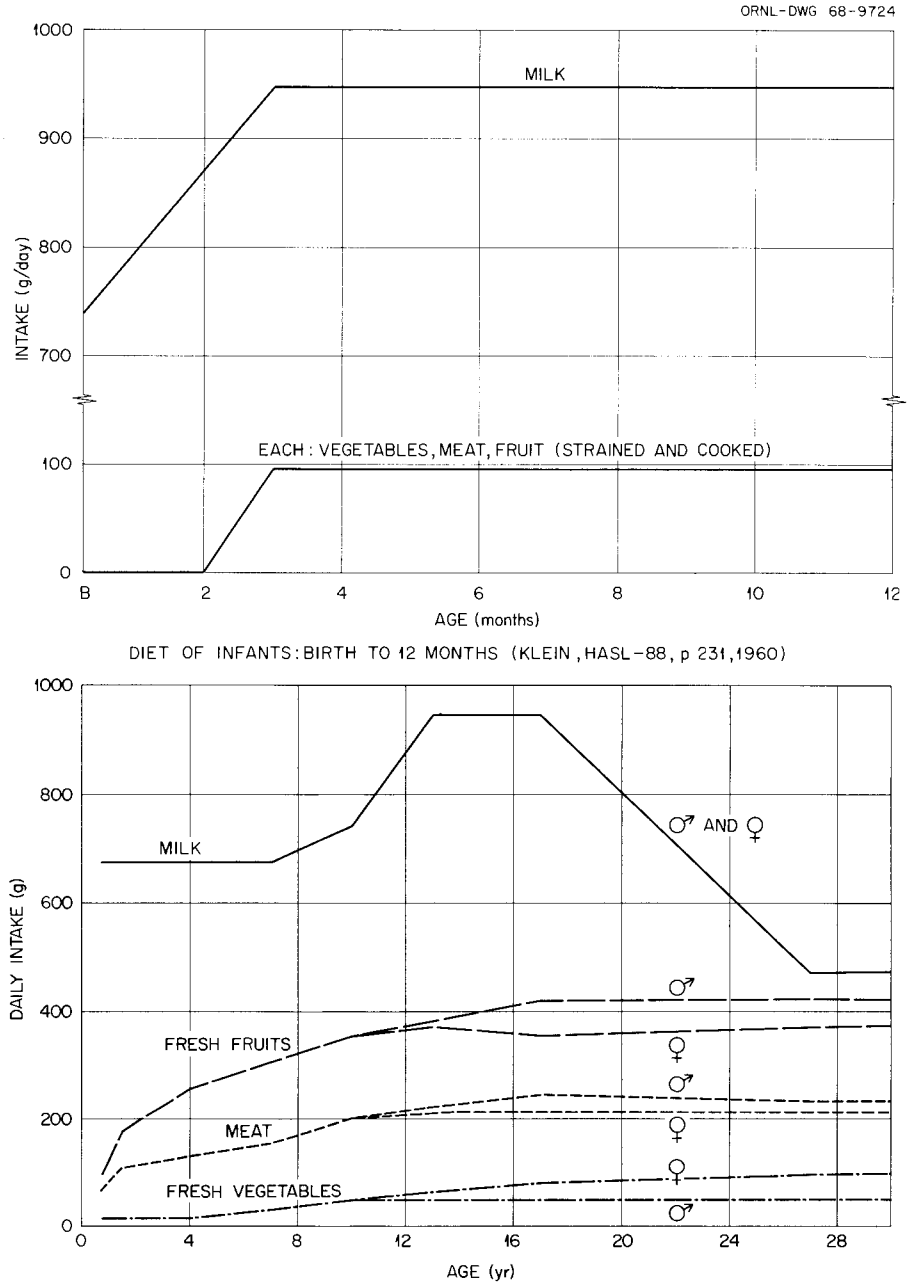

Typical Intake of Various Foods by Different Ages for a Moderate Cost Food Plan – U.S. Department of Agriculture, Revised 1964.

Fig. 25.9. Typical Intake of Various Foods by Different Ages (Newborn to 30 Years).

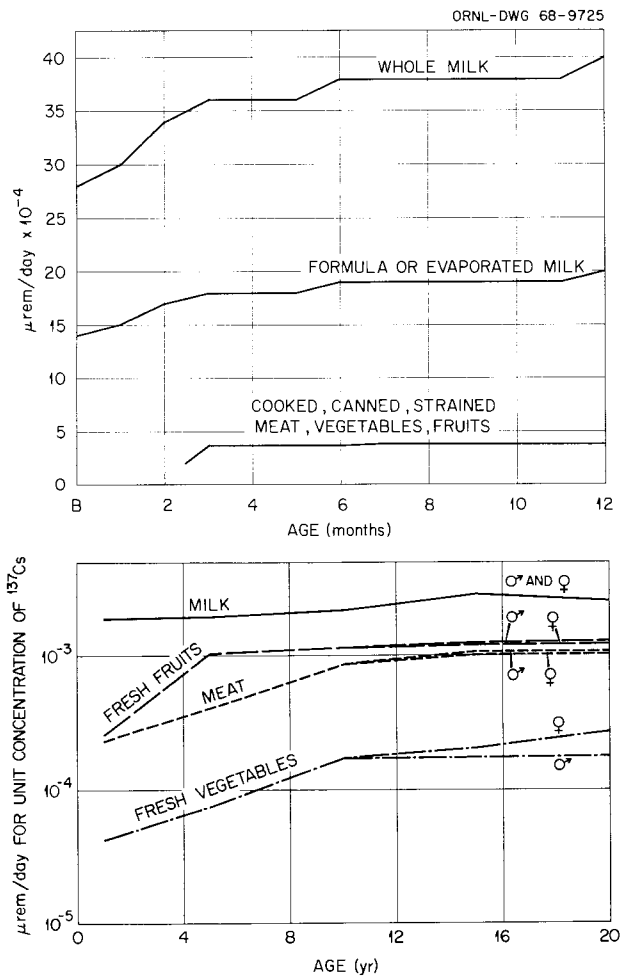

Fig. 25.10. Dose Commitment per Day of Exposure from Unit Concentration of ^{137}Cs in Various Foods (Newborn Through 20 Years).

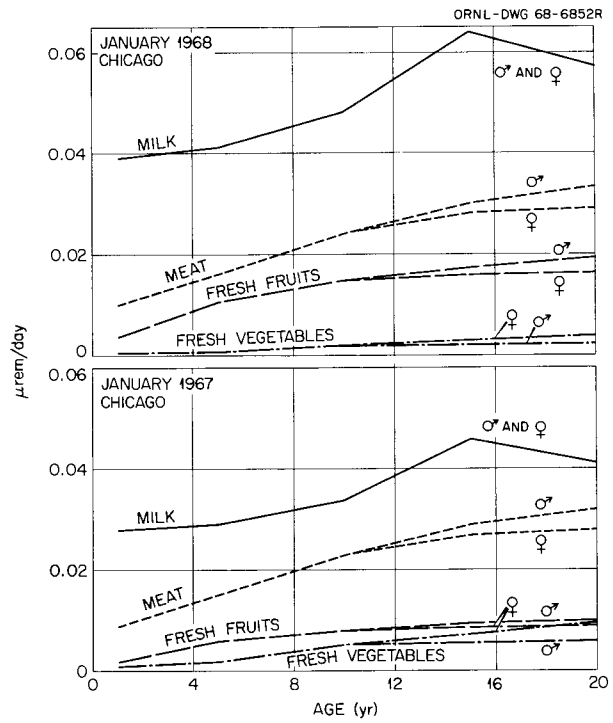

Fig. 25.11. Dose Commitment of Exposure from Fallout ^{137}Cs via Various Foods (1 Year Through 20 Years).

taken C_i as 1; that is, a unit concentration of ^{137}Cs is assumed in some one of the principal foodstuffs – milk, meat, fresh vegetables, and fresh fruits (canned vegetables and fruits during the first year of life) – which seem to be pathways for intake of ^{137}Cs. These basic data are applicable to any situation where data on concentrations of ^{137}Cs in the listed foods are available and for which the intakes are typical.

To illustrate its use for an actual situation and also to give a better idea of the relative importance of various foodstuffs in the case of contamination by fallout, values of C_i have been taken from the studies of Brar *et al.*[15,16] of Chicago foods in January 1967 and January 1968, and dose commitments per day of intake have been estimated for these levels of contamination in the four foods considered here. These estimates, plotted in Figs. 25.11 and 25.12, indicate that the relative importance of contamination in certain foods differs for different age groups, as might be expected. They also indicate how this variation may be taken into account in assessing the importance of such contamination in various foods and for the various segments of the population. For example, it appears that variation with age in the dose commitment per day of exposure due to a specified level of contamination of whole milk by ^{137}Cs varies by a factor of 2 or less if infants drank whole milk. If the infants consume formula milk or evaporated milk, which may be at quite a different level of ^{137}Cs concentration than whole milk, they may

[15] S. S. Brar *et al.*, *Health and Safety Laboratory Fallout Program Quart. Summary Rept. April 1, 1967*, HASL-181, p. III-134.

[16] S. S. Brar and D. M. Nelson, *Health and Safety Laboratory Fallout Program Quart. Summary Rept. April 1, 1968*, HASL-193, p. III-29.

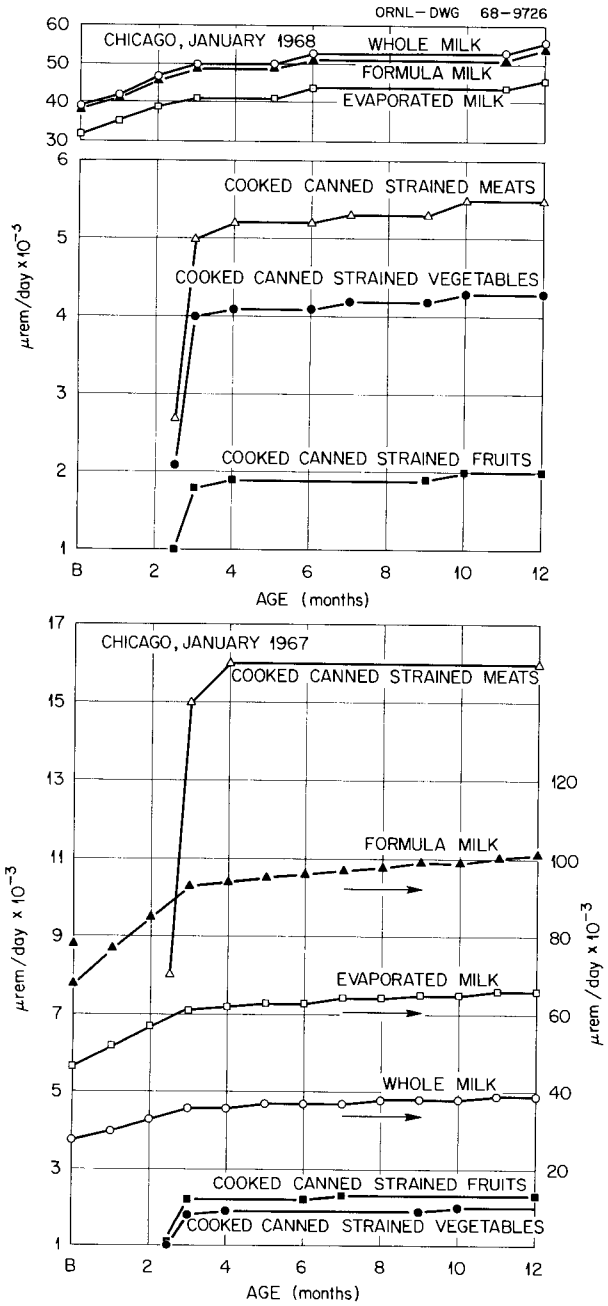

Fig. 25.12. Dose Commitment of Exposure from Fallout ^{137}Cs via Various Foods (Newborn to One Year).

have a higher dose commitment. The corresponding dose estimates due to ^{137}Cs present in meat vary widely with the age of the exposed individual. These data call attention to the rather great differences in dose commitment per day of intake with respect to age for these different foods. The trend is different when meat is the pathway for fallout ^{137}Cs intake than when milk is the pathway. Since the infant eats a very small amount of meat, his dose is quite small compared with the dose which an adult would receive, assuming that the meat was contaminated uniformly. If whole milk is contaminated, the newborn infant is low. Data are plotted in Fig. 25.12 for the infant drinking formula milk, evaporated milk, or whole milk and illustrate the wide differences to be expected.

These data are offered only as an example of the type of calculations that may be used for assessing population exposures from foods or fluids. The numerical values presented depend on estimates of intake and of contamination levels which may not be typical of other populations or other times, but the method applies for any population if the relevant data are available.

Before the age dependence problem is resolved completely, questions must be answered concerning (1) variability of the absorption of cesium into the blood when incorporated in various foodstuffs, (2) possible age dependence of this absorption factor, and (3) special diets of certain population groups.

CALCULATION OF MICROCURIE-DAYS RESIDENCE IN AN ORGAN RESULTING FROM A SINGLE INTAKE

S. R. Bernard

A computer program has been written to calculate microcurie-days, that is, the area beneath the retention curve when 1 μc of a radionuclide is initially taken into an organ or into the whole body. The microcurie-days of residence accumulated up to time t, $Q(t)$, arises in the equation for estimating the dose equivalent in rems accumulated up to time t. The daily dose rate at time t, $D_d(t)$, in rems per day received by an organ of mass m grams containing $q(t)$ microcuries of a radionuclide at time t having an effective energy of ϵ Mev per disintegration is given by the formula

$$D_d(t) = 51\ q(t)\ \epsilon/m\ , \qquad (1)$$

where 51 is the (gram-rems/microcurie-day)/(effective Mev/disintegration). The integral of Eq. (1) from time 0 to t,

$$D(t) = \int_0^t D_d(\tau)\ d\tau = 51 \int_0^t \frac{\epsilon q(\tau)}{m} d\tau\ , \qquad (2)$$

yields the dose equivalent accumulated up to time t, $D(t)$, in rems. In Eq. (2), ϵ will usually be a constant, and $q(t)/m$ is the concentration of the radionuclide in the organ at time t. For adult persons, m, the mass of the organ, is taken as a constant, and when it and ϵ are factored out, the integral (2) becomes

$$D(t) = \frac{51\epsilon}{m}\int_0^t q(\tau)\, d\tau = \frac{51\epsilon}{m} Q(t) \,. \tag{3}$$

Here, $Q(t)$ is the area beneath the retention curve $q(t)$, that is, the microcurie-days residence up to time t.

When a parent of a decay chain of radionuclides is taken into the body, the daughter elements of the chain grow in with time, and the dose equivalent for each member of the chain must be estimated in order to estimate the accumulated dose or dose equivalent to an organ. For the ith member of the chain the microcurie-days of residence in an organ is given by

$$Q_i(t) = \int_0^t q_i(\tau)\, d\tau \,.$$

Assuming ϵ_i and m constant, as before, the dose equivalent $D(t)$ in rems due to the entire chain is given by

$$D(t) = \frac{51}{m} \sum_{i=0}^{n} \epsilon_i Q_i(t) \,. \tag{4}$$

In order to calculate $Q_i(t)$ we require metabolic models, sometimes taken as sums of exponential terms, to approximate the retention of the radionuclide in the organ for extended periods of time. We list here the equations for the functions $Q_i(t)$ for the case in which the ith daughter element in the chain is only introduced into the organ by decay of its parent present in that organ. To this end let

$$R_i^s(t) = \sum_{j_i=1}^{n_i} a_{ij_i} e^{-\lambda_{ij_i}^b t} \,, \quad i = 0, 1, \ldots, n \,, \tag{5}$$

denote the fractional biological retention in an organ (i.e., the retention equation of the organ considered, corrected for radiological decay and normalized to 1 at $t = 0$) of the ith radionuclide. That is, if a unit amount of the ith daughter enters the organ at time $t = 0$, the amount present t days later is $R_i^s(t)$. In (5), the constant

$$\lambda_{ij_i}^b$$

represents the rate of biological elimination of the j_ith component of the retention.

At present the retention function for an organ generally is estimated from experimental data in which a single injection is made initially into the bloodstream. For the parent of the chain,

$$q_0(t) = q_0(0) e^{-\lambda_0^r t} R_0^s(t) \,, \tag{6}$$

where $q_0(0)$ is the microcuries initially reaching the organ and λ_0^r is the radiological decay constant. For the microcuries of the first daughter, $q_1(t)$, present in the organ, we assume linear superposition of inputs. The rate of production of daughter in $d\tau$ units of time is $\lambda_1^r q_0(\tau)\, d\tau$. The amount of daughter produced in the time interval $d\tau$ which is present at a later time t is then

$$\lambda_1^r q_0(\tau)\, d\tau\, e^{-\lambda_1^r (t-\tau)} R_1^s(t-\tau) \,,$$

where $t \geqq \tau$. We linearly superpose the incremental inputs, that is, integrate over $0 \leqq \tau \leqq t$, to obtain

$$q_1(t) = \lambda_1^r \int_0^t q_0(\tau)\, d\tau\, e^{-\lambda_1^r (t-\tau)} R_1^s(t-\tau) \tag{7}$$

$$= \lambda_1^r q_0(0) \int_0^t R_0(\tau)\, d\tau\, e^{-\lambda_1^r (t-\tau)} R_1^s(t-\tau) \,,$$

where

$$R_0(t) = e^{-\lambda_0^r t} R_0^s(t) = \frac{q_0(t)}{q_0(0)} \,. \tag{8}$$

For the level of the second daughter in the organ, $q_2(t)$, we write

$$q_2(t) = \lambda_2^r \int_0^t d\tau\, q_1(\tau)\, e^{-\lambda_2^r (t-\tau)} R_2^s(t-\tau) \,,$$

where $\lambda_2^r\, d\tau\, q_1(\tau)$ is the amount of the second daughter produced in $d\tau$ units of time and

$$\lambda_2^r\, d\tau\, q_1(\tau)\, e^{-\lambda_2^r (t-\tau)} R_2^s(t-\tau)$$

is the amount present at a later time t. In general for the level of the ith daughter of the chain present in the organ we would find

$$q_i(t) = \lambda_i^r q_0(0) \times \int_0^t R_{i-1}(\tau)\, e^{-\lambda_i^r(t-\tau)}\, R_i^s(t-\tau)\, d\tau \quad (8a)$$

as the expression for the microcuries of the ith radionuclide in the chain present in the organ at time t. Here $R_i(t) = q_i(t)/q_0(0)$.

When the $R_i^s(t)$'s are given by Eq. (5), $q_i(t)$ may be obtained in closed form, that is,

$$q_i(t) = q_0(0)\left(\prod_{k=1}^{i} \lambda_k^r\right) \times \sum_{j_0=1}^{n_0} \sum_{j_1=1}^{n_1} \cdots \sum_{j_i=1}^{n_i} \left(\prod_{h=0}^{i} a_{hj_h}\right) \times \left[\sum_{h=0}^{i} \frac{e^{-\lambda_{hj_h} t}}{\prod\limits_{\substack{p=0\\ h\neq p}}^{i} \left(\lambda_{pj_p} - \lambda_{hj_h}\right)}\right], \quad i = 1, 2, \ldots, n, \quad (9)$$

where

$$\lambda_{ij_i} = \lambda_i^r + \lambda_{ij_i}^b$$

is the effective elimination constant. Thus, the functions $Q_i(t)$ can be obtained from (6) for $i = 0$ and from (9) for all other i by straightforward integration.

In some cases it suffices to consider in the computer program only the special case when

$$R_i^s(t) = a_{ij_i} \exp\left(-\lambda_{ij_i} t\right),$$

that is, the longest-lived exponential (let it be the n_ith one). In this case, the sum of exponentials in (9) is the solution of the Bateman differential equations

$$\frac{d}{dt} q_i(t) = a_{in_i} \lambda_i^r q_{i-1}(t) - \lambda_{in_i} q_i(t), \quad i = 1, 2, \ldots, n, \quad (10)$$

$$\frac{dq_0(t)}{dt} = -\lambda_{0n_0} q_0(t).$$

After integration and rearrangement, we find

$$Q_i(t) = \frac{a_{in_i} \lambda_i^r Q_{i-1}(t) - q_i(t)}{\lambda_{in_i}}, \quad Q_0(t) = \int_0^t d\tau\, q_0(\tau) = \frac{q_0(0)}{\lambda_{0n_0}}\left[1 - R_0(t)\right]. \quad (11)$$

In the above equations $q_i(t)$ is to be estimated from Eq. (9) remembering that we only take the n_ith term in the series. Thus, from (11) and (9) the microcurie-days can be estimated, sequentially. In the simplified single-exponential case just discussed, these fractions are analogous to the f_2's in the current ICRP Committee II handbook (*Health Phys.* **3**, 1960).

We also mention that formula (8*a*) does not require that we restrict ourselves to exponential sums for $R_i^s(t)$. We can use a power function, $a_i t^{-b_i}$ (a_i and b_i are constants), for the $R_i^s(t)$. However, when we do this we do not obtain a closed form expression similar to (9). If the power function can be adequately represented by a finite sum of exponentials as suggested in the work of Bernard and Davis,[17] then the closed form expression, Eq. (9), will apply.

The computer code has been written by Sharron P. King (ORNL Mathematics Division) to evaluate the case of retention described by a single exponential term, Eqs. (9) and (11). Also, the extension of the code to handle Eq. (9) for multiexponential retention is presently under way.

A MODEL FOR ESTIMATION OF MEAN ACTIVITY PRESENT IN SEGMENTS OF THE GASTROINTESTINAL TRACT AT ANY TIME POST INGESTION

S. R. Bernard

In the papers by Eve[18] and Dolphin and Eve[19] an extensive review of the physiology of the gastro-

[17] *Health Phys. Div. Ann. Progr. Rept. July 31, 1966*, ORNL-4007, p. 232.

[18] I. S. Eve, *Health Phys.* **12**, 131 (1966).

[19] G. W. Dolphin and I. S. Eve, *Health Phys.* **12**, 163 (1966).

intestinal tract is carried out, and a new model for the dosimetry of the GI tract is presented. In their model they estimate the radiation dose to a small element of the gut walls in a segment of the tract. They compute a time average of this dose during the assumed residence time in the segment of the tract and consider this to be the mean dose throughout that section of the GI tract. Another model for residence of material in the GI tract is developed here and may serve as a basis for estimating the mean dose to segments of the tract. This other model is based on considerations of the random variable passage time through the tract.

In order to explain the basis of this other model, consider the case of passage of a stable element through the tract. Let T_1, T_2, T_3, and T_4 denote the random variable residence times of this stable element in the stomach, small intestine, upper large intestine, and lower large intestine respectively. The total time for the passage of the stable element is the sum of these random variable times, denoted by t, that is,

$$t = \sum_{i=1}^{4} T_i \,. \tag{1}$$

If the residence times in the various segments are assumed to be independent and exponentially distributed, then the probability density functions of these residence times and of the total time t satisfy the same differential equations that arise from consideration of a catenary compartment model of the tract with the flows being unidirectional. We develop here the equations along the more usual lines of compartment theory and only point out that the same equations and estimates can be given a probabilistic interpretation. Figure 25.13 shows the model; $S_{ij}(t)$ denotes the amount (in microcuries) of the ith radionuclide ($i = 0, 1, \ldots, n$) in a chain of radionuclides present in the jth region ($j = 1, 2, 3, 4$) of the GI tract at time t. Thus, when the subscript j has values 1, 2, 3, or 4 the designated quantity relates to the stomach, small intestine, upper large intestine, and lower large intestine respectively. The symbol λ^a_{ij} ($j = 1, \ldots, 4$) denotes the fractional rate of loss from compartment j by absorption into the bloodstream, λ^b_j is the fractional rate of transfer from the jth compartment to the $(j + 1)$th compartment, and λ^r_i is the radiological decay constant of the ith radionuclide in a decay chain.

The rate of change of the ith radionuclide in the jth compartment is given by

$$\frac{dS_{ij}(t)}{dt} = \lambda^r_i S_{i-1,j}(t) + \lambda^b_{j-1} S_{i,j-1}(t) - \lambda_{ij} S_{ij}(t) \,,$$

$$i = 0, 1, \ldots, n, \; j = 1, \ldots, 4 \,. \tag{2}$$

Here

$$\lambda_{ij} = \lambda^r_i + \lambda^b_j + \lambda^a_{ij}$$

is the effective elimination constant of the ith radionuclide from the jth compartment. In the differential equation (2) when $i = 0$ the term $S_{-1,j}(t) = 0$ for all t and all j, and for $j = 1$, $S_{i,-1}(t) = 0$ for all i and all t. The reader should be warned too that this equation (2) only applies when the units on the $S_{ij}(t)$ are microcuries. The values of the coefficients in the right members might be different if the $S_{ij}(t)$ are expressed in other units. We have used the Laplace transform method to obtain the general solution to these equations. The solution, assuming $S_{01}(0) = 1$, all other $S_{i,j}(0) = 0$, for the level of the ith radionuclide in the stomach is

ORNL-DWG 68-8503

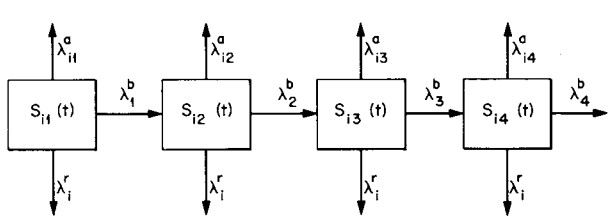

Fig. 25.13. A Catenary Compartment Model for GI Tract.

$$S_{i1}(t) = \left(\prod_{k=1}^{i} \lambda_k^r \right) \sum_{p=0}^{i} \frac{e^{-\lambda_{p1} t}}{\prod\limits_{\substack{k=0 \\ k \neq p}}^{i} (\lambda_{k1} - \lambda_{p1})}, \quad i = 0, 1, \ldots, n .$$

For the level of the ith radionuclide in the small intestine

$$S_{i2}(t) = \lambda_1^b \left(\prod_{k=1}^{i} \lambda_k^r \right) \sum_{l=0}^{i} \left[\sum_{p=0}^{l} \frac{e^{-\lambda_{p1} t}}{\prod\limits_{\substack{k=0 \\ k \neq p}}^{l} (\lambda_{k1} - \lambda_{p1}) \prod\limits_{k=l}^{i} (\lambda_{k2} - \lambda_{p1})} \right.$$

$$\left. + \sum_{p=l}^{i} \frac{e^{-\lambda_{p2} t}}{\prod\limits_{k=0}^{l} (\lambda_{k1} - \lambda_{p2}) \prod\limits_{\substack{k=l \\ k \neq p}}^{i} (\lambda_{k2} - \lambda_{p2})} \right], \quad i = 0, 1, \ldots n .$$

For the level of the ith radionuclide in the upper large intestine

$$S_{i3}(t) = \lambda_1^b \lambda_2^b \left(\prod_{k=1}^{i} \lambda_k^r \right) \sum_{m=0}^{i} \sum_{l=0}^{m} \left[\sum_{p=0}^{l} \frac{e^{-\lambda_{p1} t}}{\prod\limits_{\substack{k=0 \\ k \neq p}}^{l} (\lambda_{k1} - \lambda_{p1}) \prod\limits_{k=l}^{m} (\lambda_{k2} - \lambda_{p1}) \prod\limits_{k=m}^{i} (\lambda_{k3} - \lambda_{p1})} \right.$$

$$+ \sum_{p=l}^{m} \frac{e^{-\lambda_{p2} t}}{\prod\limits_{k=0}^{l} (\lambda_{k1} - \lambda_{p2}) \prod\limits_{\substack{k=l \\ k \neq p}}^{m} (\lambda_{k2} - \lambda_{p2}) \prod\limits_{k=m}^{i} (\lambda_{k3} - \lambda_{p2})}$$

$$\left. + \sum_{p=m}^{i} \frac{e^{-\lambda_{p3} t}}{\prod\limits_{k=0}^{l} (\lambda_{k1} - \lambda_{p3}) \prod\limits_{k=l}^{m} (\lambda_{k2} - \lambda_{p3}) \prod\limits_{\substack{k=m \\ k \neq l}}^{i} (\lambda_{k3} - \lambda_{p3})} \right], \quad i = 0, 1, \ldots, n .$$

For the lower large intestine the level of the ith radionuclide is

$$S_{i4}(t) = \lambda_1^b \lambda_2^b \lambda_3^b \left(\prod_{k=1}^{i} \lambda_k^r \right) \sum_{h=0}^{i} \sum_{m=0}^{h} \sum_{l=0}^{m} \left[\sum_{p=0}^{l} \frac{e^{-\lambda_{p1} t}}{\prod_{\substack{k=0 \\ k \neq p}}^{l} (\lambda_{k1} - \lambda_{p1}) \prod_{k=l}^{m} (\lambda_{k2} - \lambda_{p1}) \prod_{k=m}^{h} (\lambda_{k3} - \lambda_{p1}) \prod_{k=h}^{i} (\lambda_{k4} - \lambda_{p1})} \right.$$

$$+ \sum_{p=l}^{m} \frac{e^{-\lambda_{p2} t}}{\prod_{k=0}^{l} (\lambda_{k1} - \lambda_{p2}) \prod_{\substack{k=l \\ k \neq p}}^{m} (\lambda_{k2} - \lambda_{p2}) \prod_{k=m}^{h} (\lambda_{k3} - \lambda_{p2}) \prod_{k=h}^{i} (\lambda_{k4} - \lambda_{p2})}$$

$$+ \sum_{p=m}^{h} \frac{e^{-\lambda_{p3} t}}{\prod_{k=0}^{l} (\lambda_{k2} - \lambda_{p3}) \prod_{k=l}^{m} (\lambda_{k2} - \lambda_{p3}) \prod_{\substack{k=m \\ k \neq p}}^{h} (\lambda_{k3} - \lambda_{p3}) \prod_{k=h}^{i} (\lambda_{k4} - \lambda_{p3})}$$

$$\left. + \sum_{p=h}^{i} \frac{e^{-\lambda_{p4} t}}{\prod_{k=0}^{l} (\lambda_{k1} - \lambda_{p4}) \prod_{k=l}^{m} (\lambda_{k2} - \lambda_{p4}) \prod_{k=m}^{h} (\lambda_{k3} - \lambda_{p4}) \prod_{\substack{k=h \\ k \neq p}}^{i} (\lambda_{k4} - \lambda_{p4})} \right], \quad i = 0, 1, \ldots, n.$$

We have tested this model with the data of Hayes *et al.*,[20] who fed single intakes of ^{140}La (in a citrate) to patients and collected feces, which were then analyzed for the ^{140}La content. The radiological half-life of ^{140}La is ~40 hr, but Hayes *et al.* corrected the excretion data by the decay factor $e^{-0.693t/40}$ (where t is in hours), and thus their data correspond to a stable element. The mean residence times assigned by Eve for the different segments of the tract are $\frac{1}{24}$, $\frac{4}{24}$, $\frac{13}{24}$, $\frac{24}{24}$ days and consequently λ_j^b has been taken here to be 24, 6, 1.85, 1 day^{-1}, $j = 1, 2, 3, 4$, in testing the model.

Using these values and the further conditions that the stomach receives an initial input of 1 μc, all other sections have zero contents at time zero, taking $\lambda_a^j = 0$ for all j, then

$$S_{01}(t) = 1 e^{-(24+\lambda_0^r)t}, \tag{5}$$

$$S_{02}(t) = 1.33\,(e^{-6t} - e^{-24t})\, e^{-\lambda_0^r t}, \tag{6}$$

$$S_{03}(t) = (+0.36117 e^{-24t} - 1.92771 e^{-6t} + 1.56653 e^{-1.85t})\, e^{-\lambda_0^r t}, \tag{7}$$

$$S_{04}(t) = (-0.02905 e^{-24t} + 0.71325 e^{-6t} - 3.40952 e^{-1.85t} + 2.725831 e^{-t})\, e^{-\lambda_0^r t}, \tag{8}$$

while the fecal excretion is given by

$$\int_0^t 1 \cdot S_{04}(\tau)\, d\tau .$$

For $\lambda_0^r = 0$ this integral becomes

$$[-0.00121\,(1 - e^{-24t}) + 0.11887\,(1 - e^{-6t}) - 1.84298\,(1 - e^{-1.85t}) + 2.72531\,(1 - e^{-t})] . \tag{9}$$

Note that for this example, we assume no absorption from any regions of the tract into the bloodstream. Therefore (9) is applicable to the case of a single intake of a long-lived nonabsorbed substance, such as used by Hayes *et al.*[20] With their

[20] R. L. Hayes *et al.*, *Health Phys.* **9**, 915 (1963).

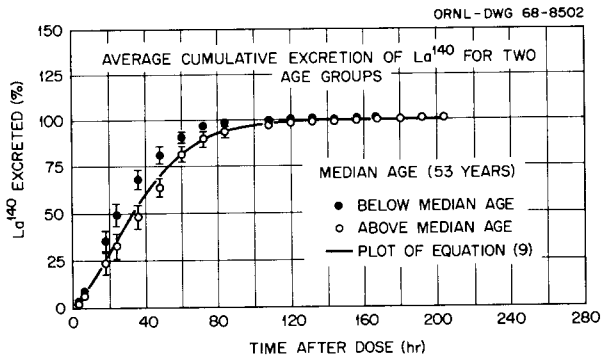

Fig. 25.14. Hayes *et al.* Average Cumulative Excretion of ^{140}La by Human Subjects Compared with Cumulative Excretion from Eq. (9).

permission, Fig. 25.14 is reproduced from ref. 20 and shows a plot of the cumulative excretion expressed in percent of that ingested at the various times after ingestion. Also shown are the estimates made by the authors from Eq. (9) [i.e., a plot of Eq. (9) as a function of time]. As can be seen, the agreement is fairly good. Some data on the levels in each region of the tract would be required to test this model adequately and see how good the estimate is in comparison with actual amounts observed at various times after ingestion of various soluble and insoluble substances.

This model permits one to estimate the mean contents of the various segments of the tract at any time following ingestion. Since an estimate of the levels of activity in the regions of the GI tract section is available, the energy deposition averaged over the entire section can be estimated rather than the peak dose or the time average over the region. However, the assumption of the exponential distributions of residence time and their independence in the various regions of the tract needs to be examined and tested with more experimental data. This model is not adequate for estimating the probability density that a given content of a radionuclide is present in a section at a given time for a given person. It only purports to give the average levels or expected levels to be found in the various sections at various times for a person having the assumed characteristics, that is, for a "Standard Man."

NUCLEAR SAFETY ENVIRONMENTAL STUDIES: BIOHAZARDS OF AEROSPACE NUCLEAR SYSTEMS

R. H. Boyett
T. G. Clark
B. R. Fish
G. W. Royster, Jr.
R. L. Walker
W. H. Wilkie, Jr.
J. L. Thompson

Microspheres of $^{238}PuO_2$ having diameters of from 50 to 250 μ are used in space electric power sources. One of the greater potential hazards they might present in the event of their accidental release to the biosphere is to the respiratory system. The probability of entry into the body through the nose is a function of the difference between the intake velocity of the airstream into the nose and the falling velocity of the particle. The ratio of the concentration of inhaled particles to the ambient concentration as a function of particle size may be calculated as follows: Let

$$U_t = Q/A ,$$

where Q = air flow rate at a time t, cm^3/sec, A = cross-sectional area of external nares, cm^2, and U_t = flow velocity at time t, cm/sec.

If the particles are assumed to be uniformly mixed and suspended in the exposure volume, the rate at which they enter the nares will be nU_tA (particles/sec), where n is the number concentration (particles/cm^3). However, if, as in the usual case, the particles have a downward velocity $-V_s$, then only $n(U_t - V_s)A$ particles/sec would gain entry. An efficiency factor e_s can then be calculated:

$$e_s = \frac{n(U_t - V_s)A}{nU_tA} ,$$

which gives the fraction of particles entering compared with the number that would have entered if they had zero settling velocity. This factor, e_s, is then adjusted for the fraction of time during inspiration that U_t occurs.

Using the respiratory air flow curves of Silverman and Billings[21] for four types of inspiratory cycles and assuming a fixed intake area of 2.5 cm^2, the

[21] L. Silverman and C. E. Billings, "Pattern of Airflow in the Respiratory Tract," *Symposium on Inhaled Particles and Vapours*, C. N. Davies, ed., Pergamon, New York, 1961.

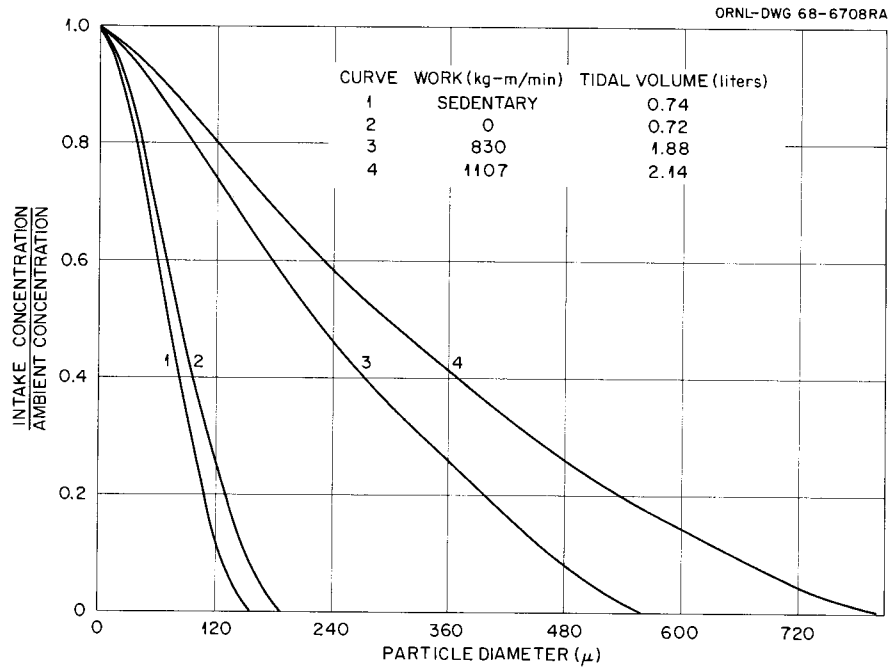

Fig. 25.15. Fraction of Plutonium Microspheres Inspired.

curves shown in Fig. 25.15 have been computed. Two factors which may be expected to give slightly lower values than those shown have been ignored: (1) the shadowing effect of the nose and (2) dilation of the nostrils and/or mouth breathing. However, these are at least partially offset by the assumption of a zero horizontal component in the path of the particle.

Using thin plastic scintillators[22] the alpha dose rate from $^{238}PuO_2$ microspheres has been measured as a function of depth in a tissue-simulating absorber (Mylar). Figure 25.16 shows average values found, and the interception of the dashed line with the abscissa is an estimate of the maximum range to be expected from a thin source. The average surface dose rate from five microspheres ranging from 123 to 225 μ diameter was 25,900 ± 2600 rads/sec.

INTERACTION OF AIRBORNE PARTICULATES WITH GASES

B. M. Smith[23] B. R. Fish

Studies are being conducted on the interaction of sulfur dioxide gas with airborne particles. Aerosols are generated by exploding wires in air, resulting in particles with diameters from about 0.01 to 0.1 μ (ref. 24). Aerosol is mixed with SO_2 tagged[25] with ^{35}S under controlled conditions in a gas-particle interaction chamber.[26] Samples for analysis are withdrawn from the chamber through diffusion tubes followed by membrane filters. The tubes are lined with lead foil coated with lead peroxide. The sample flow rate is selected so that SO_2 gas will diffuse to and be removed by the lead peroxide on the inside walls of the tubes while allowing aerosol particles to pass through the tube and be collected on the filters. For analysis, the lead-foil inserts are segmented and assayed for sulfur by radiochemical techniques. Particle samples are assayed for sorbed SO_2 in a similar manner.

---

[22]W. H. Wilkie and B. R. Fish, "Scintillation Extrapolation Dosimetry," *Symposium on Solid State and Chemical Dosimetry in Medicine and Biology*, IAEA, Vienna, 1966.

[23]Employee of National Air Pollution Control Administration (NAPCA), CPEHS, on assignment to ORNL.

[24]K. D. Duerksen *et al.*, *Health Phys. Div. Ann. Progr. Rept. July 31, 1967*, ORNL-4168, pp. 296–98.

[25]B. M. Smith *et al.*, *Health Phys. Div. Ann. Progr. Rept. July 31, 1967*, ORNL-4168, pp. 299–301.

[26]R. L. Walker, *Health Phys. Div. Ann. Progr. Rept. June 30, 1963*, ORNL-3492, pp. 187–89.

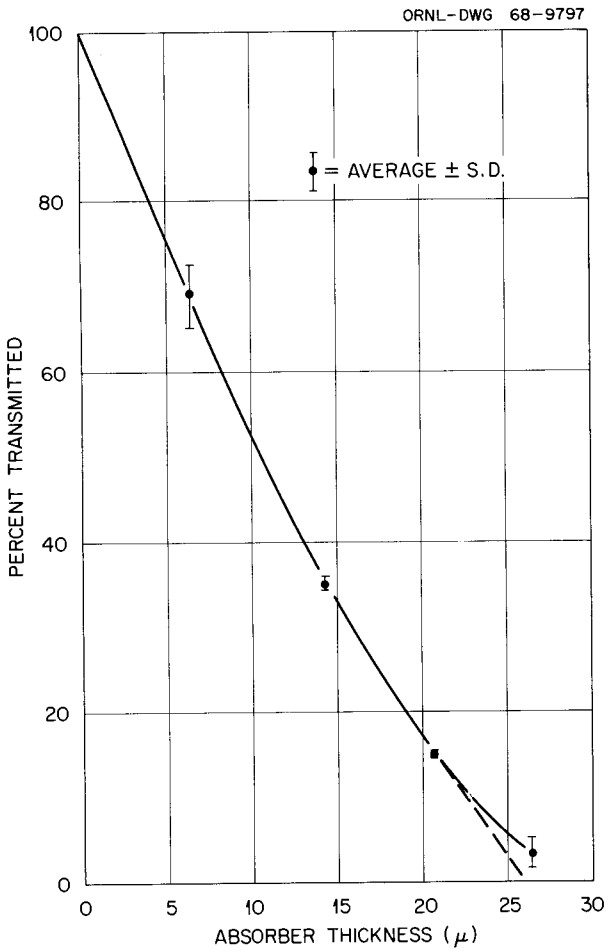

Fig. 25.16. Transmission of Alpha Rays from $^{238}PuO_2$ Microspheres Through Mylar.

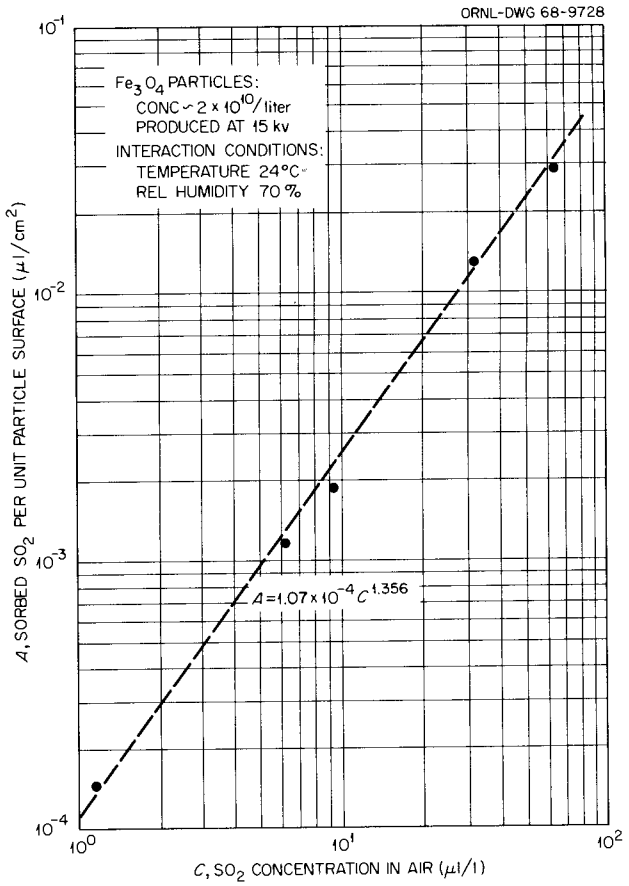

Fig. 25.17. SO_2 Sorption Isotherm. Particles dispersed in air.

Sorption of SO_2 gas on aerosol particles of lead oxides, aluminum oxides, platinum, and iron oxide has been studied. Lead oxide particles in concentrations of approximately 10^{10} particles per liter of air sorb essentially 100% of the SO_2 gas at 1 μl of SO_2 per liter of air under ambient conditions, whereas aluminum oxides and platinum particles sorb approximately 50% and 10% respectively. Preliminary indications are, however, that platinum reversibly sorbs SO_2 gas, which is subsequently released during sampling. Iron oxide (Fe_3O_4) particles sorb varying amounts of SO_2 gas in accordance with initial SO_2 concentration. A sorption isotherm for SO_2 gas on Fe_3O_4 particles in the disperse phase is presented in Fig. 25.17.

26. Stable Element Metabolism

W. S. Snyder
Mary Jane Cook
Judith Dickson[1]
F. S. Jones[2]
Peggy L. Stewart[1]
Isabel H. Tipton[1]
Cyrus Feldman[2]

PATTERNS OF ELEMENTAL EXCRETION IN LONG-TERM BALANCE STUDIES

Isabel H. Tipton Peggy L. Stewart
Judith Dickson

In the program for analysis of total self-chosen diets and total excreta for trace elements, the material from two men for 50 weeks has been analyzed for 25 elements. Statistical treatment has been made for the 250-day period September 6, 1966–May 13, 1967.

Subject C was 23 years old, 6 ft 1½ in. tall, and weighed about 220 lb. Subject D was 25 years old, 5 ft 10 in. tall, weighing about 156 lb.

Differences in the dietary habits of the two individuals are indicated by the daily gross amounts of food and drink they ingested and their fecal and urinary output. Table 26.1 shows the mean and standard deviation of the total daily dietary intake, the water content of this diet, and the daily fecal and urinary output. It is obvious that subject C drank more than subject D, and this is also reflected in his greater urinary output. Subject D, however, drank more milk than subject C, and this is reflected in the values for calcium intake. The large standard deviation for fecal excretion comes about because of the number of days on which there was no fecal excretion at all. For subject C, on more than half of the days in the period there was no fecal excretion, and there were a few periods of four days when none occurred.

Table 26.1. Gross Daily Intake and Excretion

September 6, 1966 – May 13, 1967

Mean ± standard deviation in grams

	Subject C	Subject D
Total daily intake by ingestion	3100 ± 530	2700 ± 610
Water content	2600 ± 690	2100 ± 510
Total daily fecal excretion	110 ± 130	120 ± 110
Total daily urinary excretion	1300 ± 500	1000 ± 270

Table 26.2 shows the total dietary intake and fecal and urinary output of 25 elements for this period minus three days at the beginning. The errors of the method for most elements result in an uncertainty of about ±20% in the state of balance. Therefore balance has been expressed as the ratio total excreta/total ingested rather than as the more commonly used differences between total ingested and total excreted, so that the state of balance can be more conveniently observed. If this value is between 0.8 and 1.2, the subject may be considered to have been in balance over the period under study. If the ratio is below 0.8, the intake was greater than the output, and the subject was in "positive" balance. If the ratio is above 1.2, the output exceeded the input, and the subject was in "negative" balance. The ratio of the urinary output to total excreta or to intake by ingestion is sometimes used as the lower limit of f_1, the fraction of an element absorbed from the

[1]Physics Department, University of Tennessee.
[2]Analytical Chemistry Division.

Table 26.2. Total Intake by Ingestion and Total Fecal and Urinary Excretion

September 9, 1966–May 13, 1967 (247 days)

Element	Subject	Total Ingested (g)	Total in Feces (g)	Total in Urine (g)	Total in Excreta (g)	Total Excreta / Total Ingested	Urine / Excreta	Urine / Ingested	f_1 (ICRP-59)
Aluminum	C	3.9	4.0	0.23	4.2	1.08	0.056	0.060	0.1
	D	3.8	2.8	0.19	3.0	0.79	0.063	0.050	
Barium	C	0.16	0.15	0.0028	0.15	0.95	0.018	0.018	0.05
	D	0.21	0.15	0.0034	0.15	0.73	0.022	0.040	
Beryllium	C	0.027	0.0018	0.00055	0.0023	0.086	0.24	0.020	0.002
	D	0.056	0.0012	0.00044	0.0016	0.03	0.27	0.0079	
Boron	C	0.28	0.067	0.30	0.36	1.27	0.81	1.04	0.9
	D	0.60	0.096	0.21	0.30	0.51	0.68	0.35	
Calcium	C	240	210	26	240	1.0	0.11	0.11	0.6
	D	530	290	34	320	0.62	0.11	0.067	
Cadmium[a]	C	0.0069	0.0020	0.0055	0.0075	1.1	0.74	0.79	0.0025
	D	0.012	0.0026	0.0057	0.0083	0.69	0.69	0.47	
Chromium	C	0.059	0.017	0.021	0.038	0.65	0.55	0.35	<0.005
	D	0.084	0.021	0.024	0.045	0.53	0.54	0.28	
Cobalt	C	0.083	0.0086	0.070	0.079	0.95	0.89	0.85	0.3
	D	0.12	0.014	0.064	0.078	0.67	0.82	0.56	
Copper	C	0.25	0.31	0.0055	0.32	1.28	0.018	0.022	0.28
	D	0.45	0.29	0.013	0.30	0.68	0.048	0.028	
Iron	C	3.7	3.4	0.23	3.6	0.98	0.064	0.062	0.1
	D	7.6	2.4	0.21	2.6	0.34	0.082	0.028	
Lead[b]	C	0.072	0.019	0.0074	0.027	0.37	0.28	0.10	0.08
	D	0.11	0.016	0.0084	0.024	0.22	0.34	0.075	
Magnesium	C	47	40	29	69	1.47	0.42	0.62	0.1
	D	92	46	25	71	0.78	0.35	0.28	
Manganese	C	0.79	0.67	0.0086	0.68	0.85	0.013	0.011	0.1
	D	1.3	0.68	0.0065	0.69	0.54	0.0095	0.005	
Molybdenum	C	0.068	0.027	0.035	0.062	0.92	0.56	0.52	0.8
	D	0.15	0.030	0.042	0.072	0.48	0.58	0.28	
Nickel	C	0.10	0.057	0.029	0.086	0.82	0.34	0.28	0.3
	D	0.20	0.092	0.031	0.12	0.61	0.25	0.15	
Phosphorus	C	410	110	310	420	1.02	0.74	0.75	0.75
	D	820	140	290	430	0.53	0.67	0.35	
Potassium	C[c]	410	63	660	720	1.75	0.91	1.60	1.0
	D	900	72	740	810	0.90	0.91	0.82	
Silver	C	0.046	0.0083	0.0018	0.010	0.22	0.18	0.039	0.01
	D	0.099	0.031	0.0019	0.033	0.34	0.059	0.020	
Sodium	C[c]	840	8.2	1200	1200	1.45	0.99	1.44	1.0
	D	1200	9.6	1200	1200	1.0	0.99	1.0	

Table 26.2 (continued)

Element	Subject	Total Ingested (g)	Total in Feces (g)	Total in Urine (g)	Total in Excreta (g)	Total Excreta / Total Ingested	Urine / Excreta	Urine / Ingested	f_1 (ICRP-59)
Strontium	C	0.41	0.34	0.028	0.37	0.91	0.081	0.088	0.3
	D	0.53	0.30	0.020	0.32	0.60	0.062	0.037	
Tin	C	1.5	1.1	0.026	1.1	0.72	0.024	0.018	0.05
	D	2.4	1.0	0.016	1.0	0.43	0.016	0.0068	
Titanium	C	0.20	0.11	0.096	0.20	1.01	0.47	0.47	10^{-4}
	D	0.51	0.22	0.088	0.31	0.61	0.28	0.17	
Vanadium	C	0.016	0.036	0.0052	0.041	2.48	0.13	0.32	0.02
	D	0.040	0.042	0.0073	0.049	1.23	0.15	0.18	
Zinc	C	2.7	3.6	0.38	4.0	1.48	0.094	0.14	0.1
	D	4.5	4.0	0.35	4.3	0.96	0.080	0.076	
Zirconium	C	0.12	0.036	0.024	0.060	0.50	0.39	0.20	$<10^{-4}$
	D	1.60	0.048	0.034	0.082	0.52	0.41	0.21	

[a]Cadmium data for weeks 28–36 only.

[b]Lead data for weeks 19–36 only.

[c]Subject C failed to add condiments to his duplicate meal. After he corrected this practice the apparent imbalance disappeared.

gastrointestinal tract of the total ingested. These ratios are given in Table 26.2. The ICRP Handbook 59 values for f_1 are included in the last column of the table for comparison. The agreement is good for those elements which are excreted almost entirely in urine, but it is obvious that for elements like strontium and calcium, the amount excreted in urine does not indicate the total amount absorbed, since some of the absorbed element is known to be reexcreted into the gut.

The daily variation makes it possible to study the correlation between elemental intake and excretion. Correlations between levels of excretion of an element and levels of intake by ingestion on previous days may be determined and multiple regressions obtained. If y represents the excretion of an element for any day and x_1, x_2, x_3, x_4, ... represent the dietary intake on the same day, the day before, two days before, three days before, etc., it is possible to write an equation which will predict the excretion in terms of the intake:

$$y = a_0 + a_1x_1 + a_2x_2 + a_3x_3 + \dots ,$$

where a_0 is the amount excreted which cannot be accounted for by the intake on these days. The a's are regression coefficients which indicate the influence of the variability in a corresponding day's intake on the variability of the excretion. In using the equation to predict the elemental output on any day, these coefficients are just fractions of the intake on the corresponding day.

This kind of treatment has been useful in estimating reexcretion into the gut of certain elements, and thus has made possible a better estimate of f_1. Regressions were run on fecal excretion over a four-day period and the intake over the same period, the previous four-day period, two periods previous, and so on through five periods previous, or covering a total of 24 days.

The equation in this case is

$$y_{4\ \mathrm{day}} = a_0 + a_{1-4}x_{1-4} + a_{5-8}x_{5-8} + a_{9-12}x_{9-12} + a_{13-16}x_{13-16} + a_{17-20}x_{17-20} + a_{21-24}x_{21-24} .$$

The elements for which the multiple correlation coefficient R was greater than 0.32 and for which the probability that this value could have occurred

Table 26.3. Regression Equations for Estimating Four-Day Fecal Output from Intake by Ingestion

September 6, 1966—May 13, 1967

	Subject C					Subject D				
	Cr	Mo	Ag	Sr	Sn	Cr	Mo	Ag	Sr	Sn
Regression coefficient										
a_{1-4}	0.026	0.16	0.039				0.035	0.038		0.094
a_{5-8}		0.12	0.021	0.21	0.26			0.066	0.16	
a_{9-12}	0.041						0.039			
a_{13-16}									0.15	
a_{17-20}				0.24	0.14	0.08				0.071
a_{21-24}									0.15	
a_0 (μg)	220	310	100	980	4400	240	330	290	1700	3800
R^2	0.09	0.20	0.26	0.12	0.18	0.48	0.19	0.12	0.14	0.12
Mean four-day output (μg)	280	450	140	5700	15,000	330	480	510	6300	15,000
Standard deviation	220	490	110	4000	17,000	400	550	450		17,000
Standard error of estimate	210	450	97	3800	15,000	300	500	430		16,000
Four-day intake level (μg)	940	1100	790	6500	22,000	1400	2400	1600	8600	38,000

by chance was less than 5% ($p < 0.05$) are included in Table 26.3. It is probably safe to say that correlation between fecal excretion and dietary intake within the previous week reflects the passage of all of the unabsorbed element through the G.I. tract. Some reexcretion into the gut may also take place during this time, but it is impossible to estimate the fraction from these data. Since the regression coefficients are considered to be fractions of the amount ingested, tin and chromium showed less than 10% of the amount ingested to be reexcreted within 24 days. The value 0.08 for a_{17-20} for chromium for subject D was very highly significant ($p \ll 0.0001$).

The most interesting results were those for strontium. If it is assumed that fecal excretion within one week involved only the unabsorbed element, it appears that 24 to 30% of the amount ingested was reexcreted into the gut within 24 days. When this is added to the amount excreted in urine, the total fraction absorbed of the amount ingested is about 0.34 for both subjects, which agrees very well with the ICRP-59 value of 0.3. The distribution of the excretion of absorbed quantity between urine and feces appears to be the reverse of that reported by Fujita[3] from an experiment on the ingestion of a single dose of ^{85}Sr by one man and by Bishop *et al.*[4] after intravenous ingestion of a single dose of ^{85}Sr into two subjects. That is, the reexcretion into the gut for subjects C and D was over twice as great as the urinary excretion rather than one-half as great. Actually, the situations are not comparable, since subjects C and D ingested strontium continually instead of in a single dose, and the value of the fraction of strontium in the urine of the total excreted was always closer to the value for Fujita's subject during the first two or three days than to the value which this fraction became after 90% of the dose had been excreted.

The results for calcium were not included in the table because the multiple correlation coefficient R for subject C was less than 0.32. Since the correlation for subject D was sufficient to be included ($R = 0.48$), it should be pointed out that for both subjects 11% of the amount ingested appeared to be reexcreted into the gut during the four-day period 17 to 20 days after ingestion, which is close to the value proposed by Dolphin

[3] M. Fujita *et al.*, *Health Phys.* 9, 407 (1963).

[4] M. Bishop *et al.*, "Excretion and Retention of Radioactive Strontium in Normal Men following a Single Intravenous Injection," *Intern. J. Radiation Biol.* 2, 125 (1960).

and Eve[5] as a representative value. This value added to the ~11% excreted in urine gives an f_1 of about 0.22, which is closer to the value of 0.38 proposed by Dolphin and Eve than to the ICRP value of 0.6. The discrepancy arises from the difference in urinary output. Subjects C and D excreted in the urine about 11% of the amount ingested, whereas Dolphin and Eve suggest a value nearer to 20%. The latter value is also closer to the average value for three subjects reported by Harrison *et al.*,[6] although the value for one of those subjects was 13%. It is quite reasonable to suppose that calcium (and strontium as well) has components of endogenous excretion with much longer time lags than the 24 days included in this study. As more data become available longer periods of time will be included in the regression studies.

METHOD FOR REMOVAL OF PHOSPHATE FROM BONE ASH

Cyrus Feldman F. S. Jones

The removal of phosphate from bone ash facilitates the spectrographic determination of impurities in this material by making it possible to chemically concentrate the trace elements at pH 6.5, rather than the usual pH 5.2. This substantially increases the number of trace elements which can be collected and eliminates the undesirable coprecipitation of calcium phosphate.

A practical procedure was settled on for the removal of phosphate from solutions of bone ash. After ignition at 450°C, the ash is dissolved in nitric acid, followed by formic acid. This solution is placed in the cathode compartment of a two-part electrodialysis cell; the compartments are separated by an Ionac Ma 3475 x L anion-permeable membrane. Electrodialysis at 2 amp for a few hours transfers the bulk of the phosphate to the anode compartment; cations are retained in the cathode compartment and/or deposited on the carbon cathode. The latter is wet-ashed and added to the sample solution.

Trace elements are then collected from this solution by precipitation with 8-hydroxyquinoline + thionalide + tannic acid. The precipitate is examined spectrographically.

---

[5]G. W. Dolphin and I. S. Eve, *Phys. Med. Biol.* 8, 193 (1963).

[6]G. E. Harrison, W. H. A. Raymond, and H. C. Tretheway, *Proc. Intern. Congr. Peaceful Uses At. Energy* 11, 156 (1956).

Theses, Papers, Publications, and Lectures

Theses

M-E. M. Abu-Zeid, L. G. Christophorou, and J. G. Carter
Emission and Decay of Organic Liquids Under Electron Impact, ORNL-TM-2219 (in preparation).

C. E. Baker, P. B. Dunaway, and S. I. Auerbach
Measurement of Metabolism in Cotton Rats by Retention of Cesium-134, ORNL-TM-2069 (February 1968).

R. P. Blaunstein and L. G. Christophorou
Electron Attachment to Organic Molecules, ORNL-TM-2216 (in press).

A. A. Christodoulides and L. G. Christophorou
Scattering of Thermal Electrons by Polar Molecules, ORNL-TM-2257 (in press).

B. R. Fish
Conductive Sphere on a Charged Conductive Plane, ORNL-4193 (December 1967).

R. N. Hamm, R. H. Ritchie, and J. C. Ashley
Electron Mean Free Paths in a Free-Electron Gas, ORNL-TM-2072 (in press).

J. D. Hayes and E. T. Arakawa
The Optical Properties of Vacuum-Evaporated Films of Tellurium and Amorphous Selenium, ORNL-TM-2023 (January 1968).

W. G. Hendrick, L. G. Christophorou, and G. S. Hurst
An Apparatus for Measurement of Electron Attachment and Electron Swarm Drift Velocities at High Temperatures, ORNL-TM-1444 (February 1968).

R. H. Huebner, R. N. Compton, L. G. Christophorou, and P. W. Reinhardt
Threshold Electron Impact Excitation of Organic Molecules, ORNL-TM-2156 (June 1968).

Larry Johnson and H. C. Schweinler
Oscillator Strengths in Magnesium Porphin, ORNL-TM-1951 (October 1967).

T. F. Lomenick
Accelerated Deformation of Rock Salt at Elevated Temperature and Pressure and Its Implications for High Level Radioactive Waste Disposal, ORNL-TM-2102 (March 1968).

W. T. Naff, R. N. Compton, C. D. Cooper, and P. W. Reinhardt
Transient Negative Ion States in Alicyclic and Aromatic Fluorocarbon Molecules, ORNL-TM-2260 (in preparation).

S. J. Nalley, M. Y. Nakai, F. W. Garber, R. H. Ritchie, J. A. Harter, and R. D. Birkhoff
Low-Energy Electron Studies in Aluminum, ORNL-TM-2030 (January 1968).

D. R. Nelson and F. J. Davis
Determination of Diffusion Coefficients of Thermal Electrons with a Time-of-Flight Swarm Experiment, ORNL-TM-2222 (in press).

John McKeever and H. C. Schweinler
Jacobi-Gauss Quadrature Calculations of Rydberg-Klein Potential Energy Curves for Diatomic Molecules and Solutions of the Ensuing Wave Equations for Some of Their Bound States, ORNL-TM-2167 (May 1968).

Linda R. Painter, R. D. Birkhoff, and E. T. Arakawa
Optical Properties of Liquid Water in the Vacuum Ultraviolet, ORNL-TM-2261 (in press).

H. L. Ragsdale, J. P. Witherspoon, and D. J. Nelson
The Effects of Biotic Complexity and Fast Neutron Radiation on Cesium-137 and Cobalt-60 Kinetics in Aquatic Microcosms, ORNL-4318 (in press).

Margaret S. Riedinger and L. C. Emerson
Determination of Optical Constants of Palladium by Ellipsometry, ORNL-TM-2114 (February 1968).

L. H. Toburen, M. Y. Nakai, and R. A. Langley
Part I. The Measurement of High-Energy Charge Transfer Cross Sections for Incident Protons and Atomic Hydrogen in Various Gases. Part II. The K-, L-, and M-Auger, L-Coster-Kronig, and the Conversion-Electron Spectra of Platinum in the Decay of ^{195}*Au,* ORNL-TM-1988 (November 1967).

R. C. Vehse and E. T. Arakawa
Optical and Photoemissive Properties of Evaporated Films of Palladium, Nickel, and Copper in the Vacuum Ultraviolet Spectral Region, ORNL-TM-2240 (in press).

R. E. Wilems and R. H. Ritchie
Nonlinear Interactions in Quantum Plasmas, ORNL-TM-2101 (June 1968).

H. A. Wright and W. S. Snyder
Differentiability of Set Functions, ORNL-TM-1952 (October 1967).

Papers

M-E. M. Abu-Zeid, L. G. Christophorou, J. G. Carter, R. D. Birkhoff, and J. A. Harter
Emission and Decay of Excited Organic Molecules Under Electron Impact, 11th Scintillation and Semiconductor Counter Symposium, February 28, 29–March 1, 1968, Washington, D.C.

E. T. Arakawa, L. C. Emerson, and R. D. Birkhoff
Optical Emission from Electron-Bombarded Metal Films, International Conference on Solid State Physics Research with Accelerators, September 25–28, 1967, Brookhaven National Laboratory, Upton, New York.

E. T. Arakawa, R. N. Hamm, R. H. Ritchie, and J. J. Cowan
Polarization of Light by Concave Diffraction Gratings, 2nd International Conference on Vacuum Ultraviolet Radiation Physics – Interactions with Solids, May 1–3, 1968, Gatlinburg, Tennessee.

J. C. Ashley and R. H. Ritchie
Quantum Treatment of Multiple Real Transitions, American Physical Society, Southeastern Section, November 2–4, 1967, Clemson, South Carolina.

S. I. Auerbach
Aspects of Radiation Ecology Related to Postattack Problems, OCD Staff College Seminar on Radiobiological Effects, University of Chicago, November 19–22, 1967, Chicago, Illinois.

Radiation Ecology, presented at Refresher Course, Principles of Ecology for Bio-Environmental Engineers, American Society of Zoologists, AAAS Meeting, December 27–28, 1967, New York, New York.

J. A. Auxier
Radiation Propagation and Shielding Experiments at the BRFN Tower Facility, American Nuclear Society, November 5–9, 1967, Chicago, Illinois.

K. Becker
Alpha Particle Registration in Plastics and Its Applications for Radon, Thermal, and Fast Neutron Personnel Dosimetry, Health Physics Society, June 16–20, 1968, Denver, Colorado.

The Effect of Oxygen and Humidity on Charged Particle Registration in Organic Foils, Radiation Research Society, April 21–25, 1968, Houston, Texas.

Personnel Dosimetry in Large-Scale Nuclear Emergencies, Symposium on Radiological Protection of the Public in Nuclear Mass Disasters, May 27–June 1, 1968, Interlaken, Switzerland.

K. Becker and J. S. Cheka
Silver-Activated Lithium Borate Glasses as Radiophotoluminescence Dosimeters with Low Energy Dependence, Radiation Research Society, April 21–25, 1968, Houston, Texas.

S. R. Bernard
A Random Compartment Model for Radionuclide Retention, Health Physics Society, June 16–20, 1968, Denver, Colorado.

R. D. Birkhoff
Electron Slowing-Down Spectra in Infinite Homogeneous Isotropic Media, National Bureau of Standards, July 11, 1967, Washington, D.C.

B. G. Blaylock
The Fecundity of a Population of Gambusia affinis affinis *Inhabiting a Lake Contaminated with Radioactive Waste,* Ecological Society of America, June 16–20, 1968, Madison, Wisconsin.

W. J. Boegly, Jr., F. L. Parker, and E. G. Struxness
Disposal of Radioactive Wastes in Geologic Formations, First International Congress of the International Radiation Protection Association, September 5–10, 1966, Rome, Italy.

W. J. Boegly, Jr., and E. G. Struxness
Application of Hydraulic Fracturing to Waste Disposal, National Convention of the Water Pollution Control Federation, October 8–13, 1967, New York, New York.

H. M. Butler and F. F. Haywood
Radiation Safety Practices for Handling Accelerator Targets Containing Kilo-Curie Amounts of ^{3}H, Health Physics Society, June 16–20, 1968, Denver, Colorado.

L. G. Christophorou
Emission from Organic Liquids Excited by Electrons and Photons, Radiological Physics Contractors Meeting, AEC, October 24–25, 1967, Gaithersburg, Maryland.

L. G. Christophorou and A. A. Christodoulides
Scattering of Thermal Electrons by Polar Molecules, Radiation Research Society, April 21–25, 1968, Houston, Texas.

L. G. Christophorou and J. A. Stockdale
Dissociative Electron Attachment to Molecules, 20th Annual Gaseous Electronics Conference, October 18–20, 1967, San Francisco, California.

R. N. Compton
Electron Impact Excitation and Negative Ion Formation, Health Physics Society, June 17–19, 1968, Denver, Colorado.

R. N. Compton, L. G. Christophorou, and H. W. Dickson
Electron Capture by Hydrogen Halides, 5th International Conference on the Physics of Electronic and Atomic Collisions, July 17–23, 1967, Leningrad, U.S.S.R.

M. J. Cook and W. S. Snyder
The Relative Importance of Cesium-137 Contamination in Various Foodstuffs in Terms of Total Dose for Various Age Groups of a Population, Health Physics Society, June 16–20, 1968, Denver, Colorado.

K. E. Cowser, Jacob Tadmor, D. G. Jacobs, and W. J. Boegly, Jr.
Evaluation of Krypton-85 and Hydrogen-3 in an Expanding Nuclear Fuel Reprocessing Industry, American Society of Civil Engineering National Meeting on Environmental Engineering, May 13–17, 1968, Chattanooga, Tennessee.

Julian Crowell and R. H. Ritchie
Radiative Decay of Coulomb Stimulated Plasmons in Spheres, American Physical Society, Southeastern Section, November 2–4, 1967, Clemson, South Carolina.

Patricia Dalton and J. E. Turner
New Evaluation of Mean Excitation Energies for Use in Radiation Dosimetry, Health Physics Society, June 16–20, 1968, Denver, Colorado.

Wallace de Laguna
Status of Waste Disposal by Hydraulic Fracturing, Health Physics Society Meeting, June 16–20, 1968, Denver, Colorado.

F. M. Empson, R. L. Bradshaw, W. C. McClain, and B. L. Houser
Summary of Results of a Demonstration of the Disposal of High-Level Solidified Radioactive Wastes in a Salt Mine, Health Physics Society Meeting, June 16–20, 1968, Denver, Colorado.

M. R. Ford and W. S. Snyder
A Monte Carlo Estimation of Absorbed Fractions in Body Organs of Realistic Size, Shape, Composition, and Density from a Source of Photons Distributed Uniformly in an Organ, Health Physics Society, June 16–20, 1968, Denver, Colorado.

F. W. Garber, R. D. Birkhoff, and S. J. Nalley
Determination of Low-Energy Electron Attenuation Lengths in Aluminum, American Physical Society, Southeastern Section, November 2–4, 1967, Clemson, South Carolina.

W. R. Garrett
Non-Adiabatic Target Distortion in Low-Energy Atomic Scattering, 5th International Conference on the Physics of Electronic and Atomic Collisions, July 17–23, 1967, Leningrad, U.S.S.R.

V. G. Horton, L. R. Painter, and E. T. Arakawa
Evaluation of Reflection Type Polarizers in the Vacuum Ultraviolet, American Physical Society, Southeastern Section, November 2–4, 1967, Clemson, South Carolina.

D. G. Jacobs and K. E. Cowser
The Release of Tritium from an Expanding Nuclear Power Economy and Its Long Range Behavior in the Environment, Health Physics Society Meeting, June 16–20, 1968, Denver, Colorado.

S. V. Kaye
Status of the ORNL Dose Estimation Program Related to Excavation of a Sea-Level Canal with Nuclear Explosives, Subcontractors Working Meeting, Battelle Memorial Institute, November 14, 1967, Columbus, Ohio.

S. V. Kaye, P. S. Rohwer, K. E. Cowser, and W. D. Turner
Estimating Radiation Doses to Populations for Projects Involving Reactor Siting and Peaceful Nuclear Explosives, Annual Meeting of the Health Physics Society, June 16–20, 1968, Denver, Colorado.

T. F. Lomenick
Geoseismological Factors in Power Reactor Siting, Health Physics Society Meeting, June 16–20, 1968, Denver, Colorado.

Earthquakes and Reactor Safety, Geological Society of America Annual Meeting, November 19–22, 1967, New Orleans, Louisiana.

D. R. Nelson and F. J. Davis
Thermal Electron Diffusion Coefficient Determinations from Time-of-Flight Swarm Studies, 20th Annual Gaseous Electronics Conference, October 18–20, 1967, San Francisco, California.

J. S. Olson
Productivity, Balance and Turnover in Major World Ecosystems, American Association for the Advancement of Science, December 27, 1967, New York, New York.

J. S. Olson, Giovanni Cristofolini, and Margaret Olson
Computer Processing of Information on Ecological Systems, published in Proceedings of the Symposium on Information Problems in Natural Sciences, December 1967, Universidad Nacio, Mexico.

L. R. Painter and R. D. Birkhoff
Reflectivity of Liquid H_2O in the Vacuum Ultraviolet, American Physical Society Southeastern Section, November 2–4, 1967, Clemson, South Carolina.

Linda R. Painter, R. N. Hamm, E. T. Arakawa, and R. D. Birkhoff
Electronic Properties of Liquid Water in the Vacuum Ultraviolet, 2nd International Conference on Vacuum Ultraviolet Radiation Physics – Interactions with Solids, May 1–3, 1968, Gatlinburg, Tennessee.

J. W. Poston
Radiation Dosimetry Studies at the Health Physics Research Reactor, American Nuclear Society, 7th Annual Student Conference, April 4–7, 1968, Gainesville, Florida.

D. E. Reichle
Measurement of Elemental Assimilation by Arthropods from Radioisotope Retention Patterns, AIBS Meeting, August 27–September 1, 1967, College Station, Texas.

Secondary Productivity, American Association for the Advancement of Science, December 27, 1967, New York, New York.

Productivity of the Evergreen Bagworm Thyridopteryx ephemeraeformis *(Haworth) on Different Host Plants,* Ecological Society of America, June 18–20, 1968, Madison, Wisconsin.

R. H. Ritchie
Nonlinear Interactions in Quantum Plasmas, National Bureau of Standards, July 11, 1967, Washington, D.C.

Nonlinear Interactions in Quantum Plasmas, 2nd International Conference on Vacuum Ultraviolet Radiation Physics – Interactions with Solids, May 1–3, 1968, Gatlinburg, Tennessee.

R. H. Ritchie and R. E. Wilems
Nonlinear Interactions Involving Energetic Electrons and Photons in Quantum Plasmas, International Conference on Solid State Physics Research with Accelerators, September 25–28, 1967, Brookhaven National Laboratory, Upton, New York.

P. S. Rohwer, K. E. Cowser, W. S. Snyder, and E. G. Struxness
An Approach for Assessing Potential Population Exposures, Health Physics Society Midyear Topical Symposium, January 24–25, 1968, Augusta, Georgia.

H. C. Schweinler
Determination of Symmetry Orbitals of an n-Atomic Molecule, American Physical Society, August 31–September 2, 1967, Seattle, Washington,

Determination of Normal Coordinates of an n-Atomic Molecule, Symposium on Molecular Structure and Spectra, September 5–9, 1967, Columbus, Ohio.

A. F. Shinn
Food Crops and Postattack Recovery, National Academy of Sciences, Office of Civil Defense and Office of Emergency Planning, November 6–9, 1967, Fort Monroe, Virginia.

The Effects of Ionizing Radiation on Worker Honey Bees, Apis mellifera *L. (Hymenoptera, Apidae),* Entomological Society of America, November 27–30, 1967, New York, New York.

A. F. Shinn with J. C. Bresee and S. A. Griffin
The Vulnerability of Food to Nuclear Attack, International Conference on Radiological Protection of the Public in a Nuclear Mass Disaster, May 26–June 2, 1968, Interlaken, Switzerland.

W. S. Snyder, M. R. Ford, and G. G. Warner
A Study of Individual Variation of Excretion of Plutonium by Man and of Its Significance in Estimating the Systemic Burden, Bioassay and Analytical Chemistry, October 12–13, 1967, Berkeley, California.

W. S. Snyder, H. A. Wright, J. E. Turner, and J. Neufeld
Calculations of Depth Dose from Neutrons and Protons of High Energy and Their Interpretation for Radiation Protection, American Nuclear Society, June 9–13, 1968, Toronto, Canada.

J. L. Stanford, H. E. Bennett, J. M. Bennett, E. J. Ashley, and E. T. Arakawa
Excitation of Surface Plasmons in Rough Silver Films by Normally Incident Light, 2nd International Conference on Vacuum Ultraviolet Radiation Physics – Interactions with Solids, May 1–3, 1968, Gatlinburg, Tennessee.

Peggy L. Stewart and Isabel H. Tipton
Techniques in the Analysis of Human Diets and Excreta, Southeastern Section of the Society for Applied Spectroscopy, Birmingham, Alabama, September 1967.

J. A. D. Stockdale, R. N. Compton, and P. W. Reinhardt
Measurement of Reaction Rates for the Negative Ion Molecule Reactions $H^- + H_2O \rightarrow OH^- + H_2$ *and* $D^- + D_2O \rightarrow OD^- + D_2$ *at Ion Energies near 1 eV,* American Physical Society, April 22–25, 1968, Washington, D.C.

Tsuneo Tamura
Movement of Cesium-137 by Runoff and Erosion from a Soil Under Different Cover Conditions, Post-attack Recovery Symposium, November 6–7, 1967, Fort Monroe, Virginia.

F. G. Taylor, Jr.
Radiation-Induced Anatomical Modifications in Forest Trees, Association of Southeastern Biologists, April 18–21, 1968, Athens, Georgia.

W. A. Thomas
Decomposition of Loblolly Pine Needles With and Without Addition of Dogwood Leaves, Ecological Society of America, December 26–31, 1967, New York, New York.

J. H. Thorngate and J. A. Auxier
Fast Neutron Spectrometry for Radioprotection, Symposium on Nuclear Electronics and Radioprotection, March 4–8, 1968, Toulouse, France.

Isabel H. Tipton
Trace Elements in Human Tissue – Normal Values, International Atomic Energy Panel Meeting on "Activation Analysis in the Study of Mineral Element Metabolism in Man," Tehran, Iran, June 1968.

Isabel H. Tipton, Peggy L. Stewart, and Judith Dickson
Patterns of Elemental Excretion in Long-Term Balance Studies, Health Physics Society, June 16–20, 1968, Denver, Colorado.

J. E. Turner, V. E. Anderson, and Kenneth Fox
Ground-State Energy Eigenvalues and Eigenfunctions for Electrons in a Stationary Electric Dipole Field, American Physical Society, April 22–25, 1968, Washington, D.C.

R. C. Vehse and E. T. Arakawa
Photoemission and Optical Measurements for Evaporated Films of Nickel and Copper in the Vacuum Ultraviolet, American Physical Society, January 29–February 1, 1968, Chicago, Illinois.

Evidence for Discrete Energy Losses in Vacuum Ultraviolet Photoemission from Evaporated Ni Films, 2nd International Conference on Vacuum Ultraviolet Radiation Physics – Interactions with Solids, May 1–3, 1968, Gatlinburg, Tennessee.

R. B. Vora, M. A. Prasad, and J. E. Turner
Effect of Delta-Ray Buildup in High-Energy Dose Calculations, Health Physics Society, June 16–20, 1968, Denver, Colorado (presented by J. E. Turner).

R. E. Wilems and R. H. Ritchie
A Quantum Theory of an Imperfect Bounded Plasma, American Physical Society, Southeastern Section, November 2–4, 1967, Clemson, South Carolina.

M. W. Williams, E. T. Arakawa, and R. C. Vehse
Photoelectric Emission from Al and from Al_2O_3, American Physical Society, April 22–25, 1968, Washington, D.C.

R. B. Williams and M. B. Murdoch
Compartmental Analysis of Production and Decay of Juncus roemerianus, Association of Southeastern Biologists, April 18–21, 1968, Athens, Georgia [*ASB Bull.* **15**, 59 (1968)].

J. P. Witherspoon
Genetic Modification of Radiosensitivity in Populus deltoides, Association of Southeastern Biologists, April 18–21, 1968, Athens, Georgia.

H. A. Wright
Calculation of the Buildup of Dose in Tissue Irradiated by High-Energy Neutrons and Protons, Symposium on Microdosimetry, November 13–15, 1967, Ispra, Italy.

Publications

M-E. M. Abu-Zeid, L. G. Christophorou, J. G. Carter, R. D. Birkhoff, and J. A. Harter
"Emission and Decay of Excited Organic Molecules Under Electron Impact," to be published in *IEEE Transactions of Nuclear Science.*

E. T. Arakawa, L. C. Emerson, and R. D. Birkhoff
"Optical Emission from Electron-Bombarded Metal Films," pp. 144–54 in *Proceedings of International Conference on Solid State Physics Research with Accelerators, September 25–28, 1967, Brookhaven National Laboratory* (ed. by A. N. Goland), BNL-50083 (1968).

E. T. Arakawa and M. W. Williams
"Optical Properties of Aluminum Oxide in the Vacuum Ultraviolet," submitted for publication in the *Journal of Physics and Chemistry of Solids.*

J. C. Ashley, L. S. Cram, and E. T. Arakawa
"Photon Emission from Al Foils Bombarded by Non-Normally Incident Electrons," *Phys. Rev.* **160**, 313–15 (1967).

J. C. Ashley and R. H. Ritchie
"Quantum Treatment of Multiple Real Transitions," submitted for publication in the *Physical Review.*

Leroy Augenstein, Edward Yeargers, James Carter, and DeVaughn Nelson
"Excitation, Dissipative, and Emissive Mechanisms in Biochemicals," *Radiation Res.* Suppl. 7, 128–38 (1967).

S. I. Auerbach, D. A. Crossley, Jr., and A. F. Shinn
"Postattack Insect Problems," *Proceedings of Symposium on Postattack Recovery from Nuclear War, April 1968.*

S. I. Auerbach, W. A. Thomas, and J. S. Olson
Accumulation and Cycling of Calcium by Flowering Dogwood Trees, ORNL-TM-1910 (August 1967).

J. A. Auxier

"Dosimetry and Exposures in Nuclear Accidents," *Nucl. Safety* **8**(4), 382–85 (Summer 1967).

"Special Methods in Radiation Dosimetry," pp. 215–51 in *Principles of Radiation Protection,* K. Z. Morgan and J. E. Turner (eds.), Wiley, New York, 1967.

"Physical Problems of Dosimetry of Neutrons and Protons," pp. 181–94 in *Accidental Irradiation at Place of Work,* S. A. Vaillant-Carmanne, Liege, Belgium, 1967.

Proceedings: Long-Range Biomedical and Psychosocial Effects of Nuclear War, Vol. 1, *First Interdisciplinary Conference,* DASIAC Special Report 67 (February 1968).

J. A. Auxier, W. S. Snyder, and T. D. Jones

"Neutron Interactions and Penetration in Tissue," pp. 275–316 in *Radiation Dosimetry,* vol. I, 2d ed. (ed. by F. H. Attix and W. C. Roesch), Academic, New York, 1968.

C. E. Baker and P. B. Dunaway

"Retention of ^{134}Cs as an Index to Metabolism in the Cotton Rat (*Sigmodon hispidus*)," to be published in *Health Physics.*

K. Becker

"Solid State and Chemical Radiation Dosimetry in Medicine and Biology" (book review), *Health Phys.* **14**, 526 (1968).

"Interpretation von Personendosismessungen – Ergebnisse eines OECD-ENEA Symposium in Stockholm," *Atomwirtschaft* **13**, 104 (1968).

Report of Trip to Europe by K. Becker During Period January 5, 1968–January 17, 1968, February 21, 1968 (internal memorandum).

"Alpha Particle Registration in Plastics and Its Application for Radon, Thermal, and Fast Neutron Personnel Dosimetry," to be published in *Health Physics.*

"The Effect of Oxygen and Humidity on Charged Particle Registration in Organic Foils," to be published in *Radiation Research.*

"Principles and Basic Dosimetric Properties of Radiophotoluminescence in Silver-Activated Glasses," to be published in *Proceedings of NATO Summer School on Solid-State Dosimetry, Brussels, Belgium, September 4 Through 15, 1967.*

"Nuclear Track Registration in Solids by Etching," to be published in *Biophysik.*

"Personnel Dosimetry in Large-Scale Nuclear Emergencies," to be published in *Proceedings of Symposium on Radiological Protection of the Public in Nuclear Mass Disasters, May 27–June 1, 1968, Interlaken, Switzerland.*

"Thermally Stimulated Exoelectron Emission (TSEE) as a Method for Sensitive Dose Measurements Using Unactivated Lithium Fluoride," to be published in *Health Physics.*

K. Becker and J. S. Cheka

"Silver-Activated Lithium Borate Glasses as Radiophotoluminescence Dosimeters with Low Energy Dependence," to be published in *Health Physics.*

"LET Effects on the Radiophotoluminescence in Silver-Activated Dosimeter Glasses," to be published in *Physics in Medicine and Biology.*

"High Level Glass Dosimeters with Low Energy Dependence," to be published in *Nuclear Applications.*

K. Becker and E. M. Robinson

"Dosimetry by Thermally Stimulated Exoelectron (After-) Emission," to be published in *Health Physics.*

R. D. Birkhoff

"Dose from Electrons and β Rays," chap. 8, pp. 242–67 in *Principles of Radiation Protection* (ed. by K. Z. Morgan and J. E. Turner), Wiley, New York, 1967.

R. D. Birkhoff, W. J. McConnell, R. N. Hamm, and R. H. Ritchie
"Electron Flux Spectra in Aluminum; Analysis for LET Spectra and Excitation and Ionization Yields," pp. 241–54 in *Proceedings of 1st International Symposium on the Biological Interpretation of Dose from Accelerator-Produced Radiation, March 13–16, 1967, Berkeley, California* (ed. by Roger Wallace), USAEC/DTI CONF-670305 (1967).

J. B. Birks, L. G. Christophorou, and R. H. Huebner
"Excited Electronic States of Benzene and Naphthalene," *Nature* **217**, 809–12 (1968).

R. P. Blaunstein and L. G. Christophorou
"Electron Attachment to Halogenated Aliphatic Hydrocarbons," submitted for publication in the *Journal of Chemical Physics.*

B. G. Blaylock
"Effects of Ionizing Radiation on Interspecific Competition," Proceedings of Second National Symposium on Radioecology, Ann Arbor, Michigan (in press).

"The Fecundity of a *Gambusia affinis affinis* Population Exposed to Chronic Radiation," to be published in *Radiation Research.*

W. J. Boegly, Jr., and E. G. Struxness
"Application of Hydraulic Fracturing to Waste Disposal," in *Abstracts of Technical Papers,* 40th Annual Conference of the Water Pollution Control Federation, New York, New York, October 8–13, 1967.

W. J. Boegly, Jr., F. M. Empson, W. C. McClain, and F. L. Parker
"Disposal of High Activity Power Reactor Wastes in Salt Mines: Mine Renovations Required for Project Salt Vault," *Nuclear Engineering and Design* (in press).

W. P. Bonner, H. A. Bevis, and J. J. Morgan
"Removal of Strontium from Water by Activated Alumina," *Health Phys.* **12**(12), 1681–1703 (December 1966).

R. L. Bradshaw, W. L. Beck, H. W. Dickson, and W. F. Hanson
"High Dose Response of Glass Rod Dosimeters Irradiated at Temperatures up to 250°C," *Health Phys.* **13**(8), 910–15 (August 1967).

R. L. Bradshaw, F. M. Empson, W. J. Boegly, Jr., H. Kubota, F. L. Parker, and E. G. Struxness
"Properties of Salt Important in Radioactive Waste Disposal," pp. 643–58 in *Proceedings of the International Conference on Saline Deposits, Houston, Texas, November 12–17, 1962,* The Geological Society of America, Inc., Special Paper 88 (1968).

R. L. Bradshaw and T. F. Lomenick
"Rheology of Salt in Mine Workings," *Proceedings of Symposium on the Geology and Technology of Gulf Coast Salt, Louisiana State University, Baton Rouge, Louisiana, May 1–2, 1967* (in press).

R. L. Bradshaw, J. J. Perona, J. O. Blomeke, and W. J. Boegly, Jr.
Evaluation of Ultimate Disposal Methods for Liquid and Solid Radioactive Wastes: VI. Disposal of Solid Wastes in Salt Formations, ORNL-3358 (May 1968).

W. D. Burnett, T. G. Clark, J. R. Coleman, R. S. Denham, R. J. Everett, J. W. McKelvey, and S. Z. Mikhail
The Relative Hazards of Two RTG Fuels, Plutonium-238 Dioxide and Strontium-90 Titanate, Sandia Corporation Report SC-TM-67-606 (September 1967).

J. G. Carter, L. G. Christophorou, and M-E. M. Abu-Zeid
"Emission from Organic Liquids Excited by Electron Impact," *J. Chem. Phys.* **47**, 3879–84 (1967).

J. S. Cheka
"Long-Term Stability of Radiophotoluminescence in Metaphosphate Glass," to be published in *Health Physics.*

Report of Trip Abroad by J. S. Cheka During Period June 3, 1967–June 28, 1967, August 8, 1967 (internal memorandum).

L. G. Christophorou, M-E. M. Abu-Zeid, and J. G. Carter
"Emission and Decay of Liquid Benzene and Naphthalene Derivatives Excited by Electron Impact," submitted for publication in the *Journal of Chemical Physics.*

L. G. Christophorou and R. P. Blaunstein
"Nondissociative Electron Attachment to Aromatic Hydrocarbons," submitted for publication in *Radiation Research.*

L. G. Christophorou and A. A. Christodoulides
"Scattering of Thermal Electrons by Polar Molecules," to be published in the *Journal of Physics B (Proc. Phys. Soc.).*

L. G. Christophorou and R. N. Compton
"Interaction of Low-Energy Electrons with Polyatomic Molecules," *Health Phys.* **13**, 1277–1305 (1967).

L. G. Christophorou, R. N. Compton, and H. W. Dickson
"Dissociative Electron Attachment to Hydrogen Halides and Their Deuterated Analogues," *J. Chem. Phys.* **48**, 1949–55 (1968).

L. G. Christophorou and J. A. Stockdale
"Dissociative Electron Attachment to Molecules," *J. Chem. Phys.* **48**, 1956–60 (1968).

T. G. Clark
Dose Predictions and Biological Consequences Following Burnup of a $^{90}SrTiO_3$ *Source in Space,* Sandia Corporation Report SC-CR-67-2792 (August 1967).

R. N. Compton, R. H. Huebner, P. W. Reinhardt, and L. G. Christophorou
"Threshold Electron Impact Excitation of Atoms and Molecules: Detection of Triplet and Temporary Negative Ion States," *J. Chem. Phys.* **48**, 901–9 (1968).

R. N. Compton and R. H. Huebner
"Electron Impact Excitation and Negative Ion Formation in Polyatomic Molecules," submitted for publication in *Health Physics.*

R. N. Compton and W. R. Garrett
Report of Trip Abroad by R. N. Compton and W. R. Garrett During the Period July 14–August 4, 1967, Sept. 25, 1967 (internal memoradnum).

K. E. Cowser, P. S. Rohwer, E. G. Struxness, W. S. Snyder, and S. V. Kaye
ORNL-CF-67-72-21 (July 13, 1967).

K. E. Cowser and R. E. Blanco
Waste Treatment and Disposal Semiannual Progress Report, July–December 1967, ORNL-TM-2294 (in press).

H. L. Cromroy, W. A. Goldsmith, C. R. Phillips, and W. P. Bonner
"Uptake of Cesium-137 from Contaminated Soil by Selected Grass Crops," *Radiological Health Data and Reports* **8**(8), 421–24 (August 1967).

Julian Crowell and R. H. Ritchie
"Radiative Decay of Coulomb Stimulated Plasmons in Spheres," *Phys. Rev.* (in press).

J. W. Curlin, W. M. Ciesla, and J. C. Bell, Jr.
"Color Photos and the Southern Pine Beetle," *Photogrammetric Engr.* **33**, 883–88.

J. W. Curlin and J. P. Witherspoon
"Components and Estimates of Dose to Roots of Potted Plants Exposed to Fast Neutron Radiation," *Health Phys.* **14**, 165–68 (1968).

R. C. Dahlman, J. S. Olson, and K. Doxtader
"Nitrogen Economy of Grassland and Dune Soils," Conference on Biol. and Ecol. of Nitrogen, University of California, Davis (in press).

Patricia Dalton and J. E. Turner
"New Evaluation of Mean Excitation Energies for Use in Radiation Dosimetry," *Health Phys.* (in press).

D. M. Davis, J. A. Auxier, and K. Z. Morgan
"Dosimetry and Monitoring," to be published in *Encyclopaedia of Occupational Health and Safety,* International Labour Office, Geneva.

D. R. Davy
"Prediction of Biological Damage from Stopping-Power Theory," *Health Phys.* **13**, 1159–74 (1967).

Wallace de Laguna
"*Tritium and Other Environmental Isotopes in the Hydrological Cycle* (IAEA Technical Report Series No. 73)" (Book review), *Nucl. Appl.* **4**, 448–49 (June 1968).

"*Handbook of Physical Constants* (Sydney P. Clark, Jr., Ed.; Memoir 97, The Geological Society of America, 1966)" (Book review), *Health Phys.* **13**, 1043–44 (1967).

"*Practices in the Treatment of Low- and Intermediate-Level Wastes* (Proceedings of a Symposium, Vienna, 6–10 December 1965)" (Book review), *Health Phys.* **14**, 175–81 (1968).

Wallace de Laguna, Tsuneo Tamura, H. O. Weeren, E. G. Struxness, W. C. McClain, and R. C. Sexton
Engineering Development of Hydraulic Fracturing as a Method for Permanent Disposal of Radioactive Wastes, ORNL-4259 (in press).

P. B. Dunaway
"Life History and Populational Aspects of the Eastern Harvest Mouse," *Am. Midland Naturalist* **79**, 48–67 (1968).

P. B. Dunaway, G. E. Cosgrove, and J. D. Story
"*Capillaria* and *Trypanosoma* Infestations in *Microtus ochrogaster,*" *Bull. Wildlife Disease Assoc.* **4**, 18–20 (1968).

P. B. Dunaway, L. L. Lewis, J. D. Story, J. A. Payne, and J. M. Inglis
"Radiation Effects in the Soricidae, Cricetidae, and Muridae," *Proceedings Second National Symposium on Radioecology, Ann Arbor, Michigan* (in press).

B. R. Fish
"The Electrostatic Forces of Adhesion Between Particles," *Proceedings of Symposium on Electrostatic Effects Associated with Dried Powders, Fort Detrick, Maryland, April 25–26, 1967* (in press as of 6/25/68); also, ORNL-TM-1947 (Aug. 16, 1967).

Translation of "The Particle Size Spectrum of an Aerosol Carrying Radon Daughter-Products," by R. Reiter and W. Carnuth. Originally appeared as "Das Partikelspektrum eines mit Radonfolgerprodukten beladenen Aerosols," *Naturwissenschaften* **54**, 40–41 (1967). Submitted to ORNL Library for inclusion in *Nuclear Science Abstracts* (ORNL-tr-1804) September 28, 1967.

Kenneth Fox
"Bound States of an Electron in a Point Electric Dipole Field: Quantization of a Classical Solution," *Phys. Letters* **25A**, 345–46 (1967).

"Classical Motion of an Electron in an Electric Dipole Field – II. Point Dipole Case," *J. Phys. A (Proc. Phys. Soc.)* **1**, 124–27 (1968).

W. R. Garrett and L. D. Mullins
"*l*-Averaged Exchange Term in the Hartree-Fock Equations," *J. Chem. Phys.* (in press).

A. J. P. Gore
"The Supply of Six Elements By Rain to an Upland Peat Area," submitted to *Ecology.*

A. J. P. Gore and J. S. Olson
"Preliminary Models for Accumulation of Organic Matter in an Eriophorum/Calluma Ecosystem," *Aquilo, Ser. Botanica, Jubilee Volume.*

J. D. Hayes, E. T. Arakawa, and M. W. Williams
"Optical Properties of Vacuum Evaporated Selenium and Tellurium," submitted for publication in the *Journal of Applied Physics.*

H. H. Hubbell, Jr.
Report on Trip to Japan by H. H. Hubbell, Jr., During the Period January 21 to March 4, 1968, April 22, 1968 (internal memorandum).

R. H. Huebner and R. N. Compton
"Temporary Negative Ion Formation in Pyridine and Azulene," submitted for publication in *Physics Letters.*

"Threshold Electron Impact Excitation of Azulene," submitted for publication in *Physics Letters.*

G. S. Hurst
"Ionization Methods of Mixed Radiation Dosimetry," chap. 6, pp. 192–214 in *Principles of Radiation Protection* (ed. by K. Z. Morgan and J. E. Turner), Wiley, New York, 1967.

K. B. Jacobson, J. B. Murphy, and P. B. Dunaway
"Phylogenetic Relationships in a Group of Rodents on the Basis of Isoenzymes of Lactate Dehydrogenase," submitted to *Nature.*

D. R. Johnson and W. F. Ohnesorge
"Yield, Energy, and Angular Distributions of Neutrons Produced in Graphite, Copper, and Tantalum Targets Irradiated with 63 MeV Protons," *Atompraxis* **14**, 181–83 (1968).

T. D. Jones, W. S. Snyder, and A. M. Craig, Jr.
"Distribution of Dose and Dose Equivalent in a Cylindrical Tissue Phantom from Fission Sources of Neutrons," pp. 42–50 in *Colloque International sur la Dosimetrie des Irradiations dues a des Sources Externes (Dosimetry of Irradiations from External Sources), Paris, 23–27 Novembre 1964,* Tome I, Service Central de Protection contre les Rayonnements Ionisants, Le Vesinet, 1967.

K. Katoh and J. E. Turner
"A Study of Elementary Particle Interactions for High-Energy Dosimetry," *Health Phys.* **13**, 831–43 (1967).

S. V. Kaye
"Distribution and Retention of Orally Administered Radiotungsten in the Rat," *Health Phys.* (in press).

S. V. Kaye and S. J. Ball
"Systems Analysis of a Coupled Compartment Model for Radionuclide Transfer in a Tropical Environment," *USAEC Special Symposium Series* (in press).

S. V. Kaye and D. A. Crossley, Jr.
"Radiotungsten Retention by Two Insect Species," *Health Phys.* **14**, 162–65 (1968).

S. V. Kaye and D. J. Nelson
"Analysis of Specific Activity Concept as Related to Environmental Concentration of Radionuclides," *Nucl. Safety* **9**, 53–58 (1968).

S. V. Kaye with P. S. Rohwer
Age-Dependent Models for Estimating Internal Dose in Feasibility Evaluations of Plowshare Events, ORNL-TM-2229 (June 1968).

Estimating External Dose in Feasibility Evaluations of Plowshare Events, ORNL-TM-2249 (July 1968).

"Predicting Radiation Dose Equivalents for Populations: II. Results Obtained with the Dose Models," *BioScience* (in press).

S. V. Kaye, P. S. Rohwer, K. E. Cowser, and W. S. Snyder
"Predicting Radiation Dose Equivalents for Populations: I. Dose Models and Methods of Application," *BioScience* (in press).

S. V. Kaye with W. D. Turner and P. S. Rohwer
EXREM and INREM Computer Codes for Estimating Radiation Doses to Populations from Construction of a Sea-Level Canal with Nuclear Fxplosives, K-25 Report K-1752 (July 1968).

G. D. Kerr
A Neutron-Energy Threshold Detector System Employing Solid-State Nuclear Track Detector and Fissile Radiator Units, ORNL-TM-2120 (March 1968).

"*Radiation Dosimetry,* vol. II, 2d ed." (book review), *Health Phys.* **14**, 384–85 (1968).

G. D. Kerr and J. S. Cheka
"A Lithium-7 Phosphate Glass Detector for Exposure Measurements in Mixed Neutron Gamma-Ray Radiation Fields," to be published in *Health Physics.*

G. D. Kerr, J. W. Poston, and E. M. Robinson
Health Physics and Safety Guidelines for the DOSAR Facility, ORNL-TM-1981 (September 1967).

Govind S. Khandelwal
"Characteristic X-Ray Production in Atomic *K* Shell," *Phys. Rev.* **167**, 136–38 (1968).

J. T. Kitchings III, P. B. Dunaway, J. D. Story, and L. E. Tucker
"Use of Radioiron (^{59}Fe) as an Index to Hemopoietic Damage Caused by Ionizing Radiation," *J. Tenn. Acad. Sci.* (in press).

C. E. Klots
"Transition Yields in Irradiated Gases," to be published in *Proceedings of International Conference on Radiation Chemistry, Argonne, Illinois.*

T. F. Lomenick and R. L. Bradshaw
"Some Remarks on the Role of Small-Scale Model Studies in Evaluating the Stability of Underground Activities," pp. 498–500 in *Proceedings of the First Congress of the International Society of Rock Mechanics, Lisbon, 25th September–1st October 1966,* Laboratorio National de Engenharia Civil Lisboa, Portugal (1967).

T. F. Lomenick, D. G. Jacobs, and E. G. Struxness
"The Behavior of Strontium-90 and Cesium-137 in Seepage Pits at ORNL," *Health Phys.* **13**(8), 897–905 (August 1967).

T. F. Lomenick and Herbert Robertson
"Seismological and Geophysical Instrumentation in Reactor Safety," *Nucl. Safety* **9**(2), 120–24 (March–April 1968).

R. A. MacRae, E. T. Arakawa, and M. W. Williams
"Optical Properties of Vacuum-Evaporated White Tin," *Phys. Rev.* **162**, 615–20 (1967).

W. C. McClain
"The Effect of Nonelastic Behavior of Rocks," pp. 204–16 in *Failure and Breakage of Rocks,* American Institute of Mining, New York, 1967.

"Hydraulic Fracturing as a Waste Disposal Method," pp. 135–47 in *Proceedings of IAEA Symposium on Disposal of Radioactive Wastes into the Ground, May 29 Through June 2, 1967, Vienna,* International Atomic Energy Agency, Vienna, Austria, 1967.

W. C. McClain, R. L. Bradshaw, and F. M. Empson
"Disposal of High-Level Solidified Wastes in Salt Mines," pp. 549–62 in *Proceedings of IAEA Symposium on Disposal of Radioactive Wastes into the Ground, May 29 Through June 2, 1967, Vienna,* International Atomic Energy Agency, Vienna, Austria, 1967.

W. J. McConnell, R. N. Hamm, R. H. Ritchie, and R. D. Birkhoff
"Electron Flux Spectra in Aluminum: Analysis for LET Spectra and Ionization Yields," *Radiation Res.* **33**, 216–28 (1968).

K. Z. Morgan
"Health Physics," pp. 306–9 in *The Encyclopedia of Physics* (ed. by R. M. Besancon), Reinhold, New York, 1966.

"Ionizing Radiation," pp. 1–82 in *Ionizing Radiation,* American Public Health Association, New York, 1966.

"History of Damage and Protection from Ionizing Radiation," pp. 1–75 in *Principles of Radiation Protection* (ed. by K. Z. Morgan and J. E. Turner), New York, 1967.

"Maximum Permissible Exposure Levels – External and Internal," *ibid.,* pp. 497–537.

"Common Sources of Human Exposure to Ionizing Radiation in the United States," *Am. Engr.,* July 1968, pp. 38–42.

"Protection Against Ionizing Radiation," *Salt* **4**, 8 (1967).

"Population Exposure to X-Rays," pp. 363–81 in *Electronics Products Radiation Control,* hearings before the Subcommittee on Public Health and Welfare of the Committee on Interstate and Foreign Commerce, House of Representatives, 90th Congress, First Session, on HR-10790, USGPO, Washington, 1967.

"Maximum Permissible Exposure of Miners in the United States to Radon and Its Daughters," pp. 1216–22 in *Radiation Exposure of Uranium Miners,* hearings before the Subcommittee on Research, Development, and Radiation of the Joint Committee on Atomic Energy, Congress of the United States, 90th Congress, First Session, part II, USGPO, Washington, 1967.

"Reduction of Unnecessary Medical Exposure," pp. 46–64 in *Radiation Control for Health and Safety Act of 1967,* hearings before the Committee on Commerce, United States Senate, 90th Congress, First Session, on S. 2067, USGPO, Washington, 1968.

"The Role of Nuclear Energy in the Control of Air Pollution," *Nucl. Safety* (in press as of 6/25/68).

K. Z. Morgan and L. C. Emerson
"Dose from External Sources of Radiation," chap. 9, pp. 263–300 in *Principles of Radiation Protection* (ed. by K. Z. Morgan and J. E. Turner), Wiley, New York, 1967.

K. Z. Morgan and J. E. Turner (Eds.)
Principles of Radiation Protection, Wiley, New York, 1967.

W. T. Naff, C. D. Cooper, and R. N. Compton
"Transient Negative Ion States in Alicyclic and Aromatic Fluorocarbon Molecules," submitted for publication in the *Journal of Chemical Physics.*

E. C. Neal, B. C. Patten, and C. E. DePoe
"Periphyton Growth on Artificial Substrates in a Radioactively Contaminated Lake," *Ecology* **48**(6), 918–24 (1967).

D. J. Nelson
"Microchemical Constituents in Contemporary and Pre-Columbian Clam Shell," pp. 185–203 in *Quaternary Paleoecology* (ed. by E. J. Cushing and H. E. Wright, Jr.), Yale University Press, 1967.

"Ecological Behavior of Radionuclides in the Clinch and Tennessee Rivers," in *Reservoir Fishery Resources Symposium* (in press).

"Environmental Biology" (book review), *Environ. Sci. Technol.* **1**, 444–45 (1967).

"Cesium, Cesium-137, and Potassium Concentrations in White Crappie and Other Clinch River Fish," *Proc. Second National Symposium on Radioecology* (in press).

D. R. Nelson, J. G. Carter, R. D. Birkhoff, R. N. Hamm, and L. G. Augenstein
"Yields of Luminescence from X-Irradiated Biochemicals," *Radiation Res.* **32**, 723–43 (1967).

J. Neufeld, L. C. Emerson, F. J. Davis, and J. E. Turner

"The Passage of Heavy Charged Particles, Gamma Rays, and X-Rays Through Matter," chap. 2, pp. 76–113 in *Principles of Radiation Protection* (ed. by K. Z. Morgan and J. E. Turner), Wiley, New York, 1967.

Jacob Neufeld and Harvel Wright
"Excitation of Hydromagnetic Waves by a Helical Proton Stream," pp. 121–24 in *Proceedings of Symposium on Electromagnetic Wave Theory, Delft, September 6–11, 1965,* Pergamon, London, 1967.

T. P. O'Farrell and P. B. Dunaway
"Effects of Irradiation on ^{131}IUDR Incorporation by Cotton Rats," to be published in *Radiation Research.*

"Incorporation and Tissue Distribution of a Thymidine Analog in the Cotton Rat, *Sigmodon hispidus,*" *Comp. Biochem. Physiol.* **22**, 435–50 (1967).

J. S. Olson
"Distribution and Radiocesium Transfers of Roots in a Tagged Mesophytic Appalachian Forest in Tennessee," submitted to *International Biological Program Symposium on Methods of Productivity Studies in Root-Systems and Rhizosphere Organisms, Moscow, USSR, August 1968.*

"Use of Tracer Techniques for the Study of Biogeochemical Cycles," pp. 271–88 in *Functioning of Terrestrial Ecosystems at the Primary Production Level,* Proc. of the Copenhagen Symposium, UNESCO, 1968.

J. S. Olson and V. R. R. Uppuluri
"Ecosystem Maintenance and Transformation Models as Markov Processes with Absorbing Barriers," pp. 3.1–3.5 in *Some Mathematical Models in Biology,* University of Michigan, December 1967.

L. Robinson Painter, R. N. Hamm, E. T. Arakawa, and R. D. Birkhoff
"Electronic Properties of Liquid Water in the Vacuum Ultraviolet," submitted for publication in *Physical Review Letters.*

Frank L. Parker
"Disposal of Low Level Radioactive Wastes into the Oceans," *Nucl. Safety* **8**(4), 376–82 (Summer 1967).

"Radioactive Wastes from Fusion Reactors," *Science* **159**(3810), 83–84 (Jan. 5, 1968).

J. W. Poston
Report of Trip Abroad by J. W. Poston During Period December 9, 1967–December 17, 1967, Jan. 29, 1968 (internal memorandum).

J. W. Poston, K. W. Crase, and E. M. Robinson
Thermal Neutron Fluence Measurements in the DOSAR Facility Thermal Pile, ORNL-TM-2009 (November 1967).

J. R. Reed and D. J. Nelson
"Radiostrontium Uptake in Flesh and Blood of Bluegills (*Lepomis macrochirus*)," *Proc. Second National Symposium on Radioecology* (in press).

D. E. Reichle
"Relation of Body Size to Food Intake, Oxygen Consumption, and Trace Element Metabolism in Forest Floor Arthropods," *Ecology* (in press).

D. E. Reichle and D. A. Crossley, Jr.
"Investigations on Heterotrophic Productivity in Forest Insect Communities," *Warsaw, Poland, Symposium on Principles and Methods of Secondary Productivity in Terrestrial Ecosystems,* Polish Academy of Sciences, Warsaw.

"Trophic Level Concentrations of Cesium-137, Sodium, and Potassium in Forest Arthropods," *Proc. Second National Symposium on Radioecology, Ann Arbor, Michigan* (in press).

D. E. Reichle, M. H. Shanks, and D. A. Crossley, Jr.
"Calcium, Potassium and Sodium Content of Forest Floor Arthropods," submitted to *Annals of the Entomological Society of America.*

D. E. Reichle with Eliot C. Williams
"Radioactive Tracers in the Study of Energy Turnover by a Grazing Insect, *Chrysochus auratus Fab.,*" *Oikos* **19**, 10–18 (1968).

R. H. Ritchie
"A Note on Optical Bremsstrahlung in a Dielectric Medium," submitted for publication in the *Journal of Experimental and Theoretical Physics* (Russian journal).

"The Physical Basis of Radiation Dosimetry," chap. 4, pp. 137–56 in *Principles of Radiation Protection* (ed. by K. Z. Morgan and J. E. Turner), Wiley, New York, 1967.

"Radiative Decay of Tangential Surface Plasmons," submitted for publication in *Physics Letters.*

R. H. Ritchie, M. Y. Nakai, and R. D. Birkhoff
"Low-Energy Electron Mean Free Paths in Solids," in *Advances in Radiobiology,* vol. 3 (in press).

R. H. Ritchie and R. E. Wilems
"Nonlinear Interaction in Quantum Plasmas," pp. 155–65 in *Proceedings of International Conference on Solid State Physics Research with Accelerators, September 25–28, 1967, Brookhaven National Laboratory* (ed. by A. N. Goland), BNL-50083 (1968).

L. L. Robinson, L. C. Emerson, J. G. Carter, and R. D. Birkhoff
"Optical Reflectivities of Liquid Water in the Vacuum UV," *J. Chem. Phys.* **46**, 4548–49 (1967).

P. S. Rohwer and S. V. Kaye
Age-Dependent Models for Estimating Internal Dose in Feasibility Evaluations of Plowshare Events, ORNL-TM-2229 (July 1968).

"Predicting Radiation Dose Equivalents for Populations: II. Results Obtained with the Dose Models," *BioScience* (in press).

P. S. Rohwer and E. G. Struxness
Evaluation of the Biological Effects of Radiation, ORNL-CF-67-9-60 (September 1967).

W. F. Schaffer, Jr., W. J. Boegly, Jr., R. L. Bradshaw, and F. L. Parker
"Project Salt Vault: Design of Equipment," *Nuclear Engineering and Design* (in press).

W. F. Schaffer, Jr., I. Spiewak, R. E. Blanco, and W. J. Boegly, Jr.
Survey of Potential Use of Nuclear Energy in Waste Water Treatment, ORNL-TM-2160 (June 1968).

H. A. Schroeder, Alexis P. Nason, and Isabel H. Tipton
"Essential Trace Metals in Man: Cobalt," *J. Chronic Diseases* **20**, 869–90 (1967).

H. C. Schweinler
"*Theory of Groups in Classical and Quantum Physics* – vol. I: *Mathematical Structures and the Foundations of Quantum Theory* (by Théo Kahan, American Elsevier Publishing Co., Inc., New York, 1965, 566 pp.)" (Book review), *Nucl. Sci. Eng.* **29**, 155 (1967).

A. F. Shinn
"Freshwater Fish in a Nuclear Disaster," pp. 51–54 in *Proc. Commercial Fish Farming Conference, Texas A & M University, February 1–2, 1967, College Station, Texas.*

"Grain Stocks and Protein Supplies, chap. I of ORNL-4184, part I, *Annual Progress Report, CDRP, March 1966–March 1967*, pp. 23–40.

W. S. Snyder
"The Bases of Standards for Radiation Protection: A Comparison of the Threshold Hypothesis and the Linear Hypothesis for the Dose-Effect Relation," part 2, p. 1256 in *Radiation Exposure of Uranium Miners,* hearings before the Subcommittee on Research, Development, and Radiation of the Joint Committee on Atomic Energy, Congress of the United States, 90th Congress, First Session, USGPO, Washington, 1967.

"Dose Estimation in the Context of Health Physics Regulations and Responsibilities," p. 269 in *Proceedings of the 1st International Symposium on the Biological Interpretation of Dose from Accelerator-Produced Radiation, March 13–16, 1967, Berkeley, California,* CONF-670305 (1967).

Testimony at hearings before the Subcommittee on Research, Development, and Radiation of the Joint Committee on Atomic Energy, Congress of the United States, 90th Congress, First Sesstion, Radiation Exposure of Uranium Miners, Part 1, p. 641, USGPO, Washington, 1967.

"The Variation of Dose in Man from Exposure to a Point Source of Gamma Rays," p. 7 in *Congres International sur la Radioprotection dans l'Utilisation Industrielle des Radioelements, Paris, 13–15 Decembre 1965,* Service Central de Protection Contre les Rayonnements Ionisants, Le Vesinet, 1967.

W. S. Snyder, Mary R. Ford, and Gordon Warner
"A Study of Individual Variation of Excretion of Plutonium by Man and of Its Significance in Estimating the Systemic Burden," *Proceedings of 13th Annual Bioassay and Analytical Chemistry Meeting, October 12–13, 1967, Berkeley, California* (in press).

"The Use of Excretion Data to Predict the Systemic Body Burden of Plutonium," *Proceedings of Symposium on Diagnosis and Treatment of Deposited Radionuclides, May 15–17, 1967, Richland, Washington* (in press).

Peggy L. Stewart and Isabel H. Tipton
"Shearing and Crushing Device for Mixing Powders," *Appl. Spectry.* **22**(1), 58 (1968).

J. A. Stockdale, L. G. Christophorou, and G. S. Hurst
"Capture of Thermal Electrons by Oxygen," *J. Chem. Phys.* **47**, 3267–70 (1967).

J. A. Stockdale, L. G. Christophorou, J. E. Turner, and V. E. Anderson
"Experimental Evidence for the Minimum Molecular Dipole Moment Necessary to Bind an Electron," *Phys. Letters* **25A**, 510–11 (1967).

J. A. Stockdale, R. N. Compton, and P. W. Reinhardt
"Collisions of Monoenergetic Electrons with NO_2: Lower Limits to the Electron Affinities of O_2 and NO," submitted for publication in the *Journal of Chemical Physics.*

J. A. D. Stockdale, R. N. Compton, and P. W. Reinhardt
"Measurement of the Cross Sections for the Reactions $H^- + H_2O \rightarrow OH^- + H_2$ and $D^- + D_2O \rightarrow OD^- + D_2$ at Incident Ion Energies near 2 Electron Volts," submitted for publication in *Physical Review Letters.*

G. F. Stone and J. H. Thorngate
Experimentally Determined Proton-Recoil Spectra in Tissue-Equivalent Material from 3 and 15 Mev Neutrons, ORNL-TM-1927 (October 1967).

J. C. Sutherland and E. T. Arakawa
"Optical Properties of Potassium for Protons of Energy 3.96 to 9.69 eV," *J. Opt. Soc. Am.* (in press).

Jacob Tadmor and K. E. Cowser
"Underground Disposal of Krypton-85 from Nuclear Fuel Reprocessing Plants," *Nucl. Eng. Design* **6**, 243–50 (1967).

Tsuneo Tamura
"Disposal of Radioactive Wastes by Hydraulic Fracturing: Part IV. Chemical Development of Waste-Cement Mixes," *Nucl. Eng. Design* **5**, 477–85 (1967).

"Reactions of Cesium-137 and Strontium-90 with Soil Minerals and Sesquioxides," pp. 465–78 in *Proceedings 8th International Congress of Soil Science, Bucharest, Romania, 1964,* Vol. III, Publishing House of the Academy of the Socialist Republic of Romania, 1967.

F. G. Taylor, Jr.
"Effects of Acute Gamma Radiation on Bud Production and Stem Elongation of Giant Sequoia Seedlings," *Radiation Botany* **8**, 67–70 (1968).

W. A. Thomas
"Accumulation and Cycling of Calcium by Dogwood Trees," *Ecol. Monographs* (submitted).

"Calcium Content of *Mycodiplosis alternata* (Diptera: Cecidomyiidae) Galls," *Ann. Entomol. Soc. Am.* **61**, 234–35 (1968).

"Calcium Distribution in Leaves: Autoradiography Versus Chemical Analysis," *Intern. J. Appl. Radiation Isotopes* **19**, 544–55 (1968).

"Cycling of ^{45}Ca by Dogwood Trees," *Proc. Second National Symposium on Radioecology* (in press).

"Decomposition of Loblolly Pine Needles With and Without Addition of Dogwood Leaves," *Ecology* **49** (in press).

"Dye and Calcium Ascent in Dogwood Trees," *Plant Physiol.* **42**, 1800–1802 (1967).

W. A. Thomas, S. I. Auerbach, and J. S. Olson
Accumulation and Cycling of Calcium by Flowering Dogwood Trees, ORNL-TM-1910 (August 1967).

J. H. Thorngate
"Dosimetry, Shielding, and Scattering II," in *Proceedings for the Conference on Principles of Radiation Protection, August 24–26, 1966, Oak Ridge, Tennessee,* CONF-660815 (June 28, 1968).

Report of Trip to Toulouse, France, by J. H. Thorngate During Period March 2–9, 1968, Apr. 17, 1968 (internal memorandum).

J. H. Thorngate and J. A. Auxier
"Fast Neutron Spectrometry for Radioprotection," to be published in *Proceedings of Symposium on Nuclear Electronics and Radioprotection, Toulouse, France, March 4 Through 8, 1968.*

J. E. Turner
"*Biophysikalische Probleme der Strahlenwirkung* (by H. Muth, Georg Thieme Verlag, 1966)" (Book review) *Health Phys.* **14**, 180 (1968).

"Calculation of Stopping Power of a Heavy Charged Particle in Matter," *Health Phys.* **13**, 1255–63, (1967).

"Effects of Shell Corrections to Stopping Power in Theoretical Dose Studies," pp. 53–59 in *Proceedings International Symposium on Dosimetry of Irradiations from External Sources, Paris, France, November 23–27, 1964,* Service Central de Protection Contre les Rayonnements Ionisants, Le Vesinet, 1967.

"*Health Physics: Principles of Radiation Protection* (by D. J. Rees, MIT Press, Cambridge, 1967)" (Book review), submitted for publication in *Nuclear Safety*.

"*Radiation Dosimetry*, vol. I: *Fundamentals* (ed. by F. H. Attix and W. C. Roesch)" (Book review), submitted for publication in *Nuclear Science and Engineering*.

J. E. Turner, V. E. Anderson, and Kenneth Fox
Ground State Energy Eigenfunctions for an Electron in a Stationary Electric Dipole Field, ORNL-4297 (in press); submitted for publication in *Physical Review*.

J. E. Turner, V. E. Anderson, H. A. Wright, W. S. Snyder, and J. Neufeld
"Dose from High-Energy Radiations at an Interface Between Two Media," pp. 306–17 in *Proceedings of 1st International Symposium on the Biological Interpretation of Dose from Accelerator-Produced Radiation, March 13–16, 1967, Berkeley, California* (ed. by Roger Wallace), USAEC/DTI CONF 670305 (1967).

"Radiation Dose from High Energy Nucleons in Targets Containing Soft Tissue and Bone," *Radiation Res.* (in press).

J. E. Turner and Kenneth Fox
"Classical Motion of an Electron in an Electric-Dipole Field – I. Finite Dipole Case," *J. Phys. A (Proc. Phys. Soc.)* **1**, 118–23 (1968).

J. E. Turner and Hal Hollister
On the Relationship of Collision Theory to the Interpretation of Relative Biological Effectiveness, ORNL-4215 (January 1968).

W. D. Turner, S. V. Kaye, and P. S. Rohwer
EXTREM and INREM Computer Codes for Estimating Radiation Doses to Populations from Construction of a Sea-Level Canal with Nuclear Explosives, K-25 Report K-1752 (in press).

V. R. Rao Uppuluri and S. R. Bernard

"A Two-Compartment Model with a Random Connection," pp. 175–88 in *Compartments, Pools, and Spaces in Medical Physiology* (ed. by Per-Erik E. Bergner and C. C. Lushbaugh), USAEC/DTI, Oak Ridge, 1967.

R. C. Vehse, J. L. Stanford, and E. T. Arakawa
"Discrete Energy Losses by Photoexcited Electrons in Silver and Palladium," *Phys. Rev. Letters* **19**, 1041–44 (1967).

R. C. Vehse, J. C. Sutherland, and E. T. Arakawa
"Angle-Doubler for Reflectance Measurements in Evacuated Systems," *Rev. Sci. Instr.* **29**, 268–69 (1968).

R. B. Vora, M. A. Prasad, and J. E. Turner
"Effect of Delta-Ray Buildup in High-Energy Dose Calculations," *Health Phys.* (in press).

E. B. Wagner, F. J. Davis, G. S. Hurst, and J. E. Parks
"Time-of-Flight Investigations of Electron Transport in Some Atomic and Molecular Gases," *J. Chem. Phys.* **47**, 3138–47 (1967).

R. E. Wilems and R. H. Ritchie
"A Quantum Theory of the Plasma Resonance Emission Process," *Phys. Rev. Letters* **19**, 1325–27 (1967).

W. H. Wilkie and B. R. Fish, "Scintillation Extrapolation Dosimetry of Small Beta-Emitting Sources," *Proceedings of Symposium on Solid State and Chemical Radiation Dosimetry in Biology and Medicine, Vienna, Austria, October 3–7, 1966*, IAEA, Vienna, 1967.

The Fluid Dynamics of a Spherical Particle: I. Tabulation of Settling Velocity, Reynolds Number, Drag Coefficient, Relaxation Time and Acceleration-Distance in Air and Water, SC-CR-68-3497 (1968).

M. W. Williams and E. T. Arakawa
"Optical Properties of Single Crystal Magnesium Oxide," *J. Appl. Phys.* **38**, 5272–76 (1967).

J. P. Witherspoon
"*Ecological Recovery,*" in *Project Little Harbor Summary Report,* to be published by the National Academy of Sciences.

"Effects of Internal ^{137}Cs Radiation on Seeds of *Liriodendron tulipifera,*" *Radiation Botany* **8**, 45–48 (1968).

"Radiosensitivity of Forest Tree Species to Acute Fast Neutron Radiation," in *Proc. Second National Symposium on Radioecology* (in press).

H. A. Wright
Report of Trip Abroad by H. A. Wright During the Period November 12–16, 1967, Jan. 10, 1968 (internal memorandum).

Lectures

S. I. Auerbach
Application of the Weinberg Criteria to Ecology and Study of Ecosystems, University of Georgia, May 9, 1968, Athens, Georgia.

Report of Recent Studies on Radiation Effects and Their Ecological Significance in Insects and Fish, University of Georgia, May 10, 1968, Athens, Georgia.

J. A. Auxier
The Present Status of Neutron Monitoring for Personnel Protection, U.S. Naval Reserve Meeting, December 20, 1967, Oak Ridge, Tennessee.

Nuclear Accident Dosimetry, Ten-Week Course in Health Physics, May 14, 1968, ORAU, Oak Ridge, Tennessee.

K. Becker
Nuclear Track Registration Dosimetry, Ten-Week Course in Health Physics, October 9, 1967, ORAU, Oak Ridge, Tennessee.

Radiophotoluminescence (Glass) Dosimetry, Ten-Week Course in Health Physics, October 9, 1967, ORAU, Oak Ridge, Tennessee.

Nuclear Track Registration in Dielectrics, U.S. Naval Research Laboratory, November 17, 1967, Washington, D.C.

Radiophotoluminescence (Glass) Dosimetry, University of Wisconsin, Department of Radiology, December 4, 1967, Madison, Wisconsin.

Photographic and Solid-State Personnel Dosimetry, Physikalisch-Technische Bundesanstalt, January 16, 1968, Braunschweig, Germany.

Nuclear Track Registration in Dielectrics, University of Tennessee Physics Seminar, February 12, 1968, Knoxville, Tennessee.

Neutron Dosimetry by Nuclear Track Registration in Solids, Ten-Week Course in Health Physics, May 9, 1968, ORAU, Oak Ridge, Tennessee.

Recent Work on Solid-State Dosimetry at ORNL, USAEC, Idaho Falls Operations Office, June 24, 1968, Idaho Falls, Idaho.

K. Becker and J. S. Cheka
Energy Independent Dosimeter Glasses for High Dose Levels, Third Biannual Dosimetry Workshop, April 8–9, 1968, Gaithersburg, Maryland.

B. G. Blaylock
The Effects of Radiation on Animal Populations, Tennessee Technological University, January 30, 1968, Cookeville, Tennessee.

W. C. Cate
Southern Pine Beetle (Dendroctonus frontalis) – *Detection, Life Cycle, and Control,* University of Tennessee, February 20, 1968, Knoxville, Tennessee.

L. G. Christophorou
Studies of Organic Molecules by Electron Impact, Louisiana State University, April 26, 1968, Baton Rouge, Louisiana.

R. N. Compton
Collisions of Low-Energy Electrons with Atoms and Molecules, University of Louisville, October 13, 1967, Louisville, Kentucky.

Studies of Organic Molecules by Electron Impact, Louisiana State University, November 7, 1967, Baton Rouge, Louisiana.

Studies of Organic Molecules by Electron Impact, Florida State University, November 9, 1967, Tallahassee, Florida.

Collisions of Low-Energy Electrons with Atoms and Molecules, Florida State University (School of Engineering), November 10, 1967, Tallahassee, Florida.

M. J. Cook
Biological Effects of Radiation, Department of Physics Course on Special Topics in Health Physics, University of Tennessee, May 16 and 23, 1968.

K. E. Cowser
Radioactive Waste Management, U.S. Army Nuclear Science Seminar, July 16–29, 1967, Oak Ridge, Tennessee.

Disposal of Radioactive Wastes, U.S. Army Nuclear Science Seminar, July 24, 1968, Oak Ridge, Tennessee.

Safety Evaluation of Radioactive Waste Systems, Radioactive Waste Management Seminar for Students of the University of Cincinnati, Oak Ridge National Laboratory, September 12, 1967, Oak Ridge, Tennessee.

F. M. Empson
Disposal of Radioactive Wastes in Salt Formations, Radioactive Waste Management Seminar for Students of the University of Cincinnati, Oak Ridge National Laboratory, September 12, 1967, Oak Ridge, Tennessee.

B. R. Fish
Development and Applications of ICRP Lung Model, Biohazards Study Group, Sandia Corporation, March 15, 1968, Albuquerque, New Mexico.

Physical and Mathematical Lung Models, Department of Environmental Sciences and Engineering, School of Public Health, University of North Carolina, March 20, 1968.

D. G. Jacobs
Introduction to Radioactive Waste Management, Radioactive Waste Management Seminar for Students of the University of Cincinnati, Oak Ridge National Laboratory, September 12, 1967, Oak Ridge, Tennessee.

Principles of Environmental Monitoring, Oak Ridge Institute of Nuclear Studies Health Physics Course, November 6, 1967, Oak Ridge, Tennessee.

Radioactive Releases to the Environment, Oak Ridge Institute of Nuclear Studies Health Physics Course, November 7, 1967, Oak Ridge, Tennessee.

Radioactive Waste Disposal and Principles of Environmental Monitoring, Civil Engineering Radiological Health Course, Vanderbilt University, April 23, 1968, Nashville, Tennessee.

Movement of Radionuclides in the Environment, Civil Engineering Radiological Health Course, Vanderbilt University, April 30, 1968, Nashville, Tennessee.

Principles of Environmental Monitoring, University of Tennessee Health Physics Course, April 25, 1968, Knoxville, Tennessee.

Radioactive Waste Disposal, University of Tennessee Health Physics Course, April 26, 1968, Knoxville, Tennessee.

Movement of Radionuclides in the Environment, University of Tennessee Health Physics Course, May 2, 1968, Knoxville, Tennessee.

Radioactive Waste Disposal, Field Training at ORNL for the Ten-Week ORAU Health Physics Students, Oak Ridge National Laboratory, October 23, 1967, Oak Ridge, Tennessee.

Radioactive Waste Disposal, Field Training at ORNL for the Ten-Week ORAU Health Physics Students, Oak Ridge National Laboratory, October 24, 1967, Oak Ridge, Tennessee.

Radioactive Waste Disposal and Movement of Radionuclides in the Environment, ORAU Health Physics Certification Course, May 7, 1968, Oak Ridge, Tennessee.

S. V. Kaye

Modeling the Movement of Radionuclides in the Environment, November 8, 1967; *Methods of Dose Estimation*, November 9, 1967, Health Physics Course, Oak Ridge Associated Universities, Oak Ridge, Tennessee.

Metabolism of Tungsten in the Rat, UT-AEC Farm, March 13, 1968, Oak Ridge, Tennessee.

Radiation Effects in the Environment, Sanitary Engineering Students, Vanderbilt University, April 30, 1968, Nashville, Tennessee, and Health Physics Students, University of Tennessee, May 3, 1968, Knoxville, Tennessee.

Bioenvironmental Feasibility Study for a Sea-Level Canal to Be Excavated with Nuclear Devices, Sanitary Engineering Students, Vanderbilt University, May 7, 1968, Nashville, Tennessee, and Health Physics Students, University of Tennessee, May 9, 1968, Knoxville, Tennessee.

Dose Estimation Techniques, Sanitary Engineering Students, Vanderbilt University, May 7, 1968, Nashville, Tennessee, and Health Physics Students, University of Tennessee, May 10, 1968, Knoxville, Tennessee.

T. F. Lomenick

Earthquakes and the Siting and Design of Nuclear Reactors, Radioactive Waste Management Seminar for Students of the University of Cincinnati, Oak Ridge National Laboratory, September 12, 1967, Oak Ridge, Tennessee.

Seismic and Geologic Considerations in Reactor Siting, Nuclear Safety Program Seminar, September 21, 1967, Oak Ridge, Tennessee.

Faulting, Ground Shaking, Tsunamis, and the Siting of Power Reactors, Department of Geology, University of Tennessee, October 3, 1967, Knoxville, Tennessee.

W. C. McClain

Disposal of Radioactive Wastes by Hydraulic Fracturing, Radioactive Waste Management Seminar for Students of the University of Cincinnati, Oak Ridge National Laboratory, September 12, 1967, Oak Ridge, Tennessee.

K. Z. Morgan

Health Physics; Professional Health Physics Organizations and Journals; Health Physics Certification, ORAU Health Physics Summer Institute, August 3, 1967, Oak Ridge.

Maximum Permissible Exposure of Miners in the United States to Radon and Its Daughter Products, Testimony before the Joint Committee on Atomic Energy, July 26, 1967, Washington, D.C.

Reduction of Unnecessary Medical Exposure, Testimony before the Senate Commerce Committee on Senate Bill S. 2067, August 28, 1967, Washington, D.C.

The Increasing Role of the Health Physicist, Failla Memorial Lecture, Greater New York Chapter of the Health Physics Society, September 20, 1967, New York, New York.

Population Exposure to Diagnostic X-Rays and the Resultant Damage Can Be Reduced to 10% of Their Present Levels While at the Same Time Increasing the Quality and Amount of Diagnostic Information, testimony before the House of Representatives on H.R. 10790, October 11, 1967, Washington, D.C.

Ionizing Radiation: Benefits Versus Risks, Southeastern Section of the American Physical Society, November 2, 1967, Clemson, South Carolina; Sigma Xi at the University of Tennessee, November 15, 1967, Knoxville, Tennessee; Medical College of Virginia, December 8, 1967, Roanoke, Virginia; Radiological Society of Greater Kansas City, February 15, 1968, Kansas City, Missouri; Western Pennsylvania Chapter of the Health Physics Society, June 3, 1968, Pittsburgh, Pennsylvania; Health Physics Society, June 18, 1968, Denver, Colorado.

Uranium Mining Problem as a Possible Oak Ridge National Laboratory Health Physics Research Program, 121st meeting of the AEC Division of Biology and Medicine Advisory Committee, November 9, 1967, Oak Ridge, Tennessee.

Education and Training, 121st Meeting of the AEC Division of Biology and Medicine Advisory Committee, November 9, 1967, Oak Ridge, Tennessee.

Health Physics Organization and Requirements for Certification, ORAU Ten-Week Course, November 16, 1967, Oak Ridge, Tennessee.

MPC in Air; MPC in Food, Air, and Water; Reducing Unnecessary Medical Diagnostic Exposure, West Virginia University, November 27, 1967, Morgantown, West Virginia.

Balancing Risks Against the Benefits of Medical Diagnostic Exposure, Lake Mead Chapter of the Health Physics Society, December 5, 1967, Las Vegas, Nevada.

Radiation Exposure Associated with Medical Diagnostic Studies, ORAU Medical Division Staff Meeting, December 12, 1967, Oak Ridge, Tennessee.

Maximizing the Ratio of Benefits to Risks from Ionizing Radiation, Northwestern University, March 4, 1968, Evanston, Illinois.

Internal Dose, University of Tennessee, March 28–29, 1968, April 4–5, 1968, April 11, 1968, April 18, 1968, Knoxville, Tennessee; Vanderbilt University, April 8–9, 1968, April 15–16, 1968, Nashville, Tennessee.

Health Physics – a New Science and a Challenging Profession: The Calculation of MPC for Radionuclides in Food, Air, and Water, Madison College, April 1, 1968, Harrisonburg, Virginia.

D. J. Nelson

Aquatic Ecology, U.S. Naval Reserve Research Co. 6-3, December 13, 1967, Oak Ridge, Tennessee.

Clams as Indicators of Paleochemical Environments, Department of Geology, Botany and Zoology, University of Tennessee, February 16, 1968, Knoxville, Tennessee.

Walker Branch Watershed Project, Pymatuning Laboratory of Ecology, University of Pittsburgh, July 2, 1968, Linesville, Pennsylvania.

Radioisotopes in Aquatic Ecology, Pymatuning Laboratory of Ecology, University of Pittsburgh, July 3, 1968, Linesville, Pennsylvania.

D. R. Nelson

Health Physics Research and Fellowship Opportunities at ORNL, St. John's University, October 23, 1967, Collegeville, Minnesota.

Health Physics Research and Fellowship Opportunities at ORNL, Mankato State College, October 23, 1967, Mankato, Minnesota.

Health Physics Research and Fellowship Opportunities at ORNL, St. Mary's College, October 24, 1967, Winona, Minnesota.

J. S. Olson

Systems Analysis in Ecology, University of Tennessee Engineering Seminar, March 27, 1968, Knoxville, Tennessee.

IBP Discussion of Systems Analysis, North Carolina State University, February 28, 1968, Raleigh, North Carolina.

Ecosystems Analysis of Trace Element Transfers in a Tulip Poplar Forest in Oak Ridge, University of North Carolina, February 28, 1968, Chapel Hill, North Carolina.

Stability and Change in Some Simple Ecosystem Models: Self Teaching and Simulation, Systems Ecology Symposium of The Ecological Society of America, June 18, 1968, Madison, Wisconsin.

D. E. Reichle

The Ecology of a Sphagnum Bog, Roanoke College, April 16, 1968, Salem, Virginia, and Winthrop College, March 26, 1968, Rock Hill, South Carolina.

Radiation Ecology at ORNL, Roanoke College, April 16, 1968, Salem, Virginia, and Muskingum College, December 11, 1967, New Concord, Ohio.

Trophic Dynamics of Arthropod Food Chains, Bucknell University, January 9, 1968, Lewisburg, Pennsylvania.

Biogeochemical Cycling of Cesium-137 in a Forest Ecosystem, Bradley University, October 10, 1967, Peoria, Illinois, and Muskingum College, December 12, 1967, New Concord, Ohio.

Ecology and the Ecosystem, Muskingum College, December 12, 1967, New Concord, Ohio.

R. H. Ritchie

Nonlinear Interactions in Quantum Plasmas, University of Kentucky, January 19, 1968, Lexington, Kentucky.

A. S. Rogowski

Movement of Radionuclides in Soil, Radioactive Waste Management Seminar for Students of the University of Cincinnati, Oak Ridge National Laboratory, September 12, 1967, Oak Ridge, Tennessee.

P. S. Rohwer

Evaluation of Nuclear Explosives Hazards in Plowshare, Health Physics Students, University of Rochester, May 20, 1968, Rochester, New York.

H. C. Schweinler

Molecular Potential Energy Curves, University of Kentucky, April 12, 1968, Lexington, Kentucky.

A. F. Shinn

Grain Stocks as a National Food Reserve, Civil Defense Research Project, Annual Information Meeting at Oak Ridge National Laboratory, April 25, 1968, Oak Ridge, Tennessee.

Research on the Effects of Radioactive Fallout on Honey Bees, Tennessee State Beekeepers Association Convention, October 6–7, 1967, Nashville, Tennessee.

Project Honey Bee at Oak Ridge National Laboratory, Florida State Beekeepers Association Annual Meeting, October 27–28, 1967, Perry, Florida.

Social and Economic Aspects of Nuclear Warfare as It Relates to Agricultural Crops and Animals, Seminar on Radiobiological Effects sponsored by the Staff College of the Office of Civil Defense, Battle Creek, Michigan, and the University of Chicago, at Chicago, Illinois, November 21, 1967.

W. S. Snyder

Estimation of Dose in the Body from Administration of Neohydrin Labeled with Mercury-203 or -197, South Texas Chapter of the Health Physics Society, September 7, 1967, Houston, Texas; Alabama Chapter of the Health Physics Society, May 24, 1968, Montgomery, Alabama.

Use of Excretion Data to Estimate the Systemic Burden of Plutonium, Eastern Idaho Chapter of the Health Physics Society, September 18, 1967, Idaho Falls, Idaho.

Role of ICRP, NCRP, and FRC in Establishing Permissible Limits and Concentrations, Oak Ridge Associated Universities Course in Health Physics, November 15, 1967, Oak Ridge.

The Dosimetric Aspects of Exposure to Radon Daughters in Mines, Baltimore-Washington Chapter of the Health Physics Society, December 7, 1967, Bethesda, Maryland; Southeastern Radiological Health Laboratory, May 24, 1968, Montgomery, Alabama.

A Multi-Compartment Model for Estimating Dose from HTO, Atlanta Chapter of the Health Physics Society, January 15, 1968, Atlanta, Georgia; Central Rocky Mountain Chapter of the Health Physics Society, February 28, 1968, Golden, Colorado; Southeastern Radiological Health Laboratory, May 24, 1968, Montogomery, Alabama.

Estimation of Internal Dose, University of Arkansas Graduate Students, April 25, 1968, ORNL.

Establishment of MPC's and MPD, Oak Ridge Associated Universities Course in Health Physics, June 4, 1968, Oak Ridge.

Tsuneo Tamura

Sediments: Their Physico-Chemical Makeup and Behavior, Corps of Engineers, Federal Water Pollution Control Association Board of Consultants Meeting, February 14, 1968, Buffalo, New York.

Ecological Studies in the Nuclear Industry, Taylor University, April 30, 1968, Upland, Indiana.

Crystal Chemistry of Clays, Taylor University, May 1, 1968, Upland, Indiana.

W. A. Thomas

Mineral Cycling, Kellogg Biological Station, Michigan State University, August 2, 1967, Hickory Corners, Michigan.

Research in Radiation Ecology, University of Arkansas Class in Radiological Health, April 24, 1967, Oak Ridge, Tennessee.

R. E. Wilems

Interaction of Photons with Bounded Quantum Plasmas, University of Tennessee, November 13, 1967, Knoxville, Tennessee.

R. B. Williams

Compartmental Analysis of Production and Decay of Juncus roemerianus, Association of Southeastern Biologists Meeting, April 19, 1968, Athens, Georgia.

Steady State Equilibriums in Simple Nonlinear Models, AIBS Interdisciplinary Meeting, June 20, 1968, Madison, Wisconsin.

J. P. Witherspoon

Radiation Ecology at ORNL, Winthrop College, November 7, 1967, Rock Hill, South Carolina.

Radiation Botany Studies at ORNL, U.S. Forest Service Institute of Forest Genetics, March 28, 1968, Rhinelander, Wisconsin.

Radiation Ecology, AEC Fellows, Oak Ridge National Laboratory, June 15, 1967, Oak Ridge, Tennessee.

Effects of Ionizing Radiation on Higher Plants, Tennessee Polytechnic Institute, February 20, 1967, Cookeville, Tennessee.

H. A. Wright

Research Work in Radiation Physics at ORNL and Fellowship Opportunities, University of Missouri at Rolla, October 4, 1967, Rolla, Missouri.

Research Work in Radiation Physics at ORNL and Fellowship Opportunities, State College of Arkansas, October 5, 1967, Conway, Arkansas.

Research Work in Radiation Physics at ORNL and Fellowship Opportunities, Arkansas College, October 6, 1967, Batesville, Arkansas.

HEALTH PHYSICS DIVISION

SEPTEMBER 1, 1968

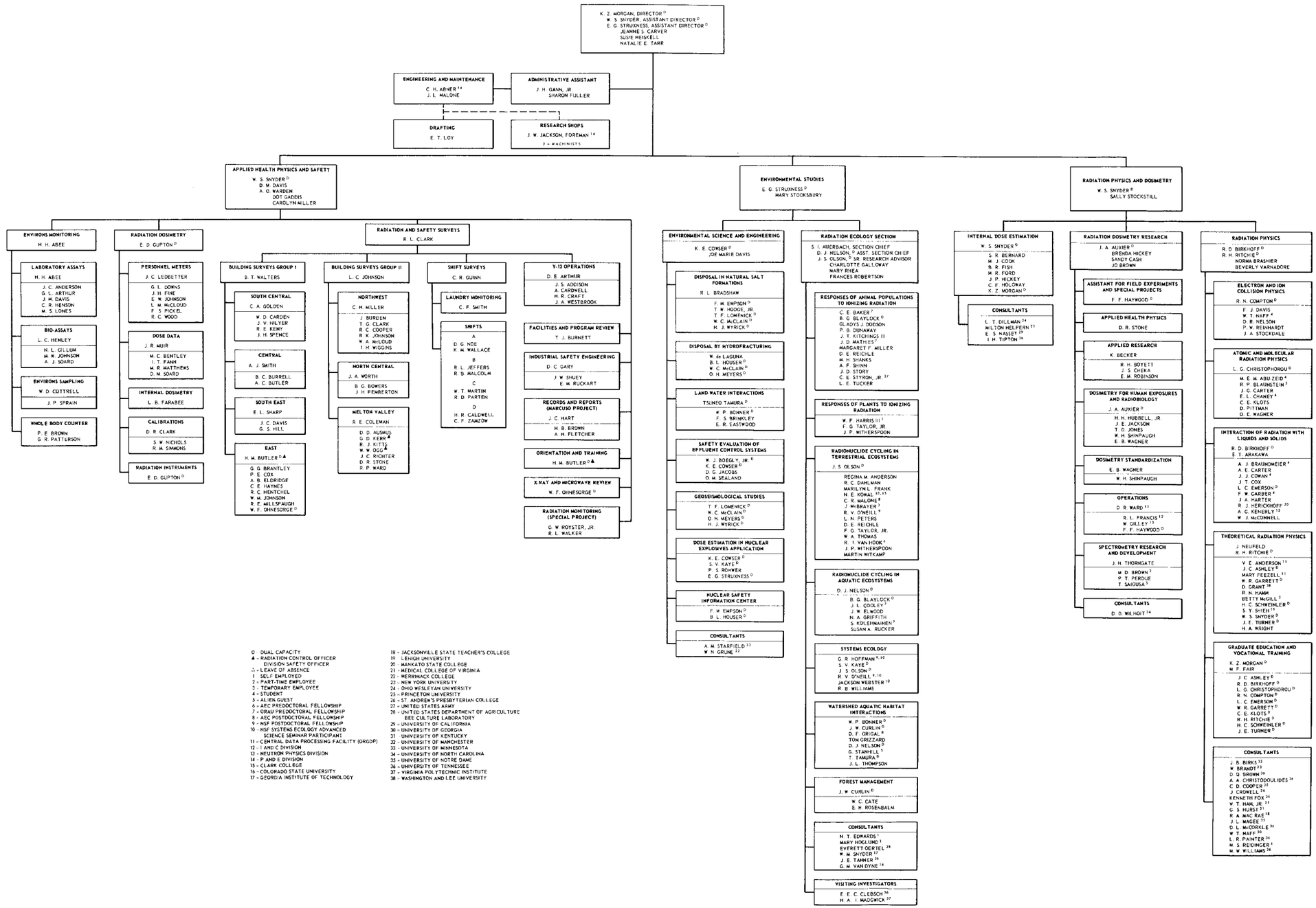

D - DUAL CAPACITY
▲ - RADIATION CONTROL OFFICER
DIVISION SAFETY OFFICER
∴ - LEAVE OF ABSENCE
1 - SELF EMPLOYED
2 - PART-TIME EMPLOYEE
3 - TEMPORARY EMPLOYEE
4 - STUDENT
5 - ALIEN GUEST
6 - AEC PREDOCTORAL FELLOWSHIP
7 - ORAU PREDOCTORAL FELLOWSHIP
8 - AEC POSTDOCTORAL FELLOWSHIP
9 - NSF POSTDOCTORAL FELLOWSHIP
10 - NSF SYSTEMS ECOLOGY ADVANCED SCIENCE SEMINAR PARTICIPANT
11 - CENTRAL DATA PROCESSING FACILITY (ORGDP)
12 - I AND C DIVISION
13 - NEUTRON PHYSICS DIVISION
14 - P AND E DIVISION
15 - CLARK COLLEGE
16 - COLORADO STATE UNIVERSITY
17 - GEORGIA INSTITUTE OF TECHNOLOGY
18 - JACKSONVILLE STATE TEACHER'S COLLEGE
19 - LEHIGH UNIVERSITY
20 - MANKATO STATE COLLEGE
21 - MEDICAL COLLEGE OF VIRGINIA
22 - MERRIMACK COLLEGE
23 - NEW YORK UNIVERSITY
24 - OHIO WESLEYAN UNIVERSITY
25 - PRINCETON UNIVERSITY
26 - ST. ANDREW'S PRESBYTERIAN COLLEGE
27 - UNITED STATES ARMY
28 - UNITED STATES DEPARTMENT OF AGRICULTURE BEE CULTURE LABORATORY
29 - UNIVERSITY OF CALIFORNIA
30 - UNIVERSITY OF GEORGIA
31 - UNIVERSITY OF KENTUCKY
32 - UNIVERSITY OF MANCHESTER
33 - UNIVERSITY OF MINNESOTA
34 - UNIVERSITY OF NORTH CAROLINA
35 - UNIVERSITY OF NOTRE DAME
36 - UNIVERSITY OF TENNESSEE
37 - VIRGINIA POLYTECHNIC INSTITUTE
38 - WASHINGTON AND LEE UNIVERSITY

ORNL-4316
UC-41–Health and Safety

INTERNAL DISTRIBUTION

1. Biology Library
2–4. Central Research Library
5. Laboratory Shift Supervisor
6–7. ORNL, Y-12 Technical Library Document Reference Section
8. MIT Practice School
9. Laboratory Records Department
10. Laboratory Records, ORNL RC
11. H. H. Abee
12. V. E. Anderson
13. E. T. Arakawa
14. J. C. Ashley
15. S. I. Auerbach
16. J. A. Auxier
17. S. E. Beall
18. K. Becker
19. S. R. Bernard
20. R. D. Birkhoff
21. R. P. Blaunstein
22. W. J. Boegly
23. W. P. Bonner
24. R. L. Bradshaw
25. P. E. Brown
26. F. R. Bruce
27. T. H. J. Burnett
28. J. G. Carter
29. J. S. Cheka
30. L. G. Christophorou
31. R. L. Clark
32. T. G. Clark
33. W. E. Cohn
34. R. N. Compton
35. M. J. Cook
36. K. E. Cowser
37. F. L. Culler
38. W. De Laguna
39. J. W. Curlin
40. D. M. Davis
41. F. J. Davis
42. P. B. Dunaway
43. L. C. Emerson
44. F. M. Empson
45. M. F. Fair
46. L. B. Farabee
47. B. R. Fish
48. M. R. Ford
49. J. A. Gabbard
50. W. R. Garrett
51. J. H. Gillette
52. E. D. Gupton
53. R. N. Hamm
54. C. S. Harrill
55. J. A. Harter
56. F. F. Haywood
57. A. Hollaender
58. L. B. Holland
59. C. F. Holoway
60. A. S. Householder
61. H. H. Hubbell
62. D. G. Jacobs
63. D. R. Johnson
64. L. C. Johnson
65. T. D. Jones
66. W. H. Jordan
67. M. A. Kastenbaum
68. S. V. Kaye
69. M. T. Kelley
70. R. F. Kimball
71. C. E. Klots
72. C. E. Larson
73. T. A. Lincoln
74. R. S. Livingston
75. T. F. Lomenick
76. H. G. MacPherson
77. F. C. Maienschein
78. W. C. McClain
79. W. J. McConnell
80. A. J. Miller
81. K. Z. Morgan
82. D. J. Nelson
83. D. R. Nelson
84. J. Neufeld
85. J. S. Olson
86–87. R. B. Parker
88. G. R. Patterson, Jr.
89. R. W. Peelle

90. J. W. Poston
91. H. P. Raaen
92. M. L. Randolph
93. D. E. Reichle
94. P. W. Reinhardt
95. R. M. Richardson
96. R. H. Ritchie
97. E. M. Robinson
98. P. S. Rohwer
99. G. W. Royster, Jr.
100. T. Saigusa
101. H. C. Schweinler
102. H. E. Seagren
103. M. J. Skinner
104. W. S. Snyder
105. J. A. Stockdale
106. E. G. Struxness
107. D. A. Sundberg
108. T. Tamura
109. E. H. Taylor
110. J. H. Thorngate
111. J. E. Turner
112. A. C. Upton
113. E. B. Wagner
114. D. R. Ward
115. A. D. Warden
116. A. M. Weinberg
117. G. C. Williams
118. J. P. Witherspoon
119. H. A. Wright
120. G. Young
121. John E. Cantlon (consultant)
122. John C. Frye (consultant)
123. Edward Gerjuoy (consultant)
124. John B. Hursh (consultant)
125. Harold O. Wyckoff (consultant)
126. J. B. Birks (consultant)
127. W. Brandt (consultant)
128. D. Q. Brown (consultant)
129. M. D. Brown (consultant)
130. J. F. Burns (consultant)
131. Thomas Callcott (consultant)
132. L. W. Cochran (consultant)
133. C. D. Cooper (consultant)
134. J. Crowell (consultant)
135. M. S. Cyrus (consultant)
136. Jack Dodd (consultant)
137. Charles Eisenhauer (consultant)
138. Ugo Fano (consultant)
139. R. E. Glick (consultant)
140. W. T. Ham, Jr. (consultant)
141. G. S. Hurst (consultant)
142. R. J. Lovell (consultant)
143. R. A. Mac Rae (consultant)
144. D. L. McCorkle (consultant)
145. Linda R. Painter (consultant)
146. J. E. Parks (consultant)
147. T. D. Strickler (consultant)
148. G. E. Thoma (consultant)
149. I. H. Tipton (consultant)
150. G. M. Van Dyne (consultant)
151. Neil Wald (consultant)
152. Donald G. Willhott (consultant)
153. M. R. Williams (consultant)

EXTERNAL DISTRIBUTION

154–323. Given external distribution
324. Radiation Physics Division, Health and Safety Laboratory, New York Operations, U.S. Atomic Energy Commission, New York, New York 10014
325. Physics Library, Vanderbilt University, Nashville, Tennessee 37203
326. Library, Room 8236, Public Service Electric and Gas Company, 80 Park Place, Newark, New Jersey 07101
327. W. W. Grigorieff, Assistant to the Executive Director, Oak Ridge Associated Universities
328. J. A. Swartout, Union Carbide Corporation, New York
329. Laboratory and University Division, AEC, ORO
330–619. Given distribution as shown in TID-4500 under Health and Safety category (25 copies – CFSTI)